The Relationship Between Extension and Magmatism in the North Sea Basin

by

David Michael Latin

Thesis submitted for the degree of

Doctor of Philosophy

University of Edinburgh

August 1990

DECLARATION

This thesis has been composed solely by myself. The work presented is my own unless otherwise acknowledged.

David Michael Latin

ABSTRACT

Recent parameterisations of melting experiments may be used to predict the volume and composition of magma generated by melting anhydrous peridotite during adiabatic decompression of the asthenosphere (McKenzie & Bickle 1988). Here they are used to predict the character of magmas generated during adiabatic upwelling which accompanies the formation of sedimentary basins. The objective of this thesis is to test the model predictions with observations from the Mesozoic North Sea Basin.

At ocean ridges the degree to which the asthenosphere melts is principally governed by its potential temperature (T_p) and the entropy change on melting (ΔS). The amount of melt produced and its average composition are controlled by the average extent and average depth of melting. The model predicts that in order to generate the normal 7 km of oceanic crust at a mid-ocean ridge, the "normal" T_p of the asthenosphere must be 1280±40°C; the error results from uncertainty in ΔS. Predicted average melt compositions agree favourably with compositions of primitive MORB (mid-ocean ridge basalt). Some ridge segments are located above anomalously hot "plumes" in the mantle. The greater thicknesses and distinctive compositions of the crust in such regions (e.g. Iceland) are consistent with model predictions for T_p's 100 to 300°C greater than normal.

The generation of melt from dry peridotite during rifting of the lithosphere depends critically on the T_p of the asthenosphere, the amount (β) and rate (ε) of lithospheric thinning, and the initial shape of the geotherm; i.e. the thickness of the mechanical boundary layer (MBL) prior to extension. In most extensional basins the steady state MBL is ~100 km thick. The maximum amount of lithospheric thinning which occurs during extension depends on the partitioning of strain between the crust (β_c) and mantle (β_m) and on whether extension is accommodated by pure shear or simple shear. At normal T_p's the amount and average composition of the melt produced during rifting is simply related to the size of the average melt fraction and the average pressure of melting. When a plume accompanies rifting, regional doming over an area 1000 to 2000 km in diameter is expected. High temperatures and rates of plume-flow may lead to the production of large volumes of alkaline magma when there is little or no stretching and flood tholeiites when β is large.

The most important episode of extension in the North Sea took place from the Middle Jurassic (180-170 Ma) to the Early Cretaceous (120-100 Ma) and resulted in the development of a trilete rift system. Associated magmatic activity occurred shortly after the onset of rifting (ca. 160-150 Ma) and was located principally in the triple-junction area, where an average thickness of 0.5-1.5 km of subaerially erupted alkali basalt comprise the Forties volcanic province. More minor volumes of nephelinites, basanites and ultrapotassic rocks, are observed on the western edge of the Egersund Basin, on the flanks of the Central Graben and in the Netherlands sector of the North Sea. Dates generated by $^{40}Ar/^{39}Ar$ stepwise degassing of the freshest samples suggest that the igneous activity is contemporaneous throughout the region; i.e. there is no migration of magmatism with time.

The North Sea rocks are variably altered and range from mildly to highly alkaline in character. The Forties basalts are chemically similar to OIB (ocean island basalt), but the ultrapotassic rocks found elsewhere in the North Sea have no oceanic equivalents. All of the North Sea rocks lie between MORB and bulk earth in terms of $^{143}Nd/^{144}Nd$ (0.51265-0.51285) and $^{87}Sr/^{86}Sr$ (0.703-0.704). Simple single stage melting calculations suggest that if the source of the Forties parental magmas was a garnet peridotite with a composition between that of bulk earth and the inferred source of MORB, then they were produced by very small amounts of melting (<3%). The extreme fractionation of LILE (large ion lithophile elements) and light REE (rare earth elements) from heavy REE seen in the magmas from other parts of the North Sea is difficult to explain by single-stage melting unless the source is more enriched in LILE and light REE than bulk earth.

The stretching factor (β) in the triple junction region is estimated from thermal subsidence and gravity data to be between 2 and 3; larger than elsewhere in the North Sea. Many of the subsidence curves are abnormal in that they show condensed, or non-existent, syn-rift subsidence, and very rapid thermal subsidence. These effects are not considered to be due to fault block rotations and do not affect the estimates of β. They may be explained by decoupling of the strain rates in the crust and mantle which results in extreme but localised thinning of the mantle at the start of rifting ($\beta_m >> \beta_c$) but, importantly, allows the lithospheric section to be balanced at all times.

The stratigraphy and the absence of a hot-spot trail during the Mesozoic is inconsistent with a plume-model for rifting. There was, however, localised uplift along the rift flanks and in the triple junction, which can be explained by the "decoupled" stretching mechanism. The simplest model for the Forties basalts involves stretching by a factor of between 2 and 3 of a MBL 90 km thick over asthenosphere with a T_p of 1280 to 1320°C. The predicted volume and composition of melt are largely consistent with these observations. A full explanation of the Forties magma compositions does, however, require an input from mantle that is enriched in incompatible elements and volatiles relative to bulk earth. This component in the Forties magmas was probably produced in a metasomatised layer at the base of the MBL. Volatile-controlled melting in the MBL was probably also responsible for the ultra alkaline rocks found in less-stretched regions of the North Sea.

ACKNOWLEDGEMENTS

I would like to thank my supervisors, John Dixon, Godfrey Fitton, and Dan McKenzie, for their interest and enthusiastic help over the last three, often frantic, years! John is thanked for continually calling my attention to the importance of detail but also for his considerable encouragement while I bullishly pursued the "big picture". Dan, who generated much of the "big picture", is also thanked for his perpetual and incredible optimism. He also provided much inspiration together with the meat and bones of many of the Fortran programs used in this thesis! I thank Godfrey for the science, the squash, the "Laughing Duck", and the beer. He also taught me to be concise! Nicky White, in many ways an unofficial fourth supervisor, is thanked for his exhaustive and very rapid proof-reading, for introducing me to the value of simplicity, β's and Beamish, *for hating footnotes and italics* and for being a good friend!

Paul Beattie was a constant source of good humour and scientific advice. Hugh Nicholson endured many of my half-cocked notions and proof-read several papers and chapters. Mike Matthews helped massively with the Fortran. Dodie James spent time introducing me to EMAS and, with Godfrey, helped me with XRF analyses throughout. Pete Hill and Stuart Kearns were always obliging when I used the electron microprobe and, more importantly, mended it every time I broke it! Nick Walsh and everyone in the chemistry lab of the Department of Geology at RHBNC were a great help. Pat Condon kindly allowed me to use his basin modelling programs. Jon Bull and Barry Heptonstall humoured me as I chased plumes under plates and showed me how to use the SUPERMAP program.

The work presented within has also benefited greatly from informal discussions with many other people, most notably Ian Bartholemew, Melvin Giles, Ben Harte, Tony Hayward, Richard Hunter, Simon Klemperer, Nick Kusznir, Alastair Robertson, Graham Ritchie, Roger Scrutton, T.O. Spring, Jon Turner, Mike Warner, Fran Waters, Sarah Watson, Bob White, Brian Upton, and Peter Ziegler with his interminable "dome"!

It is impossible to thank all of the people who have made my time in Edinburgh so enjoyable. I will long remember the heat and stench of the *Rat House* (viz. the gonad), and its internees with whom I almost shared an office! - Bjorn, Hugh, Martin, Mike & Sue. The nights on the town in Edinburgh with "batty" Steve Batty (sorry about the bureau Steve!), Chris Clark, Pete Clift, Ian Fitzsimons, Greg "the Greek" Jones, Richard Hillis, Stuart Kearns, Claire Linklater, Neil Pickard and

loads of others, are not so easily recalled (particularly the one with Bob Hunter!) but were thoroughly enjoyed.

NERC are thanked for funding the last three years in Edinburgh and for benevolently helping with jollies to the Netherlands, Germany, Greece and Turkey. Shell Expro, who provided funds for radiometric dating and for gathering data for backstripping, are thanked for their generosity and interest from the start. Ian Bartholemew, Melvin Giles (and all in UEX 33) and Larry Wakefield were a great help. The work in this thesis would not have been possible if it were not for the help, in terms of provision of data and discussion of ideas, of a number of other companies and individuals to whom I am indebted:- Amerada Hess (R. Hardman, S. Boldy); Amoco (I.D.W. Jones); Britoil; B.P. (A. Fraser, A. Hayward, & S. Rainey); Chevron (K.J. Reed); Elf; Esso (Norway); N.A.M (D. van der Baan, F. Uliczny, M. Doyle), Petroland (A.B. van der Poel), Phillips (N. Fuller); Premier (J. Davies, J.C. Parmenter); Ranger (A.D. Steele); Shell U.K. (M.R. Giles and L.L. Wakefield); Texaco (B. Rall); Total (A. Seigneurin and J. Ritchie).

Last, but far from least, I thank Judy for proof-reading this thesis in its entirety, typing tables, numbering pages (a tedious task!) and for keeping me sane (?) during its final stages. My mother, father, family and friends in Cambridge and Edinburgh have been a continual source of support. Without them none of this would have been possible.

CONTENTS

CHAPTER 1

INTRODUCTION

1.1 Background.

Basaltic magmatism is commonly observed to accompany the development of continental rifts and extensional sedimentary basins. This thesis is concerned with establishing quantitative relationships between processes operating during rifting of the continental lithosphere and the nature and location of associated magmatic activity.

Since 1978, when McKenzie proposed the uniform stretching model there has been a gradual development and consolidation of the theoretical framework which governs the formation of extensional sedimentary basins. The general consensus appears to be that, in many instances, basin morphology, heat flow and subsidence history may all be adequately explained by some quantifiable amount of lithospheric thinning[1] during rifting which is accompanied by passive upwelling of the asthenosphere from below. Although it was realised that magma generation would have important consequences for models of basin evolution (e.g. Le Pichon and Sibuet, 1981) only relatively recently has a rigorous attempt been made to incorporate magmatism into the quantitative framework.

It has long been believed that large quantities of melt are generated at mid-ocean ridges as a response to the pressure drop as the asthenosphere upwells adiabatically (e.g. Verhoogen, 1954; Green and Ringwood 1967) but the link between continental rift magmatism and magmatism at the oceanic ridges, via the adiabatically upwelling asthenosphere, has only recently been exploited. Much of the early work on rift-related magmatic activity was observational and concentrated on the East African rift system. Importantly, a number of authors (e.g. Baker *et al.*, 1978; Baker, 1987) noted the tendency for increasing silica undersaturation in rift magmas to be associated with distance away from the rift axis, and for an overall decrease in silica undersaturation to occur with time within the system.

In 1981, Dixon *et al.* made one of the first steps towards a quantitative understanding of rift magmatism. Using the concepts of lithospheric thinning and

[1] The amount of lithospheric thinning is commonly described by a factor, β which is equal to the ratio of the unstretched thickness to the stretched thickness.

adiabatic decompression of the asthenosphere (McKenzie, 1978), they suggested that the shape of the region of upwelling and the amount of adiabatic decompression would exert an important control on both the location and the composition of rift magmas. Experimental work concerning the effects of pressure on the composition of basaltic melts (Yoder, 1976) enabled Dixon *et al.* (1981) to hypothesise a relationship between the amount of thinning of the lithosphere and the composition of the resulting magmas. They suggested that areas where the amount of thinning is large should be regions where the pressure of melting is relatively low and would be characterised by relatively less silica undersaturated magmas. They noted that this qualitative relationship between degree of thinning, depth of melting, and silica saturation of the melt appeared to broadly satisfy the on-axis, off-axis and time-dependent compositional relationships observed in East Africa and the North Sea.

The first quantitative breakthrough came when Foucher *et al.* (1982) applied a simple analytical expression for the extent of melting of the mantle during decompression to the production of melt during thinning of the lithosphere. The expression used was that of Ahern and Turcotte (1979) which was based on experimental data for the melting of peridotite containing 0.01% water (Ringwood 1975). Foucher *et al.* (1982) showed that as the amount of thinning (β) increases beyond some critical value, when the solidus (melting point) is attained, the amount of melt generated will increase until the lithosphere has been thinned to zero when oceanic crust is produced. They also showed that the amount of adiabatic upwelling required for the onset of melting and the amount of melt produced would have a critical dependence on the temperature of the asthenosphere before it starts to upwell. McKenzie (1984) and Furlong and Fountain (1986) independently reached very similar conclusions.

None of these more quantitative models predicted the composition of the magmas produced and all used rather simplified expressions for the position of the solidus and for the degree of melting as a function of solidus overstep. James (1987) attempted to relate the concentrations of trace elements in rift magmas to variable amounts of thinning using a similar expression for the degree of melting. However, there are a number of serious difficulties involved when trying to use trace element concentrations to make quantitative statements about extents of melting; these were overlooked. Nor was James (1987) able to satisfactorily test his model with observations; probably for the reason that there are very few rifts in which the stretching history is sufficiently well known for such tests to be possible.

More recently, McKenzie and Bickle (1988) used a comprehensive review of experimental observations on the melting of garnet peridotite, which constrain the

temperature of the solidus, the liquidus and various intermediate melt fractions at different pressures, to obtain a simple empirical function which relates the extent of melting to the degree of adiabatic decompression of asthenosphere of a given temperature. In addition, they produced a parameterisation of the compositions of melts produced in the experiments which allowed them to predict the major-element composition as well as the amount of melt generated on decompression. Their model, when tested with observations from the oceans provides a physically reasonable explanation for the formation and composition of mid-ocean ridge basalt (MORB). The implication is that in areas where thinning of the lithosphere is not infinite, in basins and rifts, the model might also be able to relate the observed volumes and major-element compositions of magmas to the amount of stretching. This is the rationale for the present study.

1.2 Aims and Organisation.

The principal purpose of this thesis is therefore to present and test a quantitative theoretical framework, founded on the work of McKenzie and Bickle (1988), for the production of magma during rifting of the continental lithosphere. The theory is best constrained by observations from a rift system where the stretching history is both simple and well known. The Mesozoic North Sea basin appears to fit these requirements well. The vast amount of geophysical and geological data collected by the oil industry over the last 25 years of exploration in the North Sea has already allowed the application and evaluation of a number of models for basin formation (without attention to magmatism). Estimates for the amount of lithospheric attenuation have been derived from gravity, seismic refraction and deep seismic reflection studies as well as from the subsidence history of the basin and fault block restorations. Fortunately a number of exploration wells have also penetrated and cored igneous sequences within the basin.

In Chapters 2 and 3 the general theoretical framework is developed with little reference to the North Sea. Chapter 2 is concerned with decompression melting of asthenosphere. Mid-ocean ridges provide the best opportunity to study decompression of the asthenosphere because there are no lithospheric complications. The importance of asthenospheric temperature, composition and melting behaviour are discussed in some detail. Chapter 3 is devoted to the lithosphere; how it is defined and how it responds to extensional stresses. The thermal consequences of different stretching models are emphasised. Parameterisations of experimental data described

in Chapter 2 are then used to predict the volumes and compositions of melt produced from anhydrous peridotite during rifting over asthenosphere of normal and elevated temperature. The importance of parameters such as the initial thickness of the conductive portion of the lithosphere, and the rate at which lithospheric thinning takes place, is stressed.

The North Sea basin is introduced in Chapter 4 which sets out the locations, ages, approximate volumes and petrographic characteristics of four Mesozoic igneous provinces. The largest thicknesses of basaltic magma were erupted during the Middle Jurassic in a triple junction where the three major rift arms meet. In other parts of the rift system and in adjoining sub-basins small volumes of extrusive and intrusive rocks are found. In Chapter 5 the major- and trace-element characteristics of the variably altered basaltic rocks from the four igneous provinces are described. Their undersaturated and often volatile- and incompatible element rich character is emphasised. Many of the North Sea basalts, particularly those in the Forties province, are shown to be chemically and isotopically indistinguishable from ocean island basalts. The ultrapotassic character of some of the North Sea rocks, however, has no oceanic equivalent. Simple melting calculations, based on ratios of immobile and incompatible trace elements, are used to suggest that the basalts of the Forties province were produced by larger degrees of melting of garnet peridotite than is the case for any of the other Mesozoic basaltic rocks. This is consistent with their relatively large volume. The ultrapotassic rocks may, however, have been produced by still larger degrees of melting but of restricted volumes of volatile-rich, phlogopite- or amphibole-bearing, peridotite which may be probably located in the mechanical boundary layer of the lithosphere.

In Chapter 6 the degree of lithospheric attenuation which was attained in different parts of the North Sea, as a result of rifting during the Mesozoic, is estimated from an analysis of subsidence data. The discussion centres on the triple junction region since this is the most magmatically active area. The subsidence curves in this region are abnormal in that the syn-rift stage of subsidence is commonly condensed or absent while the rate and thickness of post-rift subsidence is dramatic. The cause of the abnormal curves is probably not a local tectonic one and existing stretching models are unable to explain the shapes of the curves. It is, however, shown that existing models do provide reasonable estimates for the total amount of thinning. Estimates of β from the subsidence data agree well with the degrees of crustal thinning inferred from regional seismic lines and by modelling the regional gravity field. The amount of lithospheric thinning was larger in the triple junction region than it is elsewhere in the North Sea.

Theory and observation are brought together in Chapter 7. It is shown that when reasonable values are used for the temperature of the asthenosphere, the amount and rate of stretching and the thickness of the conductive lithosphere prior to rifting, then theoretical predictions are broadly consistent with the inferred thickness and observed composition of the basaltic magmas in the most stretched part of the North Sea. The presence of more undersaturated, and sometimes ultrapotassic magmas, in other less extended parts of the North Sea is not predicted by the theory. These magmas, together with a component of the melt in the most stretched region, are probably the result of melting peridotite containing volatile-bearing phases.

CHAPTER 2

MELTING ASTHENOSPHERE

AT MID-OCEAN RIDGES

2.1 Introduction.

It is generally agreed that the generation of basaltic magmas at oceanic spreading centres occurs in response to the upwelling of asthenospheric mantle which partially melts due to adiabatic decompression. Ocean ridges provide the best opportunity to observe the results of asthenospheric melting because the melting process is not complicated by the presence of heterogeneous lithosphere. In this chapter literature concerning the melting characteristics of the asthenosphere is reviewed in an attempt to define those parameters which are fundamental in controlling the volume and composition of magma produced during adiabatic decompression. A simple quantitative model for the generation of MORB (McKenzie and Bickle, 1988) is then discussed with emphasis on its application. Other models for MORB genesis are briefly reviewed and areas of disagreement are highlighted.

2.2 Upwelling of Asthenosphere at Ridges.

Upwelling of the asthenosphere beneath mid ocean ridges is regarded as a "*passive*" process (see Figure 2.1) but this view is a relatively recent one (e.g. McKenzie and Sclater, 1973; Carmichael *et al.*, 1974). Much of the early work on sea floor spreading considered that there was a close link between the convective geometry of the asthenosphere and movement of the lithospheric plates (e.g. Hess, 1962). As such, ridges were often thought of as "*active*" features sited above the rising limbs of convection cells (Oxburgh and Turcotte, 1968; Oxburgh, 1980; see section 2.7). However, as Carmichael *et al.* (1974) and McKenzie and Bickle (1988) point out, if spreading at ocean ridges is linked to convection in this manner then there are a number of conceptual difficulties, not least in understanding how the convective system could be tied to ridges when ridges can clearly be offset by

transform faults and when they also commonly migrate and jump. Ridges are more easily explained if they are simply the result of upwelling asthenosphere in a *passive* response to plate separation. It is certainly true that in some instances ocean ridges may coincide with active upwelling of the asthenosphere (e.g. Iceland; Schilling *et al.*, 1983; R. White and McKenzie, 1989), but this does not appear to be a prerequisite either to form or to sustain spreading at a ridge. As is discussed in Chapters 3 and 7 many continental rifts do not appear to require an active convection driven component to explain their formation either.

If the response of the asthenosphere is merely passive then, as Figure 2.1 shows, the velocity at which the asthenosphere upwells directly below the ridge must be related to the horizontal plate velocity (spreading rate). Within the asthenosphere the temperature structure will be governed by convective heat transfer and will therefore be, on average, *adiabatic*. If the upward velocity of asthenosphere beneath the ridge is sufficiently fast that no heat is dissipated by conduction during upwelling, the asthenosphere will retain its adiabatic geotherm. The adiabatic temperature gradient of solid mantle is approximately 0.6°C/km (McKenzie, 1984). In general, the molar volumes and entropies of liquids are greater than those of solids and therefore melting temperatures increase with increasing pressure. As is discussed in the next section experimental data suggests that for asthenospheric mantle the gradient of this solidus will typically be greater than the adiabatic gradient. "*This observation has led to the hypothesis that melting and magma formation are caused by relief of pressure*" (Carmichael *et al.*, 1974) - see Figure 2.2.

Conservation of mass requires that all of the asthenosphere upwelled into the space beneath a ridge created by passive spreading will be converted into oceanic lithosphere upon cooling. Any melt produced during decompression will migrate upwards to form the oceanic crust. Note that again for reasons of mass conservation, the thickness of oceanic crust (melt) produced will be independent of plate velocity so long as this is rapid enough for heat loss by conduction to be ignored. This notion is supported by the observation that, despite differences in ridge topography, the relatively fast spreading East Pacific Rise has essentially the same thickness of crust as the more slowly spreading Mid Atlantic Ridge (Tréhu *et al.*, 1976). With the exception of Iceland, both ridges produce between 5 and 7 km of crust/melt.

A simple steady-state model for upwelling and melting at a ridge can therefore be envisaged in which a column of asthenosphere with some initial adiabatic (convective) geotherm is instantaneously allowed to rise to the surface, the melt produced by decompression is extracted to form the oceanic crust, and the residue produces the mantle lithosphere (see Figure 2.2 and section 2.4). The

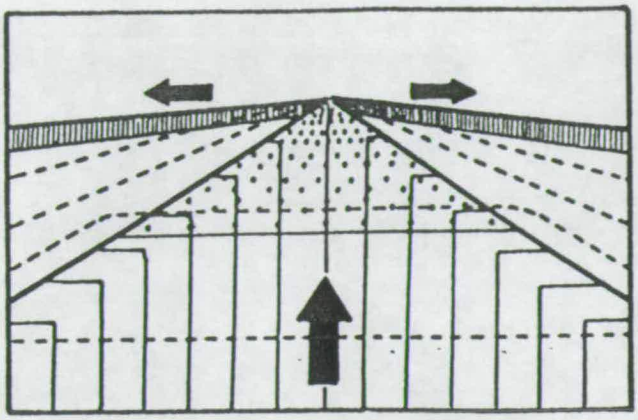

FIGURE 2.1 The formation of oceanic lithosphere by passive upwelling of asthenosphere. Dotted region, bounded at base by horizontal line, is the zone of extensive silicate melting above the dry solidus. Dashed lines are sketched isotherms for, from the base upwards, 1350°C, 1300°C, 1250°C and 1200°C. Vertical lines indicate stream lines within asthenosphere, corner flow exaggerated. Shaded area = ocean crust. The vertical flux of asthenosphere (large arrow) is related to the horizontal plate separation velocity (small arrows). The horizontal width of the diagram is ~300 Km and the vertical dimension is ~150 Km.

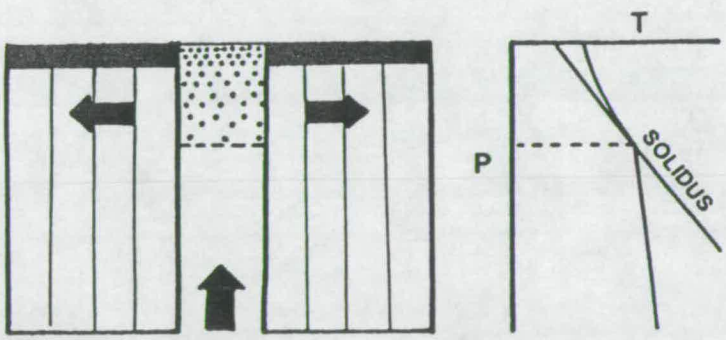

FIGURE 2.2 A simple model for the formation of crust and mantle lithosphere at an ocean ridge. The central part of the left hand diagram represents instantaneously upwelled asthenosphere which undergoes decompression melting above the dry solidus (dotted region). The melt is then extracted to form the crust (black) and mantle lithosphere on either side of the ridge. The right hand diagram shows a sketch of the temperature gradient in the upwelled asthenosphere. Below the dry solidus the gradient is adiabatic. In the melting region the gradient is governed by the entropy change on melting (see McKenzie 1984, Appendix D).

material is split as the plates separate and a new column instantaneously fills the space. To understand the factors which control the amount of melt produced and its composition evidence from melting experiments must be considered (section 2.3) together with the importance of the geometry of the melting regime in the upwelling region (sections 2.4 and 2.5).

2.3 Melting Experiments and the Melting Regime.

2.3.1 Mantle Mineralogy.

The inferred mineralogical composition of the asthenosphere, and indeed of mantle rocks in general, is that of lherzolite. The evidence for a lherzolite mineralogy comes largely from the study of carbonaceous chondrites, deep seated xenoliths found in alkali basalts and kimberlites, and ophiolite suites. A lherzolite composition is also compatible with geophysical observations, such as seismic wave velocities and mantle density, and with the parent-daughter melting constraints for basalts provided by experimental petrology (Yoder, 1976). High temperature-pressure studies of bulk lherzolite compositions suggest that the subsolidus mineral assemblage will progressively change from plagioclase to spinel and to garnet lherzolite with increasing pressure. In the CMAS (i.e. $CaO+MgO+Al_2O_3+SiO_2$) system garnet lherzolite converts to spinel lherzolite at ~2.2 GPa and 1200°C (MacGregor, 1965) via the reaction Py+Fo=En+Sp. The presence of Cr in mantle lherzolite has the effect of enlarging the stability field for spinel at the expense of garnet so that the garnet-spinel transition may occur at the slightly greater pressure of 2.5 GPa (Nickel, 1986; Kostopoulos, in press). Spinel lherzolite, in turn, converts to plagioclase lherzolite at ~0.85 GPa and 1200°C (Kushiro and Yoder, 1966) via the reaction En+Sp+Di=Fo+An. The relationship between depth (D km) and pressure (P GPa) is given by

E:2.1 $$D = P/(g\rho_m \times 10^{-6})$$

where g is acceleration due to gravity (~9.81 ms^{-2}) and ρ_m is the mantle density (~3.3×10^3 kg m^{-3}). The phase transition therefore occurs at ~75 km for garnet-spinel and at ~25 km for spinel-plagioclase. The basic 4-phase lherzolite assemblage is usually assumed to be dry in the asthenosphere.

2.3.2 Experiments and the Extent of Melting.

The relative simplicity of the ocean ridge system described above has made the understanding of mid ocean ridge basalt (MORB) petrogenesis one of the primary targets for experimental petrologists over the last 20 years. A large number of careful *equilibrium batch-melting* experiments on *dry* (volatile-free) lherzolite compositions (e.g. Ito and Kennedy, 1967; Green and Ringwood, 1967; Ringwood, 1975; Mysen and Kushiro, 1977; Stolper, 1980; Harrison, 1981; Takahashi and Kushiro, 1983; Takahashi 1986) provide invaluable constraints on the conditions necessary to cause partial melting of the asthenosphere. Many of the experiments also provide data to constrain the variation of melt fraction (X, the weight fraction of rock which melts) and melt composition (see section 2.3.6) as functions of the intensive variables, temperature (T) and pressure (P). A number of experiments have also been conducted to determine the melting behaviour of lherzolite in the presence of volatile components; these are considered in a later section because MORBs, and by inference the asthenospheric mantle (the source of MORB), appears to be effectively dry.

All of the dry batch-melting experiments show three main features:

(a) The temperature of the solidus (T_s) and liquidus (T_l) increase with increasing pressure; i.e. the Clapeyron slope (dP/dT) is positive.

(b) At a given P as the T is raised above T_s, X increases.

(c) The composition of the melt varies as a function of both X and P.

2.3.3 Quantification of Extent of Melting.

The first attempt to use such experiments to quantify the melting process beneath ridges was made by Ahern and Turcotte (1979) who derived a simple analytical expression for the variation of X with T and P to fit the experimental data of Ringwood (1975) for a garnet peridotite containing 0.1% water. In their study Ahern and Turcotte (1979) concluded that in order to produce 6 km of oceanic crust the asthenosphere must be partially molten to a depth of at least 70 km beneath the ridge and that the maximum value for X would be 0.25.

McKenzie (1984) derived a similar expression for the melting process using the experiments of Mysen and Kushiro (1977) and Takahashi and Kushiro (1983). McKenzie (1984) pointed out that, since there is no evidence for a direct link between spreading and asthenospheric convection, the adiabatically upwelling asthenosphere should have a temperature equal to the *mean temperature* of the asthenosphere and

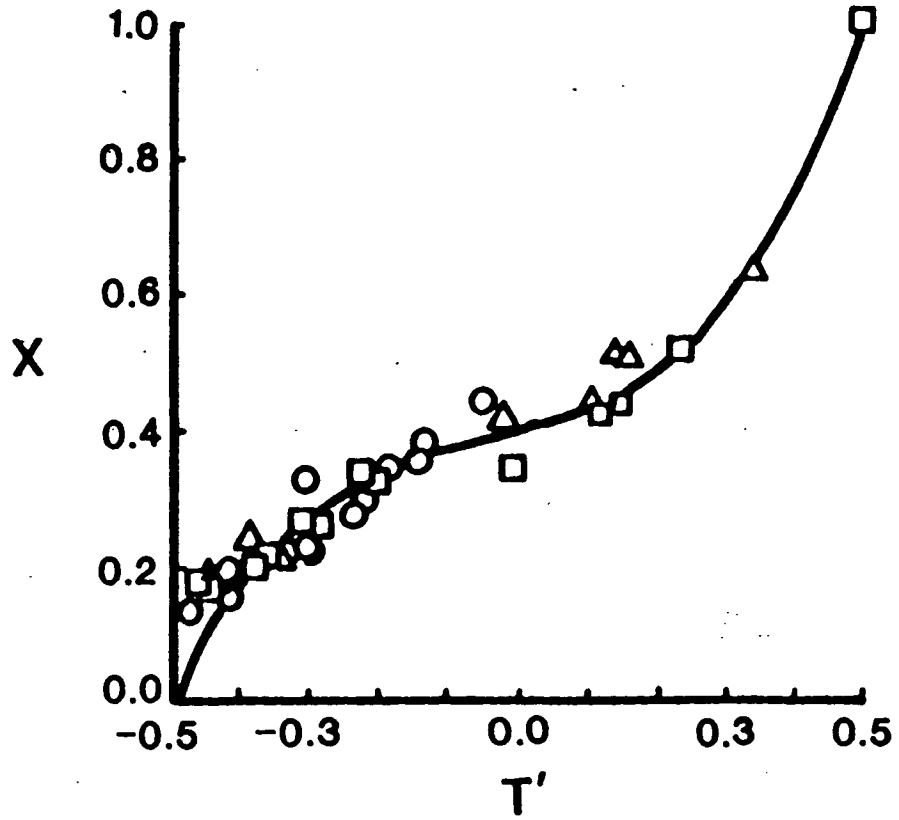

FIGURE 2.3 From McKenzie and Bickle (1988). Melt fractions produced from garnet peridotite plotted as a function of T' where

$$T' = \frac{(T-(T_l+T_s)/2)}{T_l-T_s}$$

where T_l and T_s are liquidus and solidus temperatures. Squares indicate points where P lies between 0 and 0.5 GPa; Circles 0.5<P<1.5 GPa; Triangles 1.5<P GPa. Data points are from Bickle *et al.* (1977), Arndt (1977), Bickle (1978), Green *et al.* (1979), Stolper (1980), and Jaques and Green (1980). The curve was obtained by minimising $|X_{calc}-X_{obs}|$ and calculated using the equations and coefficients given in Appendix A of McKenzie and Bickle (1988)

should be capable of producing 6-7 km of oceanic crust. This mean temperature would represent the temperature of the asthensophere in areas distant from hot upwelling limbs (plumes) or cold downgoing limbs within a large scale convective system (see section 2.7). McKenzie therefore proposed a mean temperature for the asthenosphere of 1350°C at a pressure of 2 GPa which would be capable of producing 6-7 km of melt. He also noted that on upwelling to the surface, asthenosphere with a higher than average temperature would cause melting to start at greater depths, would produce greater maximum values of X, and would result in larger volumes of melt.

Furlong and Fountain (1986) who used the experiments of Mysen and Kushiro (1977) and Jaques and Green (1980) reached very similar conclusions to those of McKenzie (1984).

More recently, using data from a much larger number of experiments on dry garnet peridotite, McKenzie and Bickle (1988) formulated a simple equation for X as a function of the degree of solidus overstep at a given pressure. First of all they obtained expressions for the variation of temperatures T_S and T_l with P. These expressions reproduced the experimental data to within estimates of the likely experimental error; i.e. to within 6°C of the solidus determinations and to within 7°C of the liquidus determinations. The variation of X between the solidus (X=0) and the liquidus (X=1) was then found as a function of a dimensionless temperature parameter T' which expresses temperature as a function of the degree of solidus overstep (for details see Figure 2.3, and McKenzie and Bickle, 1988). Thus at the solidus (when X=0) T'=-0.5 and at the liquidus (X=1) T'=+0.5 (see Figure 2.3). This simple expression allows determination of X for any value of T and P and hence, on integration, the total amount of melt produced on upwelling (Figure 2.4).

2.3.4 Problems in Using Experiments to Quantify Extent of Melting.

Two types of problems are encountered when trying to use the results of experiments to model the real world. First there are problems arising from the practical limitations of experimental techniques. Secondly there is the problem of determining how closely experiments, conducted in closed systems, reproduce real conditions. For example, can the results of batch melting experiments be applied with any accuracy to situations where the real process is not one of batch melting? This second type of problem is dealt with in sections 2.3.8 and 2.4 and concerns the modelling of processes. The first type of problem is discussed below.

While the experiments used by McKenzie and Bickle (1988) yielded a good agreement for the values of T_s and T_l at different pressures there is a significant lack of experimental data for values of X between 0 and 0.14. This paucity of data for low melt fractions results from the problems involved in the identification and modal measurement of experimental run products when X is small and the melt is largely drawn out as a fine film along grain edges or is lodged within interstices. Even in runs where X is as large as 0.4 the determination of X by point-counting the run products can lead to errors as large as 0.02 (Jaques and Green, 1980). Calculation of X by mass balance of oxides using simultaneous equations may be an even less accurate method for small values of X because it relies heavily on the melt composition which may be greatly modified by quenching when the amount of melt present is small (see section 2.3.8). Quench problems may be overcome when melt inclusions are analysed (N. Odling, pers. comm. 1990). X has also been determined by beta-track counting of samples containing highly incompatible ^{14}C spiked CO_2 (Mysen and Kushiro, 1977). However, the spiked CO_2 method is hampered by CO_2 dissolution at small amounts of melting when, even in "dry" lherzolite, a small amount of H_2O may be present as a volatile phase. In general, relative errors in the determination of a value for X get larger as X gets smaller.

The solidus position (T_s) is usually determined using the "bracketing method" in which the experimental charge is brought up to, and then quenched from, different temperatures at a fixed P. T_s is inferred to lie between runs where no melt is visible and those in which melt first appears. This method of solidus identification is reliable so long as the peridotite is only a 4 phase lherzolite which melts in a *eutectic* (invariant) manner and melt can be observed before one of the 4 phases has been melted out. If melting is not truly eutectic or if easily melted minor phases are present in the peridotite then the experimentally determined solidus will only represent the point at which melt can first be observed; this could conceivably correspond to a value of X=0.1 rather than 0 (Latin *et al.*, 1990a).

Despite this lack of data for low melt fractions the parameterisation of McKenzie and Bickle (1988) yielded a relationship between T' and X (Figure 2.3) within the X=0 to X=0.14 interval. Although the relationship shown in Figure 2.3 is not eutectic for this interval of X, it does show that in reality melting can only continue beyond the solidus if there is some input of heat (~T'). In experiments the melt fraction can jump almost instantly from 0 to 0.14 because the charge is held at constant temperature. In reality the asthenosphere must be decompressed further or have its temperature raised to get any increase in melt fraction, eutectic or otherwise.

2.3.5 Extent of Melting and Potential Temperature.

The temperature of the upwelling asthenosphere determines the pressure of solidus intersection. It is useful to discuss temperature in terms of potential temperature (T_p) because the temperature of the convecting asthenosphere is depth dependent (McKenzie, 1970; Furlong and Fountain, 1986; McKenzie and Bickle, 1988). The T_p of the asthenosphere is simply defined as the temperature it would have if it was allowed to rise adiabatically to the surface without undergoing melting; i.e. its solid adiabatic temperature at 1 atm. For any temperature (T°C) at any depth (z metres) the corresponding value of T_p is given by

E:2.2 $$T_p = T\exp((-g\alpha z)/C_p)$$

where g is acceleration due to gravity (~9.81 ms^{-2}), α is the thermal expansion coefficient for the mantle (~$4x10^{-5}$ K^{-1}) and C_p is specific heat (~$1.2x10^3$ J kg^{-1} K^{-1}). Adiabatic upwelling leaves T_p unchanged.

Figure 2.4 shows how the T_p of the asthenosphere beneath the ridge is critically important in determining the depth at which melting starts, the maximum melt fraction produced, and the corresponding thickness of oceanic crust generated. One conclusion reached by McKenzie and Bickle (1988) was that in order to produce 6-7 km of melt (the average crustal thickness) the asthenosphere should have a mean T_p of 1280°C. The average melt fraction (i.e. X integrated over depth) is 0.135 and the temperature of the erupted basalt is close to 1200°C, a value which agrees well with experimentally determined liquidus temperatures for oceanic basalts (e.g. Tilley *et al.*, 1972; Bender *et al*,. 1978). These results are discussed further in the simple quantitative model described in section 2.4. However, because of the importance which is later attached to the mean value of the asthenospheric potential temperature, some discussion of possible errors in the 1280°C value given by McKenzie and Bickle (1988) is necessary here. The value of 1280°C depends critically on an accurate knowledge of the values of two parameters; (1) The average thickness of the oceanic crust, and (2) the entropy difference between solid and liquid/unit mass (ΔS); i.e. the entropy change on melting.

Assuming for the moment that the mean thickness of the oceanic crust is equal to 7 km, the value used by McKenzie and Bickle (1988), we can concentrate on the importance of the value of ΔS. The maximum, and therefore also the average, extent of melting attained on upwelling asthenosphere of a given T_p is strongly dependent on the supra-solidus isentropic temperature gradient which itself depends

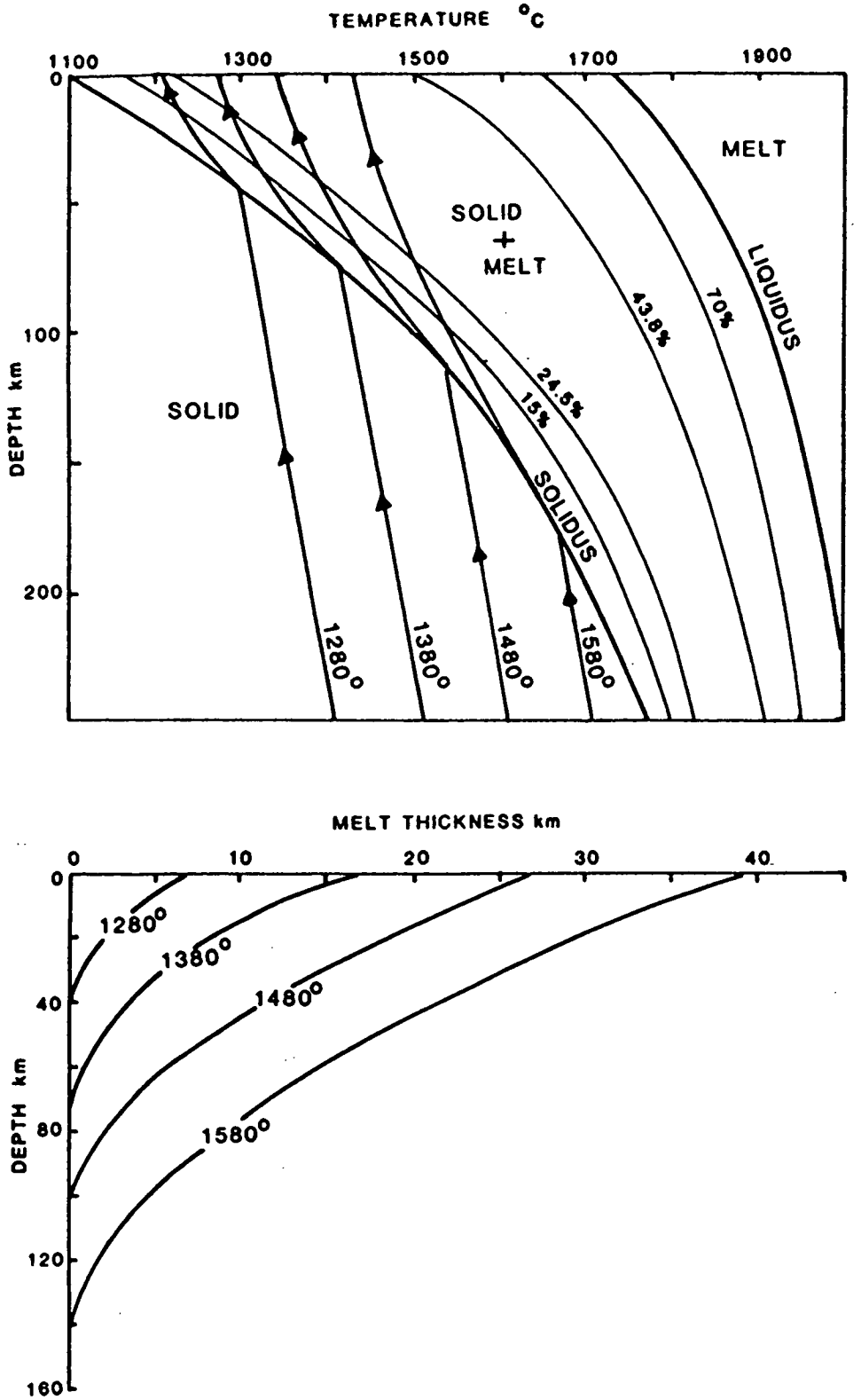

FIGURE 2.4 The upper diagram shows adiabatic decompression paths for asthenosphere with different potential temperatures. The curves between the solidus and liquidus are labelled with % melting of experimental dry peridotite (calculated from the curve in Figure 2.3). The lower diagram shows the total thickness of melt generated below a given depth plotted as a function of potential temperature. Both diagrams are from McKenzie and Bickle (1988).

on ΔS (see McKenzie, 1984). Figure 2.4 shows that asthenosphere with a value for ΔS of 250 J kg^{-1} K^{-1} in conjunction with a T_p of 1280°C will on decompression generate 7 km of melt at an ocean ridge. In Figure 2.5 the thicknesses of melt which can be expected from upwelling asthenosphere with different values of T_p is shown for five different values of ΔS. When ΔS=200 J kg^{-1} K^{-1} then 7 km of melt is produced by a T_p of ~1275°C. If ΔS is increased to 400 J kg^{-1} K^{-1} then a T_p of ~1305°C is required to produce the same amount of melt. Therefore, as ΔS increases the value of T_p required to generate some given amount of melt must also increase. Figure 2.5 also shows how the temperature of the melt at the surface (1 atm.) and the size of the average melt fraction (strictly the point and depth average melt fraction, see section 2.4.2) for a given value of T_p are dependent on the value of ΔS. For a given value of T_p larger values of ΔS lead to lower temperatures of eruption and smaller average extents of melting.

Unfortunately the value of ΔS for garnet lherzolite is only poorly constrained. As McKenzie (1984) notes, probably the best estimate of ΔS available at present is that derived from the thermodynamic relationship between dT/dP on the solidus and the volume change ΔV on melting;

E:2.3
$$\frac{dT}{dP} = \frac{\Delta V}{\Delta S}$$

Takahashi and Kushiro (1983) provide one estimate, 120°C/GPa, for the gradient of the solidus of garnet peridotite and Herzberg (1983) gives a value of 4.34×10^{-5} m^3 kg^{-1} for ΔV. McKenzie (1984) used these values of dT/dP and ΔV to calculate ΔS as being equal to 362 J kg^{-1} K^{-1}. McKenzie and Bickle (1988) do not state where they derive their value of 250 J kg^{-1} K^{-1} but it is suggestd in Chapter 3 that they use this value because it gives a potential temperature of 1280°C which at 125 km corresponds to a temperature of 1333.4°C and is therefore consistent with the temperature obtained from inverted oceanic heat flow and bathymetric data (see Chapter 3).

It seems likely that ΔS is sufficiently poorly known, especially since both ΔS and ΔV will not necessarily be constant, that it might take any value between 200 and 400 J kg^{-1} K^{-1} which, as Figure 2.5 shows, would result in an *uncertainty of ~30 °C in the value of T_p* required to generate 7 km of melt.

So far the oceanic crust has been assumed to have a constant mean thickness of 7 km. According to Hill (1957) and Raitt (1963) the average thickness of the oceanic crust, as determined by seismic refraction profiling, is close to 6.5 km. However, estimates of crustal thickness have been reported to fall within the range from 4.5 to 8.5 km (Spudich and Orcutt, 1980; R. White, 1984). This range in crustal

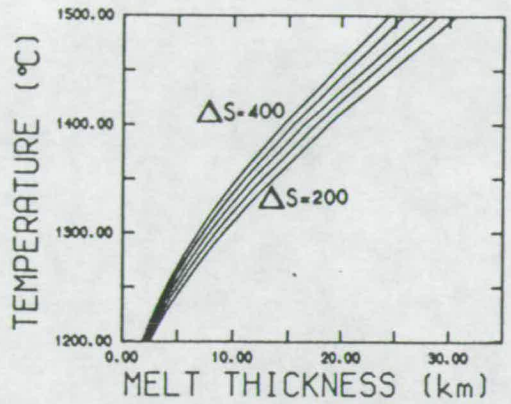

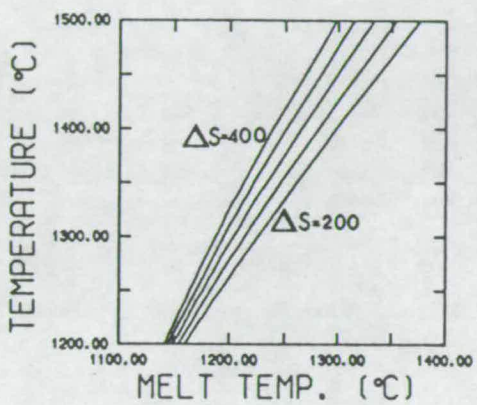

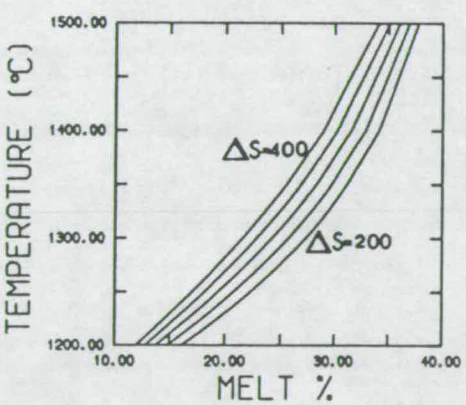

FIGURE 2.5 The dependence of melt thickness, melt temperature (at 1 atm.), and melt percent (of the point and depth average) on potential temperature (ordinate) and the entropy change on melting (ΔS). Each of the five curves in each diagram represents a different value of ΔS from ΔS=400 $Jkg^{-1} K^{-1}$ to ΔS=200 $Jkg^{-1} K^{-1}$ in steps of 50 $Jkg^{-1} K^{-1}$.

thickness led R. White and McKenzie (1989) to propose an error of ±30°C on the value of 1280°C for the mean potential temperature of the asthenosphere.

Figure 2.5 can be used to quantify the possible error on the mean Tp of the asthenosphere given the uncertainty in both the value of ΔS (200-400 J kg^{-1} K^{-1}) and the average crustal thickness (4.5-8.5 km). The outside limits on the value of T_p are ~1245°C (ΔS = 200 J kg^{-1} K^{-1}; melt thickness = 4.5 km) and ~1325°C (ΔS = 400 J kg^{-1} K^{-1}; melt thickness = 8.5 km). The value of 1280°C given by McKenzie and Bickle (1988), which lies close to the centre of this range in T_p, should therefore be qualified with an error of ±40°C. Note that uncertainties in the values of other material constants such as C_p and α have not been considered.

For a given value of ΔS (250 J kg^{-1} K^{-1} is used from here on) higher values of T_p lead to larger extents of melting and thicker oceanic crust. The observation that average oceanic crustal thicknesses are close to 7 km suggests that most ridges are sited over asthenosphere of close to the mean T_p (~1280°C). However, in some areas ridges are located above upwelling limbs (mantle plumes; see section 2.7) in the mantle convection system which are inferred to be some 200°C hotter than the mean T_p (Courtney and White, 1986). A potential temperature of 1480°C will produce 27 km of melt (Figure 2.4); a figure in agreement with the observed thickness of crust beneath aseismic ridges such as the Iceland-Faeroes ridge (Bott and Gunnarsson, 1980; R. White *et al.*, 1987). The effect of mantle plumes on melt production are discussed more fully in a later section but it is clear that wherever they are present the anomalously high T_p will lead to larger amounts of melting.

2.3.6 Melting Experiments and Melt Composition.

Equilibrium batch melting experiments also provide information concerning the major element composition of melt produced from lherzolite at a given T and P. The melt composition will largely depend upon which solid phases are present and on the proportions by which they melt. As such, the composition of the batch melt is strongly dependent on the depth and extent of melting (Yoder and Tilley, 1962; Green and Ringwood, 1967; Kushiro, 1968) and on the activities of H_2O and CO_2 (eg. Kushiro 1972; Mysen and Boettcher, 1975; Olafsson and Eggler, 1983). Simply by varying these parameters a gradational series of compositionally diverse magmas can be produced (Presnall *et al.*, 1979). Discussion of melting in the presence of volatile components is deferred to Chapter 7. In dry lherzolite, X (the melt fraction) and P (the pressure) are the most important controls on the melt composition. The

intention here is to briefly summarise those experimental observations which are important for the quantification of the melting process in terms of melt composition.

Pressure is important because it determines the mineralogical composition of the lherzolite (see section 2.3.1) and the position of the isobaric invariant melting point within the simplified CMAS system. As will be discussed in more detail later, with respect to trace elements especially, the mineralogical composition of the lherzolite exerts a particularly important control on the bulk distribution of elements between the solid and melt phases. Dry melting experiments performed on natural spinel and garnet lherzolites have shown that the composition of the initial, experimentally observable, liquid produced as lherzolite melts becomes increasingly silica undersaturated as pressure increases (e.g. Green and Ringwood, 1975; Yoder, 1976; Stolper, 1980). A generalised melting scheme for lherzolite with pressure would give rise to quartz tholeiite at < 0.5 GPa, olivine tholeiite at 0.5 to 1.5 GPa, alkali olivine basalt at 1.5 to 2.5 GPa, and alkali picrite at > 2.5 GPa. The observed increase in silica saturation with decreasing pressure results from the expansion of the olivine liquidus field and the shift of the invariant point away from olivine, as shown by the CMAS system. In terms of the major element composition of the melt, the shift with decreasing pressure is reflected by a decrease in the content of MgO and FeO and an increase in the SiO_2 content.

The extent of melting is important because the lherzolite will melt in a progressive fashion. The composition of melt produced during partial fusion will depend on the number of solid phases that are present and on the relative contributions that these phases make to the melt phase. Mysen and Kushiro (1977) have shown that a garnet lherzolite melted experimentally at 2.0 GPa gives rise to an alkali basalt when X~0.01 and T=1450°C, an olivine tholeiite when X~0.16 and T=1500°C, and a picritic melt when X>0.44 and T>1600°C. Similarly, Jaques and Green (1980) found that on melting at 1.5 GPa, spinel lherzolite produced alkali basalt when X<0.15, olivine tholeiite when 0.20<X<0.30, and a picritic liquid when 0.40<X<0.60. Jaques and Green (1980) also noted that at lower pressures (P<0.5 GPa) the first melt formed had the composition of quartz tholeiite, and as X increases this gives way to more magnesian tholeiites and komatiitic liquids.

In general, because of the olivine-rich bulk composition of lherzolite, as the extent of melting increases so will the MgO content of the melt. Since the aluminous phase and the clinopyroxene are present in relatively small amounts and tend to enter the melt in relatively large proportions they are usually exhausted before orthopyroxene and olivine. Effects on composition due to the degree of melting

cannot be separated from the pressure related effects. In adiabatically upwelling asthenosphere X is increasing as P is decreasing.

2.3.7 Quantification of Melt Composition.

From earlier discussion it should be clear that as asthenosphere of a given T_p decompresses adiabatically at an ocean ridge, it undergoes progressively greater degrees of melting (Figure 2.4). That portion of the asthenosphere which has undergone the maximum amount of decompression, and actually reaches close to the surface, has also melted by the largest extent. Within the upwelled asthenosphere the extent of melting will range from some maximum amount at the surface to zero at the solidus. This variation in the degree of melting need not imply that all of the melt remains in the matrix, but simply that some parts of the asthenosphere will have produced more melt than others. Quantification of melt composition requires that, given values for T and P, it should be possible to predict the composition of any melt produced. We have already seen that a dimensionless parameter T', which can be calculated from a knowledge of T and P, can be used to determine the value of X. If similar calculations can be performed to relate observed melt compositions to X and P, then predictions of composition will be possible.

Using all of the available experimental data (91 experiments) McKenzie and Bickle (1988) were able to plot melt composition, in terms of major element oxides, against T'. For experiments where X had been determined (38 in all) T' was simply calculated from the relationship shown in Figure 2.3. For the other experiments T' was calculated from a knowledge of T and P. McKenzie and Bickle noticed that, with the exception of SiO_2, FeO and MgO, which all show a pressure dependence, melt composition varied largely as a function of T' and hence of X. As X increases the melt composition becomes steadily less silica undersaturated. This observed variation allowed the parameterisation of compositional data in terms of P and T'. Some of the details of the parameterisation are explained in section 2.4, for further details see McKenzie and Bickle (1988), and Watson and McKenzie (in prep.). The parameterisation reproduces the melt compositions to within experimental error. The largest error occurs on SiO_2 ($\pm$1.15 wt.%) because the value for SiO_2 is calculated by subtraction of the other oxides from 100 wt.%. Together with the analytical expressions for the variation of X with T and P, the parameterisation allows the calculation of X and the associated batch melt composition at any T and P. These mathematical descriptions of the equilibrium melting regime within experimental dry

asthenosphere can now be incorporated into a quantitative model for the genesis of MORB (section 2.4).

2.3.8 Problems When Using Experimental Melt Compositions.

Just as there are practical problems in determining the precise melt fraction produced during an experiment, so too are there problems in determining, with accuracy, the melt composition. As with the determination of X these problems are most severe in the region close to the solidus. Melt composition is most commonly found by electron microprobe analyses of the liquid run product. The problems arise from the difficulties involved in preventing crystallisation during quenching. When the amount of liquid present is large, or concentrated in a small region, the problem of compositional modification of the liquid during quenching may be largely overcome by analysing glass well away from the solid-liquid interfaces. When the melt fraction is small and is drawn out along grain edges and within interstices (i.e. it is spread over a large surface area of solid) it is unlikely that the original liquid composition will be preserved on quenching. At certain pressures quench overgrowth of olivine, for example, might have the effect of reducing the apparent MgO content of the melt. For these reasons there are rarely compositional data for values of X less than ~0.10. This lack of data becomes important if melting in this low X region is non-eutectic in nature. Non-eutectic melting is certainly likely to apply in the case of the more incompatible minor components and also in the case of some of the more incompatible major element oxides (eg. K_2O, TiO_2, Na_2O, P_2O_5). For this reason the compositional data, which are used in the parameterisation, may well be suspect where low degrees of melting are concerned.

A further problem involves application of the results of batch melting experiments to real situations where the melting process may not be the same. If *fractional* or *Rayleigh melting* more closely approximates the way in which the mantle melts, then errors are likely to occur as the result of using both compositional and melt fraction data from equilibrium experiments. The mass of solid material added to the melt phase during decompression melting will depend upon the gradients in chemical potential developed for components distributed between the solid and liquid phases. In a given P-T situation, solid will be added to the melt until chemical equilibrium for all the components is attained. In Rayleigh melting the amount of melt present within the solid matrix at any time is negligible and so the matrix only needs to melt by a small amount to maintain equilibrium. The amount of melt produced will therefore depend on the amount of melt present.

The effect of Rayleigh melting on composition is equally important. The amount of any component held in the solid that enters the melt is again strongly dependent on the differences in chemical potential between the solid and melt phases. With Rayleigh melting the potential gradient is maintained at a maximum until the component in the solid is exhausted. Relatively incompatible elements are therefore likely to be stripped from the matrix much more efficiently by Rayleigh than by batch melting. McKenzie and Bickle (1988) acknowledge these problems but conclude that it is not obvious how Rayleigh melting effects can be estimated quantitatively from the existing batch melting experiments. It seems likely that, because equilibrium melting produces more melt for a given solidus overstep, *the mean potential temperature of the asthenosphere may be somewhat higher than 1280±40 ℃ when Rayleigh melting is accounted for.*

2.4 A Simple Quantitative Model for MORB Genesis.

Once able to parameterise melt fraction as a function of T and P, McKenzie and Bickle (1988) found it relatively straightforward, given certain assumptions concerning the nature of the melting process and the geometry of the region of upwelled asthenosphere, to construct a parameterisation for melt composition and hence to develop the simple quantitative model for MORB formation explained below. Considering the simplifications involved, model predictions when compared with observations show a surprisingly good agreement. Different models for MORB genesis and conflicting arguments and observations are presented in section 2.5.

2.4.1 The Shape of the Melting Region.

The discussion which follows focuses on the simple view of upwelling as a single column, similar to that shown in Figure 2.2. This approach, adopted by many authors (e.g. Gast, 1968; Shaw, 1970; Langmuir *et al.*, 1977; Klein and Langmuir, 1987; McKenzie and Bickle, 1988), assumes implicitly that each complete column of mantle processed through the melting region undergoes an equal average amount of partial melting. The production of melt during decompression can therefore be treated as a one-dimensional problem. O'Hara (1985) questioned whether this assumption would hold because the amount of decompression, and hence melting, should vary from one mantle stream line to the next; i.e. mantle which upwells directly below the ridge (Figure 2.1) will produce more melt of a greater mean extent

than mantle decompressing at the edge of the region of upwelling and that the *shape* of the melting region would therefore be of great importance in controlling the volume and composition of the melt.

For a given spreading rate, the amount of lithosphere created in any interval of time must be balanced by a similar amount of upwelled asthenosphere, and therefore the shape of the region of upwelling is unimportant. Although the melting region is triangular in shape, the result of upwelling in response to a given amount of plate separation (ξ) is to produce a column of lithosphere which, when seen at a distance from the ridge axis, has a constant width (ξ). The melt, forming the crust at the top of this column, will be equivalent to the sum of the melt extracted to leave the residual peridotite which forms the bulk of the column. Note that not all of the melt forming the crust will originate within the underlying column of mantle; i.e. the process is time integrated. The shape of the melting region beneath the ridge is therefore unimportant when the flow lines are considered at some distance from the ridge. The amount of mantle from which only a small amount of melt was extracted must balance the amount of small melt fraction mixed into the final melt.

The simple model which follows relies implicitly on the premise that no mass of material is lost or gained to the system and that all of the melt produced during a given interval of time is gathered together to form the crust. Spiegelman and McKenzie (1987) suggest that the corner flow of the matrix stream lines will, given a sufficiently high viscosity, result in a non-hydrostatic pressure gradient that will focus any melt towards a pressure minimum represented by a small region beneath the ridge. Occasionally small amounts of melt may escape the overall flow and erupt on the ridge flanks as off-axis alkalic volcanoes (Gast, 1968).

2.4.2 The Compositional Parameterisation.

Although the composition of magma erupted at the surface is a complex weighted average of melt produced over a range of depths, it is necessary, when using experimental results, to simplify the melting and extraction processes beneath a ridge into two distinct steps. First a column of asthenosphere the same thickness as equilibrium thickness oceanic lithosphere is upwelled so that its top is at the sea floor. During this stage decompression causes partial melting but no movement is allowed to occur between melt and solid matrix. In the second step, all of the melt is extracted to produce the oceanic crust. This melting scheme, although unrealistic because melt extraction is likely to be almost continuous (Ahern and Turcotte, 1979;

McKenzie, 1984; McKenzie, 1985b), allows the melt composition to be calculated from equilibrium melting experiments.

In such a melting scheme three important quantities concerning melt composition must be defined (McKenzie and Bickle, 1988; Watson and McKenzie, in prep.). The most basic of these is the *instantaneous melt composition* (C_i) which describes the composition of the melt which is added from the solid phase to increase the fraction of melt present from X to X+dX. McKenzie and Bickle (1988) first parameterised the melting experiments using a functional form based on Rayleigh's law in order to obtain C_i as a function of T', and hence of X and P. Once $C_i(X,P)$ has been determined the *average* or *batch melt composition* (C_p) of all the melt which has been generated from any particular element of solid can be found by integrating along the melting path. For an element of solid, which upon decompression, reaches some final pressure this average melt composition C_p may be described as the *point average* composition. The point average composition, C_p, for an element of solid at a given final pressure is therefore calculated in the parameterisation by integrating the instantaneous melt compositions produced for that element between melt fractions of 0 and X at the final pressure. Finally the composition of all of the melt generated in the column depends upon the average of C_p weighted for melt fraction (as each point average composition reflects a different value of X) integrated over the entire melting interval (i.e. over the entire depth). This composition, C_{pd}, will be referred to as the *point and depth average melt composition.*

An accurate description of melting using the three quantities described above depends on the assumptions concerning the melting and extraction processes. Perhaps most critical is the assumption that C_i, calculated from a Rayleigh melting function, accurately reflects the instantaneous composition of the melt produced during equilibrium batch melting. The discussion in section 2.3.8 suggested that the two compositions are likely to differ. If this assumption is flawed then the values of C_p and C_{pd} are also likely to be in error. Also, as was suggested in section 2.3.8, the value of X calculated at a given T and P from the batch melting experiments, and used thereafter in the compositional calculations, may be in error if the melting process more closely follows the Rayleigh law.

A further difficulty concerns the assumptions that melt extraction does not occur until melting is complete, and that there is then no interaction between melt and matrix. On physical grounds the arguments now strongly favour the extraction of melts at fractions less than 2-3% (e.g. Ahern and Turcotte, 1979; McKenzie, 1985b). In this case something close to Rayleigh melting is to be expected, and therefore, both

the calculated point average and point and depth average compositions might be expected to deviate from their real counterparts.

It should be noted, however, that the validity of the compositional parameterisation does not depend on the assumptions underlying the derivation of Rayleigh's law being satisfied and as McKenzie and Bickle (1988) state "*The expressions used are simply convenient functional forms whose validity should be judged by how well they fit the experimental data*".

Given all of these difficulties and simplifications, it is perhaps surprising that the parameterisations of McKenzie and Bickle (1988) are able to predict melt volumes and compositions (see discussion below) with any accuracy at all!

2.4.3 Using the Parameterisations in a Predictive Model.

In section 2.3.5 the parameterisation of melt fraction was used to suggest that, because the average thickness of the oceanic crust is 6-7 km, the mean potential temperature of the asthenosphere is close to 1280°C (see Figure 2.4). It was further suggested that regions of anomalously thick oceanic crust are produced when a ridge coincides with asthenosphere of higher than average potential temperature. These statements rely on the fact that, providing upwelling is isentropic, the thermal structure and the variation of X with P within the melting region can be calculated. The variation of X with P may then be used to predict, from the compositional parameterisation, the instantaneous (C_i), point average (C_p), and point and depth average (C_{pd}) compositions of any melt produced.

Figure 2.6 shows some examples of these calculated melt compositions, using the preferred version (version a) of the parameterisation of McKenzie and Bickle (1988), produced by asthenosphere with different potential temperatures. During melting the parameterisation treats Na_2O as a moderately incompatible element (D_{Na_2O} equal to 0.169) whilst cpx is present in the solid. Once cpx has been exhausted the concentration of Na_2O in the melt is steadily diluted. The disappearance of cpx is implied by the parameterisation to occur at X=0.245 and is represented by a kink in all of the calculated compositions shown in Figure 2.6. Diagram A shows how the extent of melting is inversely correlated with point average concentration of Na_2O. The higher the potential temperature, the greater the mean extent of melting, and the lower the corresponding value of C_{pd} for Na_2O. Because of this good correlation between Na_2O and extent of melting, Na_2O is used as the ordinate for all of the other diagrams in Figure 2.6. Other incompatible oxides,

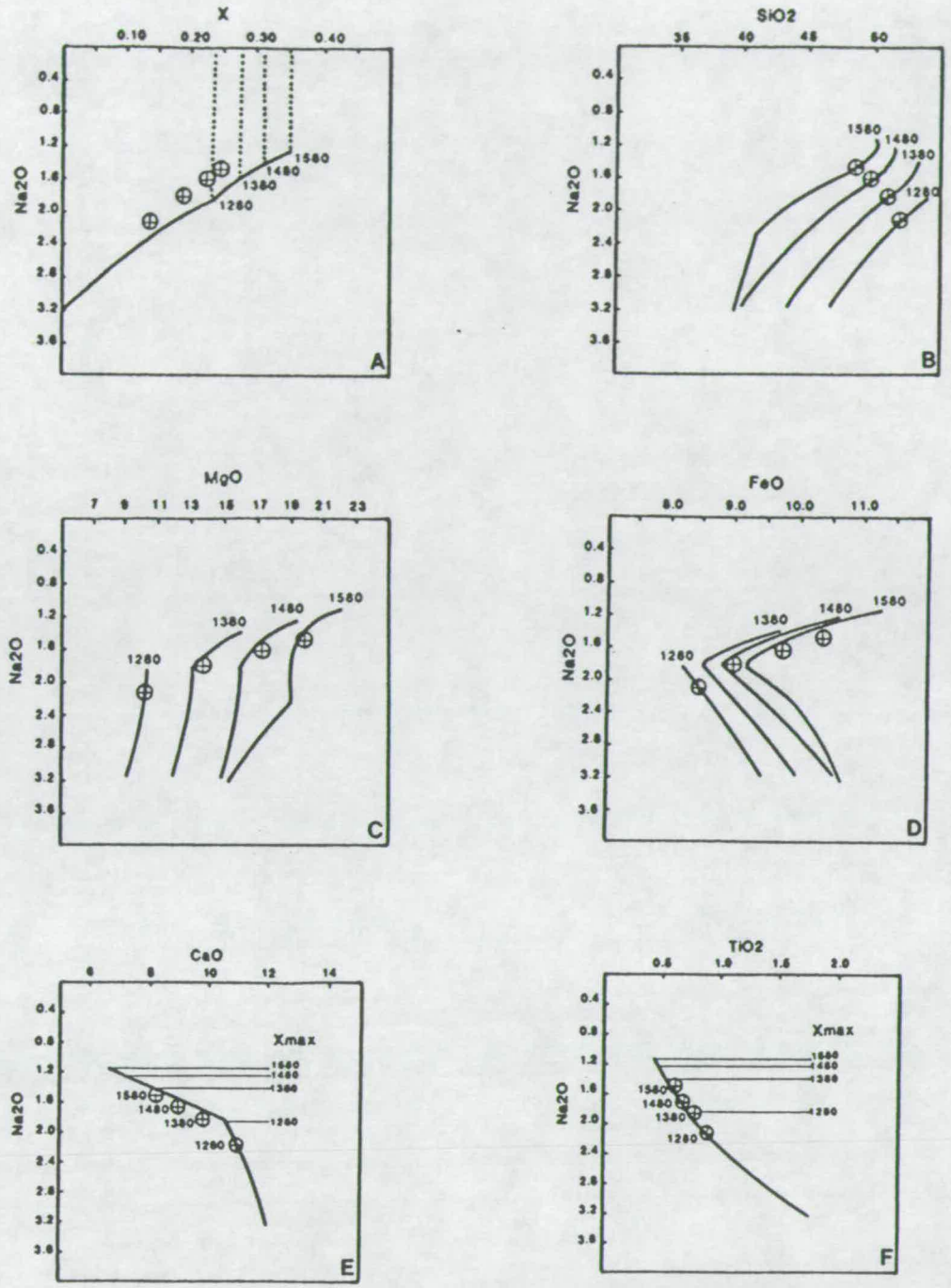

FIGURE 2.6 Point average (solid lines) and point and depth average (large circles with crosses) melt compositions for ocean ridges above asthenosphere of different potential temperatures. Values are calculated from the parameterisation (version (a) shown in Table A1 of McKenzie and Bickle (1988)). Dotted lines in diagram A indicate maximum point average melt fractions at different potential temperatures. Fine lines in E and F indicate point average compositions at the top of the melting column at different potential temperatures.

such as K_2O or TiO_2, might equally well have been used, but the parameterisation is not accurate for these (McKenzie and Bickle, 1988).

Figure 2.6B demonstrates the overall trend towards silica undersaturation and *ne* normative compositions at small extents of melting and high pressures; an observation noted in the experiments (see section 2.3.6). The pressure dependent nature of SiO_2, MgO and FeO is clearly seen in Figures 2.6B, 2.6C,and 2.6D. Notice that at melt fractions exceeding 0.245 (corresponding to Na_2O~1.8 wt.%) the point average cooncentrations of MgO and FeO both increase rapidly because ol and opx are, by this stage, the main contributors to the melt.

The value of D_{CaO} used in the parameterisation was equal to 0.5 and all of the CaO was required to have entered the melt before X=0.245. CaO is therefore treated in a way that is similar to Na_2O, but is relatively less incompatible (see Figure 2.6E). The behaviour predicted for Al_2O_3, not shown in Figure 2.6, is very similar to that of CaO. The rapid fall in the point average concentration of TiO_2 with increasing extents of melting, shown in Figure 2.6F, is a function of its relative incompatibility (D_{TiO_2}=0.103).

Details of the errors in these predicted compositions are given in Appendix A1 of McKenzie and Bickle (1988). The largest mean error (1.15%) occurs on SiO_2 which is calculated by subtraction of the other oxides from 100%, and therefore accumulates the other errors.

2.4.4 Testing the Model with Observations.

If the model as outlined above is a good approximation to reality then the range of point average compositions predicted by the model should, allowing for crystal fractionation, broadly correspond to the major element compositions of MORB. In particular, the average composition of primitive MORB should be similar to the point and depth average composition predicted for melting of normal potential temperature (T_p=1280°C) asthenosphere. Observed differences in crustal thickness, and hence ridge depth, attributed to differences in T_p, should also correlate with observable differences in basalt composition.

Figure 2.7 shows that there is a close agreement between the composition of primitive (MgO>9wt.%) MORB glasses and the predicted point average compositions for asthenosphere of normal T_p (1280°C). Note also, in Figures 2.6 and 2.7, the parameterisation predicts that for normal temperatures cpx should only just be a residual phase. This prediction is supported by the observation that, in many

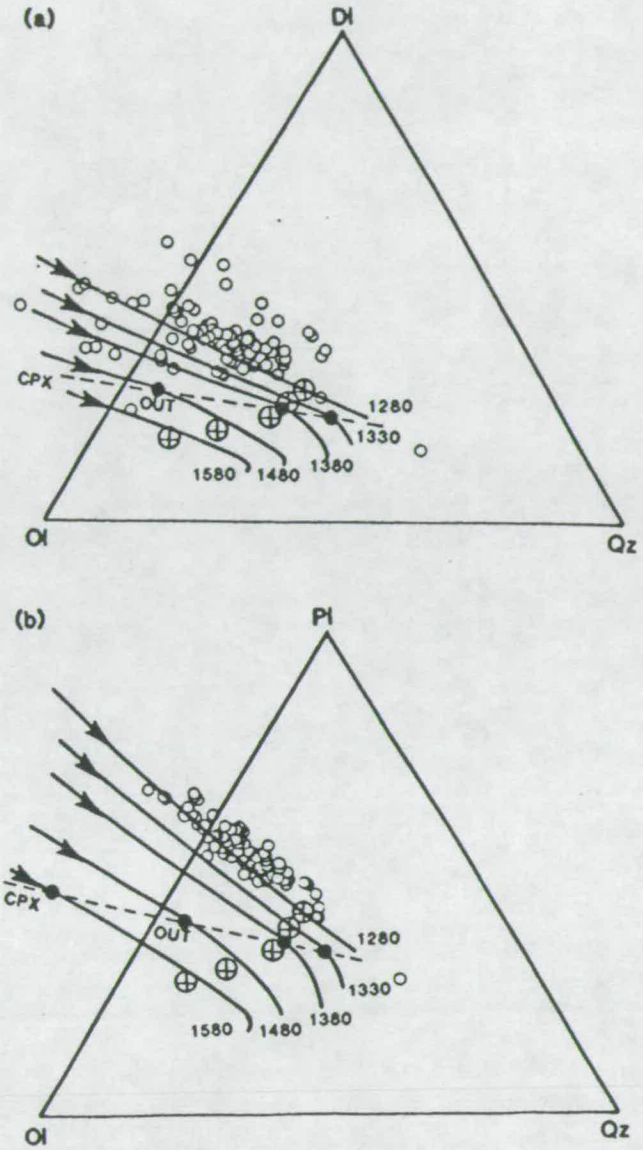

FIGURE 2.7 From McKenzie and Bickle (1988). Projections from Pl into the Ol-Di-Qz plane (a) and from Di into the Ol-Pl-Qz plane (b) of Walker *et al.*'s (1979) tetrahedron, using molar concentrations. Open circles represent oceanic glasses with MgO>9wt%. The curves are point average compositions for different potential temperatures calculated from the parameterisation (version (a) shown in Table A1 of McKenzie and Bickle (1988)). The dashed line marks a line of constant melt fraction corresponding to 0.245 (cpx-out). Crosses inside large circles show point and depth average compositions.

abyssal peridotites, enstatite is saturated in diopside but that there is little or no free diopside remaining (Dick and Fisher, 1984; Dick *et al.*, 1984).

The correlation between predicted ridge depths and compositions and observed depths and compositions is shown in Figure 2.8. The observational data in Figure 2.8, empirically corrected for crystal fractionation (Klein and Langmuir, 1987), plotted against the residual depth of the ridge axis, are from Klein and Langmuir (1987). The calculated ridge depths for different values of T_p assume Airy isostasy and use the CIPW normative mineralogy of the different point and depth average compositions to determine crustal density (see McKenzie and Bickle, 1988).

The good agreement between the predictions and observations shown in Figures 2.6 and 2.7 is very encouraging. McKenzie and Bickle (1988) also show that the point and depth average composition at 1280°C is very similar to the mean composition of MORB glasses and is quite capable of fractionating at shallow levels to produce the observed range of compositions of oceanic basalts and gabbros.

From the above discussion, covered in more detail in McKenzie and Bickle (1988), it would appear that a simple quantitative model, based on parameterisations of melting experiments, will accurately predict many of the major characteristics of MORB. If the compositions of the most MgO-rich MORB glasses do closely resemble those of primary point average compositions generated by adiabatic decompression, then the calculations support the view that primitive MORBs essentially represent primary magma (e.g. Green and Ringwood, 1967; Kushiro, 1973; Presnall et al., 1979; Fujii and Bougault, 1983; Takahashi and Kushiro, 1983; Thompson, 1987; and Klein and Langmuir, 1987).

2.5 Arguments Against the Simple Model.

One of the key tenets of the approach presented above (section 2.4) is that primitive MORB compositions from ridges sited over asthenosphere of average, rather than elevated, potential temperature represent primary magmas little modified by crystal fractionation processes. The primary origin of MORBs has been a point of considerable debate over the last 15-20 years and the views described above are not consensus ones. Many authors consider that even primitive MORB compositions represent the end products of a protracted crystallisation history at relatively high pressures (2-3 GPa) from a picritic parent containing 15 wt.% or more of MgO (e.g. O'Hara, 1968; Green *et al.*, 1979; Jaques and Green, 1980; Stolper, 1980; Elthon and Scarfe, 1980; Elthon and Scarfe, 1984).

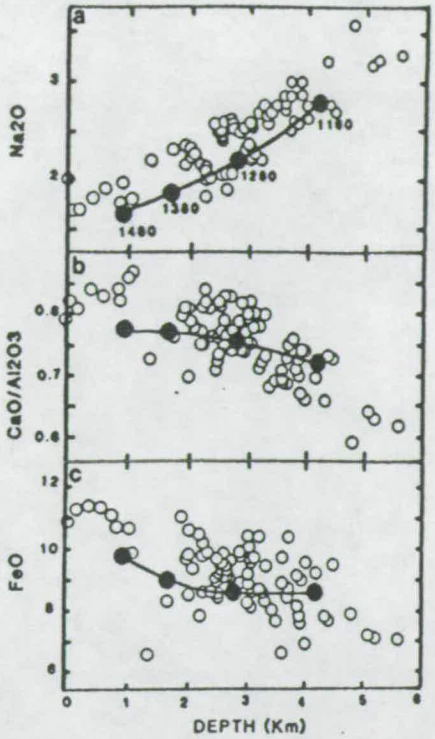

FIGURE 2.8 From Mckenzie and Bickle (1988), (a) the Na_2O, (b) the CaO/Al_2O_3, and (c) FeO concentrations in basalts containing 8% MgO plotted against depth to the ridge axis. The curves show point and depth average compositions for the potential temperatures marked in (a) obtained from the parameterisation given in Table A1 of Mckenzie and Bickle (1988). Depths were calculated by Airy compensation against a ridge axis depth of 2.8 km, a crustal thickness of 7 km and T_p=1280°C with a compensation depth of 150 km. Open circles are data points taken from Klein and Langmuir (1987).

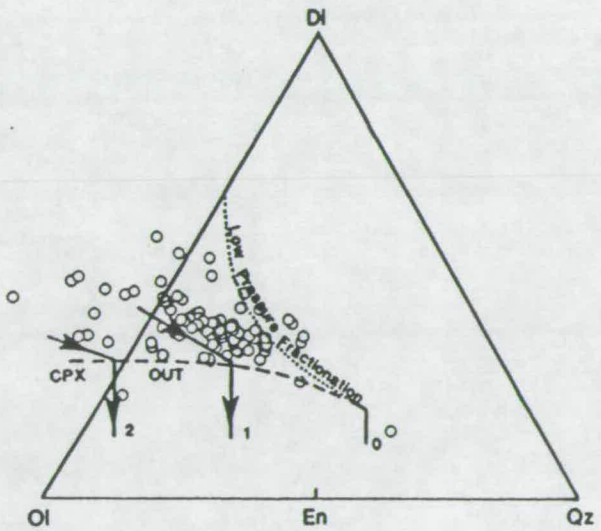

FIGURE 2.9 MORB glasses with MgO>9% (open circles) collected by Elthon (1987) projected from Pl onto the Ol-Di-Qz plane in the manner proposed by Walker *et al.* (1979). The experimental cotectics at 2, 1 and 0 GPa and the cpx-out curve are taken from Stolper (1980).

The arguments used to support the picritic parent model for MORB genesis are derived from essentially three categories of observation, as follows:

(1) Disequilibrium between MORB compositions and mantle phases.

(2) Observation of picritic bodies in many ophiolite complexes.

(3) Low pressure fractionation trends.

One of the strongest cases for a picritic parent to MORB comes from the observation that the composition of many primitive MORB glasses is not in equilibrium with opx or ol at any pressure (O'Hara, 1968; Green *et al.*, 1979; Elthon and Scarfe 1984; Elthon 1989). If primitive MORBs are primary then they should be in equilibrium with all of the phases residual to the mantle source, and therefore especially with opx and ol. If, however, primitive MORBs result from significant amounts of olivine fractionation from a primary picritic magma, containing 15-20 wt.% MgO, at pressures of 2 to 3 GPa, then there is no reason to expect them to be in equilibrium with the residual mantle.

As McKenzie and Bickle (1988) point out there are major geophysical problems associated with the picritic parent model. Figure 2.6 clearly shows that, according to the parameterisation of experimental melt compositions, in order to produce such MgO-rich magmas very large extents of melting are required (X>0.30). Such large extents of melting might, not so long ago, have been considered a virtue of the model because it was not generally believed that small melt fractions could separate to form magma bodies. Physical modelling of the melt extraction process, as well as trace element and isotopic arguments now all appear to support the extraction of small melt fractions (see section 2.6.4). Not only are the extents of melting required to form picrites greater than those attainable by asthenosphere of normal T_p (see Figures 2.4 and 2.5), but also, for such melts to be produced at pressures of 2-3 GPa requires melting at depths >70 Km. The presence of picritic magmas at such depths would imply a potential temperature in excess of 1480°C.

Perhaps a more serious problem with the picritic model concerns the prevention of extensive melting at pressures less than 2 GPa. The large volumes of melt produced at shallow levels could destroy the picritic character of the melts produced at greater depths. One way to prevent melting at low pressures is to dramatically cool the upwelling asthenosphere. As was mentioned in section 2.1, if the upwelling velocity is sufficiently slow then conductive cooling might penetrate to depths sufficient to prevent the upper parts of the upwelling column from melting, and the geotherm would no longer be adiabatic. However, the upwelling rates would need to be significantly slower than those implied by the horizontal plate separation velocities observed for most ridges. According to McKenzie and Bickle (1988) "*The*

only escape seems to be to circulate sea water to depths of 40 km, even beneath rapidly spreading ridges like the East Pacific Rise. Such a proposal generates more problems than it solves."

In recent years support for the picritic model has come from the studies of ophiolite complexes. Malpas (1978) showed that the pillow lavas in the structurally highest levels of the Bay of Islands Ophiolite (Newfoundland) were no more MgO-rich than average primitive MORB. However, when the whole ophiolite section is considered, with its abundance of extensive dunite and pyroxenite cumulates and veins of ol and opx, the estimated average composition is picritic. Elthon (1979), and Pallister and Gregory (1983) reached similar conclusions from studies elsewhere. It is clear that picrites can be found amongst or deduced from the rocks of ophiolite complexes. Whether or not these are primary magmas depends upon whether or not ophiolites are representative slices of mid-ocean ridges. Not wishing to be drawn into a protracted argument concerning the significance of ophiolite bodies, the author directs the reader to reviews by Pearce *et al.* (1984) and Thompson (1987) who conclude that the majority of ophiolites for which adequate data are available appear to have been formed in a supra-subduction-zone environment. Their often picritic nature is probably best explained by extensive melting promoted by the introduction of water. To quote Thompson (1987) "*Only the unconvinceable should by now be unconvinced that, with few exceptions, ophiolites are a dismal place to seek unambiguous evidence about the ultimate parentage of ridge basalts*"!

Another argument used by proponents of the picritic parent model concerns the compositional trend observed in the data shown in Figure 2.7. Walker *et al.* (1979) argued that the spread of data in Figure 2.7 coincides with the low pressure (1 atm) cotectic for crystallisation of olivine, diopside and plagioclase which drives the residual liquid composition towards the quartz apex. Figure 2.9, from Stolper (1980), shows how, if the primary magma composition is picritic and lies close to the Di-Ol join at 2 GPa, then crystallisation of olivine would move the composition towards the 1 atm cotectic close to the Di-Ol join. Crystallisation and magma mixing along this cotectic might then explain the observed compositional trends. However, the above model cannot explain the extension of the compositional trend across the Di-Ol thermal divide into the *ne* normative field.

McKenzie and Bickle (1988) question whether the trend in MORB glass compositions (Figure 2.7) need be explained solely by low pressure crystallisation. The data clearly coincide with the compositional vectors for point average melt compositions determined from the parameterisation (see section 2.4). If the trend

were primarily due to melting then its extension across the thermal divide causes no problems.

In summary, many of the arguments for a picritic parent to MORB appear to either contradict the geophysical evidence, or to be explicable by other means, or to be ambiguous. A further argument for extensive fractional crystallisation is based on the observed *decoupling* of compatible and incompatible elements in MORB (O'Hara and Mathews, 1981). The meaning of this term and reasons for its cause are discussed in the next section (2.6.4) which will suggest that decoupling is more likely to be an artifact of the melting rather than the crystallisation process.

2.6 MORB: Trace Element and Isotopic Character.

2.6.1 Introduction.

The literature concerning the trace element and isotopic composition of MORB and its inferred source is extensive. This section is only intended to highlight those aspects which are pertinent to the discussion of the melting process and which, in later discussions, may allow MORB-type compositions to be used as a frame of reference for melts from the asthenosphere. However, immediate difficulties appear when this sort of approach is adopted because the concentrations of, and ratios between, certain trace elements in MORB is far from constant. This observation has led to the suggestion that in some instances MORB results from melting of at least two chemically distinct types of source in the asthenosphere, normal and enriched (see Figure 2.10). There is also a degree of uncertainty concerning the effects of fractionation processes on trace element ratios and the decoupling of major and trace components during magma formation and subsequent differentiation.

2.6.2 N-MORB and the MORB Source.

Average or *normal* MORBs (*N-MORB*s) are characteristically depleted in both LILE[1] and LREE[2] relative to most other oceanic and continental basalts. As has

[1]LILE (Large Ion Lithophile Elements) include large low-valency cations (Cs, Rb, K, Ba, Pb, and Sr) and large high-valency cations (Th, U, Zr, Hf, Nb, and Ta).

[2]LREE (Light Rare Earth Elements) include La, Ce, Pr, Nd, Sm, and Eu.

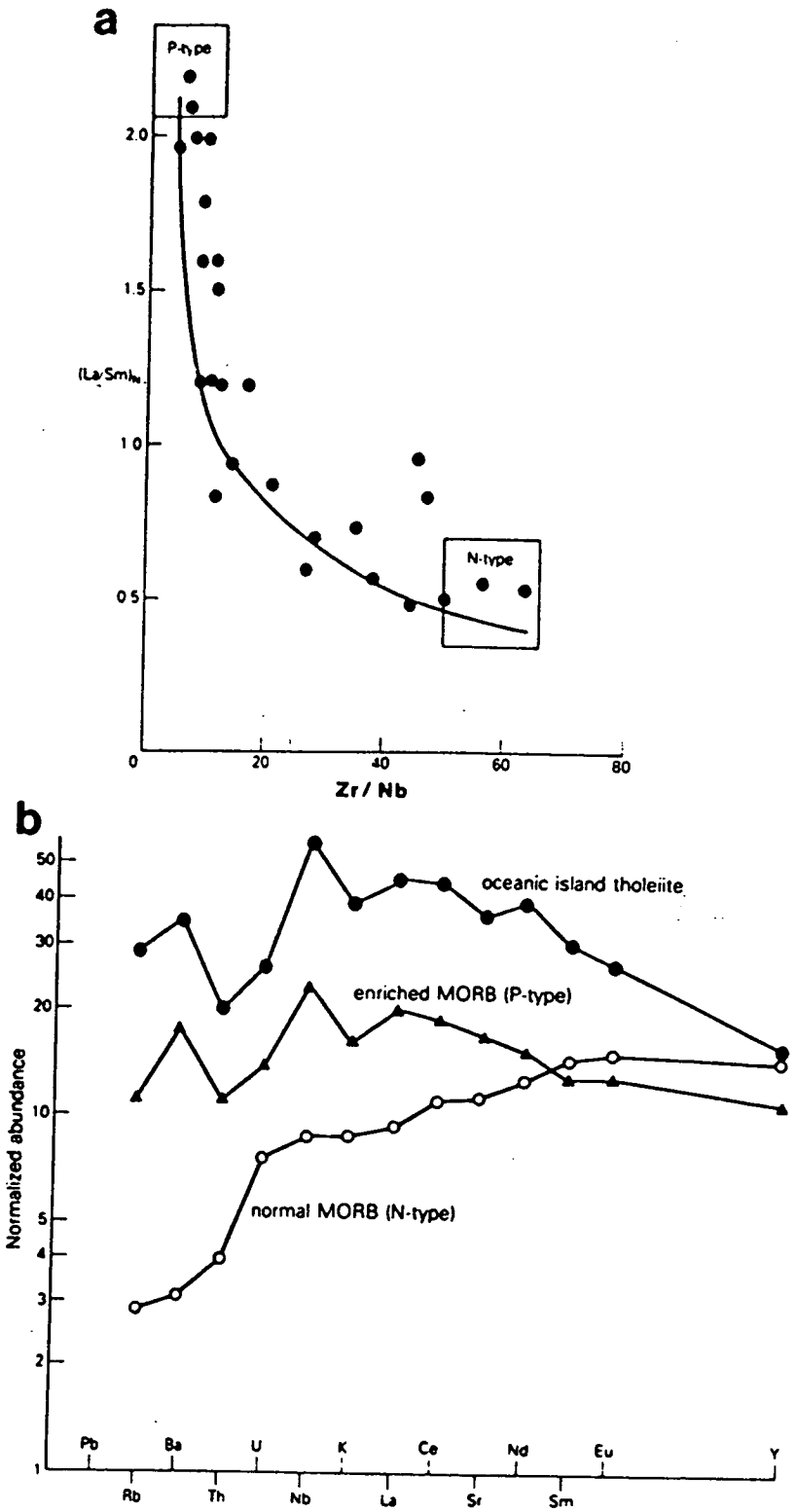

FIGURE 2.10 Differences between P-MORB and N-MORB. (a) Plot of $(La/Sm)_N$ versus Zr/Nb ratio for MORB from the Atlantic, Pacific and Indian oceans. The data array may indicate the importance of binary mixing processes in MORB source characteristics (data from Le Roex *et al.*, 1983 and Sun *et al.*, 1979). (b) Spidergrams showing the difference between N-MORB and P-MORB, and the similarity between P-MORB and ocean island tholeiites (data from Sun *et al.*, 1979). Both diagrams taken from Wilson(1989).

already been discussed MORBs produced at normal temperatures, which comprise the majority of MORBs, are believed to have evolved from relatively large degree (10-20%) partial melts of the asthenosphere. At normal temperatures melting will occur in the stability field of spinel lherzolite. If MORBs result from large extents of melting which do little to fractionate incompatible elements then, as numerous authors have noted, the concentrations of these elements in MORBs may provide direct information concerning the relative abundances of such elements in their source; the source of N-MORB will hereafter be termed the *MORB-source*. Of course the absolute abundance of such incompatible elements will always be greater in the basalt than in its source.

It follows, therefore, that because large amounts of partial melting of a chondritic, primitive upper mantle or bulk Earth (e.g. Zindler and Hart, 1986) composition will not produce the enrichment of HREE[3] over LREE and the relative depletion of LILE observed in N-MORB (see Figure 2.10), it may be concluded that the MORB source must be depleted in the most incompatible elements relative to chondrite, primitive upper mantle, or bulk Earth (e.g. Sun 1980).

This conclusion is strongly supported by isotopic evidence. The high ratios of $^{143}Nd/^{144}Nd$ and low ratios of $^{87}Sr/^{86}Sr$ observed in N-MORB relative to the bulk Earth values suggest a source which has been depleted in both Nd and Rb relative to bulk Earth for a significant part of the Earth's history (e.g. Zindler and Hart, 1986). It is comforting to note that anhydrous spinel lherzolites are among the only known mantle samples to display the Nd and Sr isotopic character of N-MORB (Zindler and Jagoutz, 1988).

A generalised model for the development of the MORB source might involve the continuous extraction, starting early in Earth history, of melts enriched in incompatible elements from the primitive upper mantle into the crust. The result of this melt removal would be to leave a chemically zoned upper mantle, strongly depleted in incompatible elements, which could later be homogenised by convective stirring. The important point to note here is that the observed fractionation of the REE in the source (e.g. Nd from Sm) requires the removal of very small melt fractions (~1%) from mantle with garnet lherzolite mineralogy (e.g. Kay and Gast, 1973; Hofmann, 1988; O'Nions and McKenzie, 1988). This concept of continuous separation of small melt fractions from the asthenosphere will be returned to below and in Chapter 7.

---

[3]HREE (Heavy Rare Earth Elements) include Er, Tb, Tm, Yb, and Lu.

There are many estimates, either directly from analyses of peridotites, or via forward and inverse modelling of N-MORB trace element compositions, for the trace element composition and modal mineralogy of the inferred MORB source (e.g. Wood, 1979; Sun, 1980; Sun, 1982; Ringwood, 1982; Hofmann, 1988). A useful review of the data and methods used in these estimates is given by Kostopoulos (1988).

2.6.3 P-MORB: an Enriched Source(s).

Although the majority of MORBs show the characteristics described above and can be ascribed to melting of a relatively depleted source, many have characteristics which reflect a source which is relatively enriched in LREE and LILE compared to the inferred source of N-MORB (e.g. Sun *et al.*, 1979; Saunders *et al.*, 1988; see Figure 2.10); these are invariably termed *E-type MORB*. It is worth noting that this type of MORB is commonly, but not always, associated with ridge segments which show anomalously shallow depths and where a mantle plume is therefore inferred to coincide with an active spreading centre (e.g. Iceland, the Azores and Jan Myen). Such observations have led to the term *P-MORB*, implying a plume-source for the enrichment.

The main differences between N- and P-MORB are shown in Figure 2.10b in which elements are ordered, from right to left, in terms of increasing compatibility in mantle phases. The relatively flat pattern shown by P-MORBs suggests melting of a source with a composition that is close to that of the primitive upper mantle, as estimated by Sun *et al.* (1979). The source of P-MORB is therefore enriched relative to that of N-MORB; or rather it has not been subject to such severe depletion in the most incompatible elements. Again such deductions are supported by the isotopic evidence; P-MORB has relatively lower $^{143}Nd/^{144}Nd$ and higher ratios of $^{87}Sr/^{86}Sr$ than does N-MORB. The Nd and Sr isotopes do, however, still suggest a time integrated depletion of Rb and Nd relative to bulk Earth.

One possible model for the source of P-MORB would involve melting of a primitive mantle reservoir which has undergone considerably less (by volume) extraction of small melt fractions than has the reservoir which now supplies N-MORB. The entire range of compositions seen in MORB cannot, however, be explained by mixing of melts from the N-MORB source (section 2.6.2) and this relatively enriched source. Important in this context is the concept of the "lead paradox" first reported by Allegre (1969). The Pb isotopes require that the U/Pb ratio in the source of P-MORB and OIB (ocean island basalt) be too high for it to be

primitive mantle. Observations such as these have led to models which involve addition of material, with already fractionated trace element assemblages, back into the asthenosphere, perhaps via the processes of subduction and lithospheric delamination (e.g. Hofmann and White, 1982; McKenzie and O'Nions, 1983; Saunders *et al.*, 1988). Mantle plumes might then return this HIMU (high U/Pb; Zindler and Hart, 1986) material to the upper parts of the asthenosphere where it would either melt or be incorporated as *inhomogeneities*. A more detailed discussion of the likely causes and consequences of mantle plumes is presented in section 2.7. See Chapters 5 and 7 for further discussion of the separate geochemical reservoirs for basaltic magmas within the Earth

2.6.4 Incompatible Element Fractionation.

Throughout the above discussion it was assumed that, because MORBs arise from large extents of melting, then the trace element characteristics of the basalts, in particular the inter-element ratios, would be signatures from their source. This assumption is, however, probably not always valid because fractionation of highly incompatible element pairs, such as U and Th, clearly does take place by some process/es (e.g. Galer and O'Nions, 1986). One example of such fractionation has already been mentioned above; P-MORBs have Nd isotope ratios indicative of a relatively high Sm/Nd ratio in their source, and yet many of the basalts themselves show low ratios of Sm/Nd. A better example is given by Galer and O'Nions (1986) in which they show that the observed range in measured parent daughter ratios (e.g. Rb/Sr) in MORBs is many times (a factor of 40) greater than the range suggested by the time integrated parent daughter ratios (e.g. $^{87}Sr/^{86}Sr$). This suggests that at least some of the chemical variations, in terms of ratios of trace elements, observed in MORBs are a function of magmatic processes rather than the composition of the source. Great care should therefore be used when attempting to define the trace element character of a source from the observed character of a basalt. Since isotope ratios cannot be changed by magmatic processes the arguments based on them (e.g. that Rb/Sr and Nd/Sm are relatively low in the source) have more certainty.

Specification of the chemical character of the mantle, and the identification of different source components from the compositions of erupted basalts requires an assessment of those processes which will operate to produce trace element ratios in the liquid that differ from those of their source; i.e. *fractionation processes*. These processes may include melt formation, melt migration and accumulation, and magma chamber differentiation.

The arguments in favour of large extents of melting generating a picritic parent to MORB and its extensive polybaric fractional crystallisation, discussed in section 2.5, led a number of authors to produce various models which ascribe the observed fractionations between incompatible elements to *open system magma chamber processes* (e.g. O'Hara, 1977; O'Hara and Mathews, 1981; Jochum *et al*,. 1983). Fractionation between incompatible trace elements while maintaining a basaltic major element composition requires that the magma crystallises in a periodically replenished/eruptive magma chamber. Buffering of the major element composition in this way accompanied by fractionation of the incompatible elements gives rise to the effective *decoupling* of these different components.

Galer and O'Nions (1986), however, argue convincingly against open system fractional crystallisation as a cause of component decoupling. The secular disequilibrium observed in the activity ratio of ^{230}Th to ^{238}U in MORBs provides a time constraint for the fractionation process of $\sim 10^5$yrs. The number of eruptive cycles that would be required to produce the observed fractionations within this short time scale appears to be unreasonably large (Galer and O'Nions, 1986) when compared to observed eruption rates at mid-ocean ridges. The same time constraint would also appear to apply for the fractionation observed in Icelandic magmas (Nicholson *et al.*, in prep).

McKenzie (1985a) argues in favour of fractionation between melt and matrix during melt migration. In this case much of the fractionation would need to occur via partitioning of elements between cpx and liquid. According to Galer and O'Nions (1986), since there is little variation in the Sr/Nd ratio of MORB, and since both Sr and Nd could be expected to be more strongly fractionated by cpx than Th and U, cpx is inferred to be relatively unimportant in terms of decoupling.

Galer and O'Nions (1986) conclude that fractionation between elements such as U and Th must be controlled by melting of minor amounts of accessory phases such as amphibole, phlogopite and carbonate. The melting of such volatile-bearing phases in the asthenosphere is likely to occur at depths which are greater (or at temperatures which are lower) than that of the dry solidus. Although basalts erupted at ocean ridges are volatile-poor they do contain minor amounts of both CO_2 and H_2O and observations by Delaney *et al.* (1978) suggest that together in the mantle they amount to <0.1wt%. The implication is that trace element fractionations will be effected by small amounts of melting (~1%) of hydrous phases. The volume of asthenosphere overstepping the volatile-controlled melting curve, which will influence incompatible element abundances in the melt, will be much larger than the volume which crosses the dry solidus (Galer and O'Nions, 1986).

Decoupling of compatible and incompatible components during melting therefore points to two significant conclusions which must be taken into account when modelling melt generation:

(1) The first melt fractions will be produced from accessory phases and are therefore not controlled by the dry solidus (see Chapter 7).

(2) The incompatible element inventory of MORB, which will be a complex function of the melting process and will relate to the depth of the melting region, will not necessarily bear any direct relationship to the major element composition.

2.7 Asthenospheric Convection

The preceding discussion has already shown the importance of the effect of differences in potential temperature in controlling the volume and composition of melt generated during decompression of the asthenosphere. Differences in potential temperature are related to the convective system in the asthenosphere, the nature of which is considered in this section.

With regard to melting it is of great importance to know the magnitude and length scale (lateral and vertical) of variations of potential temperature within the upper mantle as well as the planform and dynamics of the circulation. These aspects of convection will affect (a) the local temperature structure and (b) any compositional variations in the mantle, which may cause differences in the melting characteristics, between different parts of the convective system.

Many of the questions concerning the nature of convection in the asthenosphere have no unequivocal answer. The most important unresolved question is whether convection is mantle-wide, or whether upper and lower mantle convect separately. Peltier (1980) points out that practically all of the relevant observations can be most easily explained in terms of mantle-wide convection. However the evidence can also be accounted for in terms of separate upper- and lower-mantle convective systems. Numerical and laboratory experiments on convection in discrete layers (Richter and McKenzie, 1981) suggest that circulation may be confined to separate superimposed layers if the density contrast due to changes in chemical composition is larger than that caused by the largest temperature difference within the system.

There are no rheological objections to mantle-wide convection. Indeed the rather small viscosity increase with depth and the positive slope of the Clapeyron curve for the olivine-spinel transition would both tend to favour mantle-wide

convective schemes. However, geochemical arguments for isotopically distinct mantle reservoirs which have maintained their separate identities for periods of the order of 1 Ga or more (e.g. De Paolo and Wasserburg, 1976; O'Nions *et al.*, 1977; Jacobsen and Wasserburg, 1979; Allegre 1982) provide very strong support for proponents of separate convective systems. Numerical experiments performed by Hoffman and McKenzie (1985) suggested that the homogenisation of heterogeneities within a convective system would be very efficient and led them to argue for separate convective layers in the upper and lower mantle.

Whichever answer applies to the question of vertical length scale its importance is not likely to be great in terms of the effects on melting beneath ridges, although it may be of some importance when considering the melting beneath old abnormally thick cratonic lithosphere.

The horizontal length scale of the convective system as well as its magnitude (in terms of potential temperature) can be estimated from models of convective flow that are constrained by observations of oceanic bathymetry, the geoid and heat flow. Courtney and White (1986) combined such observations, from the Cape Verde hot spot, with a steady state axisymmetric convection model in the upper mantle in order to predict, to quote R. White and McKenzie (1989), *"a narrow (150 km diameter) plume of hot mantle rising upward at the center, and that this is deflected laterally by the overlying plate to form a mushroom-shaped head of anomalously hot mantle some 1500 km across"*. The temperature anomaly is 100°C above normal over most of the anomalous region while in the central region temperatures 200-300°C hotter than normal are to be expected (see Figure 2.11). Observations of geoid anomalies suggest that the distance between the centres of upwelling plumes is in the order of 2500 to 4000 km (McKenzie *et al.*, 1980; Watts *et al.*, 1985). It is worth noting again that in terms of melting at ocean ridges, and indeed in rifts, the area of most interest lies at the upper boundary to the convective system. Thus, while Courtney and White (1986) consider convection only in the upper mantle and others such as Olson *et al.*, (1987) consider plume generation to occur at the D" layer on the core-mantle boundary, these differences are of little direct importance to melt generation.

The scale, spacing and magnitude of the convective system, as observed from the upper boundary, may be summarised as follows (see McKenzie and Richter, 1976; McKenzie *et al.*, 1980; Richter and McKenzie, 1981; Hoffman and McKenzie, 1985; Craig and McKenzie, 1987; R. White and McKenzie, 1989):

(1) The thermally anomalous region of convective upwelling will, if axisymmetric, be between 1000 and 2000 km in diameter. In contrast relatively cold regions of downwelling within the convective system are likely to be more localised at the top

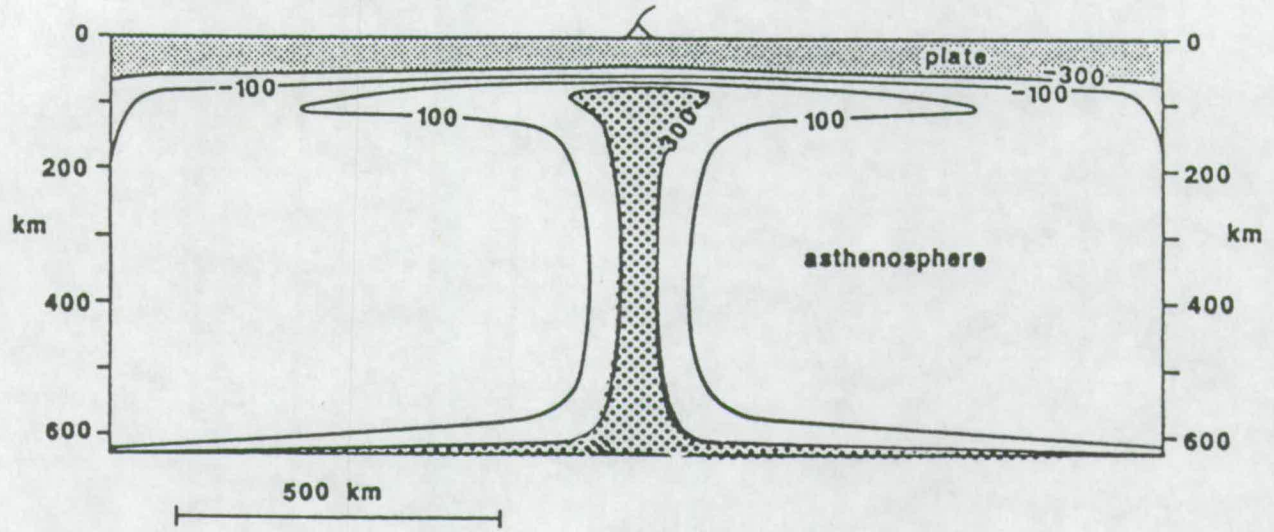

FIGURE 2.11 Temperature variations seen in cross-section through the Cape Verde swell from the best fitting axisymmetric convection model of Courtney and White (1986). Temperature anomalies are labelled in degrees Celsius with respect to the ambient asthenospheric potential temperature (~1280°C). Note the narrow central rising plume and the broad mushroom-shaped head of hot mantle deflected laterally over a distance of >1000 km by the overlying plate.

of the convective layer spreading out to similar 1000-2000 km dimensions at its base. Note that these dimensions are considerably smaller than those of the plates.

(2) The potential temperature within upwelling regions will vary from ~1380 to ~1580°C. Regions of downwelling are likely to be some 100 to 300°C cooler than ambient asthenosphere.

(3) Regions of upwelling are separated from each other by between 2500 and 4000 km. *This spacing is sufficiently wide that the horizontally averaged potential temperature of the upper mantle is close to 1280°C* even when the loci of upflow or down flow deviate from this by up to 200-300°C.

(4) The mean potential temperature of the asthenosphere is the horizontal average of the potential temperature across the whole convective system. For both internally heated and bottom driven convective systems this average is almost constant from the top to the base of the convecting region. The horizontally averaged potential temperature at the upper boundary, which is dominated by wide regions of upwelling material, is slightly hotter than the horizontally averaged potential temperature lower down, whereas at the lower boundary the converse is true (cf. Richter and McKenzie, 1981). These concepts are returned to in Chapter 3 when the upper boundary layers comprising the lithosphere are described. The region which lies between the elastic lithospheric plate and the convecting asthenosphere below is probably a region of small scale convection (see section 3.2 of Chapter 3).

Regions of upwelling within the convection system thus produce broad areas of anomalously high potential temperature at the base of the lithospheric plates. Higher potential temperatures beneath ocean ridges allow melting to take place at greater depths and to larger extents than normal. However, the temperature effect is not the only one of importance. Where a plume coincides with a ridge the dynamics require that upwelling is not passive in nature but that there will be a major active component as well (cf. Ribe, 1987; Ribe and Smooke, 1987; Watson and McKenzie, in prep.). The result is that the amount of melt produced at the given potential temperature in the steady state will far outweigh that predicted for passive upwelling alone (i.e. by McKenzie and Bickle, 1988). The shape of the melting region will be controlled by the shape and thermal structure of the plume and will be extremely important in determining the incompatible element budget of the magma (cf. Watson and McKenzie, in prep.). Quantification of the dynamic aspect of mantle plumes and its importance with respect to melting is a difficult problem which remains to be solved numerically in 3 dimensions; this discussion of the importance of plume dynamics for melting is extended in section 3.6.4.

The importance of convection with regard to the possible steady-state migration of volatile-rich small melt fractions rich in incompatible elements (section 2.6.4) is returned to in Chapter 7. If small amounts of melting occur at a volatile-controlled solidus in the asthenosphere then such melts may be easily facilitated by convective overturn in the steady state which could lead to a near continuous leakage of small melt fractions from the asthenosphere and which might explain geophysical observations of a zone of low shear wave velocity in the upper asthenosphere (e.g. Anderson, 1962; Ringwood, 1969).

2.8 Discussion.

Adiabatic upwelling of asthenosphere beneath mid-ocean ridges is a passive process, driven by plate separation, which leads to decompression melting and production of oceanic crust. Providing that the upwelling velocity is sufficient to maintain the adiabatic gradient then the thickness of the oceanic crust will be independent of spreading rate. Given that the flux of mantle into the melting region balances the sideways flux of oceanic lithosphere then the volume of melt produced and its composition will be independent of the shape of the melting region.

Simple analytical descriptions (parameterisations) of the results of equilibrium melting experiments on dry lherzolite allow the prediction of melt fraction and major-element composition when temperature and pressure conditions are known. Melt fraction increases as the solidus is progressively overstepped, either in terms of pressure or in terms of temperature. The major-element composition of the melt is strongly dependent on both the melt fraction and the pressure of melting. As either the amount of melting increases or the pressure of melting decreases melts become more tholeiitic in character. In upwelling asthenosphere melt fraction is increasing as pressure is decreasing.

The potential temperature (T_p) of the asthenosphere exerts the fundamental control on the amount of melt produced at an ocean ridge. The range in the average thickness of the oceanic crust (4.5-8.5 km) coupled with uncertainties in the value of ΔS (200-400 $Jkg^{-1} K^{-1}$) lead to an estimated value of 1280±40°C for the mean potential temperature of the asthenosphere. This value might be considered a minimum estimate given that the true melting process is more likely to be similar to Rayleigh melting.

Ridges which are located above the hot upwelling limbs of convection currents will be characterised by much greater thicknesses of crust generated, on

average, at greater pressures than at normal ridges. Such anomalous ridge segments will also have much shallower water above them. Ridge segments sited over cool downgoing limbs of the convective system will show the opposite characteristics; i.e. thinner crust and greater depths of water above them.

The simple parameterisations of McKenzie and Bickle (1988) may be used to predict, with some accuracy, the average major element compositions of primitive MORB. Empirical relationships between ridge depth and major element chemistry (cf. Klein and Langmuir, 1987) are also elegantly explained, and quantified, by the simple model.

The simple model is successful in explaining the volumes and major-element compositions of melts formed beneath spreading centres in part because it is independent of the precise composition of the source peridotite; i.e. the model will work as long as the peridotite melts on the dry solidus following the general melting scheme suggested by experiments. However, the model does not attempt to explain the trace element and isotopic characteristics of MORB.

The isotopic data from MORB suggest that very often at least two distinct components are required. One of these components, probably the most important by volume, shows a time integrated depletion in LILE and LREE relative to Bulk Earth estimates. This depleted component dominates the isotopic character of the melts at most normal ridge segments and has been termed the N-MORB source. In addition to the N-MORB component, many ridge basalts show isotopic evidence for a component which has undergone relatively less time integrated depletion and which sometimes shows evidence for time integrated enrichment relative to Bulk Earth. An input from this source component, for now termed the source of P-MORB, is seen in the isotopic character and the trace element concentrations of basalts from many anomalous ridge segments and ocean islands.

Although there is an implied relationship between P-MORB and elevated potential temperatures, often but not always supported by shallow ridge depths, the idea that plumes provide the enriched component of all P-MORB is not widely held. Many authors favour the concept of isotopic heterogeneity in the asthenospheric mantle on a range of scales from relatively small streaks to domains the size of continents.

While the isotopic character of MORB provides evidence for the evolution of its source(s) over time, fractionations between pairs of highly incompatible trace elements, such as U and Th, provide an insight into the melting process beneath ridges. The concept that very small amounts of melt can be rapidly segregated from the mantle is becoming widely accepted. The trace-element characteristics of MORB

are established by small amounts of melting of the source region to great depths beneath the ridge. The depth to which such small melt fractions are present in the upwelling asthenosphere will be controlled by the positions of the solidi for peridotite containing accessory phases such as dolomite and phlogopite and the thermal structure of the asthenosphere. The corner flow of the matrix beneath the ridge results in pressure gradients which focus most of the melt produced into a rather small region where it may mix. Much emphasis will be placed on the importance of the mobility of small melt fractions in Chapter 7 where they are looked to as a mechanism for the metasomatic enrichment of the continental lithosphere.

The major element compositions and volumes of melts produced at oceanic spreading centres are controlled by a small number of reasonably well-constrained parameters. MORBs are therefore amenable to quantitative modelling. Although the quantitative model has inherent errors because experiments cannot reproduce the dynamic polybaric melting process which operates beneath a ridge, the results obtained are surprisingly good. There are, however, some doubts as to how well the simple model operates in magmatic environments which are not so simple as the ocean ridge system.

CHAPTER 3

MELTING ASTHENOSPHERE DURING EXTENSION OF THE LITHOSPHERE

3.1 Introduction.

This thesis is primarily concerned with melting during rifting of the continental lithosphere. Volumetrically the asthenosphere is likely to be the most important source of basaltic melts produced by adiabatic decompression during extension of the lithosphere. For this reason, much discussion has already centred on the characterisation of asthenosphere as a source of basaltic magma (see Chapter 2). The asthenosphere may not be the only mantle source to undergo melting during rifting, but, it is the only source whose melting characteristics can, at this time, be predicted quantitatively from experiments. Discussion of alternative sources, much of it necessarily qualitative, is deferred until Chapter 7. This chapter is concerned only with those conditions which are required to produce melt from dry asthenosphere during rifting.

During rifting, decompression of the asthenosphere occurs in isostatic response to lithospheric thinning. The amount of decompression which takes place at any location will critically depend on the amount of lithospheric thinning which takes place and the rate at which this occurs. The thickness of the lithosphere prior to stretching is, as will be shown, also an important parameter which governs the formation of melt. The first part of this chapter is concerned with defining the thermal lithosphere and with predicting how it responds to stretching, both spatially and temporally. A number of parameters are then identified which are of critical importance in determining whether or not melting of the asthenosphere takes place during extension and, if it does, the volumes and compositions of the melt generated; e.g.:

(1) The amount of extension (β) and the shape of the lithospheric stretching envelope (see sections 3.3 and 3.4).

(2) The potential temperature of the asthenosphere (see sections 3.4 and 3.5).

(3) The thickness of the lithosphere prior to rifting (see section 3.7).

(4) The importance of multiple rift episodes and finite rates of extension (see 3.7 and 3.8).

The model of McKenzie and Bickle (1988) is used to predict the volumes and compositions of melts which accompany stretching of different types (coaxial/non-coaxial) over asthenosphere of different potential temperatures (normal/elevated). Throughout the chapter emphasis is placed on methods which might be used to externally constrain the values of important parameters such as the amount of extension (β) and the T_p in a basin such as the North Sea.

3.2 The Steady State Lithosphere: A Thermal Definition.

3.2.1 Introduction.

The key difference between magma formation in the mid-ocean ridge environment and that in continental rifts concerns the shape of the geotherm. At mid-ocean ridges, where lithosphere is absent, the steady-state thermal profile with depth is adiabatic in all but the upper few kilometres. In within-plate regions, where the asthenosphere is capped by lithosphere, the geotherm is dominated by conductive cooling.

A certain amount of confusion is evident in the literature concerning the meaning and use of the term *lithosphere* (for a recent discussion see R. White, 1988). The concept of a strong layer overlying a weak layer formed the basis of the original definition of Barrell (1914). In general there would be little disagreement over a definition of the lithosphere which described it as "the outer rigid layer of the Earth". Most of the arguments are concerned with the definition of the *base*; i.e. an isotherm, since long term strength must be temperature dependent.

3.2.2 The Plate Model.

One of the simplest definitions of the lithosphere was developed to explain the observations of decreasing heat-flow and increasing seafloor depth with increasing age of crust in the oceans (Parsons and Sclater, 1977). The subsidence of the seafloor and diminishing heat-flow can be simply and elegantly described in terms of a conductive cooling model in which asthenosphere is converted, via cooling, into lithosphere which sinks as it cools away from the ridge. In this model the lithosphere

is defined simply as the *outer conductive part* of the Earth which overlies a convecting and therefore *adiabatic interior*; the asthenosphere. No compositional difference between lithosphere and asthenosphere is implied by this model although the upper parts of the lithosphere will be different because they consist of asthenosphere which has been separated, upon melting, into basaltic crust and residual lherzolite (or harzburgite).

The variation in heat flow and bathymetry observed in the ocean basins can be reasonably accurately predicted using a variety of simple thermal models which differ chiefly in their description of the lower boundary condition; i.e. it may be described by a fixed temperature, a rheological change or a phase transition. The simplest model involves a *rigid plate of constant thickness and constant bottom temperature* which cools as it moves at constant velocity away from a hot vertical boundary at the ridge crest (e.g. McKenzie, 1967; Sclater and Francheteau, 1970). The variation in the temperature distribution within the plate with age and spreading rate can be calculated (analytically or numerically) by assuming a value for the thermal diffusivity and by neglecting internal sources of heat. The seafloor topography and ocean depth can then be calculated from a knowledge of the thermal expansion coefficient and by assuming isostatic equilibrium. The plate used in such models was modelled with a constant thickness in order to reproduce the approximately constant background heat flux and bathymetry observed in the older (>80 Ma) parts of the ocean basins. It was, however, realised that the plate is not created at its full thickness and that the model would, therefore, deviate from reality close to the ridge. As the model is thermal it is not concerned with real changes in plate thickness so long as the modelled thermal structure, assuming constant thickness, is able to predict the heat flow and bathymetry well.

The simple plate model described above clearly deviates from reality when the oceanic crust is less than 80 Ma, since the "plate" is not created at constant thickness. The alternative model of Parker and Oldenburg (1973) treated the plate, from the ridge outwards, as a cooling half-space in which the depth to any isotherm increased progressively from zero. Both models contain the relation that depth and heat-flow are proportional to $\sqrt{t}$ between 0 and ~80 Ma. The present concensus appears to be that the heat flow and bathymetric data are consistent with a rate of thickening of old plate (i.e. >80 Ma) which is considerably less than the cooling half-space model of Parker and Oldenburg (1973) would predict. The implication is that the lithospheric plate, created at the ocean ridge, approaches a condition of greatly slowed thickening or some steady-state constant thickness, within about 80 Ma.

There are, however, a number of problems with the plate model described above. Perhaps most important, in the context of the present discussion, is the fact that both the plate thickness and the temperature at its base are arbitrarily prescribed. Parsons and Sclater (1977) were able to invert depth, age and heat flow data from the North Pacific to obtain estimates of the equilibrium plate thickness (125±10 km), the temperature at its base (1333±274°C)[1] and the thermal coefficient of expansion ($3.28\pm1.19 \times 10^{-5}$°C^{-1}). Inversion of data from the North Atlantic gives very similar values for the three parameters. It should be noted that because each parameter is used in calculation of the next, errors propagate; hence the ~30% error on the thermal expansion coefficient. Parsons and Sclater took no account of errors in the values of assumed parameters, such as specific heat and diffusivity. The error bars on the three unknown parameters are therefore minimum errors. Of the three, plate thickness is best constrained, the thermal expansion coefficient agrees well with measured values for lithospheric minerals, but the temperature at the base of the plate is poorly constrained. It is perhaps unfortunate that a value of 1333°C for the temperature at the base of the lithosphere appears to have propagated through much of the literature seemingly without much attention to its inherent error (±300°C).

The implication of a constant plate thickness is that heat must be supplied to the base of the plate by some mechanism which is more effective than simple conduction of heat from a constant temperature convecting region to the base of the conductive layer. If this were not the case then the conductive layer would not cease to thicken. Some mechanism of periodically removing the base of the thickening plate and maintaining both constant heat flux and time-integrated thickness is required. This observation led Parsons and McKenzie (1978) to suggest that a convective instability is responsible for removing material from the base of the old conductively cooled plate and replacing it with hotter material. *Small scale convection* within a *thermal boundary layer* at or close to the base of the plate may therefore maintain the equilibrium lithosphere thickness.

---

[1] It is interesting that the independently determined normal potential temperature of the asthenosphere (1280°C; McKenzie and Bickle, 1988) should be equal to a real temperature of 1333.4°C at a depth of 125 km. In Chapter 2 (section 2.3.5). It seems likely that for consistency McKenzie and Bickle (1988) have assumed the value of 1333°C and have adjusted the value of ΔS to produce the correct volume of melt (7 km) at that temperature (see section 2.3.5).

3.2.3 The Boundary Layer Model.

Boundary layer theory (Parsons and McKenzie, 1978; Richter and McKenzie, 1981) leads to a more rigorous and geochemically more useful definition of the upper parts of the Earth than does the simple plate model. The assumption of a simple conductive geotherm within the lithosphere is an over-simplification of the thermal structure since small scale convection within the thermal boundary layer will allow for a smooth transition between the conductive portion and the convecting (adiabatic) interior. Despite this, the plate thickness or apparent lithospheric thickness remains a useful concept providing that the mean geotherm in the plate model (shown by the two straight lines which intersect at the broken line in Figure 3.1) is the same as the true time-averaged equilibrium thermal structure beneath old oceanic crust (curved line in Figure 3.1) as derived by Richter and McKenzie (1981). Even though the plate model description of the lithospheric thermal structure has been widely used (e.g. in models of basin subsidence) it is not clear that it is useful in a study of melt generation. From a geochemical viewpoint it is extremely important to determine those parts of the lithosphere/asthenosphere system which can be treated as isolated geochemical reservoirs and on what time scale this can be done.

It is convenient, therefore, to split the lithosphere/asthenosphere system into three parts on the basis of Péclet number[2] which may be used to express the relative importance of convection and conduction as modes of heat transport (Ranalli, 1987; McKenzie and Bickle, 1988). The upper part of the system is referred to as the *mechanical boundary layer* (MBL, Figure 3.1). The MBL has a more or less linear temperature gradient which is governed by conductive heat loss. In the steady state, the MBL is perhaps 100 km thick (McKenzie and Bickle, 1988); although, as is shown below, this steady-state MBL thickness depends on the viscosity of the uppermost asthenospheric mantle. Because of the isolation of the MBL from the convective part of the system, it constitutes the geochemists "lithospheric reservoir". Beneath the MBL, acting as a buffer to the convecting asthenosphere, is the *thermal boundary layer* (TBL, Figure 3.1). The TBL is a region where the Péclet number is close to critical and which maintains an horizontal isotherm by undergoing some convective overturn. The base of the lithosphere as defined by the thermal plate model lies within this region (as shown in Figure 3.1). Such a model will generate essentially the same heat-flow and depth relationships as the plate model with a

---

[2] The Péclet number (*Pe*) is defined as $Pe = vl/k$ where v is a characteristic material velocity, l is a characteristic length for the convecting system, and k is the thermal diffusivity. When $Pe \gg 1$ heat transfer is dominated by convection. When $Pe \ll 1$ conduction dominates.

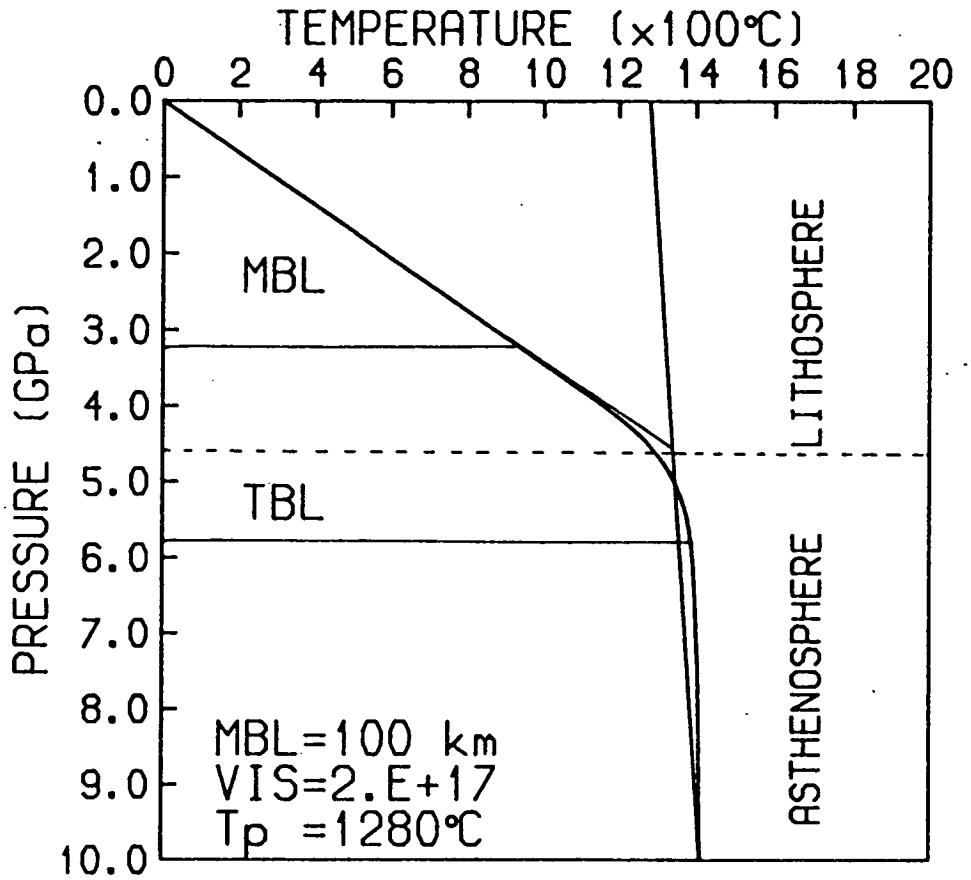

FIGURE 3.1 The horizontally averaged thermal structure of the lithosphere (convective geotherm; curved line) for a T_p of 1280°C, an interior viscosity of 2×10^{17} m^2 s^{-1} and a MBL (mechanical boundary layer) thickness of 100 km. Dashed line indicates the base of the lithosphere as defined by the plate model (see text) which lies within the TBL (thermal boundary layer). Near vertical line represents the adiabat for solid mantle. Note that the base of the plate (dashed line) is defined by the intersection of the adiabat with the projection from the conductive part of the geotherm. The maximum in T_p which occurs within and just below the TBL is a feature of all horizontally averaged convective temperatures which is produced by the fact that the average temperature at the top of the asthenosphere is dominated by the mushrooming heads of hot upwelling plumes (cf. McKenzie and Bickle, 1988).

gradual transition from conductive to advective geotherms if the intersection of the continuations of the conductive and advective curves is used to define the plate base (see Figure 3.1). The thickness of the TBL is controlled by its viscosity (which affects the characteristic velocity and Rayleigh number of the convective system); see Figure 3.2.

The viscosity of the upper mantle and of the TBL in particular is poorly constrained. Estimates for the value of the average kinematic viscosity[3] of the mantle vary considerably. The rates of post glacial rebound suggest that $2x10^{17}$ m^2 s^{-1} may be a good value for the bulk viscosity of the upper mantle; although such estimates of viscosity do depend weakly on the type of rheological model adopted (Ranalli, 1987). A variety of arguments, such as its relatively low shear wave velocity and the absence of a step in the geoid across fracture zones, favour values closer to $4x10^{15}$ m^2 s^{-1} for the uppermost part of the asthenosphere and therefore for the TBL (cf. Craig and McKenzie, 1987). Figure 3.2 shows the difference in effective plate thickness obtained for the same MBL thickness (100 km) at the two different viscosities. The lower viscosity ($4x10^{15}$ m^2 s^{-1}) gives rise to a thinner TBL which together with a MBL thickness of 100 km gives a convective geotherm that is very similar to a 125 km plate geotherm. With the higher viscosity ($2x10^{17}$ m^2 s^{-1}) the corresponding lithospheric plate, shown by the dotted line, is closer to 150 km thick essentially because conductive cooling is important to greater depths. Although the MBL is still 100 km thick with the higher viscosity the TBL is thicker and more of its thermal structure is controlled by conduction. The temperature at the base of the MBL is, therefore, correspondingly cooler. In order to obtain the same steady-state plate thickness (125 km) at the higher viscosity the thickness of the MBL must be reduced to ~70 km. To avoid confusion the combination of a viscosity of $4x10^{15}$ m^2 s^{-1} and a MBL thickness of 100 km is adopted, throughout the remainder of this thesis, as a steady-state standard for old oceanic areas.

However TBL overturn is achieved and whether it is continuous or episodic, it must do so on a time scale which is at least comparable with the thermal time constant for the oceanic lithosphere (~60 Ma). The nature and time scale of TBL overturn have important implications for possible geochemical reservoirs and for within plate processes of melt generation. If the TBL overturns steady state creep then it is not likely to be chemically different from the asthenosphere. If however, overturn is more episodic, and if small melt fractions have migrated into the region,

---

[3] Kinematic viscosity (m^2 s^{-1}) is equal to dynamic viscosity (Pa s) divided by density; for the mantle ~3300 kg m^{-3}.

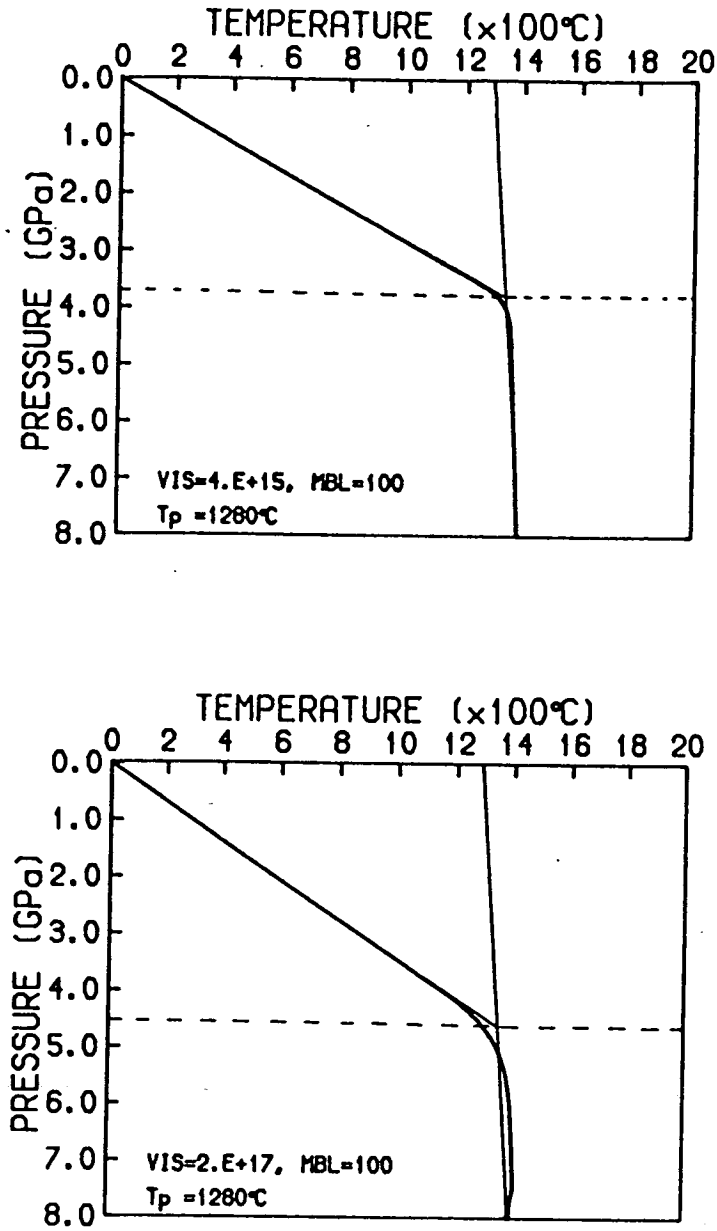

FIGURE 3.2 Convective geotherms for the lithosphere for Tp=1280°C and MBL=100 km but with different interior viscosities. Top diagram is for an interior viscosity of 4×10^{15} m^2 s^{-1} while bottom diagram is for an interior viscosity of 2×10^{17} m^2 s^{-1}. Note how the lower viscosity results in a thinner lithospheric plate because the conductive portion of the TBL is thinner.

then given the likely enrichment of such melts in LILE, the generation of a reservoir that is isotopically distinct from the asthenosphere may be possible (see Chapter 7).

The discussion has so far been concerned with modelling observations from the ocean basins and it is perhaps not obvious that the same models should be applied to continental lithosphere. One important observation is that in areas of continental lithospheric thinning, thermally controlled subsidence occurs with time constants which are virtually identical to those determined from the subsidence of the ocean basins. Therefore, the subsidence history of sedimentary basins such as the Michigan Basin (Sleep, 1971) and the North Sea Basin (Sclater and Christie, 1980; Barton and Wood, 1984) led Sclater *et al.* (1980) to suggest that the continental lithosphere in such areas has an equilibrium plate thickness of ~125 km; equivalent to a MBL ~100 km thick; assuming an interior viscosity of $4x10^{15}$ m^2 s^{-1}. It is important, however, to note that this does not necessarily mean that the MBL/lithosphere beneath any particular basin was at its equilibrium thickness prior to a given phase of extension (see Chapter 7). As will be shown later in this chapter the thickness of the MBL at the start of a rift episode is an extremely important parameter in so far as melting is concerned.

3.2.4 Shield and Non-Shield Regions.

The North Sea Basin, which becomes central to the discussion in Chapters 4 onwards, is inferred to have an equilibrium plate thickness of ~125 km and therefore a MBL thickness of ~100 km. It should, however, be pointed out that at least some continental rifts are formed on lithosphere of considerably greater thickness. The East African and Baikal rifts, for example, both occur in shield areas. Shield regions often display convincing evidence for lithospheric thicknesses in excess of 125 km. Lateral variations of the velocity of compressional (P-) and shear (S-) waves exist through the upper mantle to depths of ~700 km and have led Jordan (1978, 1988) to argue for the existence of lithosphere that is as least as thick as 400 km beneath shield regions. It is, however, not obvious how seismic velocities relate to the thermal structure of the Earth. Isotope studies of inclusions in diamonds (Richardson et al., 1984) provide better evidence for a thickness of MBL of at least 180 km beneath Archaean regions. McKenzie (1989) has been able to show that the geotherms in the Kaapvaal Craton, as defined by P,T estimates from mineral barometers and thermometers, are compatible with a MBL of ~150 km thick overlying a convecting interior (viscosity of $4x10^{15}$ m^2 s^{-1}) whose potential temperature is close to 1280°C; this corresponds to a plate thickness of ~170 km.

It appears that the equilibrium thickness of the continental lithosphere varies largely as a function of its age, tectonic history, and composition. The oldest, anorogenic, and potentially most refractory lithosphere (having been depleted in komatiitic liquids) occurs in the Archaean shield areas which are inferred to have the thickest steady-state MBLs (>150 km). Younger (Phanerozoic) orogenic areas, which may have similar lithospheric mantle mineralogy to the ocean basins, have steady-state MBL thicknesses close to 100 km.

3.2.5 Melting and the Steady-State Lithosphere.

It is a fact that basaltic melts are not appearing at the Earth's surface everywhere all of the time. Clearly rather special conditions are required for melting to occur and these conditions are not met in the steady state. In order for the asthenosphere to melt it must intersect its solidus (see Chapter 2). In the steady state the continental geotherm is a long way below the experimentally determined solidus for dry peridotite (Figure 3.3); thus if this solidus controls melting, it will not occur. If however, the solidus drawn in Figure 3.3 is not the true initiation of melting line, but represents only the line of experimentally visible melt generation (e.g. >5%) then small volumes of melt could occur widely in the mantle at significantly lower temperatures (for a given pressure)[4]. It is none the less clear that for significant volumes of melt to be produced from the asthenosphere the equilibrium system must be perturbed in one of three ways (Figure 3.3):

(1) By changing the position of the solidus, for example by the addition of water, as in the case of melting below island arcs;

(2) By increasing the potential temperature of the asthenosphere thereby moving the equilibrium geotherm to higher temperatures where it may intersect the dry solidus; this appears to be the case for ocean island volcanoes (e.g. Hawaii) located over hot spots (plumes) in the mantle, and may also be important for some segments of ocean ridges (Iceland) and continental rifts (East Africa);

(3) By raising the base of the lithosphere closer to the surface (i.e. by thinning), thus causing adiabatic upwelling of the asthenosphere below. This is the process operating at normal ocean ridges, where thinning is infinite, and is implied by the various stretching models for passively formed extensional sedimentary basins, discussed in the next section.

---

[4] As was discussed by McKenzie (1989) such small melt fractions are unlikely to carry sufficient heat to stray from the temperature of their surroundings. They will therefore usually freeze in the MBL (see also Latin *et al.*, 1990a and Chapter 7 of this thesis).

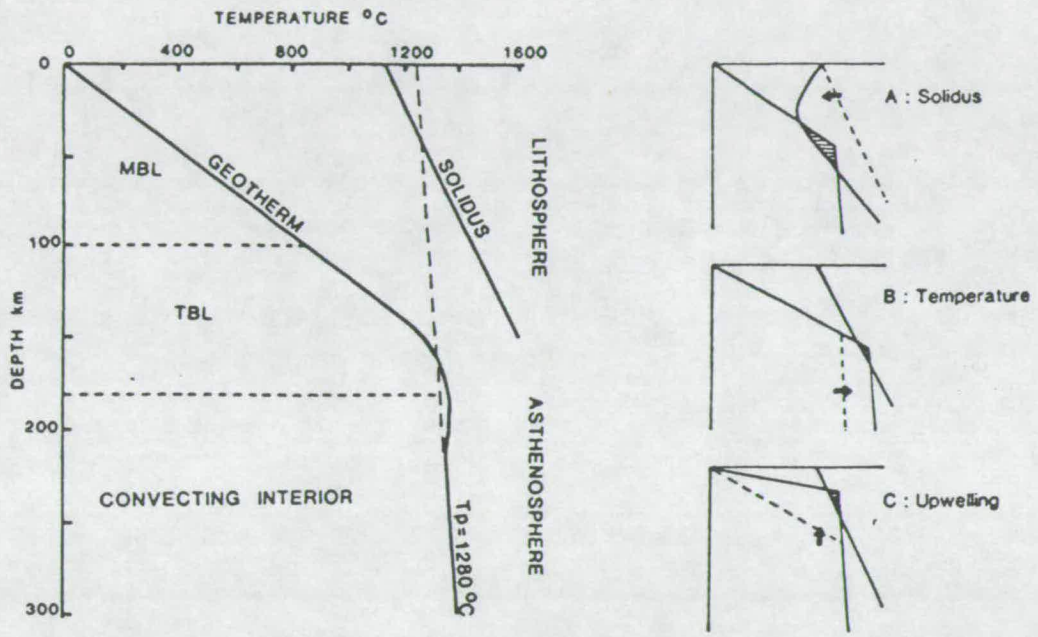

FIGURE 3.3 The horizontally averaged thermal structure of the lithosphere for T_p=1280°C, MBL=100 km, and a viscosity of $2x10^{17}$ m^2 s^{-1}. The corresponding upwelling curve, assuming no melting, is shown dashed. The solidus for dry peridotite from the parameterisation of McKenzie and Bickle (1988) is also shown. The highly schematic cartoons to the right of the main diagram show three end-member melting mechanisms: A. melting due to a change in solidus position, B. melting by raising the T_p, and C. melting by adiabatic upwelling. From Latin *et al.* (1990a).

In both the normal ridge and ridge+plume cases mentioned in Chapter 2, the amount of primary melt produced and thus its composition, is governed largely by potential temperature because upwelling continues all of the way to the seafloor as the plates separate; the entropy change on melting and mantle source composition are of secondary importance. In the case of a continental rift such as the North Sea, the amount of extension (β) is finite and so controls the degree of upwelling of mantle for any given potential temperature. The initial thickness of the MBL, prior to stretching, is also important. Clearly for thinner initial thicknesses the convecting asthenosphere is already closer to the dry solidus and so for a given amount of thinning will not need to rise as far before it starts to melt. Slow rates of extension will reduce the amount of melting if the rate of heat loss by conduction is faster than the upwelling velocity. The composition of the asthenosphere and the relevant solidus position are obviously of critical importance, but as has already been stated it is assumed, for now, that the asthenosphere is dry and produces melts which have the major element characteristics of the experiments used in the parameterisation of McKenzie and Bickle (1988). If the asthenosphere is dry then it is clear from Figure 3.3 that melting will always occur first in the TBL and then, with greater perturbations to the geotherm, in the asthenosphere.

In the following sections, different models of lithospheric attenuation are reviewed; attention is focussed specifically on two end member types of extension (coaxial and non-coaxial), how these models differ in their melt producing capabilities and how they might be discriminated between in real basins. The importance of differences in potential temperature, rates of extension, initial MBL thickness, and the effects of multiple stretching events are stressed.

3.3 Models of Lithospheric Attenuation.

3.3.1 Introduction.

Over the last 10-15 years considerable progress has been made in understanding the development of basins and rifts within continental plates. Such basins can broadly be divided into two types, flexural and extensional (Beaumont *et al.*, 1982). The formation of *flexure basins* does not involve thinning of the lithosphere but rather occurs in response to loading. Such flexure basins are therefore amagmatic and of no interest here. *Extensional basins*, on the other hand, such as the

North Sea Basin (Sclater and Christie, 1980; Barton and Wood, 1984; N. White, 1990) and the Pannonian Basin (Sclater *et al* ., 1980) clearly form by lithospheric stretching and most are magmatic; although the scale to which different extensional rifts are magmatically active varies by orders of magnitude.

Extensional basins are characterised by the deposition of fault controlled syn-rift sediments which are later overlain by substantial thicknesses of post-rift sediment. When the total sediment thickness is decompacted and the effect of its load on the basement is removed then the basement subsidence follows an exponential decay with time during the post-rift phase. The exponential curve is thought to be controlled by the cooling of upwelled asthenosphere (McKenzie, 1978) and suggests a thermal time constant comparable to that seen in the ocean basins.

Models for the development of extensional sedimentary basins essentially fall into two types:

(1) *Coaxial* stretching models in which thinning of the crust and subcrustal lithosphere occur symmetrically about the rift. The simplest of these is the *uniform* stretching model of McKenzie (1978) which was first applied to the North Sea Basin.

(2) *Non-coaxial* stretching models in which the zones of maximum crustal and subcrustal thinning are displaced from one another and which therefore are not, in terms of thinning, symmetric about the rift axis. This type of model was first proposed by Wernicke (1981, 1985) for account for different features observed in the Basin and Range Province, but has since been applied to the North Sea Basin and a number of passive margins.

The differences between these two types of model particularly with respect to their thermal consequences are detailed below. The importance of these differences in the generation of basaltic magmas from the asthenosphere in extensional sedimentary basins and on passive margins are discussed in section 3.4 (cf. Latin and White, 1990; Latin *et al.*, 1990b).

3.3.2 Coaxial Stretching Models.

The simplest coaxial stretching model is the uniform stretching model, proposed by McKenzie (1978). Figure 3.4 shows the main features of the uniform stretching model. The continental lithosphere is uniformly extended by a factor β. In the seismogenic upper crust, the upper 10 km or so (Jackson, 1987), extension is accommodated by block faulting. In the lower crust and mantle, extension takes place via penetrative flow. If extension is instantaneous then the temperature of any particle within the lithospheric column remains unchanged but every particle is

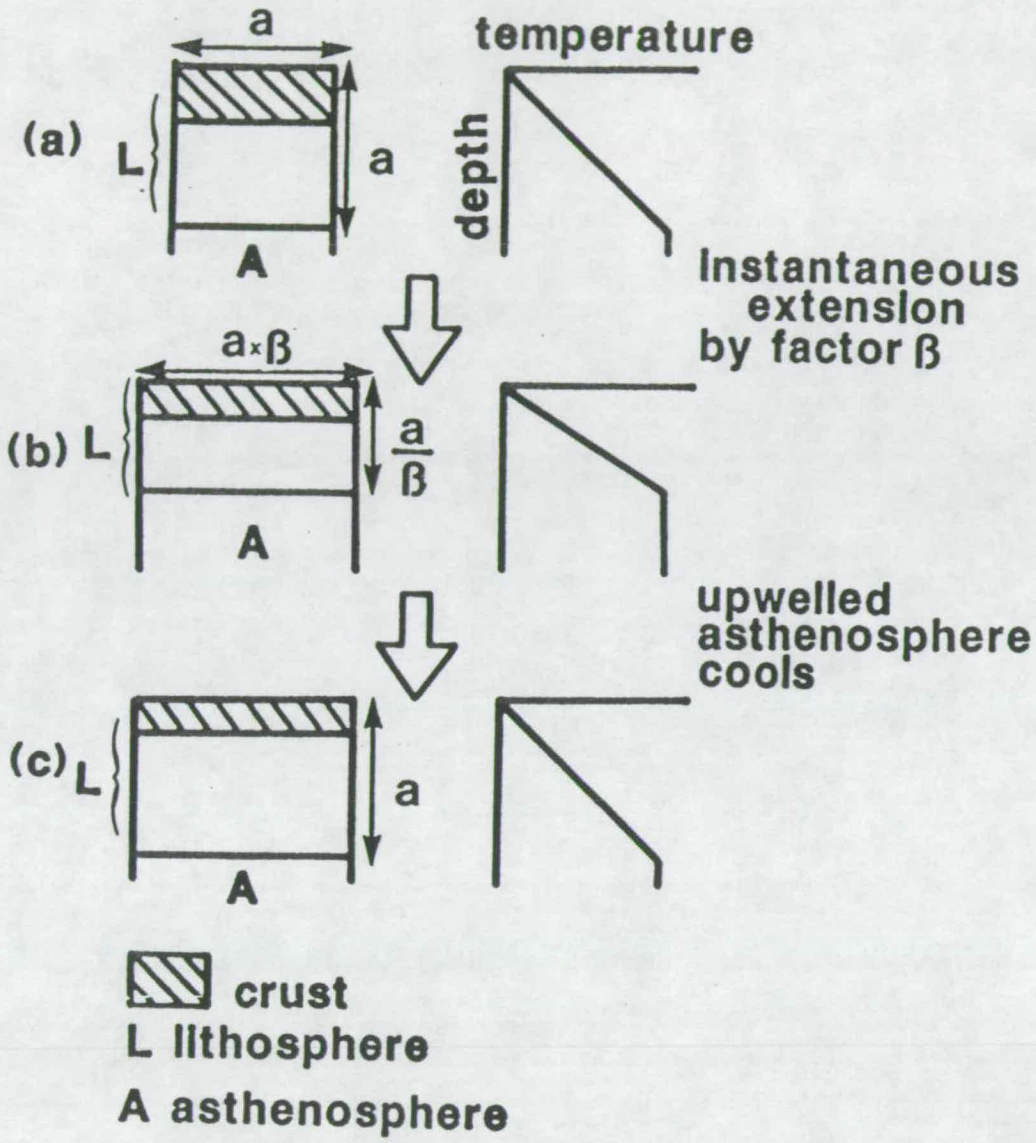

FIGURE 3.4 The uniform stretching model for the development of extensional sedimentary basins (McKenzie, 1978). (a) Column of thermally equilibrated lithosphere. (b) Instantaneous stretching. Note perturbation of the temperature gradient. (c) Perturbed temperature gradient gradually returns to steady state position. From N. White (1988).

brought to a shallower level lowering its pressure and resulting in a hotter geotherm and increased surface heat flow. Isostatic compensation of the lithospheric column after extension requires that the asthenosphere upwells. For a lithospheric plate initially ~125 km thick, provided that the crust is initially greater than about 20 km thick, isostatic compensation will also result in an initial fault-controlled subsidence (McKenzie, 1978).

After instantaneous thinning slow thermal subsidence will take place in isostatic response to the exponential cooling of the temperature perturbation. The surface heat flux will also decay back to its equilibrium value. The total subsidence of the basement (assuming no sediment loading) and the temporal variation of subsidence and heat flux with time are purely functions of β and the equilibrium geotherm. Figure 3.5 illustrates coaxial pure shear (the uniform stretching model). Both the initial lithospheric configuration immediately after instantaneous rifting and the final geometry after 300 Ma of conductive cooling are shown. The model in Figure 3.5 was calculated assuming a maximum extension factor of 2 in the centre of the basin. There are a number of important observations which can be used to discriminate between coaxial models and non-coaxial models:

(1) In pure shear or coaxial models the subsidence distribution is symmetrical about the rift. Symmetry is usually best observed in the thermal subsidence sediments whose distribution is less strongly controlled by rift topography (N. White, 1988; Klemperer and White, 1990).

(2) In the coaxial stretching model the ratio of thermal subsidence to initial subsidence is ~3:1 (N. White, 1989, 1990; Klemperer and White, 1990)

(3) In coaxial stretching models, because crustal and mantle thinning are superimposed, the maximum amount of asthenospheric decompression will occur in the basin centre. This will have profound implications for the location, character, and volume of rift-related basaltic melts; see section 3.4.

If stretching is strictly uniform then the crust and mantle lithosphere are thinned by the same amount, β, in all parts. The uniform stretching model can be tested because the value of β can be determined in a number of different ways (subsidence, crustal thinning, measured extension on faults, and heat flux) which should all give, to within error, similar values. The methods most commonly used are measurements of crustal thinning and measurement of extension on normal faults; basement subsidence cannot be reliably used in very young rifts and heat flux is of little value in rifts older than ~10 Ma. In some parts of some basins and on some passive margins the uniform stretching model appears to satisfy the observations and its predictions work very well; e.g. parts of the North Sea (Sclater and Christie, 1980;

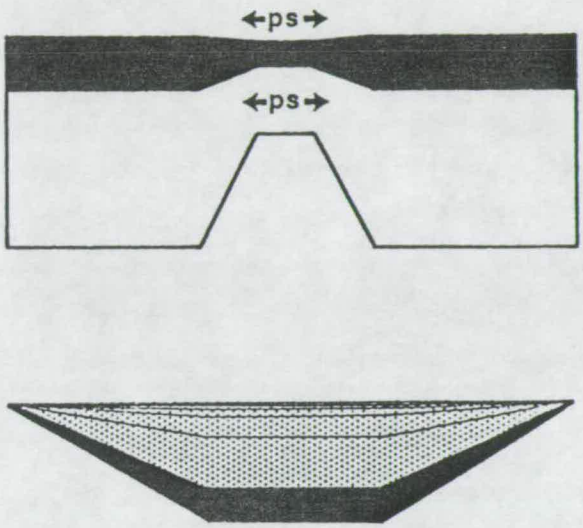

FIGURE 3.5 Results of numerical modelling of coaxial stretching which reaches a maximum β factor of 2 in the centre of the basin. Top diagram shows isostatically compensated crust (shaded) and lithospheric mantle. Bottom diagram shows subsidence with time. Initial subsidence (shaded) and thermal subsidence (stippled); isochrons are drawn for every 60 Ma. Bottom diagram is exaggerated by x20 and flat base of the basin is 100 km across. ps = pure shear. After N. White (1990).

Christie and Sclater, 1980; Wood, 1982; Barton and Wood, 1984; N. White, 1988; Klemperer and White, 1989; N. White, 1990), the Biscay margin (Le Pichon and Sibuet, 1981), the Baltimore margin (Sawyer *et al.*, 1982) and the Pannonian basin (Royden *et al.*, 1983).

Despite the applicability of the uniform stretching model in many areas, there are some parts of some rifts which, although apparently coaxial in character, have not undergone uniform stretching *sensu stricto* (see Chapter 6). For example the "Steer's Head" geometry observed in the onlap of the thermal subsidence sediments in the Viking Graben of the northern North Sea requires, given negligible flexural rigidity (Wood, 1982; Barton and Wood, 1984) or lateral conduction of heat, a depth dependent "two layer" stretching model (N. White and McKenzie, 1988).

In two layer stretching models the crust and mantle lithosphere are stretched by different amounts (Hellinger and Sclater, 1983). It is however, most important, in terms of mass and volume conservation, that the amounts of crustal (β_c) and mantle (β_m) thinning, when summed over the entire region, should balance; a consideration which has often been ignored (N. White and McKenzie, 1988). Thus in the model of N. White and McKenzie (Figure 3.6) in order for β_m to exceed β_c at the basin margins, and so generate the "Steer's Head" geometry, β_c must exceed β_m in the centre of the basin. Therefore, in White and McKenzie's two layer stretching model the stretching is coaxial even though it is not strictly uniform (see Chapter 6 for further discussion of stretching models).

The uniform stretching model described above is often adapted to incorporate rifting over a finite duration (cf. Jarvis and McKenzie, 1980). Rifting is rarely instantaneous and the rate of heat loss by conduction in a vertical sense becomes important when the duration of rifting exceeds the value of the thermal time constant for conduction (~$60/\beta^2$ Ma; Jarvis and McKenzie, 1980). The importance of finite rates of rifting, which is not confined to coaxial models, is further discussed in section 3.8 which concerns upwelling rates and melting (see also Chapters 6 and 7).

3.3.3 Non-Coaxial Stretching Models.

Non-coaxial models for extension of the lithosphere are those in which areas of maximum crustal and maximum subcrustal thinning are not directly superimposed. The most obvious of these models is the *lithospheric simple shear model*, first proposed by Wernicke (1981, 1985), which was developed to explain observations based on field mapping, seismic experiments and considerations of magmatism and topography in part of the Basin and Range province. The lithospheric simple shear

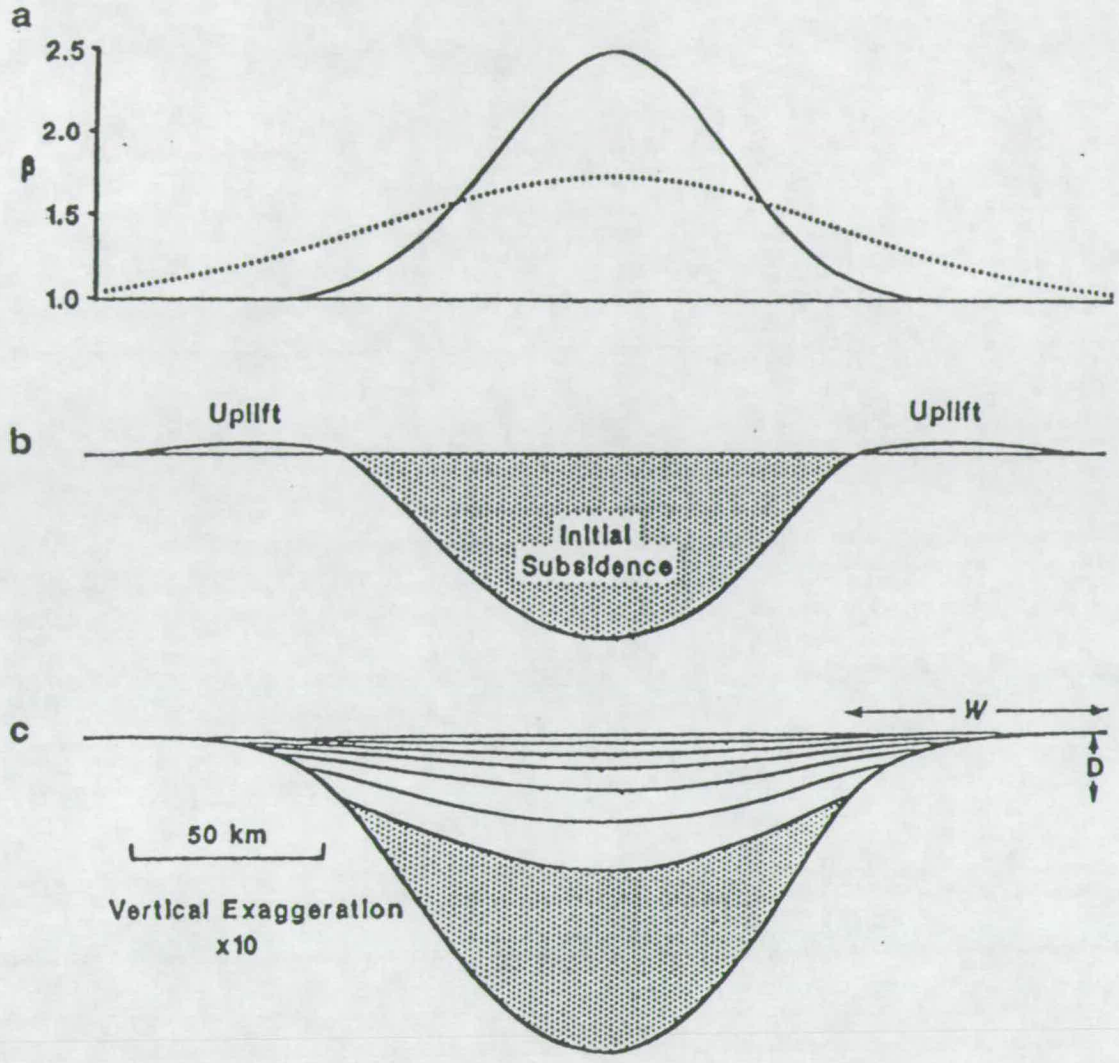

FIGURE 3.6 Distributed stretching modelled using a Gaussian function to describe the variation in crustal and mantle stretching. **a.** The variation of β_c (solid line) and β_m (dotted line) with distance across a model rift. **b.** Initial subsidence showing flank uplift. **c.** Total subsidence 150 Ma after rifting (isochrons every 25 Ma). W and D are horizontal extent and thickness of onlap. After N. White (1988) and N. White and McKenzie (1988).

model assumes that extension is accommodated by slip along a very low-angle (less than 30°) normal fault or "detachment" which penetrates the entire lithosphere (Figure 3.7). Since it was first proposed the lithospheric simple shear model has been widely applied throughout the Basin and Range province (e.g. Bartley and Wernicke, 1984; Wernicke *et al.*, 1985; Howard and John, 1987) as well as to other sedimentary basins and passive margins; e.g. the North Sea (Beach, 1986; Beach *et al.*, 1987; Gibbs, 1987,1990), the East African Rift (Bosworth, 1987) and passive margins in general (Lister *et al.*, 1986, 1990).

Figure 3.7 shows the main features of the lithospheric simple shear model as envisaged by Wernicke (1981, 1985). Extension in this model is largely accommodated by slip along the detachment fault which divides the lithosphere into two "plates"; an upper plate and a lower plate. As extension proceeds the upper crust in the upper lithospheric plate breaks into a number of fault-bounded blocks while the lower plate remains undeformed. The undeformed nature of the lower plate is extremely important because it means that thinning in the crust and mantle must all occur in the upper plate and that *crustal and mantle thinning will be spatially separated.* As the lower plate is unloaded it responds isostatically causing some uplift within the rift zone and generating a downward steepening profile on what was an originally planar detachment fault. Uplift of the upper plate also occurs in areas distant from the crustal rift, where the mantle is thinned more than the crust ($\beta_m > \beta_c$). As with the uniform stretching model there are two stages of development. First there is a rift stage in which subsidence is fault controlled and occurs in direct response to the thinning of the crust. This is followed by a thermal subsidence stage as the upwelled asthenosphere cools and the base of the lithospheric plate returns to its original position.

Over the past eight years there has been considerable debate concerning whether or not the lithospheric simple shear model (or other types of non-coaxial model) is more applicable to basin development than coaxial (or pure shear) models. A variety of arguments have been used to try to distinguish between the two end-member models. For example, Jackson (1987) showed on the basis of seismological data from areas of active extension such as the Aegean, Yunnan (China), East Africa, Suez, and the Basin and Range, that the majority of active normal faults do not have dips of <30° and that they are approximately planar down to the base of the seismogenic layer (~10 km in most regions) where brittle failure ends. On the other hand, according to Gibbs (1987) and Beach (1986), unmigrated deep seismic reflection data from the northern North Sea can be interpreted to show evidence in favour of low angle detachments from the presence of some strong shallow angle

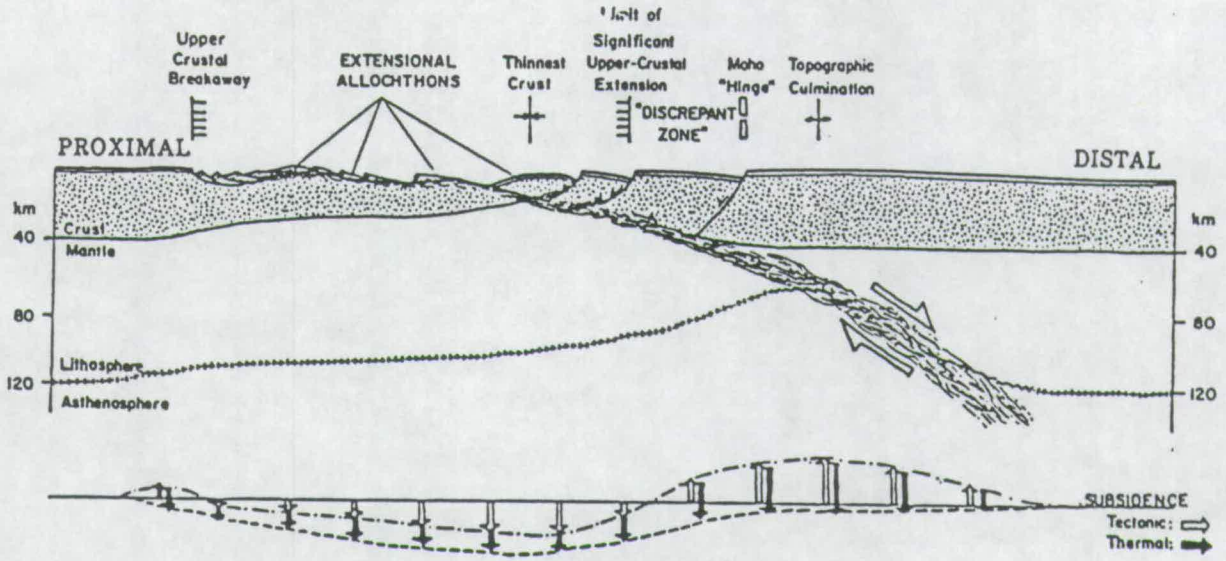

FIGURE 3.7 Cartoon illustrating the lithospheric simple shear model. Details of crustal deformation and the qualitative thermal consequences of lithospheric simple shear are shown. After Wernicke (1985).

reflectors penetrating the mantle and because of zones of differing reflectivity. Diametrically opposed to Gibbs (1987) and Beach (1986), Klemperer (1988) argues that the data when depth-migrated are quite consistent with the uniform stretching model because the crust appears to have been thinned symmetrically and because both syn-rift and post-rift sediments are superimposed directly on top of thinned crust.

More recently numerical models of the thermal response of the lithosphere to simple shear have provided quantitative predictions (for a given amount of horizontal extension) of the distribution and extent of asthenospheric upwelling, and the distribution and thickness of initial and thermal subsidence through time (Voorhoeve and Houseman, 1988; Buck *et al.*, 1988; N. White, 1988, 1989; Latin and White, 1990; Latin *et al.*, 1990b). In the numerical models the lithosphere is assumed to deform via instantaneous slip along a planar low-angle normal fault, and heat flow is assumed to be one-dimensional (cf. N. White, 1988, 1989).

Figure 3.8 (from N. White, 1988) shows how for the purpose of the thermal model the lithosphere, immediately after slip on the fault, is divided into 7 distinct sections. An assumption of negligible flexural rigidity, and therefore local Airy isostasy, allows each vertical column within the 7 sections to be treated independently in the calculations. For a given amount of extension ($\in$) the values of β_c and β_m can be calculated in each vertical column. For example, in column C-D β_m=1 (no thinning in the mantle) and β_c is found by dividing the initial crustal thickness by the final crustal thickness. The isostatic and thermal response to stretching in each column, and therefore across the whole region can then be calculated using equations which are similar to McKenzie's (1978).

Figure 3.9 shows the results of the numerical calculations assuming that stretching took place 300 Ma ago and that the maximum value for β_c, achieved in column C-D, was equal to 2 (see footnote [5]). According to these calculations, lithospheric simple shear will produce crustal thinning that is symmetric about the basin and the locus of initial and thermal subsidence sediments will coincide, spatially, with the crustal rift; so eliminating Klemperer's (1988) main arguments against simple shear for the North Sea. However three important observations arise from the modelling which may allow the distinction between pure and simple shear models in the field:

---

[5] Note that β_c and β_m can only be related to $\in$ when the initial dip of the detachment fault is known but, importantly, also note that provided the fault is initially planar its dip will not effect the conclusions of the thermal model. See the discussion on dip angle and melting in the next section.

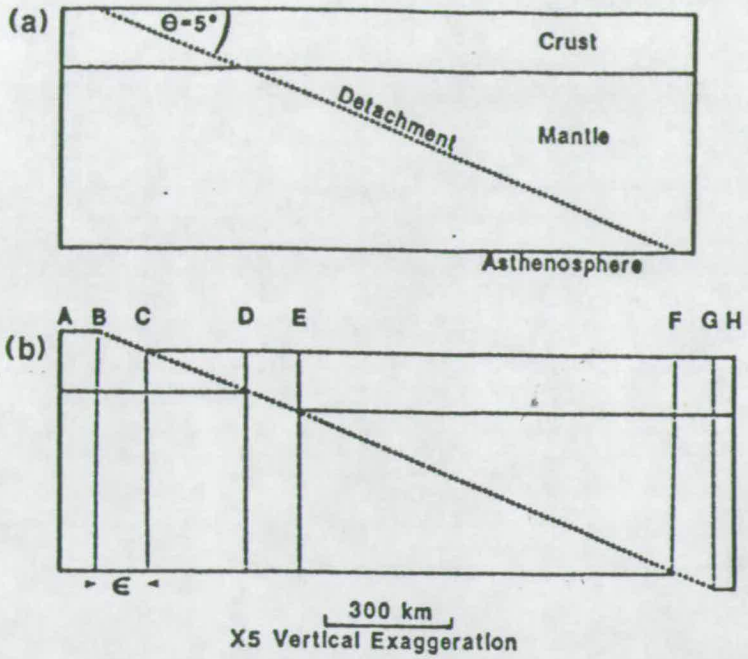

FIGURE 3.8 (a) Cross-section of lithosphere with incipient planar detachment fault. (b) Same section after extension by simple shear but before isostatic compensation. After N. White (1988).

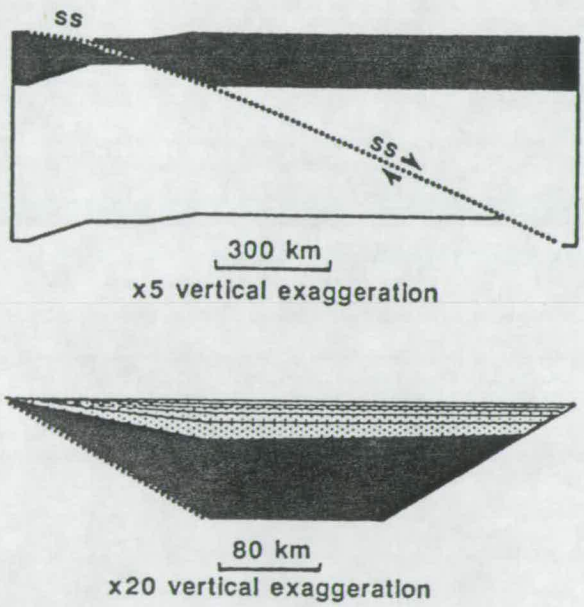

FIGURE 3.9 Results of numerical modelling of lithospheric simple shear in which the crustal stretching which reaches a maximum β factor of 2. Top diagram shows isostatically compensated crust (shaded) and lithospheric mantle. Bottom diagram shows subsidence with time. Initial subsidence (shaded) and thermal subsidence (stippled); isochrons are drawn for every 60 Ma. ss = simple shear. After N. White (1990).

(1) Whereas in coaxial/pure shear models the sediment sequences are symmetrically distributed about the rift (Figure 3.5), in the simple shear model both initial and thermal subsidence packages pinch out towards the detachment; this would give rise to a marked asymmetry within the sedimentary fill of a mature simple shear basin.
(2) In the pure shear models, particularly the uniform stretching model, the thickness of thermal subsidence sediment predicted is greater than the thickness of the initial subsidence package (in Figure 3.5 the ratio is ~3:1 for instantaneous stretching). In the simple shear model, however, the converse is true and the basin fill should be dominated by syn-rift sediments which should be ~3 times more abundant than sediments of the post-rift/thermal sequence. The lesser importance of thermal subsidence in the simple shear model relates to the distributed nature of the extension; unlike the pure shear model all of the thinning does not occur in the same place.
(3) Following on from the last point, it is important to note that in the simple shear model the region of maximum asthenospheric decompression occurs away from the rift axis. In this case any melting would be expected to occur first in the asthenosphere in the region below E-F in Figure 3.8. The full implications of this model, as opposed to the pure shear model, for the locations, compositions and volumes of magmas are discussed in detail in the next section.

3.4 Extension by Pure Shear at Normal T_p.

Adiabatic decompression of normal potential temperature asthenosphere, as it wells up in isostatic response to lithospheric thinning, will lead to melting if the perturbed geotherm intersects the relevant solidus. In this chapter the dry solidus and X,T,P functional forms of McKenzie and Bickle (1988) are used and convective geotherms are derived from the parameterisations of Richter and McKenzie (1981) as discussed in McKenzie and Bickle (1988).

Figure 3.10 shows what happens to the steady state convective geotherm when the lithosphere (MBL=100 km) is instantaneously and uniformly thinned by different amounts (β). Note that melting will not occur on the dry solidus until the asthenospheric mantle (T_p=1280°C) has decompressed to a pressure of ~1.45 GPa (~45 km); for uniform stretching of lithosphere with an initial MBL thickness of 100 km (an effective plate thickness of ~125 km) this requires β to exceed 2.75. Whether extension is uniform or non-uniform, coaxial or non-coaxial, at normal potential

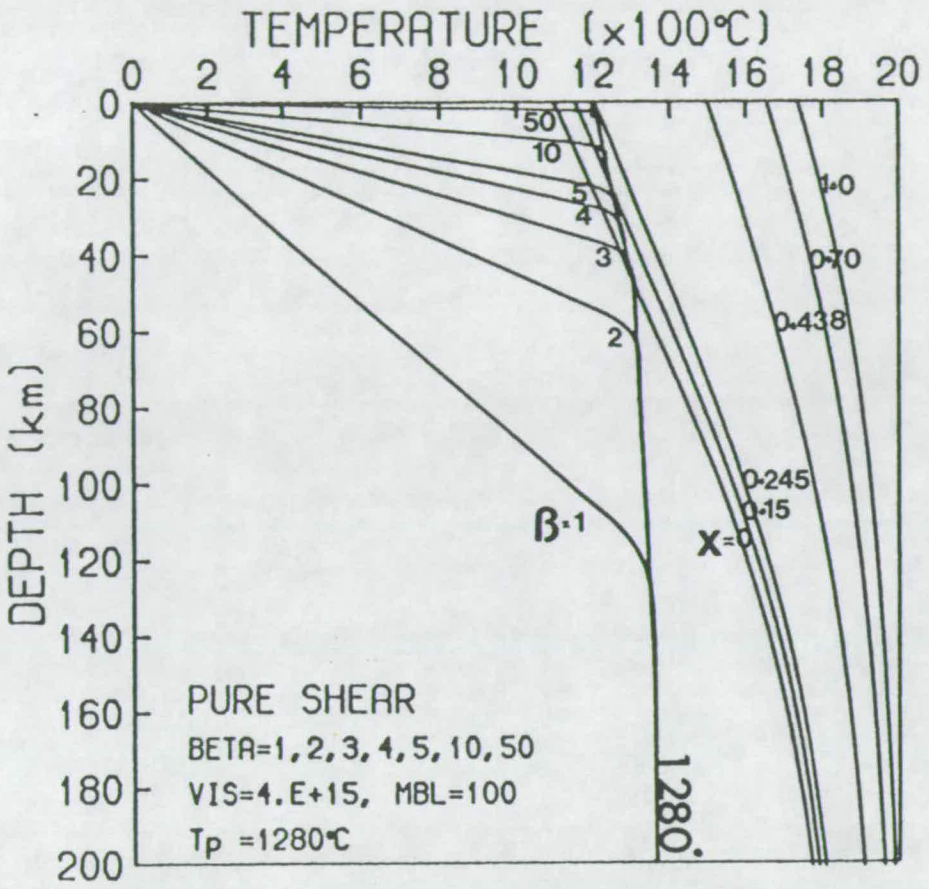

FIGURE 3.10 Convective geotherms (T_p=1280°C, MBL=100 km and interior viscosity of $4x10^{15}$ m^2 s^{-1}) which have been stretched by instantaneous pure shear for different values of β (1,2,3,4,5,10, and 50). Lines of constant melt fraction X are shown for 0, 0.15, 0.245, 0.438, 0.70, 1.0 by weight.

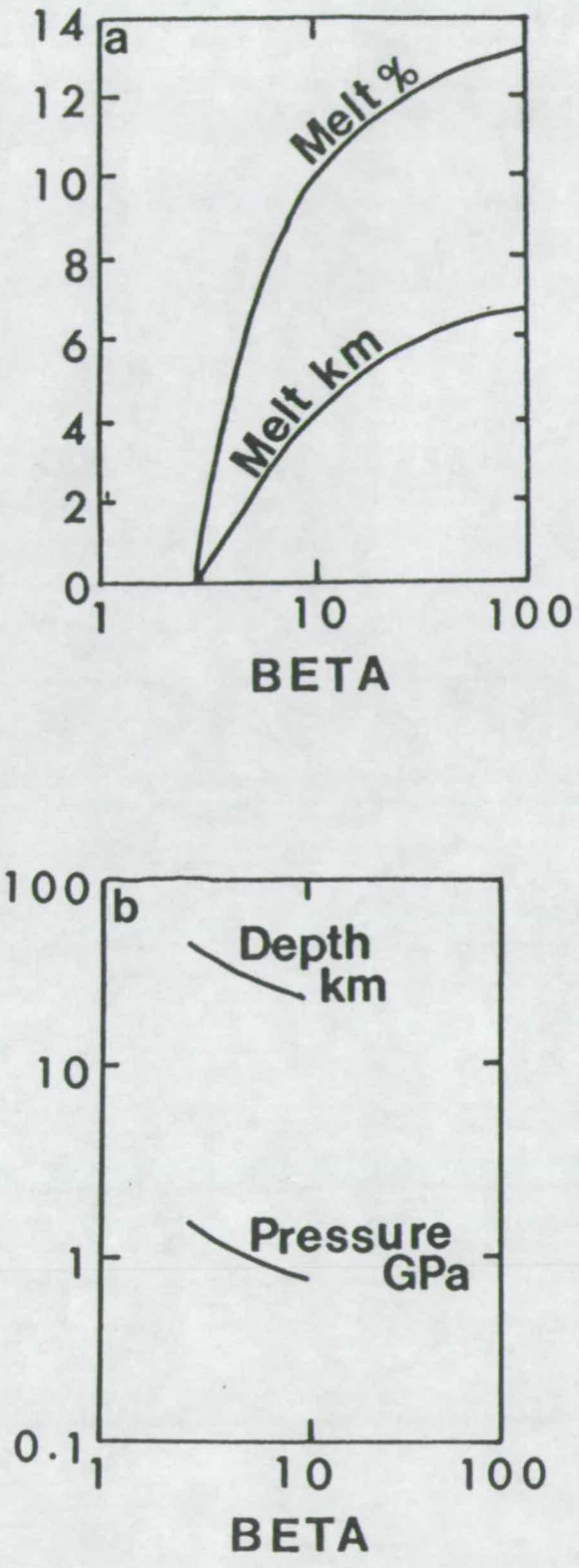

FIGURE 3.11 T_p=1280°C; MBL=100 km; viscosity=$4x10^{15}$ m^2 s^{-1}. Top: Melt thickness (km) and average percentage melting of the point and depth average as a function of β. Bottom: Average pressure in GPa and average depth in km of point and depth average melt fraction as a function of β.

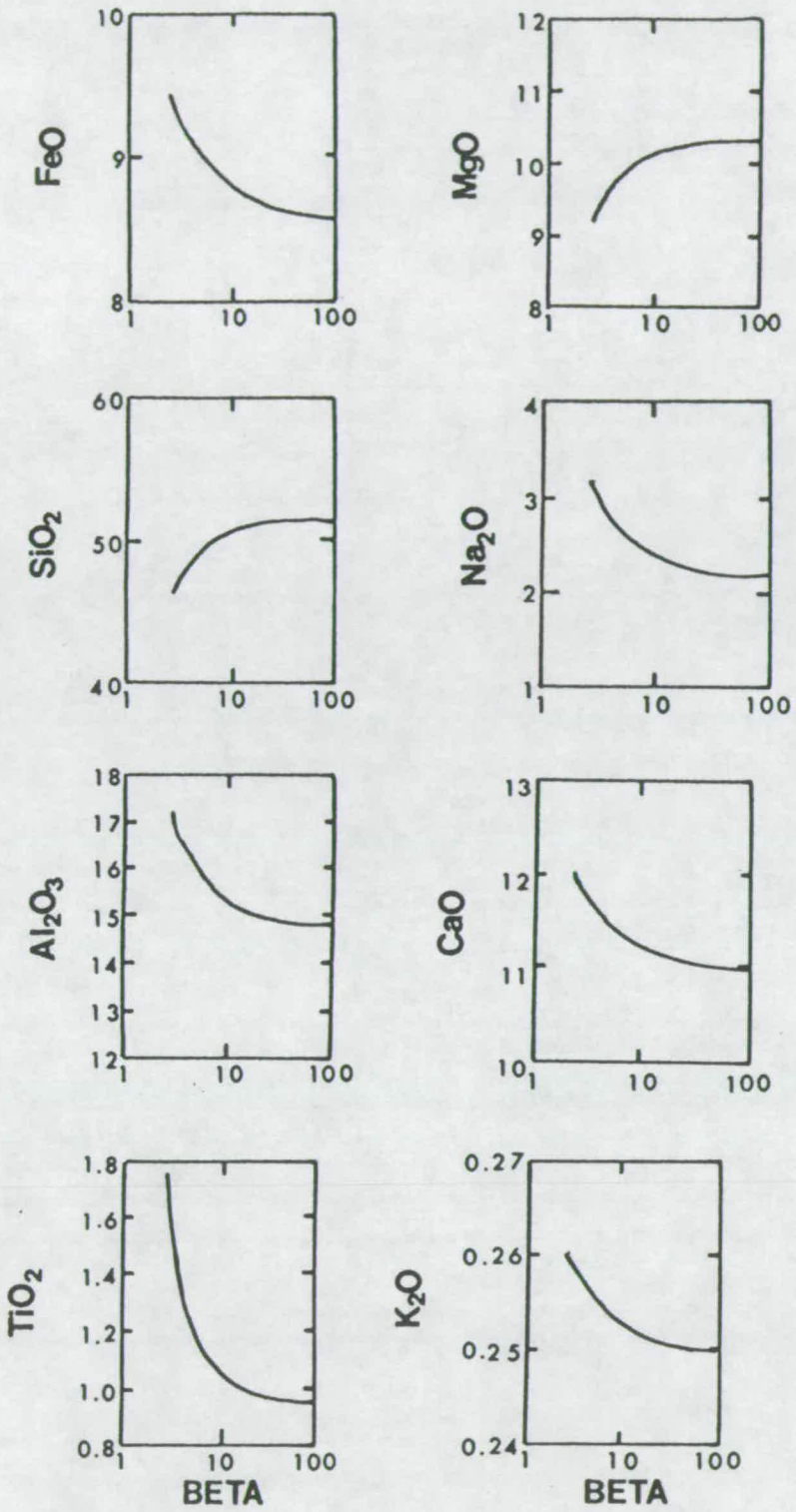

FIGURE 3.12 Point and depth average melt compositions (as wt.% oxides) plotted as a function of β using the same model parameters as in Figure 3.11. Compositions were generated from the parameterisation (a) of McKenzie and Bickle (1988).

temperatures melting should not occur until enough thinning has taken place to allow decompression to 1.45 GPa.

Notice in Figure 3.10 that for values of $\beta>2.7$ the knee in the stretched geotherm becomes truncated as latent heat is lost on melting. The path of the geotherm within the melting region is calculated, assuming isentropic upwelling, in exactly the same manner as it is beneath ocean ridges and consequently has the same dependence on the entropy change (ΔS) on melting.

Figure 3.11a shows how the amount of melt produced (melt thickness) and its point and depth average melt fraction vary as a function of β. When β exceeds ~50 the lithosphere is thinned to less than 2.5 km and the melt thickness and average extent of melting are those of a normal oceanic ridge. Notice in Figure 11b that the average pressure and depth of melting decrease smoothly as β increases.

The point and depth average melt compositions predicted using the compositional parameterisation are shown as different oxides (in wt.%) for a range of β values in Figure 3.12. Note how, as β and therefore the extent of melting increases, so do the concentrations of SiO_2 and MgO in the point and depth average melt composition. The concentrations of all other oxides in the melt decreases (they are diluted) as the amount of stretching increases. The general prediction is, as would be expected, more silica deficient, alkaline magmas at smaller values of β and small extents of melting. The importance, in terms of melt chemistry, of melting at relatively low pressures, because of the normal potential temperature, is stressed when compositions at different temperatures are compared in section 3.6.

3.5 Extension by Simple Shear at Normal T_p.

In the simple shear model, just as with pure shear, the largest extents of melting will occur where there is greatest decompression of the asthenosphere; i.e. in the *region of maximum mantle thinning*. The region of maximum mantle thinning occurs directly below and beyond the region where the detachment fault passes along the Moho and into the lithospheric mantle; i.e. where the crust returns to its normal thickness, between E and F in Figure 3.8. The value of β_m for this region can be related to the maximum amount of thinning of the crust (β_c) which itself relates to the horizontal extension ($\in$) between the two plates and the dip of the detachment fault (θ) provided that the plates separate cleanly.

Figure 3.13 shows the lithosphere after extension along a planar detachment fault before the section has been isostatically balanced. Crustal thinning is related to detachment dip and horizontal plate separation by

(E:3.1) $$\beta_c = t_c/(t_c - \in \tan\theta)$$

where t_c is the thickness of the crust prior to extension and $\in \tan\theta$ is equal to the vertical separation of the two plates, y_c in Figure 3.13. Similarly the amount of mantle thinning is found from

(E:3.2) $$\beta_m = (a - t_c)/(a - t_c - \in \tan\theta)$$

where a is the thickness of the lithospheric plate prior to extension. Equation E:3.1 can be in terms of $\in$ to give

(E:3.3) $$\in = t_c(1 - 1/\beta_c)/\tan\theta$$

which when substituted into E:3.2 allows β_m to be expressed as a function of β_c such that,

(E:3.4) $$\beta_m = (a - t_c)/(a - 2t_c - 1/\beta_c).$$

From E:3.4 it is clear that when thinning occurs as the result of slip along an initially planar fault then, for a given value of β_c, the value of β_m is independent of the dip of the detachment and the horizontal separation of the two plates.

Using equation 3.4 the maximum value of β_m, occurring in region E to F in Figure 3.8, can be calculated forny maximum amount of crustal thinning. In the region of maximum mantle thinning the crust remains intact and therefore the effective thinning of the whole lithosphere in that region is given by

(E:3.5) $$\beta_{lith} = (a\beta_m)/(a - t_c + \beta_m t_c)$$

where β_{lith} is the stretching factor for the whole lithosphere (crust + mantle) in the region of maximum mantle thinning. Note that, as is consistent with the crust not being thinned, β_{lith} remains finite even when β_m tends to infinity. In terms of melt generation it is important to be able to calculate the pressure at the base of the

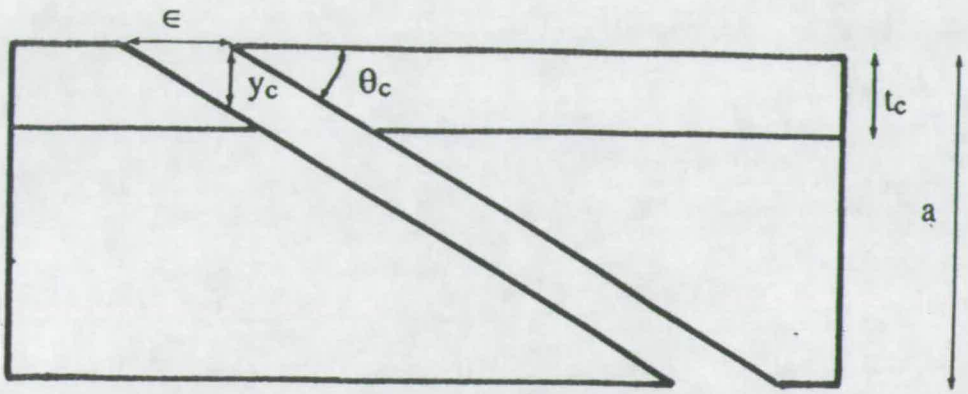

FIGURE 3.13 Extension ($\in$) along an initially planar detachment fault which has a dip of q_c in the crust and the same dip in the mantle. Diagram shows lithospheric section after extension but prior to isostatic balancing; y_c, vertical separation in the crust, t_c, crustal thickness, a, lithospheric thickness.

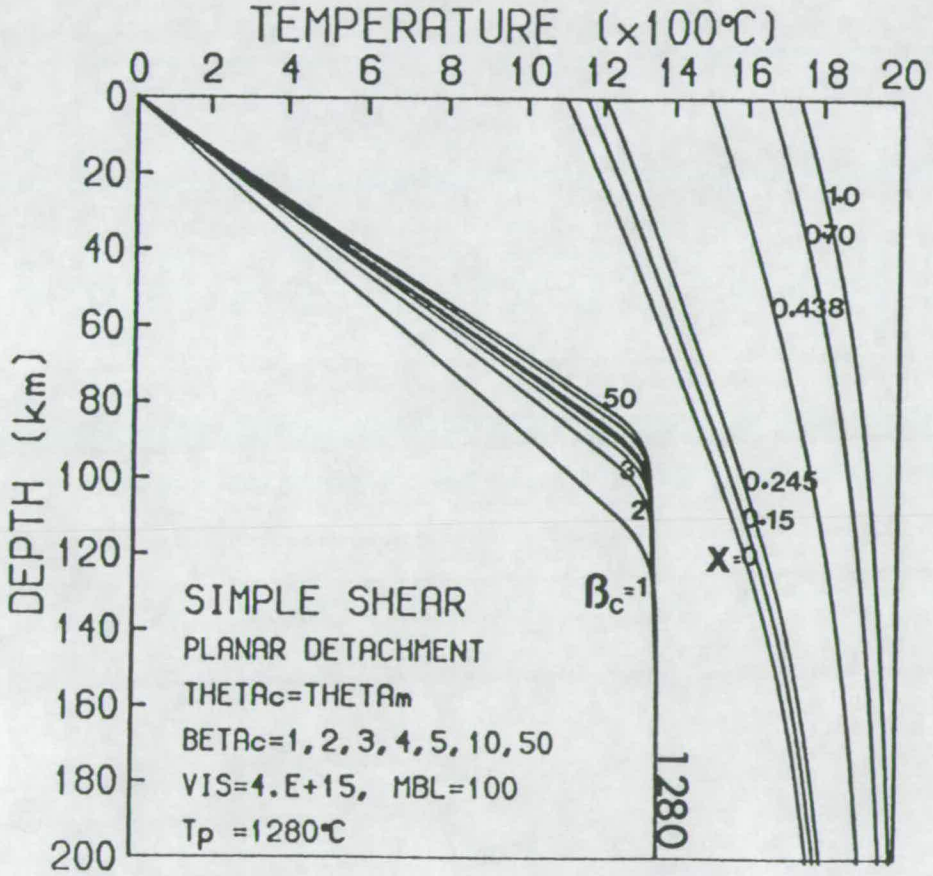

FIGURE 3.14 Convective geotherms (T_p=1280°C, MBL=100 km and interior viscosity of 4×10^{15} m^2 s^{-1}) which have been stretched by instantaneous simple shear along a planar detachment fault for different values of β_c. Notice that no melting takes place even when β_c is at infinity.

lithosphere; this is easily obtained from the equations above by substituting in the appropriate densities of crust and mantle.

Figure 3.14 shows what happens to the steady state geotherm when the lithosphere (MBL=100 km) is extended along an initially planar detachment fault. The different geotherms correspond to different values of β_{lith} but are more usefully labelled with values of β_c as this is the parameter most easily measured (by crustal thickness or faulting) in many stretched basins. For normal potential temperatures it is clear that the perturbed geotherm does not intersect the dry solidus even when the values of crustal thinning are extremely large (e.g. β_c=50). No asthenospheric melt is produced because the effective thinning of the lithosphere (<1.4) is such that the base is still at ~90 km (~3 GPa). This is in marked contrast to the uniform stretching model in $\beta_{lith}=\beta_c$ resulting in oceanic crust when β=50 at normal temperatures. Note that although the calculations are critically dependent on the value used for t_c, because of its relatively low density, the lithosphere would need to be almost entirely made of crust before upwelling as a result of isostatic compensation at β_c~50 could result in melting on the dry solidus at normal temperatures!

So far the modelling has only be concerned with an initially planar detachment fault. It is, however, just as simple to model the consequences of extension along a fault which initially dips differently in the crust and mantle. Figure 3.15 shows a situation, prior to isostatic balancing, where the dip of the fault in the crust (θ_c) is different to that in the mantle (θ_m), i.e. the fault is initially non-planar. An equation similar to 3.4 can be written to obtain β_m from β_c in this situation (cf. Latin and White, 1990; Latin et al., 1990b),

(E:3.6) $$\beta_m = (a-t_c)/\{a-t_c-t_c(1-1/\beta_c)\tan\theta_m/\tan\theta_c\}.$$

Figure 3.16 shows the results of this calculation with β_c and β_m plotted against one another for a range of θ_m (from 5° to 45° in steps of 5°) where θ_c is constant in each diagram. Note from these diagrams that the same values of β_m and β_c are obtained if the fault is planar ($\theta_c=\theta_m$), whatever the dip. If the fault more than doubles its dip on passing from crust to mantle, then it is possible to intersect the dry solidus at normal temperatures if the change in dip and the amount of crustal thinning are very large (Figure 3.17). Given that the original lithospheric simple shear model (Wernicke, 1981, 1985) proposed a *planar low-angle fault* (<30°) and that in terms of rheology a shallowing of dip is more likely, then such circumstances are unlikely to be realistic!

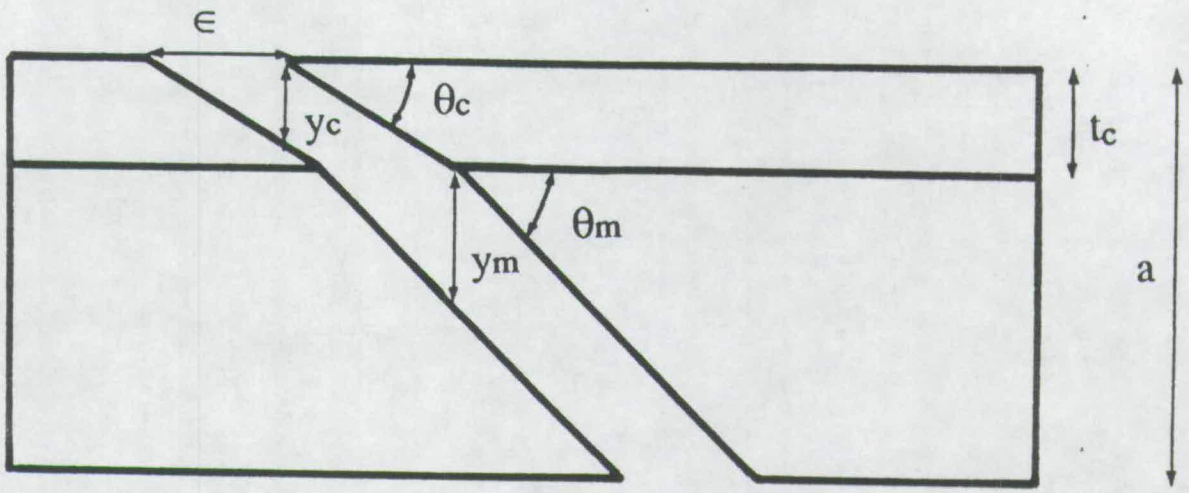

FIGURE 3.15 Extension (∈) along an initially non-planar detachment fault with dip θ_c in the crust and dip θ_m in the mantle. Diagram shows lithospheric section after extension but prior to isostatic balancing; y_c, vertical separation in the crust, y_m, vertical separation in the mantle, t_c, crustal thickness, a, lithospheric thickness.

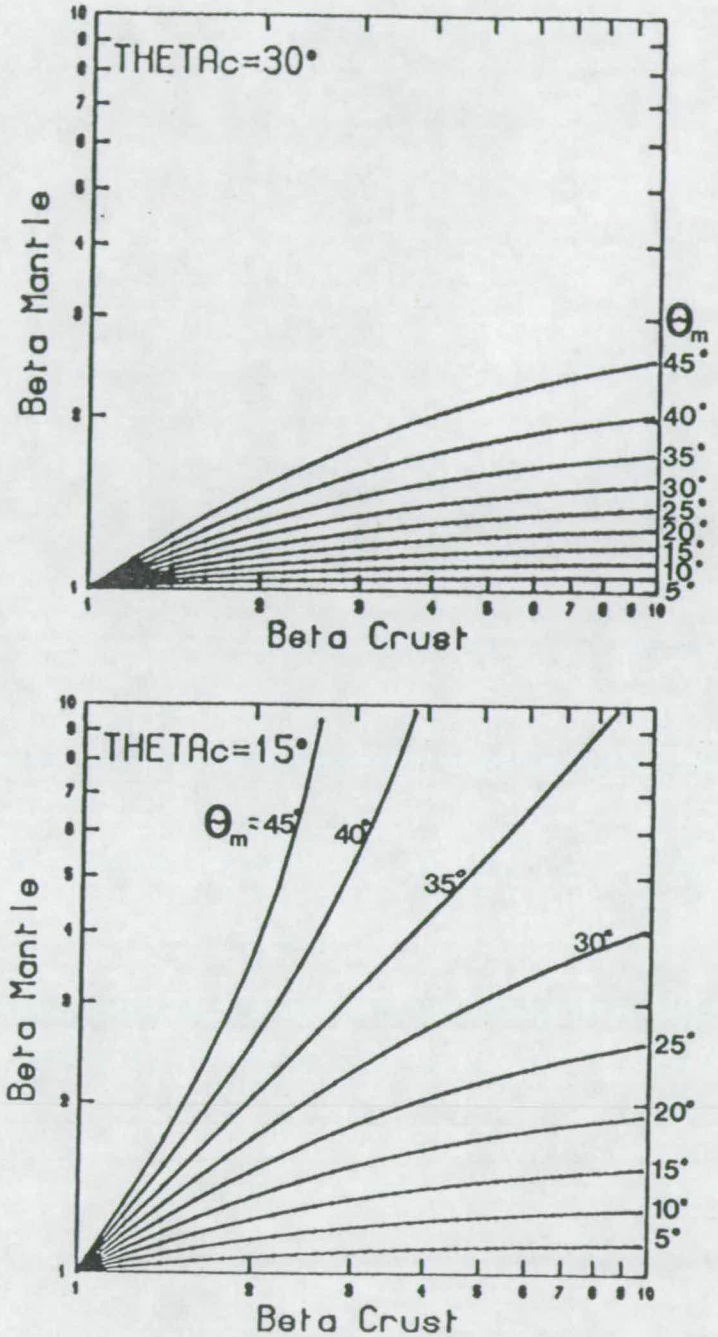

FIGURE 3.16 The variation of crustal(β_c) and mantle (β_m) thinning with detachment dip calculated from E:3.5 (see text). Upper diagram is for constant value of θ_c=30° whereas in lower diagram θ_c=15°. Curved lines are for constant θ_c with θ_m which varies from 5° to 45° in steps of 5°.

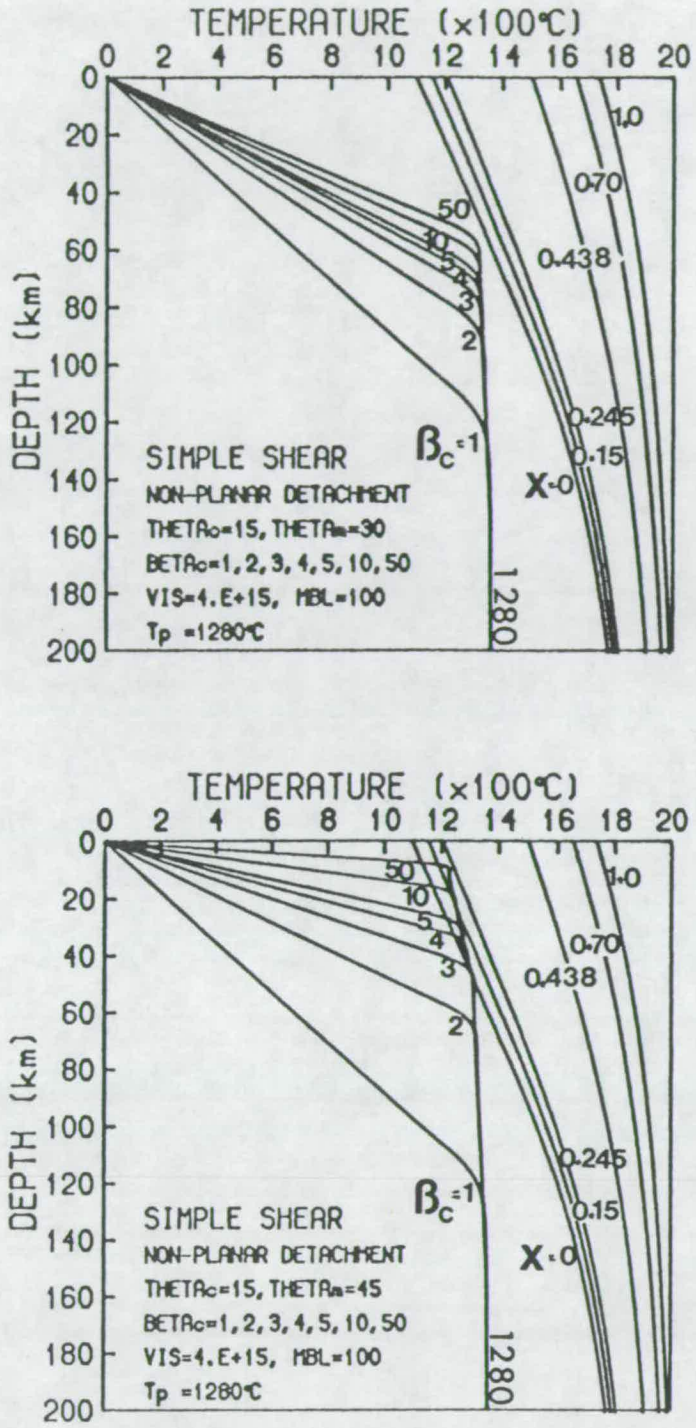

FIGURE 3.17 Convective geotherms (T_p=1280°C, MBL=100 km and interior viscosity of $4x10^{15}$ m^2 s^{-1}) which have been stretched by instantaneous simple shear along a non-planar detachment fault for different values of β_c. Upper diagram is for a fault with θ_c=15° and θ_m=30°, while lower diagram is for θ_c=15° and θ_m=45°. Notice how melting only occurs in the second case when the change in dip is very large.

The observation that it is difficult to produce melt by lithospheric simple shear is not new (Buck et al., 1988; Lister et al., 1990). However, the simple quantitative analysis presented above suggests that at normal asthenospheric potential temperatures *melting of dry peridotite will not occur* if extension is by lithospheric simple shear unless:

(1) The amount of extension along an initially planar fault is greater than that required to reduce the crust to zero thickness; depending on the dip of the detachment fault, such large amounts of crustal thinning might require horizontal separation of hundreds of km between the two plates. Providing the plates separate cleanly, production of a mid-ocean ridge would not occur until mantle had been exposed over a very wide region implying large areas of ocean floor/margin without magnetic lineations.

(2) The dip of the detachment fault more than doubles as it passes from crust to mantle; the value of β_c would still need to be large, i.e. in excess of 3 when θ_m=45° and θ_c=15°.

Any melt that is formed would, assuming vertical migration, be found away from the crustal rift.

Other non-coaxial models which require a large lateral offset between crustal and lithospheric mantle thinning (e.g. Lister *et al.*, 1990) are equally unsatisfactory for the generation of MORB at normal temperatures. For example, suppose that the crust is stretched by a factor of 50 in one place, and the lithospheric mantle is stretched by the same amount elsewhere. Beneath the sediment-loaded crustal rift, the base of the lithosphere rises by about 16 km to a depth of ~90 km from the surface; no melt is predicted in this region at normal temperatures (90 km >> 1.45 GPa). In the zone of major lithospheric mantle attenuation the upwelling is far greater, but the base of the lithosphere is still ~30 km below the surface (~0.8 GPa assuming a crustal density of 2800 kg m^{-3}), and therefore decompression only generates <2 km of melt under normal asthenospheric temperature conditions. Clearly, in order for non-coaxial models to produce even modest amounts of basaltic melt from dry peridotite, elevated temperatures will be required.

3.6 Extension, Melting and Uplift at Elevated T_p.

Just as some mid-ocean ridges may coincide with active regions of upwelling in the asthenosphere (e.g. Iceland), so too may some continental rifts. Plumes may predispose the lithosphere to rupture above them when it is put in tension, by

inducing local stress through uplift, elevating the heat flow and so causing mechanical softening, they may cause thermal thinning by conductive heat transfer, or even active thinning by convective processes, but no mechanism is known whereby stretching the lithosphere can initiate a plume or influence the location of one in the short term.

The potential temperature of the asthenosphere at the time of rifting is therefore a parameter of critical importance not only in terms of melt generation but also with regard to the history of relative uplift and subsidence within the basin. The discussion so far has been concerned with basin formation above asthenosphere of normal potential temperature (inferred from MORB to be 1280±40°C). At a normal value of T_p only relatively modest amounts of melt (<7 km) are generated even at extremely large amounts of extension. At higher potential temperatures large volumes of melt may be generated more easily at, on average, greater pressures. The presence of a large scale thermal anomaly in the asthenosphere which allows the production of large volumes of melt at relatively small amounts of extension has profound implications for basin subsidence whichever extensional model is employed.

3.6.1 Pure Shear and Elevated T_p.

When the T_p is more than 100°C above the normal T_p the dry solidus is overstepped by relatively small amounts of coaxial stretching; i.e. $\beta<2$. Figure 3.18 shows the result of instantaneous uniform extension of the steady-state lithospheric geotherm (MBL=100 km) over asthenosphere of 1380 and 1480°C. For a T_p as great as 1480°C melting commences on the dry solidus at a depth of ~100 km (~3.3 GPa; see Figure 3.19) which requires a value of β as modest as 1.25. At a T_p of 1380°C the dry solidus is intersected when β exceeds 1.6.

In Figure 3.19 the amount of melt generated, the point and depth average melt fraction, and average pressure of melting, are all shown as functions of different instantaneous amounts of uniform extension over asthenosphere of T_p=1480°C and T_p=1280°C. Clearly values for a T_p of 1380°C will lie in between the other two. Notice that in all cases when β is small melting occurs at depth by a small average extent and produces relatively small volumes of magma. Higher potential temperatures allow melting to occur at smaller values of β and the melts are therefore produced, on average, at greater depths in the mantle.

When the T_p is 1480°C the melt thickness exceeds that produced at a normal ocean ridge by the time β has reached 2.25 (when the melt thickness is ~9 km). In

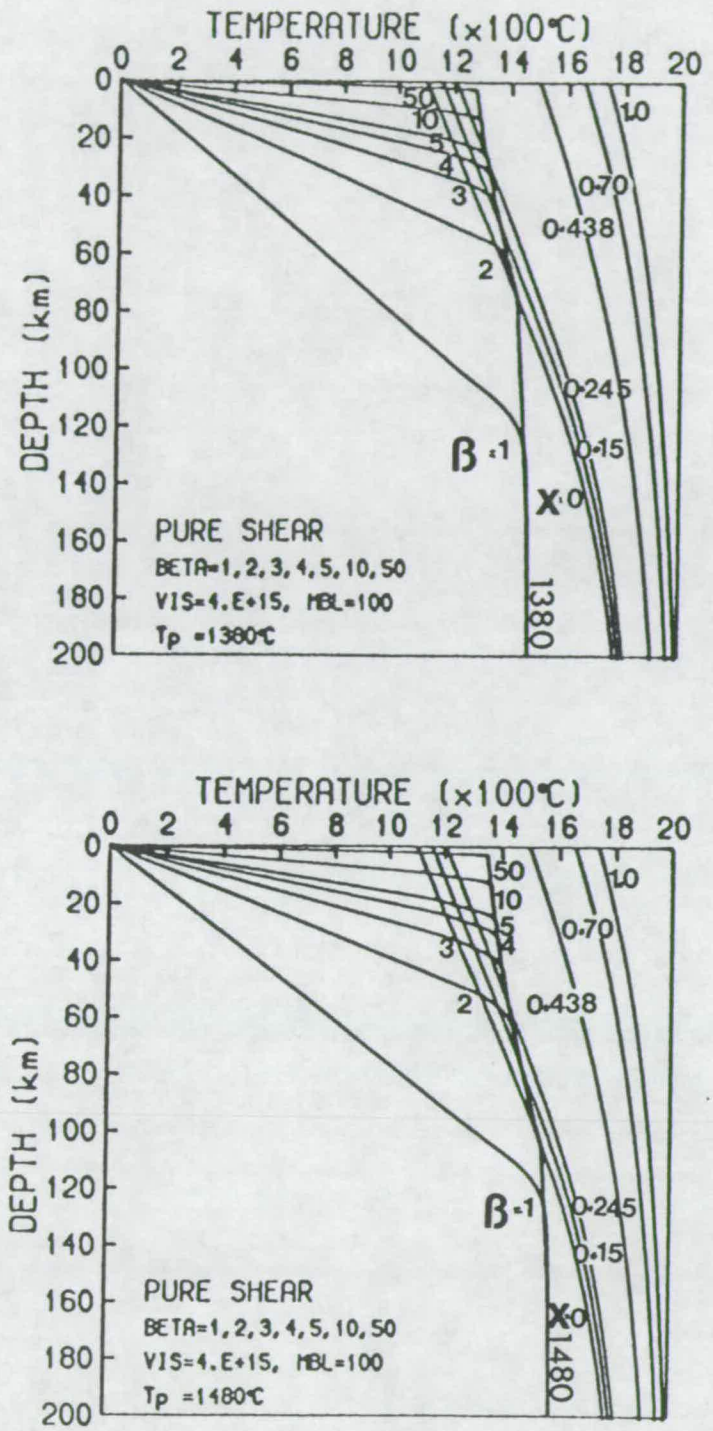

FIGURE 3.18 Elevated potential temperatures. Convective geotherms (MBL=100 km and interior viscosity of $4x10^{15}$ m^2 s^{-1}) which have been stretched by instantaneous pure shear for different values of β. Top; T_p=1380°C. Bottom; T_p=1480°C.

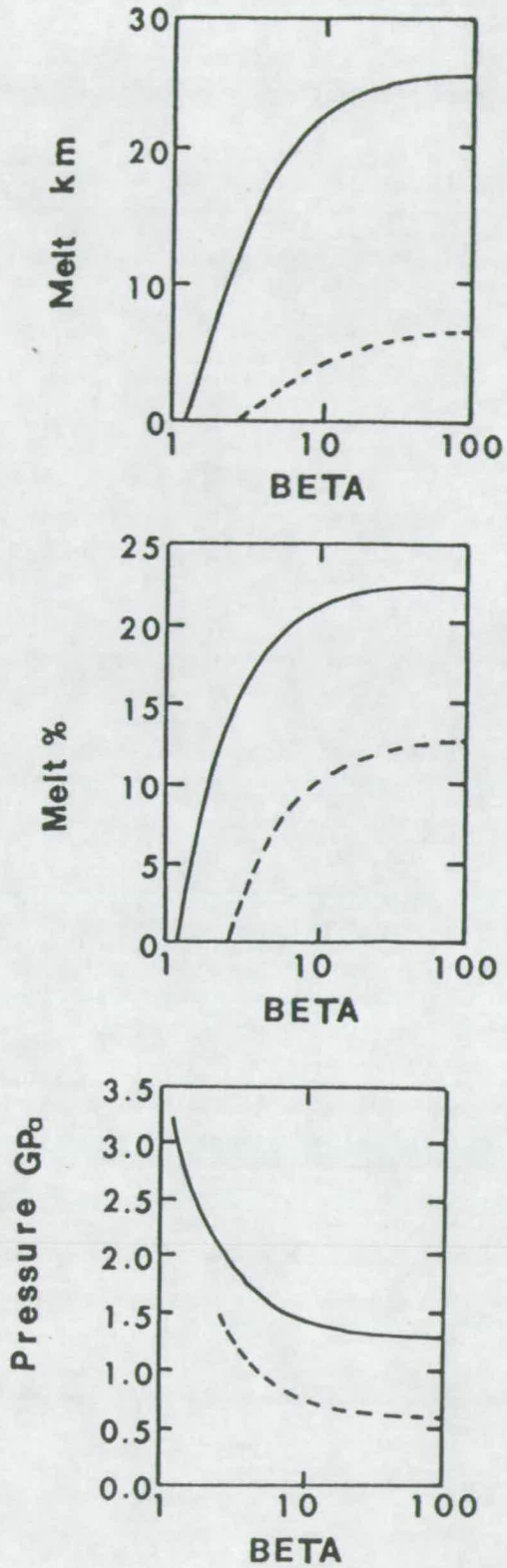

FIGURE 3.19 The variation of melt thickness (top), melt percent and pressure of point and depth average melt, with β at two different potential temperatures. In all cases upper curved line of points is for T_p=1480°C whereas lower dashed line is for T_p=1280°C. MBL=100 km and interior viscosity = 4×10^{15} m^2 s^{-1}.

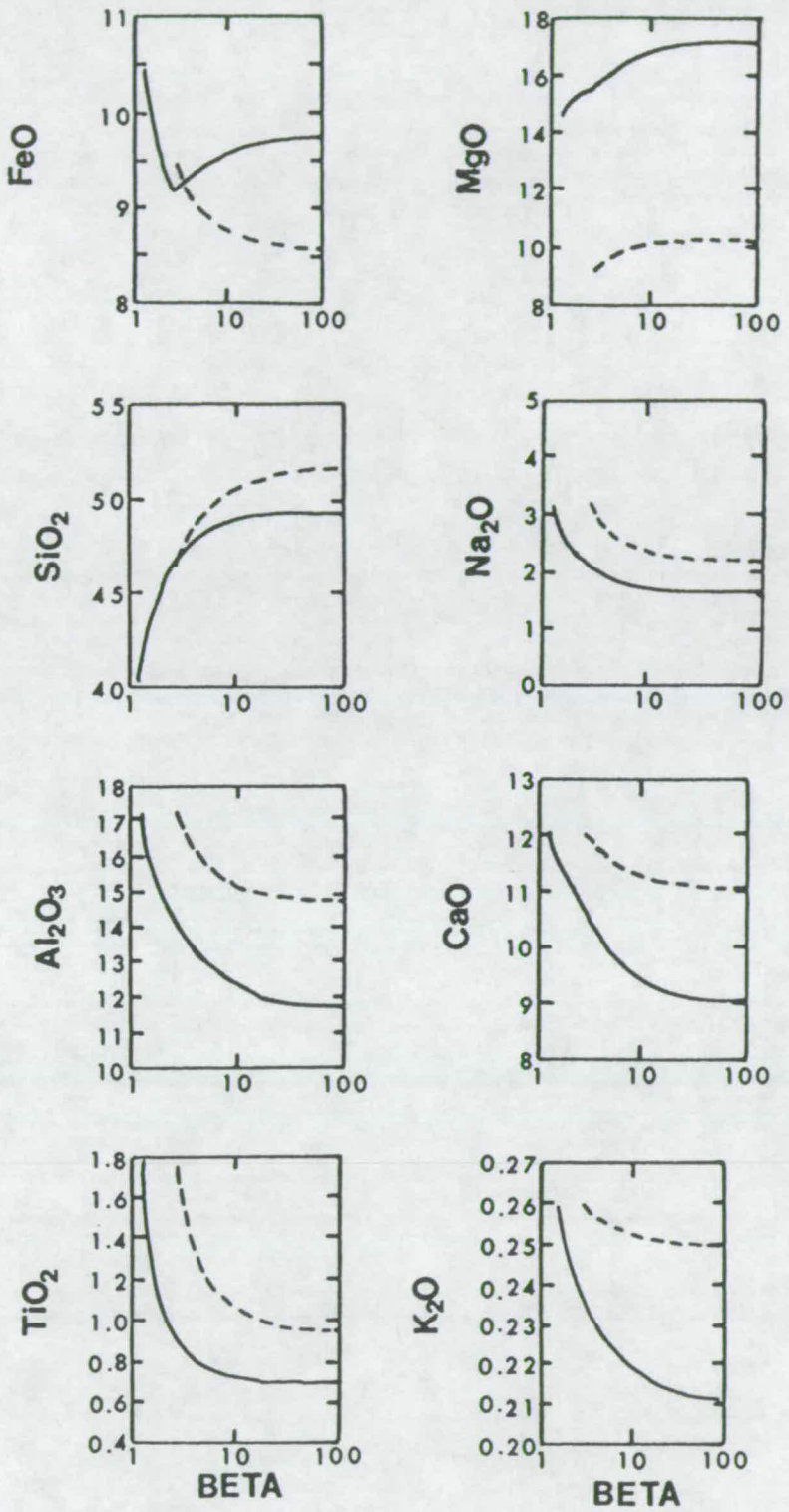

FIGURE 3.20 Point and depth average melt compositions (as wt.% oxides) plotted as a function of β using model parameters as in Figure 3.19. Compositions were generated from the parameterisation (a) of McKenzie and Bickle, 1988. In all diagrams solid curves are for T_p=1480°C while dashed curves are for T_p=1280°C.

contrast, for a T_p of 1280°C no melt is generated until β exceeds 2.75. It is clear that pure shear thinning at elevated potential temperatures can generate very extensive thicknesses of basaltic magma. This theoretical observation enabled R. White *et al.*, (1987) to explain geophysical observations, particularly variations in seismic velocity, at dipping reflector margins such as Hatton Bank (N. Atlantic), in terms of massive basaltic outpouring and underplating due to rifting in the vicinity of a mantle hot-spot or plume. The same explanation has also been put forward for the development of flood basalt provinces such as Deccan, Paraná and Karoo (R. White and McKenzie, 1989).

The compositional parameterisations of McKenzie and Bickle (1988) can be used to predict the compositions of the primary magmas generated by rifting over high temperature plumes in the asthenosphere. Because the melting occurs, on average, at greater pressures than at normal temperatures, the earlier formed melts are considerably more magnesian and iron rich; see Figure 3.20. The predicted oxide concentrations for different values of β at T_ps of 1480°C and 1280°C are shown in Figure 3.20. Notice that at low values of β (<<10) the diagrams imply that FeO and SiO_2, which unlike MgO are largely buffered during subsequent crystallisation of olivine, may be useful for discriminating between basalts produced by similar amounts of stretching at the two different temperatures.

3.6.2 Simple Shear and Elevated T_p.

The lithospheric simple shear model, presented in section 3.5, predicts no melting at normal potential temperatures, even at values of β_c in excess of 10, unless the detachment fault more than doubles its dip on passing from crust to mantle. As Figure 3.21 shows, stretching on an initially planar detachment fault will not cause melting at a T_p of 1380°C even when the crust has been thinned to zero, and will only cause very small extents of melting at T_p=1480°C when β_c exceeds 3 (see footnote [6]). It should be clear by now that the initially planar fault version of the lithospheric simple shear model is simply not capable of producing anything other than trivial amounts of melt even at very large amounts of extension at elevated asthenospheric potential temperatures. The result of extension at elevated potential temperatures along a detachment fault which doubles its dip with depth is shown in Figure 3.22.

---

[6] Note that Figure 3.21 is different from Figure 2 of Latin and White (1990) in that much less melt is predicted at T_p=1480°C when the effects of latent heat on melting are allowed to modify the stretched geotherm.

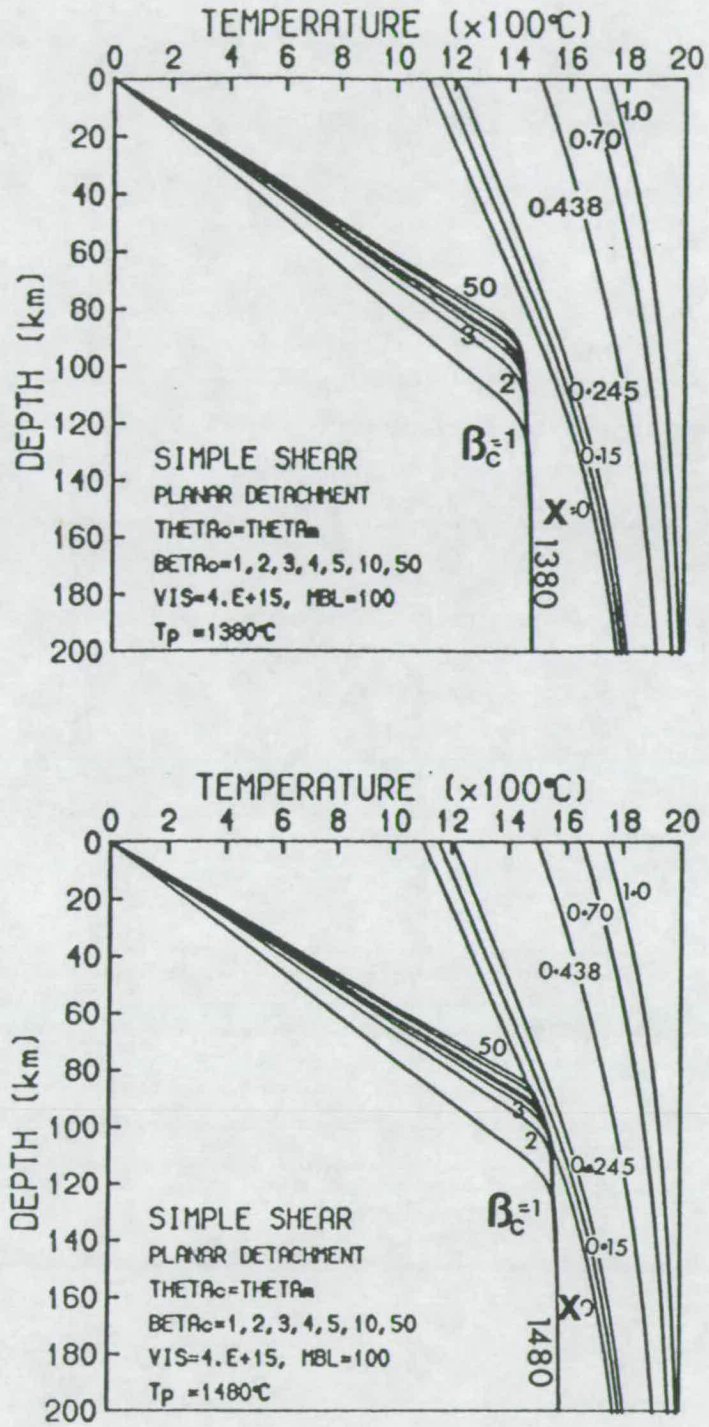

FIGURE 3.21 Elevated potential temperatures. Convective geotherms (MBL=100 km and interior viscosity of 4×10^{15} m^2 s^{-1}) which have been stretched by instantaneous simple shear along a planar detachment fault for different values of β_c at different values of T_p. Top, T_p=1380°C; Bottom; T_p=1480°C. Notice that only very small amounts of melting take place even at high T_p's and large values of β_c.

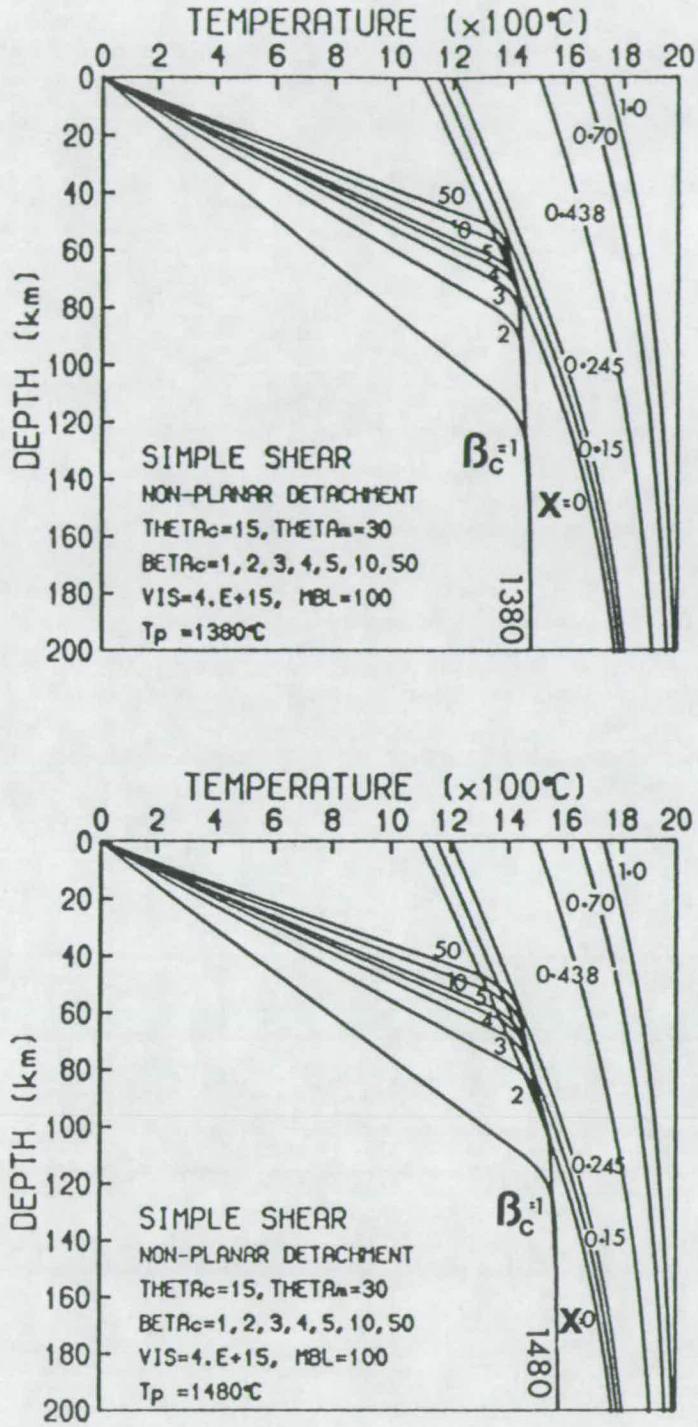

FIGURE 3.22 Elevated potential temperature. Convective geotherms (MBL=100 km and interior viscosity of 4×10^{15} m^2 s^{-1}) which have been stretched by instantaneous simple shear along a non-planar detachment fault (θ_c=15° and θ_m=30°) for different values of β_c at different values of T_p. Top, T_p=1380°C; Bottom, T_p=1480°C.

This non-planar model is clearly able to produce quite significant amounts of melt when a mantle plume is present.

The lithospheric simple shear model has been widely applied to the evolution of passive margins (e.g. Lister *et al.*, 1986, 1990). Conjugate margins are described as either upper or lower plate in character depending on their particular geometries. Emphasis has been placed on the need to produce between 5 and 15 km of melt below upper plate margins to account for permanent uplift and evidence for underplating and surface volcanism. As has already been mentioned R. White *et al.*, (1987) and R. White and McKenzie (1989) can account for the development of most volcanic margins by uniform stretching over mantle hotspots. The calculations discussed in section 3.5 together with their predictions presented in Figures 3.21 and 3.22 suggest that little, if any, melt will be produced by lithospheric simple shear, even for very large values of β_c and extension over a mantle plume. Magmatism has also been invoked to explain the widespread and persistent uplift of lower plate margins (the undeformed plate in Figure 3.7). However, the simple observation from Figures 3.8 and 3.9 is that considerably less melt is likely to be produced from beneath the lower plate than is produced from beneath the upper plate.

3.6.3 Basin Subsidence and Elevated T_p.

There are a number of lines of evidence which may indicate that a mantle plume was present during rifting of the continental lithosphere. Elevated potential temperatures are likely to give rise to differential uplift and subsidence on a regional scale, abundant surface volcanism, discrepancies between different estimates for the amount of extension, temporal migration of plume-induced uplift-related unconformities, and the migration of the locus of volcanic activity through time. In the identification of plume involvement one of the most important considerations concerns the size of the plume-affected region.

Uplift of the order of 0.5 to 2 km over a region some 1000 to 2000 km in diameter will occur *prior to and during rifting*. Large scale regional uplift of this sort is likely to cause widespread truncation and erosion of pre-rift sequences. The syn-rift sedimentary facies and their pattern of distribution pattern will also be highly sensitive to regional doming. Plume-induced doming, because of its regional nature, should be easily distinguished from more localised fault-footwall effects.

At normal potential temperatures the isostatic response to stretching is subsidence; shown by the normal T_p line in Figure 3.23. Regional uplift of the

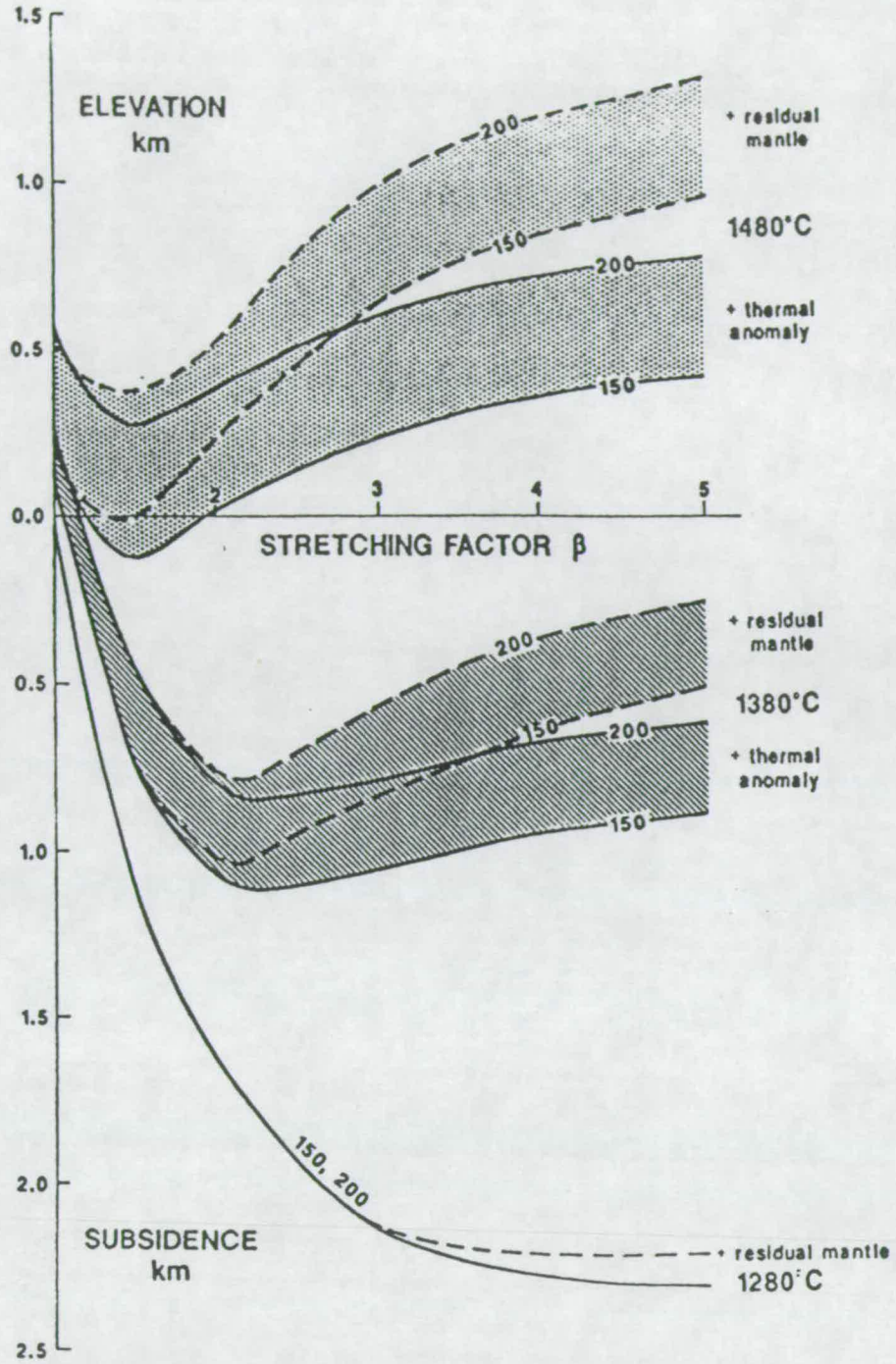

FIGURE 3.23 Amount of subsidence at the time of rifting as a function of the degree of instantaneous uniform stretching β over different T_p asthenosphere. Subsidence calculation includes the effect of lithospheric thinning, and the effect of adding basaltic melt to the crust. Uplift including the estimated dynamic effect of a mantle plume, calculated by assuming a compensation depth of between 150 and 200 km below the lithospheric plate, is shown by solid lines. The additional effect of reducing the density of the asthenosphere by melt extraction is shown by dashed lines. Curves are calculated assuming initial MBL=100 km which has its unstretched surface at sea level prior to the introduction of the thermal anomaly in the asthenosphere. From R. White and McKenzie (1989).

lithosphere over a plume, causing the geoid anomaly associated with hotspots such as Hawaii, results from 2 main factors:

(1) Dynamic support due to the presence of hot low density plume flow in the asthenosphere. This support can only be accurately quantified by modelling the whole flow of the plume. R. White and McKenzie (1989) approximate its effects by assuming that abnormally hot mantle replaces the ambient mantle at the base of the lithosphere down to some chosen depth; they choose 150-200 km as the depth to the base of the mushroom shaped head of the plume (Courtney and White, 1986). The amount of uplift resulting from the isostatic response to this hot mantle can then be calculated assuming Airy isostasy using the simple equation given by Latin *et al.*, 1990a. It is important to note that this component of the uplift forms the entire component during the pre-rift stage so long as no melting takes place; see Figure 3.23 for β=1

(2) Uplift related to the formation of large volumes of low density basaltic melt and a relatively low density residual mantle. The amount of uplift is proportional to the amount of melt underplating and thickening the crust. In Figure 3.23 (from R. White and McKenzie, 1989) stretching is assumed to be instantaneous and uniform. The density of the solidified melt is calculated from the normative mineralogy of its predicted composition. R. White and McKenzie (1989) calculate the effects of melt removal on the density of the residual (asthenospheric) solid by assuming that it had changed from lherzolite to harzburgite. If the density of hot liquid melt and the normative density of the residual mantle had been used, the effective uplift, shown in Figure 3.23, would have been even greater. Notice that in Figure 3.23 at a normal T_p so little melt is produced, even when β is very large, that the true subsidence path deviates little from that predicted without melting. At high potential temperatures the large volumes of melt produced during rifting combined with the effects of the dynamic support mean that subsidence will not occur until rifting has ceased and the plate has moved away from the plume. Figure 3.23 suggests that there will be a gradation in the amount of uplift across the rift according to β and across the plume according to its temperature, which will be greatest in the centre.

If the effect of a plume is to cause widespread uplift, even during rifting, then it should be recorded in a rather dramatic way in the stratigraphy of any basin. Not only would such doming be likely to restrict rift sedimentation to terrestrial facies types but it would also cause the develop of a marked regional erosional unconformity and it would have a dramatic effect on the regional drainage patterns. The migration of the lithospheric plate over the plume with time might be expected to

lead to a predictable younging of the erosional unconformity in a direction opposite to the direction of plate motion.

If stretching is coaxial then the presence of a mantle plume will result in abundant volcanism even at rather small values of β. Indeed as is shown in section 3.8, if the lithosphere is still cooling from some prior stretching event, and therefore has a MBL which is less than its steady state thickness, melting may occur before rifting. In non-coaxial models the amounts of melt will be small unless the detachment fault is non-planar or the plume actively thins the MBL (see the next section). In these models the first melts will be most likely to occur off-axis.

Just as uplift-related regional unconformities might be expected to migrate and erode younger sequences with time, so too might we expect to see a temporal migration in the locus of magmatic activity. This migration will not necessarily be reflected in compositions or volumes, because these depend on the degree of decompression, but it should be reflected in a decrease in the ages of volcanism in a direction which is opposite to the plate vector (in the hot-spot reference frame).

As is discussed in the next section, the plume itself may cause erosion of the base of the MBL. This would result in a discrepancy between the amount of crustal thinning, due only to extension during rifting, and the amount of total lithospheric thinning. The presence of a plume during rifting might, therefore, be indicated if there is evidence that $\beta_c << \beta_m$ over a large part of the rifted region; see discussion in Chapter 7.

3.6.4 Plume Dynamics and Melting.

So far in the discussion the dynamics of mantle plumes which are responsible for regions of elevated potential temperature have largely been ignored. The predictions made by the model of McKenzie and Bickle assume that decompression of the asthenosphere, of whatever T_p, is instantaneous and that it only occurs as a passive response to lithospheric thinning. In reality, regions of elevated T_p, mantle plumes, are dynamic phenomena which continuously undergo upwards flow and decompression which are largely independent of the motion of the overriding lithospheric plates. Melting at elevated T_p's must therefore be considered to result from two, essentially independent processes:

(1) Passively driven decompression melting which occurs in response to thinning of the lithospheric plate immediately above the plume.

(2) Actively driven decompression melting which results from the plume sustaining flow.

The latter of these two processes is best explained with reference to oceanic hotspots, such as Hawaii, where there is no extensional thinning of the lithosphere.

Melting takes place beneath Hawaii as asthenosphere of elevated T_p within the Hawaiian plume undergoes actively driven decompression to the base of the oceanic plate. The oceanic plate below Hawaii was perhaps 70-80 Ma old at the time of loading (McNutt and Menard, 1982) and so would have been approaching its steady state thickness (100-125 km). A plume with a central T_p of ~1480°C would be on or just over its solidus at these depths. The amount of melt generated from the Hawaiian plume is essentially governed by (1) the degree to which the plume asthenosphere upwells over the solidus, which is controlled by the thickness of the plate above, and (2) the flow rate within the plume which determines the rate at which unmelted asthenosphere is passed through the melting region. The Hawaiian ridge, which extends for ~100 km, is built from crust that is ~20 km thick (McKenzie, 1984) which implies that a thickness of melt in excess of 10 km has been added to the oceanic crust in this region. Given the alkaline to transitional nature of the Hawaiian magmas the average extent of melting is unlikely to exceed ~7% (e.g. Fitton and James, 1986). Such a relatively small amount of melting will not give rise to the required melt thickness in a single upwelling event. Watson and McKenzie (in prep.) show how the volume and composition of melt produced above the Hawaiian plume is consistent with large volumes of mantle being processed, by plume flow, through a narrow melting zone (i.e. a small average melt fraction) at the base of the lithosphere.

East Africa may provide a similar example of the importance of plume dynamics in melt generation beneath a continental rift. The very large volumes of alkaline felsic rocks with mantle isotope ratios (~70,000 km^3; Baker, 1987), coupled with the huge volumes of alkaline mafic magma (~150,000 km^3) which have been produced over the last 30 Ma are difficult to explain simply in terms of extension produced decompression at an elevated T_p especially as the observed amount of crustal extension in the East African rifts appears relatively small (i.e.β_c<1.25; Kusznir, pers. comm. 1989). Given the initially rather thick MBL (see next section) and small amounts of extension, perhaps the best explanation for such large volumes of undersaturated melt would involve a dynamic plume cycling fertile peridotite through a narrow melting zone at the base of the continental lithosphere.

The theoretical quantification of the effects of plume flow on the volume and composition of melt produced at continental rifts and oceanic ridges is a difficult problem since it requires 3 dimensional modelling of convecting material that is also melting. Although plumes have been numerically modelled in 3 dimensions (Craig and McKenzie, 1987), plume-related melting has only been considered in 2

dimensional numerical models (e.g. Ribe and Smooke, 1987; Ribe, 1987; Watson and McKenzie, in prep.) which usually assume a planar stress free upper boundary and which ignore the possible effect of buoyant melt on plume flow. The interaction of plume flow with an uneven upper boundary, such as would occur at a ridge or rift, has not yet been studied. When the amount of decompression of a plume is large, as it is at Iceland, the large amounts of melt present in the plume flow, and associated buoyancy forces, must exert an important influence on the nature of plume flow; this has not at the present time been modelled. Despite these problems, which make it difficult to quantify the effects of plume flow on melt generation, it is possible to use the one dimensional model of McKenzie and Bickle to make an absolute minimum estimate of the volumes of melt produced over decompressing mantle plumes. The melt composition predicted from the average extent of melting in the parameterisation may, for the one dimensional case, be in significant error if melts from throughout the head of the plume are gathered towards the pressure minimum at its apex (much as are melts beneath a ridge; cf. Spiegelman and McKenzie, 1987). If melts are focussed in this manner then the average extent of melting is likely to be dominated by large volumes of low degree, relatively high pressure, melt formed around the edge of the central flow (cf. Watson and McKenzie, in prep.). However, Ribe and Smooke (1987) in their 2 dimensional stagnation-point model for melt extraction from a mantle plume, suggest that the flow of melt is likely to be governed by its buoyancy, rather than by the nonhydrostatic pressure gradient, and that it will therefore flow almost vertically upwards, regardless of the matrix streamlines, across the whole of the melting region. If Ribe and Smooke (1987) are correct then the reason for the relatively small size of the zone of intrusion and eruption (the Hawaiian ridge) above the Hawaiian plume is that it is only the central region of the plume which is hot enough to cross the solidus at the base of the lithosphere; a region some 200 km in diameter.

Finally there is the possibility that the elevated temperatures and flow within a plume may lead to thinning of the lithospheric plate. If plumes do thin the overriding plate then predictions of melt volume from known amounts of extension, even if models take account of plume flow, might be significant underestimates. A stationary or slow moving plate above a plume is likely to have its base eroded because the material at the base of the MBL will be warmed conductively as vigorous secondary convection is generated in the TBL due to the viscosity drop induced by the elevated T_p (Yuen and Fleitout, 1985). As the base of the MBL is warmed it becomes unstable and may be swept away by the high Raleigh number plume flow. Yuen and Fleitout (1985) suggest that, by this process alone, lithosphere initially 200

km thick could be thinned by a factor of 2 in approximately 50 Ma. Wendlandt and Morgan (1982) suggest that in East Africa actively driven thinning of the lithosphere operates in conjunction with extensional stresses and, with time, leads to a progressively decreasing depth of melt generation. The observed temporal trend in magma compositions from small volume highly undersaturated (kimberlites, carbonatites and nephelinites) to larger volume less highly undersaturated rocks (flood basalts of alkaline to transitional character) suggests a shallowing of the magma source. Using the age of eruption of the different melt compositions in conjunction with estimates for their depths of origin, Wendlandt and Morgan (1982) attempt to determine the ascent rate of the asthenosphere and the amount of lithospheric thinning. Unfortunately their arguments fall down because they assume that flood phonolites and trachytes are formed by melting at shallow levels (< 50 km) and that the lithosphere has therefore been very dramatically thinned. Most workers would consider that the phonolites, in particular, and trachytes result from the fractional crystallisation of alkaline basaltic magmas (see Baker, 1987; Macdonald, 1987). It is also difficult to see why, if the lithosphere is thinned ~30 km today (as Wendlandt and Morgan (1982) suggest), there are not huge volumes of tholeiitic rocks within the rift. It seems more likely therefore that the African lithosphere has been thinned to ~80 km over a plume allowing production of large volumes of alkaline flood basalt which fractionates to form the felsic varieties in the upper mantle and lower crust.

3.6.5 Rift Induced Convection: An Alternative to Elevated T_p

Although the large volumes of melt inferred to occur on dipping reflector margins are adequately explained by elevated potential temperatures due to rifting over a plume (R. White and McKenzie, 1989), a number of authors favour small scale convection as an alternative mechanism (e.g. Buck, 1986; Keen, 1987; Mutter *et al.*, 1988; Zehnder *et al.*, 1990). Small scale convection cells may be developed in the TBL beneath rifts if the horizontal temperature gradients are sufficiently large that the critical value of the Grashof number (the equivalent of the Rayleigh number for side-driven convection; Hughes and Brighton, 1967 p.67) is exceeded. If such convective systems do indeed operate beneath rifts then they will certainly augment melt production and may also lead to active thinning of the lithosphere (Steckler, 1985).

There are two major arguments against small scale convective models. First they require a very sharp break between rifted and non-rifted lithosphere in order to generate suitable horizontal gradients in temperature (R. White and McKenzie, 1989).

Perhaps more important is the fact that because the susceptibility to the initiation of convection, as defined by the Raleigh or the Grashof number, is strongly proportional to the thickness of the layer under consideration. Because the TBL is thinned during stretching the effect is to stabilize it against convection (McKenzie. pers comm. 1989). To get around this problem, models of small scale convection require that very large reductions in viscosity occur in the TBL as rifting takes place. If melting is initiated during rifting then such a drop in viscosity may be possible, but if there is at all times a small amount of melt present in the TBL, giving rise to the seismic low-velocity zone, then the drop in viscosity, merely as a result of increasing its volume during rifting, may not be sufficient.

3.7 MBL Thickness and Finite Duration Rifting.

3.7.1 The Initial Thickness of the MBL.

Throughout this chapter there has been an implicit importance attached to the shape of the geotherm prior to rifting. The shape of the geotherm, given that the arguments from boundary layer theory presented in section 3.2 stand, is controlled by the potential temperature and the thickness of the MBL; which may thin with time if vigorous convection in the TBL is induced by plume heating. So far little attention has been paid to the thickness of the MBL prior to rifting; in all the diagrams a steady-state thickness of 100 km has been assumed. However as Figure 3.24 clearly shows, different starting thicknesses for the MBL mean that for any given T_p different values of β are required to cause melting. If the MBL is thinner than its steady state thickness then melting is achieved more easily because it is already closer to the solidus. Thus for an initial MBL thickness of 70 km the dry solidus is intersected when β exceeds 2, for 100 km β must exceed 2.7 and for 150 km β must be significantly greater than 3. Note however, that when β reaches infinity then the amount of melt produced will be the same, whatever the initial thickness of the MBL, and it will only be controlled by the T_p.

The thickness of the MBL prior to extension is obviously a critical parameter. Differences in the steady-state thickness of the MBL were discussed in section 3.2. Here the concern is with short term changes in the thickness of the MBL which may result from thermal effects produced by tectonics; thus the MBL may thicken during continental collision and it will be thinned during extension. It is therefore extremely

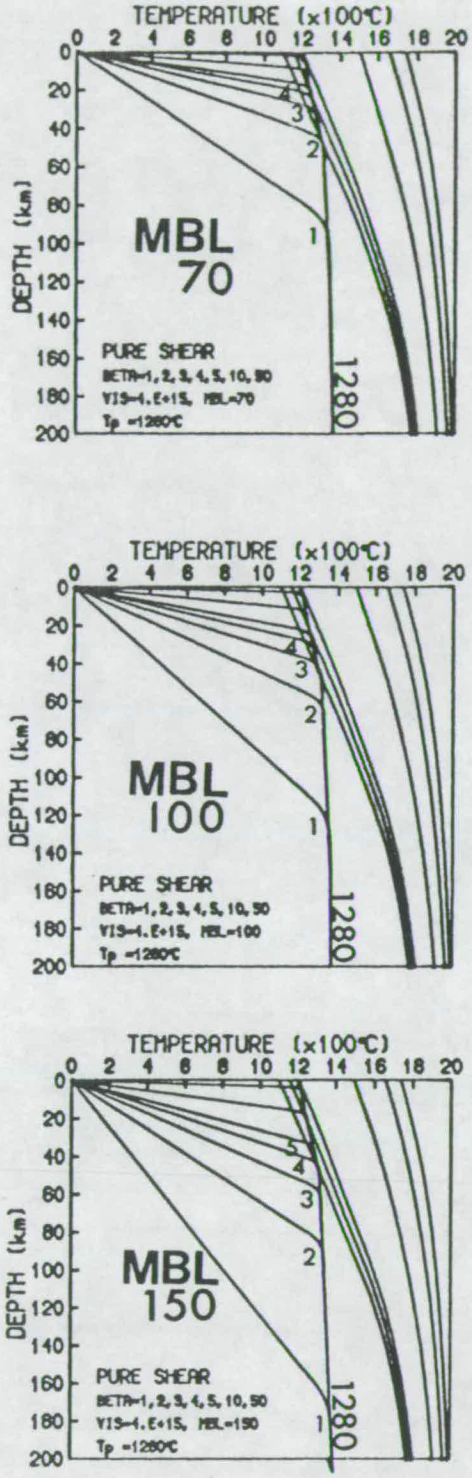

FIGURE 3.24 The effect of initial MBL thickness on melt generation at a given value of β for instantaneous uniform stretching over asthenosphere with T_p=1280°C. In all three diagrams the stretched geotherms are for different values of β. Top, MBL=70 km; Middle, MBL=100 km; Bottom, MBL=150km. Notice how melting is achieved at smaller perturbations of the geotherm when the initial thickness of the MBL is less (top) than the steady state thickness (middle).

important to know the recent thermal history of the area under study; by recent a time equal to about one thermal time constant (~60 Ma) is implied (see below and Chapter 7). For example, when considering the relationship between extension and magmatism in the Basin and Range, Western Anatolia, or Tibet it would be foolish to ignore the effects of recent thickening. In the North Sea the thermal effects of a rifting event which occurred during the Triassic, but which is difficult to quantify, should not be ignored when considering rifting and magmatism in the Jurassic. It is, however, shown in Chapter 7 that the effects of Triassic rifting on the thickness of the MBL prior to Jurassic rifting are likely to have been very minor.

3.7.2 Finite Duration Stretching.

In all of the predictive diagrams presented in this chapter the assumption of instantaneous rifting has been inherent to the calculations. Instantaneous rifting will maximise the predicted amount of melt for a given combination of β, T_p, and initial thickness of MBL and is an extremely attractive assumption since it considerably simplifies the calculations. However, as a number of authors point out, when rifting is not instantaneous, then the vertical (in particular) and lateral temperature gradients developed during thinning may lead to considerable conductive heat loss (e.g. Jarvis and McKenzie, 1980; Cochran, 1983). In terms of the subsidence history of a model basin the effect of conductive cooling during stretching is simply to superimpose syn-rift and thermal subsidence sequences. The rate of stretching will be a critical parameter with respect to solidus intersection and melt formation. If the duration of rifting is sufficiently slow then conductive cooling may keep pace with tectonic thinning and maintain the lithosphere at its steady state thickness; in this case no melting could occur even if the amount of extension was extremely large. Interestingly, this emplaces relatively unmelted (fertile) upper mantle into the mantle lithosphere, whereas widespread thermal events or rapid stretching replace the thinned part with melt-depleted mantle.

The effects of vertical heat conduction during finite duration rifting on the shape of the geotherm and on the size of the temperature perturbation for a given value of β at different stretching rates have been studied using a "staggered leapfrog" finite difference scheme (see Press *et al.*, 1986 pp. 632) to numerically solve the one dimensional heat flow equation:

(E:3.7)
$$\frac{\delta T}{\delta t} = \kappa \frac{\delta^2 T}{\delta z^2} - V \frac{\delta T}{\delta z}$$

where T is temperature, t is time, z is depth, κ is thermal diffusivity and V represents the upwards velocity, or strain rate, of the base of the lithosphere. The boundary conditions are that, at the surface T=0°C whilst at the base of the finite difference mesh T corresponds to a depth converted T_p of 1280°C. The initial conditions were obtained from the steady state geotherm. V is determined from the total amount of extension (β) and the stretching duration. The geotherm at the end of rifting is calculated using equation 3.7, and from then onwards the geotherm is modified according to the more simple conductive cooling equation (E:3.7 minus the advective term).

The results of stretching a simple plate geotherm by a factor of 2 over different durations are shown in Figure 3.25. Conductive cooling after the end of the rift phase has not been considered. In Figure 3.25 the dashed line represents the conductive lithospheric plate, 120 km thick, prior to extension or after extension that is infinitely slow. Notice that once the duration of stretching exceeds ~50 Ma the size of the thermal perturbation is more than halved. Jarvis and McKenzie (1980) provided a useful approximation which states that the duration of rifting will be of limited importance, with respect to the subsidence of a basin, provided that it is less than the thermal time constant for the stretched lithosphere; i.e. ~$60/\beta^2$ Ma. Figure 3.25 shows that for a duration of between 5 and 10 Ma, which lies within the time limit of Jarvis and McKenzie ($60/\beta^2$=15 Ma), the change in the shape of the geotherm is still noticeable and may well be important when melting is considered.

The finite difference scheme was then used to calculate the effects of extending a convective geotherm, rather than just a simple plate geotherm. Although finite duration rifting cannot be easily incorporated into the model of McKenzie and Bickle (1988), which is instantaneous, it is possible to model the effect that a prior rift episode of finite duration has on the initial convective geotherm used in the melting model. If the time elapsed since the last rifting episode is sufficiently large then it may have no effect on the geotherm which will have retumed to its steady state position.

Figure 3.26 shows stretched geotherms for β=3 over a number of different stretching and cooling durations. The upper diagram shows the initial geotherm, (MBL=100 km, T_p=1280°C) and then that geotherm perturbed by stretching by a factor of 3 over 30 Ma, 20 Ma, 10 Ma, and instantaneously. Note how only the case of instantaneous thinning results in intersection of the solidus. The lower diagram shows the same initial geotherm again stretched by a factor of 3 but this time all of the curves are for instantaneous thinning and the differences reflect differences in the

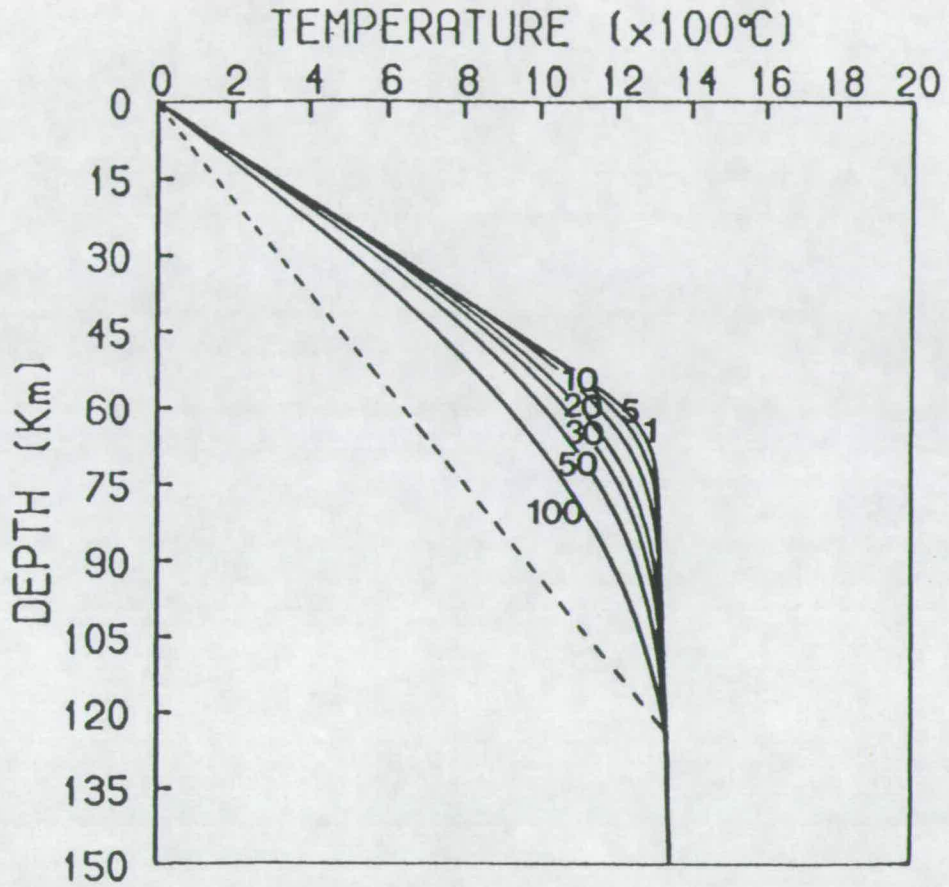

FIGURE 3.25 The effect of uniform extension over a finite rifting duration. Initial geotherm (dashed line) is for a plate model 120 km thick and T_p=1280°C. Stretched geotherms are all for β=2 with stretching durations of 100, 50, 30, 20, 10, 5 and 1 Ma. The effects of conductive heat loss, which causes the loss of the sharp corner in the initial plate geotherm, are calculated from a finite difference scheme using E:3.7 (the one dimensional heat flow equation, see text). Notice how the temperature perturbation is least severe at the end of a stretching episode with a long duration. A value of 8.04×10^{-3} cm^2 s^{-1} is used for the thermal diffusivity.

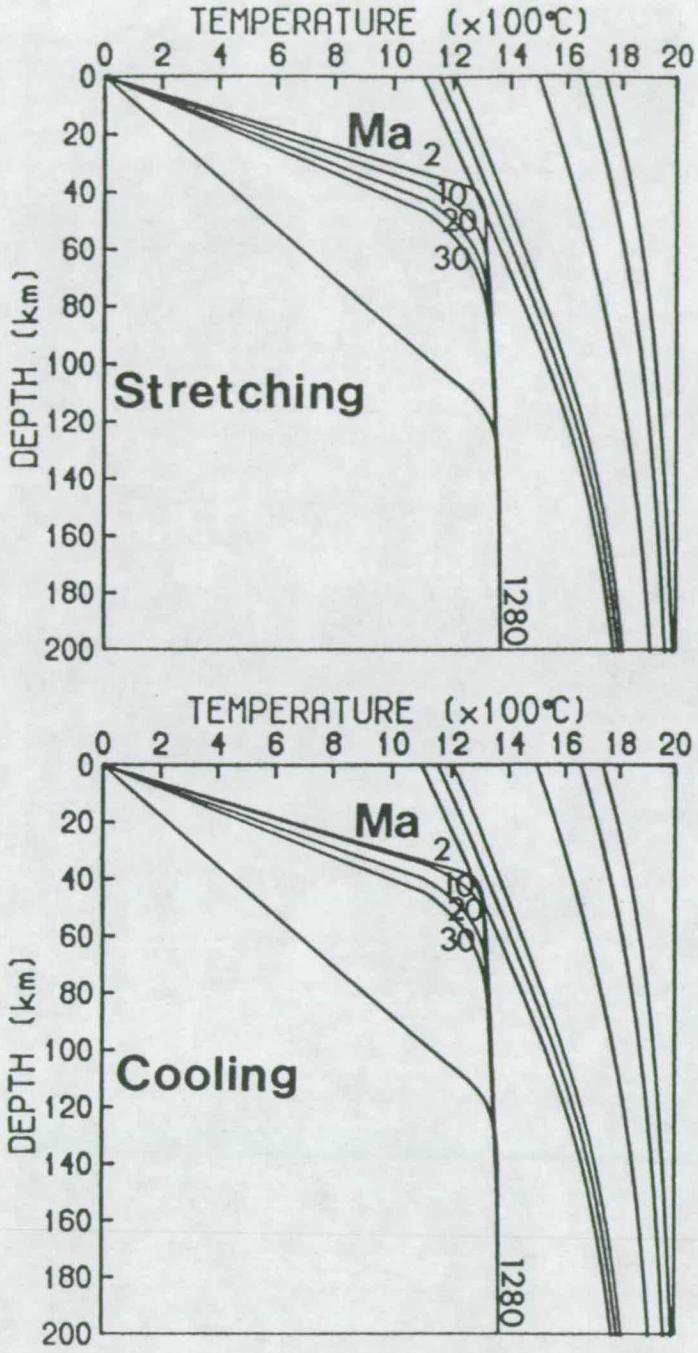

FIGURE 3.26 Upper diagram shows extension of a convective geotherm by a factor of 3 (uniform stretching) over a duration of 2, 10, 20 and 30 Ma. Lower diagram shows instantaneous extension by a factor of 3 followed by conductive cooling for 2, 10, 20 and 30 Ma respectively. Curves in both diagrams are for T_p=1280°C, MBL=100 km and viscosity=4×10^{15} m^2 s^{-1}. A value of 8.04×10^{-3} cm^2 s^{-1} is used for the thermal diffusivity.

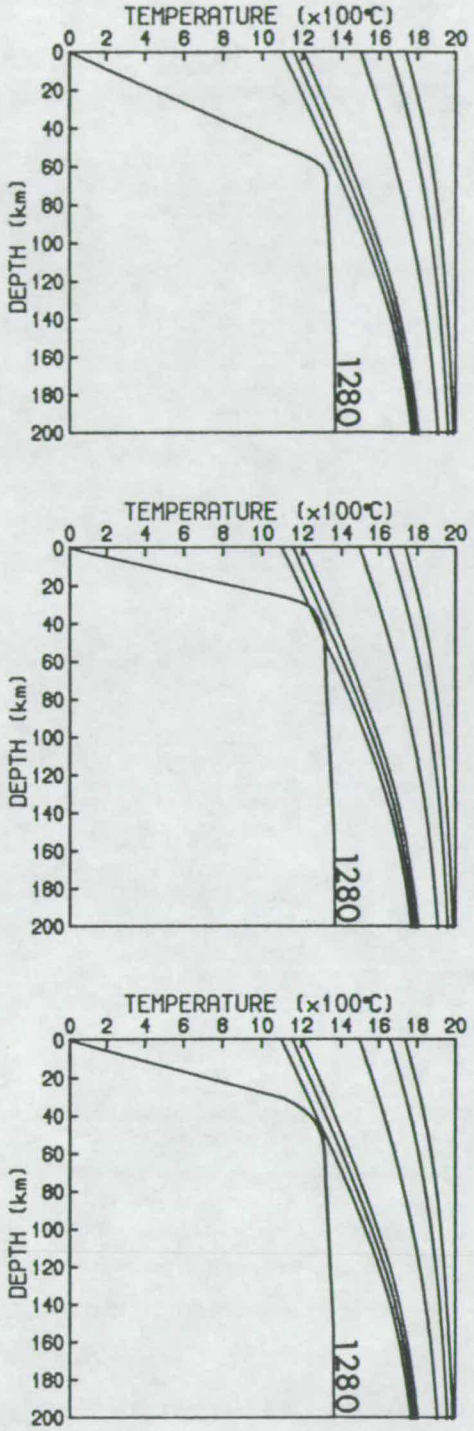

FIGURE 3.27 More than one uniform stretching event. In all three diagrams T_p=1280°C, MBL=100 km and viscosity=4×10^{15} m^2 s^{-1}. Top diagram shows a convective geotherm which has been instantaneously stretched by a factor of 2, no melting results. Middle diagram is for the case of instantaneous stretching by a factor of 2, followed by conductive cooling for 10 Ma, followed by instantaneous stretching with β=2; melting results and ~0.67 km of melt is produced. Bottom diagram is for the same conditions as the middle diagram except that the first stretching event is followed by 30 Ma (rather than 10 Ma) of conductive cooling; no melting. A value of 8.04×10^{-3} cm^2 s^{-1} is used for the thermal diffusivity.

period of conductive cooling; from the initial geotherm upwards the curves are for cooling of 30, 20, 10 and 0 Ma.

Figure 3.27 shows three examples of thinning by a factor of 2. In the uppermost diagram the stretching is instantaneous and no melting occurs. In the middle diagram the geotherm had already been instantaneously stretched by a factor of 2 in an event which occurred 10 Ma ago; when this geotherm is stretched again by a factor of 2 then 0.67 km of melt is produced. In the lowermost diagram the prior stretching event, again for an instantaneous β value of 2, was allowed more time to cool (30 Ma) before stretching occurs again; the cooling was just sufficient to prevent melting on the second stretch.

Finite rates of stretching and previous phases of rifting must clearly be carefully considered when any attempt is made to apply the model to one particular phase of rifting in a real basin. This discussion will be returned to in Chapter 7 when the arguments presented above are used to suggest that the thermal effects of a Triassic stretching event had negligible effect on the geotherm at the time of rifting in the Middle Jurassic.

3.8 Summary.

If the amount of adiabatic decompression of asthenosphere of a given potential temperature is sufficient to induce melting of anhydrous peridotite, then the volume and average composition of the melt generated may be predicted using the parameterisations of experimental data (McKenzie and Bickle, 1988) described in Chapter 2.

The present chapter has been concerned with quantifying the volumes and compositions of melt which may be generated on decompression of anhydrous peridotite during rifting of the lithosphere. The amount of adiabatic decompression depends critically on the amount and rate by which the lithosphere is extended, how thick the lithosphere was prior to extension, and how the strain is partitioned between the crust and mantle; i.e. whether coaxial or non-coaxial models are more appropriate. The potential temperature (T_p) of the asthenosphere depends on the presence or absence of asthenosphere of anomalously high temperature beneath the rifting lithosphere. Since it seems likely that convection in the upper mantle is not tied to the motion of the plates, the value of the potential temperature parameter rather depends on chance location.

The most important conclusions of the present chapter are summarised as follows:

(1) Melting of dry peridotite is more likely to occur if extension of the lithosphere is accommodated by coaxial stretching (e.g. the uniform stretching model) than it is if extension takes place by non-coaxial stretching (e.g. the lithospheric simple shear model). This conclusion holds at normal or elevated potential temperatures. The distribution of subsidence and the location of magmatic activity can be used to discriminate between different modes of extension.

(2) When rifting occurs above a mantle plume the volumes of melt produced may be very large. Since the existing quantitative theory does not incorporate plume upflow in the calculations predictions are likely to be minimum estimates. Underestimates in the amount of melt produced will also occur if mantle-plumes are able to thermally erode the overlying mechanical boundary layer. The presence of a plume should be recorded in basin stratigraphy by the temporal migration of regional uplift and erosion and the locus of magmatic activity.

(3) The thickness of the MBL immediately prior to rifting, which controls the shape of the geotherm, is one of the most important parameters controlling the amount of melt for a given amount of decompression. It is therefore necessary to establish whether or not the lithosphere in the rifted region was at thermal equilibrium prior to rifting or whether it was still recovering from some previous thermal event.

(4) The rate at which stretching takes place is of critical importance. At present theoretical framework is only concerned with instantaneous thinning and all upwelling is therefore assumed to be adiabatic. Non-adiabatic upwelling is likely to seriously reduce the amount of melt produced when stretching episodes are more than $\sim 60/b^2$ in length.

If the predictions of the theory are to be tested with observations of magmatism in a rifted region then model-independent values for the potential temperature, the amount and rate of lithospheric thinning, and the thickness of the MBL prior to rifting are required. This discussion is returned to in Chapter 7 when an attempt is made to assign values to these parameters in the North Sea.

CHAPTER 4

MAGMATISM IN THE NORTH SEA BASIN: I LOCATION, AGE, PETROGRAPHY

4.1 Introduction.

In the preceding Chapters a general theoretical framework has been described which is potentially able to predict, given the values of a number of important parameters (e.g. β, T_p, initial MBL thickness, rates of extension), the volumes and compositions of magmas which are likely to be produced from the asthenosphere during extension of the continental lithosphere. The main aim of this thesis is to assess whether or not predictions made by the theory are consistent with observations from the North Sea region[1] where, during the Mesozoic, there is a well defined crustal rift for which the timing, location and degree of extension is known, where there is magmatism, and where there is no shortage of the sorts of geological and geophysical information needed to assign values to the critical parameters. In order to test the theory it is therefore necessary to establish the timing, location, volumes and chemical character of the basaltic magmatic activity with a view to estimating the volumes and compositions of the parental magmas.

This chapter is therefore concerned chiefly with describing the locations, volumes, ages, petrographic and mineralogical character of basaltic igneous rocks associated with rifting in the North Sea. Chapter 5 concerns the chemical characteristics of these basaltic rocks. Most emphasis is placed on those basaltic rocks that were generated during the phase of Mesozoic rifting which resulted in the prominent N-S trending Viking and Central grabens and the E-W trending Witch Ground graben which meet each other at a triple junction in the Outer Moray Firth area (Figure 4.1). The North Sea has, however, undergone several periods of extension, with associated magmatism, since the Silurian/Devonian closure of Iapetus (e.g. Ziegler, 1975,1981,1982; Glennie, 1984; Ziegler and Van Hoorn 1990) and the Mesozoic phase is only one of these. Essentially three important phases of rifting and magmatism may be identified in the North Sea:

[1] The North Sea region is defined here as that area approximately bounded by latitudes 61° and 51° N and longitudes 5°E and 9°W although most of the discussion will centre on a rather smaller area.

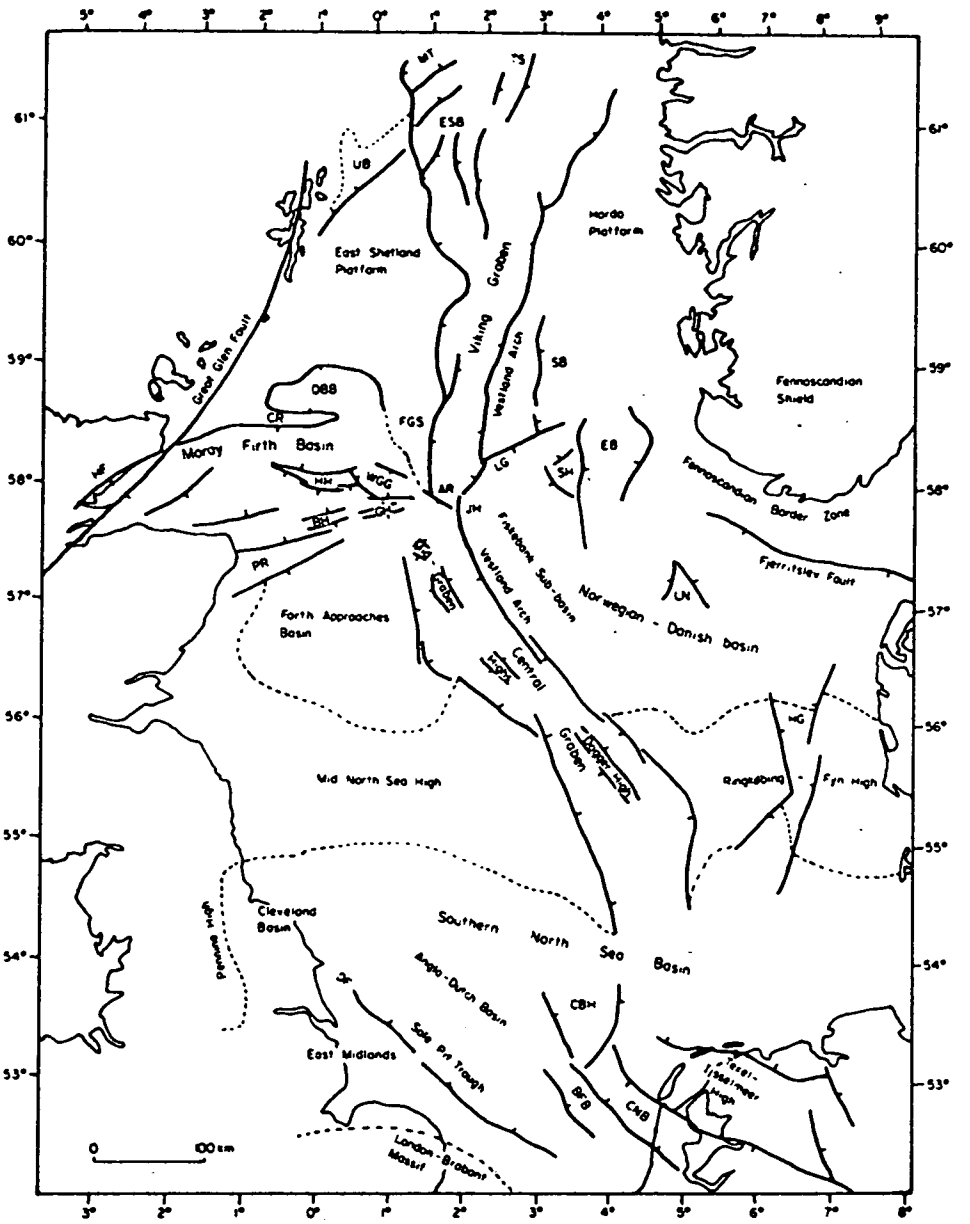

Fig. 6.1. Structural elements of the North Sea Basins.
Abbreviations:

AR	Andrew Ridge	ESB	East Shetland Basin	LN	Lista Nose
BFB	Broad Fourteens Basin	FGS	Fladen Ground Spur	MT	Magnus Trough
BH	Buchan Horst	GH	Glenn Horst	PR	Peterhead Ridge
CBH	Cleaver Bank High	HF	Helmsdale Fault	SB	Stord Basin
CNB	Central Netherlands Basin	HG	Horn Graben	SH	Sele High
CR	Caithness Ridge	HH	Halibut Horst	TS	Tampen Spur
DBB	Dutch Bank Basin	JH	Jaeren High	UB	Unst Basin
DF	Dowsing Fault	LG	Ling Graben	WGG	Witch Ground Graben
EB	Egersund Basin				

FIGURE 4.1 A map to show the main structural elements of the North Sea region, from Brown (1984).

(1) Palaeozoic rifting and magmatism occurred in Lower Carboniferous through to Early Permian times and resulted in a widespread magmatic province stretching across the North Sea from Northern Britain to East Germany. This rift episode, which resulted in the dominantly E-W Northern and Southern North Sea Permian Basins (Glennie, 1984), is relatively poorly understood and few parameters of importance can be quantified. The mildly alkaline basaltic rocks of Early Permian age from the North Sea are not discussed in this thesis although some analyses may be found in Appendix A. For details of Early Permian magmatism see Dixon *et al.*, (1981) and Latin *et al.*, (1990a).

(2) Mesozoic rifting, which produced the structural trends which dominate the region to the present day (Figure 4.1), occurred as two separate episodes, one in the Triassic, and a second in the Mid-Jurassic to Early Cretaceous period. The former episode was probably largely amagmatic and the latter, which is magmatic and which is structurally relatively simple, well defined, and quantifiable, forms the basis of most of the discussion in the remaining sections and Chapters of this thesis.

(3) Tertiary rifting and magmatic activity on the northern periphery of the North Sea region and in North West Scotland, which is related to the final stages in the opening of the North Atlantic (e.g. Upton, 1988) and is not considered further here.

The locations, ages and petrographic details of the various Mesozoic igneous occurrences are discussed in the following sections. For the purpose of this discussion the Mesozoic igneous rocks are divided into four major provinces (see Figure 4.2):

(1) The Forties province (section 4.2).

(2) The Central North Sea province (section 4.3).

(3) The Egersund Basin (section 4.4).

(4) The Netherlands province (section 4.5).

Although this grouping was initially somewhat arbitrary it happens that the provinces are fairly distinct in terms petrographic character and chemistry. In addition to the four provinces identified within the North Sea region a number of other nearby areas were magmatically active during the Mesozoic (e.g. The Sunnhørdland area of western Norway and the Skåne district in southern Sweden). These are discussed in section 4.6. In the following sections the locations of samples, all taken from exploration wells, are recorded by using the standard oil company licensing format; i.e. the location 15/21-1 relates to the location of well number 1 in the 21st block of quadrant number 15 in the U.K. section of the North Sea. A number of the wells have only recently been released into the public domain and they have therefore been given code names elsewhere (i.e. in Latin *et al.*, 1990a, 1990b); e.g.

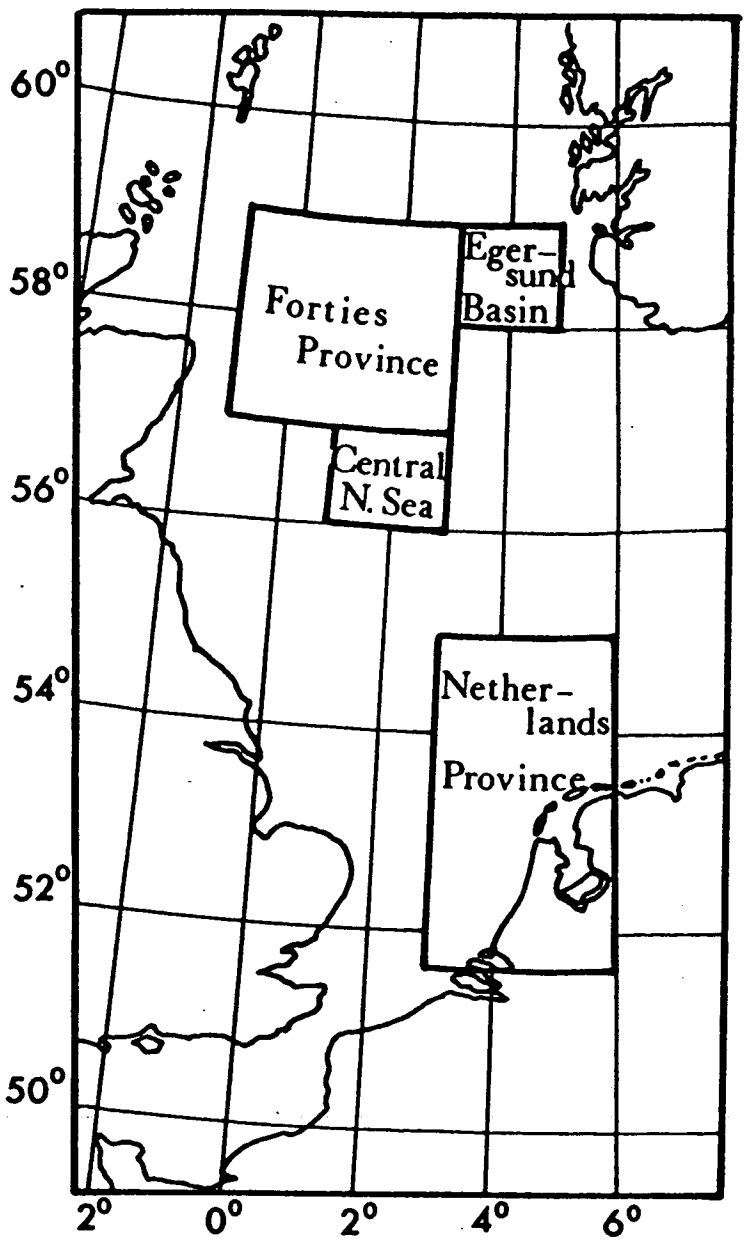

FIGURE 4.2 A map to show the 4 main areas of Mesozoic igneous activity in the North Sea region.

well 15/21a-8 was previously given the code name AH1. These code names are now given together with the well locations in the text but because they are shorter the code names are often retained in the diagrams. For similar reasons it is also convenient to discuss particular samples from particular wells in terms of a code. Thus AH1/42 relates to the 42nd sample in well AH1 (viz. 15/21a-8).

4.2 The Forties Province.

4.2.1 Location and Stratigraphic Age.

4.2.1.1. Location.

The preponderance of volcanic activity in the area of the Moray Firth-Central Graben-Viking Graben triple junction (see Figures 4.1 and 4.2) is the most striking feature of the magmatism during the Mesozoic in the North Sea. The igneous province, which is largely volcanic and of Middle Jurassic age, was first discovered in 1970 when exploratory wells were drilled in what is now the Forties Field (Howitt *et al.*, 1975). Igneous rocks have since been cored in at least 12 wells and there are many more from which cuttings have been recovered. Figure 4.3, which was compiled from a survey of well log data (conducted at the offices of Shell U.K, in London) and a review of the published literature on the Forties province (Howitt *et al.*, 1975; Gibb and Kanaris-Sotiriou, 1976; Woodhall and Knox, 1979; Fall 1980; Fall *et al.*, 1982), shows those wells which are known to have penetrated igneous rocks in the province (filled circles) and those wells which despite penetrating to similar stratigraphic levels failed to sample igneous rocks (open circles). For the course of the present work samples were only taken from core. It is possible to use cuttings but the quality of the sample is often much poorer in such cases and it was clear from an extensive study of both cores and cuttings which had already been conducted (Fall, 1980), that the province as a whole was relatively homogeneous in character and that the few core samples would therefore probably be representative. The wells in which igneous rocks were sampled for the purposes of the present study are shown by the large filled circles in Figure 4.3 and are labelled with code names in Figure 4.4. Details of these samples are given in Appendix A.

Figure 4.4 shows the locations of the wells containing igneous rocks in relation to the major structural elements of the Forties area. The stippled region,

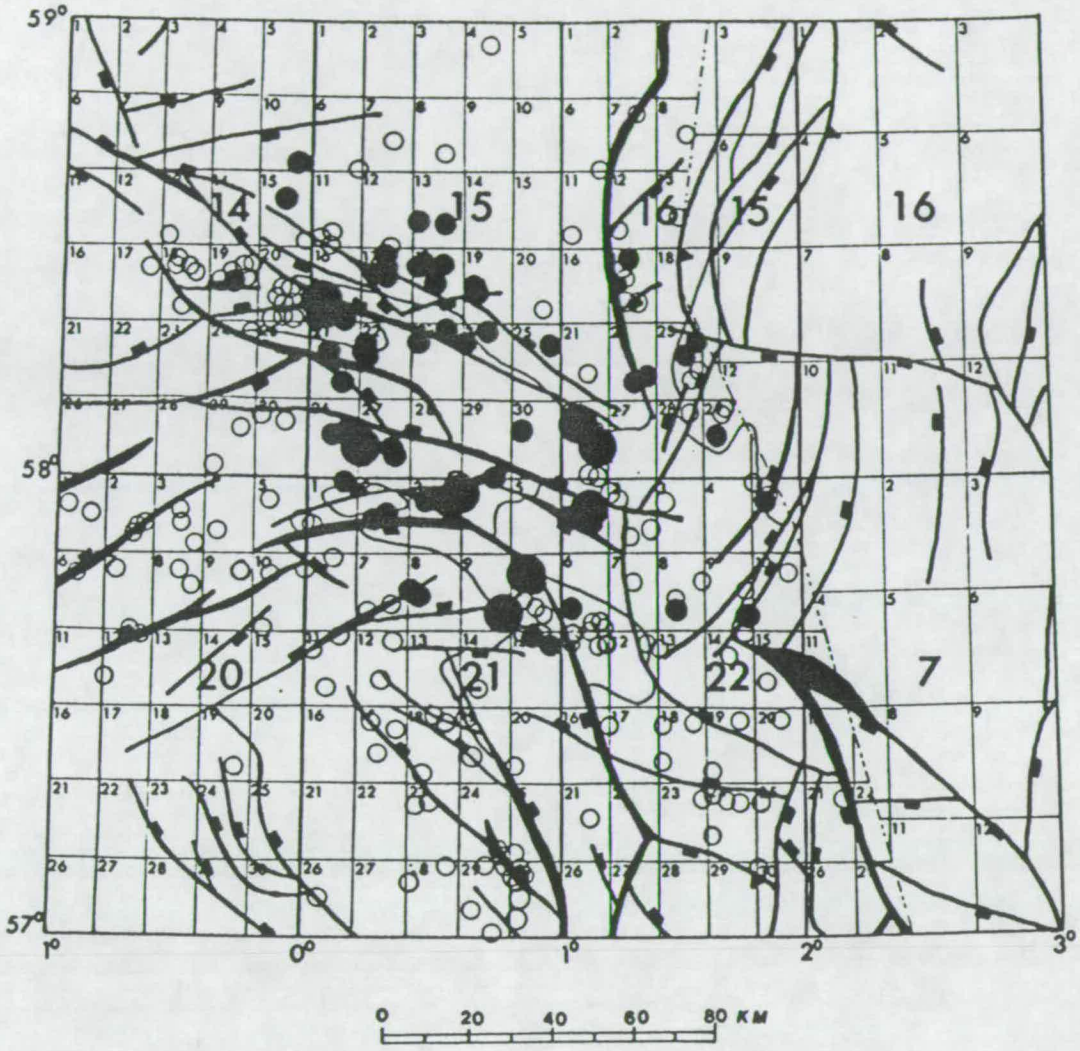

FIGURE 4.3 Location of igneous rocks in the Forties province. The map shows the locations of wells penetrating igneous material in the Middle Jurassic (small filled circles), wells in which volcanics were cored and used in the present study (large filled circles - see Figure 4.4) and wells which penetrated Triassic sediments without sampling igneous rocks (small open circles). The large numbers correspond to the standard U.K and Norwegian quadrant numbers while small numbers note individual licensing blocks.

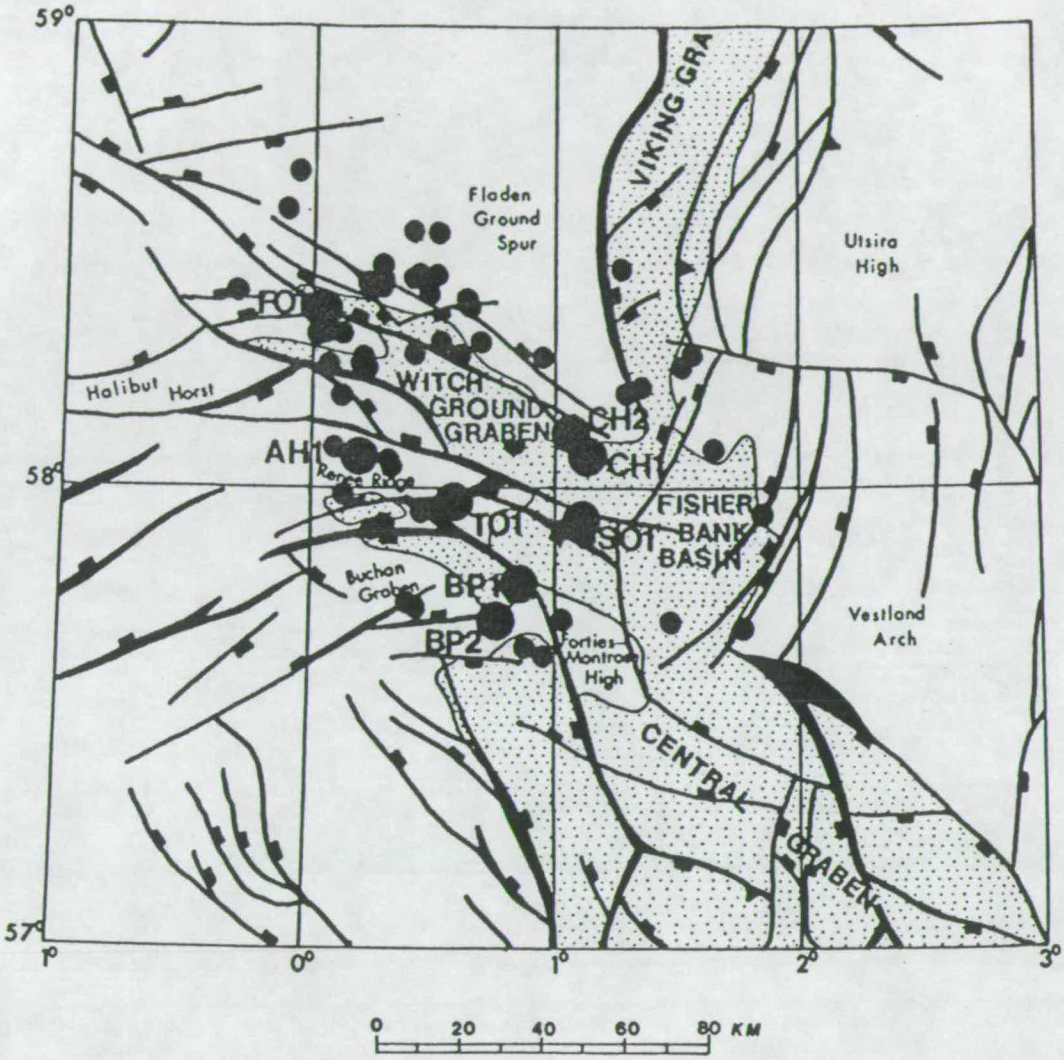

FIGURE 4.4 The main structural elements of the *triple junction* region are shown. Wells from which cored samples of igneous rocks were analysed (Appendix A) are labelled with code names and are indicated by large filled circles. As in Figure 4.3 small filled circles indicate other wells which penetrate igneous rocks. The base map is the *Tectonic Map of the North Sea* which was published in 1989 by GECO Exploration Services and Alastair Beach Associates. The dotted region indicates the main graben defined by the 3.0 second TWT contour at Base Cretaceous level.

which covers the area where the Base Cretaceous or "X unconformity" is found at >3 seconds two-way seismic travel time, marks the deepest parts of the basin. Notice how most of the wells, whether or not they penetrate the igneous rocks of the province, are restricted to structural highs and how they often cluster together at the sites of major hydrocarbon plays. The lack of igneous rocks in the deep parts of the region, particularly in the centres of the Fisher Bank and Witch Ground basins is largely a function of exploration economics! The lack of well information in these deep areas is a very real problem when trying to unravel the subsidence history in these parts of the basin (see Chapter 6). It is clear from Figure 4.3 that the limits of the province can be quite sharply defined. The igneous province therefore covers a roughly circular area which is some 100 km in diameter. This region also coincides with at least two large isolated total field positive magnetic anomalies which are attributable to mafic rocks (R. Hunter and D. Smythe pers. comm. 1990). One of these anomalies is sited over the Witch Ground Graben and the other lies close to the Andrew oil field (ca. quadrants 16/28 to 22/3) on the northern edge of the Fisher Bank Basin.

4.2.1.2 Stratigraphy.

The stratigraphy of the Witch Ground Graben area was most recently reviewed by Andrews and Brown (1987, see Figure 4.5) and Harker *et al.* (1987). In terms of lithostratigraphy the igneous province is termed the Rattray Volcanic Formation whose lateral equivalent is the Pentland Formation which consists in part of reworked Rattray rocks together with interbedded siltstones, shales and coals deposited in alluvial to marginal marine conditions. Both formations comprise the Fladen Group, named after the structurally-high Fladen Ground Spur which separates the Viking and Witch Ground grabens (Figure 4.4). Although the units within the Fladen group are sparsely fossiliferous the palynoflora apparently contains distinctive spore-dominated assemblages which are characteristic of Bathonian-Bajocian deltaic facies (Harker *et al.*, 1987). A Middle Jurassic (Bathonian/Bajocian) age was also determined from microfossils (foraminifera, ostracodes, spores, microspores, and dinoflagellates) found in interbedded sediments and in sediments from beneath the volcanic pile which are occasionally sampled at the edges of the province (Howitt *et al.*, 1975). However, questions have been raised as to the validity of the microfossil evidence (Ritchie *et al.*, 1988), because it is quite possible that the palynomorphs used for dating may have been reworked, and the volcanic rocks might therefore be somewhat younger.

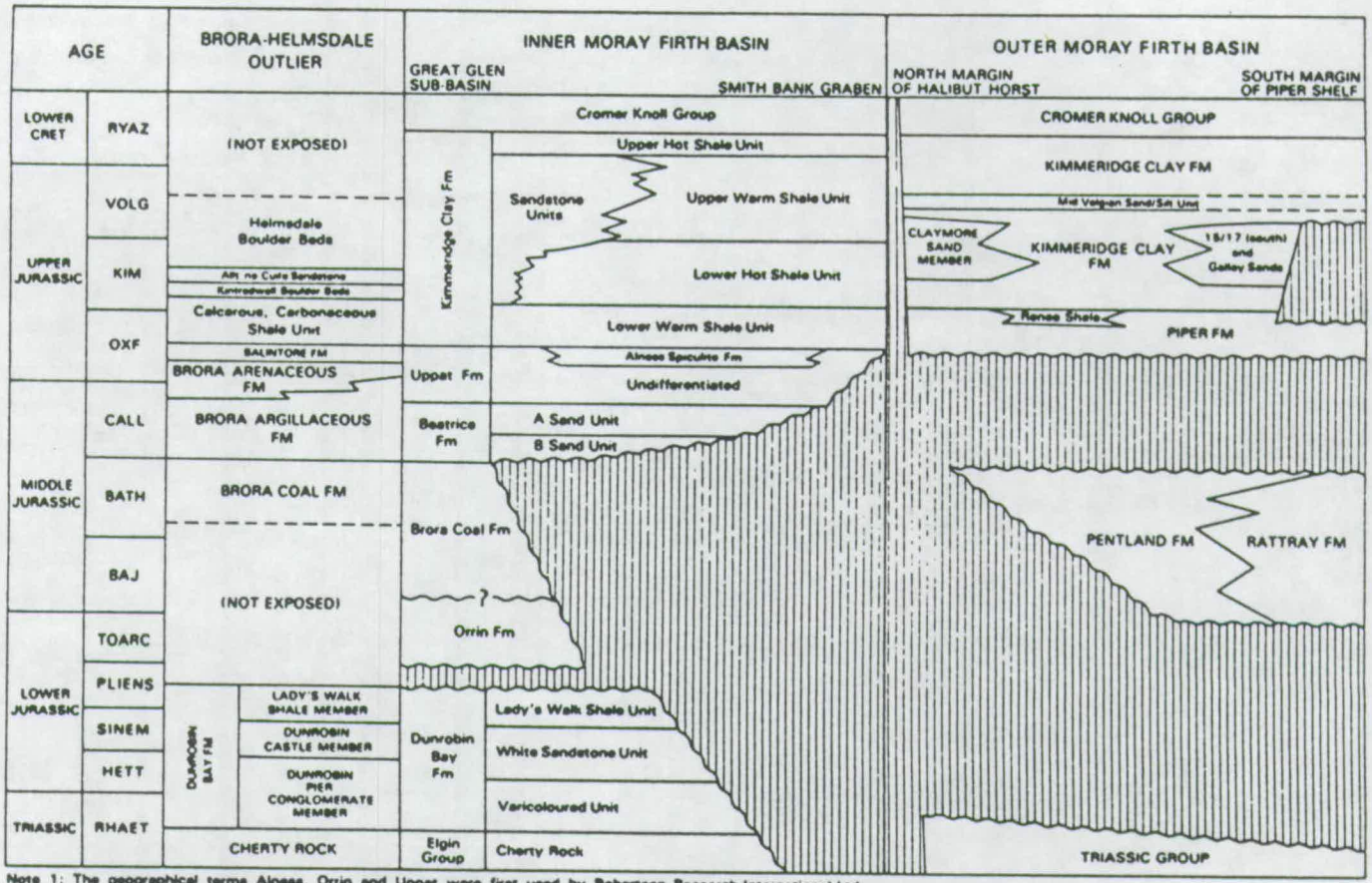

Note 1: The geographical terms Ainess, Orrin and Uppat were first used by Robertson Research International Ltd.
2: Lower case denotes that a lithostratigraphic term or its usage is informal
3: Renee Mudstone Unit occurs south and south-east of Halibut Horst

FIGURE 4.5 Summary of Jurassic lithostratigraphy in the Moray Firth, from Andrews and Brown (1987).

The igneous rocks of the Forties province are overlain by 2-3km of younger Mesozoic and Cenozoic sediments and, when the base of the pile is seen, lie unconformably above barren red beds of inferred Triassic age (Howitt *et al.*, 1975, Harker *et al.*, 1987). In all of the wells studied during the course of this work sediments of Lower Jurassic age were never positively identified in the area. The apparent lack of Lower Jurassic sediments (see Figure 4.5) over large parts of the Central North Sea has been attributed by Ziegler (1975, 1981, 1982) and Ziegler and Van Hoorn (1990) to widespread erosion during "*regional doming*", prior to and during magmatic activity in the Middle Jurassic (see Figure 4.6). The scale and regional significance of any uplift and erosion is discussed at greater length in Chapters 6 and 7. In all of the wells studied, the sediments directly above the igneous rocks are upper Oxfordian (Piper Formation, see Figure 4.5) or younger in age and therefore provide a minimum stratigraphic age constraint. The contact between the Fladen group and overlying Late Jurassic sediments is commonly shown as an erosional unconformity but in reality there is rarely evidence for significant amounts of erosion and the contact is more of a disconformity than an unconformity.

Precisely when rifting occurred during the Mesozoic in this area is very difficult to establish. There may well have been a Permo-Triassic event (e.g. Ziegler 1982, Barton and Wood, 1984), the scale of which is difficult to ascertain but which is likely to have been relatively minor (Barton and Wood, 1984; N. White, 1990; see Chapter 6). A number of authors place the main phase of crustal extension in the Mid to Late Oxfordian when the sands of the Piper formation were deposited on top of the Fladen Group as thick sequences in the hanging walls of major faults (e.g. Rawson and Riley, 1982; Turner *et al.*, 1984). However, as Andrews and Brown (1987) point out, the transgression which led to the deposition of the Piper sands can be correlated with a global high stand in sea level which was attained during the Late Oxfordian. Barton and Wood (1984) place the main phase of extension in the Mid Jurassic whereas Ziegler (1982) considers the main phase to start at the beginning of the Middle Jurassic but notes further crustal extension in the Late Jurassic. Roberts *et al.*, 1990 also consider that there were separate rift phases in the Mid and Late Jurassic and place most importance on the latter. Perhaps the most important evidence for stretching occurring contemporaneously with, and perhaps also prior to, the basaltic volcanism comes from the fault controlled subsidence and growth of the Fladen Group noted by Woodhall and Knox (1979). Woodhall and Knox (1979) suggest that the Forties province volcanics were extruded onto an already faulted topography, that they attain their maximum thickness in the deepest parts of the rift system, and that they are cut by later fault movements.

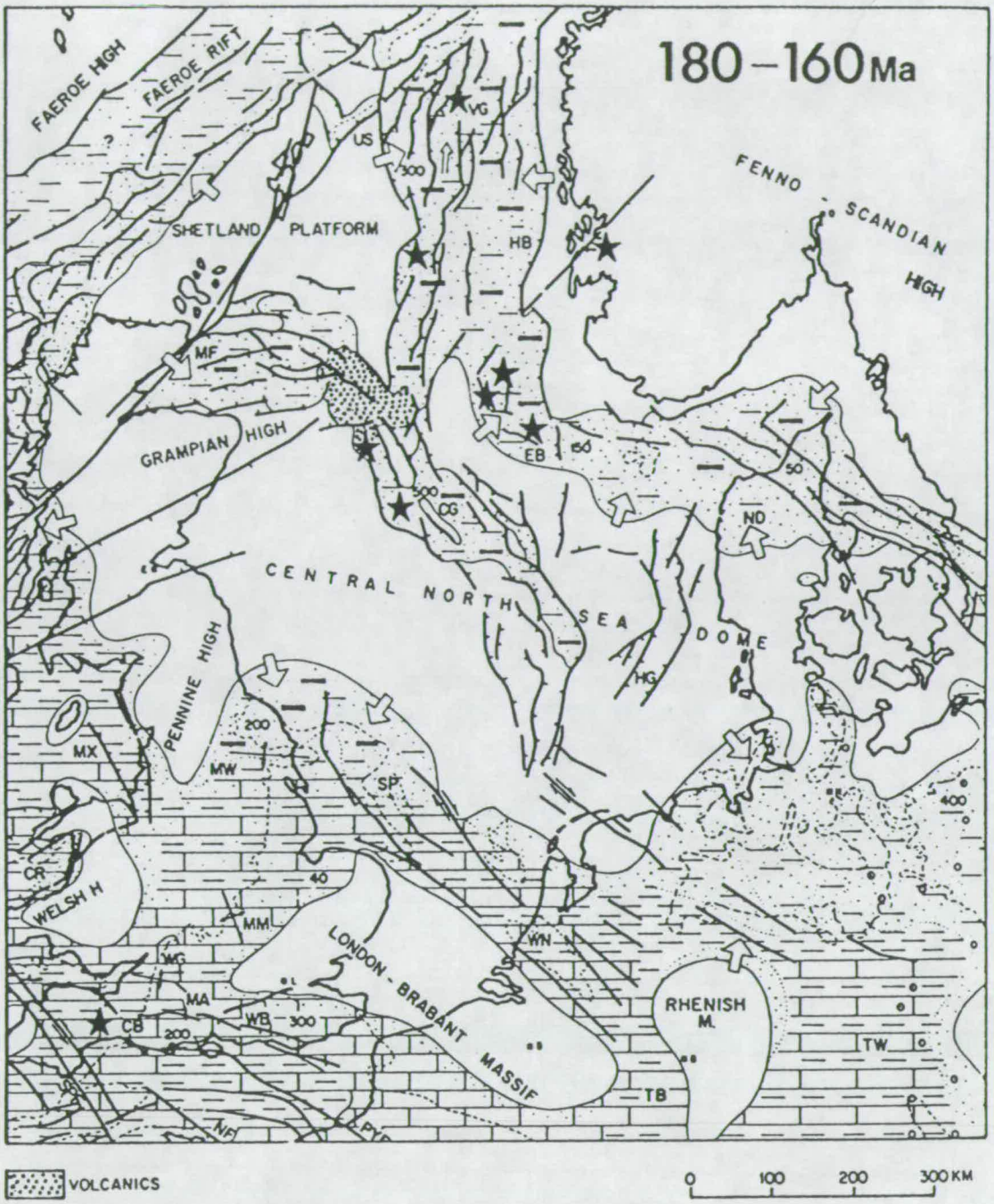

BAJOCIAN - BATHONIAN

FIGURE 4.6 Bajocian-Bathonian palaeogeography of the North Sea, from Ziegler and Van Hoorn (1990). Note that over much of the North Sea there is no deposition of sediments. The stars represent active intrusion of igneous rocks which (with the possible exception of the dykes in Norway) were probably not intruded until somewhat later (probably ~150 Ma see section 4.7). The Forties province is also shown but, as is noted later in this section, may not have been active until the Callovian (i.e. ~150 Ma).

In summary it seems most likely that the main phase of rifting during the Mesozoic in the area of the Outer Moray Firth and Fisher Bank basins started in, or at the beginning of, the Middle Jurassic (ca. 180 Ma, see Figure 4.6). The rift episode was protracted and crustal strain rates may have increased during the Late Jurassic (see Chapter 7). It is generally accepted that rifting ceased at some stage during the earliest Cretaceous and that by Upper Cretaceous times subsidence was largely thermally driven (Barton and Wood, 1984). The precise change from syn- to post-rift sedimentation is difficult to identify and need not relate to the point at which faults cease to be important since faults may continue to be active, due to differential loading, well into the thermal subsidence stage.

4.2.2 Radiometric Ages.

Severe alteration (see section 4.2.3, Chapter 5 and Plates in Appendix A) makes radiometric dates unreliable. The radiometric dates which were available at the start of the present study were reviewed by Latin *et al.* 1990a. A Middle Jurassic *minimum age* was given by Howitt et al. (1975) on the basis of conventional K/Ar dating on whole-rock samples of volcanic rocks. These dates, revised by Ritchie *et al.* (1988) using more recent IUGS constants (Steiger and Jäger, 1977), are given as 169±4 Ma (21/3-1a, Total), 155±6 Ma (15/21-1, Monsanto), 147±5 Ma and 164±12 Ma (21/10-1, BP.). The oldest of these dates is Bajocian on most time scales, but the overall spread is from Bajocian to Oxfordian (on the scales of Hallam *et al.*, 1985, and Van Hinte, 1976) or Tithonian (on the scales of Harland *et al.*, 1982, 1990). The oldest dates so far reported, which are~188±10 Ma, come from K/Ar determinations conducted for Ranger Oil on two samples of alkali olivine basalt from a sidewall core in 22/8a-3 and are interpreted as Lower Jurassic on most time scales. Ritchie *et al.* (1988) have challenged the minimum-age hypothesis of Howitt *et al.* (1975) on the grounds that the K/Ar age may be reduced or increased, depending upon the relative proportion of radiogenic Ar lost to the proportion of K lost or gained during the various alteration processes.

Ritchie *et al.* (1988) have produced what are probably the most reliable dates for the province. They carried out a detailed $^{40}Ar/^{39}Ar$ stepwise degassing study of rocks from well 21/3b-3 (Occidental). This is one of the few ways of producing reliable radiometric dates from altered rocks (another being U/Pb studies on zircons). The study produced two $^{40}Ar/^{39}Ar$ dates of 148±2 Ma and 154±2 Ma. Of these dates, only the former meets the somewhat arbitrary 50% Ar-loss constraint of Fleck *et al.* (1977), but both are probably reliable estimates. The Ritchie *et al.* (1988) dates

suggest that the province could be as young as Tithonian, or as old as Callovian (depending on the time scale used!). The Callovian age is considered more likely because the province is overlain by sediments of Oxfordian age.

At the start of the present study it was clear that there was a considerable amount of disagreement concerning the age of the Forties province. This also turned out to be the case for the ages reported for the other Mesozoic igneous provinces in the North Sea. From the discussion in Chapter 3, concerning the impact of a mantle plume on basin development, it should be clear that one key piece of evidence for the presence of mantle plume would be a shift in the locus of magmatic activity with time. It was therefore considered vital to have good radiometric dates for the various igneous provinces in the North Sea. A careful $^{39}Ar/^{40}Ar$ stepwise degassing study of four of the freshest of the Forties samples (AH1/42 (15/21a-8), BP1/33 (21/9-1), TO1/20 (21/3-2) and SO1/8 (22/1-4a)), see Appendix B), generously funded by Shell Expro, was therefore carried out in conjunction with Dr J.A. Miller at Cambridge University and Dr A.N. Halliday at the University of Michigan in Ann Arbor. The following is a summary of the results of the dating study and full details are given in Appendix B of this thesis.

Of all of the Forties province samples, **AH1/42** was petrographically the freshest (the only sample to contain fresh olivine) and it was therefore hoped that it would give a good age spectrum. The same sample was dated by Miller in Cambridge and by Halliday in Ann Arbor. Miller obtained an excellent age plateau, representing 80% of the total ^{39}Ar released at the high temperature steps, which gave a best estimate for the age of 156 Ma (Callovian using the scale of Harland *et al.*, 1990). Halliday, on the other hand, did not obtain a single plateau and concludes that, although 183±5 Ma (Aalenian) may represent the crystallisation age of the rock, the results are ambiguous. The difference in the quality of the age spectrum in the two cases probably reflects the variably altered nature of the sample coupled with the fact that there is no major K-bearing phase in the rock. Miller's date is considered, from the good age plateau obtained, to represent the best estimate of the true age of the rock.

BP1/33, which was studied by Miller, yeilded a U-shaped spectrum which he interprets to be caused by excess ^{40}Ar contained in zeolite (see Appendix B). The maximum percentage release of ^{39}Ar corresponds to the trough in the U which may be used to estimate the *maximum age* of the rock (196±3 Ma; Pliensbachian). In his report Miller notes that the data do not require that the sample is older than AH1/42.

Halliday obtained an irregular age spectrum, without a plateau, for SO1/8. He notes that its crystallisation age is probably best represented by *at least* 131±4 Ma (Valanginian) which is the highest temperature age recorded during step heating.

The $^{40}Ar/^{39}Ar$ data are highly ambiguous for TO1/20 and Halliday was unable to comment on its age other than to say that the total degassing age, equivalent to a K-Ar age, is 107±11 Ma.

Only one of the four samples studied (AH1/42) gave a satisfactory age plateau. Considering that these samples were petrographically and chemically considered to be least altered of all the Forties province rocks these results are disappointing. The main result appears to be that none of the previous dates, excepting the convincing $^{40}Ar/^{39}Ar$ date of Ritchie *et al.* (1988), should be trusted. It is concluded that there is no radiometric evidence that the rocks of the Province are any older than 150 to 160 Ma (~Callovian) in age.

4.2.3 Volumes.

Although the area covered by the province is well constrained the total amount of igneous material in the province is still uncertain. In the northern part of the province, wells have been drilled through the entire igneous sequence, where it is rather thin (often less than 200m thick). Woodhall and Knox (1979) report a total of 580m of volcanics penetrated in a well "*close to latitude 58 N*", and an adjacent well penetrated 1100m without reaching the base. The only well sampled during the course of the present study to pass through more than 1 km of volcanics was FO1 (15/27-2, Phillips) which reaches its total depth after penetrating of 1125m of the Rattray formation. According to Ritchie *et al.* (1988) the thickest sequence encountered to date is 1492m recorded from 21/3b-3 (Occidental). Howitt *et al.* (1975) suggested that total thicknesses might reach 1.5 km. Woodhall and Knox (1979) integrated the evidence from well stratigraphy, seismic, and aeromagnetic surveys, to produce an isopach map for the province, which indicates a maximum thickness of 3-4 km in some places (see Figure 4.7). However, more recent geophysical modelling (J.L. Swallow in prep.) suggests that the thickness only very rarely exceeds 2.5 km.

It is difficult to be conclusive without detailed seismic refraction and magnetic surveys but the implication is that the average thickness of extrusive rocks in the area is probably considerably less than 3 km. Given that geophysical models for magnetic anomalies give non-unique solutions and cannot easily discriminate between high level gabbroic bodies and volcanic rocks of similar magnetic

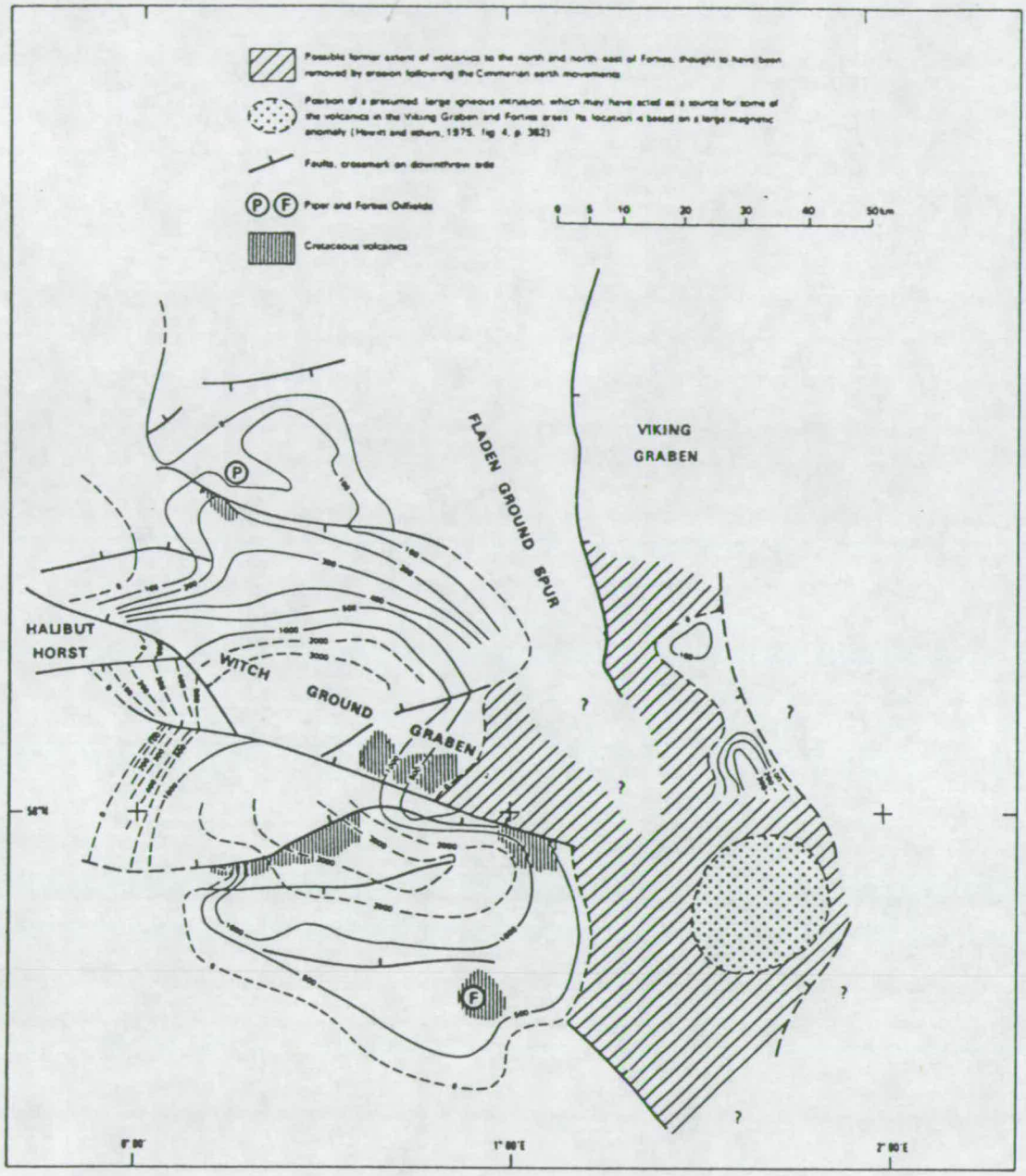

FIGURE 4.7 From Woodhall and Knox (1979) "*Distribution of Mesozoic volcanics in the eastern Moray Firth Basin. Thickness isopachs (metres) are shown for the Middle Jurassic volcanics, although in some central and southern areas this thickness includes volcanics of possible Triassic age. The 0 to 500m isopachs in the north and north-west are based on well evidence. The position of the 1000m isopach is more conjectural because it is based on only very limited well evidence. The 2000m and 3000m isopachs are based only on magnetic interpretations.*"

susceptibility then, unless there has been significant crustal underplating, this value of *3 km is likely to be an absolute maximum for the average total thickness of basaltic melt.* Large magma chambers at depths which correspond to temperatures that are greater than the Curie point, and which therefore do not give rise to magnetic anomalies, are unlikely because, as is discussed below, the basalts appear to have undergone only relatively small amounts of fractional crystallisation.

4.2.4 Petrography and Mineralogy.

The dominant rock type in the Forties province is an extrusive, mildly undersaturated, porphyritic alkali basalt or ankaramite. The basalts, which are often occellar, are typically strikingly enriched in large euhedral olivine and titanaugite phenocrysts (ca. 30-40% by mode) which may be accompanied by microphenocrysts of calcic plagioclase. Variations in the modal proportions of these three phenocryst phases may be used to explain most of the variations in whole rock chemistry seen between the different rocks of the province (see Chapter 5). However, in a large number of samples alteration is so pervasive and severe that there is almost complete loss of igneous texture and mineralogy (see Plates A to F in Appendix A). Alteration is usually most intense at the top of the volcanic pile close to the sediment-basalt interface which appears, commonly, to have acted as a pathway for hydrothermal fluids at some later stage in the history of the region. Similar zones of intense alteration are also commonly observed to occur between individual flows. Unfortunately most exploration wells terminate close to the sediment-basalt interface! Fortunately, in the Forties province at least, a sufficiently large number of wells have penetrated to considerable depths within the volcanic sequence and from these at least some moderately fresh rocks have been recovered. Discussion of the effects of alteration, which is a more severe problem in other parts of the North Sea where there are far fewer igneous samples, is continued in Chapter 5.

The petrographic and mineralogical characteristics of the Forties province rocks have been described in detail elsewhere (Fall, 1980; Fall *et al.*, 1982) and are therefore only briefly reviewed here. Further details and Plates representing specific features may be found in Latin *et al.* (1990a) and in the Appendices of this thesis which contains detailed petrographic description of the 4 Forties rocks used in the Shell-funded age determinations.

In general alkali basalts and ankaramites (basalts rich in accumulated olivine and clinopyroxene) are by far the most abundant rock types in the province. Basaltic hawaiites and hawaiites are also present in more minor amounts and may be

identified petrographically on the basis of an increasing modal proportion of feldspar and decreasing amounts of mafic phases. Apart from olivine, clinopyroxene and plagioclase, the most obvious phase in the groundmass of many of the Forties rocks is kaersutitic amphibole which is particularly abundant in ocellar patches. Other groundmass phases are potash feldspar, opaque spinel, apatite, and more locally, biotite.

In most samples olivines are completely transformed to chlorites, clays, carbonate, zeolite or even hydrothermal silica. In many samples there appear to be at least two distinct stages of olivine alteration (see the description of AH1/42 in Appendix B and Plates A to D in Appendix A) one which is probably high temperature and magmatic and a later lower temperature hydrothermal phase. However, a rare few samples contain unaltered olivines. Fall (1980) found fresh olivines in one sample of alkali basalt from well 15/22-1. The olivine phenocrysts in this sample were apparently zoned from Fo86 to "*at least Fo74*" and the groundmass olivine was Fo70. Fresh olivines have now also been discovered in two samples of ankaramite from well 15/21a-8 (samples AH1/41 and AH1/42; see Plates A and G in Appendix A of this thesis and Plate 6.1a from Latin *et al.*, 1990a). The largest olivine phenocrysts (3-5 mm in size) in these samples show a marked zonation from Fo81 in the cores to Fo69 at the rims, associated with a slight increase in birefringence. Microphenocrysts (1-2 mm) are slightly zoned from Fo69 to Fo67, and the smallest generation of groundmass olivines are Fo67-66. The ankaramites often contain up to 25% of olivine by mode and of this more than half is made up by large phenocrysts. In the alkali basalts the modal proportion of olivine is usually considerably lower (ca. 10%) and in the hawaiites olivines are relatively rare (<5%). Large olivine phenocrysts sometimes contain inclusions of clinopyroxene and spinel suggesting their coprecipitation at quite an early stage in the crystallisation history of the alkali basalt magma.

Clinopyroxenes, which are commonly well preserved, are titaniferous augites characteristic of silica deficient magmas. Euhedral clinopyroxene phenocrysts, when intact, may reach 10 mm in size and are ubiquitously zoned from light coloured cores of diopside or augite to darker coloured pink/brown rims of titanaugite or salite (see Plate C in Appendix A). The overall increase in the abundance of Ca, Ti, Al and total Fe from core to rim, which is inversely correlated with Mg, Si and Cr, mimics the overall behaviour of the alkali basalt magma as crystallisation proceeds and reflects the incorporation of both Ca- and Ti-Tschermak molecules into the pyroxene structure. Microphenocrysts of clinopyroxene, which commonly occur as glommeroporphyritic clusters, are variable but are usually of a composition which is

intermediate between the core and rim compositions of the large phenocrysts. Groundmass titanaugites are also variable in composition, presumably reflecting local melt compositions and diffusion gradients, but generally match the highest Ti and Al values observed in the phenocryst rims. Ankaramites often contain 45% modal clinopyroxene of which more than half is comprised of large phenocrysts. In the alkali basalts and the hawaiites the amount of pyroxene is less (ca. 30% and 20% respectively) and in the hawaiites it is largely confined to the groundmass. In the ankaramites, from TO1 (21/3-2) in particular, the large phenocrysts of clinopyroxene frequently contain inclusions of olivine, spinel and kaersutite.

In the alkali basalts and hawaiites calcic plagioclase occurs as microphenocrysts (1-2 mm) which are often sericitised and which commonly occur in stellate clusters. In the alkali basalts these microphenocrysts are zoned in a simple manner from large cores of ~An80 to narrow rims of ~An70. In the more evolved rock types the plagioclase phenocrysts become more abundant and are generally less calcic (ca. An40). The groundmass feldspar is frequently unaltered and ranges from ~An70 to potash oligoclase (~An20 Ab65 Or15) via sodic plagioclase. In the alkali basalts and ankaramites feldspar comprises less than 30-40% of the mode whereas in the more evolved hawaiitic varieties modal feldspar exceeds 50%. As the amount of modal feldspar increases the rocks can acquire a marked trachytoid, or flow aligned, texture of plagioclase laths and microlites. The more evolved varieties are also commonly more rapidly quenched and vesicular in character (see Plate J in Appendix A of this thesis and Plate 6.1b in Latin *et al.*, 1990a).

Ocelli, sub-spherical patches up to 10 mm in diameter, with a modal mineralogy and texture sharply distinct from the enclosing host rock, are locally common; e.g. in ankaramites from 21/10-1 (BP2), 21/3-2 (TO1) and 21/3-1a - see Plate I in Appendix A and Plate 6.1c in Latin *et al.*, 1990a. The ocelli are richer in kaersutite, magnetite, feldspar and apatite than the host groundmass, they are always more coarsely crystalline and the ocellus-groundmass contact is always abrupt. Kaersutite, which occurs as euhedral prismatic crystals which are often elongate (up to 1.5 mm in length) comprises up to 30% of the mode of the ocelli, the remainder of which is largely feldspar. Many of the ocelli are associated with amygdales containing carbonate or zeolite, which are usually defined by a tangential alignment of amphibole crystals. Ocelli are usually interpreted as evidence for the separation of an immiscible volatile-rich silicate liquid (Fall, 1980) and are not uncommon in alkali basalts. In some of the ankaramites the ocellar patches comprise ca. 10% of the mode. In this instance their occurrence in relatively mafic basaltic rocks, which have clearly not undergone substantial amounts of low pressure fractionation, may attest to

some enrichment of H_2O and K_2O in the parental Forties magmas. Indeed the presence of groundmass amphibole, biotite and ocelli in the Forties rocks all point towards a parental magma which was not completely free of volatiles.

Although the majority of the Forties rocks appear to be extrusive a few minor intrusives have been recognised. Fall *et al.* (1982) comment on intrusive hawaiites in 21/3-1a, and in 21/10-1 (BP2) a thin vein of hawaiite was observed to cut across the ankaramite. In 21/9-1 a number of alkali basalt flows may be identified by the presence of very fine grained reddened (oxidised) tops, a feature which may indicate subaerial eruption. Flow front breccias and hyaloclastite-like glassy and variolitic textures are developed in rapidly quenched highly vesicular hawaiitic rocks from wells CH1 (16/26-3) and SO1 (22/1a-4) in the deeper central parts of the region (see Figure 4.4), but generally the Forties basalts are not rapidly cooled and show no evidence for eruption into either water or wet sediments. It is concluded that the Forties basaltic rocks were erupted in a generally subaerial setting in a deltaic type of environment.

4.2.5 Summary.

Those features of the Forties province which are likely to be of importance when testing the theoretical framework (see Chapter 7) can be summarised as follows:

(1) The Forties province is Middle Jurassic in age and is located at the intersection of the three main Mesozoic North Sea graben structures. This may have implications for the degree of lithospheric attenuation in the area - see Chapter 6.

(2) The magmatic activity, which is largely extrusive and subaerial, occurs at a relatively early stage in the Jurassic syn-rift sequence and predates the Upper Jurassic (Oxfordian) extensional phase, considered by many to be the most important, at least in terms of fault movement and sediment growth. The timing of the magmatic activity must be providing information about the rate of decompression of the base of the lithosphere - see Chapter 7.

(3) The province covers a roughly circular area some 100 km across (~8000 km^2). The average thicknesses of igneous rocks in the province, including any gabbroic intrusions in the upper parts of the crust, is unlikely to exceed 2-3 km and is probably much less (0.5-1 km).

(4) The rocks are mildly undersaturated alkali basaltic rocks which have undergone only limited amounts of fractional crystallisation (to hawaiite).

4.3 Central North Sea Province.

4.3.1 Location and Stratigraphic Age.

The igneous rocks described in this group are restricted to quadrants 29 and 30 on the western flank of the deepest parts of the Central graben (see filled circles in Figure 4.8). The cores sampled from this area are from one production well, SH1 (30/16-A13Y, Shell) in the Auk oil field, and two exploration wells, SH2 (29/25-1, Shell) and AH2 (29/14b-1a, Britoil), on the Auk Ridge. At least 10 wells have penetrated igneous rocks, of intrusive, extrusive and epiclastic varieties, in this part of the North Sea which may, volumetrically, be second only to the Forties province in terms of its importance. The location of this province, close to the edge of the Central Graben, is of interest because in terms of the simple stretching model this region should be less stretched than the centre. However, as with the deep parts of the Witch Ground and Fisher Bank basins, there is a sampling problem in the deeper parts of the Central Graben. Figure 4.9 shows the location of positive magnetic anomalies, compiled from BGS regional total field anomaly maps, in the northern parts of U.K. sector of the North Sea (D. Smythe, pers. comm. 1990). Three distinct anomalies, attributable to mafic rocks, occur along the flanks of the graben close to the Cod, Auk, and Valhall fields, but none occurs in its centre. However, igneous rocks have, to this authors knowledge, only been recorded in wells from the Auk area. If these anomalies do represent igneous bodies then perhaps it is noteworthy that all three regions occur very close to major basin bounding faults. Upwardly migrating melts could be expected to diverge laterally in the upper crust and travel horizontal distances of up to about 20-30 km along major faults in the seismogenic layer; the upper 10-15 km of the crust. Similar observations have been attributed to melt migration along shallowly dipping detachment faults in East Africa (Bosworth, 1987).

The rocks of the Central North Sea province, like the Forties province, appear to be primarily extrusive in nature. However, in wells 29/14c-2, 29/19-2 and 29/25-1 (SH2) intrusive igneous bodies are encountered in the Zechstein part of the sequence. A number of wells penetrate conglomerates which are formed by large (up to 10 cm in diameter) rounded cobbles of altered basaltic material supported in a matrix which is chalky and fossiliferous. (e.g. 29/14b-1a (AH2), 30/16-3, 30/16-A13Z). In well 30/16-A13Y (SH1) a similar, but more clast supported and brecciated layer, 2-3m in thickness, occurs directly above a sequence of lava flows which have been cored and

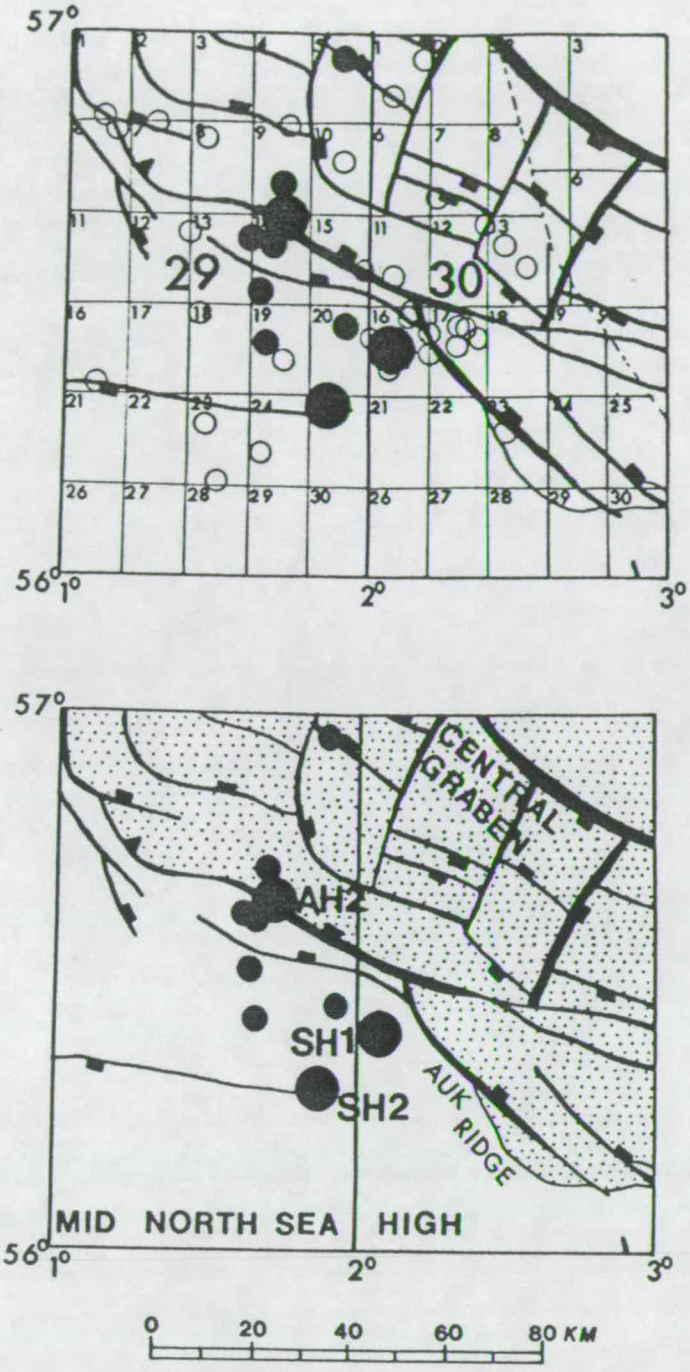

FIGURE 4.8 Location of igneous rocks in the Central Graben province. Upper diagram shows the locations of wells penetrating igneous material (small filled circles), wells in which igneous rocks were cored and used in the present study (large filled circles) and wells which penetrated Triassic sediments without sampling igneous rocks (small open circles). Large numbers correspond to standard U.K quadrant numbers while small numbers note individual licensing blocks. The main structural elements of the region are shown in the lower diagram and wells from igneous rocks were analysed (Appendix A) and are labelled with code names. The base map is the *Tectonic Map of the North Sea* published in 1989 by GECO Exploration Services and Alastair Beach Associates. Dots indicate the main graben defined by the 3.0 second TWT contour at Base Cretaceous level.

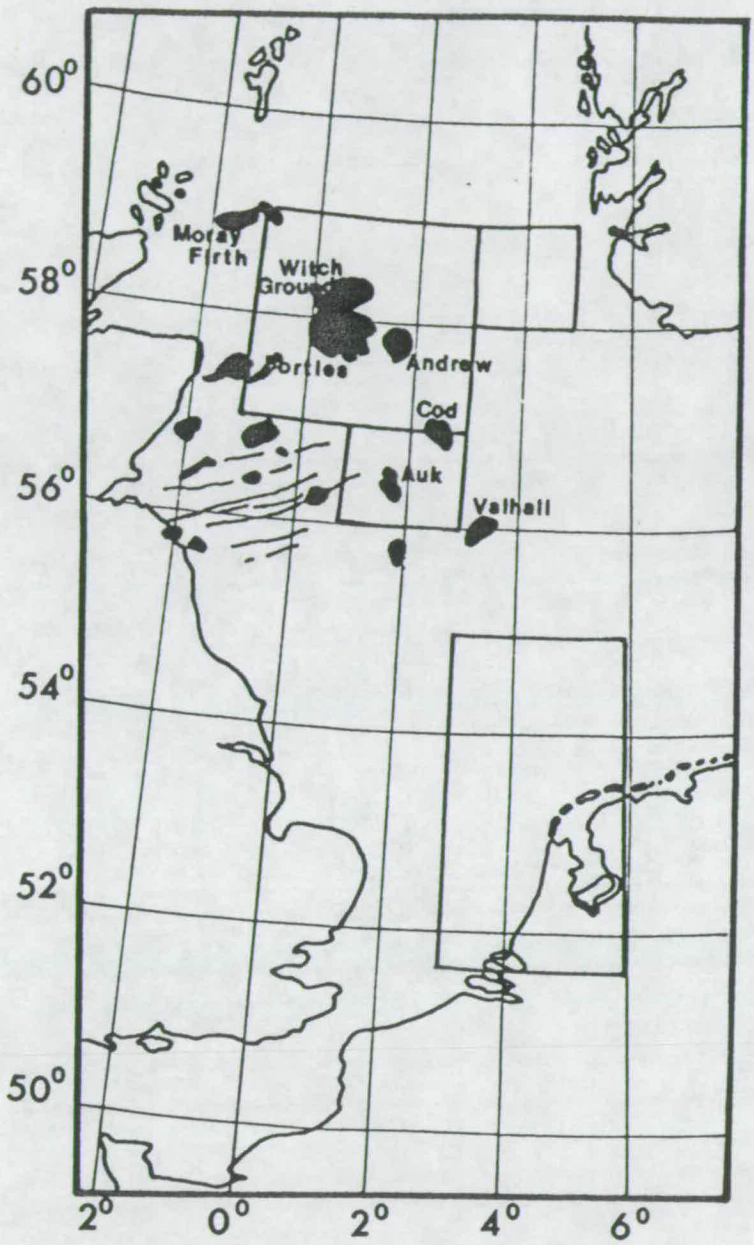

FIGURE 4.9 Total field magnetic anomalies attributable to mafic rocks which are either deeply buried volcanics, plutonic bodies or in some instances dykes. Copied from an unpublished diagram provided by D. Smythe (Glasgow university). The main areas of igneous activity during the Mesozoic are outlined. Hydrocarbon fields close to individual anomalies are named.

were sampled during the course of the present study. Although flows are only cored in 30/16-A13Y they are noted in the well reports of a number of wells (e.g. 29/14b-3, 29/14b-1a, and 29/20-1). Other wells sample polymict epiclastic (or agglomeratic) deposits composed largely of angular fragments of basalt which fine upwards into sandy shales containing coal fragments (e.g. 29/14b-4 (Texaco) and 29/9b-2 (Premier)).

In all of the wells studied the extrusive flows, volcaniclastic and epiclastic deposits are overlain by Upper Jurassic (Kimmeridgian or Volgian) sands and shales. Some of these sandy sediments contain glauconite and are therefore inferred to represent shallow marine conditions. The stratigraphic age of the overlying sediments appears to be well constrained, mainly on the basis of palynoflora. In none of the wells are there reliable palynomorphs for the igneous part of the sequence which is commonly inferred to belong to the Middle Jurassic. The Central Graben igneous province rests on fluviatile sands which are generally considered to be Triassic in age. The overall statigraphic sequence is therefore very similar to that described for the Forties region (see Figure 4.5). Basement subsidence curves for 3 of the wells in this area, (29/14b-1a, 29/14a-4, and 29/9-1) are presented in Chapter 6.

4.3.2 Radiometric Ages.

In well 29/25-1 (SH2), on the edge of the Mid North Sea High, two sequences of rocks were discovered, one in the Upper Permian, the other a few hundred metres lower in the Lower Permian, both very similar texturally. $^{40}Ar/^{39}Ar$ age spectra showed a plateau oscillating about 135 Ma, with a best estimate age of 138±4 Ma and outside limits of 128 and 157 Ma (Dixon *et al.*, 1981; Latin *et al.*, 1990a). When these samples were originally dated in the late 1970's it was thought that the high age at the low temperature end of the spectrum was probably due to a gain in ^{40}Ar from the surrounding salts (J. Miller pers. comm. 1988). However, $^{40}Ar/^{39}Ar$ dating funded by Shell has since been conducted on a mineralogically similar whole rock sample (PL1/6), also intruding salts, in the Netherlands province. Although a similar spectrum, with apparent ^{40}Ar gain causing old ages at low temperature steps, was obtained from the whole rock sample (Miller, see Appendix B), when fresh kaersutite separates were analysed from the same sample they gave old ages (Halliday, see Appendix B). It is therefore suggested that the probable age of the intrusive rocks in 29/25-1 is closer to 157 Ma which would place them in the Oxfordian or Callovian on most time scales.

Four samples from the extrusive rocks from well 30/16-A13Y were dated in 1988 using K-Ar by P.J Hamilton and R.M. Macintyre (SURRC) for Shell (A. Heward, pers. comm. 1989). In an unpublished report to Shell, Hamilton and Macintyre state that because of later alteration events "*the ages of 127-101 Ma should be considered minima*". One sample (SH1/10) has now been the subject of a $^{40}Ar/^{39}Ar$ stepwise degassing study, conducted by A. Halliday, which yielded a good age plateau providing a reasonably reliable estimate of 130±2 Ma (Valanginian-Hauterivian) for the age of the sample (see Appendix B for further details). Given that the extrusive rocks in SH1 (30/16-A13Y) are reportedly overlain by Lower Cretaceous sediments, this young age need not be at odds with the statigraphic constraints.

4.3.3 Volumes.

Individual wells (e.g. 29/14b-1a and 29/14a-4) penetrate close to 300 m of volcanics and tuffs before reaching the Triassic part of the section. There is no evidence that the thickness of melt extruded in this province exceeds 300 m and on average it may be less. The magnetic anomaly in the Auk region could be modelled in terms of some volume of mafic rock but this has not yet been done. In short the volume of melt generated in this part of the North Sea during the Middle Jurassic is not constrained but it does appear that this may be the second most important igneous centre, after the Forties province, in the Mesozoic of the North Sea.

4.3.4 Petrography and Mineralogy.

All three cored sequences encountered "basaltic" rocks which are more undersaturated and which, by inference from their mineralogy, are more enriched in K_2O and H_2O than the Forties alkali basalt suite. The most common extrusive rock type in the province appears to be a largely aphyric, kaersutite-rich, undersaturated rock (basanite to leucitite), containing prominent ocelli and late stage segregation veins (see Plate N in Appendix A) which are probably the result of filter pressing (Middlemost, 1985). The intrusive rocks are mineralogically similar but biotite occurs instead of kaersutite, which is only found in ocelli, and they contain pseudomorphed phenocrysts of clinopyroxene and olivine (see Plate O in Appendix A). High pressure phenocrysts/xenocrysts of phlogopite, now resorbed, are common in the intrusive rocks. Both intrusive and extrusive rock types are altered, sometimes severely.

4.3.4.1 Extrusive Rocks.

The extrusive rocks in the province are most easily studied in well 30/16-A13Y (SH1) which penetrates three flows (each ~10m thick) whose tops are marked by brecciation and intense alteration. The highly altered ?extrusive igneous rocks sampled as cobbles from the conglomerate cored in 29/14b-1 (AH2) appear to be of two varieties, one type similar to the SH1 suite described below, and another type, containing some groundmass plagioclase and pseudomorphed phenocrysts of olivine and augite, which is more reminiscent of the basaltic rocks seen in the Forties province.

The rocks in SH1 are fine grained, ocellated, and are dominantly composed of euhedral titanaugite and amphibole prisms, in a groundmass of alkali feldspar and feldspathoid with large crystals of spinel and apatite (see Plate N in Appendix A). Rare microphenocrysts of titanaugite as stellate clusters and early spinel octahedra, also as clusters, occur. They have been termed *kaersutite leucitites*.

Pyroxene is largely a groundmass phase (0.2-0.3mm in length by 0.02mm across), occurring as euhedral prisms which form ~20% of the mode and which are titanaugites compositionally richer in Al and Ti than the cores of the phenocrysts in the Forties province. Al_2O_3 ranges from 4 to 5 wt. % and TiO_2 varies from 2 to 3 wt. %. Individual pyroxene microphenocrysts fall close to the lower end of this compositional range in terms of Al and Ti and are usually less than 1mm in length. Spinel, which forms up to 15% of the mode of these rocks, occurs both as microphenocryst (octahedra up to 0.8mm across) and groundmass generations (as 0.025mm grains). Amphibole, which occurs as euhedral prisms usually 0.1mm by 0.05mm in size, is entirely restricted to the groundmass, ocelli and veinlets, and comprises ~10-15% of the mode. Compositionally the amphiboles are kaersutites, rich in TiO_2 (5 to 6.3 wt.%) and K_2O (1 to 1.15 wt.%).

The mafic crystals described above are surrounded by felsic material which has two main components. One of these is a clear untwinned alkali feldspar (ca. 20-25% by mode) and the other is a colourless or slightly brownish zeolite inferred (from the high K_2O content of the whole rock, see Appendix A) to be a pseudomorph after a potassic feldspathoid (?leucite) and silica-undersaturated glass which together constitute ~30% of the mode. Apatite is abundant and commonly occurs as large hollow prisms (0.5mm long) which may attest to the relatively evolved nature of these rocks.

The severe alteration of the igneous samples in 29/14b-1 (AH2) makes petrographic classification difficult. It is however clear that there are two varieties. Samples AH2/9, AH2/5 and AH2/6 are all fine grained and largely aphyric, although

microphenocrysts of clinopyroxene (now pseudomorphed) and spinel do occur. The groundmass is characterised by microlites of alkali feldspar, patches of carbonate after pyroxene, and colourless octahedra of zeolite after ?feldspathoid. Small crystals of biotite (0.25mm across) are locally abundant and amphiboles occur in ocellar patches observed in two of the thin sections. These rocks are tentatively classified as basanites which, from their relatively large modal proportion of felsic material (>50%), are probably moderately evolved; i.e. the undersaturated equivalent of the Forties province hawaiites. The other variety, seen in samples AH2/4, AH2/7 and AH2/11 is more similar to the basalts of the Forties province but is still probably more undersaturated (see Plate E in Appendix A). They are noticeably more coarsely crystalline and porphyritic than the variety described above. Pseudomorphs of clinopyroxene and olivine are abundant. Groundmass plagioclase, notably less abundant than in the alkali basalts of the Forties province, is altered but still shows multiple twins. The presence of large (1 to 2mm) poikilitic plates of alkali feldspar suggests slow cooling. They are again tentatively classified as basanitic.

4.3.4.2 Intrusive Rocks.

The intrusive rocks from well 29/25-1 (SH2) were described by Dixon *et al.* (1981). The intrusive rocks in the Central North Sea can be broadly termed lamprophyres. They are fine grained and contain conspicuous flakes of pale brown mica (up to 10 mm across) scattered through them (see Plate O in Appendix A). In thin section these micas are perfectly fresh, smoothly rounded, phlogopites interpreted as high pressure phenocrysts or xenocrysts. Rounded xenocrysts of ?orthopyroxene pseudomorphed by carbonate are also common. Phenocrysts of clinopyroxene (up to 2.5 mm across) often in stellate clusters, are pseudomorphed by granular ore and carbonate. Euhedral olivines (up to 1 mm across) pseudomorphed by chlorite are scattered across the slide. Microphenocrysts (0.1 mm across) are small spinels and 6- and 8-sided pseudomorphs in carbonate and zeolite after a feldspathoid (?leucite). The groundmass is composed of finely prismatic pyroxene pseudomorphs, abundant biotite, and a low birefringence interstitial phase thought to be analcime. Alkali feldspar and amphibole are confined to ocelli 1-2 mm. These intrusive rocks, which show many similarities to the kaersutite-leucitites identified in 30/16-A13Y (SH1), were termed mafic biotite phonolites by Dixon *et al.* (1981). They might alternatively be described as potassic lamprophyres.

4.3.5 Summary.

(1) The Central North Sea igneous province, which occurs on the western margin of the Central Graben, is, like the Forties province, probably Middle Jurassic (Callovian) in age. The episode of igneous activity is followed by an Upper Jurassic to Lower Cretaceous marine transgression.
(2) The igneous rocks of the province are largely subaerial, lava flows, tuffs and epiclastic rocks, although a number of intrusions are found within the Zechstein part of the sequence.
(3) The amount of igneous material in this area of the Central Graben is difficult to estimate. Aeromagnetic data (Figure 4.9) suggest that the province extends along both the E and the W flanks of the Graben, that locations may be controlled by faults, and that the total area covered by mafic rocks may be of secondary importance only when compared with the Forties province.
(4) The rocks are highly potassic, volatile rich, undersaturated basanites, leucitites and lamprophyres. They cannot be the direct product of melting of dry garnet peridotite (see Chapter 5).

4.4 The Egersund Basin.

4.4.1 Location and Stratigraphic Age.

Two sequences of igneous rocks, first reported by Dixon *et al.* (1981) and later described by Furnes *et al.* (1982) were cored in well 17/9-1 (Esso, ES1) on the western edge of the Egersund basin in the Norwegian sector of the North Sea (Figure 4.10; see also Figure 4.2). The area is one with very few exploration wells and no other igneous rocks are known to have been cored. The upper igneous sequence in well 17/9-1 comprises approximately 400m of volcanic rocks and interbedded sediments which are overlain by claystones of Oxfordian age, and which overlie Lower Jurassic shales and limestones of the Fejerritslev and Gassum formations. The rocks of this upper igneous sequence are reported to be interbedded with sediments of the Haldanger formation which is Bajocian-Bathonian in age (Furnes *et al.*, 1982). The second, lower, igneous sequence intrudes sandstones belonging to the Triassic Skagerak formation.

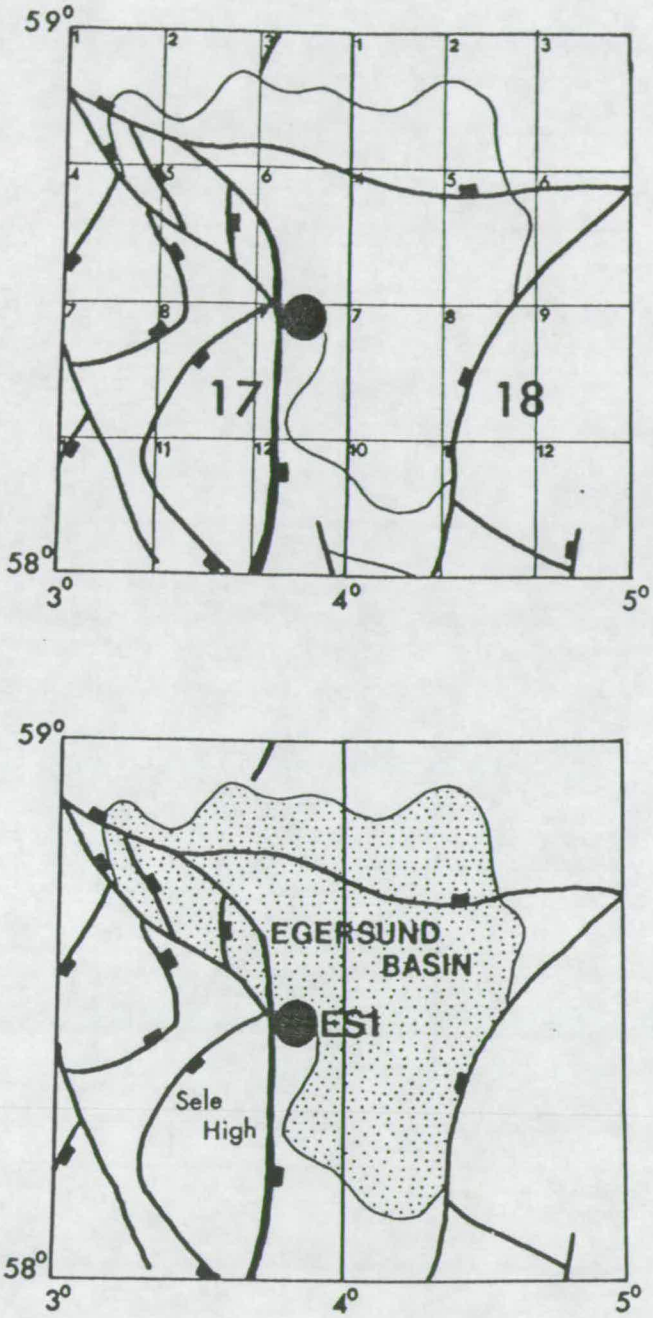

FIGURE 4.10 Location of igneous rocks in well 17/9-1 from the Egersund Basin in the Norwegian sector of the North Sea. Large numbers in upper diagram correspond to standard Norwegian quadrant numbers while small numbers note individual licensing blocks. The main structural elements of the region are shown in the lower diagram and the analytical code name (ES1) is given (see Appendix A). The base map is the *Tectonic Map of the North Sea* published in 1989 by GECO Exploration Services and Alastair Beach Associates.

According to Brown (1984) the Egersund Basin was largely developed during the Late Jurassic, although Ziegler (1982) notes the Stord-Egersund Basin as one of the outstanding structural features during the Triassic. The Stord Basin, just to the north of the Egersund Basin, certainly contains large thicknesses (up to 1 km) of Triassic strata which show clear evidence of north-south fault control (Biddle and Rudolph, 1988). Basement subsidence curves for 17/9-1 (see Chapter 6) suggest that subsidence accelerated during the Middle to Upper Jurassic but was on-going from the Triassic to the present day.

4.4.2 Radiometric Ages.

The lower suite of intrusive rocks contain large phlogopite phenocrysts which were dated, using conventional K/Ar techniques, by Fumes *et al.* in 1982. They report a range of ages from 177 to 180 Ma. Both igneous sequences are pervasively altered and even the phlogopite phenocrysts are veined by carbonate. The reliability of dates determined by standard K/Ar techniques may therefore be in some doubt. Phlogopites from the lower sequence and a whole-rock sample from the upper sequence have now been dated using the $^{40}Ar/^{39}Ar$ stepwise degassing technique (see Appendix B).

J. Miller (Cambridge) conducted a step wise Ar degassing study onthe whole-rock sample from the upper sequence (see Appendix B); sample 7N, an extrusive nephelinite. Unfortunately more than 90% of the ^{39}Ar was lost during the first three heating steps and no reliable estimate could be made for the age of the sample. A conventional K-Ar date would have been 244±40 Ma! Stepwise degassing of irradiated phlogopite separates (by Halliday) from the lower sequence was much more successful and an excellent age plateau was obtained which gave an estimated crystallisation age of 170±2 Ma (Bathonian/Bajocian).

4.4.3 Volumes.

It is not possible to say much about the volume of igneous rock in this area. Fumes *et al.* (1982) suggest from seismic evidence that the extrusive sequence may cover an area some 600 km^2. The average thickness of melt produced in the Egersund Basin is probably much smaller than in the preceding areas. i.e. considerably less than 0.5 km.

4.4.4 Petrography and mineralogy.

The igneous rocks from well 17/9-1 are highly undersaturated extrusive nephelinites, rich in titaniferous pyroxenes, and potassic alkaline lamprophyres (?alnöites) rich in large, often fractured, phenocrysts of phlogopite, and pseudomorphs after clinopyroxene and olivine phenocrysts.

4.4.4.1 Extrusive Rocks.

The lava samples studied are relatively fresh porphyritic rocks with either a fine grained holocrystalline, or a turbid brown glassy sometimes brecciated, groundmass. The samples are highly vesicular and many contain chlorite filled or zeolite (?natrolite) filled amygdales. At rapidly chilled flow tops streamers of vesicles are observed. The hyaloclastite-like textures of some samples suggest rapid cooling of flows, some of which may have been erupted into water. All samples contain prominent, euhedral, multiply twinned, rectangular phenocrysts of a brown clinopyroxene up to 6mm in length, which also show sector and complex fine scale oscillatory zoning and anomalous birefringence (see Plate K in Appendix A). Compositionally they are titaniferous salites typical of undersaturated basic rocks. Zoning reflects variation between a relatively low-Ti, Al-poor salite (TiO_2~1 wt.% and Al_2O_3~4 wt.%) and a high-Ti, Al-rich salite (TiO_2~5 wt.% and Al_2O_3~10.5 wt.%). The high Ti zones are also enriched in total Fe. Microphenocrysts of pyroxene, showing similar zonations, are common as glommeroporphyritic clusters. Rare, larger, euhedral, serpentine pseudomorphs after olivine occur in a number of sections. Altered nepheline, clinopyroxene and ore make up the groundmass. A few samples (e.g. 8N and ES1/5) contain 6-, 7- and 8-sided phenocrysts (up to 1mm across) and groundmass crystals after another feldspathoid phase, now analcime, but probably a sodalite group mineral originally (see Plate K in Appendix A). Contrary to Furnes *et al.* (1982) no samples were found containing any feldspar, despite the study of more than 30 thin sections, and the rocks have thus been classified as nephelinites.

4.4.4.2 Intrusive Rocks.

Samples from the intrusive sequence show abundant, large, pseudomorphed, euhedral phenocrysts of clinopyroxene and olivine, both now replaced by similar aggregates of carbonate and green chlorite (see Plate L in Appendix A). Large, slightly rounded, phlogopite phenocrysts are prominent and are only partially altered along cleavage traces. No phenocrysts of feldspathoid have been positively

identified. The groundmass is dominated by opaque ore, small flakes of mica and a pale brown low birefringence phase which is probably an altered feldspathoid or possibly melilite. Contrary to Fumes *et al.* (1982) leucite phenocrysts were not identified in the samples studied. Several distinctive, rounded, carbonate and chlorite pseudomorphs rimmed by phlogopite and magnetite are thought to be partially resorbed orthopyroxene xenocrysts which have undergone subsequent hydrothermal alteration (see Plate L in Appendix A). The rock's texture is striking, arising from abundant euhedral microphenocrysts of phlogopite and altered clinopyroxene and highly irregular fractured larger grains, suggesting transport in a rapid moving volatile-rich matrix which was then partly extracted concentrating the phenocrysts. The presence of phenocrysts of phlogopite, clinopyroxene and olivine would, if melilite could be positively identified, lead to classification of these rocks as alnöites. Alternatively, a safer classification would be that of an ultrapotassic alkaline lamprophyre. These rocks show many similarities to the lamprophyres described from 29/25-1 (SH2) in the Central North Sea.

4.4.5 Summary.

(1) The Egersund Basin, which has been subsiding since Triassic times, is sited approximately half way between the Forties province and southern Norway. Volcanism, possibly submarine, and intrusive magmatic activity, occurred on the south western edge of the basin in the early Middle Jurassic (~170 Ma).

(2) The amount of basaltic material is difficult to estimate but it seems likely that there is less than in the Central North Sea province and much less than in the Forties province.

(3) The igneous rocks from the Egersund Basin are extremely silica undersaturated, highly alkaline, nephelinites and phlogopite bearing lamprophyres (alnöites). Their generation almost certainly involves the presence of CO_2 and/or H_2O.

4.5 The Netherlands Province.

4.5.1 Locations.

The known locations of igneous rocks in the Netherlands region, onshore and offshore, are shown in Figures 4.11 and 4.12. The occurrences can essentially be split into 3 groups on the basis of location.

(1) The Cleaver Bank Terrace group on the western edge of the Dutch Central Graben; F/10-1 (PL1, Petroland) and E/6-1 (N.A.M.).

(2) The Waddensee occurrence close to Texel Island; Zuidwal-1 (PL2, Petroland).

(3) Broad Fourteens Basin group; K14-FA103 and L13/3 (both N.A.M.).

(4) West Netherlands Basin group; Andel/2, Andel/4 and Loon-op-Zand/1 (all N.A.M.).

It is most convenient to discuss the stratigraphic position, age and petrographic and mineralogical character of the igneous rocks from each group in separate sections. It should be noted that the rocks of the Netherlands province are probably the most severely altered of all of the North Sea occurrences sampled. The subsidence history is not known in detail because the entire region is subject to salt withdrawal and diapirism and because many of the basins have been inverted. Unlike the regions already discussed, estimates of β are not made for the Netherlands basins in Chapter 6.

4.5.2 Cleaver Bank Terrace.

In the Dutch Central Graben and Cleaver Bank Terrace the stratigraphic relationships are very similar to those observed in the Central North Sea province. According to Clarke-Lowes *et al.* (1987) thermal subsidence occurs after a Triassic rift phase but is abruptly terminated during the Middle Jurassic (Bajocian-Bathonian) by an erosional unconformity which heralds "*the onset of major basin extension*" and the deposition of thick sequences of Oxfordian sediments. The igneous rocks in F/10-1 (PL1), like some of the Central North Sea occurrences, are intrusive into the Zechstein sequence and have often, wrongly, been assigned to the Permian. The igneous rocks in E/6-1 have not been sampled during the course of this work because the side wall core was completely used up in dating. According to N.A.M. the rocks are intrusive, granites (!!), within the Carboniferous.

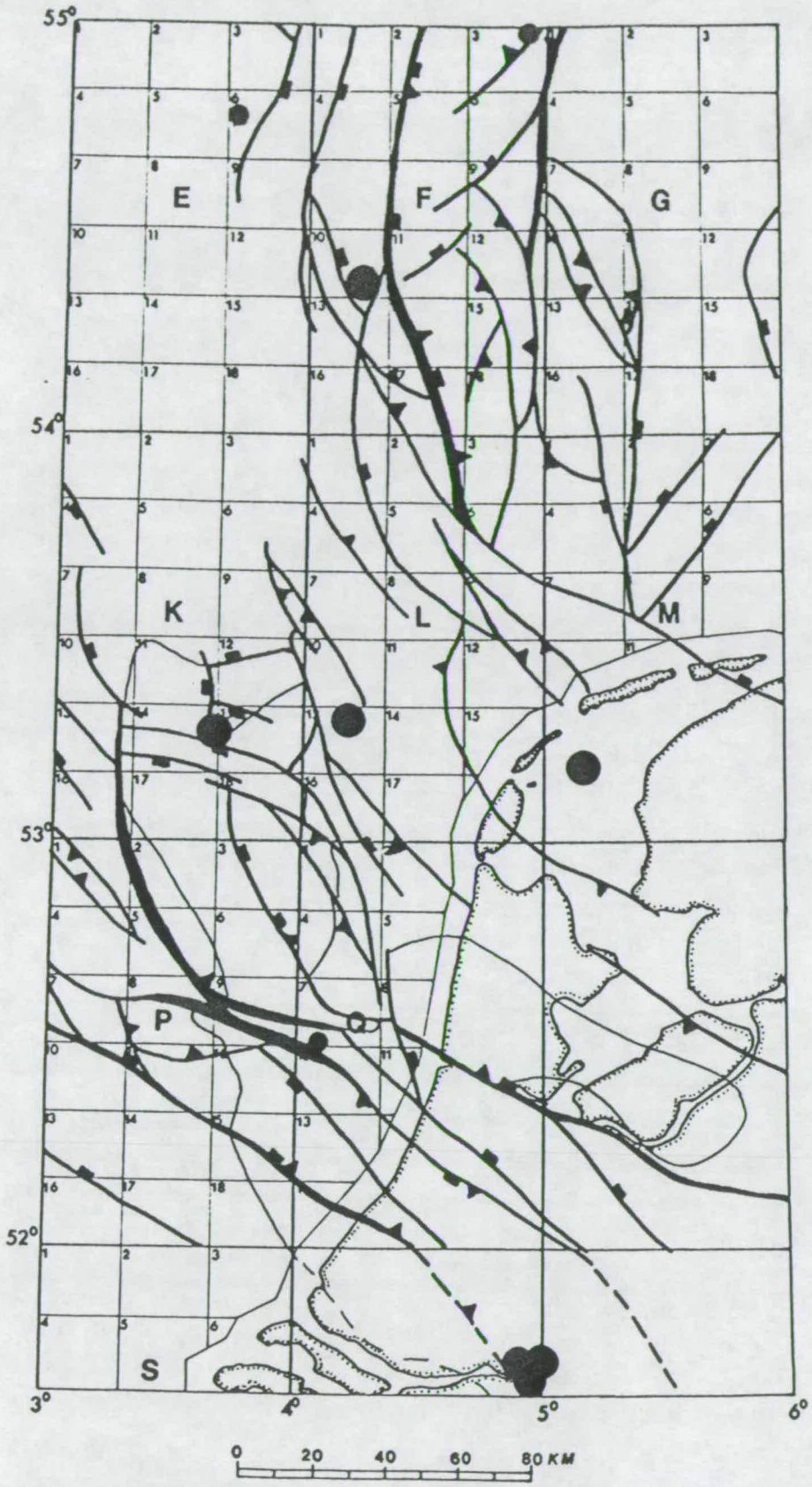

FIGURE 4.11 Location of wells containing igneous rocks in the Netherlands province. The map shows wells in which igneous rocks were cored and used in the present study (large filled circles) and wells which penetrated igneous material that was not used (small filled circles). Large numbers correspond to standard Netherlands quadrant numbers while small numbers note individual licensing blocks.

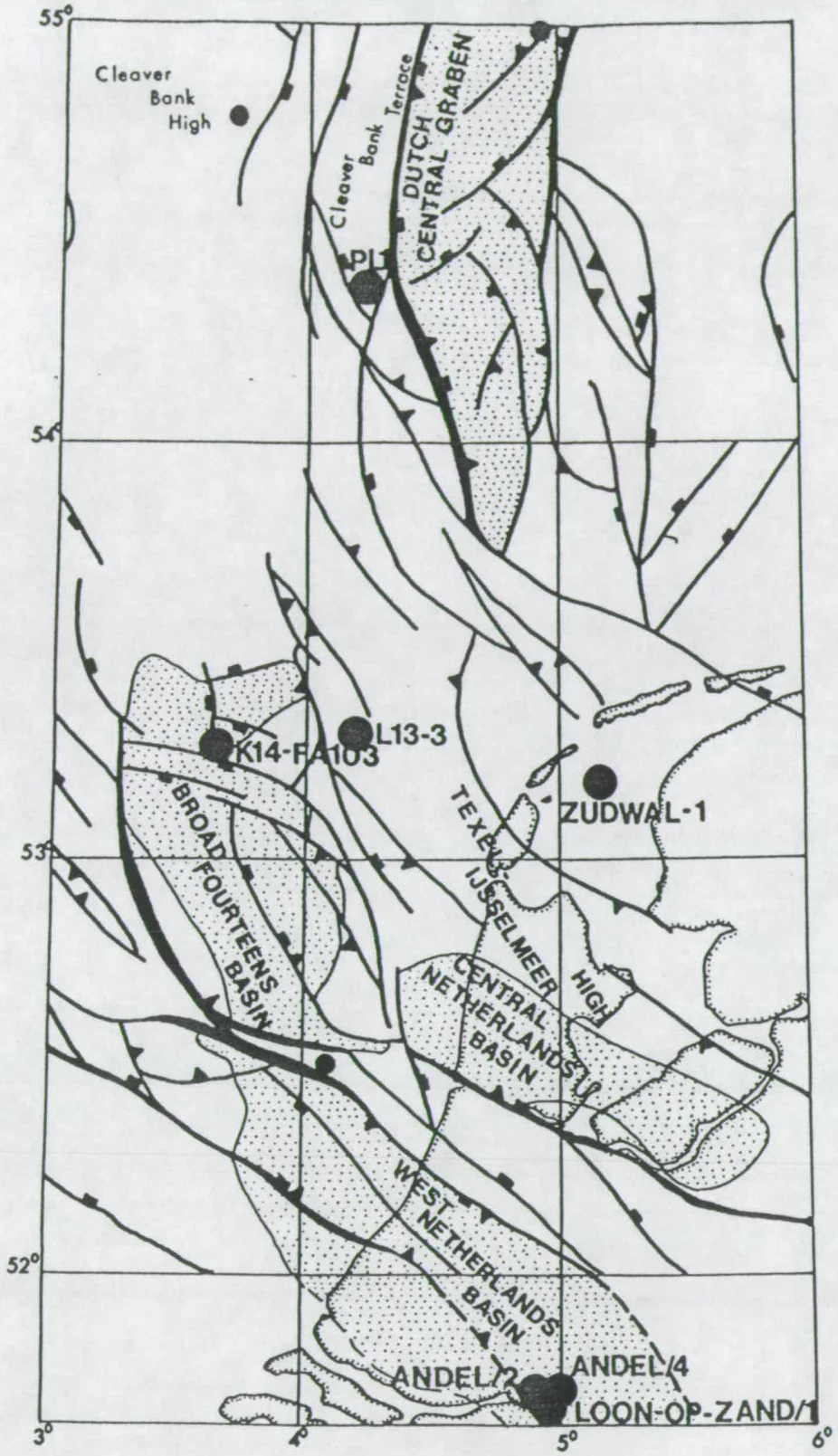

FIGURE 4.12 The main structural elements of the Netherlands region are shown and wells from which igneous rocks were analysed (Appendix A) and are labelled (large filled circles). The base map is the *Tectonic Map of the North Sea* published in 1989 by GECO Exploration Services and Alastair Beach Associates. Dots indicate the main graben defined by the 3.0 second TWT contour at Base Cretaceous level.

The intrusive rocks in E/6-1 and F/10-1 were dated using whole rock K/Ar methods and gave ages of 161±4 Ma (~Callovian/Bathonian) and 95±5 Ma (~Albian) respectively (unpublished data of N.A.M.). The rocks in F/10-1 have now been dated again using the $^{40}Ar/^{39}Ar$ stepwise degassing technique on a whole rock sample (J. Miller at Cambridge) and on kaersutite phenocrysts separated from the same sample (A. Halliday at Mitchigan). The whole rock spectrum on sample PL1/6 would conventionally be interpreted to give an age of 101.6±2.5 Ma at the highest temperature steps. The ages obtained from the ^{39}Ar released at lower temperatures are greater, and give a maximum plateau age of 125±5.8 Ma. However, the amphiboles separated from this sample give a very consistent spectrum through all of the degassing steps which gives a best estimate of the closure age as 151±2 Ma (Kimmeridgian/Tithonian). The lower ages given by the whole rock spectrum are almost certainly an artifact of an alteration event which must have affected the region at ca. 100 Ma. *The older date obtained by study of the amphibole phenocrysts calls into question all of the previous K/Ar and whole rock $^{40}Ar/^{39}Ar$ dates on rocks in the southern North Sea* (see Latin *et al.* 1990a).

The intrusive rocks in F/10-1 (PL1) are characterised by sparse large euhedral phenocrysts of kaersutitic amphibole and even less abundant phenocrysts of titaniferous clinopyroxene (see Plate M in Appendix A). A very small number of euhedral olivine phenocrysts, now pseudomorphed by clay, may also be identified. The rest of the rock is largely composed of euhedral microphenocrysts of kaersutite and pyroxene, with interstitial feldspar, zeolite, apatite and spinel. These rocks, which look essentially like coarse equivalents of the lava flows described from the Auk area in the Central Graben, have been termed alkaline lamprophyres (?sannaites) and one of the freshest samples (PL1/6) is described in detail in Appendix B.

4.5.3 The Waddensee.

The only occurrence of igneous rocks known from this area comes from wells in the Zuidwal gas field and they have only been cored by Zuidwal-1 (Petroland; samples denoted by ZU in Appendix A). The well is located north of the Texel Ijsselmeer High and south of the southern extension of the Central Graben (see Figure 4.12). The exploration well was drilled in the hope of finding a gas field in a domal structure which had been defined by gravity, magnetic and seismic data (Cottençon *et al.*, 1975; Perrot and van der Poel, 1987). After penetrating gas-bearing Valanginian sands and ~1 km of volcanic agglomerate, drilling was discontinued in the volcanics. Seismic data shows that Zuidwal-1 evidently scored a direct hit on the vent of a major

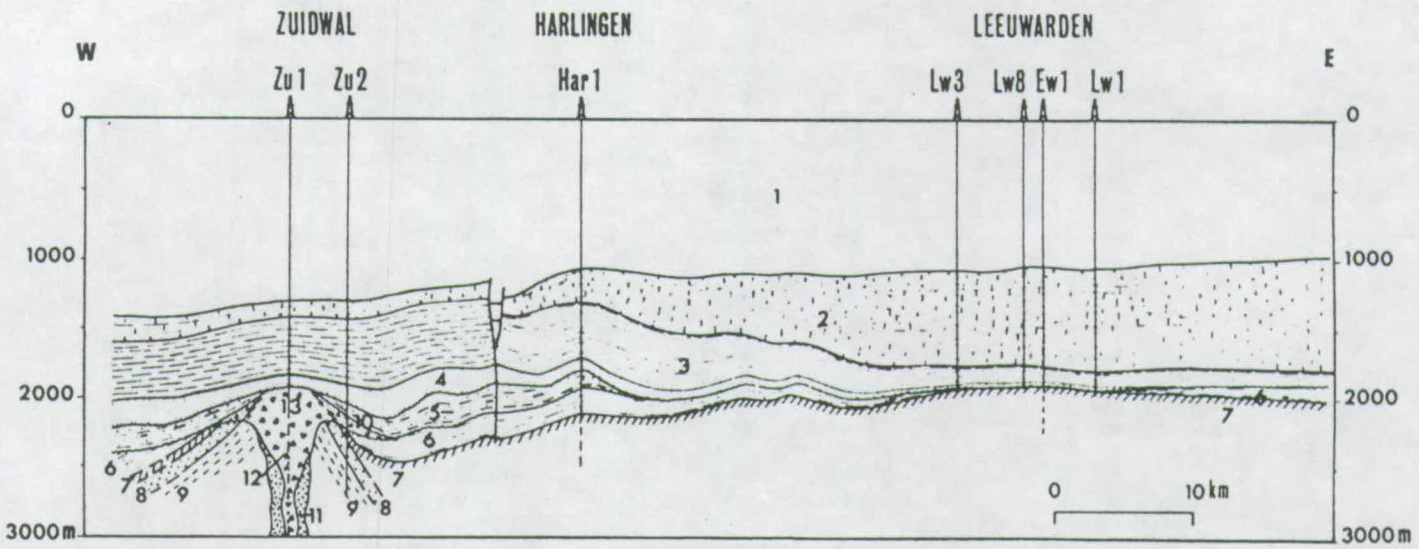

FIGURE 4.13 From Cottençon *et al.* (1975). A structural cross-section of the Netherlands Lower Ctetaceous gas-fields also showing the volcano at Zuidwal.

volcanic edifice. The stratigraphy in the area is shown in Figure 4.13, taken from Cottençon *et al.* (1975). In Zuidwal-2 and Zuidwal-3 volcanic breccias are overlain by uppermost Jurassic and Lower Cretaceous (Wealden) coal bearing sandstones and shales. Stratigraphically the igneous rocks are constrained as being older than Lower Cretaceous and probably younger than Triassic. It appears that, once again, the igneous rocks occur just prior to the main phase of subsidence in the area. The Zuidwal volcano is evidently an eroded volcanic dome, some 12 km across, now buried by Lower Cretaceous sediments. Zuidwal is clearly a major edifice perhaps comparable to off-axis volcanoes in East Africa, such as Mount Elgon (Dixon *et al.*, 1981). No reliable estimate of the volume of basaltic parental magma can be made from the available data.

Samples of volcanic material have been dated using K/Ar (Harrison *et al.*, 1979), $^{40}Ar/^{39}Ar$ (Dixon *et al.*, 1981) and $^{40}Ar/^{36}Ar$-$^{40}K/^{36}Ar$ techniques (Perrot and van der Poel, 1987). Of these the latter gives the oldest, and probably the most reliable, age of 152±3 Ma which would be Kimmeridgian/Tithonian on the timescale of Harland *et al.* (1990). This makes the Zuidwal occurrence the same age, to within analytical error, as the intrusive rocks from F/10-1 (151±2 Ma) and this is similar to the oldest age (157 Ma) reported for the intrusive rocks from 29/25-1 in the vicinity of the Auk field.

The core from Zuidwal-1 encountered a great range of different rock types (often severely altered), from feldspathoidal basalts through to evolved types rich in feldspathoid alone (e.g. leucitophyre or leucitite; see Plate P in Appendix A of this thesis and Plate 6.1g in Latin *et al.*, 1990a) or feldspar and feldspathoid (phonolite). Jeans *et al.* (1977) report trachytes but these have not been observed in the sections studied during the course of this work. The more evolved varieties dominate the suite of samples. Some of the basic varieties appear to have abundant modal nepheline (basanites and tephrites) while others contain microphenocrysts of leucite (leucite basanites and tephrites). The freshest mafic rocks sampled (ZU5 and ZU6) are rather evolved leucite basanites (mafic phonolites) which contain two, distinct phenocrystal pyroxenes (see Plates Q and R in Appendix A). One is a green pleochroic aegirine augite, while the other, a brown titaniferous salite, is very similar to those observed in the nephelinite suite of the Egersund Basin, suggesting a similar degree of undersaturation (see Dixon *et al.*, 1981).

The key feature of the igneous rocks of the Zuidwal volcano is the implied, but not necessarily large, variability in the ratios of Na_2O to K_2O and of total alkalis to alumina and silica in the parental basaltic undersaturated magmas. Low pressure fractionation has then operated to exploit what may be small bulk chemical

differences between parents to produce a wide range of evolved rock types. It is however clear that the Zuidwal volcanics are a nephelinite to phonolite suite which requires there to have been volatiles present in the region of melt generation.

4.5.4 Broad Fourteens and West Netherlands.

No new wells have been reported to have penetrated igneous rocks in these two basins and the localities shown in Figures 4.11 and 4.12 are those first described by Dixon *et al.* (1981). The Broad Fourteens Basin contains two occurrences of intrusive rocks, both at its northern end, K14-FA103 in the basin and L13-3 on the SW edge of the Texel Ijsselmeer High. The West Netherlands Basin has three wells which penetrate intrusive rocks; Andel/2, Andel/4 and Loon-op-Zand. Between the two basins, which are described together because of their similar stratigraphic histories, igneous rocks were encountered and dated in Q/7-2.

According to Ziegler (1982) the basins in the onshore and offshore areas of the Netherlands started to develop in the Early Triassic as a result of crustal extension. The main phase of subsidence, governed by the now evident NW-SE trending fault systems (Figure 4.12), occurred in the Middle to Upper Jurassic and extension is likely to have been dominated by dextral motions (van Wijhe, 1987). Seismic sections across the basins show thick sequences of Jurassic and Cretaceous sediments which become less affected by fault motions during the Upper Cretaceous and Tertiary as regional thermal subsidence occurred. Subsidence was interrupted and the basins were inverted during the Palaeocene as Alpine shortening to the south made itself felt.

The igneous intrusions associated with these basins are not found in sequences younger than Middle Jurassic in age. Radiometric dates were given by Dixon *et al.* (1981) and are summarised in Table 6.1 in Latin *et al.* (1990a). None of these ages are greater than 133±2 Ma (Andel/4) and so if they are correct the igneous rocks in these two basins must be younger than those in the Waddensee and Cleaver Bank Terrace. The rocks are, however, all extremely altered and the dates given are most likely to be minimum age estimates. Given that Q/7-2, L/13-3 both give whole rock $^{40}Ar/^{39}Ar$ ages that are close to 100 Ma (95±2 to 106±2 and 101±1 Ma respectively) and that the whole rock $^{40}Ar/^{39}Ar$ age for F/10-1 was ~100 Ma when its true age is probably closer to 150 Ma, these low ages should be treated with considerable suspicion. Unfortunately all of the samples collected so far are too altered to date effectively.

Petrographically the rocks all appear to be more undersaturated than the Forties province alkali basalts. The samples from K/14-FA103 (samples DL1 to DL2A in Appendix A) are severely altered, rather evolved (hawaiitic), undersaturated potassic rocks, similar to those 30/16-A13Y (SH1), rich in pseudomorphs after amphibole and containing ocelli dominated by abundant large acicular amphibole pseudomorphs. Andel/2, Andel/4, Loon-op-Zand/1 and L/13-3 are all rather similar altered mafic rocks rich in pseudomorphs after olivine and clinopyroxene phenocrysts set in a glassy base, rich in olivine and pyroxene but also containing kaersutite, biotite and apatite. They are largely free of feldspar and analyses of rare unaltered pyroxene cores from Loon-op-Zand samples showed them to be chemically indistinguishable from the titaniferous salites see in the Egersund Basin rocks (Dixon *et al.*, 1981). Some samples from Andel-2 contain possible pseudomorphs after nepheline and minor amounts of feldspar are present in the rocks from L/13-3. The group as a whole is comparable with, but possibly slightly less undersaturated than, the Egersund basin nephelinites.

4.5.5 Summary.

(1) The Netherlands region consists of a number of broadly NW-SE trending basins which, together with the southern end of the Central Graben, have been subsiding since the Triassic.
(2) The main phase of subsidence and basin extension occurred in the Middle to Upper Jurassic and was accompanied by minor intrusive activity (ca. 150-160 Ma) and the eruption of a major off axis volcano (Zuidwal) in the Waddensee area.
(3) The igneous rocks of the Netherlands province are undersaturated, variably potassic, nephelinites and basanites to phonolites and trachytes which are in character similar to, and probably intermediate between, the potassic basanites and leucitites of the Central Graben and the nephelinites of the Egersund Basin.

4.6 Other Occurrences.

In the south ***Viking Graben*** there are two locations where igneous rocks have been reported. In quadrant 9, close to the Beryl field, Ziegler (1982) indicates volcanic activity during the Middle Jurassic. In well 9/8-4, also in the Beryl embayment, B.P. report cuttings of a Permo-Carboniferous dolerite (see Figure 4.14). Cuttings examined during the course of this study from the Middle Jurassic sands

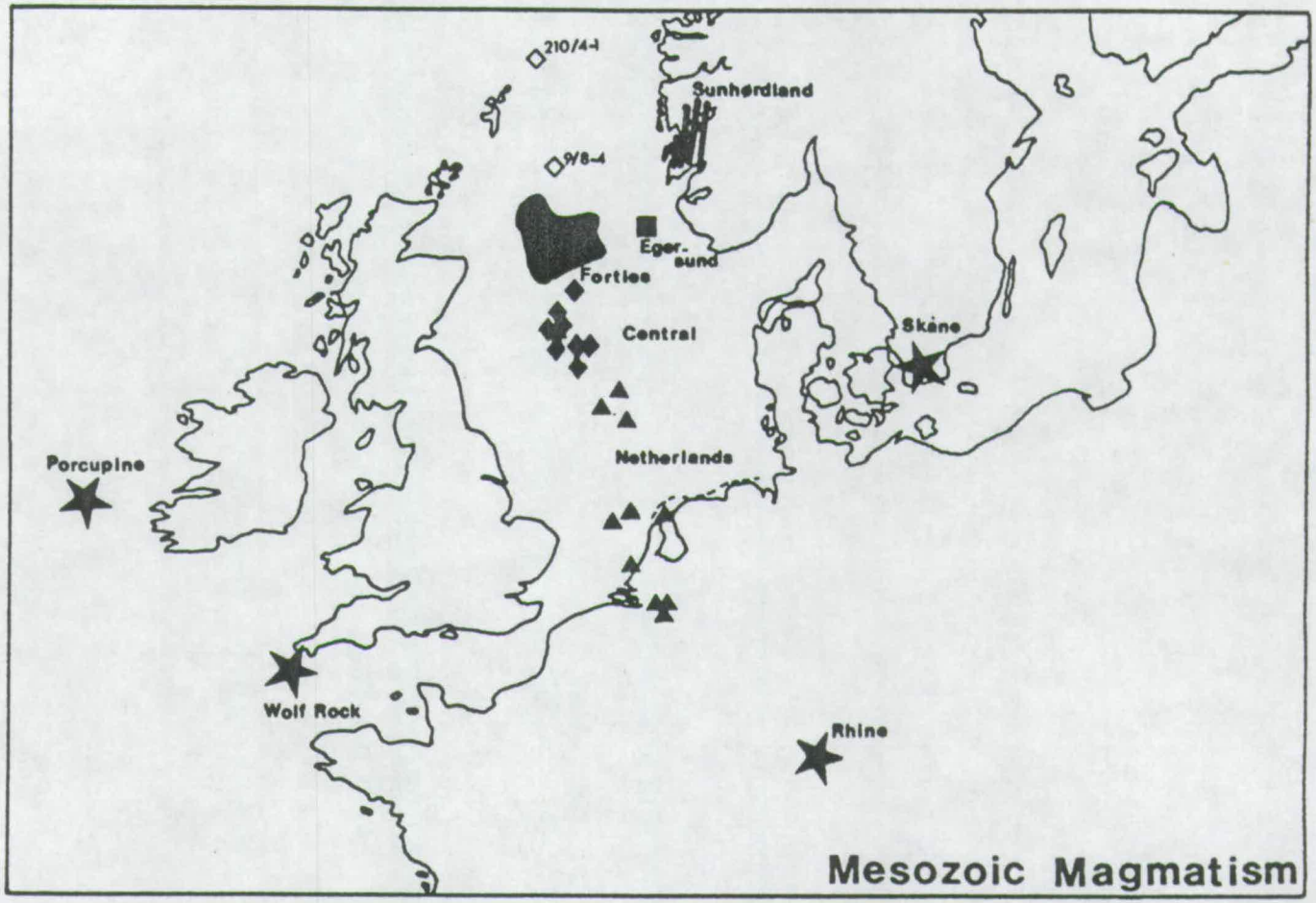

FIGURE 4.14 Locations of Mesozoic igneous provinces in the North Sea and surrounding areas (see text).

(?Heather Formation) in well 9/8-4 did show some small amounts of volcanic debris. Other wells may contain volcanic material but no volcanic flows, intrusive rocks, or tuffs, have been cored in this area.

Dixon *et al.* (1981) reported igneous rocks, probably hawaiites or mugearites, intrusive in Permian sediments from well 210/4-1 in the northern part of the Viking Graben (see Figure 4.14). The rocks in this well were dated as Kimmeridgian (152±3 Ma) by conventional K/Ar methods. Unfortunately no material was left from these samples and they have not been studied here.

In the ***Sunnhørdland*** region of West Norway (Figure 4.14), just west of the Triassic Stord and Egersund basins, there is a suite of more than 60 northerly trending (coast parallel) alkaline (lamprophyre) dykes intruded into Precambrian gneisses and the overlying metasedimentary rocks of Lower Palaeozoic age (Faerseth *et al.*, 1976). According to Faerseth *et al.* (1976), on the basis of K/Ar dates, the dykes were largely intruded during the Triassic (ca. 220 Ma), although some may have been intruded during the Permian (~275 Ma) and two may be Middle Jurassic in age (~160 Ma, Callovian). Three different age episodes are supported by cross cutting relationships observed in the field.

Faerseth *et al.* (1976) describe fresh (except for olivine), porphyritic, ocelli-rich, vesicular rocks which in many ways sound similar to the Forties alkali basalts, although are possibly more undersaturated. Pyroxene phenocrysts are fresh and compositionally are titaniferous augites and salites showing the typical sympathetic variations of Ti, Al and total Fe from core to rim. Kaersutitic amphiboles are common, especially in ocelli where they occur with alkali feldspar. Plagioclase is common as a groundmass phase in all but the slightly less undersaturated Permian occurrences in which plagioclase phenocrysts are observed. The two Jurassic dykes which are slightly more alkaline than the other rocks in the area, are olivine free and are dominated by amphibole. These two youngest samples (termed D10 and D33 by Faerseth *et al.*, 1976) may be very similar to the amphibole rich rocks from the flanks of the Central Graben.

The Sunnhørdland dykes are of interest for a number of reasons. They provide evidence for 3 discrete episodes of magmatic activity which must in some way be related to the regional tectonics. Similar alkaline, essentially N-S trending, dykes of apparent Permian age have been reported from Orkney (Upton *et al.*, in prep.) and Early Permian magmatic activity was also widespread in the Midland Valley of Scotland (Wallis, 1989), in the Central North Sea and in the Oslo Graben (Dixon *et al.*, 1981). In the Triassic the Sunnhørdland dykes represent the only reported incidence of Triassic magmatic activity in the North Sea region (Ziegler,

1982). The very close correlation between the Middle Jurassic magmatism and the onset of extension in the North Sea suggests that the Triassic dates obtained from the dykes might be used to date the onset of the Triassic phase of extension which laid the structural framework for the later, more major, Jurassic episode. Dykes were intruded again in the Middle Jurassic at ~160 Ma, at essentially the same time as the Forties province and the Egersund Basin, and represent magmatism at the western edge of the Egersund Basin; for this reason they might have earlier been included in the Egersund Basin group. The dykes have not been analysed during the course of this study and since the tectonics and subsidence history have not been studied either they are not included in later discussions. A full investigation of the tectonic significance and petrogenesis of the dyke suite in Sunnhøhordland is an area of possible future research.

Klingspor (1976) describes a province of undersaturated volcanic and intrusive rocks from Skåne in southern Sweden (see Figure 4.14) in which two episodes of activity, Middle Jurassic (167±4 Ma, Bathonian) and Middle Cretaceous (108±3 Ma, Albian), are tentatively distinguished on the basis of radiometric age determinations. Of these determinations only the Middle Jurassic age is supported by a good K/Ar isochron and the younger age is much more uncertain. The rocks are described as alkali basalts and may be similar to the rocks of the Forties province. However, they are not considered further as there is no chemical data available and because they are a long distance away from the main region of interest, i.e. the North Sea.

Other marginal areas of activity (see Figure 4.14) include the nosean phonolite at Wolf Rock (south west of Cornwall, Dixon *et al.*, 1981) dated as ~130 Ma by various workers (see Harrison *et al.*, 1979), and the Mid Jurassic to Early Cretaceous volcanism reported by Tate and Dobson (1988) in the Porcupine Trough (west of Ireland). Dixon *et al.*, also draw attention to the early olivine nephelinites of the Rhine Graben which date back to the Early Cretaceous. Mesozoic magmatic activity was clearly not restricted to the area of study because much of western Europe underwent phases of extension during this time (see Ziegler, 1982). However, as the nature of each occurrence or group of occurrences will depend largely on the local tectonics, the local degree of stretching, the local stretching history and the asthenospheric temperature, only the North Sea region, because it is best known, is considered further in this thesis. Indeed, even within the North Sea most attention will focus on the Forties Province. It is however worth noting that a recent study of the extension in the Porcupine Basin suggests that there is a clear and

predictable relationship between the inferred volumes of volcanic rocks and the degree of extension (N. White and M. Tate pers. comm., 1990).

4.7 Summary and Discussion.

The Mesozoic igneous rocks in the North Sea are placed into 4 provinces on the basis of location. The Forties province is the most important, in terms of volume, and occurs in an area where the three main rift arms meet. The dominantly subaerially extruded rocks of the Forties province comprise an alkali basalt suite from ankaramites, through alkali basalts to hawaiites. The alkali basalts occur over an area of ~8000 km^3 and their average thickness is considered to be less than 3 km. The Central Graben province contains ultrapotassic extrusive and intrusive rock types and, of all 4 provinces, is second only to the Forties province in terms of its volumetric importance. The Egersund basin contains a relatively minor amounts of extrusive nephelinites and intrusive lamprophyres similar to the Central Graben province. Petrographically the rocks from the Netherlands province are predominantly undersaturated basanites and nephelinites although mafic ultrapotassic dykes are found in two places and ultra-alkaline evolved rocks are associated with a major volcano in the Waddensee. In the areas bordering the North Sea ocurrences of magmatism are noted throughout the Mesozoic. Most important of these in terms of its close proximity to the North Sea is the Sunnhørdland region of western Norway in which alkaline dykes of Permian, Triassic and Middle Jurassic age are found.

There are a large number of radiometric dates, both K/Ar and $^{40}Ar/^{39}Ar$, for igneous rocks from the North Sea. A compilation of dates is plotted against latitude in Figure 4.15. Figure 4.15 is similar to those used by Latin *et al.* (1990a,b) to suggest that there was a temporal shift in the locus of magmatic activity, from north to south, in the Mesozoic North Sea. Latin *et al.* (op. cit.) suggested that such a trend, if real, might relate either to a gradual southwards propagation of the rift system, or to northwards motion of the European plate over a stationary hot-spot.

Rocks from the North Sea suite are, however, commonly very altered. Recently conducted $^{40}Ar/^{39}Ar$ step wise degassing studies of 10 of the freshest North Sea samples suggest that previously obtained K/Ar and $^{40}Ar/^{39}Ar$ dates should be treated with considerable care. Figure 4.16 shows a compilation of $^{40}Ar/^{39}Ar$ dates, which all give good age plateaux, and that are therefore considered to be most reliable of all the North Sea dates in Figure 4.15. Note how the apparent southerly

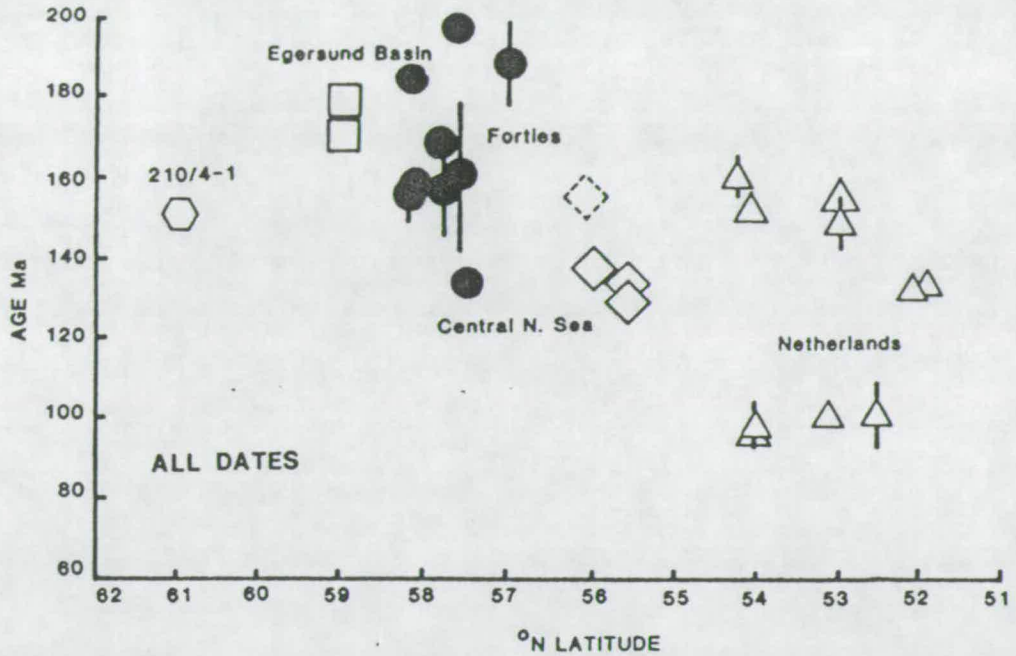

FIGURE 4.15 A compilation of radiometric age data for the Mesozoic rocks of the North Sea (see Table 6.2 in Latin *et al.*, 1990a and the new dates in Appendix B of this thesis). Longitude coordinates for the locations of dated samples have been projected onto the 2°E line of latitude. Ages are therefore plotted against distance down the rift axis from N to S. When errors exceed the size of the symbol they have been shown by vertical lines. The dashed triangle represents the new age interpretation for the sample from 29/25-1 (see text). Note that if no preferential weighting is given to certain dates then there appears to be a southwards migration of activity.

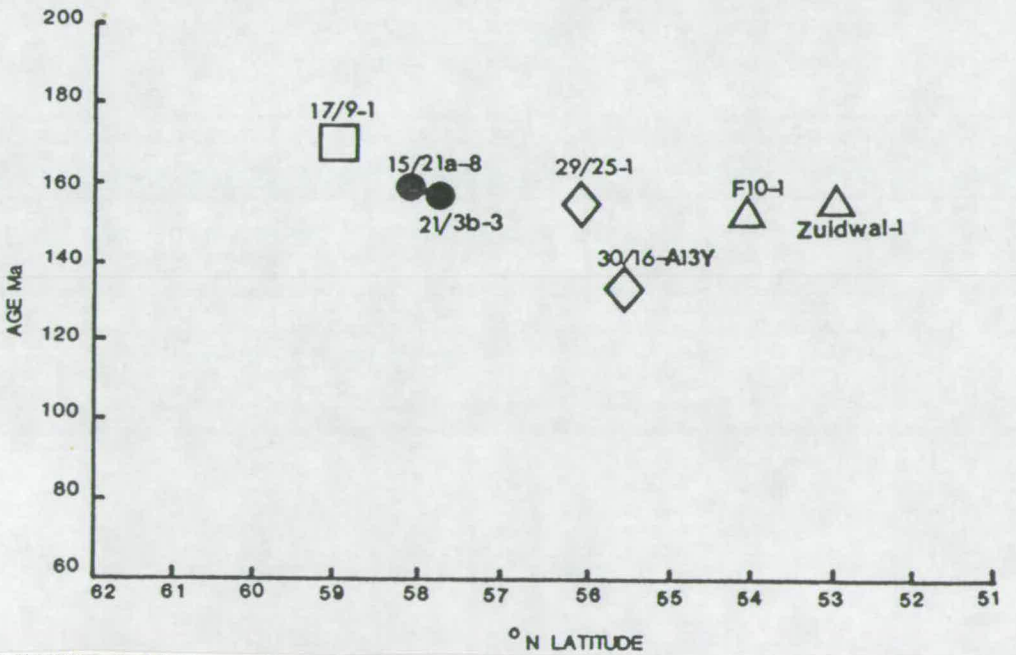

FIGURE 4.16 Dates from igneous samples projected onto the 2°E line of latitude as in Figure 4.15. However, on this diagram, unlike Figure 4.15, only those dates obtained from $^{40}Ar/^{39}Ar$ age spectra which met with the criteria of Fleck *et al.* (1977) are plotted. These dates all correspond to good "age plateaux" on step wise degassing (see Appendix B) and are therefore considered the most reliable. Notice that the migration of igneous activity with time which was observed in Figure 4.15 has largely disappeared.

migration of magmatic activity with time in Figure 4.15 is not present in Figure 4.16 and that the rocks from all 4 provinces are, to within ±10 Ma, all of the same age.

According to Ziegler (1982) and Ziegler and Van Hoorn (1990) the igneous activity of the Forties province is associated with a phase of regional updoming in the Middle Jurassic (see Figure 4.6) which was marked by the development of deltaic and shoreface sedimentary facies. The conclusion that the initiation of rifting appears to be coeval with regional doming associated with approximately contemporaneous, but sporadic, igneous activity, is an area of potential disagreement with the models in Chapter 3.

The simplest coaxial stretching models (McKenzie, 1978; Jarvis and McKenzie, 1980) have no mechanism (short of invoking a pre-rift crustal thickness of < 18 km) whereby the onset of extension should be marked by uplift rather than subsidence. Perhaps even more important is the observation by many workers that the main phase of crustal extension, marked by the development of major faults and syn-rift sedimentary packages, commonly post dates the magmatic activity. The simple models of Chapter 3 would suggest that magmatism should start after the onset of extension and would continue until the end!

At first sight many of these problems might be reconciled with a model that incorporates a mantle plume. This would cause regional uplift and might allow some magmatism to predate major faulting. However, the lack of a temporal shift in magmatic activity in Figure 4.16 is the first sign that the simple plume-model may not work either. This problem is coupled with the fact that the magmatism should not switch off, but rather should intensify, in the Upper Jurassic. When these problems with the plume-model are considered together with whether a *hot-spot trail* is in accordance with reconstructions of the palaeofacies of the whole North Sea region through the Mesozoic (see Chapter 7), they become insurmountable.

In Chapter 7 a model which involves co-axial stretching with time-integrated differential partitioning of strain between the crust and mantle, is forwarded in an attempt to reconcile the above observations with finite duration stretching at normal temperatures. However, for the next two Chapters different stretching models are set aside as an attempt is made to place constraints on the extent of melting which gave rise to the basaltic rocks (Chapter 5) and the degree of lithospheric thinning which took place in the North Sea during the Jurassic (Chapter 6).

CHAPTER 5

MAGMATISM IN THE NORTH SEA BASIN: II

WHOLE-ROCK GEOCHEMISTRY

5.1 Introduction.

The quantitative models presented in Chapters 2 and 3 make predictions about the major element compositions and volumes of basaltic melts produced from garnet peridotite during adiabatic decompression as a result of rifting of the lithosphere. Those areas where the degree of extension is greatest should, in theory, be characterised by the least undersaturated, largest degree, melts of the rifted region. The main aim of this section is to try to establish the chemical character, essentially the *degree of undersaturation*, of the primary basaltic magmas produced during Mesozoic rifting in the North Sea so that their chemistry may later be used to test the quantitative models (see Chapter 7). In Chapter 4 the petrographic and mineralogical characteristics of the suite of variably altered Mesozoic rocks from the North Sea were described. Their undersaturated often volatile-rich nature was emphasised. In this chapter attention is focussed on the whole-rock chemistry of Mesozoic samples, from the locations shown in Figure 5.1 (also see Appendix A). The severity of the alteration in all but a few samples from the Mesozoic suite renders a detailed study of major element chemistry across the whole suite impossible. The major element chemistry of a few fresh samples which have undergone relatively small amounts of low pressure fractionation is presented at the start of this chapter and is used, in Chapter 7, together with estimates of β from Chapter 6, to test the models presented in Chapter 3. In order to study the entire suite, including even the most altered samples, emphasis is placed on establishing chemical indicators of degree of undersaturation which are not affected by alteration. Ratios of trace elements which are both incompatible and immobile are used to place constraints on the composition of the source to the basalts and on the degree of melting that took place in their production. Estimates for the extent of melting are calculated from simple equilibrium melting models (section 5.6) and are used later, in Chapter 7, to provide a constraint on the relative degrees of adiabatic decompression in different parts of the

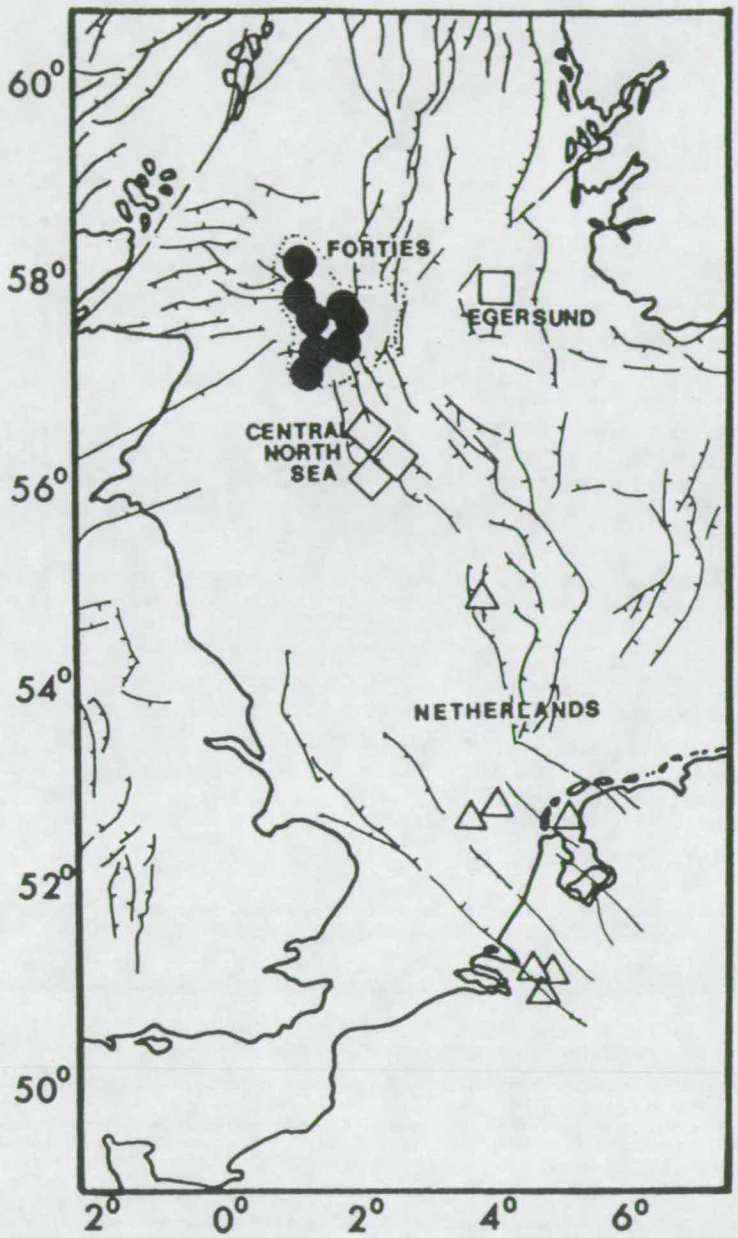

FIGURE 5.1 Location of wells in the North Sea region containing Jurassic-Cretaceous igneous rocks which have been sampled and whose whole-rock chemistry is presented in Appendix A of this thesis. Samples are grouped into 4 provinces; the Forties province (filled circles), the Central North Sea province (diamonds), the Egersund Basin province (square) and the Netherlands province (triangles).

North Sea which are independent of the estimates made from the major element chemistry.

The chemical composition of an igneous rock at the Earth's surface is the result of a number of processes and variables. Subsequent to extraction from its partially molten source region in the asthenosphere or lithosphere, where it gains its primary character, a magma must migrate upwards through the lithosphere, cooling and fractionally crystallising prior to eruption and then perhaps undergoing chemical changes resulting from low temperature surface hydrothermal alteration and weathering. To establish the original chemical character of the rock it is necessary to work backwards along this path of chemical evolution. The effects of alteration must first be removed and then, to establish the chemical character of the primary magma the effects of fractional crystallisation must also be accounted for. The mineralogy of the source region together with the extent of melting will be the primary control on major and trace element chemistry of a magma prior to its ascent and fractional crystallisation.

Analytical procedures are briefly described in section 5.2. In section 5.3 the major and trace element characteristics of the freshest of the North Sea rocks, mainly from the Forties province, are used to determine the degree of undersaturation and overall chemical character of the magmas from the different provinces. In 5.4 the effects of alteration, which is often severe, on major and trace element whole-rock concentrations is discussed. It is shown that ratios of immobile trace elements (e.g. Nb, Zr, Ce, Y) are largely unaffected by the alteration process. In section 5.5 it is shown that the effects of fractional crystallisation (as well as alteration) can be eliminated by use of ratios of immobile incompatible trace elements; i.e. they may be used to investigate the primary magma characteristics. Ratios of immobile and incompatible trace elements are used to determine empirically the degree of undersaturation of rocks where the concentrations of more mobile elements (e.g. MgO, SiO_2 and alkalis), commonly used in calculation of the CIPW norm, cannot be trusted. These incompatible element ratios reflect the ratios of the original primary magma, and they will therefore be largely a function of source composition and degree of melting. In section 5.6 it is shown that the North Sea rocks result from different degrees of melting and that the Forties alkali basalts represent the largest extents of melting, or melts from the least LILE enriched source, of all the Mesozoic occurrences. Normalised trace element patterns, together with the Sr and Nd isotope characteristics of three North Sea samples, suggest that the source of the North Sea basaltic rocks is similar to that of OIB (ocean island basalt). The geochemical data

for all but the most potassic samples is not inconsistent with melting of garnet peridotite but melting is not necessarily volatile-free.

5.2 Analytical Techniques.

Approximately 200 whole rock major- and trace-element analyses were determined using X-ray fluorescence techniques in Edinburgh (using a Philips PW1450/20 automatic XRF spectrometer as in Fitton and Dunlop (1985), except that a Rh-anode tube was used; also see Wallis (1989) and Smedley (1986) for details) and are presented, together with data concerning their accuracy and precision (reproducibility), in Appendix A. In view of the often highly altered nature of the rocks from the North Sea, all powders used for major element determinations were dried at 110°C and then ignited at 1100°C for one hour to remove volatile material. Percentage weight loss on ignition (LOI) was calculated, and the ignited material was used in preparation of fused glass discs. Major element concentrations, determined using glass discs, and trace element concentrations, determined using pressed-powder pellets with matrix corrections calculated from major element compositions, are therefore presented on an *anhydrous* basis in Appendix A. REE were determined on 40 powdered whole-rock samples using the Philips PV8210 1.5-m inductively coupled plasma atomic emission spectrometer (ICP-AES) at Royal Holloway and Bedford New College (see Walsh *et al.*, 1981, for details of the analytical procedure). The REE data together with information on accuracy and precision is presented, on a *hydrous* basis in Appendix A.

5.3 Chemistry of Rare Fresh Rocks.

Degree of undersaturation is typically measured using the CIPW norm. Normative compositions depend heavily on the total amount of alkalis (Na_2O+K_2O) and silica in a rock. These oxides are among the most mobile during hydrothermal alteration (see section 5.4). Figure 5.2 highlights the problem in the North Sea where a large proportion of analyses have high LOI. Notice also the inverse correlation between LOI and SiO_2 which probably reflects the fact that the most glassy undersaturated rocks are commonly the most altered, rather than leaching of silica

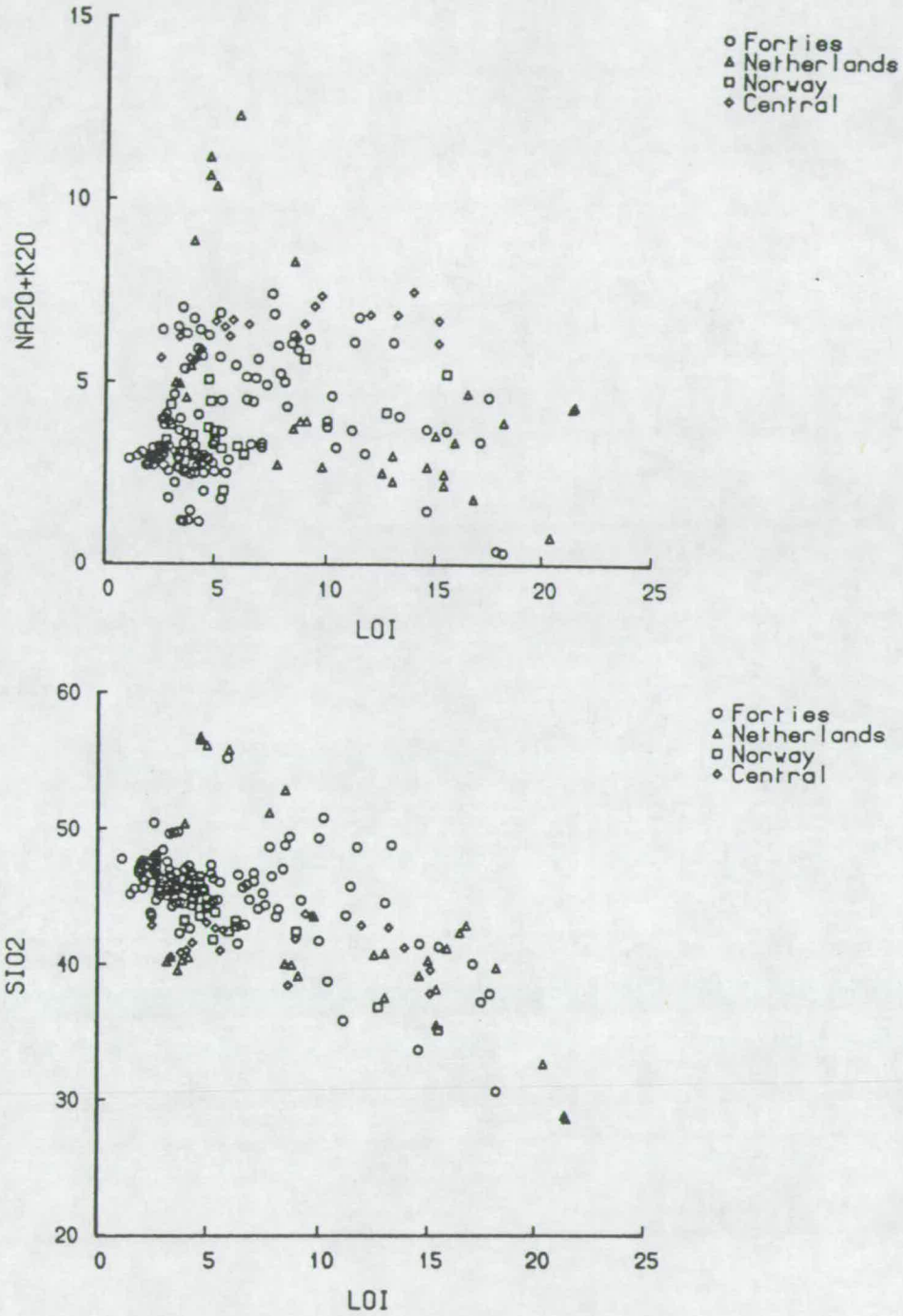

FIGURE 5.2 Total alkalis (upper diagram) and silica (lower diagram) plotted as wt.% oxides against LOI (% wt. loss on ignition) for the entire North Sea data set. See diagram for symbol key and see text for discussion.

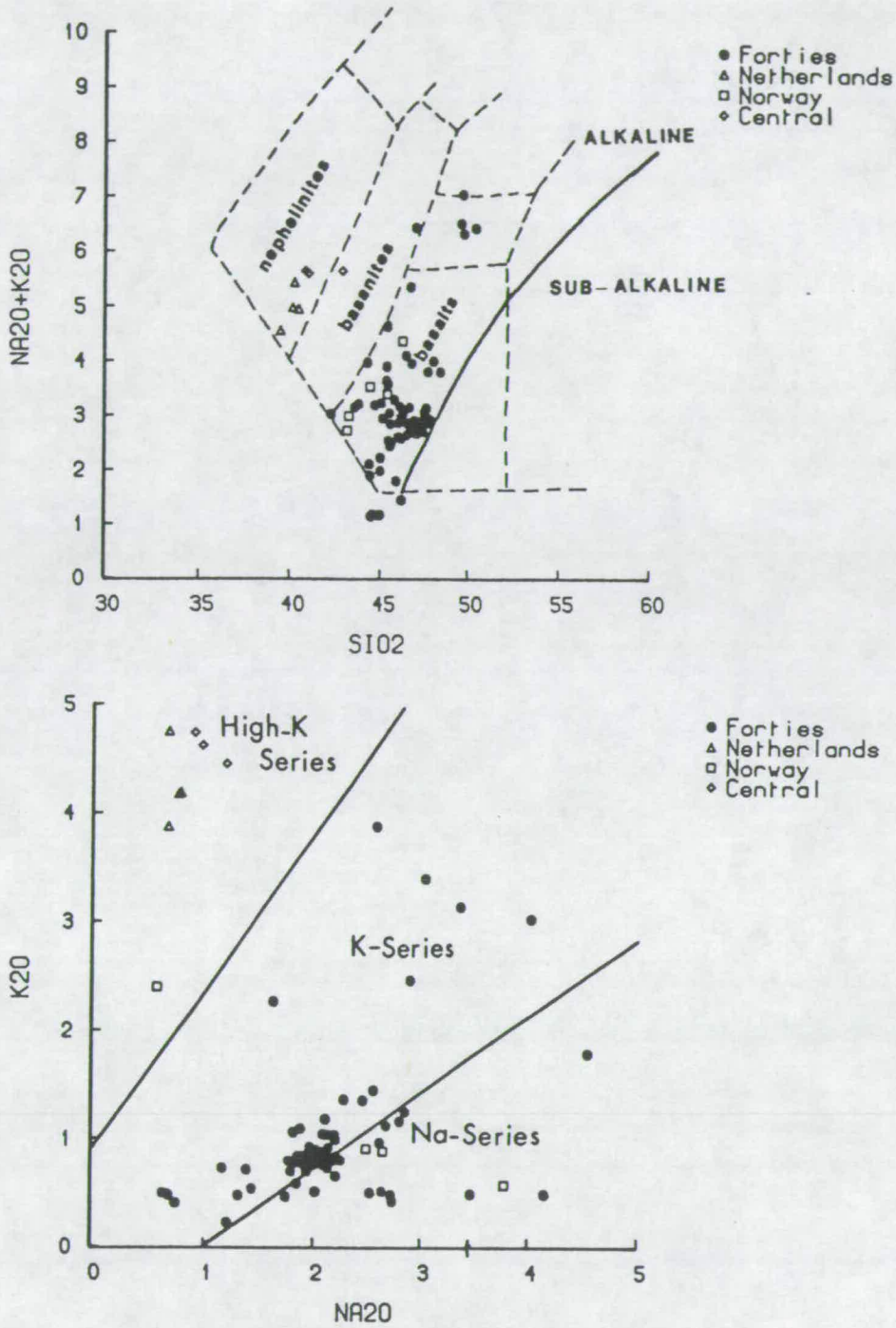

FIGURE 5.3 Upper diagram shows the freshest subset of mafic North Sea rocks (LOI < 4 wt.% and MgO > 4 wt.%) plotted on the alkali silica diagram of Cox *et al.* (1979). Lower diagram shows K_2O vs. Na_2O (both in wt.%) for the same subset of rocks. The fields for the different basaltic series (shown in the lower diagram) are from Middlemost (1975).

which is often added during alteration[1]; see section 5.4. It should be noted that LOI is not always a good indicator of alteration. Many of the ultrapotassic rocks, although petrographically very fresh, contain abundant volatile bearing phases (e.g. biotite and kaersutite). Out of a total of 194 analyses only 77 have LOI values of 4 wt.% or less; i.e. only 40% of the analyses. There is no reason to suppose that rocks with LOI less than or equal to 4 wt.% are undisturbed chemically. However, if a lower value of LOI is used to separate altered from unaltered analyses the remaining number of analyses becomes so small as to be virtually useless. Given that 4 wt.% LOI is a rather arbitrary value to choose the following discussion of the chemistry of this data subset should be treated with some caution. Note also the very small number of samples with <4wt.% LOI which are from outside the Forties province; 3 samples from the Central Graben (all from 30/16-A13Y (SH1)), 4 from the Netherlands province (all from F10-1 (PL1)) and 5 from the Egersund basin (all from the upper, ?nephelinite, sequence in 17/9-1). The positions of the analyses of samples from different groups, with the exception of the Forties province, in the diagrams discussed below should not, therefore, necessarily be regarded as representative. Indeed the rocks from F/10-1 (Netherlands) are much more similar to the rocks from Central Graben than they are to any of the other Netherlands occurrences.

The total alkali content of the very freshest rock samples (LOI<4 wt.%) from the four North Sea provinces is shown plotted against SiO_2 in the upper diagram in Figure 5.3. In terms of total alkalis *vs.* silica all of the freshest Mesozoic rocks fall in the alkaline field (after Middlemost, 1975). Using the nomenclature of Cox *et al.* (1979) the Forties province samples are basalts and hawaiites whereas the samples from the Central Graben and Netherlands fall largely in the nephelinite field. The chemistry of the freshest rocks from these three provinces therefore broadly agrees with the conclusions from their petrography presented in Chapter 4. Perhaps surprisingly the rocks from the Egersund Basin, which petrographically and mineralogically looked at least as undersaturated as the Central Graben and Netherlands occurrences, fall inside the basalt, rather than the nephelinite, field. The relatively high SiO_2 and low total alkalis in these samples is partly an artefact of alteration which, despite their relatively low LOI, has had severe consequences on the distribution of oxides. In thin section abundant, large, analcime pseudomorphs after a feldspathoid are present.

The lower diagram in Figure 5.3 highlights the ultrapotassic nature of the rocks from F/10-1 and 30/16-A13Y which all belong to the High-K series

---

[1] This effect is not due to dilution with volatiles since SiO_2 is expressed on a volatile-free basis.

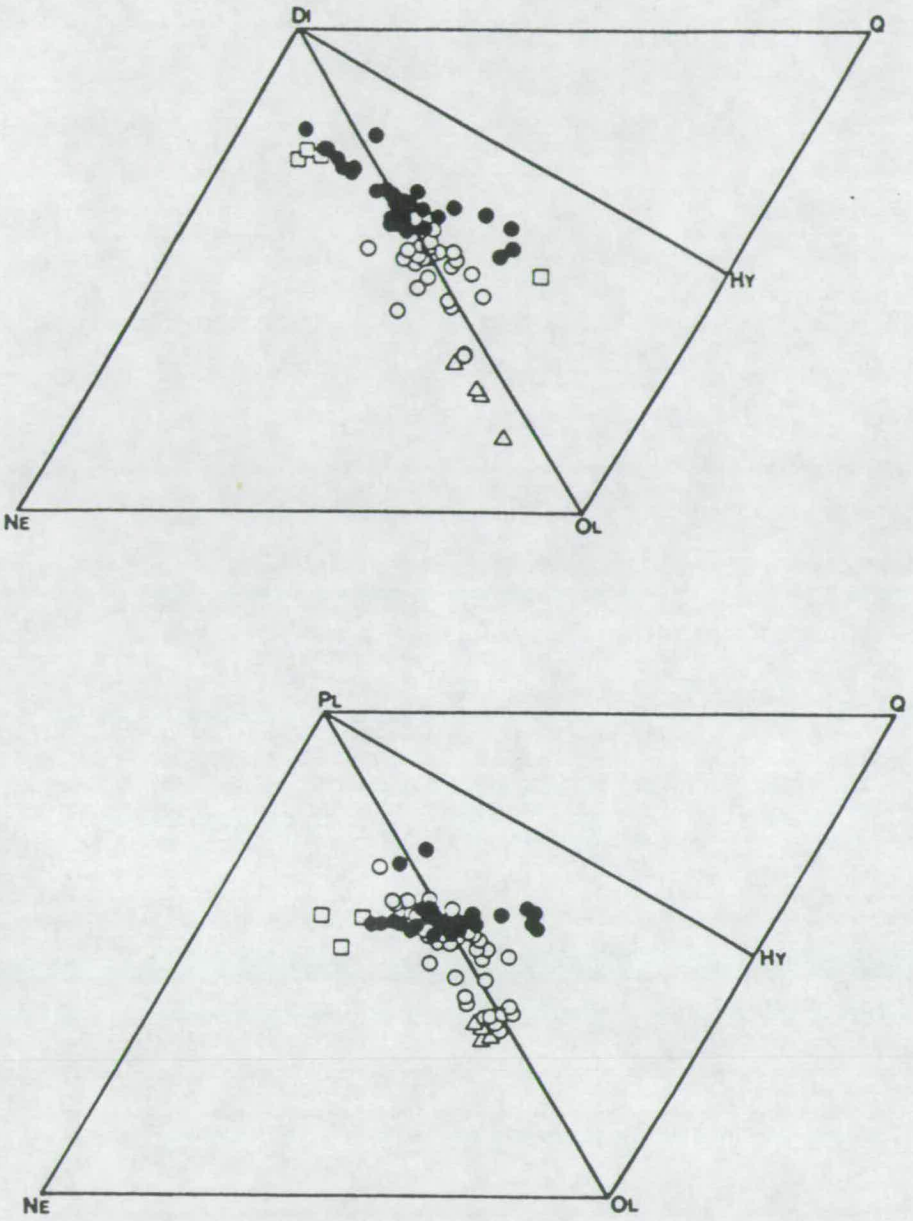

FIGURE 5.4 Normative compositions (as molecular %) of the freshest subset of North Sea mafic rocks (LOI < 4 wt.% and MgO > 4 wt.%). $Fe_2O_3/(FeO+Fe_2O_3)$ was nomalised to 0.2 for the norm calculations.

(Middlemost, 1975). The Forties basalts and Egersund rocks, on the other hand, are transitional between the K- and Na-Series.

As might be expected, many of the low LOI subset are *ne*-normative (see Figure 5.4) although a number of Forties samples, and one of the altered Egersund samples, project into the *hy*-normative field of the basalt tetrahedron. The strongly potassic rocks from the Central Graben are *lc*-normative and do not plot in Figure 5.4. The overall trend in both diagrams in Figure 5.4 is suggestive of fractionation of olivine and clinopyroxene, confirming the petrographic observations. The filled circles in Figure 5.4 correspond to samples which are all from the same flow (from AH1) in the Forties province (see section 5.4 and Figure 5.7) in which subtle chemical variations, largely in the CaO concentration, resulting from alteration, have led to the trend away from *hy*. It is clear that, even in this small relatively unaltered subset of rocks, chemical effects of alteration cloud interpretation.

It is convenient to be able to display the degree of undersaturation without having to resort to calculation of normative composition. Figure 5.5 shows a plot of MgO *vs.* an index of saturation (S.I.; see Latin *et al.*, 1990a) which is defined as

E:5.1 $$S.I. = \frac{Si-(11(Na+K)+3Ca+Al+Fe+Mg))}{2}$$

where Fe is Fe^{II}. The critical plane of silica undersaturation in the basalt tetrahedron is defined on this index by a value of S.I. = 0. Increasingly negative values of S.I. indicate rocks which are increasingly undersaturated, while positive values indicate a saturated to oversaturated composition. In general nephelinites and basanites would plot at between -5 and -15 whereas alkali basalts might be expected between -5 and +5. The main advantage of the saturation index is that it allows *ne*-, *lc*-, *hy*- and *q*-normative compositions, together with extremely potassic rocks containing K-orthosilicate in their norm, to all be portrayed on the same simple bivariant diagram. Figure 5.5 therefore displays the undersaturated nature of the *lc*-normative Central Graben rocks which do not project into the basalt tetrahedron. The poorly visible negative correlation between MgO and S.I. may be a function of the speed of ascent and therefore limited fractional crystallisation of the more undersaturated magmas. Note also that there is no positive correlation which suggests that the more *ne*-normative samples (i.e. effectively those with the most negative values of S.I.) are not the result of high pressure fractional crystallisation of *hy*-normative basalt. Finally notice that the effects of alteration, as in the basalt tetrahedron, are to make the whole-rock chemistry more silica saturated (see section 5.3).

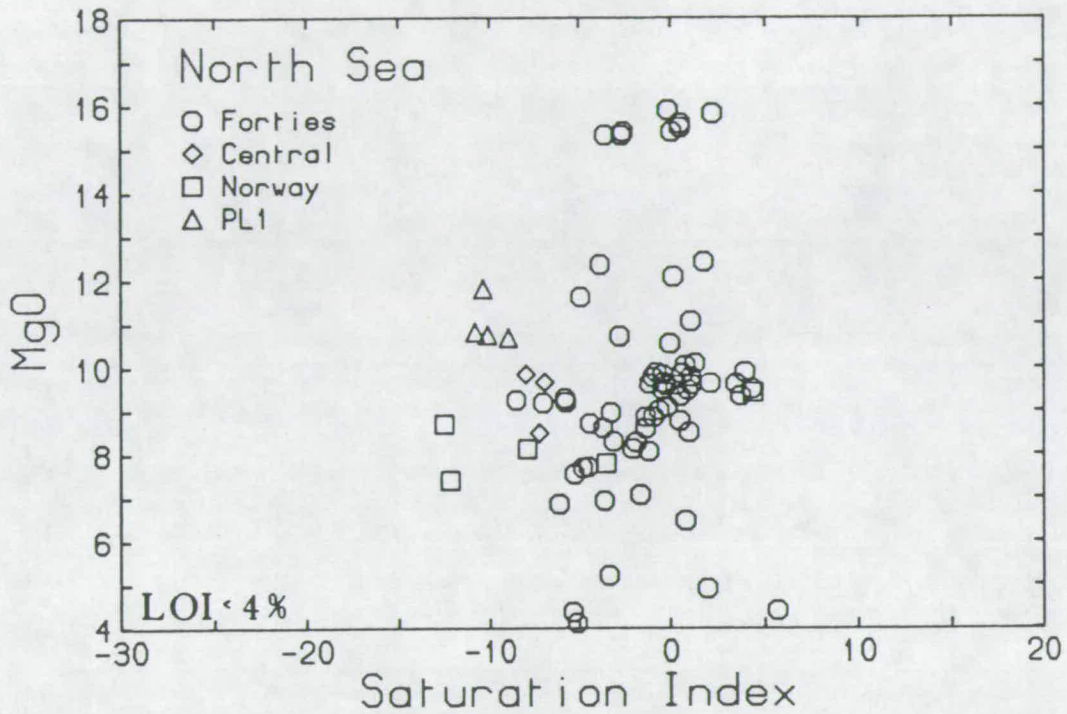

FIGURE 5.5 MgO (wt.%) against an index of silica saturation for the freshest subset of mafic North Sea rocks (LOI < 4 wt.% and MgO > 4 wt.%). The Saturation Index (SI) is defined as

$$SI = [Si-(11(Na+K)+3Ca+Al+Fe^{II}+Mg)] / 2$$

so that the critical plane of silica undersaturation is at 0 and -ve values therefore represent undersaturated compositions while +ve values reflect saturated and oversaturated compositions.

Fall *et al.*, (1982) have already carried out a comprehensive study of the chemical classification, using various indices, and crystallisation history, using least squares models, of the Forties basalts and there is no intention to repeat their work here. The basic observations can be very briefly summarised, with reference to the diagrams in Figures 5.6 and 5.7, which are for samples with LOI of 4 wt.% or less, as follows:

(1) The basaltic rocks of the Forties province form a suite which range from ankaramites, with MgO greater than about 10 wt.% and Cr in excess of ca. 700 ppm, through alkali basalts and basaltic hawaiites, to hawaiites with MgO between 4 and 5 wt.%, SiO_2 close to 50 wt.%, both Na_2O and K_2O close to 3 wt.%, and with Ni and Cr less than 100 ppm.

(2) The variations with MgO of most of the major and trace elements are dominated by fractionation or accumulation of olivine and clinopyroxene.

(3) There is some evidence, from the very slight drop in Fe_2O_3 and V, and to lesser extent TiO_2, at 4-5 wt.% MgO, for the increasing importance of magnetite fractionation at the more evolved end of the suite.

(4) The excellent inverse correlation of Al_2O_3 (and Na_2O) with MgO and CaO suggests that plagioclase was not an important fractionating phase.

(5) Notice a group of five samples which at 7 and 9 wt.% MgO are consistently at higher values of TiO_2 (~4 wt.%), P_2O_5 (~0.75 wt.%), La (~70 ppm.) and Ce (~150 ppm.) than the other Forties samples of comparable MgO content. These same samples are the only ones from the suite with SiO_2 concentrations below ~45 wt.% and, as will become clear in section 5.6, are part of a subset of Forties rocks which are rather more undersaturated (basanitic) than the norm.

5.4 Alteration and Immobile Elements.

The North Sea rocks have undergone variable degrees of alteration from iddingsitisation or chloritisation of olivines through pervasive groundmass alteration, chloritisation, zeolitisation and veining by hydrothermal minerals (natrolite, sphene, carbonates and quartz) and pseudomorphing of all primary magmatic phases, to total destruction of the original igneous rock texture. A key to the petrographically determined severity of the alteration is provided with the chemical data in Appendix A. The alteration assemblages present in the North Sea samples, some of which are described in detail in the sections on petrography in Appendix B, often attest to the

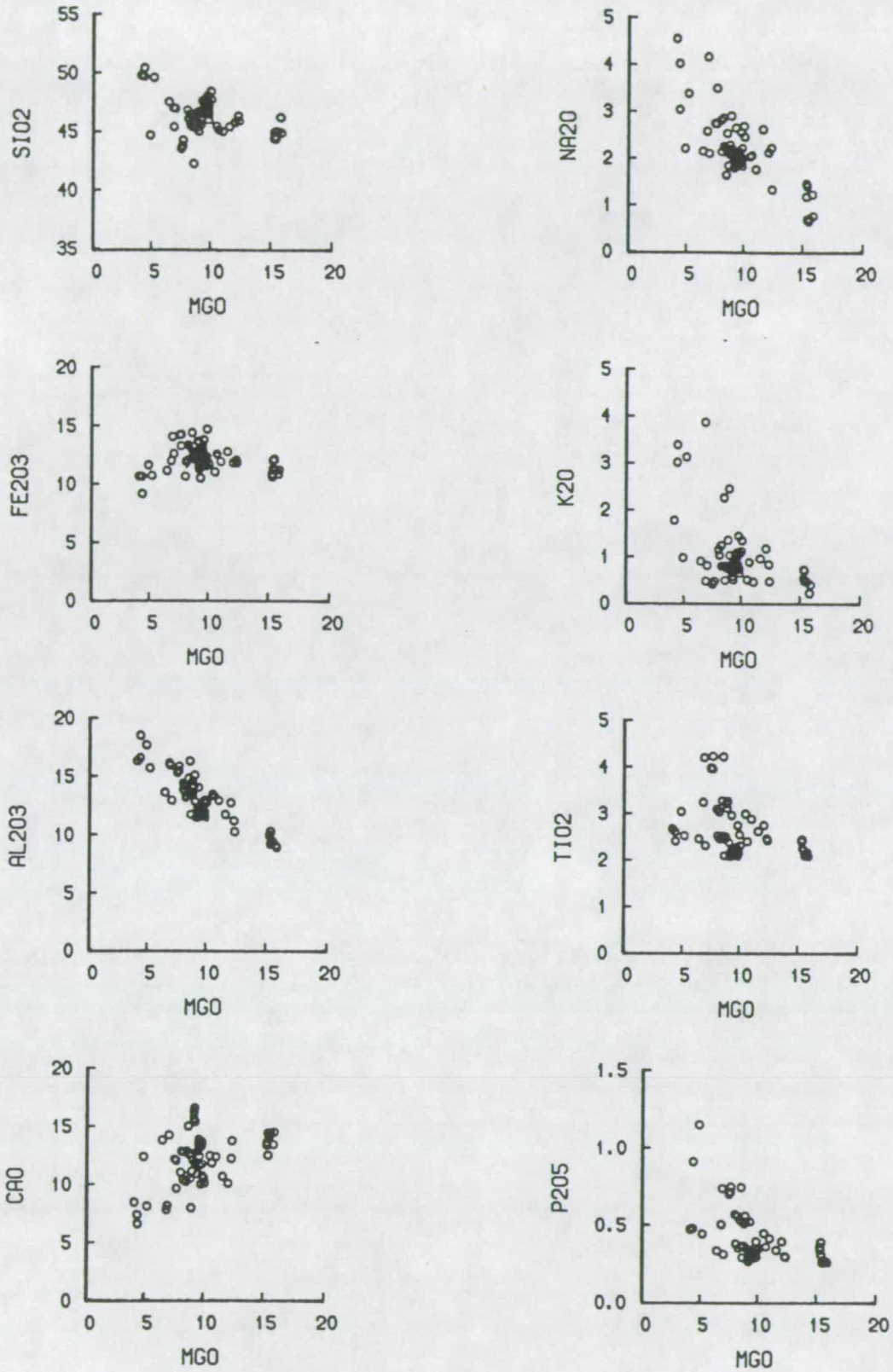

FIGURE 5.6 The variation in the concentrations of major elements (as wt.% oxides) with MgO (wt. %) for the freshest rocks from the Forties province (LOI < 4 wt.%).

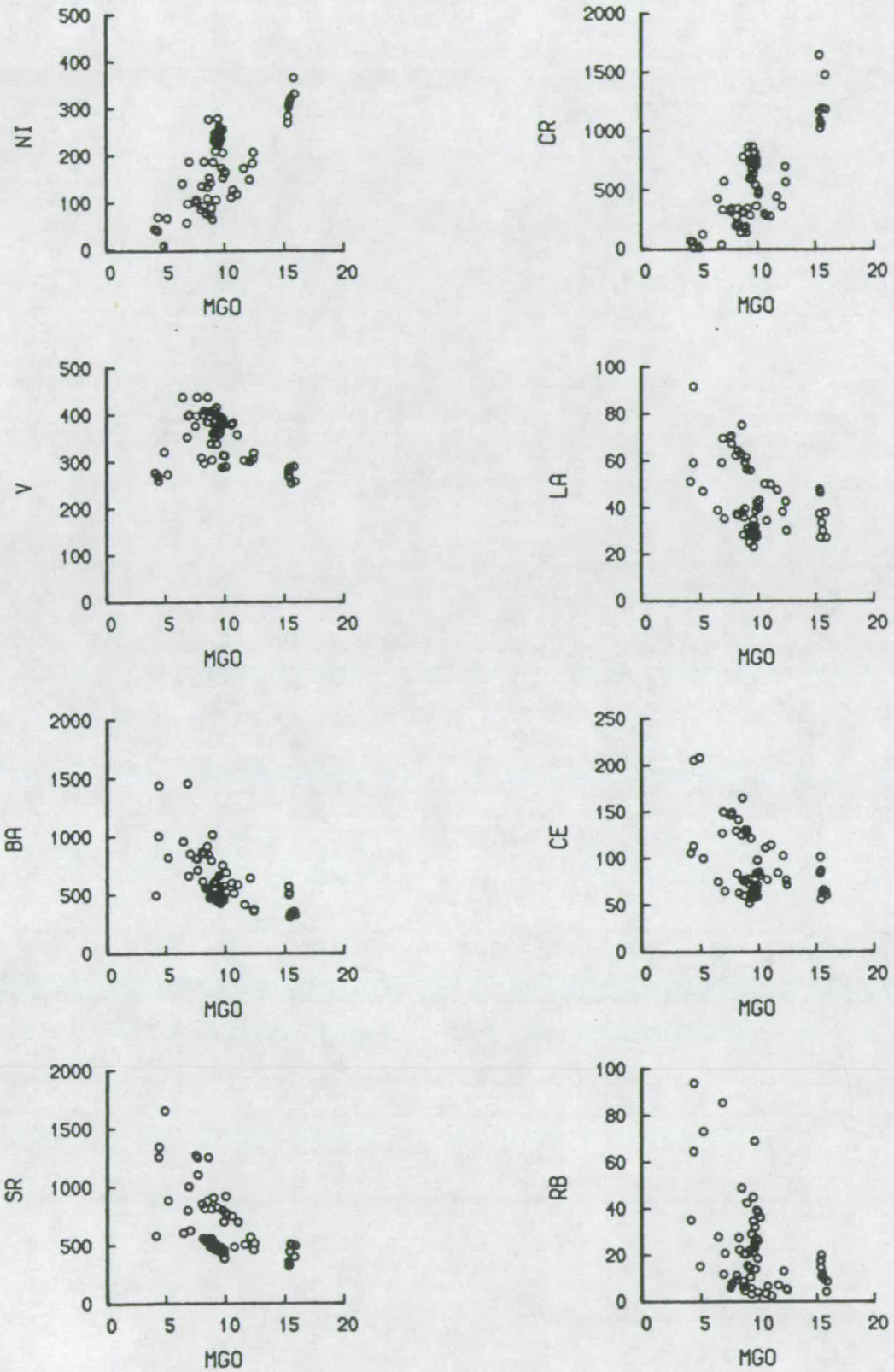

FIGURE 5.7 The variation of selected trace element concentrations (in ppm.) with MgO (wt. %) for the freshest rocks from the Forties province (LOI < 4 wt.%).

mobility, at least locally, of many of the major rock forming constituents (e.g. MgO, SiO_2, CaO, TiO_2, K_2O, Na_2O etc).

The often marked effects of alteration on the more mobile elements (e.g. Mg, Si, Ca, K, Na, Sr, Rb, Ba and Pb) means that the sorts of conventional chemically based systems of classification can only be used on the rare fresh rocks found in the North Sea; these are largely from the Forties province. Although some idea of the relative degrees of alkalinity and silica saturation between different samples can be obtained from the petrographic characteristics of the rocks and from relict mineral compositions it would be desirable if there were an alternative chemically based method of classification which did not suffer from the problems of alteration.

The effects of alteration on the major and trace element concentrations of samples from a 15 m core of an ankaramite flow from 15/21a-8 (well AH1) in the Forties province have been studied. The samples, taken at approximately 30 cm intervals throughout the flow, are all very similar petrographically but show local variations due to the intensity of alteration (crudely measured by wt.% LOI) or the degree of olivine and clinopyroxene phenocryst enrichment. Figures 5.8 and 5.9 show major and trace element variations, together with the variation of LOI, as a function of depth though the core. Notice the marked increase in the LOI towards the top of the core where it reaches 17 wt.%. In general, as LOI increases, SiO_2, Na_2O, K_2O, Ba, Sr, Rb as well as all of the elements traditionally regarded as immobile (many of the trace elements and TiO_2, Al_2O_3, P_2O_5), increase, while MgO, CaO, and Fe_2O_3 decrease in abundance. The increase in alkalis may be explained by their introduction, while the increases observed in the immobile elements are thought to reflect their concentration in the residue. The two samples closest to the top of the core do not however follow the general trend with LOI. In these two samples (AH1/3 and AH1/1) veining by zeolite and carbonate, most obviously reflected in the doubling of the CaO content and a marked decrease in SiO_2, is intense and causes a rather variable decrease (effectively dilution) of most other elements. Most of the core is remarkably homogeneous chemically throughout its length and only shows a deviation from the average towards its base which is relatively less enriched in olivine and clinopyroxene phenocrysts (total phenocryst content drops from 35 to 20 % by mode) a fact that is reflected by the sudden drop in Cr and Ni.

In their Table 6.2 Latin *et al.* (1990a) summarise the observed effects of alteration on the major element composition of two ankaramite flows (from 15/21a-8 (AH1) and 21/3-1a (TO1)), together with those noted by Fall (1980) for the Forties province in general. The overall leaching of CaO, MgO and SiO_2 and gain in alkalis

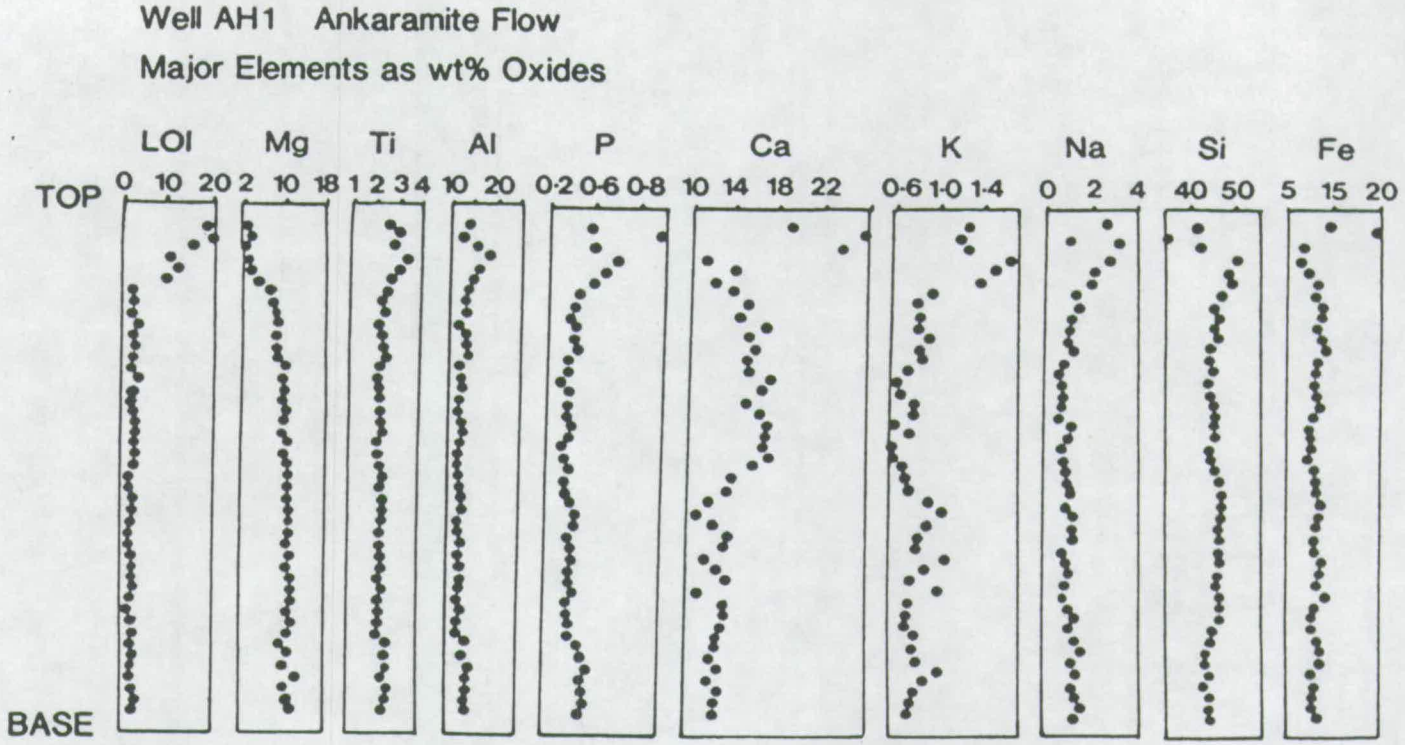

FIGURE 5.8 The variation in the concentration of major elements (wt.% oxides) and LOI (wt. %) with depth through an ankaramite flow (AH1) from well 15/21a-8 in the Forties province. Total thickness of the flow is approximately 15 metres. Note the effect of alteration on all of the elements in the top part of the flow. Note also the variability of the more mobile elements (Ca and K) throughout the flow.

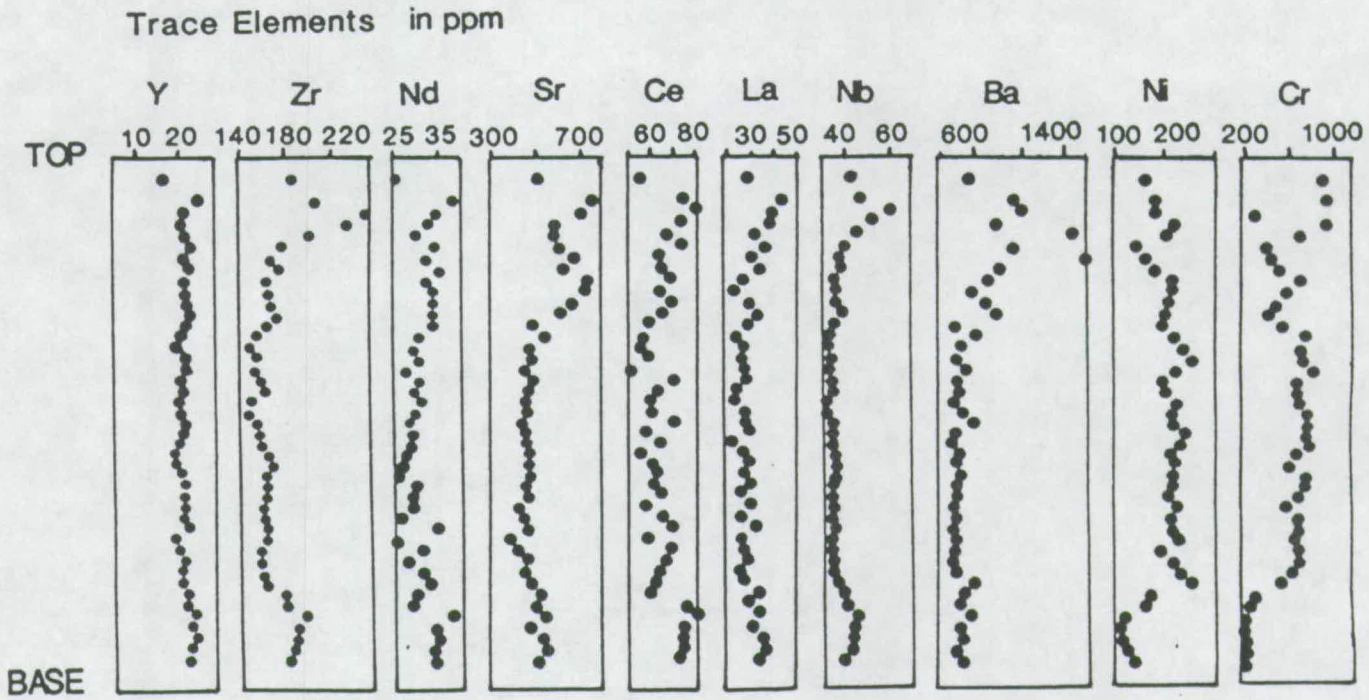

FIGURE 5.9 The variation in the concentration of selected trace elements (in ppm.) with depth through an ankaramite flow (AH1) from well 15/21a-8 in the Forties province. Total thickness of the flow is approximately 15 metres.

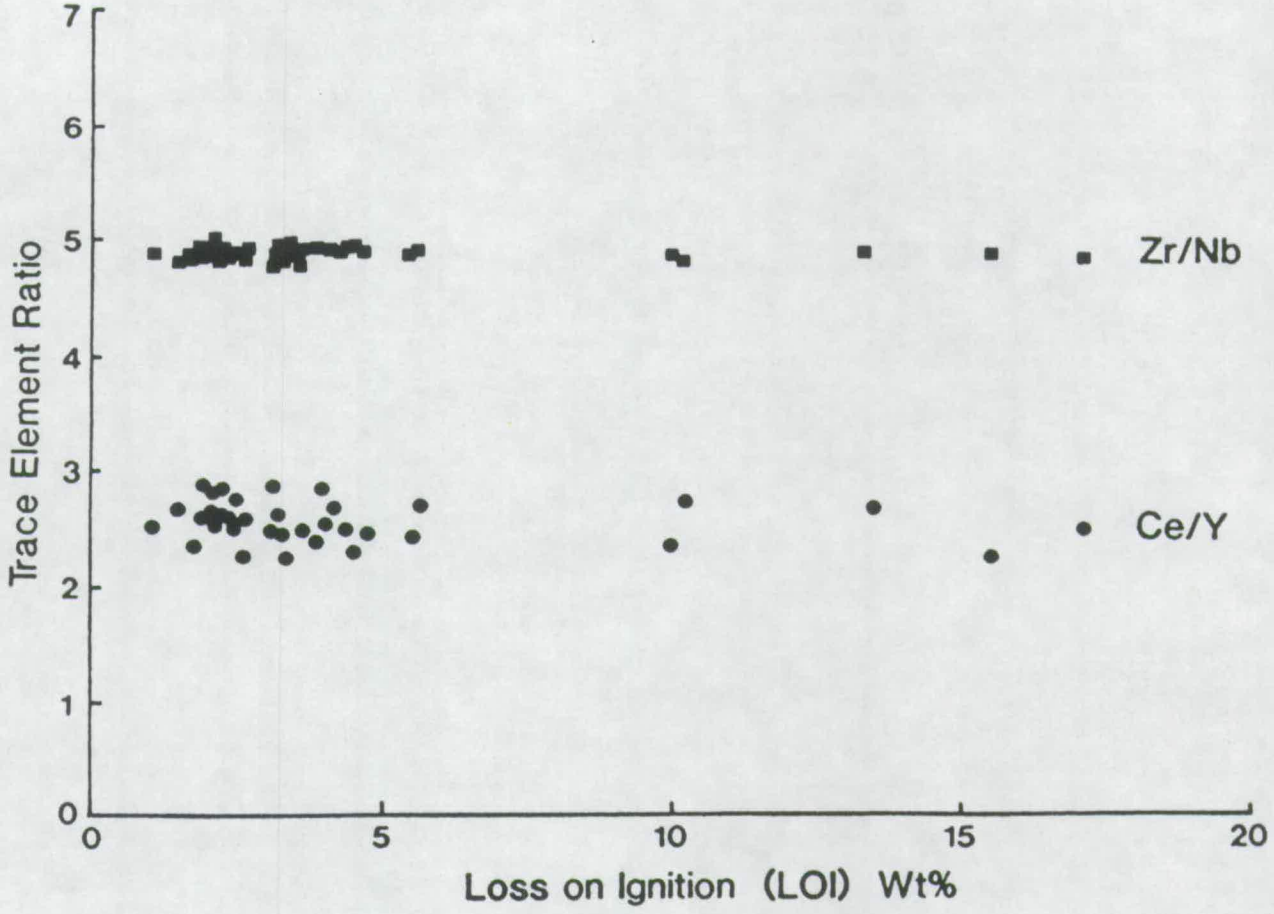

FIGURE 5.10 Ce/Y and Zr/Nb plotted as a function of LOI (wt. %) for samples from the ankaramite flow in well 15/21a-8 (see also Figures 5.8 and 5.9). Note how ratios of immobile trace elements are undisturbed by alteration.

observed in the altered rocks of the Forties province is comparable with the effects of low temperature alteration by sea water noted by Hart (1973).

In a chemical study of altered rocks the immobile elements are clearly the only reliable sources of information concerning the original chemical character of the rocks. Although immobile elements may increase in concentration during alteration, ratios between such elements remain unaffected. The concept of using ratios of immobile trace elements to study altered rocks is not a new one (e.g. see Pearce and Cann, 1973) but the remarkably constant values for such ratios shown in Figure 5.10 for the samples through the core in 15/21a-8 shows just how immobile these elements are. The ratios are unchanged even when LOI reaches almost 20 wt.%. The same is true of ratios of immobile major element oxides such as TiO_2, P_2O_5 and Al_2O_3 and of other immobile trace and rare earth elements.

It has not been possible to do a systematic study of the chemical effects of different styles of alteration on all of the different rock types present in the North Sea because fresh and variably altered samples of the same flow or intrusion are rarely available. The constancy of the ratios of immobile trace elements, such as Ce/Y and Zr/Nb, shown in Figure 5.10 does, however, inspire a certain amount of confidence that such ratios may be used to see through the effects of alteration on the original chemistry of the rock.

5.5 Crystallisation and Immobile Elements.

Fractional crystallisation is usually the most important process which operates to change the composition of a magma, once it has segregated from its mantle source. Its effects can be described with reference to TiO_2 and P_2O_5, which are immobile, but which will be subject to enrichment in highly altered rocks.

Small degrees of melting give rise to primary magmas with higher TiO_2 and P_2O_5 concentrations than do large degrees of melting since both Ti and P are incompatible in major mantle phases. Therefore, in general, at a given level of fractional crystallisation, more undersaturated magmas have higher values of TiO_2 and P_2O_5. The observation that the Forties basalts are the least undersaturated of the North Sea rocks is therefore confirmed in the upper diagram in Figure 5.11. In the lower diagram in Figure 5.11 all of the North Sea data set is shown and the overall dispersion of the different North Sea groups in terms of TiO_2 and P_2O_5 might, at first sight, be explained in terms of differing degrees of partial melting. However both elements are involved in the subsequent crystallisation of these melts and the very

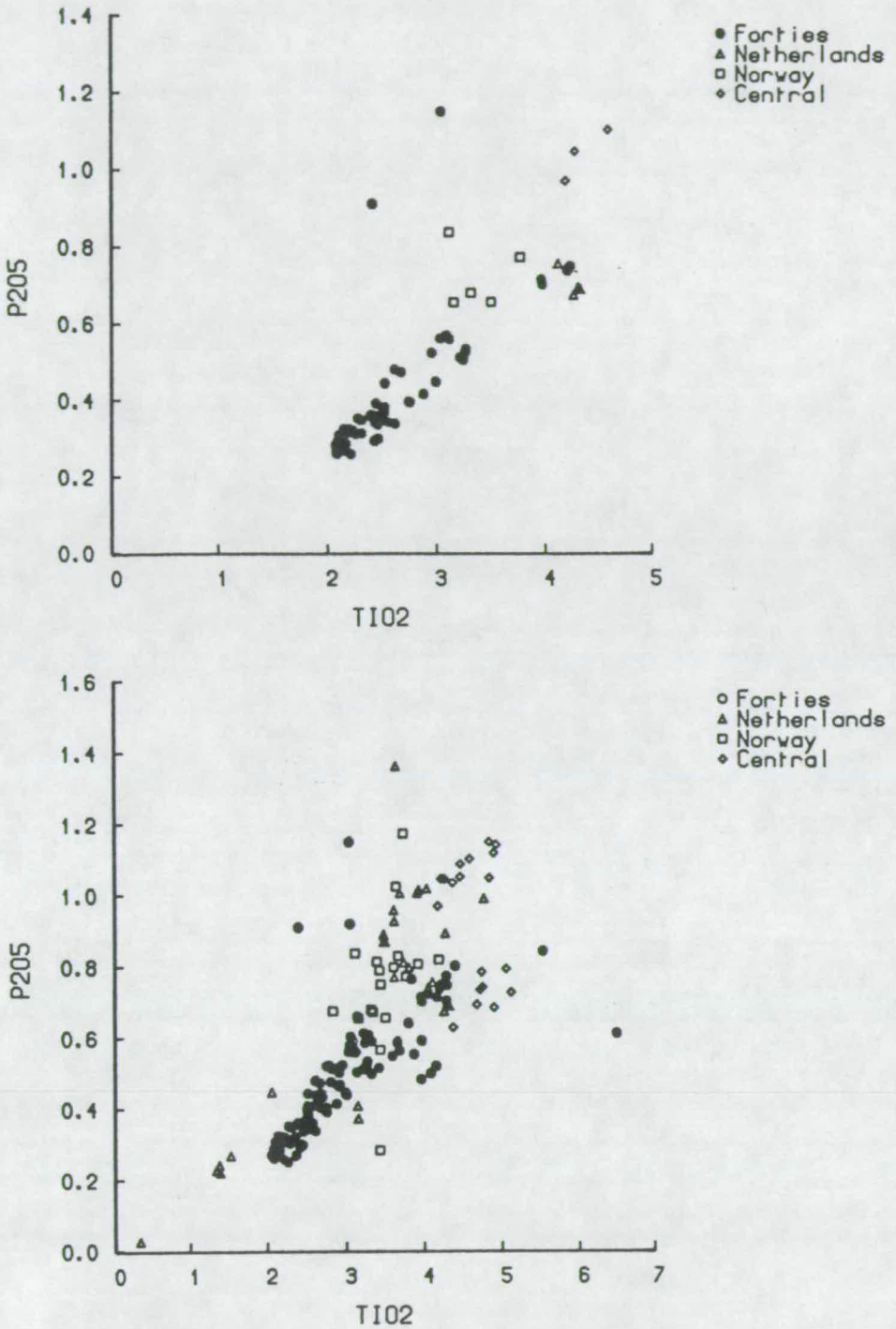

FIGURE 5.11 P_2O_5 vs. TiO_2 (wt.%). Upper diagram shows only the freshest subset of mafic North Sea rocks (LOI < 4 wt.% and MgO > 4 wt.%). Lower diagram shows all Mesozoic data.

low values of both oxides in some of the Netherlands samples relate to the more evolved, leucitophyre and phonolite, samples. Figure 5.12 shows the extent of Ti and P variation attributable firstly to varying degrees of equilibrium partial melting of a simple MORB type source[2] and in addition to the effects of progressive crystallisation and extraction of the expected mineral phases from the basaltic parent. Varying the source composition would introduce still more dispersion. Removal of olivine, with no Ti or P, concentrates both elements in the residual liquid in much the same way that alteration concentrates immobile elements. Clinopyroxene contains significant Ti but no P. Magnetite and apatite contain abundant Ti and P respectively. The net effect is to generate a wide range of TiO_2, P_2O_5 and TiO_2/P_2O_5 values in rocks still broadly basaltic (> 4wt% MgO), thus completely obscuring the values in the parent magmas generated on partial melting of the source.

Ratios of immobile trace elements such as Zr/Nb and Ce/Y have already been shown to be unaffected by low temperature alteration of the sort observed in the basalts from well AH1 (15/21a-8). Figure 5.13 depicts Zr/Nb and Ce/Y plotted against wt.% MgO for 116 analyses (J.G. Fitton, unpublished data) of unaltered, variably evolved alkaline rocks (similar in character to the alkali basalts from the North Sea) from the ocean island of São Tomé, part of the Cameroon line of West Africa (Fitton 1987). Note that for rocks which are the result of little or only moderate degrees of fractional crystallisation (MgO > 4%) the ratios are remarkably constant, a sign that the elements concerned are equally incompatible in the fractionating phases. In the more evolved rocks (MgO < 4%) the ratios start to increase and become highly variable. Clearly the elements concerned are not equally incompatible during this late stage in the crystallisation history.

From this study of fresh material we conclude that the ratios Zr/Nb and Ce/Y can be used to "see through" both the alteration and fractional crystallisation of igneous rocks, provided that only data from moderately or unevolved (MgO > 4%) samples is used. Values of Ce/Y and Zr/Nb from such samples should thus only depend on the composition of the mantle source and the degree of partial melting which produced the primary magma. The concentrations of the individual elements will be clearly subject to strong enrichment by fractional crystallisation and by alteration or by both processes.

---

[2] Melting path calculated using simple modal melting equation (see section 5.6) of Shaw (1970), bulk distribution coefficients (D), of 0.11 for Ti and 0.053 for P, from Fitton and James (1986) and the MORB source composition of Fitton and Dunlop (1985); i.e. the concentration of Ti and P in the source is assumed to be 1632 ppm and 95 ppm respectively.

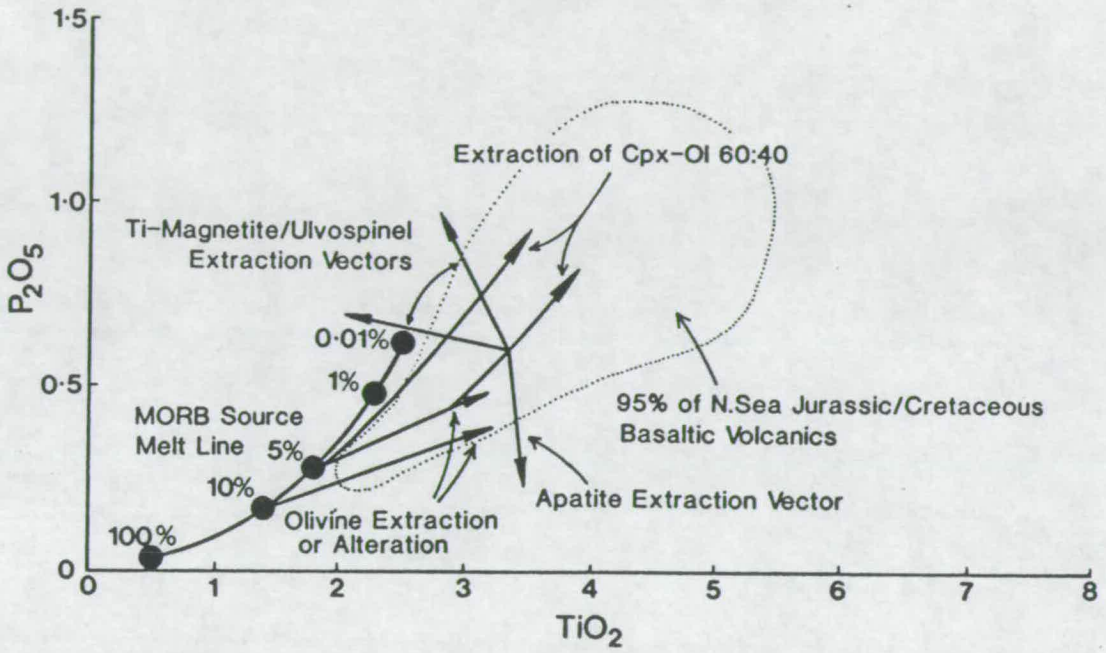

FIGURE 5.12 The dotted line indicates the field occupied by the Mesozoic North Sea data on the diagram of P_2O_5 vs. TiO_2 shown in Figure 5.11. A simple equilibrium partial melting path (from a MORB source, see text) is shown by the curved line and the per cent melting at different positions on the line are given. Vectors indicate the effects of alteration and fractional crystallisation on selected compositional points (see discussion in text).

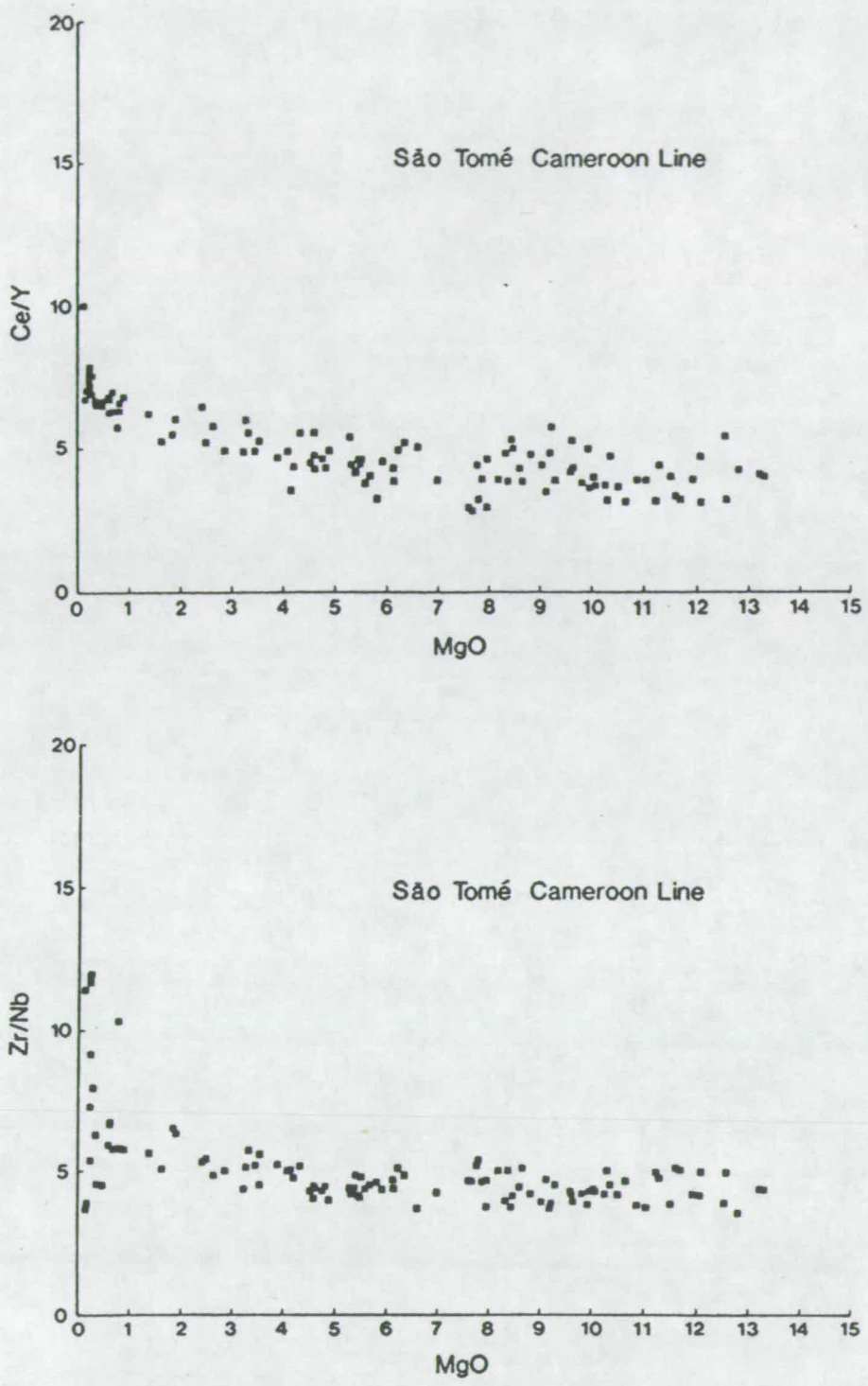

FIGURE 5.13 Variations in ratios of Ce to Y (upper diagram) and Zr to Nb (lower diagram) with MgO (wt.%) in a suite of alkaline lavas from the ocean island of São Tomé (Cameroon Line, West Africa). Data are from the unpublished data set of J.G Fitton (Edinburgh). Note that in mafic rocks (MgO > 4 wt.%) Ce/Y and Zr/Nb are almost constant suggesting that crystallisation does not fractionate these elements from one another in mafic rocks.

5.6 Partial Melting.

The main aim of this chapter is to establish the relative degrees of partial melting which resulted in the primary magma compositions observed in different parts of the North Sea. The undersaturated nature of the rocks suggests that the primary magmas resulted from small degrees of melting but in order to determine approximately how small these extents of melting were it is necessary to establish (1) some index of extent of melting that is free of the problems associated with alteration and fractional crystallisation, and (2) the chemical character of the source of the primary magmas.

Elements such as Ce, Y, Zr, Nb, and Sm are particularly useful for a study of the primary magma characteristics of a suite of variably altered variably fractionally crystallised rocks. These elements are approximately equally incompatible and it is well known that small extents of melting, unlike small amounts of crystal fractionation, can exploit what are rather small differences in the bulk distribution coefficients between different incompatible elements, fractionating them from one another. Ratios of such elements in any melt produced will therefore differ from those originally present in the source. For example, Nd must have been fractionated from Sm in order to explain the time integrated depletion, relative to the bulk earth, of the N-MORB reservoir (see Chapter 2). Extreme fractionation of elements such as La, Sm or Ce from Y and the HREE is commonly attributed to small extents of melting of a source containing garnet. Whereas the ratio of K to Ba or to Nb may critically depend on the presence or absence of K bearing phases such as phlogopite or K-richterite in the source region (see 5.6.2).

5.6.1 Ratios of Incompatible Trace Elements: An Index of Silica Saturation.

Smaller-degree melts are likely to be more undersaturated and form at greater depths than larger degree melts. From the discussion above it would therefore seem likely that differences in the ratios of incompatible trace elements should correlate directly with differences in the degree of undersaturation. Higher values of Ce/Y ($D_{Ce} < D_Y$) and lower values of Zr/Nb ($D_{Zr} > D_{Nb}$) would be expected in smaller degree melts which should also be more undersaturated. The value of Ce/Y might be expected to be especially high when garnet is a residual phase (at depths > 60km or so; pressures > 2.0 GPa; see Chapter 2) because Y tends to reside in the garnet.

In order to test the idea that ratios of immobile incompatible elements such as Ce/Y and Zr/Nb could be used to estimate, as a first approximation, the saturation of an altered rock the Ce/Y and Zr/Nb values of over 800 analyses of fresh, mafic (> 4wt% MgO) ocean island basalts (J.G. Fitton and D. James, unpublished data) were plotted against the saturation index defined in section 5.3. The results of this analysis are encouraging. The ocean island basalt data set shows a marked negative correlation of Ce/Y with S.I. and a positive correlation of Zr/Nb with S.I. (see Figure 5.14). In Figure 5.15 the values Ce/Y and Zr/Nb for the freshest of the North Sea samples (LOI<4 wt.%) are similarly plotted against S.I.. The correlations noted in Figure 5.14 do appear to be present but are masked slightly by the effects of olivine and clinopyroxene fractionation, and possibly also by alteration, which shifts points to higher values of S.I.

Figures 5.14 and 5.15 imply that in altered basalts, where the saturation index is useless, ratios of immobile incompatible trace elements may be used to give an indication of the degree of saturation of the primary melt. A diagram of Ce/Y *vs.* Zr/Nb or Ce/Y *vs.* Zr/Y (see Figure 5.16) can therefore be used to study the relative degrees of undersaturation of altered mafic rocks. Of the freshest North Sea rocks, those with highest Ce/Y (8-10), highest Zr/Y (~16) and lowest Zr/Nb (~2.5) are the Egersund basin nephelinites which could therefore be considered the most undersaturated rocks in the region, and probably reflect the smallest degrees of partial melting from the greatest depths. Such an interpretation is supported by their petrographic characteristics but was not apparent in the major element chemistry of even the least altered samples. Following the same logic, the Forties Province alkali basalts would be regarded as the least undersaturated, largest degree melts from the shallowest levels, of all of the Mesozoic rocks. Notice how the same general picture is retained in Figure 5.17 even when all of the mafic rocks (MgO > 4 wt.%) from the North Sea data set, whatever their LOI, are plotted. Of course it would be possible to obtain all of the North Sea rocks at similar extents of melting simply be varying the source composition but one might not then expect them to also be different in terms of degree of undersaturation; this discussion is returned to in section 5.7. Assuming, for the time being, that all of the North Sea rocks resulted from different degrees of melting of the same source, then these conclusions about undersaturation are in accordance with the petrographic observations and confirms and extends the conclusions of Dixon *et al.* (1981) which were based on the major element chemistry of rare fresh rocks in each region and on compositions of relict pyroxenes.

If differences in the values of ratios such as Ce/Y, Zr/Nb, and Zr/Y reflect different degrees of melting of some starting composition then, if the starting

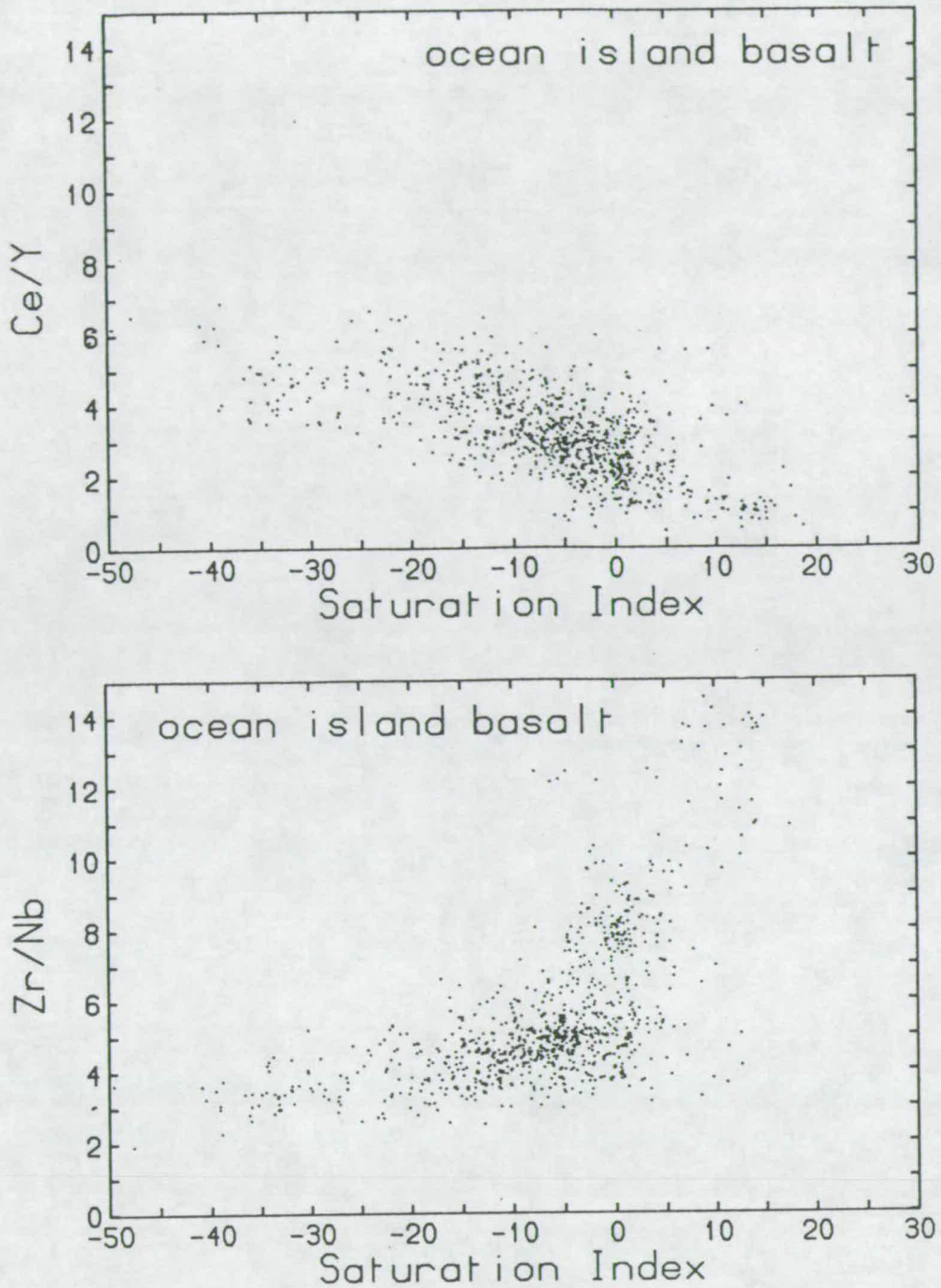

FIGURE 5.14 Variations in trace element ratios (Zr/Nb and Ce/Y) of OIBs with silica saturation as defined by the Saturation Index (SI) where

$$SI = [Si-(11(Na+K)+3Ca+Al+Fe^{II}+Mg)] / 2$$

and negative values of SI indicate undersaturated compositions. Note that undersaturated OIBs generally have Zr/Nb < 6 (upper diagram) and Ce/Y > 2. The OIBs plotted are all mafic volcanic rocks (MgO > 4 wt.%) from the unpublished data set of J.G. Fitton and D. James (Edinburgh).

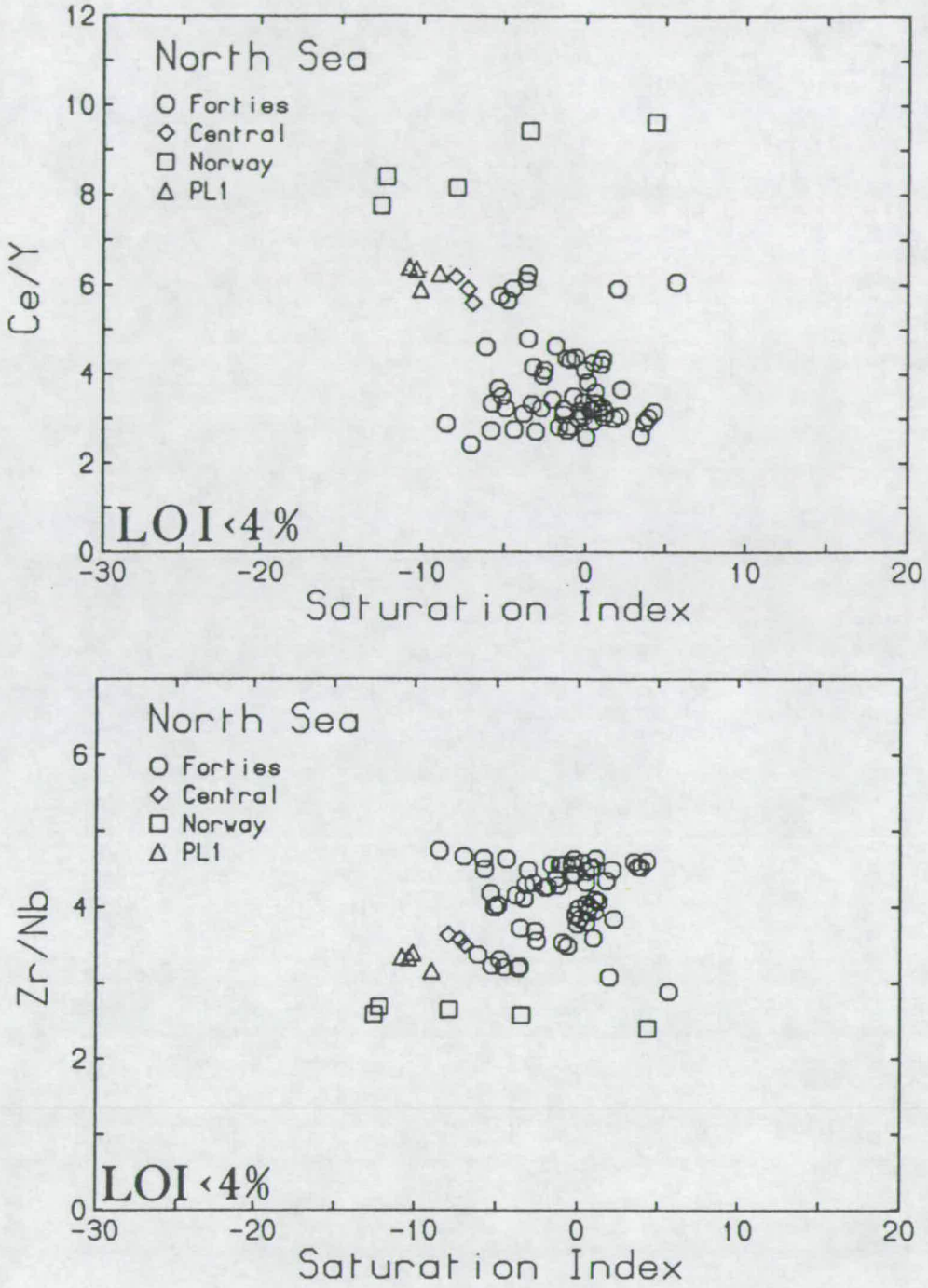

FIGURE 5.15 Variations in trace element ratios (Zr/Nb and Ce/Y) of the freshest subset of mafic Mesozoic North Sea rocks (LOI < 4 wt.% and MgO > 4 wt.%) with silica saturation as defined by the Saturation Index (SI; see Figure 5.14 for definition). Note that all of the North Sea rocks plotted have Zr/Nb < 6 and Ce/Y >2, an observation which is consistent with their generally undersaturated chemical character.

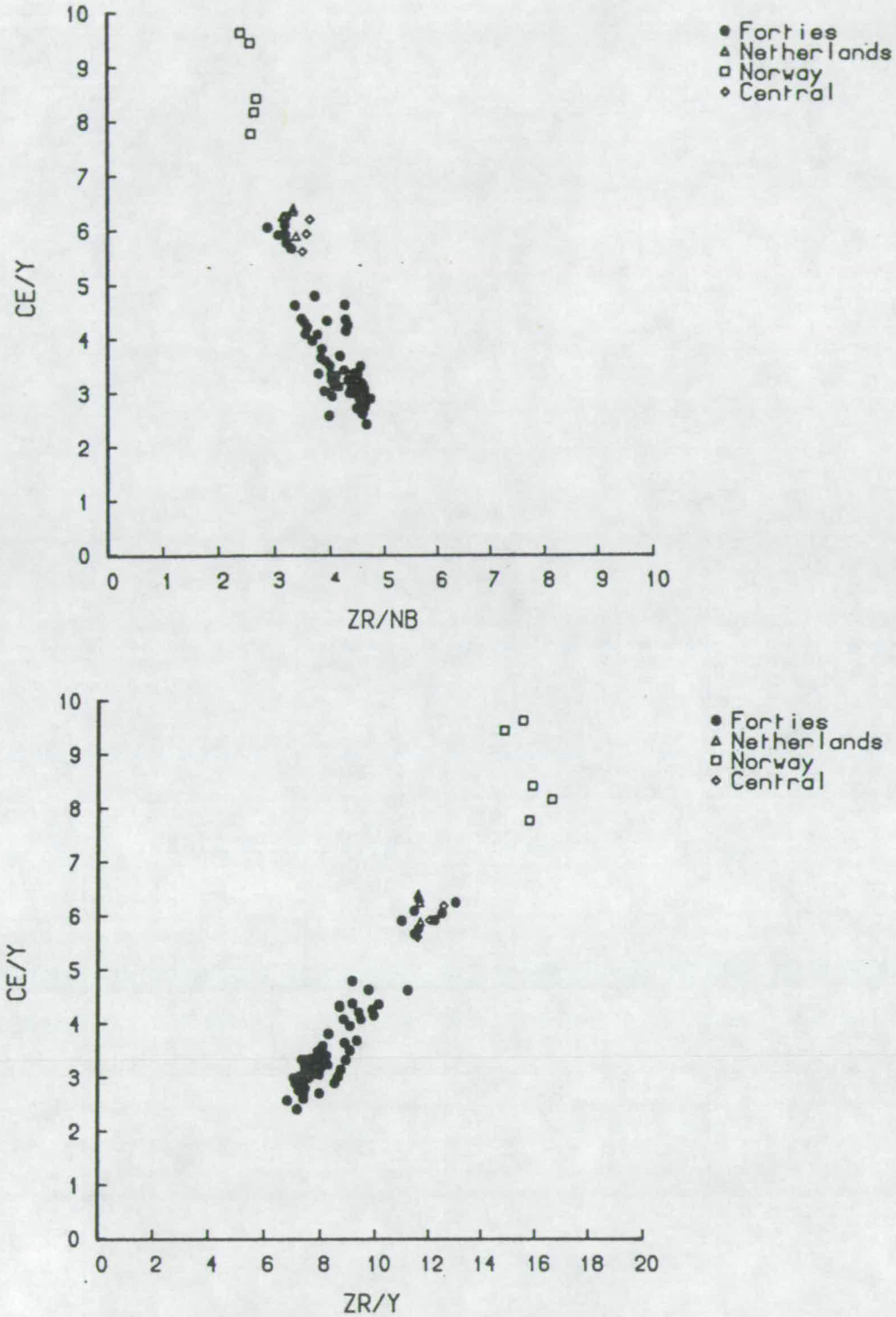

FIGURE 5.16 Variations in Ce/Y with Zr/Nb (upper diagram) and Zr/Y (lower diagram) for the freshest subset of mafic Mesozoic North Sea rocks (LOI < 4 wt.% and MgO > 4 wt.%).

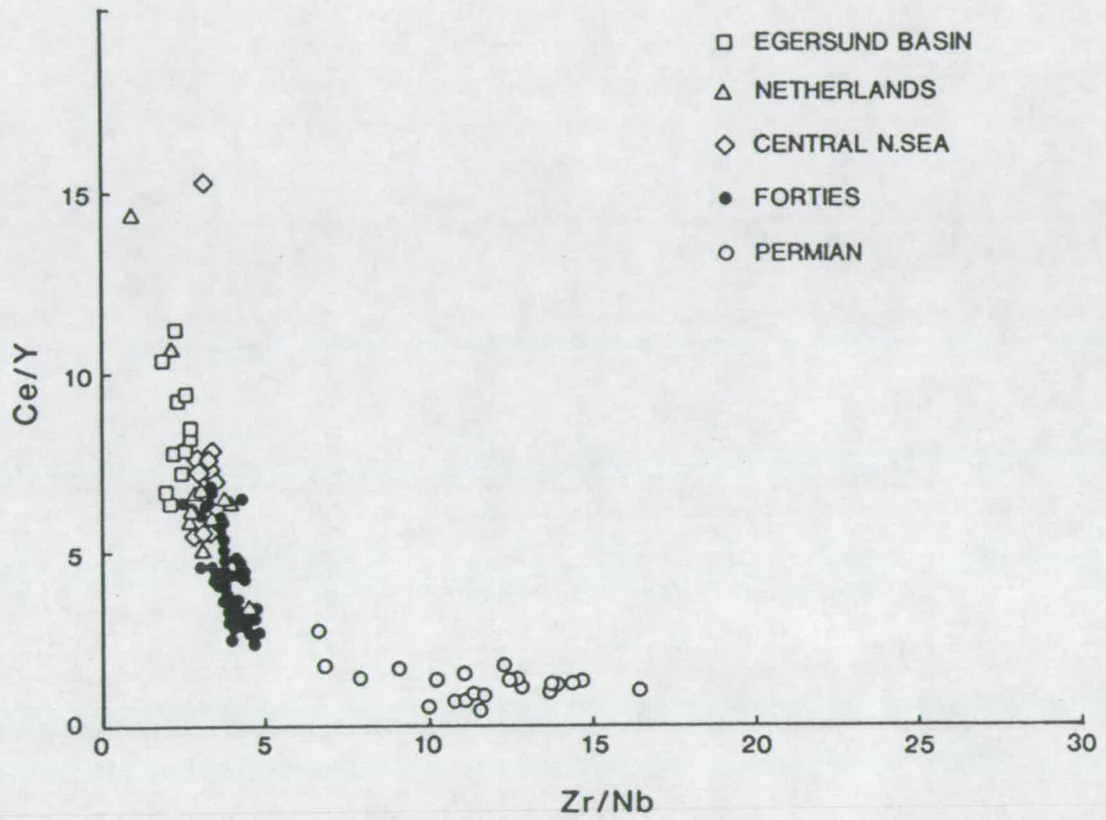

FIGURE 5.17 Variation of Ce/Y with Zr/Nb for all of the mafic rocks from North Sea data set (MgO > 4 wt.%) irrespective of LOI. Note that the overall grouping seen in Figure 5.16 has not changed. Note also the lower Ce/Y and higher Zr/Nb values of the Lower Permian mildly alkaline basalts which are included on this plot.

composition (source) can be shown to be similar for all of the North Sea rocks, differences in the degrees of melting can be estimated from equilibrium melting calculations. Any such differences should relate to different degrees of extension in the different areas of the North Sea.

5.6.2 The Nature of the Source(s) of the North Sea Magmas.

The quantitative models presented in chapters 2 and 3 are dependent on the assumption that the mantle melts with the characteristics of anhydrous garnet lherzolite studied in experiments. The question addressed in this section is that of whether the trace element compositions of any or all of the North Sea suite can be reconciled with melting of a simple four phase lherzolite assemblage, containing olivine, two pyroxenes and garnet or spinel. The time-integrated nature and possible location of the source of the melts is then discussed with reference to ratios of isotopes of Sr and Nd.

5.6.2.1 Evidence from Normalised Trace Element Patterns.

In Figures 5.18, 5.19, and 5.20, averages of samples with LOI<4 wt.% and MgO>8 wt.%, from each of the four groups, have been normalised against MORB (average value of J.A. Pearce, pers. comm. 1989), chondrite (after Sun, 1980) and OIB (average value of J.G. Fitton and D. James, pers. comm. 1990) respectively (see captions for normalisation factors). Note that in all three diagrams the most mobile elements are likely to be Rb, Ba, K and Sr and any interpretation based on these four elements should be tentative.

On the MORB-normalised and chondrite-normalised diagrams all of the North Sea samples show the LILE-enriched humped patterns which are so characteristic of oceanic and many continental within-plate basalts. All of the elements plotted on such diagrams are generally considered incompatible during the early stages of fractional crystallisation of basaltic magmas and therefore the steepness of such patterns, effectively the La/Y ratio, is generally considered to reflect the degree of melting at source (e.g. Fitton and Dunlop, 1985) although it may also vary according to the modal proportion of garnet and the source composition. In the simplest possible geochemical model, assuming only one source composition, the Egersund samples would be considered the smallest degree, and therefore the most highly undersaturated melts, whereas the Forties basalts would be considered to be the largest degree, least undersaturated, melts of the Mesozoic suite. These arguments are consistent with those presented above based on ratios of pairs of trace elements.

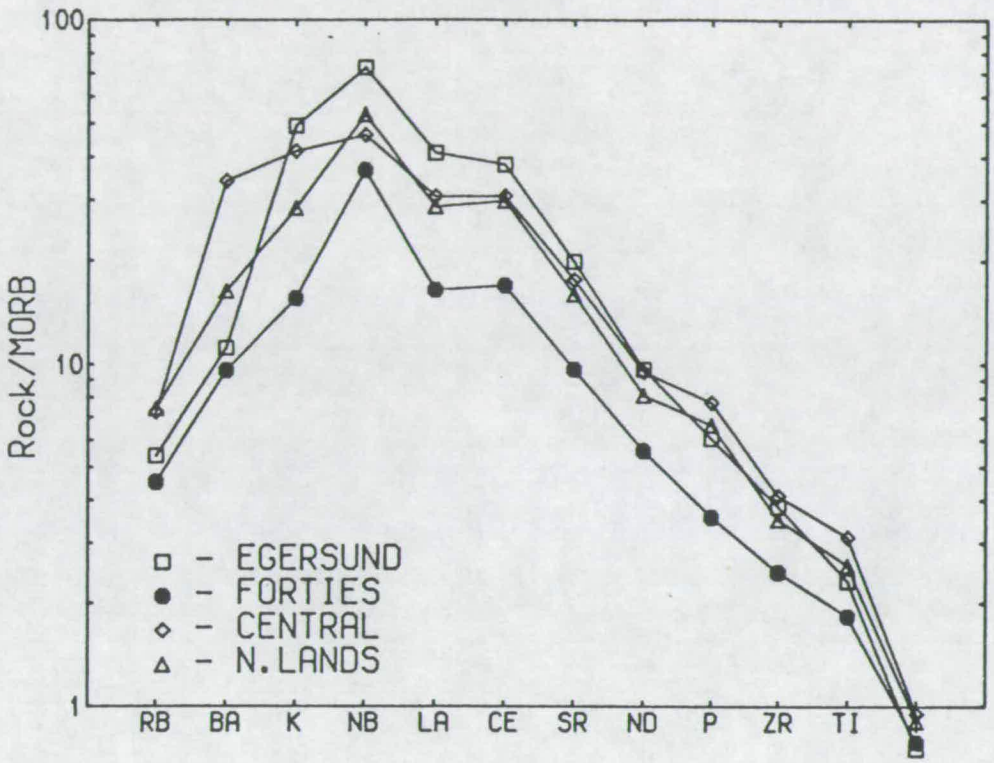

FIGURE 5.18 Average MORB-normalised trace element patterns of the freshest (LOI < 4 wt. %) most mafic (MgO > 8 wt.%) Mesozoic rocks from the North Sea. The normalisation factors used for average MORB were supplied by J.A. Pearce (pers. comm. 1989) and are (in ppm. unless otherwise stated) 1.28, 14.7, 0.077 (wt.% oxide), 2.48, 2.73, 8.12, 92.4, 7.54, 0.09 (wt.% oxide), 81.5 and 1.32 (wt.% oxide) respectively for Rb, Ba, K, Nb, La, Ce, Sr, Nd, P, Zr and Ti.

Notice how the overall gradient of all of the North Sea rocks on Figure 5.20 suggests that, on average, the North Sea rocks reflect a rather smaller degree of melting than average OIB.

The overall similarity of the patterns between the four groups on all three normalised diagrams is important because it suggests that the gross chemical characteristics of their source was the same. In particular the similarity with average OIB is apparent. However, the differences, when they are not merely differences of slope or artefacts of alteration or fractional crystallisation, may provide important information concerning the mineralogy of the source. For example the very low normalised values of Y suggests that in all cases the North Sea melts were at some stage in equilibrium with garnet. Values of Y on the MORB-normalised diagram (Figure 5.18) which are lower than 1 are generally thought to reflect the importance of garnet in the source region of alkaline magmas, while the higher value in MORB, despite its larger degrees of melting, could be explained by melting at shallower depths in the spinel stability field or by the complete melting-out of garnet in the source. The fact that the Egersund samples show the steepest slope on the MORB- and chondrite-normalised patterns and yet have the lowest values of normalised Y suggests that not only are they the result of the smallest degrees of melting but also that their source was richer in garnet.

The trough at K on the chondrite-normalised diagram (Figure 5.18) suggests that K was relatively compatible in the source of all but the Central Graben samples. K troughs have commonly been attributed to the presence of an accessory phase such as the amphibole K-richterite. Phlogopite may also be a K-bearing accessory phase in the mantle but is unlikely to be an important residual phase in the generation of the North Sea melts because there is no pronounced trough at Ba or Rb. It should be noted that it would not be necessary to invoke an accessory phase to explain the K trough if a small amount of K (like Na) could be incorporated in clinopyroxene (jadeite) at high pressures (ca. > 2 GPa). The apparent peak at K for the Central Graben samples (which is also apparent in the patterns from the rocks from F/10-1 when these are plotted alone rather as a part of a Netherlands average) may well be an artefact of Ba and Rb mobility (relative depletion), but it is clear that there is no K trough which may suggest that, if present in the source, phlogopite or K-richterite formed a major component of the melt and that it was completely melted out of the source region. The ultrapotassic nature of these samples (4-5 wt.% K_2O) together their high concentrations of TiO_2 (4-5 wt.%), their very low Na_2O content (< 1 wt.%), and low concentrations of Ni and Cr (both less than 200 ppm) at high values of MgO (10-12 wt.%) is shown in Chapter 7 to be compatible with melting of a

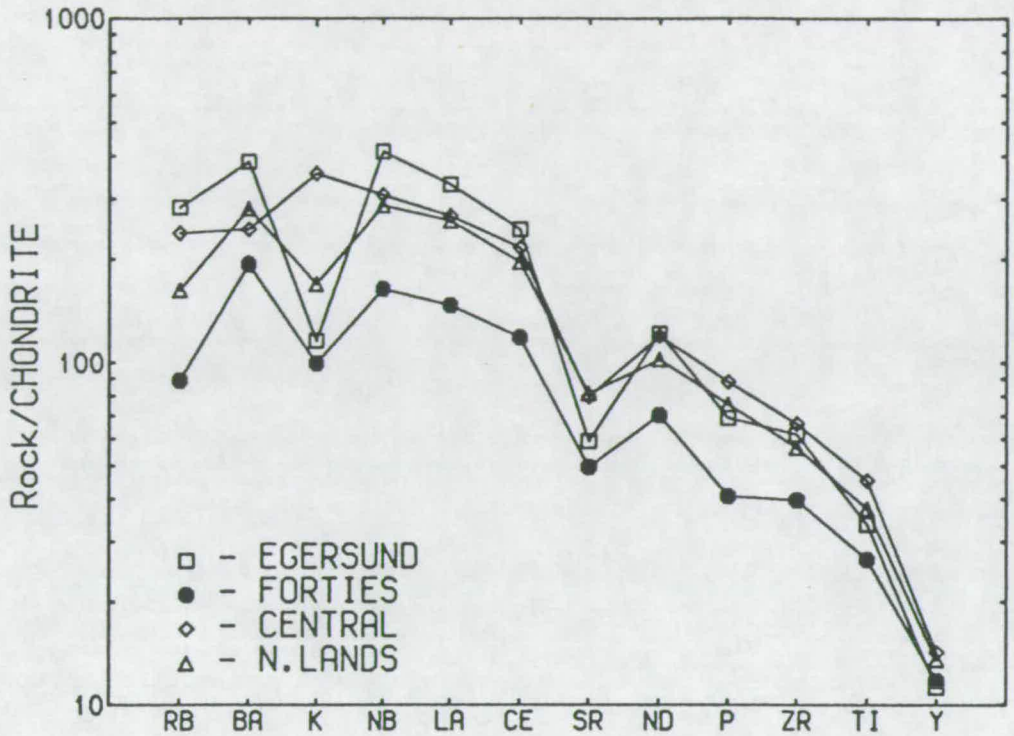

FIGURE 5.19 Average chondrite-normalised trace element patterns of the freshest (LOI < 4 wt. %) most mafic (MgO > 8 wt.%) Mesozoic rocks from the North Sea. The normalisation factors of Sun (1980) were used.

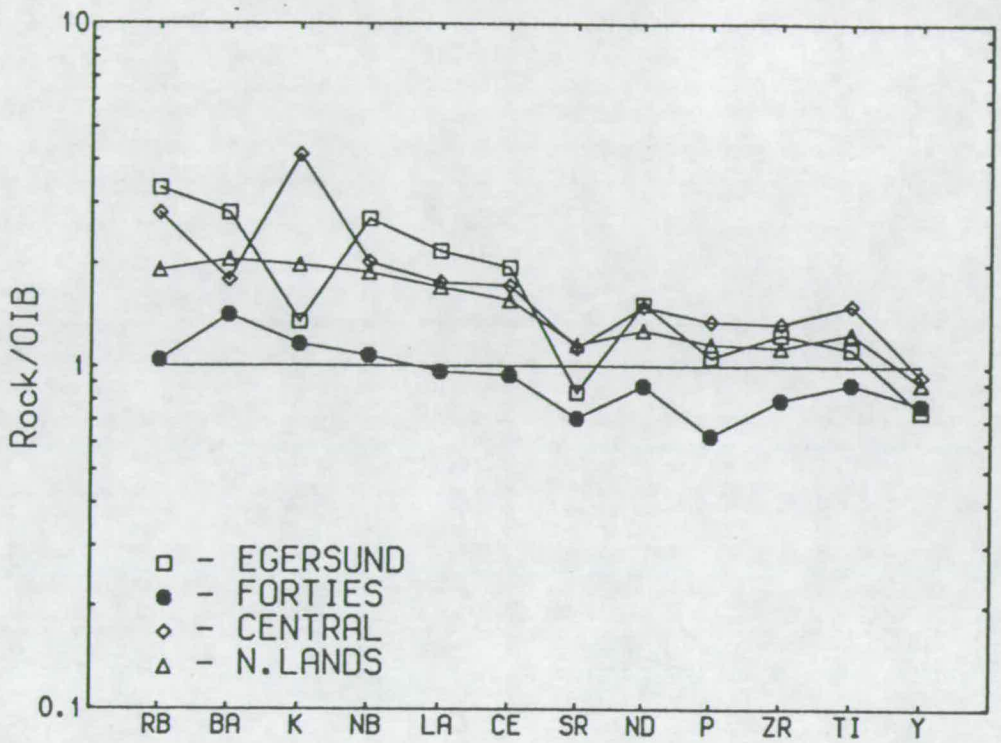

FIGURE 5.20 Average OIB-normalised trace element patterns of the freshest (LOI < 4 wt. %) most mafic (MgO > 8 wt.%) Mesozoic rocks from the North Sea. The normalisation factors used for average OIB were supplied by J.G. Fitton and D. James (pers. comm. 1990) and are (in ppm. unless otherwise stated) 29.65, 517.71, 1.235 (wt.% oxide), 53.30, 47.71, 101.91, 769.18, 47.60, 0.681 (wt.% oxide), 277.26, and 3.08 (wt.% oxide) respectively for Rb, Ba, K, Nb, La, Ce, Sr, Nd, P, Zr and Ti.

phlogopite-clinopyroxenite, poor in olivine, rather than a garnet peridotite. Note that because of their mafic composition their high K chemistry cannot be easily explained in terms of crustal melting. On the OIB-normalised diagram (Figure 5.20) a K trough is only present for the Egersund basin rocks, a feature which may be due to their rather altered nature even at relatively low values of LOI (i.e. < 4 wt.%). Since average OIB show a K trough the peak at K for the Central Graben lamprophyres is emphasised on Figure 5.20.

A prominent trough in Sr is also clear, for all provinces, on all three diagrams. There is little evidence of substantial plagioclase fractionation in the Forties province basalts and similar troughs are commonly observed in melilitites and nephelinites (J.G. Fitton, pers. comm. 1990) and this feature is therefore considered to be primary. Sr is only moderately incompatible in clinopyroxene, with a partition coefficient of between 0.07 and 0.43 (Henderson, 1982), and is therefore unlikely to be fractionated by the relatively small amounts of clinopyroxene crystallisation inferred to have taken place in basaltic rocks. Although the chondrite-normalised patterns of most OIBs contain a trough at Sr, the North Sea data contain a pronounced Sr trough on the OIB-normalised diagram. This trough may in fact be an artifact of the large amount of data from Hawaii, which do not contain a dip at Sr and, which contribute to the OIB average. There is at present no satisfactory explanation for the trough at Sr. The very slight flattening of the chondrite normalised curves for Forties and Egersund between Zr and P is thought to reflect the fractionation of apatite, in the more evolved of the Forties and Egersund samples, from the alkali basalt and nephelinite melts.

In summary, the evidence from normalised trace element patterns suggests that the mantle source of the mafic North Sea rocks, with the exception of the ultrapotassic varieties, is similar to that of average OIB and should therefore be broadly represented by garnet lherzolite (Norry and Fitton, 1983). Simple equilibrium melting calculations of garnet lherzolite might therefore be used to adequately reproduce the sorts of normalised incompatible element patterns discussed above (e.g. Norry and Fitton, 1983; Fitton and Dunlop, 1985; Fitton and James, 1986); see section 5.6.3.

5.6.2.2 Isotopic Evidence.

A study of the ratios of $^{86}Sr/^{87}Sr$ and $^{143}Nd/^{144}Nd$ was carried out by F.G. Waters at Cambridge University on three of the freshest whole rock samples from the North Sea; AH1/42 an ankaramite from well 15/21a-8, PL1/12 a potassic alkaline lamprophyre from well F/10-1, and ES1/24 a nephelinite from well 17/9-1. Clinopyroxene separates from these same samples were also studied and gave similar

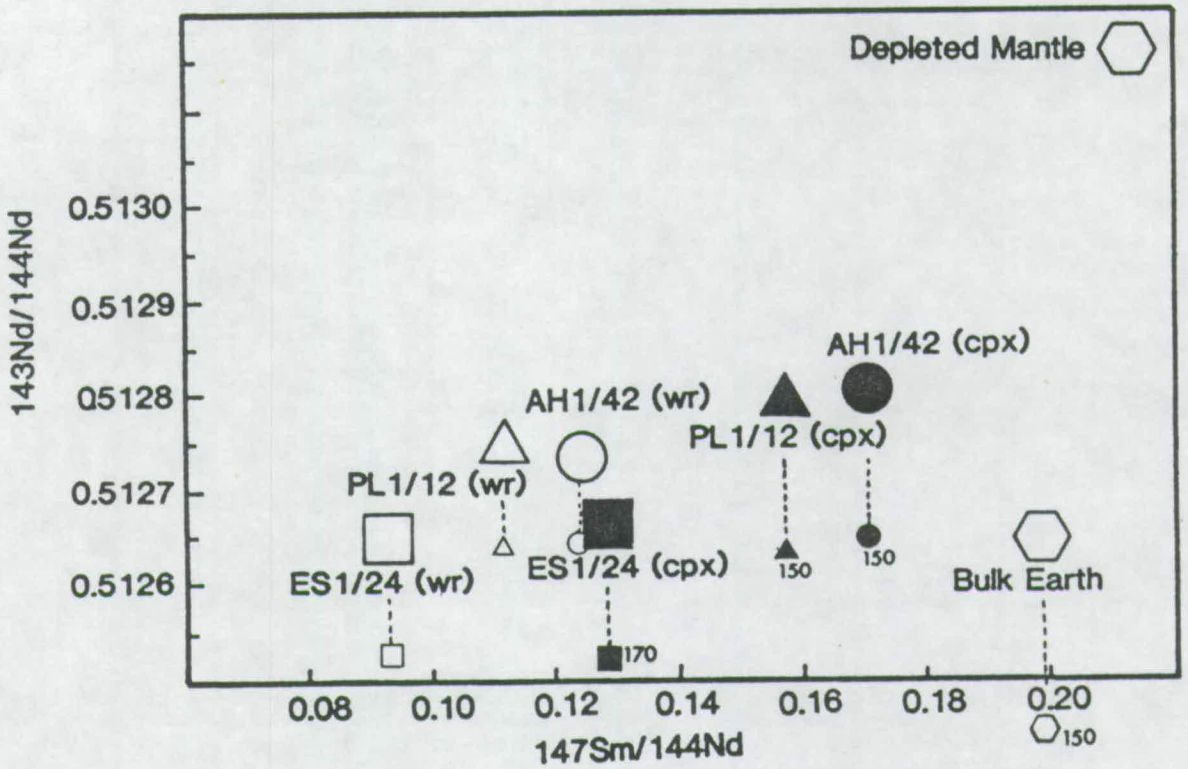

FIGURE 5.21 $^{143}Nd/^{144}Nd$ vs. $^{147}Sm/^{144}Nd$ for clinopyroxene (cpx) separates (filled symbols) and whole-rocks (wr; open symbols) from samples AH1/42 (15/21a-8; alkali basalt from the Forties province), PL1/12 (F/10-1; ultrapotassic lamprohpyre from the Netherlands province) and ES1/24 (17/9-1; nephelinite from the Egersund Basin). Note that the small symbols are at $^{143}Nd/^{144}Nd$ values which have been age-corrected (correction of 170 Ma for ES1/24 and 150 Ma for AH1/42, PL1/12 and bulk earth). This diagram which contains unpublished data was kindly supplied by F.G Waters (Cambridge).

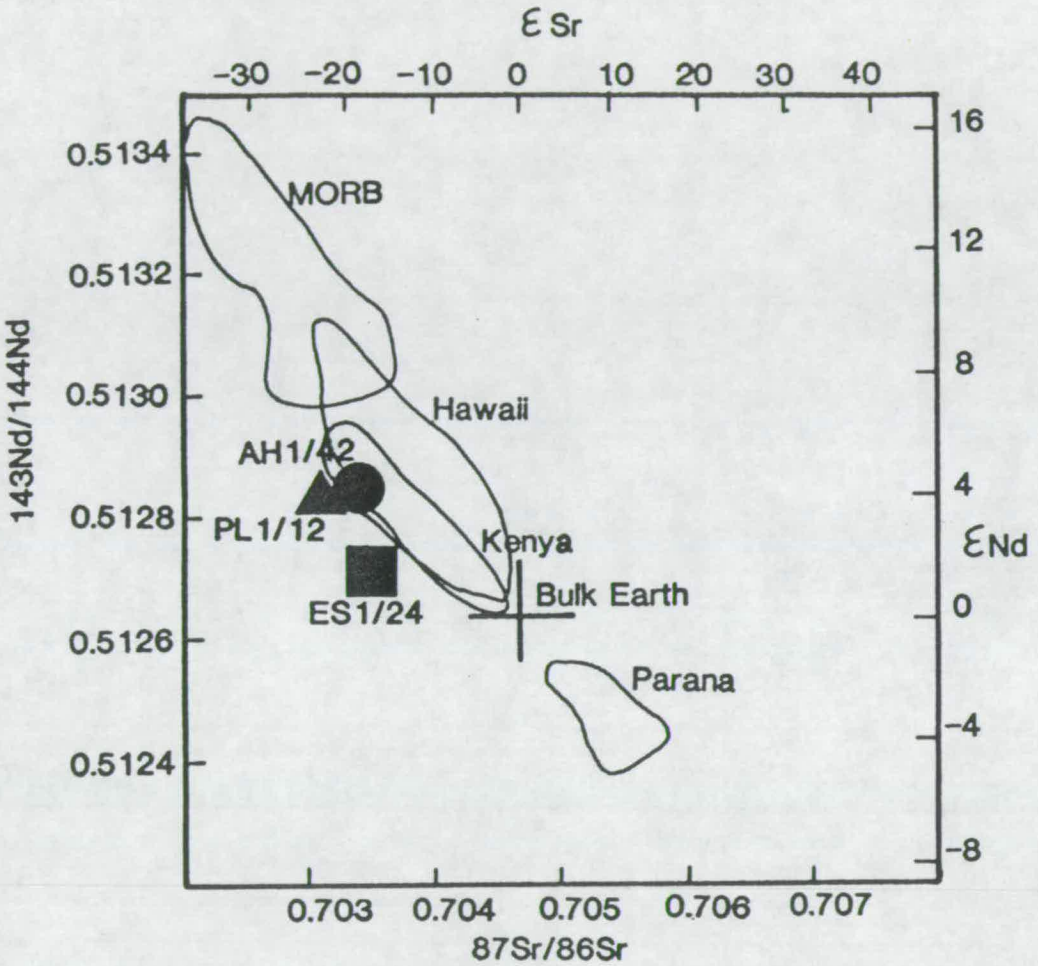

FIGURE 5.22 εNd vs. εSr for the clinopyroxene separates from AH1/42, PL1/12 and ES1/24. The fields for OIB and MORB are from Wilson (1989). Unpublished data provided by F.G. Waters (Cambridge).

results. Full details of this study, which is as yet unfinished, will be presented elsewhere.

The preliminary results of the isotope study, kindly provided by F.G. Waters, are shown in Figures 5.21 and 5.22. The slightly higher values of $^{143}Nd/^{144}Nd$ and $^{147}Sm/^{144}Nd$ observed for the pyroxenes, when compared to the whole rock values, reflects the fact that, in clinopyroxene, Sm is marginally more compatible than Nd and this over the last 150-170 Ma has led to a slightly greater increase in radiogenic ^{143}Nd in the pyroxenes than in the whole rock. Notice that the differences between whole-rock and mineral-separate values for $^{143}Nd/^{144}Nd$ are the same after an age correction has been applied (see small symbols in Figure 5.21). The most important conclusion to be drawn from Figures 5.21 and 5.22 is that, like OIB, despite their LILE enriched nature (relative to bulk earth) the mafic rocks of the North Sea were produced by melting of a source (or sources) which was, on average, more LILE depleted than bulk earth but which was more LILE enriched than the MORB reservoir. Because of the uncertainties involved in selecting a value for an age correction for each of the samples, it is not possible to say categorically whether or not the more undersaturated Egersund sample (ES1/24) was derived from an isotopically more enriched source than that of the lamprophyre (PL1/12) and alkali basalt (AH1/42). If sample ES1/24 is ~170 Ma old whereas the other samples are closer to 150 Ma in age then this may well be the case. On the basis of the somewhat limited data at present all three samples are considered to have an isotopically very similar source. Note that this need not necessarily imply that the sources are mineralogically the same (PL1/12 is probably a melt from phlogopite pyroxenite rather than garnet peridotite; see Chapter 7) or even that they are all located in the same part of the mantle; lithosphere or asthenosphere.

5.6.2.3 Discussion.

At this point it is not intended to digress to discuss at great length the various hypotheses for different possible geochemical reservoirs which need to be invoked to explain the isotopic characteristics of continental rift zone basalts and OIB, which are commonly very similar but which are isotopically distinct from N-MORB. There is little agreement in the literature concerning the location of the LILE-enriched material which is apparent in the isotopic signature of such rocks. Without considering all of their pros and cons, the more popular hypotheses, which essentially fall into 3 groups and which were discussed at some length by Latin *et al.* (1990a,b), may be very briefly summarised as follows :

(1) Streaky asthenosphere models (e.g. Sleep, 1984; Fitton and Dunlop, 1985; Fitton and James, 1986; Allègre, 1987) have been called upon to explain the similarity between OIB and continental rift basalts. These models rely on a *host* asthenosphere that is more depleted, isotopically and in terms of LILE, than the ideal inferred source of N-MORB, but which contains *streaks* of more easily fusible, isotopically- and LILE-enriched (relative to MORB) material. At large degrees of melting both streaks and host homogenise to produce average MORB, while at lower degrees of melting the chemical characteristics of the magmas are dominated by the streaks.

(2) Enriched or metasomatised lithosphere models have been popular in the literature concerning the origin of continental rift basalts (e.g. Frey *et al.*, 1978; Menzies and Murthy, 1980; Bailey, 1982; Harte, 1983; Wyllie, 1987). Early models for rift magmatism, because of the problems perceived with extracting small amounts of melt from the mantle, invoked widespread metasomatic enrichment of the lithosphere in order to explain the origin of LILE enrichment without invoking small extents of melting. More recently, as a consequence of physical modelling of melt extraction (McKenzie, 1984), the concept of LILE enrichment due to small degrees of melting has met with more acceptance. The most recent models concerning enriched lithosphere advocate metasomatism of the base of the MBL, produced by time-integrated, or event-driven, migration of, and veining by, LILE-and volatile-rich small melt fractions from the asthenosphere, as a reason for isotopic compositions which are enriched relative to MORB and sometimes even relative to bulk earth (e.g. McKenzie, 1989; Thompson *et al.*, 1990). Metasomatism of the lithosphere by melts or fluids which are enriched in LILE, with the exception of Nb and Ta, may occur over subducting lithospheric slabs or simply as a result of the continual convective overturn and decompression within the asthenosphere. Old metasomatised lithosphere is often invoked as a source of ultrapotassic rocks, like those of the North Sea, because such *high-K rocks are never found in the oceans* (e.g. Latin *et al.*, 1990a,b; Thompson *et al.*, 1990).

(3) Plume models (e.g. Hofmann and White, 1982; Allègre, 1982; McKenzie and O'Nions, 1983) have long been popular. In this case material that is LILE and isotopically more enriched than N-MORB is transported upwards from some reservoir in or near the lower mantle. In terms of chemistry the plume models are a very attractive explanation for many OIB and for the source of P-MORB. Plumes, like processes of subduction and lithospheric delamination, may also add heterogeneities to the asthenosphere and provide a source of the isotopically distinct streaks required in the first model. However, such models do require elevated potential temperatures beneath every ocean island, anomalous ridge segment and

continental rift. In Chapter 7 it is shown that the presence of a mantle plume during rifting in the North Sea is inconsistent with other observations.

Even with a perfectly fresh suite of rocks from a continental rift it would be extremely difficult to make definite, or unique, quantitative conclusions concerning the mineralogical, chemical and isotopic composition of their source, let alone its physical location. Indeed many of the arguments would become circular. For example, the observation that some basalts have Pb isotope ratios, which suggest high U/Pb ratios, requires separation of a high U source for considerable periods of time. This source could either reside in the lower mantle, or it may reside in the continental lithosphere, or it may relate to a plume source which is fuelled by U-rich lithosphere either oceanic, via subduction, or continental, via delamination. There are at present a great many interdependent scenarios for the formation and existence and significance of different chemical reservoirs within the Earth. Detailed examination of such arguments does little to help our understanding of the links between extension, decompression and rift magmatism! To reiterate, the main purpose of this study is to establish whether or not there are differences in the degrees of melting which produced the primary basaltic magmas in different regions of the North Sea and, if this is the case, whether such differences may be related quantitatively to the nature and degree of extension. This purpose will not be achieved by any amount of discussion concerning the relative merits of different models for enrichment. Therefore, bearing possible oversimplifications in mind one way forward is to use simple calculations to estimate the relative extents of melting from a garnet peridotite mantle.

5.6.3. Estimating Relative Degrees of Partial Melting.

If differences between the values of ratios of immobile, incompatible trace elements (e.g. Ce/Y, Zr/Nb) from various parts of the North Sea, and differences in the slope of normalised trace element patterns are related to differences in the degrees of melting, then it should be possible to make estimates of the relative degrees of melting from calculations which assume a simple modal melting model (cf. Shaw, 1970). The values obtained from such melting calculations are very much model-dependent, particularly with respect to the D values (i.e. bulk distribution coefficients) and source compositions used. Thus a large degree melt from a very LILE enriched source, which might itself have been produced by small degrees of melting of a more depleted source, may look very similar to an ultrasmall degree melt from a rather more LILE depleted mantle.

There are, however, some constraints on the source composition. Firstly the Sr and Nd isotope ratios of the three North Sea samples suggest that the bulk source(s) of these melts is rather more LILE enriched than the source of N-MORB. By using a source composition which will generate the trace element ratios observed in N-MORB some lower limit may be placed on the extent of melting. The isotope ratios imply a mantle source more LILE depleted than bulk earth. A source composition close to that estimated for bulk earth should therefore give some sort of upper limit to the degrees of melting. Of course no model will uniquely explain the data and more complex models involving mixing of melts from sources of different composition could equally well be devised.

5.6.3.1 Simple Model with Ce/Y and Zr/Nb.

For the first trace element model the bulk mantle D values presented by Fitton and Dunlop (1985) were used (D_{Ce}=0.012, D_Y=0.183, D_{Zr}=0.049, D_{Nb}=0.0057). Because of the critical dependence of melt fraction on D at very small degrees of melting small changes in the value of D lead to large differences in melt fractions calculated during the modelling. The values of Fitton and Dunlop (1985) were used because they produce reasonable melt fraction estimates in the calculations for alkali basalts (< 5% melting; Gast 1968) and MORB (15-20%), and because they are consistent with experimentally-determined values for mantle phases. The D values are appropriate for a garnet lherzolite source containing a small amount of a K-rich phase such as the amphibole richterite. It must be stressed that these D values are model-dependent and must not be regarded as accurate absolute values. They will, however, be internally consistent and may therefore be used to calculate relative degrees of melting.

The MORB source of Fitton and Dunlop (1985), calculated from average MORB by assuming that MORB is produced by 15% melting of garnet lherzolite leaving a residue of 70% olivine, 23% orthopyroxene and 7% clinopyroxene, is employed. This source, which is depleted relative to estimates for bulk earth, has Ce/Y equal to 0.27 (Ce=1.4 and Y=5.1 ppm.), Zr/Nb equal to 28.1 (Zr=13.5 and Nb=0.48 ppm.), and reproduces the ratios commonly found in MORB (0.3-0.4 and 25-26 respectively) as a result of 15-20% partial melting.

As an example of relatively more enriched mantle a Bulk Silicate Earth (BSE) source is also used in the calculations (S. James 1987; Kostopoulos, 1988). The BSE source, which is considerably less depleted in LILEs than the MORB source, has Ce/Y = 0.40 (Ce=1.6 and Y=4 ppm.) and Zr/Nb = 19.2 (Zr=10.9 and Nb=0.57), and is

used to assess the effects of bulk-mantle enrichment with respect to the depleted MORB source.

All melting models have the property that as the degree of melting (F) tends to zero then C_l/C_o (concentration in liquid / concentration in the source) tends to 1/D and so will give similar values for the liquid composition. All models are also constrained such that when F=1 (100% melting) then $C_l=C_o$. Because of these constraints the computed concentration of a given element in the liquid for high and low degrees of melting of the mantle will vary little between the different models. The simplest form of the equilibrium modal melting equation

E:5.2 $$C_l = C_o / (F+D - (FD))$$

was used in the calculations (Shaw, 1970). This model assumes that melt once formed remains in contact with and, therefore in equilibrium with, the solid residue, until it is extracted in one step; i.e. it is a batch melt. The use of this model is justified for two reasons. First, because the amounts of melting are small (the North Sea rocks are undersaturated) there is little or no difference between results generated using this model and those produced by using other more complex models (i.e. non-modal melting, zone refining, dynamic melting etc.). Secondly, the exact nature of the melting process in the mantle is not yet fully understood. Simple equilibrium melting cannot strictly be the true process, which is more likely to be somewhere between equilibrium and fractional melting, but it provides a sufficiently accurate description when the melt fractions involved are small.

The results of the equilibrium melting calculations are displayed, together with the data, in Figure 5.23. On this diagram there are two non-linear trends of decreasing Ce/Y and increasing Zr/Nb with increasing degrees of partial melting, one trend for each of the two sources. The trends are labelled for degrees of melting along their length. Notice that at large degrees of melting (ca. 20%) there is a significant positional discrepancy between the two paths, the more enriched BSE source producing much lower Zr/Nb values (and slightly higher Ce/Y) than the melts from the depleted MORB source. However, at small degrees of melting (<2%) the discrepancy is not so large and tends to be dominated by Ce/Y rather than Zr/Nb. In addition to the Mesozoic rocks discussed throughout this and the last chapter Figure 5.23 also shows fields for the mildly alkaline Lower Permian basalts from the North Sea, and ocean island basalts (OIB; J.G. Fitton and D. James, unpublished data). The majority of the North Sea rocks coincide with the OIB field. The BSE source will not produce the ratios required for MORB (Ce/Y = 0.3-0.4, Zr/Nb = 25-26) at any degree of melting, nor will it produce many OIBs.

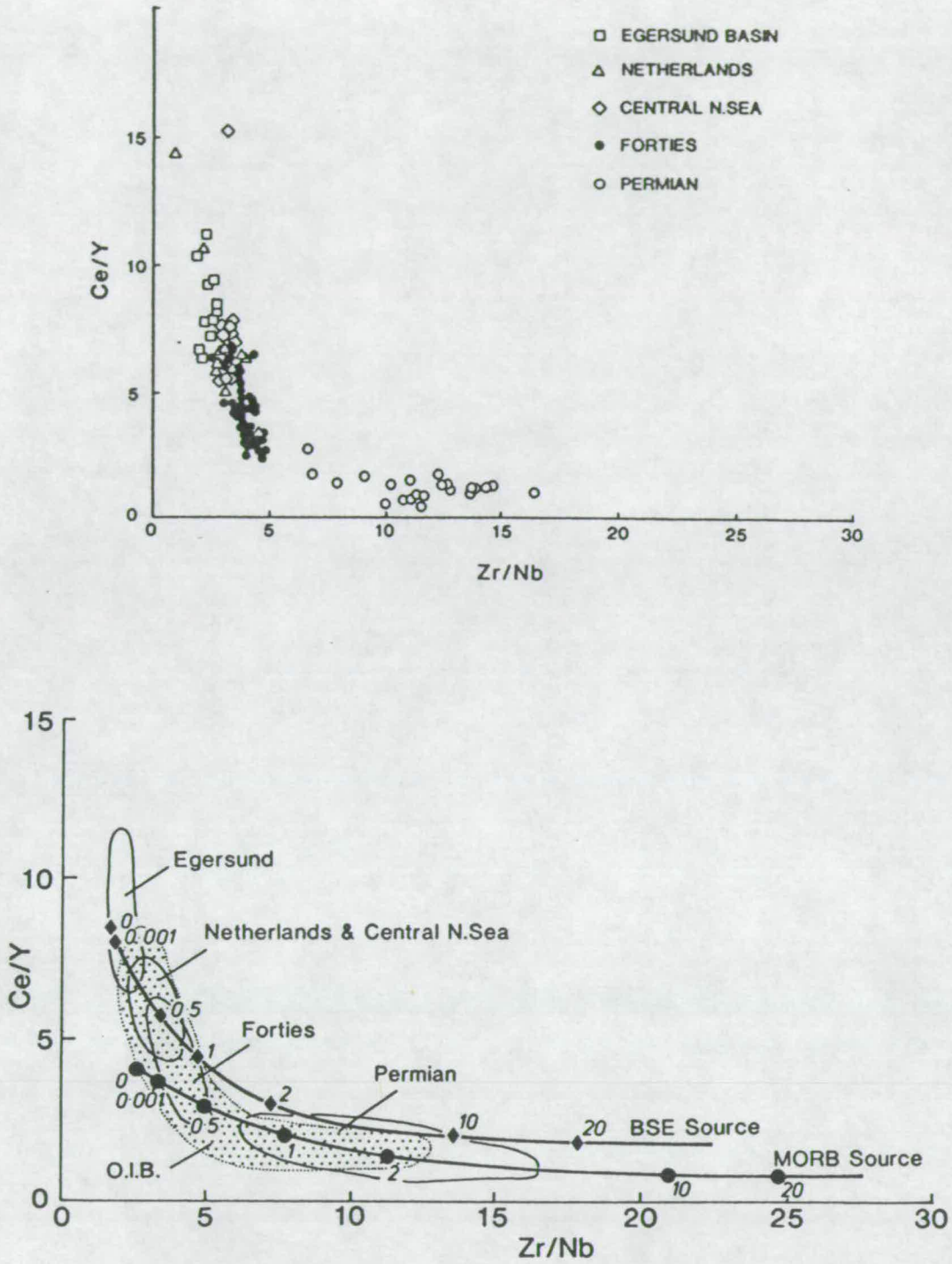

FIGURE 5.23 Upper diagram is from Figure 5.17 and shows the variation of Ce/Y with Zr/Nb for all of the mafic rocks from North Sea data set (MgO > 4 wt.%) irrespective of LOI. Lower diagram shows equilibrium partial melting lines for Ce/Y vs. Zr/Nb for melting of a MORB source (Fitton and Dunlop, 1985) and a BSE source (James, 1987; Kostopoulos, 1988). The melting lines are marked for per cent melting and were calculated assuming simple, single-stage, modal melting using the bulk distribution coefficients calculated by Fitton and Dunlop (1985). Fields for mafic igneous rocks from the North Sea (taken from the upper diagram) and OIBs (unpublished data of J.G. Fitton and D. James) are also outlined. See text for further details.

The Forties province alkali basalts, as was suspected, give the largest melting estimates of all the Mesozoic groups with 1% to 0.5% for the BSE source and 0.5% to 0% for the depleted MORB source, for those with the lowest Ce/Y (around 3.5 to 4). All other Mesozoic groups represent less than 1% melting of the BSE source and cannot be produced by single-stage melting of the depleted MORB source. That the other Mesozoic rocks can only be derived from a more enriched source is no surprise since their isotopic character suggested that their source should be LILE enriched relative to the source of N-MORB. The mildly alkaline Lower Permian basalts from the North Sea have Ce/Y and Zr/Nb values suggestive of much larger degrees of melting; 5% to 0.5% from the depleted MORB source, and 15% to 2% from the BSE source.

5.6.3.2 Simple Model with $(Ce/Sm)_N$ and Ce_N.

Figure 5.24 shows a plot of chondrite-normalised values (after Nakamura, 1974) of Ce/Sm *vs.* Ce for the freshest of the North Sea samples for which REE data has been obtained (see Appendix A). Also shown on Figure 5.24 is a melting curve calculated by assuming equilibrium modal melting of garnet peridotite. The parameters used in the calculation are those used by O'Nions and McKenzie (1988). The starting peridotite is assumed to have a mode of 55% olivine, 25% orthopyroxene, 11% clinopyroxene and 9% garnet, and a bulk earth composition for Ce and Sm equal to 1.4 and 0.35 ppm respectively. Bulk distribution coefficients are taken from Set 5 of Frey *et al.* (1978) and are equal to 0.0115 and 0.0420 for Ce and Sm respectively.

The bulk of the Forties province samples lie within the 1 to 2% melt region in Figure 5.24 with an upper limit of ~3% melting and a few samples which lie close to the 0% melting region. The few Forties samples with high values of Ce_N and $(Ce/Sm)_N$ are hawaiites and presumably the Ce/Sm ratio has been increased slightly by the partitioning of Sm into clinopyroxene. The Central Graben and Netherlands samples fall in the 0.5% to 0% melt region and the Egersund samples, as with Ce/Y *vs.* Zr/Nb (Figure 5.23), go off the end of the melting scale.

5.6.3.3 Discussion of Single Stage Melting.

The key conclusions from the analysis above, using Ce/Y, Zr/Nb, and Ce/Sm and very simple, single stage equilibrium melting calculations are:

(1) In terms of single stage melting of a garnet peridotite the North Sea suite can only be explained by very small degrees of melting (< 3%). This is true even when a

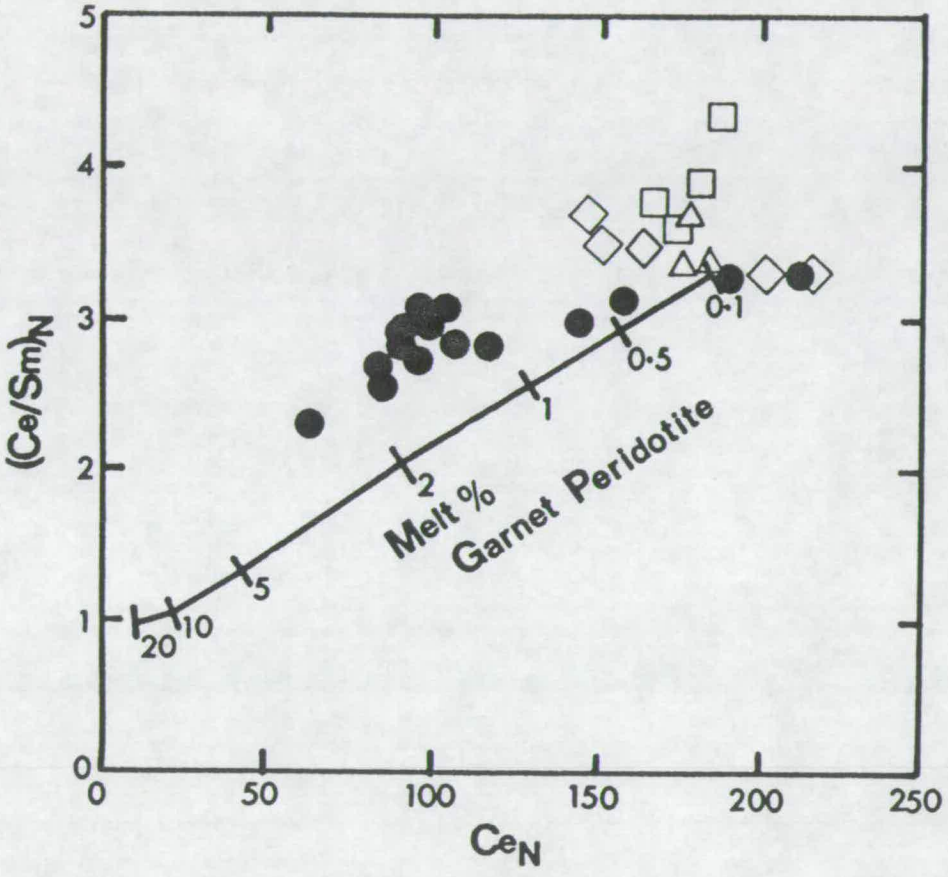

FIGURE 5.24 Chondrite normalised values of Ce/Sm vs. Ce plotted for the set of North Sea rocks which were analysed for REE by ICP-AES (see Appendix A of this thesis). Symbols are the same as in previous diagrams. A curve which represents the effects of modal melting of a garnet peridotite with an estimated bulk earth composition (from O'Nions and McKenzie, 1988) is also shown. See text for further details.

relatively LILE enriched, compared to the source of MORB, BSE or bulk earth composition is used in the calculations.

(2) At least some of the Forties basalts, can be produced by small amounts of melting of a garnet lherzolite composition which will also produce MORB. However such peridotites, which liberate MORB at 15-20% melting, will not generate the full range of OIB or the North Sea rocks at smaller amounts of melting.

(3) Although essentially all of the trace element compositions of the North Sea rocks can be adequately explained by small but differing amounts of partial melting of a BSE source, such a model is not realistic because the isotope ratios suggest that the bulk time-integrated composition of the source is depleted with respect to bulk earth.

If a single stage melting model is to be applied to the North Sea suite then it must be melting of a mantle composition that is intermediate between bulk earth and the source of N-MORB. Such a model would involve melting of streaky asthenosphere or a plume component. However a slightly more complex model involving melting and mixing of depleted and enriched mantle reservoirs might equally well be invoked.

In Figure 5.25 calculated curves for Ce/Y *vs.* Zr/Nb are shown for single and multi-stage melting models. The purpose of the diagram is simply to show that it is possible to produce the values shown by the North Sea data through melting of sources with compositions other than those of the MORB source, BSE or bulk earth. It is important to notice that the ratios observed in the North Sea suite can easily be produced by rather large amounts of melting (5 to 10%) of garnet peridotites containing phlogopite. A phlogopite bearing source mineralogy will be called upon in Chapter 7 to explain the presence and chemical character of the ultrapotassic rocks in the North Sea.

5.7 Summary and Discussion.

In this chapter the undersaturated nature of the North Sea suite which was suggested by their petrography and mineralogy (Chapter 4) has been confirmed by major and trace element geochemistry. It has been shown that, even in highly altered rocks, it is possible to use the ratios of trace elements which are both immobile and incompatible to indicate the degree of undersaturation. Such incompatible element ratios are largely undisturbed by fractional crystallisation or low temperature alteration, and so their values represent those of the primary North Sea magmas.

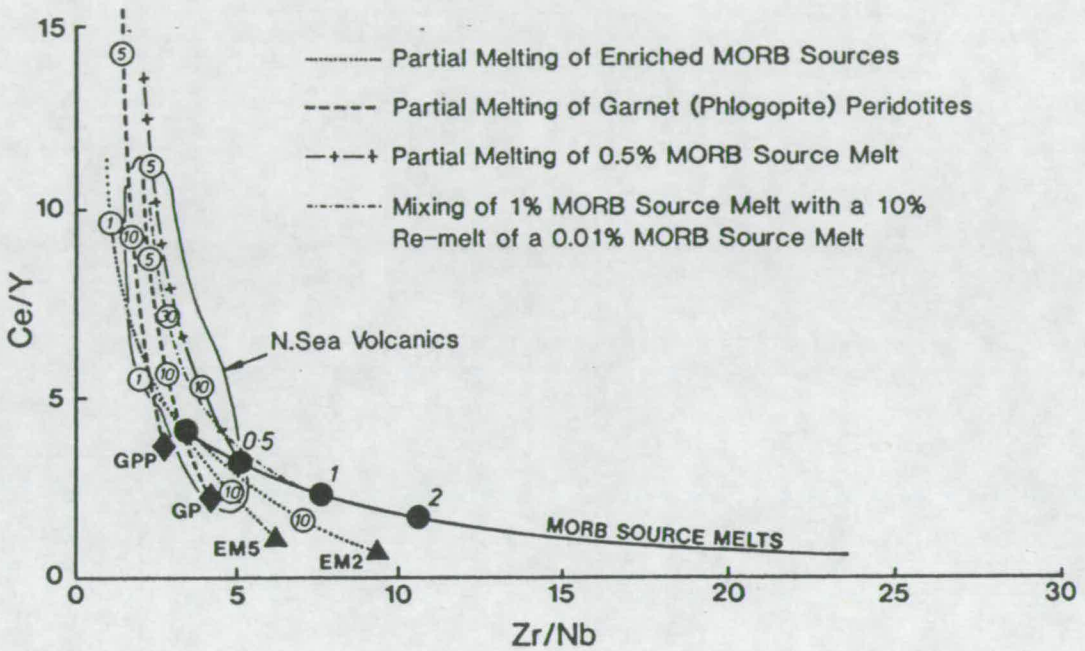

FIGURE 5.25 Ce/Y vs. Zr/Nb relations for single- and multi-stage melting models. The bold curved line shows Ce/Y vs. Zr/Nb values for different degrees of melting of a MORB source (see Figure 5.23). The other curved lines refer to different hypothetical melting models which could all lead to the high values of Ce/Y shown by the North Sea rocks. Each line relates to a different source composition and each is marked with values relating to the per cent melting of that particular source. Note that these values should be treated with caution since the bulk distribution coefficients used (Fitton and Dunlop, 1985) in the calculations were only intended for use with garnet peridotite. EM2 and EM5 are enriched MORB sources produced by mixing 98% and 95% (by volume) of the MORB source respectively with 2% and 5% by volume of a 0.1% melt of the MORB source. GP is a garnet lherzolite xenolith composition and GPP is an average garnet phlogopite lherzolite xenolith composition. Both GP and GPP are from the data of Erlank *et al.* (1987) for xenoliths from Kimberley, South Africa.

The major and trace element chemistry of the rare fresh rocks together with the values of ratios such as Ce/Y, Zr/Nb, and Ce/Sm, for the whole suite suggest that the Forties province alkali basalts are the least undersaturated rocks in the North Sea whereas the rocks from the Egersund basin are highly LILE enriched nephelinites. Other occurrences are, in terms of silica saturation, transitional between these two groups. Normalised trace element patterns are identical to those of OIB and are consistent with melting of garnet peridotite. The ultrapotassic rocks from the Central Graben and Netherlands may, however, require another source mineralogy which is rich in K and Ti but poor in Na, Ni and Cr. Their ultrapotassic character makes them quite distinct from oceanic rocks which are generally sodic.

Sr and Nd isotope ratios for three whole rock and clinopyroxene samples suggest that the North Sea suite as a whole had a source(s), very similar to that of OIB, which had suffered time integrated depletion in LILE relative to bulk earth but which was enriched relative to the more depleted source of N-MORB. Simple single-stage equilibrium melting calculations on garnet peridotite mineralogies with different bulk compositions, although highly model dependent, suggest that the extents of melting in the North Sea were very small (< 3%). This conclusion is in agreement with the rather small volumes noted in Chapter 4 and does not preclude models involving small volumes of very large degree melts from extremely LILE enriched sources mixing with larger amounts of less LILE enriched melt.

It seems likely that the alkali basalts of the Forties province were produced by melting of garnet lherzolite, which if anhydrous or near to anhydrous, would upon decompression, according to the discussion in Chapter 3, first liberate melt in the asthenosphere. If the asthenospheric melts have the isotopic characteristics of N-MORB then a more LILE enriched component must be added from elsewhere. Their isotopic composition can be explained by preferential melting of more easily fusible streaks, or as is advocated later, may be derived by the addition of a small amount of highly LILE- and volatile-rich melt, similar in composition to the ultrapotassic rocks, from the metasomatised mechanical boundary layer (see Chapter 7).

The nephelinites and basanites of the Egersund basin and Netherlands province were again produced by small amounts of melting of garnet lherzolite. Their more undersaturated nature may attest to melting in the presence of CO_2 which has the effect of shifting the eutectic melt composition away from garnet towards clinopyroxene (Brey *et al.*, 1983). If CO_2 is required in the source of these melts then its recognition is important for two reasons. First the estimated abundance of CO_2 in the asthenosphere is small (ca. <0.1 wt.%) and since it is highly incompatible it is likely to enter the first formed melt fractions. Secondly CO_2, like H_2O, has the effect

of lowering the solidus of garnet peridotite considerably (cf. Wyllie, 1987) making it more accessible at small amounts of extension or lower potential temperatures (see Chapter 7 and Latin *et al.*, 1990a,b).

CHAPTER 6

MEASURING EXTENSION IN THE NORTH SEA BASIN

6.1 Introduction.

Estimates for the amount of extension (β), or more importantly the degree of adiabatic decompression, in different parts the Mesozoic North Sea are vital if the main aim of this thesis is to be realised; i.e. the determination of whether or not extension and magmatism may be related to each other in a quantifiable way.

Section 6.2 of this chapter summarises existing estimates of extension, made using a variety of techniques, for the Mesozoic North Sea. Unfortunately previous work, although extensive in its coverage, provides little quantitative information about the amount of lithospheric thinning in the most magmatically active part of the North Sea; i.e. the Forties province at the intersection of the three rifts. A major component of the present study has therefore been to obtain subsidence profiles from this important "*triple junction*" region by backstripping well data and to interpret them in terms of models of lithospheric thinning (see Figures 6.1 and 6.6). Subsidence analysis has also been conducted on several wells from the region of the Central Graben igneous province, and one from the Egersund Basin (see Figures 6.1 and 6.6). Determination of subsidence curves from the stratigraphy of wells in the Netherlands part of the North Sea has not been attempted because here the interpretation is made much more difficult by Tertiary reactivation and uplift (inversion) and by the widespread presence of salt.

The method used for determining curves describing basement subsidence is explained in section 6.3 and the philosophy used in their interpretation, together with the main results of the subsidence study, are presented in section 6.4. Unlike many other parts of the North Sea region, the syn-rift subsidence in the triple junction, and in much of the Central Graben, is considerably less than would be predicted by fitting a simple stretching model to the thermal part of the subsidence curve, even in the hanging wall regions of large fault blocks. The abnormal shape of the subsidence may have important implications for the temporal and spatial partitioning of strain between crust and mantle during extension in the North Sea. At the end of section

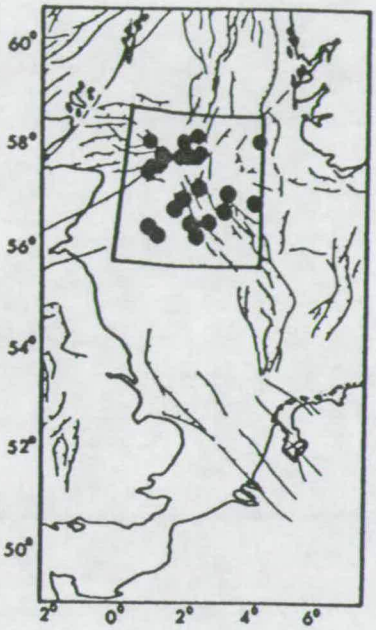

FIGURE 6.1 Region of interest in subsidence analysis. Filled circles indicate the locations of wells used to estimate β later in this chapter (see also Figures 6.6 and 6.20).

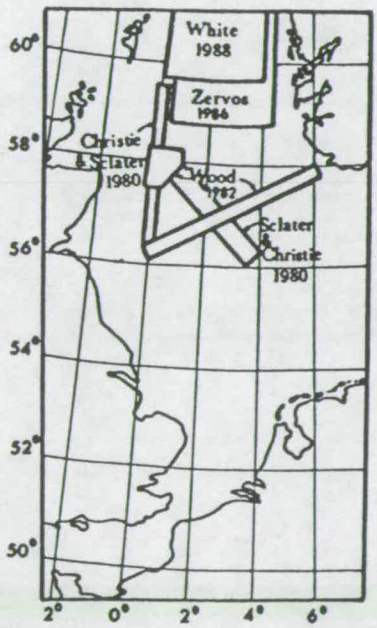

FIGURE 6.2 A map showing areas covered by previous detailed studies of subsidence, crustal thinning and faulting in the North Sea. Note how none of these study areas are centred on the region of most interest; i.e. close to 58°N and 2°E.

6.4 the *minimum amount* of lithospheric thinning implied by the subsidence study is shown to be in agreement with recent estimates for the amount of crustal thinning in the critical region.

6.2 Previous Work.

Since McKenzie first proposed the simple stretching model in 1978, the North Sea has been used as a test area for models of extension. It is not the intention here to summarise all previous work concerning the nature, style, and scale of extension in the North Sea[1]. Instead reference is made to a relatively small number of detailed studies which provide estimates for the degree of extension in different parts of the North Sea (see Figures 6.2 and 6.3). Figures 6.2 and 6.3 show that there are two main areas in the North Sea for which this has been done:

(1) The Central Graben and Outer Moray Firth. The subsidence of these areas was studied by Sclater and Christie (1980) and later by Wood (1982). Two seismic refraction lines have also been shot and allow determination of crustal thinning across the Witch Ground Graben (Christie and Sclater, 1980) and Central Graben (Barton and Wood, 1984).

(2) The North Viking Graben and Shetland Terrace areas. Solli (1976) presented probably the first estimate for β from a seismic refraction line in the North Viking Graben. Zervos (1986, 1987) used the Bouguer gravity field in the northern North Sea to model crustal thinning. N. White (1988, 1990) used the displacement on faults and basement subsidence curves to estimate β, assuming uniform stretching, in the area of the Shetland Terrace. Klemperer (1988) and Holliger and Klemperer (1989) present estimates of crustal thinning from deep seismic reflection lines (NSDP-1, -2, -3 and -4) and from models of the regional gravity field.

6.2.1 Measuring Extension.

Estimates for the amount of extension in a region are conventionally made by using one or more of the following methods:

(1) Subsidence Analysis. Basin stratigraphy, either from seismic or well data, is decompacted and is used to progressively *unload* the basement; i.e. the sediments are "stripped-off". Curves which show the water-loaded subsidence of the basin as a

[1] For a more comprehensive coverage of these subject areas see papers in Blundell and Gibbs (1990).

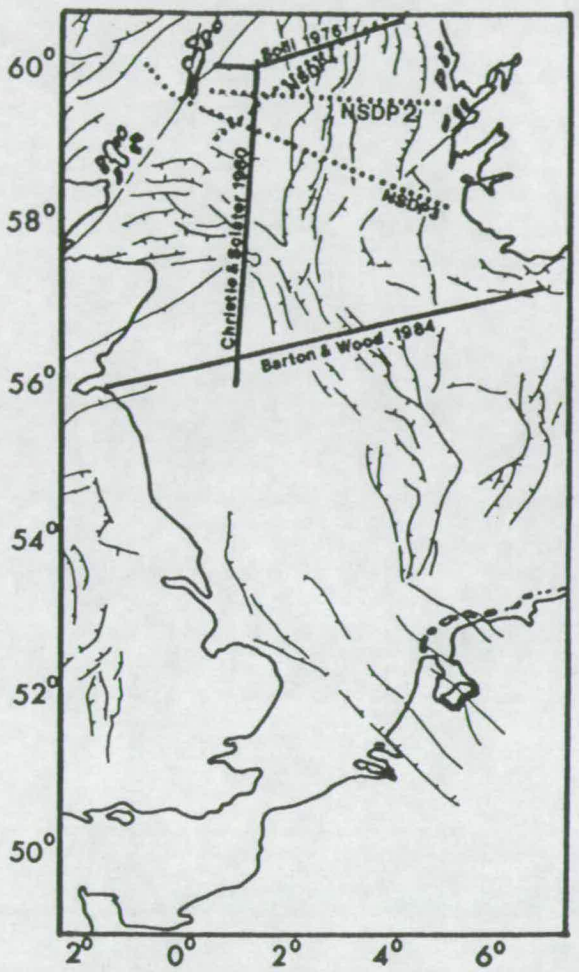

FIGURE 6.3 A map showing seismic refraction lines (bold lines) and deep seismic reflection lines (dotted lines) which have been used to estimate crustal thinning in the North Sea.

function of time are generated (see section 6.3). The water-loaded subsidence of a basin is usually interpreted as representing the tectonically-driven component of subsidence. The observed curves may then be compared with theoretical water-loaded subsidence curves, generated by assuming some model for stretching (see section 6.4). Subsidence analysis has the advantage that in an area where there have been a number of discrete rifting episodes the amount of extension during each phase of rifting may be evaluated. Use of subsidence to determine β requires that the thermal perturbations from different rift episodes do not significantly overlap in time.

(2) Crustal Thinning. Unlike subsidence analysis this method only provides a time-integrated measure of β. The method uses measurements of crustal thickness (more correctly basement thickness) within the rifted region and uses similar estimates in areas unaffected by rifting, to estimate the amount of thinning in the rift. The method relies on the assumption that the crustal section is conserved during rifting; i.e. that there was no addition of material due to magmatic underplating. In ancient rifts crustal thinning has commonly been determined by seismic refraction lines, modelling of the regional gravity field, and more recently by identification of the Moho on deep seismic reflection profiles.

(3) Measuring Extension on faults. Palinspastic reconstruction of faults across rifted regions was one of the first methods ever used to calculate degrees of extension (for a recent example see Ziegler and Van Hoorn, 1990). Such methods assume that all of the important faults in the basin, together with all of the statigraphic displacements caused by these faults, can be identified and measured with accuracy. The fact that estimates from palinspastic methods are commonly very much smaller than estimates from any of the methods described above suggests that there may be problems with such reconstructive methods. Another method applies simple trigonometry to the geometries of fault blocks to measure extension by assuming that they may be represented by rigid rotating dominoes. The method is inherently difficult to apply and, as N. White (1988, 1990) has shown, commonly provides *minimum estimates* for the amount of extension. The dip of the faults, together with the amount of fault block rotation, need to be accurately known before extension can be calculated assuming the simplest possible "rigid domino" model.

6.2.2 Central Graben and Outer Moray Firth.

Sclater and Christie (1980) carried out the first study of basin subsidence and crustal thinning in the North Sea. They examined the subsidence over the last 100 Ma, shown by the stratigraphy of 8 wells six along the Central Graben and two on the

graben flanks (see Figure 6.2). In the centre of the rift, theoretical (model) subsidence curves for instantaneous uniform stretching (McKenzie, 1978) by β factors of between 1.5 and 2 were found to compare favourably with observed basement subsidence curves. The two wells at the edges of the rift showed, as might be expected, considerably less subsidence suggesting smaller amounts of stretching; $\beta<1.5$. It is important to take note at this stage that the "good fit" between the calculated and observed subsidence curves in the wells studied by Sclater and Christie (1980) occurs largely because they only consider the post-rift, or thermal, phase of subsidence (see section 6.4). By only considering subsidence for the last 100 Ma, when rifting probably started at between 180 and 160 Ma (e.g. Ziegler 1982), Sclater and Christie (1980) ignored syn-rift subsidence. In addition they assumed that rifting was instantaneous, and occurred just prior to the phase of thermal subsidence, rather than being of finite duration, and they used only very poorly constrained palaeowater depth corrections in the backstripping calculations. Such simplifications may lead to potentially large errors on their estimated values of β. However, perhaps fortuitously, the overall approach taken by Sclater and Christie (1980), in only attempting to fit the thermal part of the subsidence curve, was almost exactly the right one for the area of the North Sea under consideration (see section 6.4).

Christie and Sclater (1980) studied the crustal structure across the Buchan and Witchground Graben in the Outer Moray Firth using a 400 km long seismic refraction line (see Figures 6.2 and 6.3). The refraction line suggested that, assuming an initial thickness of 35 km, the crust had been thinned by a factor of ~1.8 in its most stretched part[2]. Analysis of the thermal part of the subsidence profile of 5 wells along the refraction line and comparison with theoretical curves (in a similar manner to that of Sclater and Christie, 1980) led to estimated β values which reached 2 in the most stretched region.

The important conclusions of the work of Sclater and Christie (1980) and Christie and Sclater (1980), were that (1) the subsidence-derived value of β was, to within error, the same as the value of β derived from estimates of crustal thinning, (2) the shape of the subsidence curve, in its thermal part, in basins such as the North Sea, was controlled by conductive cooling as McKenzie (1978) had postulated.

---

[2] Unfortunately it must be noted that estimates of β from crustal thinning are usually associated with rather large errors (see N. White, 1990) because errors in the estimates of initial (±1-2 km) and stretched crustal thickness (±2-3 km) are propagated during calculations. As the thinning gets larger so do the errors so that when β values of 2 are reported from crustal thinning the error may be as large as ±0.5.

In 1982 Wood confirmed and extended the work of Sclater and Christie (1980) by studying the subsidence history preserved in 19 wells in the Central Graben and Outer Moray Firth areas. The wells used in her study are shown later by the open circles in Figure 6.6. There are a number of important differences between Wood's subsidence analysis and that of Sclater and Christie (1980):

(1) Following the reasoning of Jarvis and McKenzie (1980), Wood (1982) incorporated finite duration rifting, with a constant strain rate, in the uniform stretching model used to generate her theoretical subsidence curves. When the duration of rifting is large compared with the value of the thermal time constant for conduction (i.e. > $60/\beta^2$ Ma; Jarvis and McKenzie, 1980) then some thermally-driven subsidence should occur during syn-rift subsidence. In line with reported geological evidence (e.g. Ziegler, 1982) Wood chose to start the model Jurassic rift episode at the beginning of the Bajocian (~180 Ma). Rifting was considered to last for 60 Ma terminating in the Early Cretaceous (~120 Ma).

(2) Rather than attempting to fit only the thermal part of the data, Wood chose theoretical curves which would give the best possible fit for all of the data, syn- and post-rift (see section 6.4 and Figure 6.14 later in this chapter). This philosophy, however, ignores the fact that the amount of syn-rift sediment deposited, or preserved, in a well is extremely sensitive to the well's location with respect to basement structures (e.g. Barr, 1987; N. White, 1988; Yielding, 1990).

(3) An extensive study of the microfauna (mainly benthic foraminifera) enabled Wood (1982) to make realistic corrections to the subsidence curves for fluctuating water depths (depths of deposition) through time; see section 6.3 for further discussion.

Initially Wood (1982) and Barton and Wood (1984) used a pre-rift crustal thickness[3] of 31.2 km as one of the lithospheric parameters used in the generation of model subsidence curves (see section 6.4). When theoretical and observed subsidence curves were compared, the maximum β value interpreted by Wood (1982) for any of the 19 wells was 1.55 (e.g. well 30/2-1, see Figure 6.14 later in this chapter) and β was seen to decrease in a predictable manner from the centre to the edges of the basin.

When the β values determined from the subsidence curves were later compared with estimates of the crustal thinning from a seismic refraction line (Barton and Wood, 1984; see Figure 6.2) a considerable mismatch was noted. Where

[3] This value (31.2 km) was obtained by estimating the unstretched thickness of the crust in the North Sea region from the seismic refraction line of Christie and Sclater (1980). Despite its apparent precision it is in fact rather poorly constrained.

consideration of the subsidence in well 30/2-1 led Wood (1982) to suggest a stretching factor of 1.55, the amount of crustal thinning observed at the same point on the refraction line was considered to lie between 1.83 and 2.85 (depending on the density used for different crustal layers in the seismic model). The observed discrepancy between subsidence-derived and crustal-thickness-derived estimates of stretching was attributed by Wood (1982) and Barton and Wood (1984) to the effect on the thickness of the crustal section of pre-Jurassic rifting events, involving a maximum integrated stretching factor of between 1.1 and 1.4. Wood (1982) used the mismatch observed at each well to refine the estimate of the initial (pre-Jurassic) crustal thickness, used in calculation of the theoretical subsidence, downwards from 31.2 km to whatever value was appropriate to eliminate the discrepancy. This somewhat circular argument allowed Wood (1982) to produce a new set of theoretical curves, with broadly similar values to the initial ones, which appeared to fit the observed subsidence curves slightly better.

In section 6.4 it is suggested that in the region of interest such pre-Jurassic events were likely to have been very small ($\beta<1.2$) and that a reinterpretation of the subsidence data from well 30/2-1, based on a rather different philosophy for evaluating the "goodness of fit" between theoretical and observed curves, might easily indicate a β value in excess of 1.8.

In summary, the highest published value of β reported for the Central Graben is 2.85 (Barton and Wood, 1984). However, this value is model-dependent (a different density in the modelling reduces it to 1.8) and it may represent the accumulative effect of a number of different stretching events on the crustal section. The largest value for β derived from the analysis of subsidence curves, assuming instantaneous rifting, is 2 (Sclater and Christie, 1980), but when rifting of finite duration is considered the largest value recorded is only 1.55 (Wood, 1982). A significant pre-Jurassic stretching event has been suggested by Wood (1982) and Barton and Wood (1984) to explain the mismatch between subsidence determined values of β, derived using a finite-duration stretching model, and those implied by crustal thinning.

6.2.3 North Viking Graben and Shetland Terrace.

The refraction line of Solli (1976), which runs orthogonal to the northern part of the Viking Graben (see Figure 6.3), suggests that in its most thinned part the crust is ~14 km thick. Since the crust at either end of the line reaches a thickness of ~35

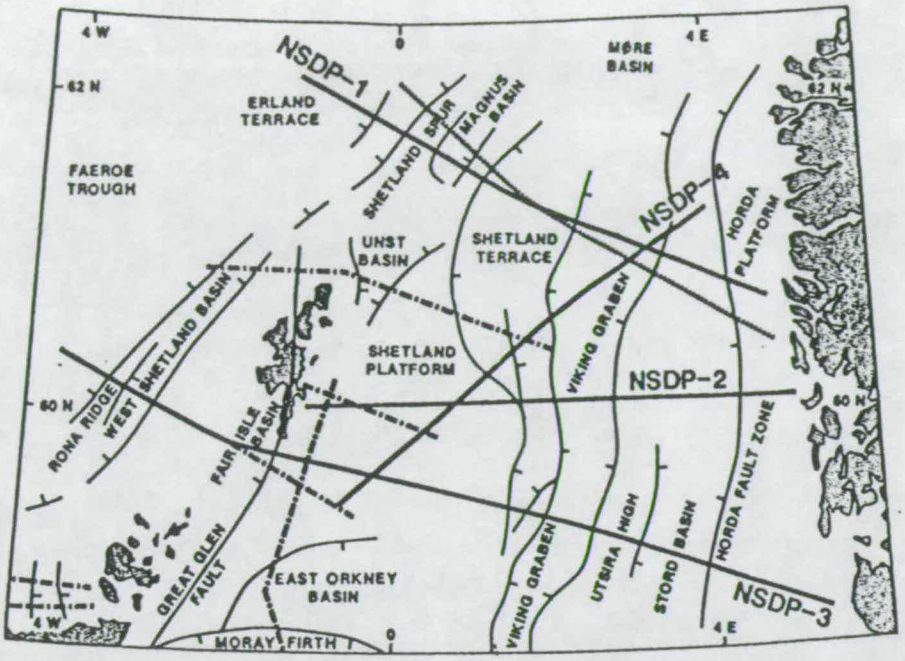

FIGURE 6.4 Map of the northern North Sea showing the location of NSDP deep seismic lines (in bold). Dot-dash lines mark locations of the SHET (McGeary, 1987), MOIST (Brewer and Smythe, 1984) and DRUM (McGeary and Warner, 1985) deep seismic reflection surveys conducted by BIRPS. Dotted line marks location of Britoil deep seismic profile (Beach, 1986). Figure taken from Klemperer (1988).

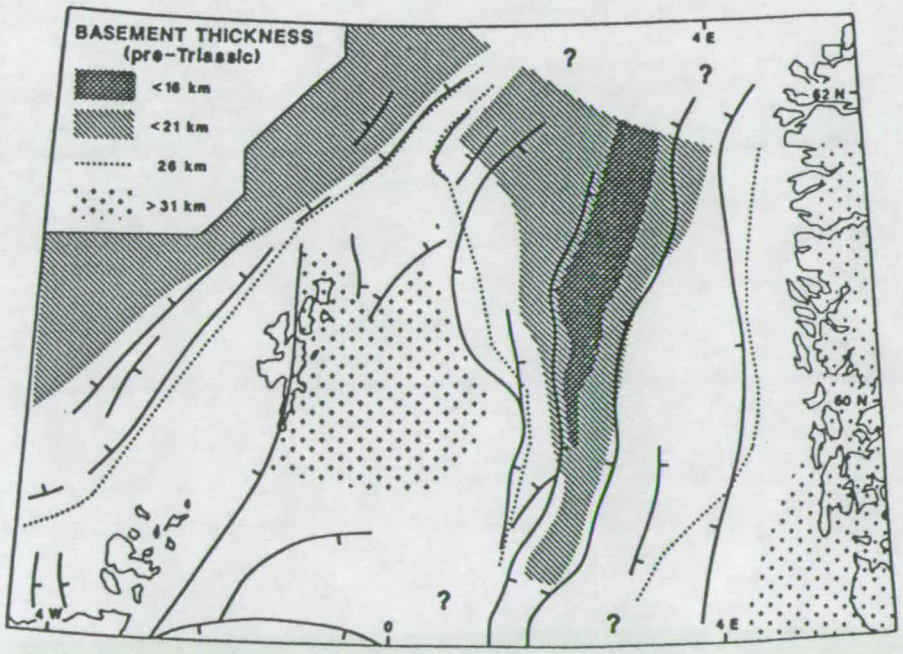

FIGURE 6.5 Contour map of thickness of pre-Mesozoic basement, interpreted from NSDP lines by Klemperer (1988), superimposed on main structural features of northern North Sea (from Klemperer, 1988).

km a time-integrated maximum β value of ~2.5 is implied for this part of the North Sea.

More recently a number of deep seismic reflection profiles (NSDP 84 lines 1 to 4, and a Britoil line) have been shot across the main structures in the northern North Sea (see Figure 6.4). Figure 6.5, taken from Klemperer (1988), shows his interpretation of crustal thickness from the reflection lines in the northern North Sea across the Viking Graben, where he suggests total thinning by a factor of at least 2. Holliger and Klemperer (1989), who modelled the gravity along the NSDP 84 deep seismic lines, found that gravity-derived and seismic depths to the Moho in the northern North Sea were very similar. An absolute maximum, time-integrated, thinning factor of 3.2, which should perhaps have an attached uncertainty of ±0.5, was reported for the Viking Graben from the gravity modelling of NSDP-2 (Holliger and Klemperer, 1989).

The inferred topography of the Moho, derived from three dimensional modelling of the filtered regional Bouguer anomaly field, was presented by Zervos (1986, 1987) for a region of the Viking Graben similar to, though slightly smaller than, that shown in Figure 6.5. According to the gravity model the maximum amount of thinning occurs close to 2°E and 60°N and results in a Moho depth of ~21 km which represents thinning by a factor of ~2.5 assuming ~8 km of basin fill and an original crustal thickness of ~32 km. This value for the stretching is rather smaller than the maximum of 3.2 suggested by Holliger and Klemperer (1989) for the inferred thinning on the NSDP-2 line, although it is from almost exactly the same part of the Viking Graben.

N. White (1988 and 1990) carried out a detailed study of the different methods of measuring extension in the Shetland Terrace region of the northern North Sea. The main result of his 1988 study was to show that estimates of β from consideration of fault block rotations, and from subsidence analysis, were essentially the same. N. White (1990) also showed that when estimates of β from the faults and the subsidence[4] are compared with estimates of β from observations of crustal thinning from the NSDP-84-1 line, there is a small but consistent discrepancy which may be accounted for by invoking a very minor amount of Triassic rifting. N. White (1990) suggests that the Triassic stretching factor need be no greater than 1.2, decreasing to 1.05 at the eastern edge of the East Shetland Terrace, in order to account for the observed differences in β derived from the different measurements.

---

[4] N. White (1988) like Wood (1982) uses theoretical subsidence curves for finite duration stretching with a period of 60 Ma. White (1988) chooses to start the theoretical model at 160 Ma, 20 Ma later than Wood (1982), and rifting ceases at 100 Ma.

The maximum Jurassic stretching factor, inferred from the analysis of the faults and subsidence, is between 1.5 and 2.2.

6.2.4 Discussion.

None of the studies described in the previous two sections favour Jurassic stretching factors in excess of 2. The consensus opinion appears to be that, although the time-integrated stretching in the Central and Viking Grabens, from estimates of crustal thinning, may be greater than 2, the Jurassic rifting event probably involved β factors which were closer to 1.5. However, none of the subsidence studies was based on wells from the very deepest parts of the North Sea rift system. The wells used by Wood (1982) and by Christie and Sclater (1980), were located largely on the edges of the system or were sited on major intra-graben highs (see Figure 6.6). Given the large number of new wells which have been drilled during the last decade, some in the deeper sections of the rift, another study of the subsidence seemed worthwhile.

6.3 Subsidence Analysis.

The stratigraphy reported from 19 wells (see Figure 6.6) was used to obtain water-loaded subsidence curves for those parts of the North Sea relevant to the present study (not including the Netherlands). Some of the wells are as yet unreleased to the public and the data are therefore not presented in this thesis. Released well data are available from the British Geological Survey or from individual oil companies. Backstripped subsidence curves for all 19 wells, which were calculated using the software of N. White (Cambridge), are presented in the next section (section 6.4). The basic technique for obtaining a water-loaded subsidence curve from well data follows the approach of Steckler and Watts (1978), Sclater and Christie (1980) and Wood (1982), and involves the following steps:

(1) The thickness and average sediment type (sand, shale, chalk etc.) deposited over different stratigraphic intervals throughout the history of a well are established (see 6.3.1).

(2) The effects of sediment compaction on the thickness of the sediment column at different time intervals are removed via the process of decompaction (see 6.3.2).

(3) The loading of the sedimentary pile is calculated together with its effect on the basement subsidence (see 6.3.3).

(4) The subsidence curve is corrected for the depth of water at the time of sediment deposition (see 6.3.4).
(5) A correction may be also be included in an attempt to take account of global fluctuations in sea level (see 6.3.5).

6.3.1 Well-Log Information.

One of the most important aspects which should be considered when choosing wells for backstripping is their location within the basin. Wells sited on the footwall tips of fault blocks are unlikely to have preserved a complete syn- and post-rift sequence. In such areas, depending on the size of the particular fault block, the syn-rift sequence is often missing or condensed, and continued fault movement into the thermal phase of subsidence may also be important. The locations of the 19 wells used in this study are shown in Figure 6.6. The wells were chosen for four main reasons. First, they all occur within the region of general interest. Second, they all contain near complete Cretaceous and Tertiary, post-rift, sequences. Third, many of them, unlike the wells used by Wood (1982), are from the deep parts of the basin; e.g. wells 16/27-3 and -4; 16/26-2, -3 and -4; 16/13-2, 16/28-3, 22/15-1, 22/21-4, and 29/9-1. These wells from the deeper parts of the basin, many of which are sited in the centres, or close to the hanging walls, of fault blocks should, in theory, preserve the entire stratigraphy. The final reason is that, of the wells available during the course of the present study, these appeared to be the best of those which had not been previously presented in terms of backstripped subsidence curves.

Of the 19 wells only 5 penetrate large parts of the Triassic (16/28-3, 22/15-1, 22/21-4, 29/14-1, 29/14-4, and 17/9-1). Most of the other wells reach their total depths at an unconformity which marks the contact between Triassic sands and sedimentary, volcaniclastic or volcanic rocks belonging to the Middle Jurassic (Fladen Group) part of the sequence. The Jurassic part of the sequence in all of the wells is characterised by prominent unconformities and disconformities, commonly between (1) the Triassic (Rhaetian) and Middle Jurassic (Bajocian-Callovian), (2) the Middle Jurassic (Bathonian-Callovian) and Upper Jurassic (Upper Oxfordian), and (3) between the Upper Jurassic (Kimmeridgian-Portlandian) and the Early Cretaceous (Valanginian to Barremian). The sequence from the late Early Cretaceous through to the present is complete in most of the wells.

During the backstripping process the stratigraphy recorded in a well is divided up into a number of layers; each is assumed to have a homogeneous lithology and to have been deposited during a given interval of geological time. It is common practice

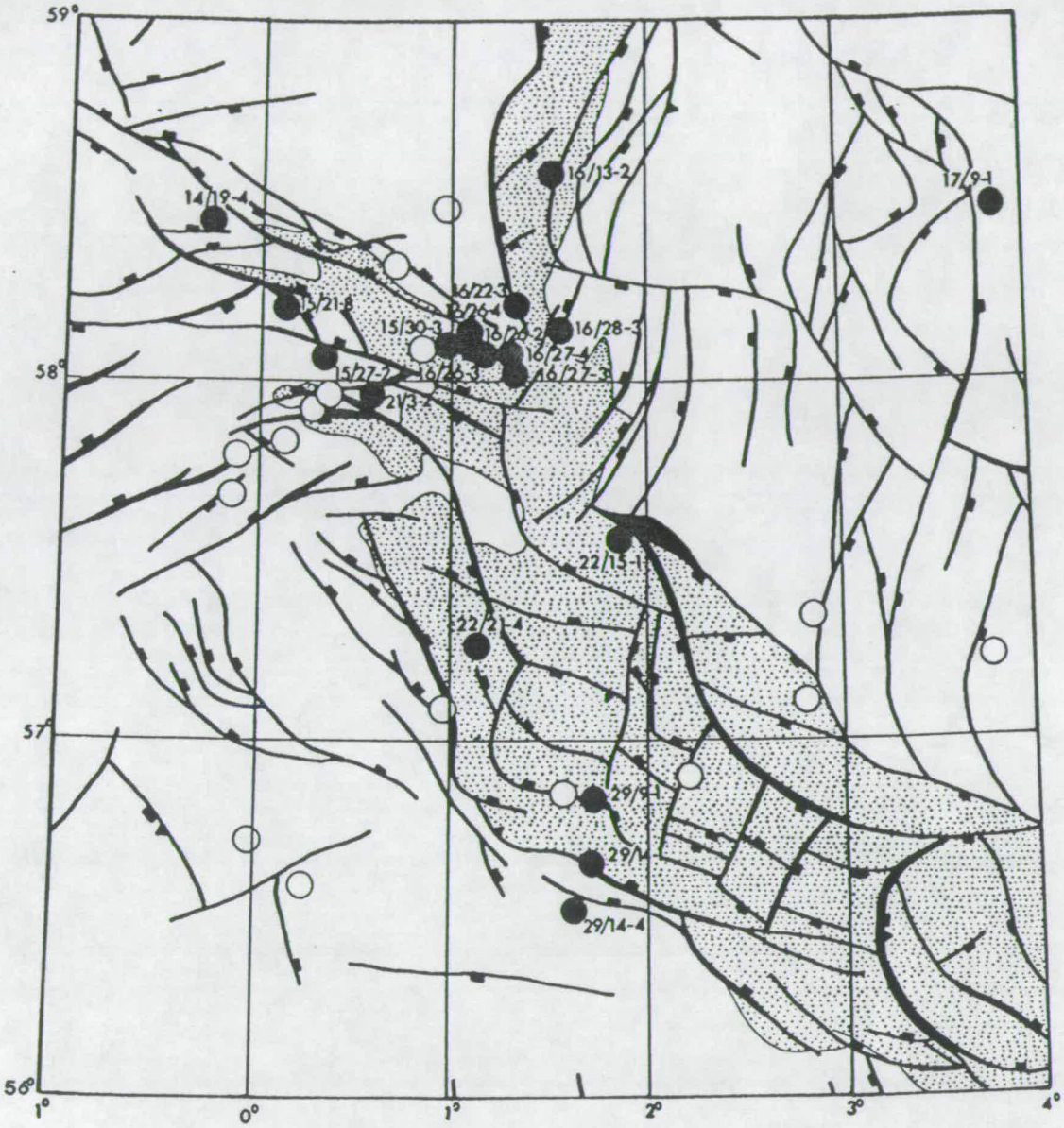

FIGURE 6.6 Map showing locations of wells used in subsidence analysis during the present study (filled circles) and the study of Wood (1982; open circles). Base map taken from the North Sea tectonic map published in 1989 by GECO Exploration services in conjunction with Alastair Beach Associates. Dotted region indicates main graben area defined by the 3.0 second TWT contour at Base Cretaceous level.

to identify layers as packages of rock lying between positions of known stratigraphic age within the well. The number of layers therefore depends on the number of age points within the well.

The sediment type within each layer is recorded. This information is needed for the decompaction and unloading procedure. Where several types of sediment occur within a layer, for example as alternating horizons of sand and shale, the sediment type within the layer is recorded in terms of percentages of the following ideal lithological end members; (1) shale, (2) shaly sand, (3) chalk, and (4) sand.

The stratigraphic ages recorded in the oil company well records are most commonly based on studies of assemblages of microfossils, frequently conducted by service companies. The time-scale of Harland *et al.* (1982) has been used to convert stratigraphic age to absolute age, as in similar recent studies (e.g. Wood, 1982; N. White, 1988). Errors in the detailed shape of the subsidence profile resulting from errors in the stratigraphic ages assigned to the tops of different layers, and in their corresponding dates on the time scale, are difficult to quantify and are often ignored. There was no time during the present study to investigate the size of these errors but because they are likely to be small (probably $<\pm 5$ Ma) relative to the temporal spacing of most of the points on the curves (often >10 Ma) such errors are considered unlikely to affect the overall shape of the subsidence curves.

6.3.2 Sediment Decompaction.

Compaction of the sediment pile during its progressive burial means that the thickness of any layer observed at the present day represents only some fraction of the original thickness of the layer. The decrease in the thickness of a sedimentary layer as it is buried may be related to the decrease in its porosity. Sclater and Christie (1980) observed that the decay of porosity (ϕ) with depth of burial (z) was exponential and could be approximated by the relationship

E:6.1 $$\phi(z) = \phi_0 \exp(-z/\lambda)$$

where ϕ_0 is the initial porosity and λ is the characteristic decay length. On the basis of a study of porosity-depth relationships, using sonic log porosity data from the North Sea, Sclater and Christie (1980) identified values for ϕ_0 and λ for four different lithologies; sand, shale, shaly sand and chalk. The values of ϕ_0 and λ for each sediment type are those used by Sclater and Christie (1980) and subsequently by Wood (1982), Barton and Wood (1984), N. White (1988), and many other workers; see Figure 6.7 taken from Wood (1982).

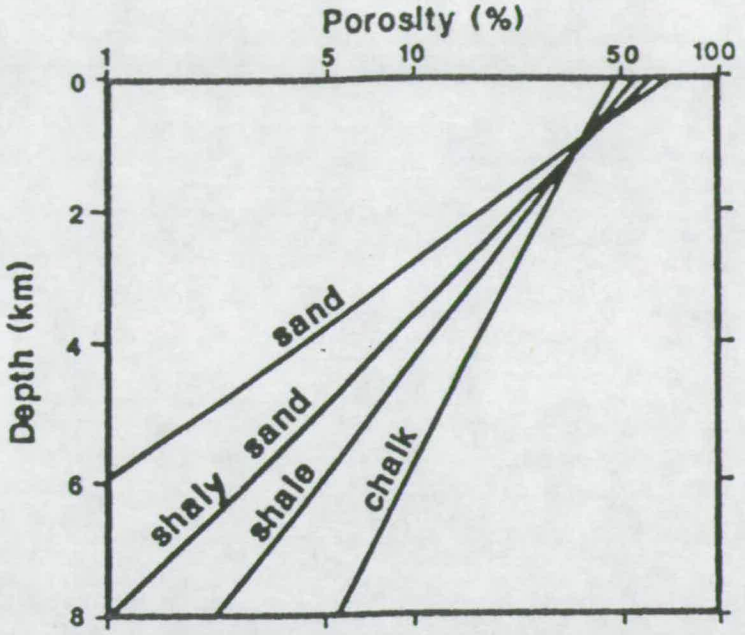

FIGURE 6.7 Logarithm of porosity vs. depth for four sediment types (from Wood, 1982). Diagram from N. White 1988. See Equation E:6.1 in text.

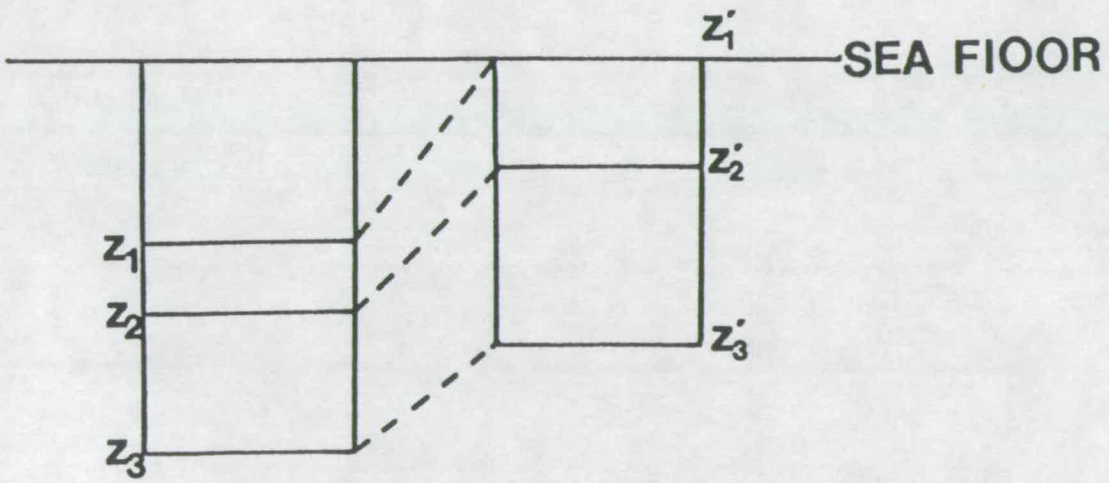

FIGURE 6.8 Decompaction of sediment layers (Z_2 and Z_3) as a layer of sediment (Z_1) is removed; after Sclater and Christie (1980). See text and Equation E:6.2 for details.

Decompaction of the layers, and therefore the entire column, in every well was carried out using the method described by Sclater and Christie (1980). Based on this approach the thickness of a unit varies during decompaction according to

E:6.2 $$Z_{2'} = (Z_2-Z_1) - \phi_0\lambda[\exp(-z_1/\lambda)-\exp(-z_2/\lambda)] + \phi_0\lambda[1-\exp(-z_{2'}/\lambda)]$$
$$Z_{3'} = Z_{2'}+Z_3-Z_2 - \phi_0\lambda[\exp(-z_2/\lambda)-\exp(-z_3/\lambda)] + \phi_0\lambda[\exp(-z_{2'}/\lambda)-\exp(-z_{3'}/\lambda)]$$

where Z_1, Z_2 and Z_3 represent the original depths to the top of units 1, 2 and 3, and where $Z_{2'}$ and $Z_{3'}$ represented the decompacted depths to the top of units 2 and 3 when $Z_{1'} = 0$; see Figure 6.8 taken from Wood (1982).

The sediments observed in each well are assumed to lie on top of a completely compacted basement. For all but 5 of the 19 wells used in the present study the top of the fully compacted "*basement*" is assumed to correspond to the top of the Triassic (~213 Ma). In the 5 wells which contain Triassic sediments the top of the basement is assumed to be at the top of the Permian (~250 Ma). As each layer of sediment is successively removed, the whole of the sedimentary column beneath is brought to the surface and decompacted by the appropriate amount. This is repeated until the top of the nominated basement is at the surface.

Figure 6.9A shows subsidence curves for one of the 19 wells (17/9-1) prior to the decompaction correction (circles), and after (triangles), but before any correction for sediment and water-loading (see next section; Figure 6.9B). The main effect of decompaction is to increase the depth to the basement at any instant.

It is noted that at least two effects make the decompacted subsidence a maximum estimate. Firstly it is likely that the basement will not have been fully compacted at the time of deposition of the first sediments in the well. Unaccounted for compaction of the basement will lead to a slight overestimate in the total amount of subsidence. Secondly the calculations assume that the stratigraphic sections are not overpressured. In overpressured sections pore fluids support some of the overburden weight. In overpressured sections the decompacted subsidence will therefore be overestimated because a layer at a given depth will appear thicker than it would at normal pore fluid pressures.

6.3.3 Sediment Loading Correction.

The sediment pile itself constitutes a lithospheric load which, depending on its thickness and density, will cause a component of basement subsidence. During backstripping, as each layer is removed and the underlying units are decompacted, the

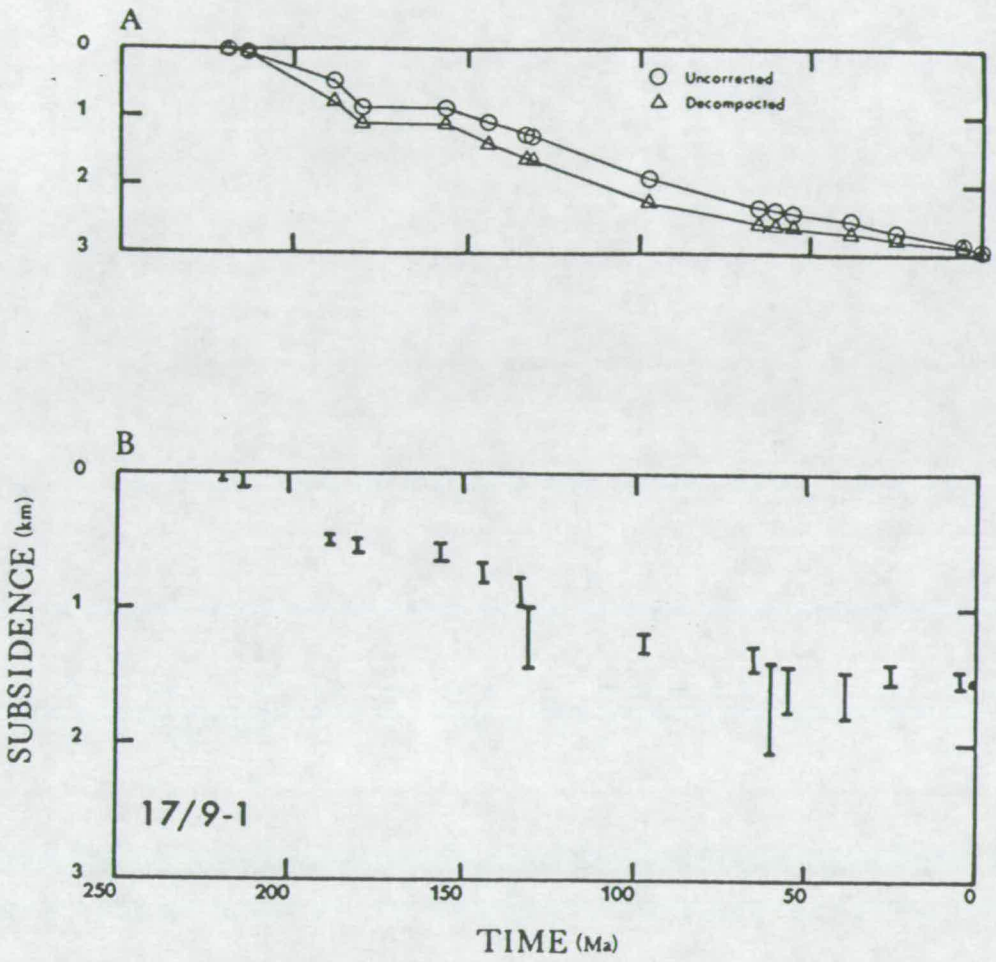

FIGURE 6.9 Subsidence curves for well 17/9-1 (from the Egersund Basin). Upper diagram (A) shows uncorrected (circles) and decompacted (triangles) basement subsidence. Lower diagram (B) shows water-loaded basement subsidence (error bars); i.e subsidence after the effects of sediment loading have been removed and a palaeowater depth correction have been applied.

depth to basement is recomputed, and the mean sediment density of the remaining column (ρ_s) is evaluated using the relationship

E:6.3 $$\rho_s = \sum\{\phi_i\rho_w + (1-\phi_i)\rho_{sgi}\}Z_{i'}/S$$

where ϕ_i is the mean porosity of the i^{th} layer, ρ_{sgi} is the sediment grain density of the i^{th} layer, $Z_{i'}$ is the recomputed depth to the top of the i^{th} unit, and S is the recomputed total sediment thickness (Sclater and Christie, 1980). The decompacted thickness of the sediment column (less any layers already stripped off) is then unloaded and the space left is filled by water to leave the water-loaded depth to basement (D). By assuming Airy isostasy this is

E:6.4 $$D = S(\rho_m-\rho_s)/(\rho_m-\rho_w)$$

where ρ_m is the average density of the mantle (3.33 g cm^{-3}) and ρ_w is the density of water (1.0 g cm^{-3}).

The assumption of Airy isostasy is critical to these calculations. If the lithosphere has a finite elastic strength then the response to a load at a particular point will depend not only on the size of the load directly above the point, and the surrounding load, but also on the effective elastic thickness (strength) of the plate (Turcotte and Schubert, 1982). For the assumption of Airy isostasy to be valid the elastic thickness (T_e) of the plate should be zero, in which case the lateral strength of the lithosphere will be zero and it will therefore respond only to the load directly above. Through studies of admittance[5], Wood (1982) and Barton and Wood (1984) concluded that the value of T_e for the North Sea plate was <5 km for the whole of the post-rift phase and that the assumption of Airy isostasy would therefore be valid. This conclusion is supported by other studies of passive margins and sedimentary basins (e.g. Walcott, 1970; Nunn and Sleep, 1984; Le Pichon *et al.*, 1984), which similarly suggest that low values for T_e are maintained long after rifting. Such values are significantly smaller than those reported for oceanic lithosphere of a similar thermal age where T_e is approximately the depth to the 450°C isotherm (Watts, 1978). Differences in elastic behaviour, between continental and oceanic lithospheric plates, may be largely controlled by rheology (e.g. England, 1983; N. White, 1988). Differences in the value of T_e between different areas within continental plates (e.g. Karner and Watts, 1982; Lyon-Caen and Molnar, 1983; Ahern and Mrkivicka, 1984;

[5] The study of admittance, which uses perturbation theory to relate the free-air gravity anomaly to the size and shape of a load, can be used to determine the elastic thickness of a plate (Lewis and Dorman, 1970; McKenzie and Bowin, 1976).

Bechtel *et al.*, 1987; Watts and Cox, 1989) may in part be due to differences in rheology and thermal structure. However, the consistent, very low values of T_e associated with many extensional sedimentary basins, might also be related to the higher intensity and closer spacing of crustal fractures within such areas.

6.3.4 Water Depth Correction.

Few basins are kept completely filled with sediments at all times and palaeobathymetry has therefore a very important contribution to make to the determination of the depth of the unloaded basement. The water depth at the time of deposition is, however, a difficult parameter to determine. Typically two methods are used to estimate palaeobathymetry. One approach uses sedimentary facies indicators (e.g. glauconite-bearing sands, coal horizons, red beds) to make distinctions between different environments of deposition. Another, commonly more useful, method is to use assemblages of fossils known to have lived in certain depth ranges (e.g. benthic foraminifera). Fortunately for the purposes of the present study Wood (1982) used both of these methods to determine fluctuations in water depth through time in the Central Graben and Moray Firth areas of the North Sea. The approach taken in the present study has been to combine estimates for palaeobathymetry given by Wood (1982) with additional data from individual wells. The method has been to err wherever possible on the side of caution and whenever there is any doubt, to adopt shallower rather than deeper values for the water depth so as to minimise the overall subsidence. When the effects of water depth are added, complete with the uncertainties attached, to the unloaded decompacted subsidence curve in Figure 6.9A the result is a water-loaded subsidence curve of the type shown in Figure 6.9B.

6.3.5 Global Sea-Level Correction.

Apparent changes in water depth may result from changes in the position of the sea-level datum used in the backstripping calculations. Corrections for global fluctuations in sea-level should ideally be made to maintain the backstripping datum at the same level. Pitman (1978) related such sea-level changes to changes in the volumes of spreading centres in the oceans. On the basis of the identification of onlap, supposedly unrelated to any tectonic mechanism, recognised in the seismic stratigraphy of a number of "key" areas, Vail *et al.* (1977), Vail and Todd (1981), and Haq *et al.* (1987) have argued for changes in sea-level of up to 1 km. It is, however, essential to be certain that onlapping sequences are truly unrelated to tectonics.

Careful study of one of the "key" areas, from the Inner Moray Firth Basin in the North Sea, suggests that one of the original sections was parallel to the major fault blocks in the area which are clearly the main control on onlapping Upper Jurassic and Lower Cretaceous sequences (J. Underhill, pers. comm. 1990)! In the few cases where very rigorous attempts were made to disentangle the effects of tectonic uplift from sea-level fall, and tectonic subsidence from high stands in sea level, only small fluctuations in the order of tens of metres were inferred (Watts and Thorne, 1984). Given the overall uncertainty involved in using a correction for global sea-level change, and given that when such corrections are applied they usually cause extreme irregularities to appear in otherwise smooth subsidence curves (Wood, 1982; J. Turner, pers. comm., 1990), it was decided that the corrections would not be applied in the present study.

6.4 Modelling Subsidence.

The end result of the subsidence analysis described in the previous section is to produce a set of water-loaded basement subsidence curves. These curves are expressed as a series of error bars reflecting the uncertainty in the palaeowater depth correction (see Figure 6.9B). The approach traditionally employed, and discussed in section 6.4.1, has then been to attempt to fit such backstripped curves (observed curves) with theoretical (model) subsidence curves. Figure 6.10 shows a set of theoretical subsidence curves for finite duration homogeneous stretching ($\beta_c=\beta_m$) generated from the equations of Jarvis and McKenzie (1980) by assuming that stretching started at 160 Ma and continued with a constant strain rate for 60 Ma. The syn-rift phase in the model therefore occurs between 160 and 100 Ma and is followed by thermal cooling from 100 Ma to the present. The lithospheric parameters used in the modelling are listed in Table 6.1.

When the observed subsidence curve is similar in shape, over its entire length, to the theoretical curves there is little difficulty in fitting the data; these are simple well-behaved subsidence curves (see section 6.4.1). There are, however, circumstances when the observed subsidence profile is very difficult to explain in terms of the simplest homogeneous stretching models and more complex models, involving heterogeneous stretching need to be invoked. Many of the subsidence curves from the critical region of interest are of this second, *abnormal*, type (see section 6.4.2). In section 6.4.3 it is shown how homogeneous stretching curves may be used, even when the mechanism is one of heterogeneous stretching in space or

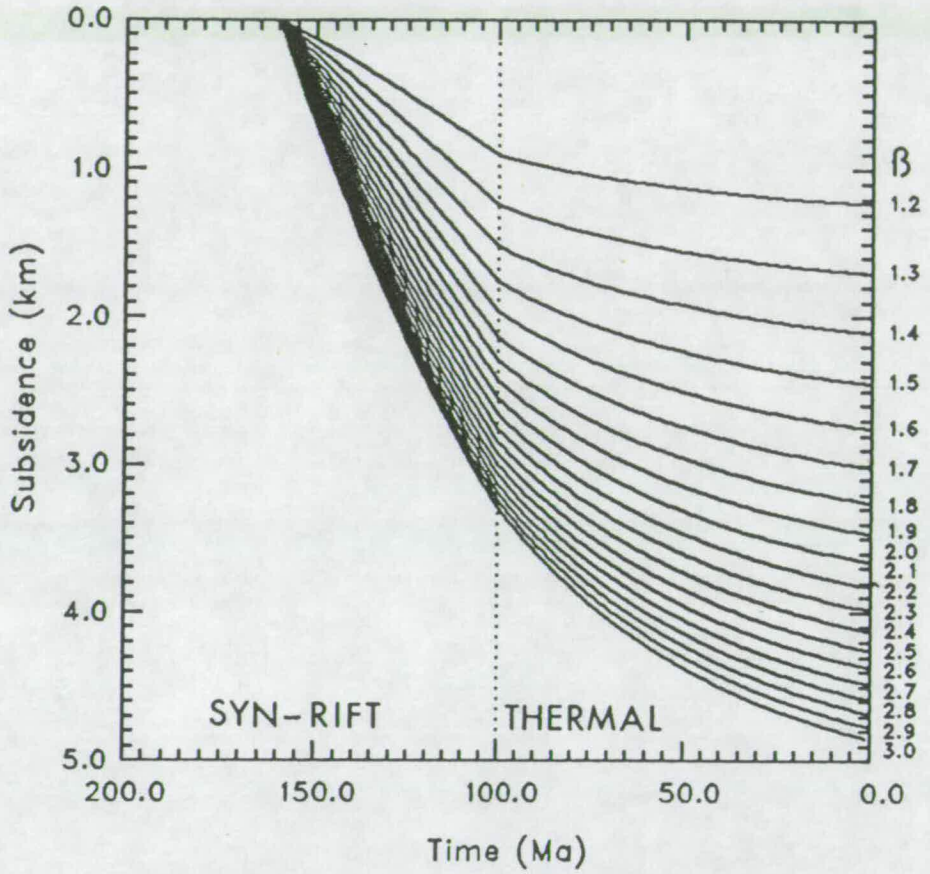

FIGURE 6.10 Theoretical subsidence curves for a range of β values (1.2 to 3.0). Homogeneous stretching is assumed to have started at 160 Ma and to have continued with a constant strain rate for 60 Ma (see Equation E:6.5 in text). Subsidence over the last 100 Ma is purely related to thermal cooling. See Table 6.1 for model parameters.

subsidence profiles. The results of these estimates for β are presented in 6.4.6 and in section 6.4.7 they are shown to be in good agreement with, but slightly less than, estimates of the total crustal thinning in the region.

TABLE 6.1 : Model Parameters

a	lithospheric thickness	125 km
t_c	crustal thickness	30 km
ρ_w	sea water density	1.0 g cm^{-3}
ρ_s	sediment density	2.0 g cm^{-3}
ρ_c	crustal density (at 0°C)	2.8 g cm^{-3}
ρ_m	mantle density (at 0°C)	3.33 g cm^{-3}
ρ_a	asthenosphere density (at 1333°C)	3.2 g cm^{-3}
T_a	asthenosphere temperature (at 125 km)	1333°C
α	thermal expansion coefficient	3.28×10^{-5} $°C^{-1}$
κ	thermal diffusivity	$8 \times 10\text{-}7 m^2$ s^{-1}
τ	decay time	62.8 Ma

6.4.1 Simple Well-Behaved Subsidence Curves.

Figure 6.11 shows the observed subsidence, as error bars, for well 17/9-1 (see also Figure 6.9B) together with best fit model curves. The interpretation of the data from 17/9-1 involves identification of two separate homogeneous rifting episodes, one during the Triassic which was in its cooling phase during the Lower/Middle Jurassic, and a second which starts in the Middle Jurassic (~160 Ma) and has an approximately 60 Ma duration. The evidence for two rift phases in the Egersund and Stord basins is well documented (e.g. Ziegler, 1982; Biddle and Rudolph, 1988; Ziegler and Van Hoorn, 1990) and the subsidence data from well 17/9-1 in general fits very well with two separate stretching events each involving thinning by β between 1.15 and 1.2. Notice that, because the well only penetrates as far as the Middle Triassic, the model curve is continued into negative subsidence space implying that if the well were to penetrate deeper it would encounter more Triassic syn-rift sediments. The relatively simple subsidence pattern displayed by 17/9-1 is an example of subsidence that is well-behaved. Wells from many parts of the North Sea show simple well-behaved subsidence curves of the type shown by 17/9-1; see for example wells from the Shetland Terrace and Viking Graben in N White (1988 and 1990) and some of the subsidence curves for the flanks of the Central Graben and western parts of the Outer Moray Firth in Wood (1982). However, in many of the wells in the area of the Outer Moray Firth, Fisher Bank Basin, in the northern parts of

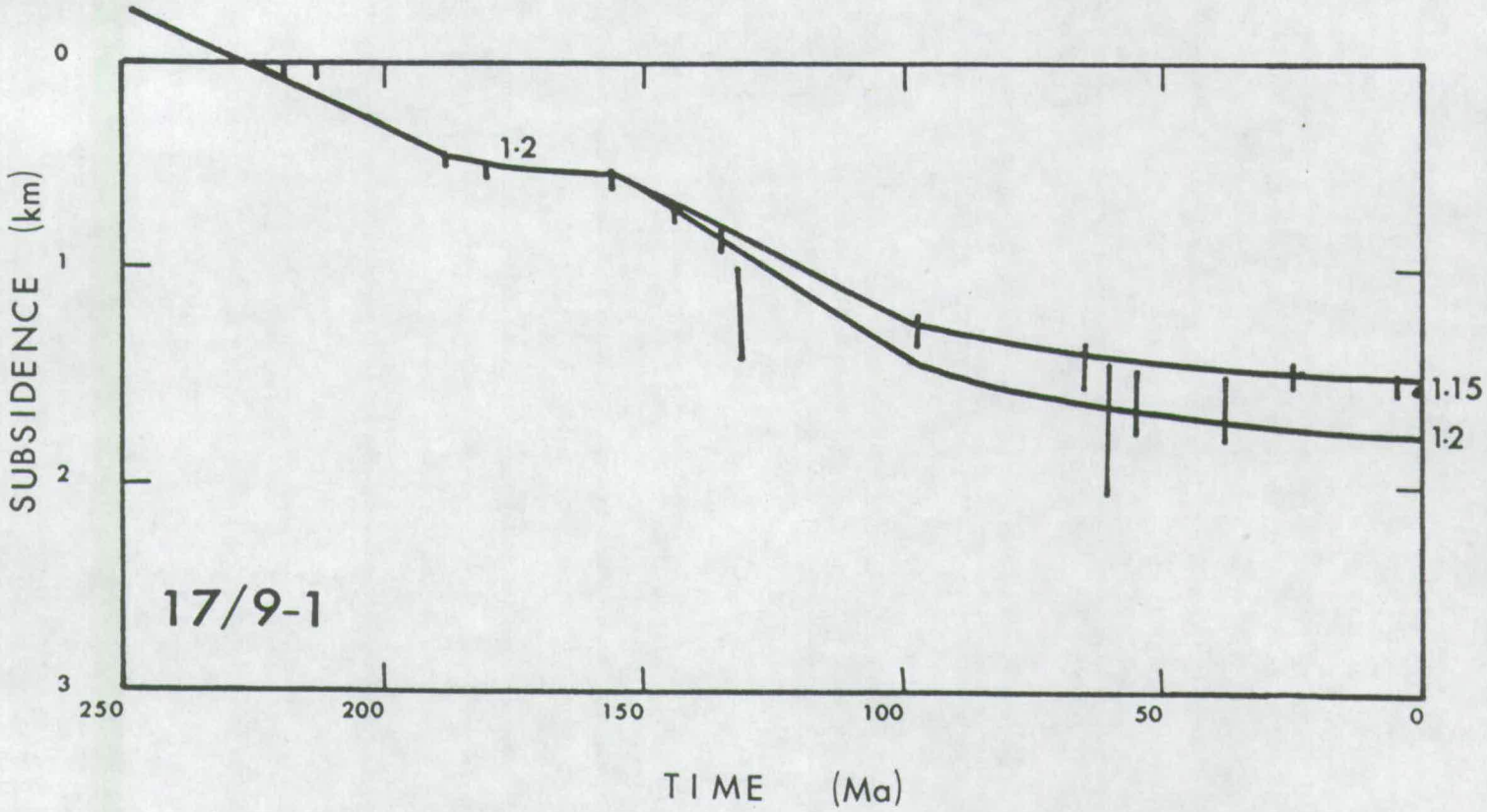

FIGURE 6.11 Water-loaded subsidence of 17/9-1 with palaeowater depth errors is interpreted in terms of two episodes of homogeneous stretching. The most recent episode appears to have occurred at ~160 Ma, to have continued for ~60 Ma, and to be best explained by stretching by $1.15<\beta<1.2$. The earlier rift phase is Triassic and, although it has been interpreted as representing stretching by a factor of ~1.2, the uncertainties due to missing data are large.

the Central Graben and southern Viking Graben, the subsidence does not appear to be nearly so well-behaved.

6.4.2 Abnormal Subsidence Curves.

The subsidence profiles of a large number of the wells from the area of interest are characterised by a syn-rift sequence (Middle-Jurassic to Early Cretaceous) that is relatively condensed in comparison with the often very large thicknesses of post-rift sediments (e.g. see subsidence data in Figure 6.12). The relative lack of syn-rift subsidence observed in wells is often interpreted as being due to their location on structural highs in the basement (e.g. Barr, 1987; N. White, 1988; Yielding, 1990). If basement highs and the tips of rotating fault blocks are areas of *condensed* or *non-deposition* during the syn-rift stage, then the converse should be true of the deeper parts of the basin, where the whole syn-rift sequence should be preserved. It might also be expected that those areas close to the hanging walls of fault blocks should show very thick syn-rift sequences, which might even be overthickened (relative to model curves) due to syn-faulting sediment growth during fault block rotation.

At the start of the present study the frequently observed paucity of syn-rift stage sedimentation (e.g. see Figure 6.12) was attributed to the location of the exploration wells. Figure 6.6 however shows that a large number of the wells used in the present study are within the deeper parts of the basin, lie in the centres of fault blocks, or are even apparently placed within the hanging walls of fault blocks. Figure 6.13 shows two E-W regional geological cross-sections (after Ziegler, 1982), one across the centre of the Viking Graben at ~60°N (near the Frigg field) and the other across the Forties Montrose High which, at ~57.5°N, is in the centre of the region shown in Figure 6.6. Notice how the thickness of Jurassic and Lower Cretaceous syn-rift sediments decreases dramatically from the Viking Graben in the north to the Central Graben further south, while the thickness of Tertiary and Upper Cretaceous sediments is approximately the same in both areas.

Figure 6.14 shows two different attempts to fit observational data with theoretical curves. The dashed curve ($\beta = 1.55$) is the interpretation of Wood (1982). The two bold curves ($\beta = 1.8$ to 2.0) represent this authors interpretation of the data (see section 6.4.5 for an explanation). These two rather different interpretations reflect very different interpretational philosophies.

The philosophy adopted by Wood (1982) was to attempt to find "*the closest fitting theoretical curve*" which was apparently chosen to give the "*closest fit to the thermal part of the subsidence, while not exceeding the amount of initial* (syn-rift)

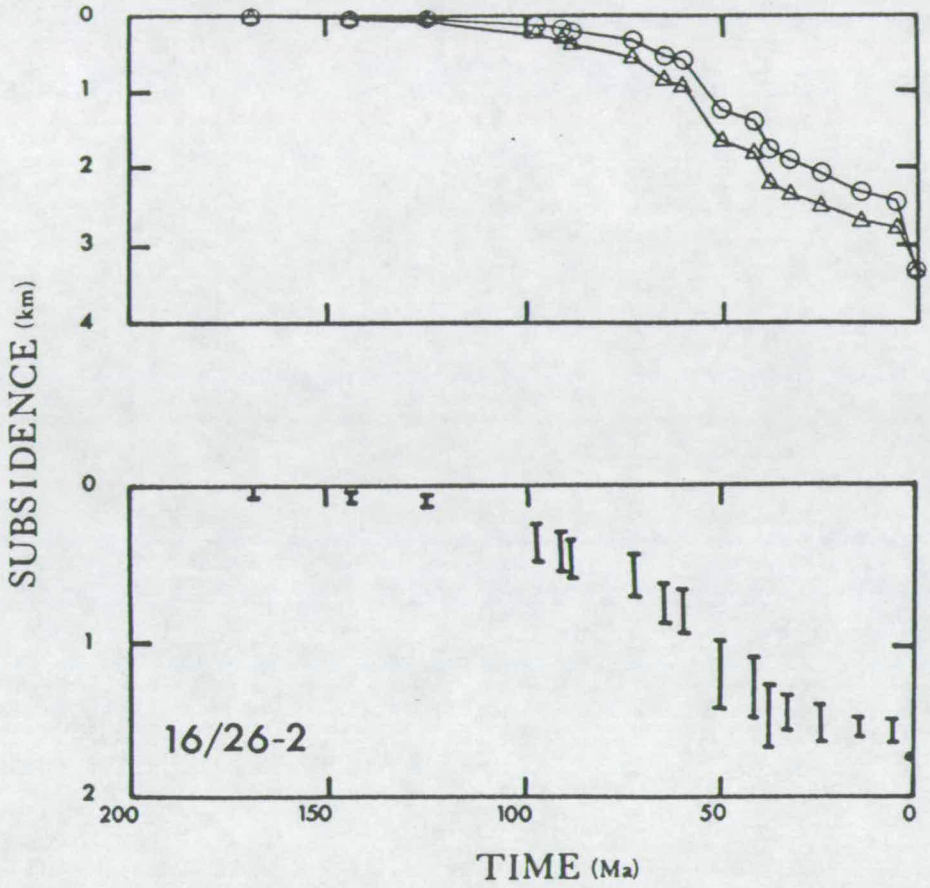

FIGURE 6.12 Subsidence curves for well 16/26-2 (from near the Alba field, triple junction region). Upper diagram shows uncorrected (circles) and decompacted (triangles) basement subsidence. Lower diagram shows water-loaded basement subsidence corrected for errors in palaeowater depth. Notice that these curves are very different to those for 17/9-7 which are shown in Figure 6.9 and interpreted in Figure 6.11. The subsidence in 16/26-2 is *abnormal* since although the well is not sited on the tip of a fault block the syn-rift stage of subsidence is highly condensed while the amount of thermal subsidence recorded is large and its gradient is steep.

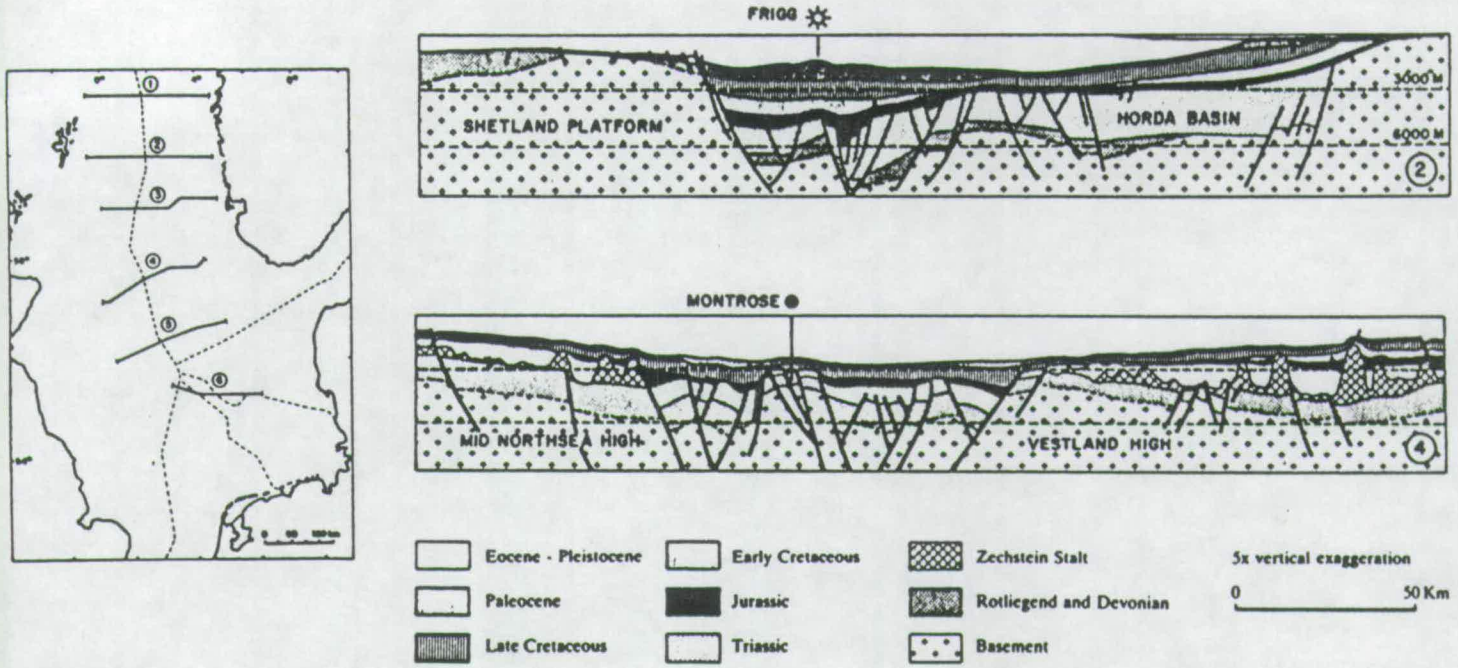

FIGURE 6.13 Two regional geological cross-sections (sections 2 and 4 from Ziegler, 1982) together with map showing their location. Note that the sequence of Jurassic and Lower Cretaceous, syn-rift, sediments is much thinner in the Central Graben (section 4) than it is in the Viking Graben (section 2) while the thickness of Upper Cretaceous and Tertiary, post-rift, sediments is similar in both regions.

subsidence apparent in the well". Wood's main concern is that the model curve should not exceed the syn-rift subsidence phase as "*the total initial subsidence must still be compatible with the estimate of* β *obtained from matching the thermal subsidence*". Underlying Wood's interpretation is the fundamental tenet that *stretching is at all times uniform* in a vertical section. It is at exactly this point that the philosophy adopted here, and explained below, diverges from that of Wood (1982) (see sections 6.4.3 and 6.4.4).

At an empirical level it has already been noted that many exploration wells are located on structural highs and there is therefore no reason why the syn-rift sequence should not be much less than would be predicted by a simple model curve. More important it was also noted that even in the deep parts of the basin the syn-rift phase of sedimentation is remarkably thin. Figure 6.14 shows just how badly model homogeneous curves, of the sort shown in Figure 6.10, fit the *overall* subsidence pattern. This observation may suggest that simple, vertically-uniform, homogeneous *stretching of finite duration is not the correct mechanism* for the formation of all parts of a sedimentary basin. Despite this suspicion the bold curves in Figure 6.14 (which represent this authors attempt to fit homogeneous stretching curves to the data) have been used to estimate β because although homogeneous stretching may not be the correct mechanism, it is later shown (see 6.4.3 and 6.4.4) that, whatever the correct mechanism, *fitting homogeneous model curves does give reasonable estimates for* β. Unlike Wood (1982) this author has only attempted to fit curves to the thermal part of the subsidence profile in Figure 6.14. The thermal subsidence part of the sequence is complete in most wells and it therefore represents the very best data. According to almost any type of extensional model this phase of subsidence relates purely to cooling of the rift-induced thermal perturbation

It is clear from Figure 6.14 that different approaches to fitting the observed subsidence will result in rather different estimates for β. It is also clear that, unlike the subsidence curve for 17/9-1 (Figure 6.11), it is not possible to fit a simple homogeneous model curve to all of the data points on the observed subsidence curve in 30/2-1. The following discussion centres on the different types of mechanism which can be invoked to produce the observed subsidence profiles during stretching.

The main aim of the subsidence study is to obtain a reliable estimate for the amount of Jurassic stretching in the critical region, or more crucially an estimate for the amount of decompression of the asthenosphere during rifting. Such estimates are easily made if the observed subsidence follows a pattern similar to that predicted by a simple homogeneous stretching model (e.g. Figure 6.11). The observation, however, that the subsidence of a significant number of wells in the critical region, selected by

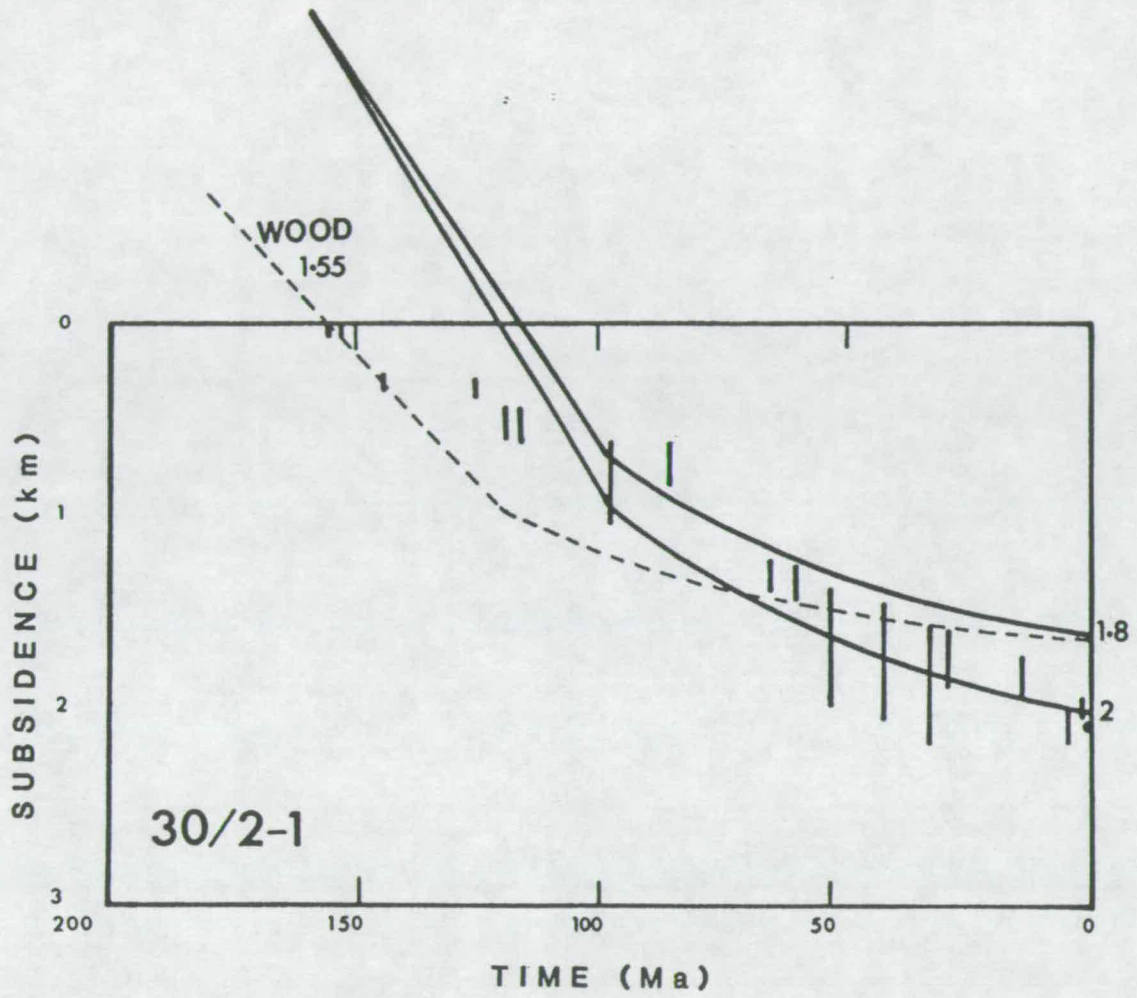

FIGURE 6.14 Two different sets of theoretical curves fitted to the water-loaded subsidence data from 30/2-1. The dashed curve is from Wood (1982) and is for homogeneous stretching (from 180 to 120 Ma) by a factor of 1.55. The two bold curves are estimates of β (1.8 and 2.0) obtained by fitting only the thermal subsidence part of the data (see text).

location for their presumed freedom from local tectonic effects, does not closely match theoretical curves for simple homogeneous stretching suggests that some other, more complex, stretching mechanism may need to be invoked.

The most obvious mechanism for reducing the amount of syn-rift relative to post-rift subsidence, without resorting to local tectonic effects, involves stretching the crust (β_c) by less than the mantle (β_m); *heterogeneous stretching*. In 1983, Hellinger and Sclater proposed heterogeneous stretching as a mechanism to explain similar, abnormal, subsidence curves in the Pannonian Basin. It is intuitively obvious that if the crust remains unthinned (β_c=1) while the more dense lithospheric mantle undergoes some amount of thinning (β_m), then upwelling of hotter and therefore less dense asthenosphere, in isostatic response to thinning, will cause uplift. If the crust is thinned by some amount which is less than the thinning in the lithospheric mantle ($\beta_m > \beta_c$) then the syn-rift phase of subsidence will be considerably less than would be predicted by a simple homogeneous stretching model in which $\beta_c = \beta_m$. The main objection to heterogeneous stretching models arises when the total amount of stretching across the rifted region is left unbalanced between the crust and mantle. Assuming for the moment that section-balancing poses no problem, and that there is no space problem at any stage, then there are essentially two types of heterogeneous stretching model which may be possible:

(1) *Coupled Strain Rate Model.* In which the rates of strain in the crust and mantle may be different and variable but are coupled such that, for example, if the crustal strain rate increases by some amount then so does the mantle strain rate by proportionally the same amount. In this case, if β_c is set to be less than β_m in any vertical column of lithosphere at the start of rifting then, within that column, β_c will be less than β_m throughout the rift phase (see Figure 6.15 and section 6.4.3).

(2) *Decoupled Strain Rate Model.* In which the rates of strain in the crust and mantle are different from each other and may vary disproportionately with time during rifting. In this case the relative values of β_c and β_m may be varied within a single vertical column during rifting. For example, if the crust was thinned according to an increasing strain rate while the mantle deformed according to a decreasing stain rate, then it is possible to imagine how β_m may exceed β_c at the start of rifting but at the end of rifting β_c might be equal to or even exceed β_m. In this type of model while stretching at any stage during rifting may be heterogeneous the time-integrated total stretching need not be (see section 6.4.4).

Application of these two types of model to explain the observed subsidence profiles is described below. It is also shown that the values of β obtained by fitting homogeneous model curves to the thermal part of the subsidence data will provide

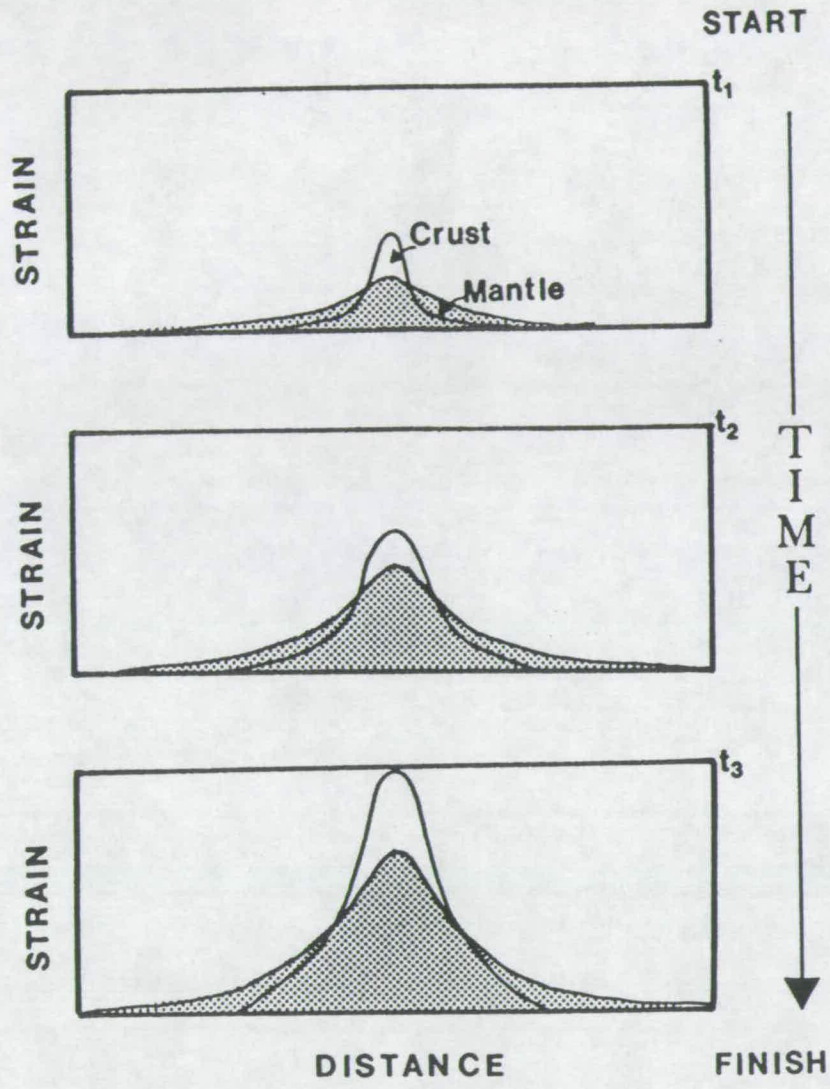

FIGURE 6.15 Coupled strain rate heterogeneous stretching. This diagram shows, qualitatively, that β_c and β_m must balance at any time across the rifted region. In this coupled strain rate model β_c is always greater than β_m in the centre of the rift while β_m is always greater than β_c at the rift flanks. This sort of model was used by N. White and McKenzie (1988) to explain the Steer's Head geometry of the subsidence in the northern North Sea.

lower estimates for the total lithospheric thinning than those predicted by either of the more complex models.

6.4.3 Coupled Strain Rate Models.

Most previously published and unpublished modelling of heterogeneous stretching (e.g. Sclater *et al.*, 1980; Royden and Keen, 1980; Hellinger and Sclater, 1983; Zervos, 1986; Rowley and Sahagian, 1986; Condon, 1988; Hillis, 1988; N. White and McKenzie, 1988), and indeed of homogeneous stretching (e.g. Jarvis and McKenzie, 1980; Wood, 1982; and N. White, 1988,1990), involves the use of either constant or coupled strain rates in the crust and mantle. As such the *relative values of* β_c *and* β_m *cannot be varied with time.* For example, in their depth-dependent stretching model for the northern North Sea, which successfully reproduces the "Steer's Head" geometry of basin subsidence (see discussion in Chapter 3), N. White and McKenzie (1988) used different Gaussian distributions for the stretching of the crust and mantle across the rifted region. Coupled strain rates are, however, implicit in their model, as they are in all other similar models. Thus N. White and McKenzie (1988) assume that throughout rifting β_m is always greater than β_c, by the same proportion, beneath the flanks of the rift, while in the centre of the rift β_c always exceeds β_m by the same proportion (see Figure 6.15; also Figure 3.6 in Chapter 3).

Two water-loaded subsidence curves, from 16/26-3 and 29/14-1, were chosen in order to evaluate the effect of applying a coupled strain rate heterogeneous stretching model to subsidence curves from the region of interest (see Figure 6.16). Theoretical curves were generated for finite duration (160 to 100 Ma) using a program developed by Condon (1988)[6]. The model curves in Figure 6.16 are for heterogeneous stretching where $\beta_c < \beta_m$ and in which the crust is stretched at a constant rate equal to ε_c which is less than the constant mantle strain rate ε_m where

E:6.5 $$\varepsilon_c \propto \beta_c/60 \text{ and } \varepsilon_m \propto \beta_m/60$$

and 60 is the rifting duration in Ma. In order to generate the subsidence profile observed in 16/26-3 by constant strain rate heterogeneous stretching, values for β_c of

---

[6] The program developed by Condon (1988) for finite duration heterogeneous rifting was used. In order to overcome the technical problem arising from having two boundaries (base crust and base lithosphere) moving upwards at different velocities during rifting (i.e. deforming at different constant strain rates to arrive at different total values of β for the crust and mantle by the end of rifting) Condon followed the mathematical approach of Cochran (1983) which assumes that the rift episode can be approximated by a large number of infinitesimal heterogeneous increments.

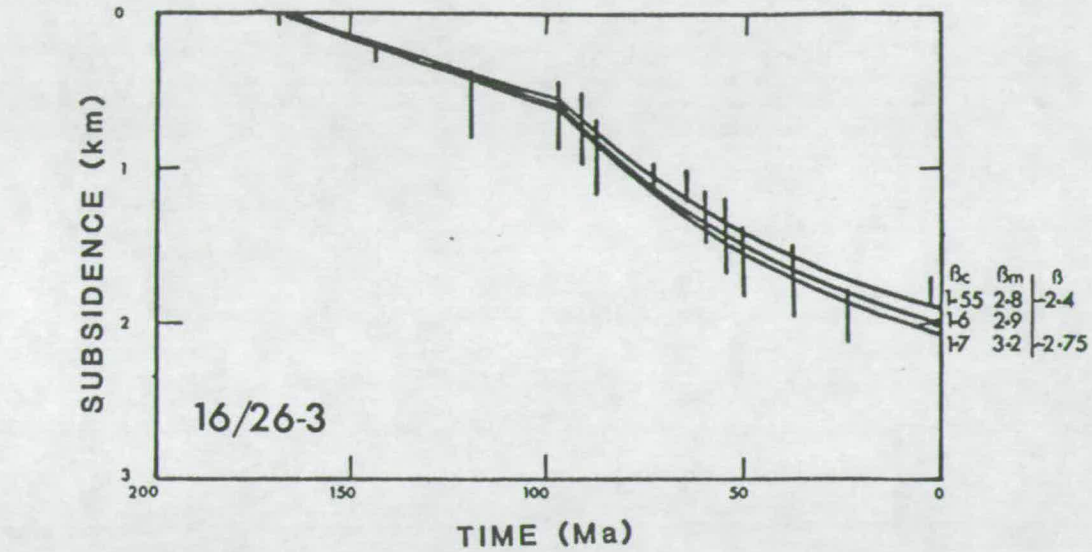

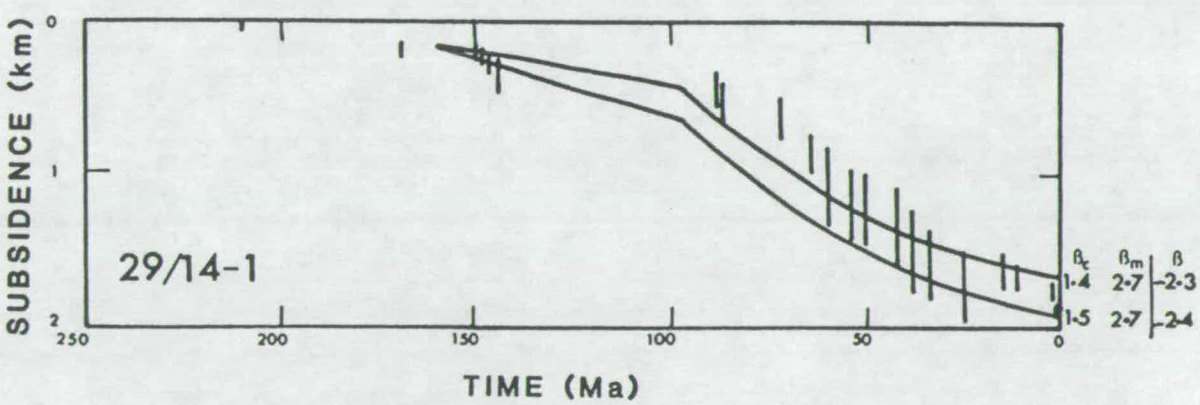

FIGURE 6.16 Fitting curves for heterogeneous stretching to water-loaded subsidence data (shown by error bars) from 16/26-3 and 29/14-1. Curves for constant strain rate heterogeneous stretching are used (see text). Rifting is assumed to start at 160 Ma and to finish at 100 Ma. Model curves are labelled with β_c and β_m and the *effective value of* β which represents an equivalent amount of decompression is also noted (see text for explanation).

between 1.55 and 1.7 and corresponding values for β_m of between 2.8 and 3.2 are required. For the water-loaded subsidence pattern in 29/14-1 values of β_c between 1.4 and 1.5 with β_m at ~2.7 are required. Similar values for β_c and β_m are obtained when this coupled strain rate heterogeneous model is applied to the subsidence in the other wells from the region. In terms of understanding the magmatism some value representing the total lithospheric thinning, and therefore decompression, is of more importance than the values of β_c or β_m. The values of β_c and β_m can be used to calculate the total amount of decompression which may then be expressed in terms of an *equivalent homogeneous stretching factor*[7] (β). The equivalent homogeneous stretching factors are $\beta \sim 2.4$ to 2.75 for 16/26-3 and $\beta \sim 2.3$ to 2.4 for 29/14-1; see Figure 6.16.

Although the model described above appears to fit the data it does, however, have serious difficulties when its implications are considered in a regional context. If, as seems likely, during stretching the lithospheric section must at all times be conserved, then the crustal and mantle sections must balance in two dimensions. The implication is that if β_c was significantly smaller than β_m in the centre of the North Sea rift during the Jurassic, then there should be corresponding off-axis regions where $\beta_c >> \beta_m$ and where there is therefore a large amount of crustal thinning associated with only very small amounts of thermal subsidence. Such off-axis regions are not observed. Indeed, off-axis areas in the North Sea are commonly observed to have undergone relatively little or no crustal thinning and yet have subsided thermally to give rise to the Steer's Head geometry!

It is clear that the coupled strain rate heterogeneous model cannot simultaneously explain all of the observations concerning subsidence in the North Sea. It is, however, of interest to note that if a constant strain rate homogeneous stretching model is used to estimate a value for β, using only the thermal part of the subsidence in wells 16/26-3 and 29/14-1, it predicts very similar, but slightly smaller values, than the values for the *equivalent homogeneous stretching factor* predicted by the heterogeneous model. Thus, Figure 6.17 shows that the best fit homogeneous stretching curves (from Figure 6.10) for 16/26-3 are $\beta = 2.3$-2.5 and for 29/14-1 are $\beta = 2.1$-2.3. The reason for the similarity in the amount of decompression predicted by both of these models is that in both cases the model curves have to fit the steep thermal part of the observed subsidence curves. Since the shape of the thermal part of the subsidence curve is a direct result of cooling and is related to the size of the

---

[7] The pressure drop as a result of thinning the crust by β_c and the mantle by β_m is calculated. The homogeneous stretching factor β which results in approximately the same amount of decompression is then found. The *equivalent homogeneous stretching factor* is defined by this value of β.

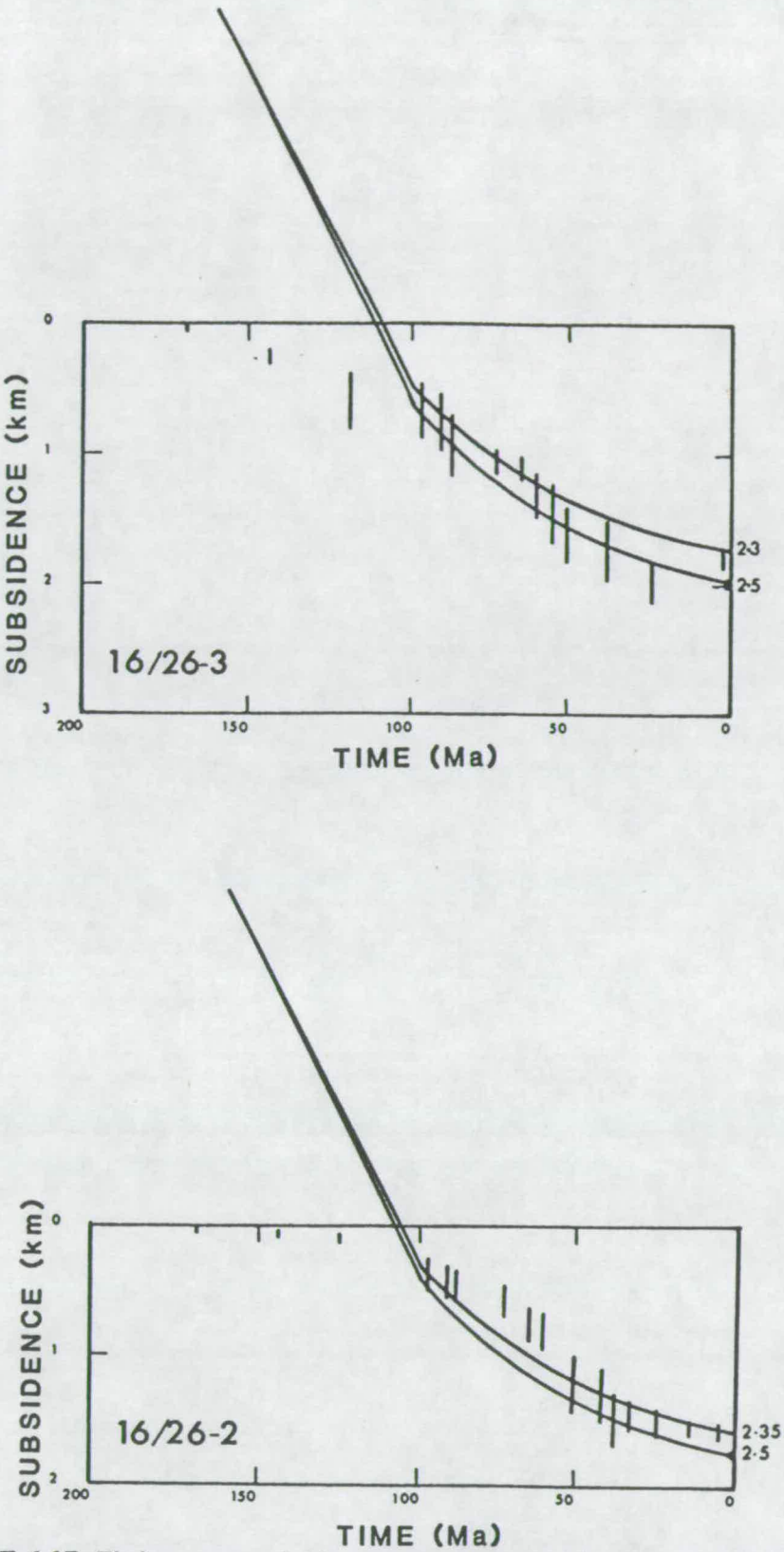

FIGURE 6.17 Fitting curves for homogeneous stretching to water-loaded subsidence data (shown by error bars) from 16/26-3 and 29/14-1. Curves for constant strain rate homogeneous stretching are used (see text and Figure 6.10). Model curves are labelled with values of β. Note that the values of β are very similar to the effective β-values produced by modelling the same subsidence profiles with heterogeneous stretching (see Figure 6.16).

thermal perturbation which remained at the end of rifting, it is perhaps no surprise that both models predict similar amounts of total thinning. These observations in part justify the use of fits from homogeneous model curves to derive β values, representing probably a lower estimate for total amount of decompression, from the subsidence of all 19 wells in section 6.4.5.

6.4.4 Decoupled Strain Rate Models.

Coupled strain rate models, whether homogeneous or heterogeneous, are unable to balance the crustal and mantle sections at all times and simultaneously explain observed on- and off-axis variations in syn-rift and thermal subsidence. A decoupled strain rate model is not subject to these problems. One of the simplest examples of decoupling might be a situation where, although the rift episode was protracted, the maximum amount of thinning of the mantle in the centre of the rifted region was attained very soon after the start of rifting, while the maximum amount of crustal thinning was not attained until near the end of the rift episode. The mantle might therefore have an exponentially decreasing strain rate while the crust has an exponentially increasing strain rate. In this example β_m is >> β_c at the start of rifting but by the end of rifting β_c may exceed β_m.

To this author's knowledge no quantitative model for stretching with decoupled strain rates has yet been published. A number of papers have commented on the effects on basin morphology of applying different bulk strain rates to the lithosphere during stretching (e.g. Kusznir, 1982; Kusznir and Park, 1984, 1987; Ranalli, 1987). None of these papers has indicated whether or not the rates of strain in the mantle and crust may vary locally and with time across a rifted region, so long as the overall strain at any one time balances. Kusznir and Park (1984) did, however, note that the olivine rheology of the mantle at depth may favour creep at stresses which are lower than those required for brittle failure of a quartz rheology at near surface pressures and temperatures.

The mechanism favoured as an explanation for the abnormal subsidence curves in the central North Sea involves heterogeneous extension with decoupled strain rates. Although a quantitative model that is able simultaneously to fit all of the observations has yet to be developed it is possible to consider the implications of certain end-member models which follow this type of approach. One rather extreme scenario to explain the abnormal subsidence curves may be considered in two stages as follows (see Figure 6.18):

(1) At the start of rifting at the very centre of the rift $\varepsilon_m >> \varepsilon_c$ and β_m reaches its maximum value within a very short period of time. During this first stage $\beta_m >> \beta_c$ and therefore the initial result of stretching in this central part of the rift will be uplift and erosion. After this first stage ε_m falls to a very low value similar to or less than ε_c. This first stage, shown in Figure 6.18, has been modelled, using Condon's heterogeneous stretching program, by thinning the mantle by a factor of 3 at 160 Ma over a duration of 5 Ma while keeping β_c equal to 1.

(2) The second stage occurs some time later in the syn-rift period and is marked by a dramatic increase in ε_c. Most of the crustal thinning is associated with this phase of rifting and as β_c becomes as large as, or exceeds, β_m subsidence ensues. The second stage has been modelled by assuming that 55 Ma after the start of the first stage (i.e. at 105 Ma) the crust is thinned by a factor of 3 over a duration of 5 Ma but that no more mantle thinning occurs.

The model described above and shown by the bold curve in Figure 6.18 is clearly rather extreme. The model curve in Figure 6.18 does however highlight two important points:

(1) Positive syn-rift subsidence only occurs in the last 5 Ma of the 60 Ma rift phase and is relatively minor because for most of the rift phase the region is uplifted by the effect of mantle thinning. A less extreme model, in which crustal thinning occurs throughout the 60 Ma, might easily allow for a small amount of syn-rift subsidence at an earlier stage. The important point that comes out here is that the syn-rift stage of subsidence cannot, if it contains erosional unconformities or periods of non-deposition, be used to constrain models since there is no way of measuring the amount of negative subsidence which is missing.

(2) Since much of the total lithospheric thinning occurs at an early stage in the rift episode the thermal part of the subsidence curve has already dropped through cooling to the extent, that it appears to be the result of a significantly smaller amount of constant strain rate homogeneous stretching (β = 2.15 to 2.35; see dashed curves in Figure 6.18) over the same total duration (60 Ma). If the duration of mantle stretching was increased to occur over more than 5 of the 60 Ma then the thermal curve would be steeper and the resulting estimate of β using homogeneous curves would be closer to the true value. Figure 6.18 suggests that, if some form of decoupled strain-rate mechanism is responsible for the abnormal subsidence patterns observed in the central North Sea, then a *lower estimate of* β may be obtained by fitting the gradient of the thermal subsidence part of the data with model curves for homogeneous stretching.

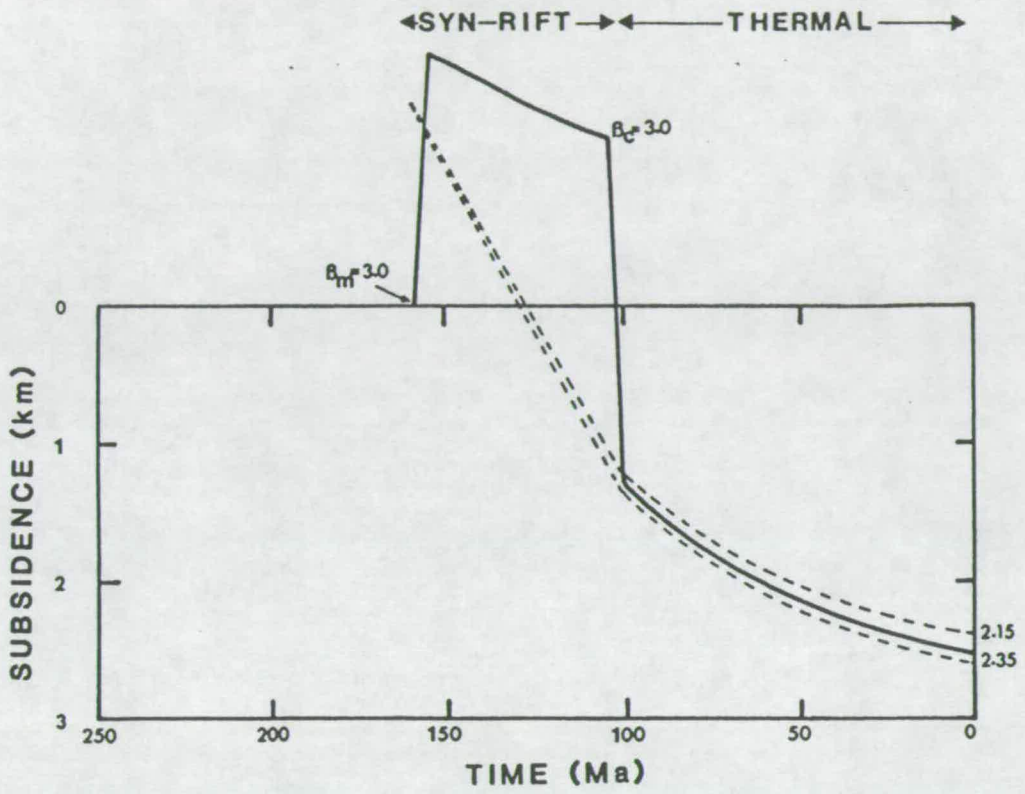

FIGURE 6.18 Stretching when crustal and mantle strain rates are decoupled (bold curve). In this extreme model all of the mantle stretching (β_m=3) occurs in the first 5 Ma of rifting (between 160 and 155 Ma) and all of the crustal stretching (β_c=3) occurs in the last 5 Ma of rifting (between 105 and 100 Ma). This model is heterogeneous at any instant during the rift phase but at the end of rifting the crust and mantle have been thinned by the same amount. The time integrated effect is therefore homogeneous. The shape of the subsidence curve, however differs significantly from the homogeneous theoretical curve for a constant strain rate where β=3 (see Figure 6.10). When model curves for constant strain rate homogeneous stretching are used to estimate β from the thermal subsidence stage (see dashed curves) they give values of β of between 2.15 and 2.35, somewhat lower than the true value.

6.4.5 Summary and Discussion.

A general feature of *all* stretching models is that the syn-rift stage is characterised by some path of β vs. time. In coupled strain rate models, whether they are homogeneous or heterogeneous, the amount of thinning of the crustal and mantle layers of the lithosphere will proceed maintaining the same proportionality with time. In more complex decoupled strain rate models the variation of β_c may not be proportional to that of β_m and complex β/time paths for the different layers may occur during the syn-rift phase. The complex nature of the syn-rift phase of subsidence, which is so intimately related to local tectonic controls and to the precise shape of the β/time path, makes it inherently difficult to model in a unique manner. The path of thermal subsidence on the other hand, depends primarily on the size of the thermal perturbation which remains at the end of the rift phase. In this case a maximum estimate of β would be obtained by fitting the thermal subsidence to the thermal part of model curves for instantaneous stretching at the start of the Jurassic rift phase. The model curves would, in this case, have already been cooling for ~60 Ma by the start of the thermal phase seen in the data. The values of β determined in this way turn out to be rather large. Alternatively an *absolute minimum* value for β could be obtained from instantaneous model curves by assuming that extension only started at ~100 Ma. When this approach was applied to the thermal part of the model curve in Figure 6.18, a β value of only 1.5 was estimated. The latter was the approach of Sclater and Christie (1980). By using curves for finite duration stretching to fit the thermal part of the data, something close to an *average* value should be obtained.

6.4.6 Results.

The discussion above has shown that regional occurrence of abnormal subsidence curves can be explained by heterogeneous extension with coupled or decoupled strain rates. It has also been shown that model curves for homogeneous stretching may be used to estimate values for β from the thermal parts of the subsidence curves, whichever heterogeneous stretching mechanism applies. A decoupled strain rate mechanism is considered most likely since, as is discussed in Chapter 7 (see Figures 7.19 and 7.20), it seems likely, at least qualitatively, that it can account for observations of pre-crustal-rift uplift, magmatism, and abnormal subsidence curves in the centre of the rift together with rift-flank thermal uplift and later subsidence.

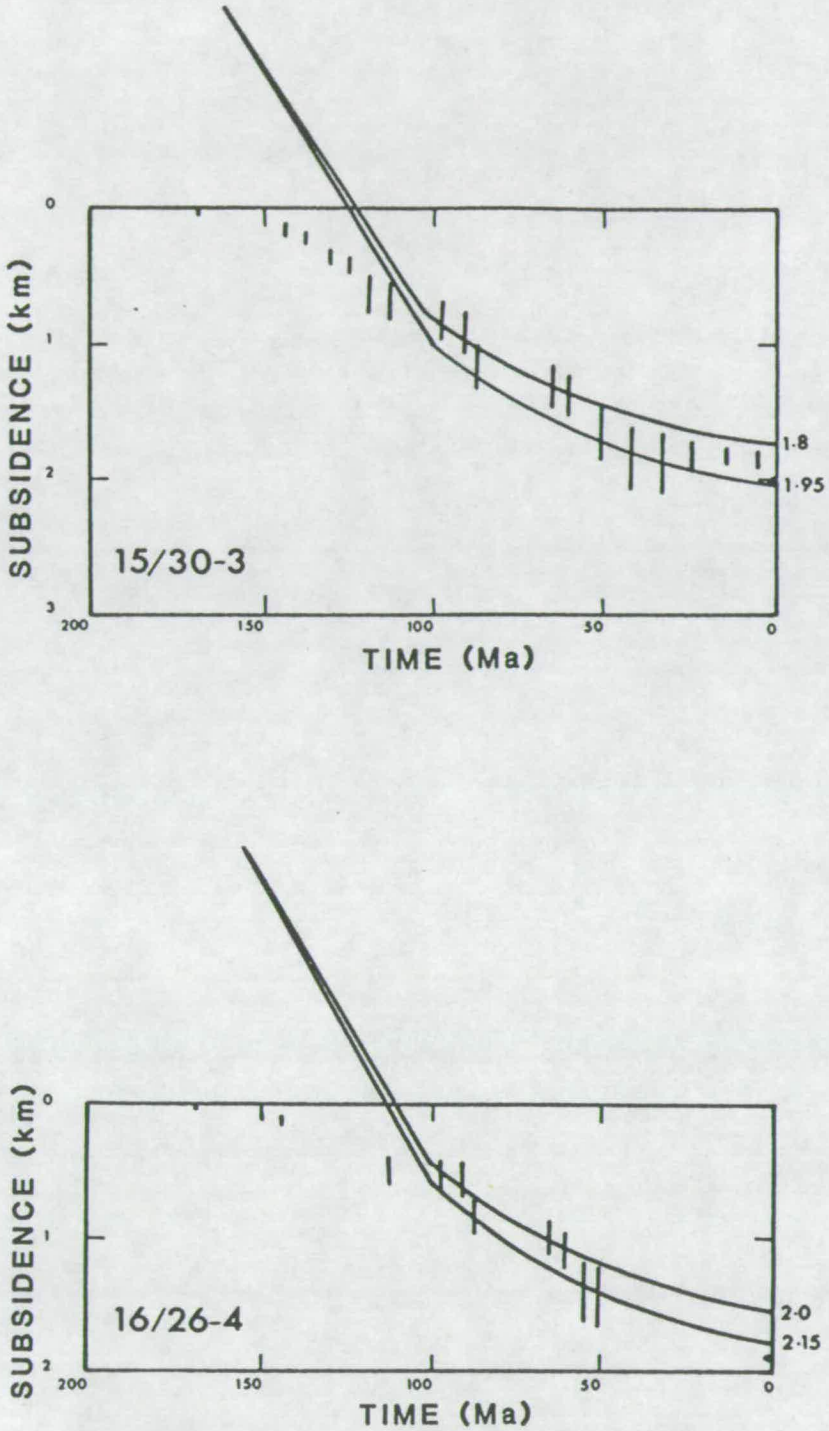

FIGURE 6.19 Water-loaded subsidence data (error bars) together with estimates of β for 18 wells from the region of interest (see Figure 6.6 for locations). β has been estimated by assuming that model curves for constant strain rate homogeneous stretching, when fitted to the thermal stage of subsidence observed in the data, give reasonable estimates for the amount lithospheric thinning even if the true mechanism is not constant strain rate homogeneous stretching (see text for justification).

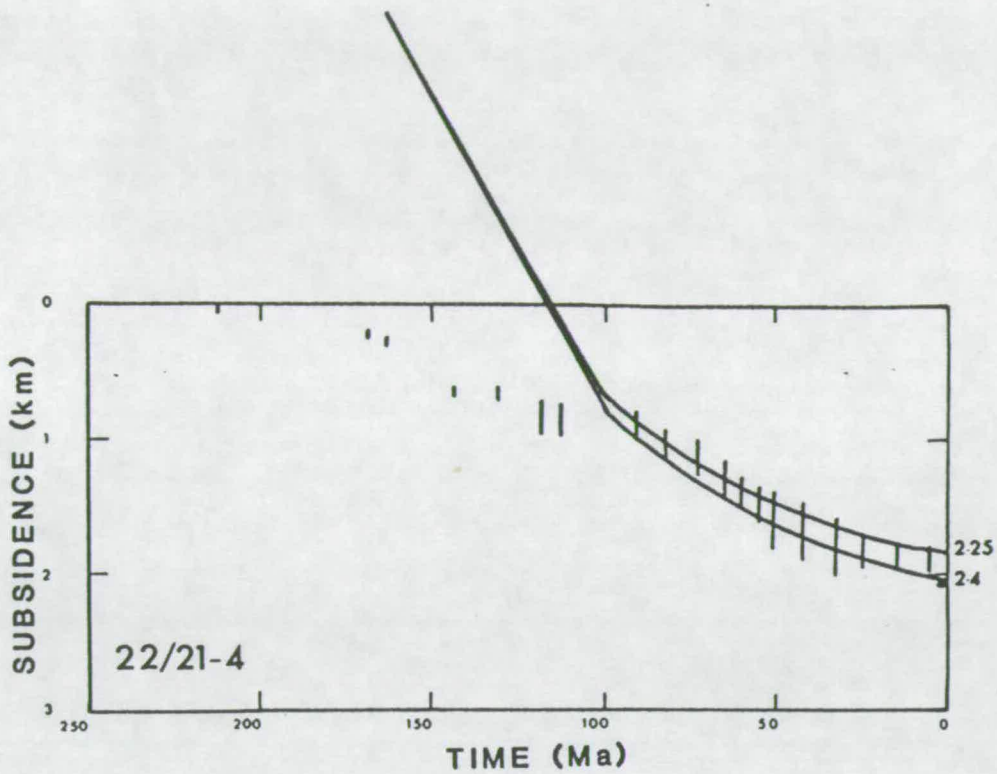

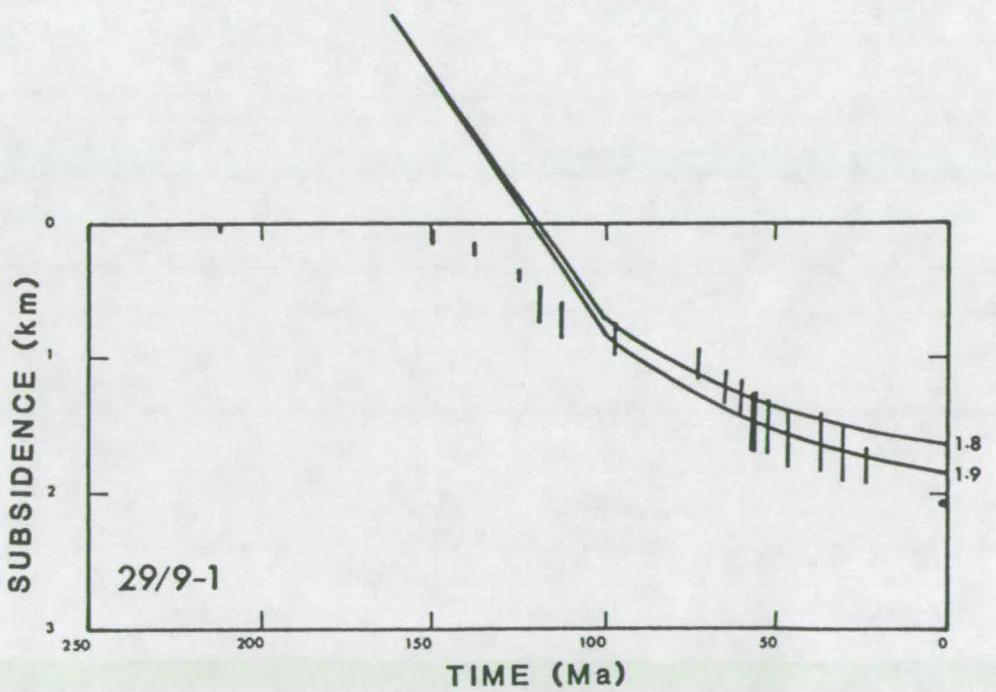

FIGURE 6.19 continued.

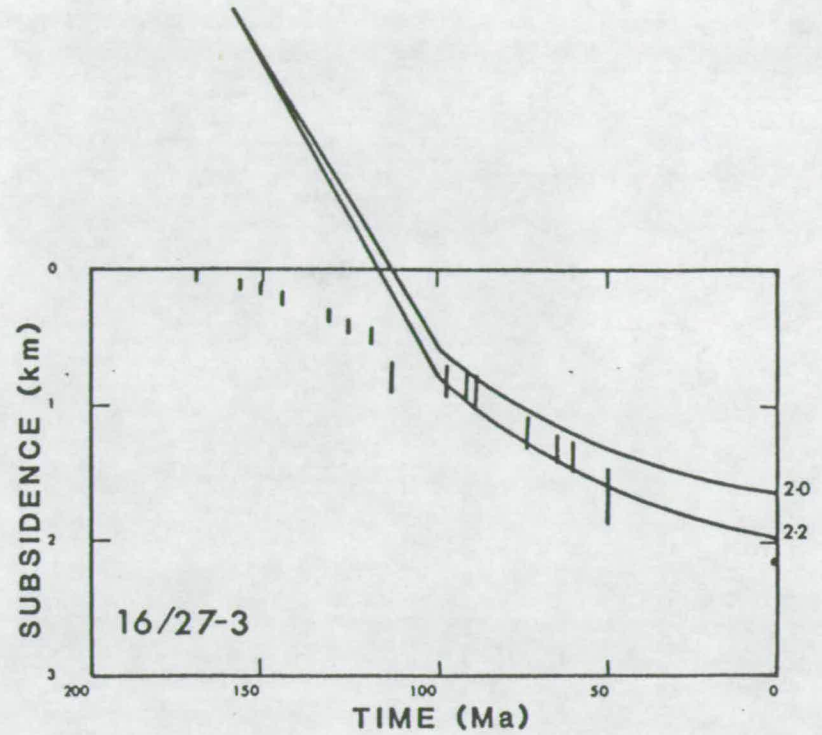

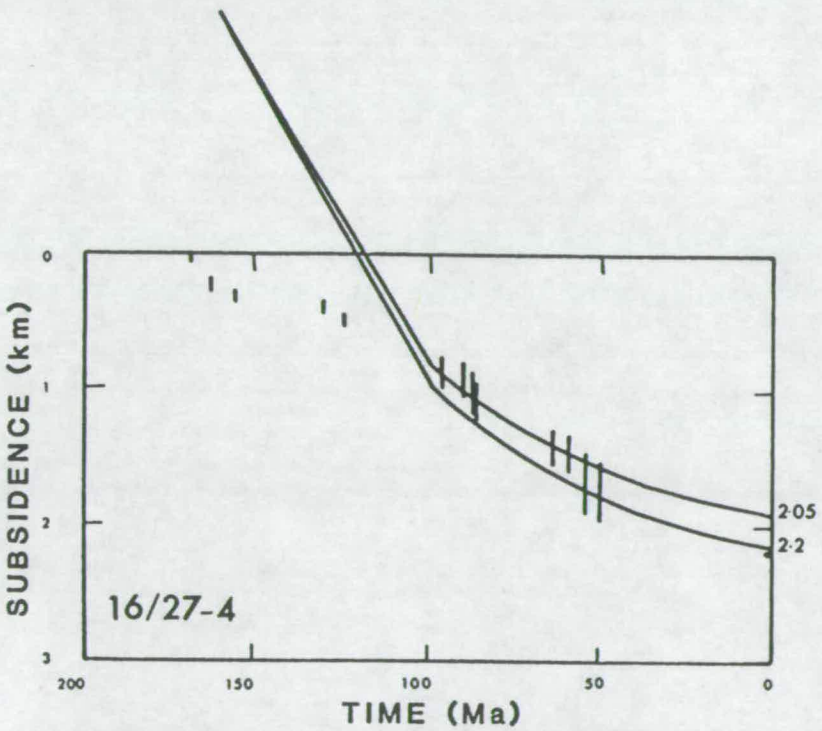

FIGURE 6.19 continued.

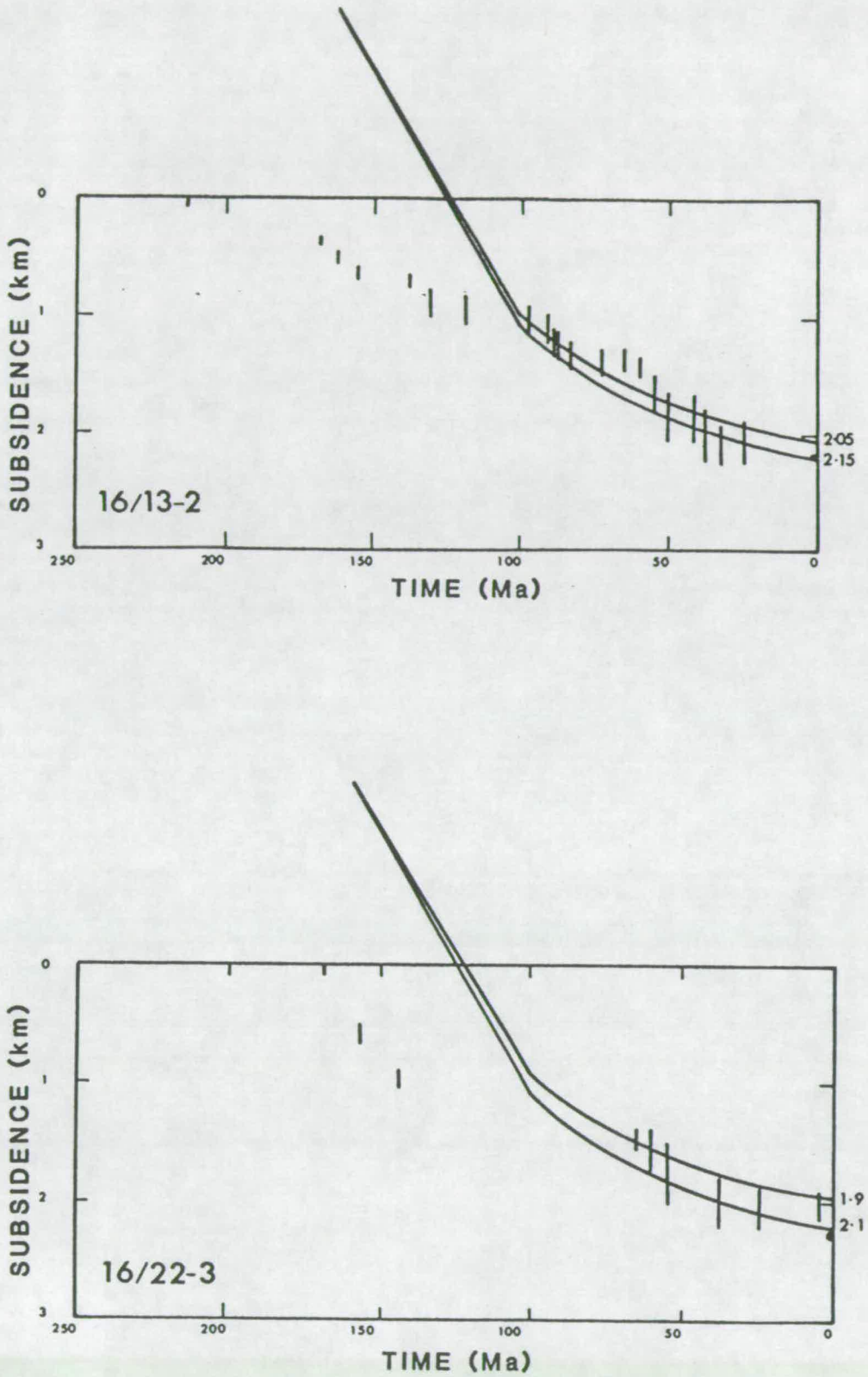

FIGURE 6.19 continued.

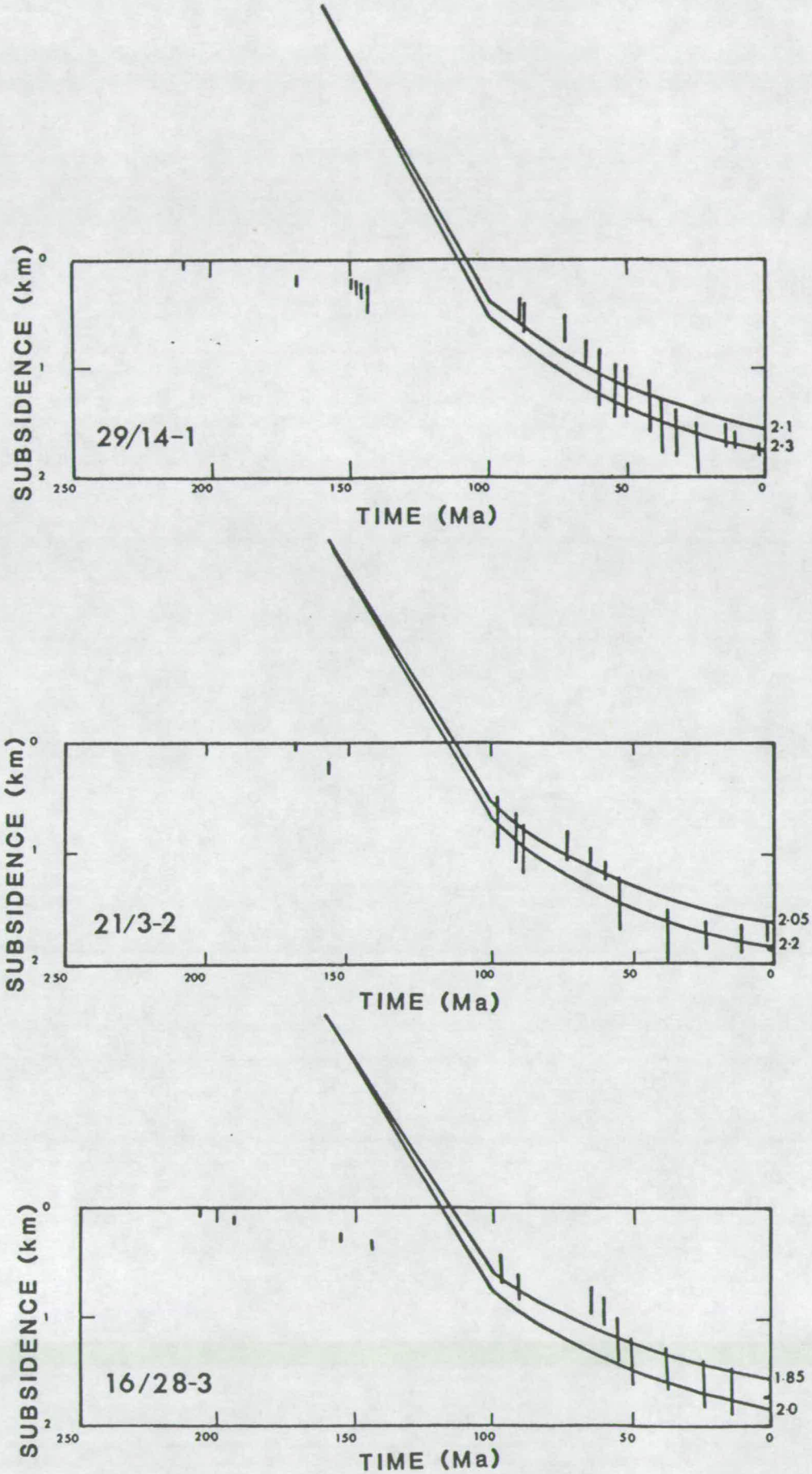

FIGURE 6.19 continued.

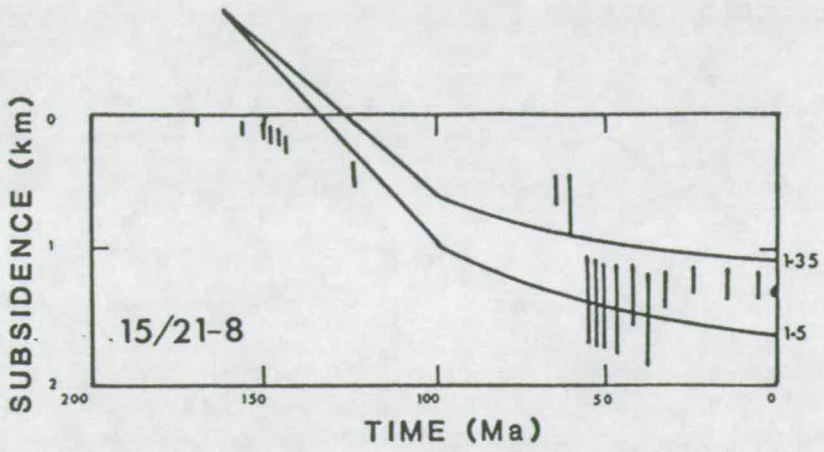

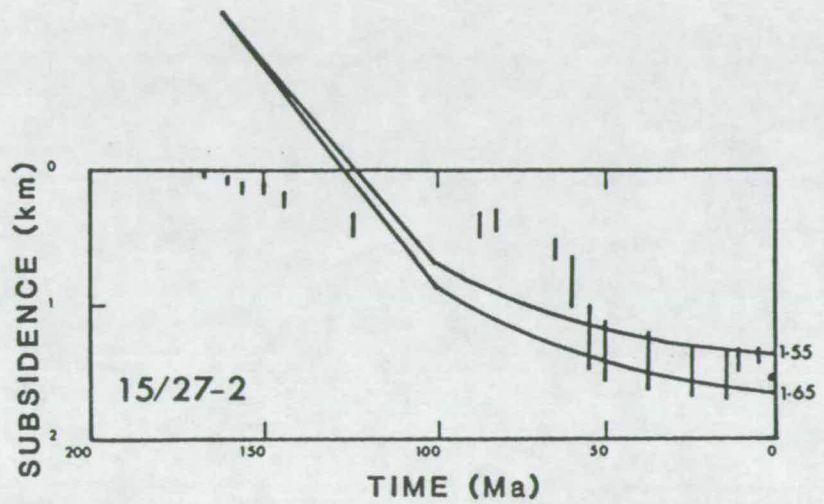

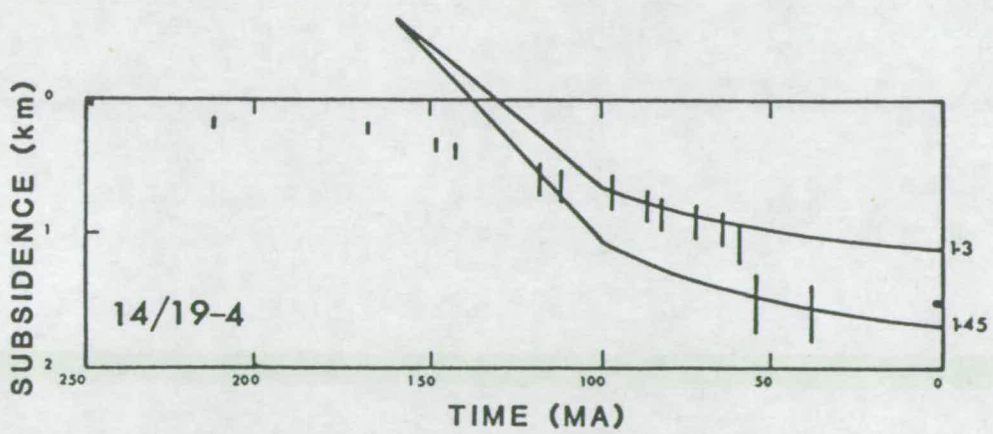

FIGURE 6.19 continued.

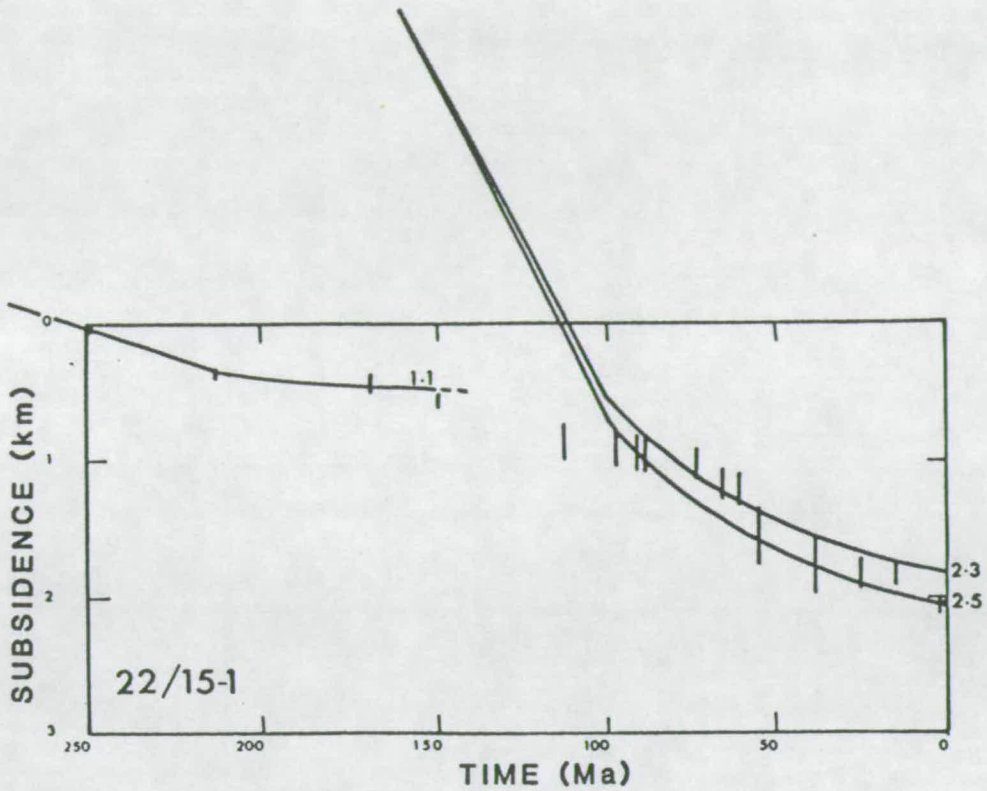

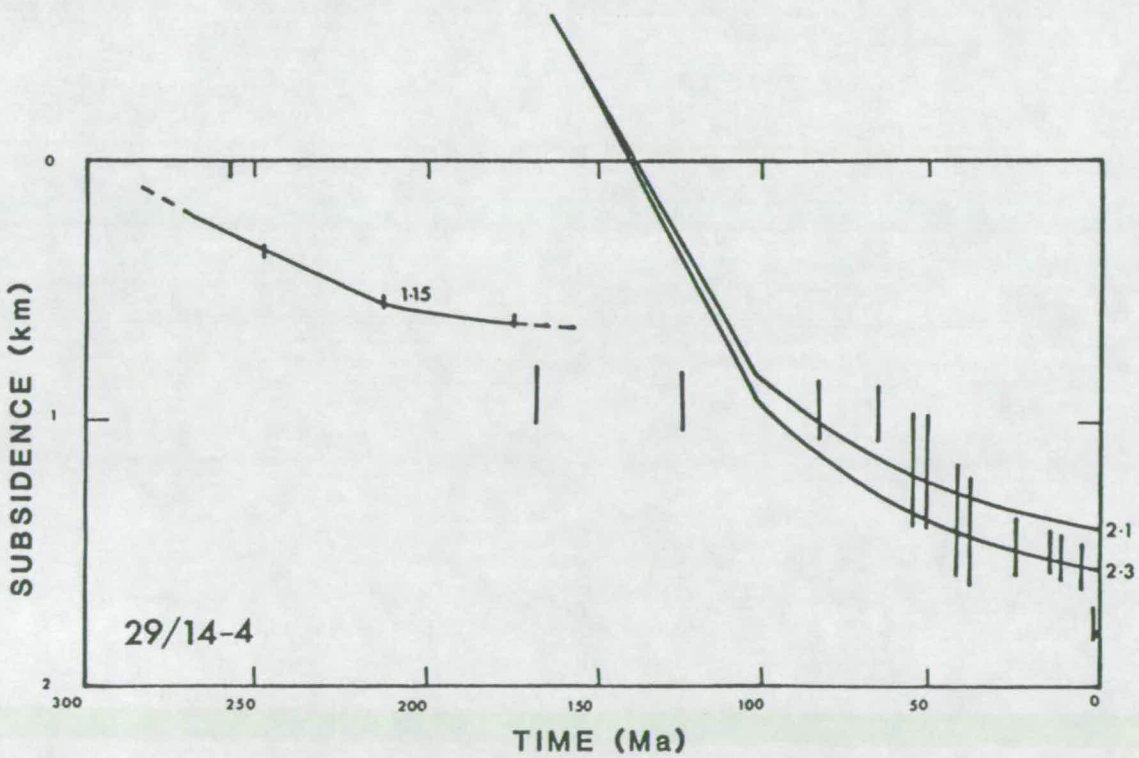

FIGURE 6.19 continued.

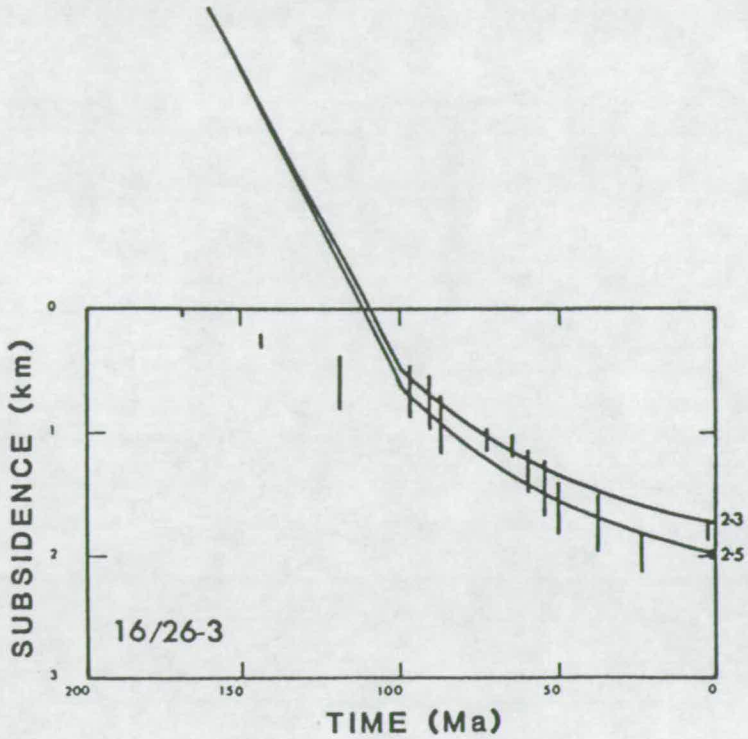

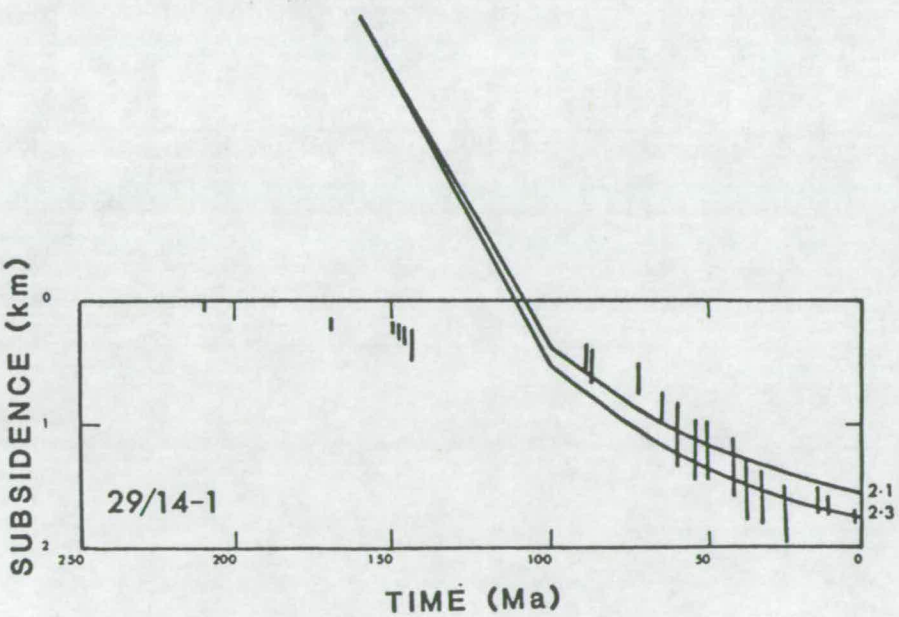

FIGURE 6.19 continued.

It is therefore suggested that the bold curves in Figure 6.14, rather than the dashed curve of Wood (1982), provide a better fit for the last 100 Ma of subsidence and are the most appropriate estimates of β. The rift episode is taken to be from 160 to 100 Ma, rather than 180-120 Ma, for three reasons. First, in Chapter 4 it was suggested that there is little evidence for major fault-controlled extension prior to the eruption of the Forties volcanic province, which on the basis of new dates is interpreted as Callovian (~160-150 Ma). Second, if the older rift phase were to be used it would result in larger estimates of β for a given curve because proportionally more cooling, and therefore flattening of any given model curve, will have taken place prior to the steep part of the observed subsidence curves. Thirdly, the 160 to 100 Ma duration for rifting in the area under study would make it compatible with rifting in the Viking Graben (N.White, 1988), where there is no reason to believe that rifting necessarily started any later and where some believe that it may even have started somewhat earlier (A. Hayward, pers. comm. 1990).

Figure 6.19 shows the water-loaded subsidence curves for the 18 of the 19 wells (17/9-1 not included) which have been produced during the course of this study. Each water-loaded curve has been interpreted in terms of the simple approach described above (bold curves) and model curves, labelled with β, are also shown. Note in particular that wells that are not obviously on fault block tips (Figure 6.6), such as 22/21-4, 22/15-1, and 16/27-4, show especially good examples of "abnormal" subsidence curves. Estimates of β, maximum and minimum, for all of the wells backstripped during the present study, together with a reevaluation of Wood's (1982) curves[8], are presented on the map in Figure 6.20. It is clear that, using the philosophy described above, the average value of β in the deeper parts of the basin is at least 2 and near the very centre of the triple junction (e.g. wells 22/21-4, 22/15-1, 16/26-3, 16/26-2) β may reach values which are as high as 2.5. These estimates of β, which are certainly not maximum estimates, *are considerably larger than any previously presented* from subsidence studies in the North Sea.

6.4.7 Subsidence Compared with Crustal Thinning.

In an as yet unpublished study, R. Hunter (Imperial College, pers. comm. 1990) has recently modelled the Bouguer anomaly field to estimate the depth to the Moho (Figure 6.21A) and effective crustal thinning (β_c, Figure 6.21B) in the region

[8] Many of Wood's (1982) curves were not abnormal and there was therefore no disagreement in their interpretation.

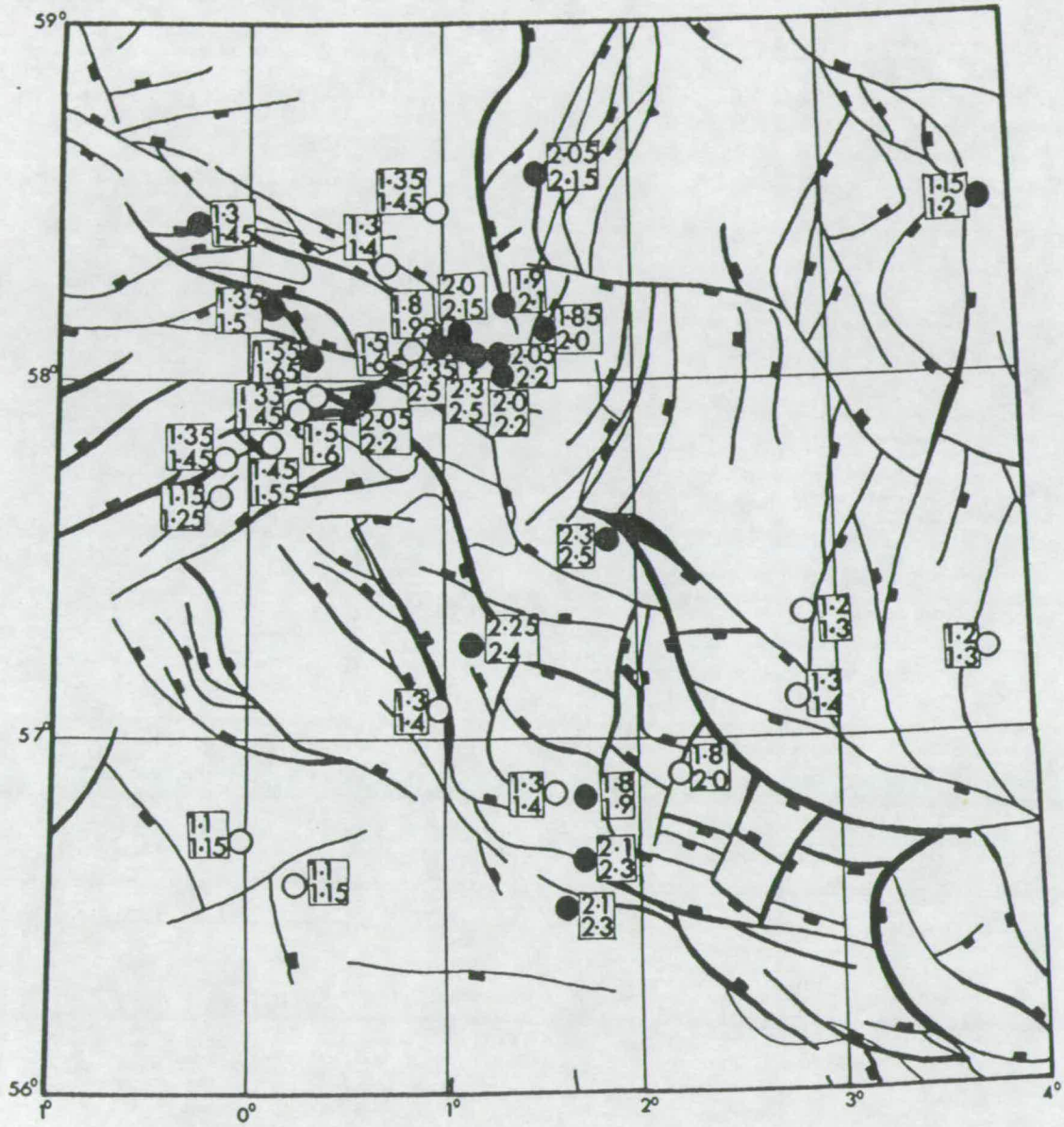

FIGURE 6.20 A map showing estimated values of β in the Middle-Upper Jurassic for the wells analysed in Figure 6.19 together with the value from 17/9-1 (see Figure 6.11) and reinterpreted values for the wells presented by Wood (1982). The base map is the same as the one used in Figure 6.6.

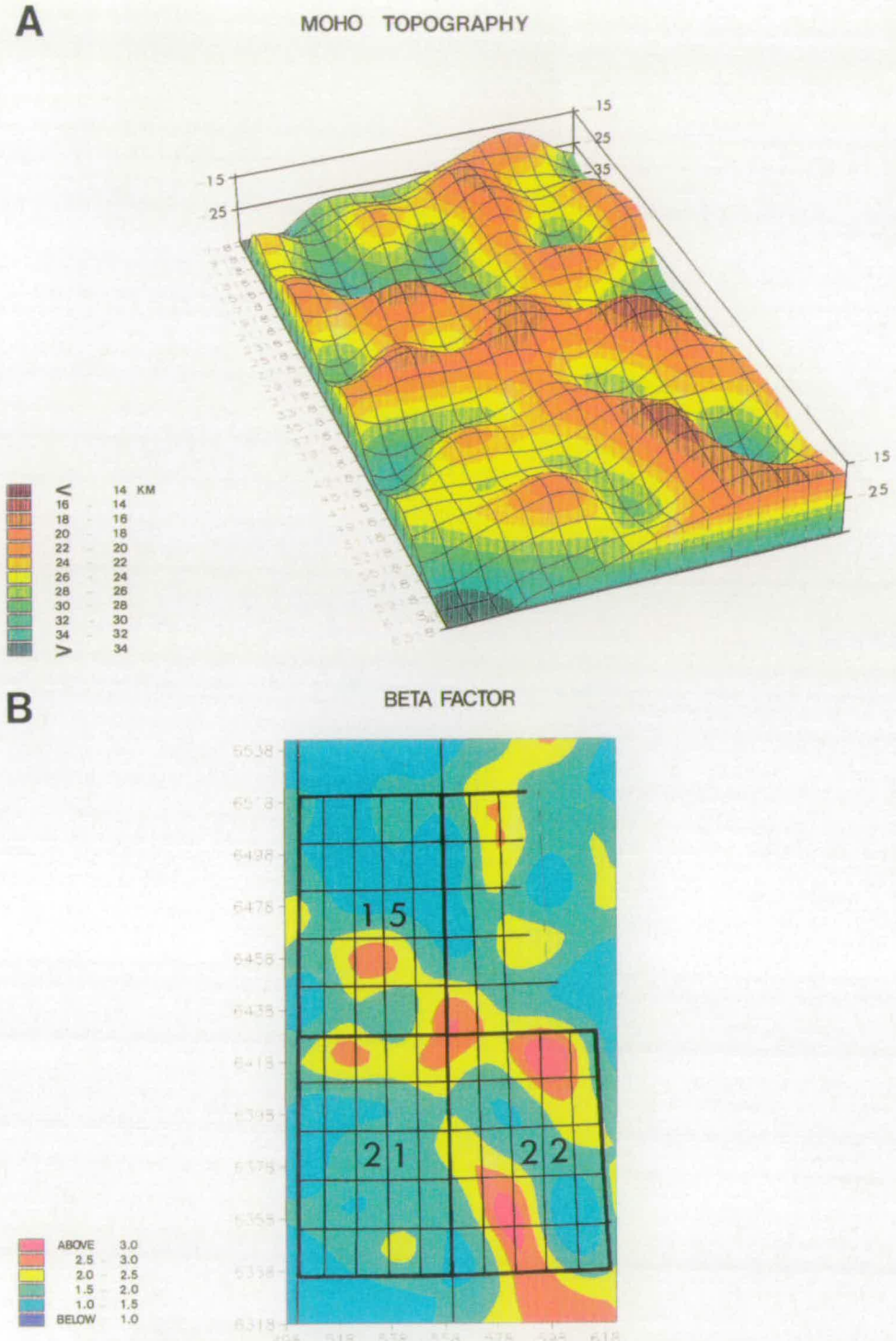

FIGURE 6.21 Upper diagram (A) shows the Moho topography (depth to the Moho) predicted by modelling the filtered residual Bouguer gravity anomaly field, after the effects of low density basin fill had been removed. The location of the area covered by the gravity model is shown by the numbered U.K. North Sea quadrants in the lower diagram. The lower diagram (B) shows contours of estimated minimum crustal thinning (BETA = β_c; assuming an original crustal thickness of 35 km) in the modelled region (see text for details). Both diagrams are from unpublished work and were kindly supplied by R. Hunter (Imperial College, London).

of interest. Figure 6.21A shows Hunter's model for Moho depth, whereas in Figure 6.21B contours of minimum β_c are shown; determined by assuming β = 35/(depth to Moho - depth to base Cretaceous) where the initial thickness of the crust is assumed to be 35 km. In order to prevent extreme variations in the Moho topography generated during modelling of the gravity field, the depth to the Moho was only allowed to vary between 12 and 35 km (see Figure 6.21A). The Moho model, which involves the removal of the total thickness of low density sediments, uses the Cretaceous and Tertiary isopachs of Day et al. (1981). Note that because thicknesses of Jurassic, Triassic and older low density sediments are not accounted for, the apparent crustal thinning is a minimum. Note also that the effects of the relatively high density volcanic and intrusive rocks from the region have not been accounted for; this will have the effect of maximising the apparent thinning. Modelling of the associated magnetic anomalies is under way in order to take account of these effects (R. Hunter, pers. comm., 1990).

When values for β_c from the gravity-determined crustal thickness, contoured on Figure 6.21b, are compared with the values for β determined using the subsidence (see Figure 6.20) the general agreement is striking. The maximum value of β_c (>3) is somewhat larger than the value of β from the subsidence (~2.5) but given that there is a large error (±0.5) on the value of β from crustal thinning, the two values are in excellent agreement. This conclusion supports the suggestion made by N. White (1990) that Triassic rifting is likely to have been a rather minor event.

6.5 Discussion.

The most important conclusions from the study of well subsidence presented in this chapter may be summarised as follows:

(1) The maximum amount of thinning, suggested by the gradient of the thermal subsidence observed in wells, in the triple junction area of the North Sea during the Jurassic corresponds to a *stretching factor of at least 2.5*. This value is supported by the crustal thinning suggested by modelling of the gravity field. The large values of β observed for this central part of the North Sea support claims that the geometry of the region, with its three intersecting rift arms, is likely to result in large degrees of thinning (Latin *et al.*, 1990a,b; Latin and White, 1990).

(2) The estimates of β from the subsidence and the crustal thinning in the triple junction, on the flanks of the Central Graben, and on the edge of the Egersund Basin may be summarised in Table 6.2 on the following page.

TABLE 6.2 : Estimates of β			
	Forties	Central Graben	Egersund
Seismic β_c	>2	>1.8	--
Gravity β_c	>3	--	--
Maximum β_{subs}	>2.5	2.1-2.3	1.2
Minimum β_{subs}	~2.0	1.3-1.4	1.15

(3) The abnormal shape of the subsidence curves in the central region is difficult to explain in terms of any simple homogeneous stretching model. The observations require that syn-rift subsidence be minimal throughout the most stretched region while the thermal stage dominates the subsidence curves. However, the very large amount of crustal thinning observed from gravity modelling and on seismic refraction lines in the area suggests that a simple coupled strain rate heterogeneous model in which $\beta_c << \beta_m$ cannot be used to explain the subsidence observations unless the pre-Jurassic component of the crustal thinning is rather large (> 50%). A decoupled strain rate heterogeneous stretching model in which β_m is larger than β_c in the early stages of rifting is consistent with many of the observations (see Chapter 7, Figures 7.19 and 7.20).

CHAPTER 7

THE RELATIONSHIP BETWEEN EXTENSION AND MAGMATISM IN THE NORTH SEA

7.1 Introduction.

Previous chapters of this thesis fall into two different categories. Chapters 2 and 3, together with part of Chapter 6, are theoretical while Chapters 4 and 5, together with most of Chapter 6, are based on observation. The main concern of this chapter is to establish whether or not predictions made by the theory of McKenzie and Bickle (1988) are consistent with the observations from the North Sea.

The essence of the theory is as follows. If the amount of *adiabatic* decompression, or "*upwelling*", of asthenosphere of a given potential temperature (T_p) is sufficient to induce melting of dry peridotite, then the volume and average composition of the melt generated may be predicted using parameterisations of experimental data (see McKenzie and Bickle (1988) and Chapters 2 and 3 of this thesis). The amount of adiabatic upwelling that occurs during extension of the lithosphere, is controlled by the amount and rate of lithospheric thinning (β and ε) and the thickness of the mechanical boundary layer (MBL) prior to rifting. To be able to predict the volume and composition of melt generated during rifting in the North Sea it is necessary to determine model-independent values for the lithospheric parameters (β, ε, and initial MBL) and the potential temperature of the asthenosphere at the time of rifting.

In section 7.2 the "*normal*" value of 1280±40°C (see Chapter 2) is shown to be the most appropriate potential temperature during Jurassic rifting in the North Sea. When this T_p is combined with the most likely value for the initial thickness of the MBL (100±10 km) and with estimates for β and ε, the Forties province is shown to be the only region predicted to have igneous activity during extension in the North Sea (see section 7.3). The central location of the Forties province is also consistent with coaxial stretching (pure shear) rather than non-coaxial stretching (simple shear); see Chapter 3 and Latin and White (1990). When the major-element compositions of the Forties basalts are compared with the predicted melt compositions, the degree of misfit is small (see section 7.3). The small volume of alkali basalt observed in the

Forties area is shown to be consistent with the theory. The ultrapotassic lamprophyres and the nephelinites observed in other parts of the North Sea (see Chapters 4 and 5) are not predicted, have very different compositions when compared to the predicted melts, and require the presence of volatiles in their mantle source region (see sections 7.4 and 7.5).

The existence and composition of the ultrapotassic rocks from the North Sea are shown to be consistent with melting of phlogopite-pyroxenite, or some other phlogopite-bearing peridotite, which was probably resident in the MBL of the lithosphere (see sections 7.4 and 7.5). The addition of a small volume of ultrapotassic melt to the alkali basalt melt generated in the Forties region will also be suggested as a possible explanation for the misfit in K_2O and TiO_2 observed when the Forties basalts are compared with the predicted melt compositions.

Although the volume and composition of the basalts in the Forties province is shown to be broadly consistent with the predictions of McKenzie and Bickle (1988) and the more undersaturated magmas may be explained by volatile controlled melting at smaller amounts of lithospheric thinning, there remain a number of observations which are difficult to explain. Most important of these are (1) that the magmatic activity occurs very early in the syn-rift phase, and (2) that magmatism is absent in most parts of the rift system. A qualitative model involving decoupled strain rates and coaxial-stretching is proposed in the discussion at the end of this chapter (section 7.6) in an attempt to explain the timing of magmatism. The second observation is more difficult to explain but its answer may be related to differences in the rheology and thermal history of the lithosphere in different parts of the North Sea.

7.2 Assigning Values to Parameters.

7.2.1 Potential Temperature: A Mantle Plume in the Jurassic North Sea?

The potential temperature of the asthenosphere at the time of rifting exerts a fundamental control on the volume and composition of any melt generated during rifting (see Chapters 2 and 3). Indeed, in some instances anomalously high potential temperatures may be the direct cause of melting unaccompanied by lithospheric thinning (e.g. Hawaii). Evidence for or against the presence of a mantle plume in the Jurassic North Sea must be carefully reviewed and needs to yield a firm conclusion if the main aim of this thesis is to be realised.

In sections 2.7 and 3.6 there was lengthy discussion of the likely effects on basin development of an anomalously high T_p due to the presence of a convective plume in the asthenosphere. Three predictable consequences of plume involvement were noted:

(1) *Regional Doming*: The anomalous temperatures together with the dynamic support of a plume would be expected to lead to axisymmetric uplift of the order of 1-2 km over a region of 1000 to 2000 km in diameter. This uplift should be apparent in both the pre- and syn-rift stages of basin development and would be accentuated in the syn-rift stage if stretching were sufficient to produce large volumes of melt.

(2) *Plume Trail*: Migration of the European lithospheric plate over a relatively stationary convective plume within the asthenosphere should lead to a predictable temporal migration of plume-induced, uplift-related unconformities in the geological record. The locus of any magmatic activity might also be expected to show a temporal migration and so define a hot-spot trail.

(3) *Convective Thinning*: A hot, vigorously convecting plume beneath the lithospheric plate might be expected to cause some thinning of the lithosphere due to the temperature-dependent nature of viscosity (Yuen and Fleitout, 1985). The result of such convective thinning would be a very serious mismatch between mantle and crustal thinning. The crust would be observed to be thinned by an amount that was significantly smaller than the amount of total lithospheric thinning inferred from the subsidence of the basin.

In the following discussion the evidence for and against regional doming at the onset of Middle Jurassic rifting in the North Sea is considered. If a plume had been present beneath the Central North Sea during the Middle Jurassic then its likely path through time can be predicted from the motion of the European plate relative to the hot-spot reference frame. The predicted path suggests that the centre of the plume would have remained within the North Sea region from 200 to 100 Ma. Evidence for regional doming prior to and subsequent to the onset of rifting is therefore considered together with the observed timing of magmatic activity. It is shown that although the observations may be consistent with rift-related doming in the Middle Jurassic they do not necessarily support its interpretation in terms of a mantle plume. It is further shown that there is no unambiguous evidence for convective thinning.

7.2.1.1 Regional Doming in the Middle Jurassic?

Early interpretations of the origin of the main graben system of the North Sea all suggested that *the three rift basins developed as a failed triple junction over a plume-generated dome* (e.g. Whiteman *et al.*, 1975; Kent, 1975; Ziegler, 1981;

Eynon, 1981). Such an interpretation may in part have simply reflected the widespread view, at the time, that plumes were an integral part, and probable cause, of rifting, and that triple junctions, in particular, were plume-generated (e.g. Burke and Dewey, 1973). However, as Brown (1984) notes, the stratigraphic evidence for regional doming during the Early Jurassic, which relies on the marked lack of Lower Jurassic sediments and deep truncation of Palaeozoic series over much of the North Sea, is striking.

Eynon (1981) favoured a mantle plume on the basis of four lines of evidence: (1) The erosion of Lower Jurassic sediments over a very large part of the North Sea, (2) the presence of volcanic rocks at the locus of the uplift, (3) the development of a trilete rift system for the dispersal of erosional products, and (4) the development of a concentric pattern of sedimentary facies, from terrestrial to marine, about the focus. Ziegler (1981) describes the development of a large "*rift dome*" in the Central North Sea at the transition from the Aalenian to the Bajocian. According to Ziegler (1982), describing a dome with dimensions of 600 km by 450 km, "*its structural relief is difficult to assess but, to judge from the estimated thickness of the eroded strata could have been of the order of 2000-3000m in its crestal parts*".

More recently Ziegler and Van Hoorn (1990) describe a dome which first "*appears*" in the early Middle Jurassic, which has a relief of 1.5 to 2 km, which covers an region with dimensions of 700 km by 1000 km, and which "*founders*" during the Late Middle and Upper Jurassic (see Figure 7.1). Ziegler and Van Hoorn (1990) summarise their observations by stating that "*the rate of the resultant thermal uplift of the Central North Sea area exceeded the contemporaneous differential subsidence rate of the Central Graben that was induced by continued crustal stretching*".

Many of the conclusions noted above hinge on the observed absence of Lower Jurassic sediments and on the often deep truncation of Triassic and even Permian (Zechstein) strata in the Central North Sea. However, the absence of Lower Jurassic sediments, which are represented by a rather thin sequence of marine shales elsewhere in the North Sea (Brown, 1984), need not imply large amounts of erosion. Indeed widespread non-deposition, rather than erosion, would appear to be just as possible. The deep truncation of pre-Jurassic strata noted by Ziegler (1982) and Ziegler and Van Hoorn (1990) appears to occur mainly along the flanks of the Central Graben and may well be related to uplift of the rift flanks or on the footwalls of major faults. No data have been presented to suggest that the floor of the main graben shows extensive erosion. Since data are rarely presented in an uninterpreted form it is difficult to decide whether or not such extreme amounts of erosion, of the order of

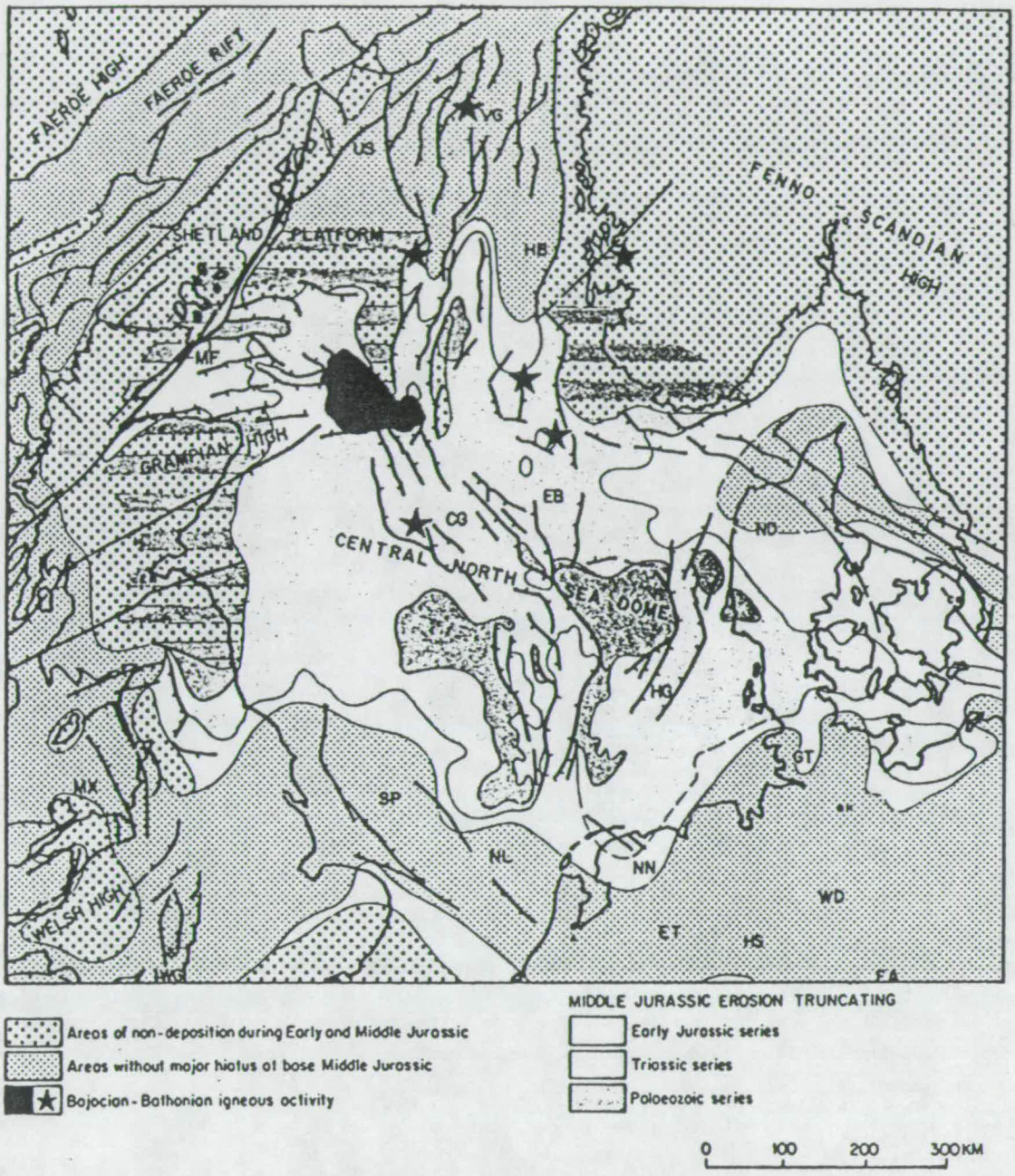

MID-JURASSIC TECTONICS

FIGURE 7.1 Middle Jurassic "doming" of the Central North Sea. From Ziegler and Van Hoorn (1990).

1 km or more, are merely the result of local tectonics or whether they point to regional uplift on the scale favoured by Ziegler and Van Hoorn (1990). As Leeder (1983) notes "*the direct stratigraphic evidence for uplift is present on the up-dip portions of tilted fault blocks whose subsidence kinematics may be expected to yield erosion in such areas*". Perhaps the abnormal subsidence curves presented in Chapter 6 provide the best evidence for non-deposition or erosion and implied uplift during the early syn-rift stage in the central parts of the Central Graben and Outer Moray Firth during the Middle Jurassic. Although the abnormal subsidence curves of Chapter 6 may therefore support the concept of regional doming they do not, however, necessarily require *large* amounts of uplift or erosion.

Contrary to Ziegler (1982) and Ziegler and Van Hoorn (1990), Leeder (1983) gives a rather more conservative estimate of "*a few hundred metres*" for the *regional* relief during the Lower Middle Jurassic which he considers as quite adequate to have provided a source for fluvio-deltaic clastics weathered from Permo-Triassic and Upper Palaeozoic hinterlands. It should further be noted that erosion of 2-3 km of sediment in a region is not in itself evidence for a relief of 2-3 km, but rather it indicates that the region has maintained some amount of positive relief for a period of time. In other words the large amounts of uplift reported by Ziegler (1982) and by Ziegler and Van Hoorn (1990) should be integrated over the period of time involved.

In summary there does appear to be evidence for early-syn rift uplift, on a regional scale, in the Central North Sea. The scale of this uplift is unclear since local and regional tectonic influences are difficult to disentangle in data which are rarely presented in an uninterpreted form. The absence of Lower Jurassic sediments, if due to Middle Jurassic erosion, does not provide incontrovertible evidence for the scale of syn-rift uplift. Similarly, if the absence of Lower Jurassic sediments results from of pre-rift uplift, and if, as most workers suggest, this uplift was centred on the Forties volcanic province, then (as is discussed below) the occurrence of marine shales of Lower Jurassic age in many other parts of the North Sea region (e.g. the Inner Moray Firth, Viking Graben, Danish Central Graben) is difficult to reconcile with plume related uplift on the scale and planform favoured by R. White and McKenzie (1989).

7.2.1.2 Motion of the European Plate in the Hot Spot Frame.

The Mesozoic motion of the European plate in the hot-spot reference frame was calculated using the set of poles and angles of rotation given by W. Morgan (1981) and the different set given by Livermore and Smith (1985). Figure 7.2 shows the temporal migration of a plume, assumed to have been centred on the Forties province (approximately 58°N and 1°E) at 160 Ma, which is predicted by the two

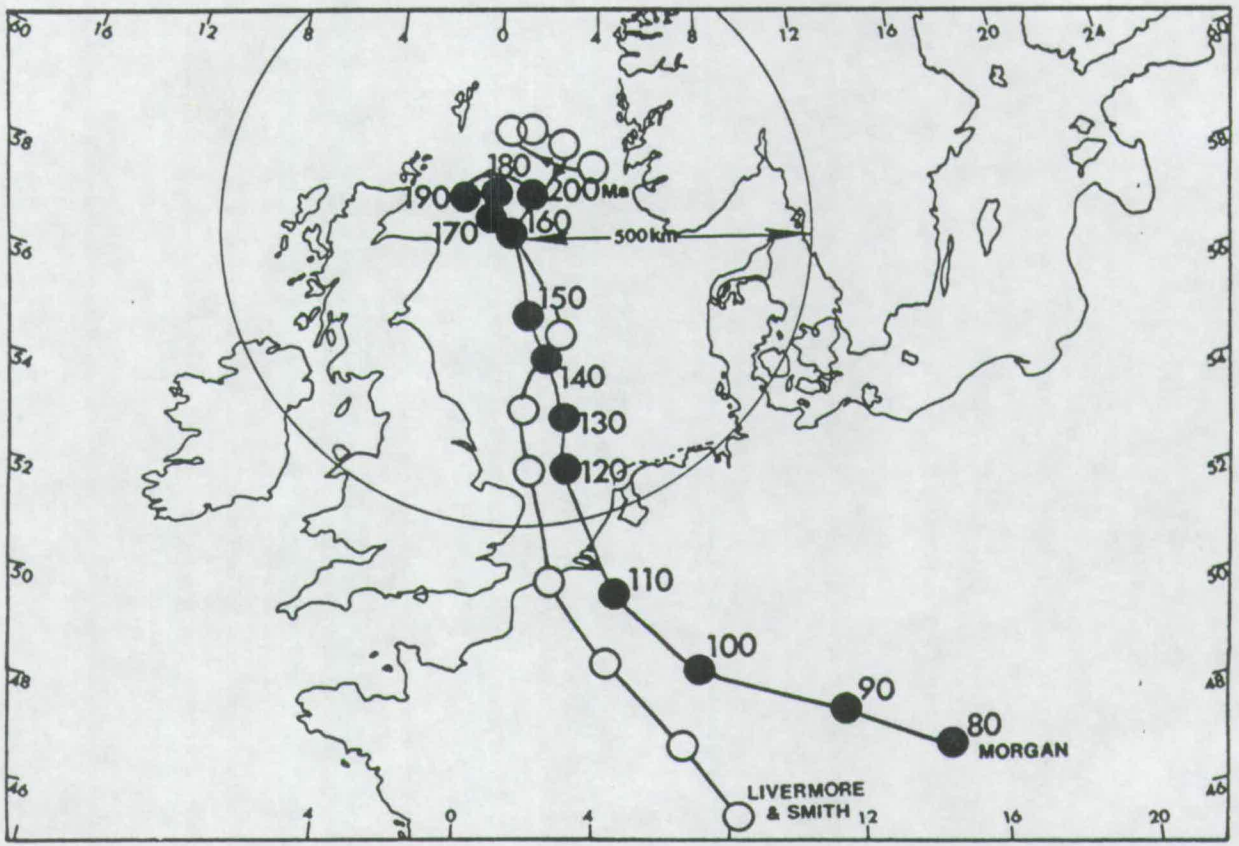

FIGURE 7.2 Motion of the European plate from 200 Ma to 80 Ma in the hot-spot reference frames of Morgan (1981; filled circles labelled with time in Ma) and Livermore and Smith (1985; open circles). Points mark position of a stationary hot spot, assumed to lie initially at 58°N and 1°E at 160 Ma, at different times. Large circle (1000 km in diameter) marks the (minimum) region of plume-related uplift predicted by R. White and McKenzie (1989).

different schemes. If plumes cause uplift over regions 1000 to 2000 km across (R. White and McKenzie, 1989; see Figure 3.23) then it is clear that the entire North Sea should have been uplifted from early Lower Jurassic to at least middle Cretaceous times. If rifting was continuous in the North Sea from ~180-160 to 120-100 Ma, as most authors suggest (e.g. Ziegler, 1982; Barton and Wood, 1984; N. White, 1988, 1990; Roberts *et al.*, 1990), then a southwards shift in the timing of magmatic activity might be expected as the plate rode over the hot centre of the plume.

7.2.1.3 Evidence for Doming Before and After Rifting?

The five diagrams (A to E) in Figure 7.3 which are taken directly from Ziegler and Van Hoorn (1990) show their interpreted palaeogeography of the North Sea region at a number of different time intervals between 200 and 100 Ma. Each diagram also shows a circle, 1000 km in diameter, centred on the approximate position of the hot-spot at that time (from Figure 7.2). This circular region is, on every diagram in Figure 7.3, expected to approximate the region affected by anomalous potential temperatures, and therefore uplifted, if a plume were present. The diagrams also show locations of extrusive and intrusive activity (stars). Note that the dates of these occurrences, many of which were determined on altered rock samples, were reinterpreted in Chapter 4 and are discussed in the next section.

During the Sinemurian and Aalenian (Lower Jurassic, ~200-180 Ma) Ziegler and Van Hoorn (1990) suggest that the North Sea region is dominated by shallow marine conditions (see Figure 7.3 A). If there were a plume present during this time then marine conditions would be highly unlikely. However, the uninterrupted subsidence observed throughout the Lower Jurassic in a number of the wells presented in Chapter 6 (e.g. 17/9-1, 29/14-4, and 22/15-1), which is attributed to thermal cooling after Triassic rifting, indicates that there was no uplift in these areas during the Lower Jurassic. If a plume is required to explain the regional doming and the magmatism in the Middle Jurassic then it must clearly be initiated at that time. This is the first case of special pleading for the plume model.

The Bajocian to Bathonian period in Figure 7.3 (diagram B) is, as was discussed in section 7.2.1.1, characterised by doming over a large part of the Central North Sea. It is conceivable that this doming is related to a plume even though the area of uplift is somewhat less that that shown by the 1000 km circle in Figure 7.3. Along the main graben structures which developed at this time fluviatile, deltaic and shore-face facies, characterised by coals, were being deposited (e.g. Brown, 1984; see Chapter 4). Ziegler and Van Hoorn (1990) attribute the volcanic rocks of the Forties province to this period of rifting although a Callovian age is now considered most

likely (~160-150 Ma; see Chapter 4). The Callovian to Oxfordian period (Diagram C in Figure 7.3) is not greatly different to the Bajocian-Bathonian and a dome remains in evidence in Ziegler and Van Hoorn's diagram. According to Brown (1984) coal bearing strata remain characteristic of the Callovian but marine conditions and deposition of shales, similar to those in the Sinemurian and Aalenian, are returned to in the Oxfordian. In Chapter 4 it was stressed that the start of the Upper Jurassic (Oxfordian-Kimmeridgian) is considered by many workers to herald the main phase of rifting in the North Sea.

From the Late Oxfordian onwards, through the Kimmeridgian and Tithonian (Diagram D in Figure 7.3) and the remaining Upper Jurassic the North Sea region is characterised by marine conditions. The domed region has "*foundered*". Marine conditions continued and deepened into the Cretaceous. Note that in Diagram E of Figure 7.3 deep marine conditions are indicated over the *entire* region, even the areas outside the main rift. The main areas of non-deposition are those which have remained as mountainous highs throughout much of the Mesozoic (e.g. the Grampians, Fenno-Scandian High, the London Brabant Massif). Indeed the domed region in diagram B is rather less impressive if these high areas are discounted and appears to be concentrated within and along the flanks of the three main rifts.

The main conclusions to be drawn from study of the palaeogeographic reconstructions of Ziegler and Van Hoorn (1990) is that the North Sea rift dome was (1) absent immediately prior to rifting, (2) in evidence at the start of Middle Jurassic extension in the Bathonian-Bajocian but remained visible for less than 30 Ma, and (3) was concentrated along the flanks of the three main rift arms. There is no strong support for the southwards migration of a large region of plume-induced uplift.

7.2.1.4 Migration of Magmatic Activity?

The discussion at the end of Chapter 4 suggested that erroneous dates on altered samples may have misled previous authors in their interpretations (e.g. Ziegler, 1982; Dixon *et al.*, 1981; Latin *et al.*, 1990 a,b; Ziegler and Van Hoorn, 1990). Latin *et al.* (1990a) suggested that a southwards migration of igneous activity with time was evident in the dates of igneous rock from the rift system. This effect, which was shown in Figure 4.15, is implicit in the diagrams of Ziegler and Van Hoorn (1990) in Figure 7.3. None of the publications specifically attributes the observed migration in activity to the presence of a plume, indeed Latin *et al.* (1990b) suggested that the same effect might have been produced by a southwards propagation of the rift. It was, however, shown in Chapter 4 that many of the younger dates and some of the older dates should be treated with considerable caution

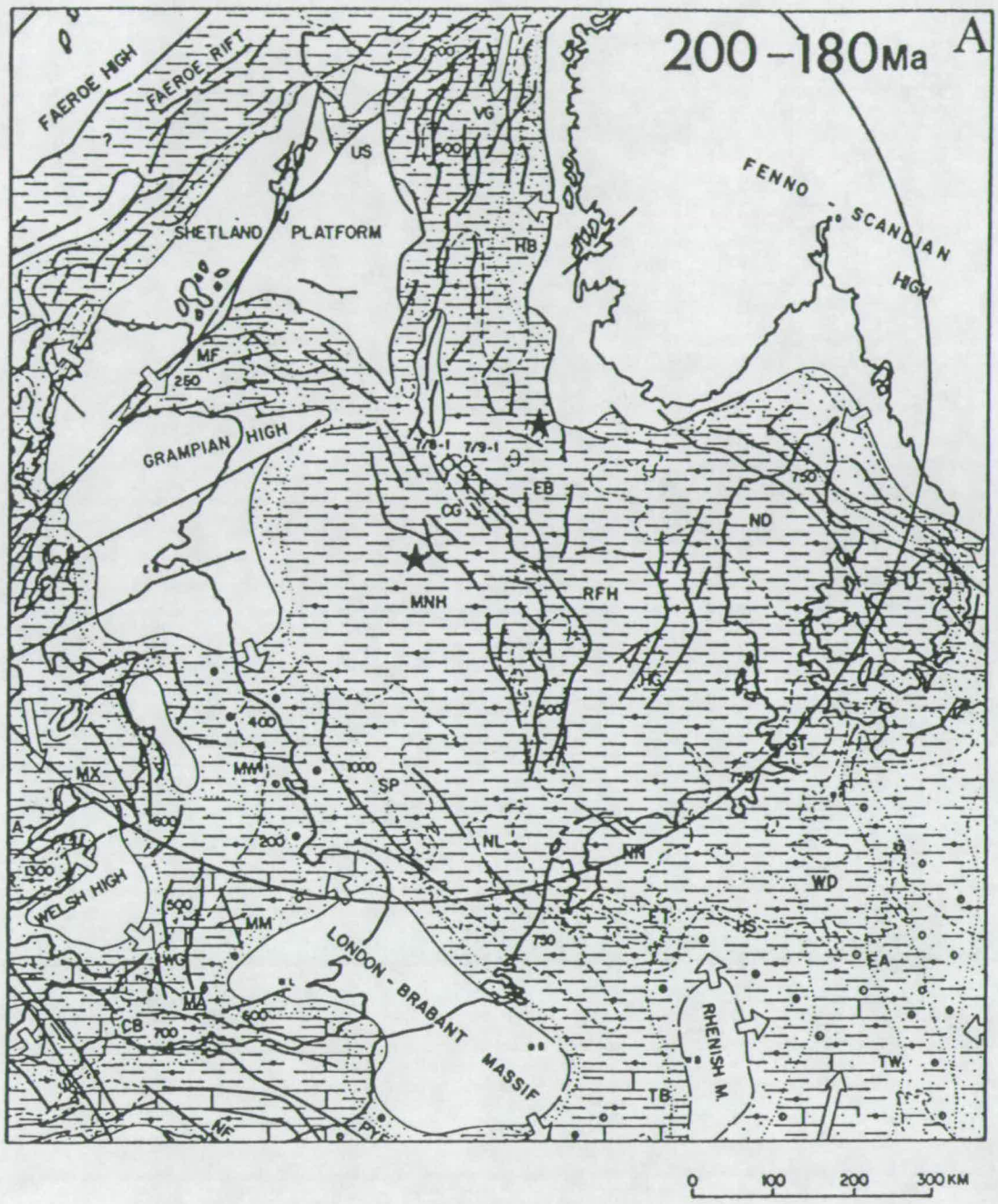

SINEMURIAN - AALENIAN

FIGURE 7.3 Palaeogeographic maps of Ziegler and Van Hoorn (1990) for the North Sea region at different periods in geological time. Each diagram (A to E) also shows a 1000 km circle centred on the appropriate hot spot location from Figure 7.2. Blank areas represent regions of uplift or non-deposition. Dashes show regions of marine shale deposition while dots indicate shallow water/terrestrial sands. See Ziegler and Van Hoorn for a detailed key and see text for details.

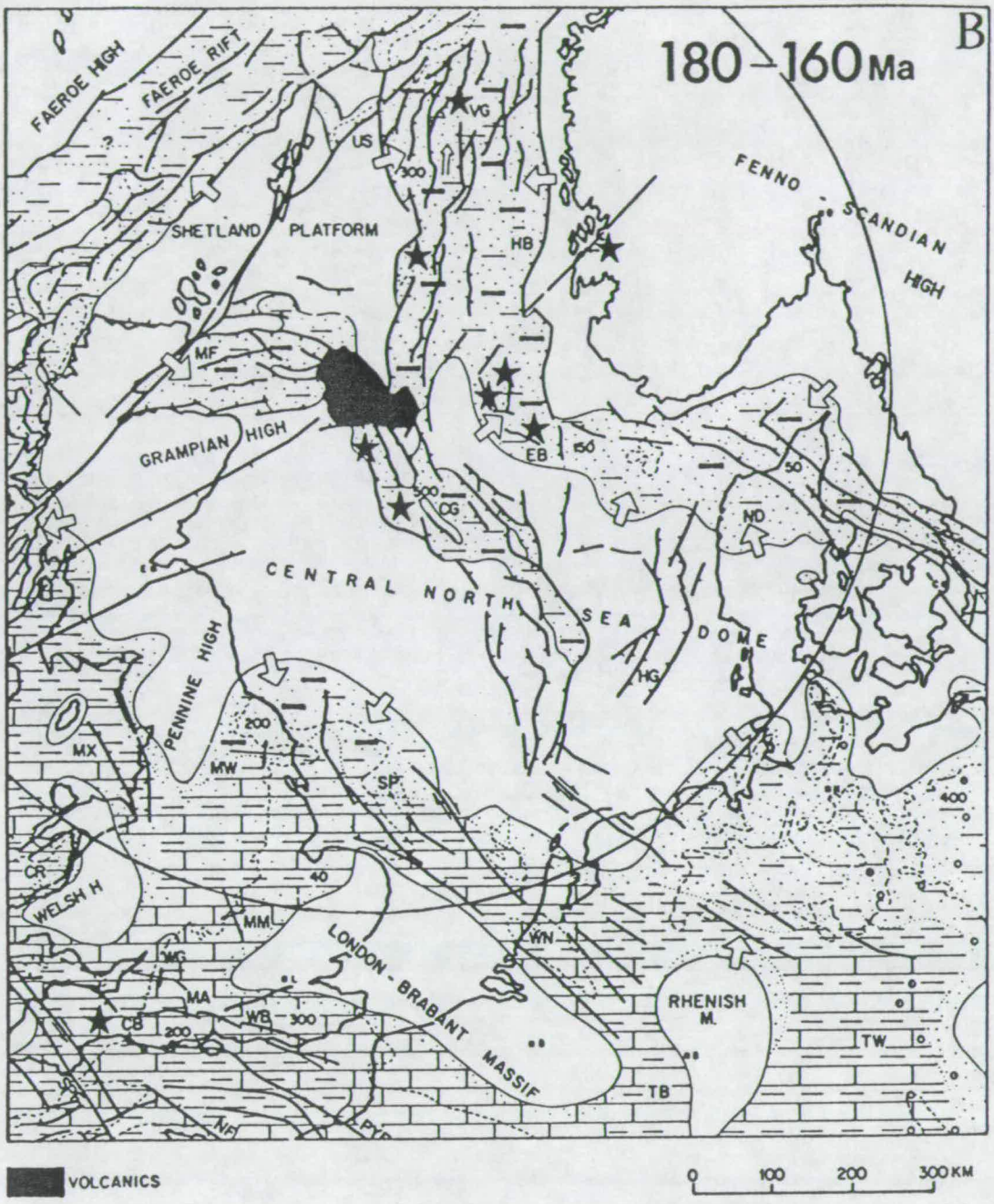

BAJOCIAN - BATHONIAN

FIGURE 7.3 Continued.

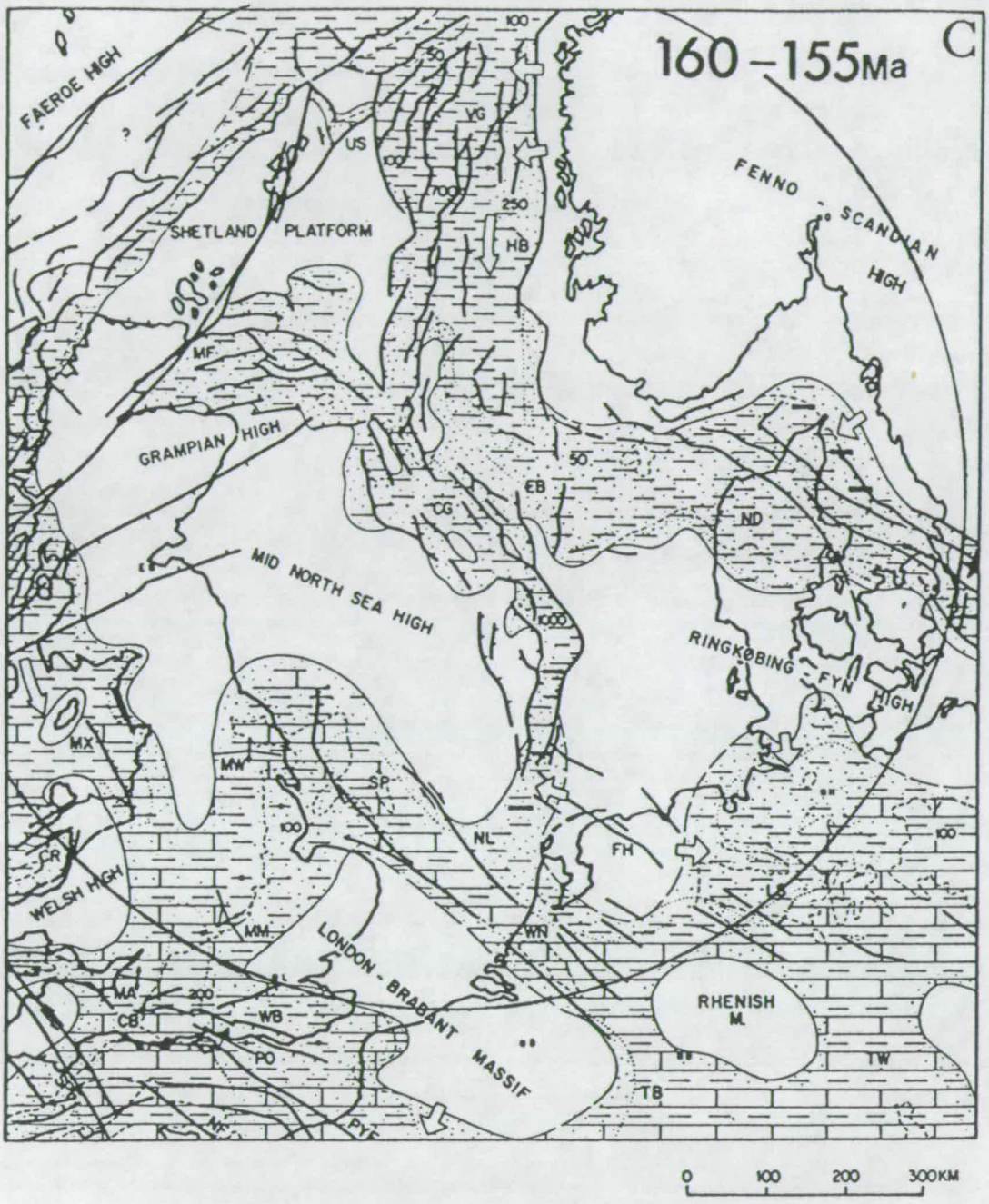

CALLOVIAN-OXFORDIAN

FIGURE 7.3 Continued.

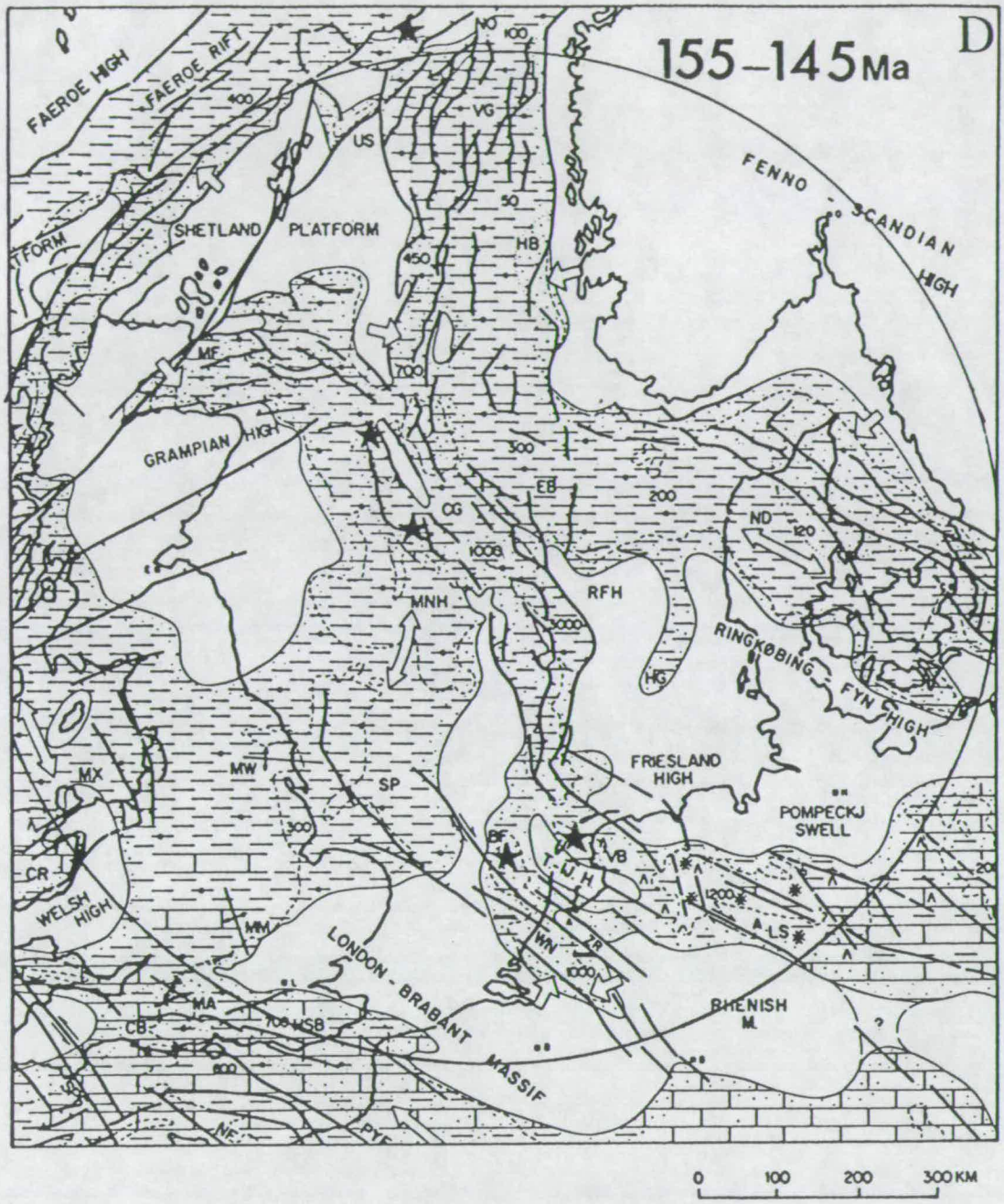

KIMMERIDGIAN - TITHONIAN

FIGURE 7.3 Continued.

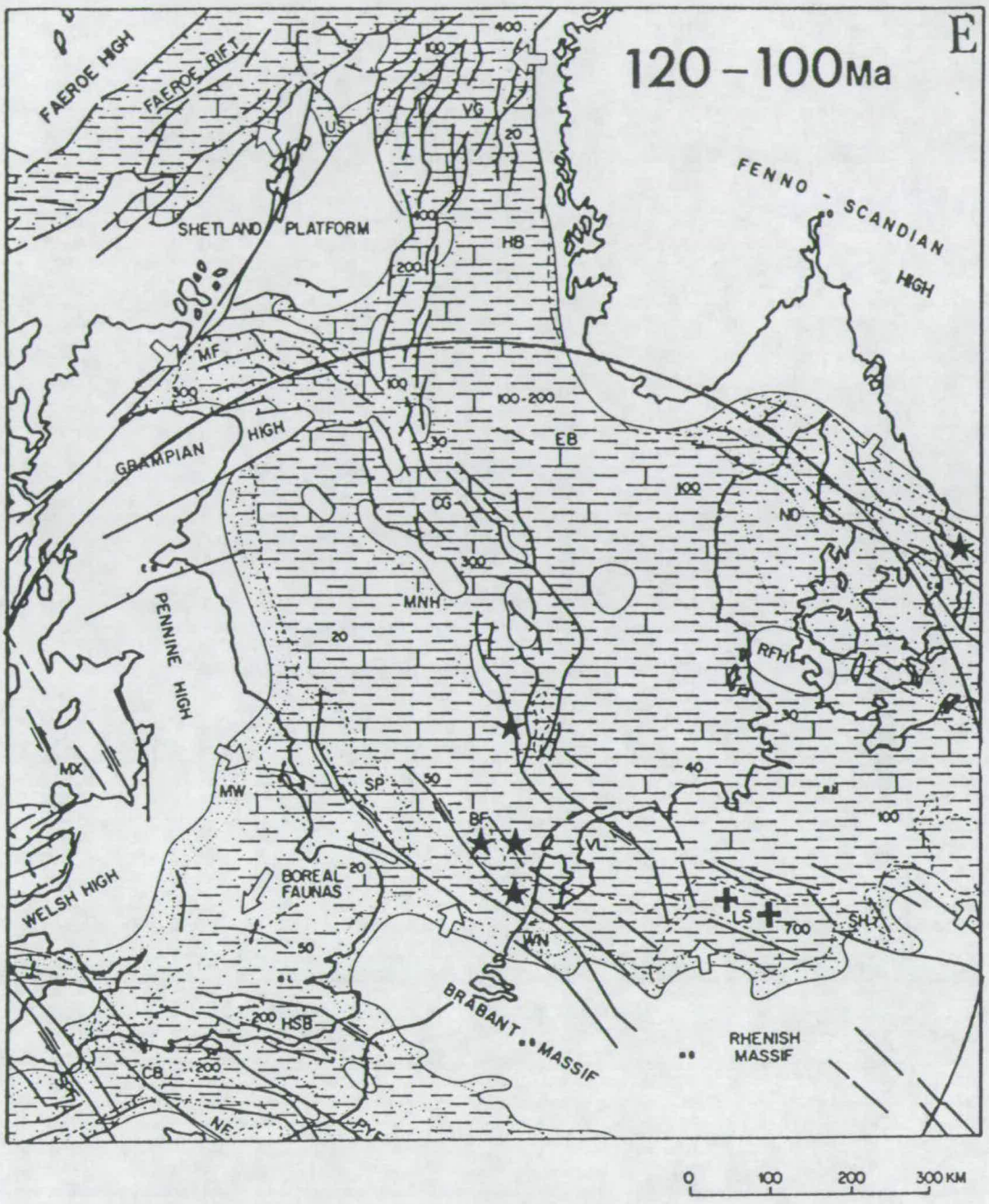

APTIAN - ALBIAN

FIGURE 7.3 Continued.

(see also Appendix B). When only the most reliable dates are plotted (see Figure 4.16) the igneous activity in the Forties region appears to be no older than the lamprophyre intrusion at F/10-1 or the undersaturated volcano at Zuidwal (both in the Netherlands province). Most of the dates fall between 160 and 150 Ma. Even when the slightly older date (~170 Ma) from the Egersund basin or the rather younger, and probably less trustworthy, date from the Central Graben (~130 Ma) are considered they hardly constitute good evidence for a hot-spot trail.

7.2.1.5 Lithospheric Thinning *vs.* Crustal Thinning.

The presence of a vigorously convecting plume beneath the lithosphere might lead to thermal thinning without crustal thinning. Therefore when lithosphere is stretched over a plume the amount of crustal thinning, which results only because of stretching, may be rather less than the total lithospheric thinning which is the result of both mechanisms; there being no longer any need to balance the lithospheric section. The thermal part of the subsidence curves examined in Chapter 6 suggested that the size of the thermal perturbation remaining at the end of rifting in the triple junction region could be approximated by lithospheric thinning by a factor of at least 2 and possibly as much as 3. The minimum estimate from gravity modelling for amount of crustal thinning in this most stretched region is in excess of 3. Therefore unless most of this crustal thinning had occurred as a result of extension in pre-Jurassic times there is no obvious, very large, mismatch between crustal and whole-lithosphere thinning. There is little evidence, from the thickness of pre-Jurassic sediments or from the steepness of pre-Jurassic thermal subsidence curves, for very large amounts of pre-Jurassic extension in this, or indeed any, part of the North Sea.

7.2.1.6 Discussion.

The evidence for regional doming of the Central North Sea during the Middle Jurassic appears to be incontrovertible. The uplift is, however, relatively short lived and appears to be intimately tied to development of the crustal rift rather than to some deeper detached asthenospheric mechanism. Although the dated igneous rocks appear to define a hot-spot trail from ~160 Ma in the north to ~100 Ma in the Netherlands there is no stratigraphic evidence for ages as young as 100 Ma. No temporal shift is observed in magmatic activity when only the dates obtained from unaltered samples are considered. Further, there is no unambiguous evidence of convective thinning due to a plume.

The main conclusion to be drawn from the discussion above is that the observations do not support the presence of a long-lived mantle plume beneath the

lithosphere in the North Sea during the Mesozoic. It is noted that the observations cannot rule out the possibility that rifting may have been initiated over a mantle plume which itself was initiated in the Middle Jurassic and which was relatively short-lived. One further problem with the plume-model was mentioned at the end of Chapter 4 and concerns the timing of the magmatic activity. It is difficult to explain why, if the Forties province is the result of melting over a plume, there is not an intensification of magmatic activity in the Upper Jurassic which is reportedly the main phase of crustal extension. These observations are also difficult to explain using conventional stretching models (see Chapter 6 and section 7.6). The doming and contemporaneous magmatic activity early in the rift phase must therefore be explained by some other mechanism. In section 7.6 it is suggested that both the doming and the occurrence of the Forties province prior to the main upper Jurassic rifting event may be the result of localised, very rapid strain rates in the lithospheric mantle as a result of decoupling of mantle and crustal strain rates (see Chapter 6).

The observations are not consistent with elevated potential temperatures. In this case the simplest approach is to adopt the "normal" potential temperature of 1280±40°C which was justified in Chapter 2. It is noted that this temperature value is itself dependent on the model of McKenzie and Bickle (1988). Arguments which used model-derived values to test models are somewhat circular. In this instance there appears to be no alternative to using the value of McKenzie and Bickle (1988) since the only other estimate for the temperature of the asthenosphere has an error of ±274°C (Parsons and Sclater, 1977; see Chapter 3). While the value of 1280±40°C is adopted in the arguments from this point on the reader is reminded that it is based on the results of equilibrium melting experiments. It was suggested in Chapter 2 that these experiments may overestimate the amount of melt produced if the true process is closer to Rayleigh melting. The "normal" value of McKenzie and Bickle (1988) may therefore be closer to a minimum value.

7.2.2 Initial MBL Thickness.

The thickness of the mechanical boundary layer at the start of rifting determines the minimum pressure obtained by upwelled asthenosphere after lithospheric stretching by a factor β. For a given value of β the pressure at the base of the MBL after stretching is greater for a larger initial thicknesses of MBL. There are a number of ways of estimating the thickness of the MBL in the steady state or the thickness of the "lithosphere" at the present time. Unfortunately there is no direct way of measuring the thickness of the MBL of the North Sea lithosphere prior to

rifting in the Middle Jurassic. Three arguments may be used to estimate the thickness of the MBL in the North Sea:

(1) The thermal time constant method (Barton and Wood, 1984; McKenzie and Bickle, 1988; Latin *et al.*, 1990 a,b; Latin and White, 1990): This argument depends upon the observation that the form of the subsidence in the North Sea depends upon a thermal time constant which is similar to that of the oceans (~60 Ma) and thus a similar steady state lithosphere thickness is implied (see Chapter 3). In the oceans the plate thickness is reported to be 125±10 km (Parsons and Sclater, 1977) with a MBL thickness of 100 km (McKenzie and Bickle, 1988). The implication is that the North Sea like many other continental non-shield areas (see Chapter 3) has a steady state MBL thickness of ~100 km. It seems likely that the error on this value will be similar to that on the value of the plate thickness; i.e ±10 km. A value of 100±10 km may be appropriate for the initial thickness of the MBL prior to Jurassic rifting in the North Sea. This does, however, assume that the thermal effects of any pre-Jurassic rifting events had completely decayed away before the start of the Jurassic rift phase. As is discussed below this assumption would appear to be valid.

(2) The Rayleigh wave dispersion method (Stuart, 1978): Studies of Rayleigh wave dispersion data may be used to estimate the depth to the top of the seismic low velocity zone which is inferred by some authors to mark the base of the lithosphere (cf. Dziewonski, 1971; Bott, 1982; Calcagnile, 1982). The low seismic velocity zone does not, however, necessarily mark the base of the MBL or long term "plate" as seismic velcities are a measure of a short term property. Stuart (1978) used a dispersion study to determine a regional phase velocity curve for the North Sea. A velocity model was then used to calculate the depth to the top of the low S-wave velocity zone by inversion methods. Stuart reports a "lithospheric thickness" of between 80 and 90 km but remarks that values as low as 70 km or as high as 100 km give equally good results. The best estimate of the depth to the low velocity zone is therefore 85±15 km, a value in close agreement with the value for the thickness of MBL estimated from the subsidence. Unfortunately this measurement does not necessarily provide any information about the pre-rift thickness of the MBL.

(3) The ultra-deep seismic reflection method (Lie *et al.*, 1990): Recent ultra-deep seismic reflection studies have revealed "*continuous and virtually horizontal reflectors in the lower continental lithosphere down to depths of 100-110 km below the Skagerrak (Scandinavia)*" (Lie *et al.*, 1990). According to Lie *et al.* (op cite.) these reflectors occur close to the base of the "lithosphere" in the area which occurs between 110 and 120 km when it is measured from Rayleigh wave dispersion (Calcagnile, 1982) and is at ~125 km according to the thermal subsidence (Pederson

et al., in press). If such reflectors are real, and are not artefacts of data processing, then they may represent either shearing or magmatic underplating at the base of the present day MBL. The anisotropies responsible for the reflections are not expected to be preserved in the convective TBL.

The difference between the values obtained from the different methods may be due to two main reasons; (1) The methods are measuring responses to different physical properties over different time scales, and (2) the first method measures an inferred steady-state condition while the second and third measure the present condition; the lithosphere in the North Sea may not yet have fully returned to the steady state. None of the measurements necessarily give accurate values for the thickness of the MBL immediately prior to Jurassic rifting.

In order to determine the initial thickness of the MBL it is necessary to establish the likely degree of thermal reequilibration of the lithosphere at the start of rifting. It is difficult to estimate the position of the geotherm at the start of Jurassic rifting because the precise timing, duration, and importance of Triassic rifting is not known. The method used here to determine the thermal structure at the start of Jurassic rifting is as follows:

(1) Magmatism in the Middle Jurassic of the North Sea appears to occur close to the start of rifting (i.e. within 10-20 Ma). If this observation is true of most rifts then perhaps the suite of Triassic dykes in the Sunnhørdland region of Norway provide the best indication of the onset of Triassic rifting (ca. 220 Ma). The subsidence record preserved in well 17/9-1 (see Figure 6.9) clearly goes back as far as 220 Ma and perhaps a better estimate for the timing of Triassic rifting is 250 Ma. The second estimate is in agreement with the rift phase suggested by Beach *et al*, (1987) while the first (220 Ma) is used by Giltner (1987) for modelling the northern Viking Graben.

(2) The Triassic rift episode is assumed to be instantaneous. There is no good reason for assuming instantaneous rifting but it does make the calculations simpler.

(3) The amount of lithospheric thinning during the Triassic rift episode is not known. In the wells examined in Chapter 6 (e.g. 17/9-1, 29/14-4, 22/15-1) its thermal effects never appeared to be large (i.e. β of 1.15-1.25). To maximise the effect of Triassic rifting on the starting geotherm in the Jurassic, the stretching factor is assumed to be 2.

(4) The effects of Triassic rifting on the Middle Jurassic geotherm were calculated[1] by assuming instantaneous homogeneous stretching by a factor of 2 at 250 Ma and

[1] The calculation was performed using the finite difference scheme described at the end of Chapter 3.

then conductive cooling for 70 Ma until 180 Ma when the Middle Jurassic phase is assumed to start. Cooling over 70 Ma rather than 90 Ma will maximise the remnant thermal perturbation if Jurassic extension did not start until 160 Ma. It was necessary to assume that the lithosphere was in equilibrium at the start of Triassic rifting (i.e. that the MBL had a value of 100 km). The calculated geotherm at the end of this Triassic phase is shown in Figure 7.4 where it is compared with the steady state geotherm for a MBL of 100 km. The effective thickness of the MBL prior to Jurassic rifting in this rather extreme example is ~80 km. Bringing the rift phase forward, from 250 to 220 Ma, would increase the thermal perturbation which remained at the start of Jurassic rifting. Decreasing β would decrease the temperature anomaly while adding the effects of finite duration rifting will increase the importance of the Triassic event on the Jurassic geotherm.

Figure 7.4 clearly shows the problems involved when attempting to determine the time-temperature path of a *convective* geotherm. The key question concerns whether or not overturn of the TBL (thermal boundary layer) occurs in the 70 Ma cooling period. Figure 7.4A shows the geotherm assuming that no TBL overturn occurs between the Triassic rift phase and 180 Ma. If TBL overturn did occur then the stretched geotherm in Figure 7.4A only shows the minimum temperature perturbation which remained by 180 Ma. TBL overturn would have the effect of replacing the material between ~80 and 120 km with hotter asthenosphere. In this case the geotherm prior to Jurassic stretching would correspond to that for lithosphere with a MBL of 80 km in the steady state (the dashed line in Figure 7.4A). Given that the TBL must overturn at least once in ~60 Ma beneath the oceanic MBL (see Chapter 3), the curve labelled for 180 Ma in Figure 7.4B (the dashed line in Figure 7.4) seems most likely.

In conclusion the steady state MBL in the North Sea is probably close to 100 km thick. The effects of Triassic stretching on the thermal structure of the lithosphere are unlikely to be significant in the Jurassic since even a relatively extreme example, which involves Triassic stretching by a factor of 2 and TBL overturn, only results in an initial MBL of 80 km for the Middle Jurassic. Given that the effects, however small, of Triassic rifting may remain in the Middle Jurassic, the thickness of the MBL prior to rifting is considered to be closer to 90 km than to 100 km. It is impossible to say whether or not this value is applicable to all parts of the North Sea. All of the areas considered later, however, have probably been subject to some small amount of Triassic extension.

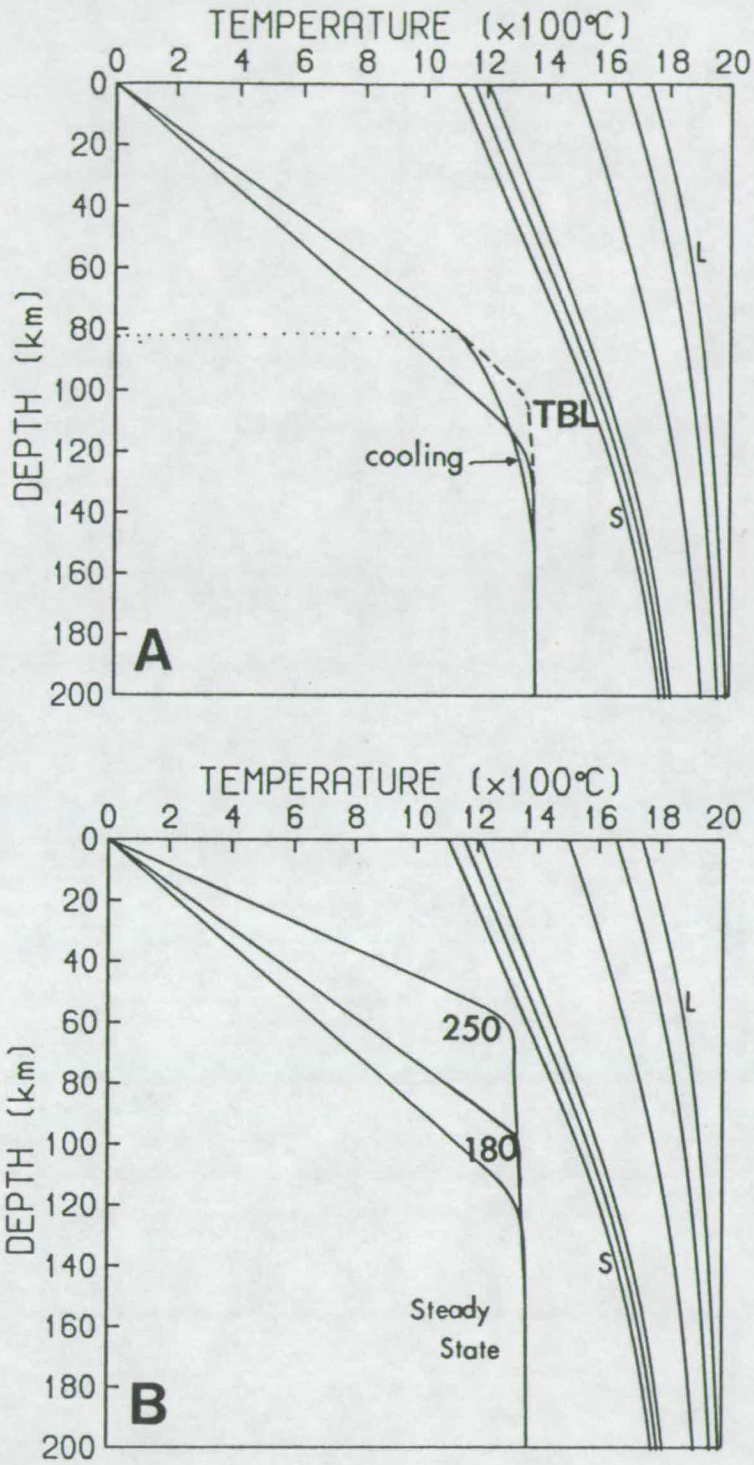

FIGURE 7.4 The effects of Triassic stretching on the thickness of the MBL prior to rifting in the Middle Jurassic. Upper diagram (A) shows geotherm in the steady state and after conductive cooling for 70 Ma following stretching by a factor of 2. The MBL, 100 km thick in the steady state, is ~80 km thick after this amount of cooling. Note how the TBL has been allowed to cool below its steady state potential temperature (dashed curve). Lower diagram (B) shows the position of the geotherm at 3 different times. (1) Directly after instantaneous homogeneous stretching by a factor of 2 in the Triassic (250 Ma). (2) At 180 Ma after 70 Ma of conductive cooling of the MBL but maintaining the potential temperature of the TBL by convective overturn. (3) In the steady state.

7.2.3 Lithospheric Thinning (β and ε).

The amount (β) and rate (ε) of stretching are also very important parameters. Less discussion of their values for the Jurassic North Sea is required in this section since they were discussed in Chapter 6. If, as seems likely, a mantle plume was not present beneath the North Sea region in the Mesozoic, then a rapid rate of strain is implicit in the fact that the Forties province occurs so early in the rift phase. The early occurrence of the largest degree, shallowest level melts (see Chapter 5) so early during rifting suggests that within the first 10-20 Ma of rifting the maximum amount of decompression had occurred beneath the Forties region (see section 7.5). The same is presumably true of the other regions of magmatic activity. In this case the assumption of instantaneous rifting is probably justified; this is fortunate since it simplifies the melting calculations considerably.

Estimated stretching factors were given in Table 6.1 at the end of Chapter 6. In Chapter 6 it was suggested that model curves for homogeneous stretching could be used to give reasonable estimates of β providing that they were only compared with the thermal part of the subsidence curves. The steepness of the thermal part of a subsidence curve is proportional to the size of the thermal perturbation which remains at the end of rifting. The values of β obtained in this way, which are probably close to minimum values, were between 2 and 2.5 for the Forties region. Because the subsidence path during the syn-rift period is poorly constrained and because estimates for the amount of total crustal thinning and the amount of pre-Jurassic stretching are associated with large errors, the true value of β in this triple junction region may have been as large as 3 in the Middle Jurassic. The amount of stretching on the flanks of the Central Graben was probably between 2 and 1.5. The Jurassic β value observed on the edge of the Egersund basin was close to 1.2 but it was probably greater in the centre (hence the value of <1.5 in Table 7.1).

7.2.4 Summary of Parameter Values.

The potential temperature of the asthenosphere is unlikely to have been any different from the average potential temperature. The average value is 1280±40°C, however, for reasons explained earlier and in Chapter 2, values slightly higher than 1280°C are probably most likely. The thickness of the MBL in the North Sea is probably close to 100 km in the steady state. Immediately prior to Jurassic rifting the lithosphere may have still been cooling from the effects of Triassic rifting. A value of ~90 km is preferred for the initial thickness of the MBL. The rate of stretching

appears to have been sufficiently rapid that it may be assumed instantaneous. The amounts of stretching are estimated to have been between 2 and 3 in the Forties region, between 2 and 1.5 in the region of the Central Graben province, and probably less than 1.5 in the Egersund region. Note that the stretching factor in the Netherlands area is unconstrained. Note also that for the purpose of the following discussion the solidus position is assumed to be that of dry peridotite. The preferred parameter values are summarised in Table 7.1; see Chapter 6 for β values (β_{Jur} = Jurassic, β_c = total time-integrated stretching from crustal thinning).

TABLE 7.1 : Preferred Parameter Values.

Location	T_p°C	MBL	β_{Jur}	β_c
Viking. G.	1280±40	90-100	1.5-2.25	2.0-2.5
Forties.	1280±40	90-100	2-3	>3
Central.	1280±40	90-100	2-2.3	<3
Egersund.	1280±40	90-100	<1.5	?

7.3 Quantitative Predictions *vs.* Observations.

7.3.1 Locations of Magmatic Activity.

By using the parameter values given in Table 7.1 in conjunction with the parameterisations of McKenzie and Bickle (1988) it is possible to predict those locations where the solidus for anhydrous peridotite will have been intersected during rifting in the North Sea (see Chapters 2 and 3 for a more detailed discussion).

Figure 7.5 shows the region of parameter space in which melting of dry peridotite is first expected to occur. Each diagonal line corresponds to the values of β and T_p required to intersect the solidus for a given initial MBL thickness. It is clear that if the initial MBL was 90 km thick, then melt would be expected to occur within the Forties province for almost the entire spectrum of preferred values of T_p and β (see Table 7.1). As long as the normal T_p is equal to or greater than 1280°C (see dashed line in Figure 7.5) then melt is predicted in the Forties region for all three

MBL thicknesses for all possible values of β (i.e. from 2 to 3). The observation of melt in the Forties province is therefore entirely consistent with the large amounts of stretching in that area.

The Viking and Central Graben areas appear to have been stretched by a smaller amount than the area of the triple junction during the Middle Jurassic. Melt is only predicted for these regions when T_p>1280°C if the initial thickness of the MBL is <100 km and only then at the upper range of predicted β values (i.e. 2-2.25). It is perhaps not surprising, therefore, that very little magmatism is noted in the Central and Viking Graben areas, and indeed elsewhere in the North Sea region. The Central Graben igneous province may reflect very small amounts of melting (see Chapter 5) but the ultrapotassic nature of these rocks may point to volatile-controlled solidi and large amounts of melting of peridotite which is more LILE enriched than the source of the alkali basalts (see section 7.4). It is possible that a very small amount of melt was produced beneath the Viking and Central Grabens but that it was underplated.

In an attempt to account for a discrepancy between the depth to the Moho inferred from gravity modelling and that observed on deep seismic reflection profiles Holliger and Klemperer (1989) suggest that as much as 3 km of basalt may have been added to the crust beneath parts of the Viking Graben. It is noted that they make two very significant assumptions before arriving at this figure. Their first assumption is that the value of β_c estimated from crustal thinning can be used to make predictions concerning melting. This is clearly not so since β_c results from several events (at least two) and is therefore time integrated. Second they use Stuart's (1978) *minimum* estimate for the present day lithospheric thickness (70 km) as their value for the initial thickness of the MBL. Perhaps their discrepancy may be more due to problems inherent in the methods for locating the seismic- and the gravity-Moho than a real feature. There seems to be no justification for deducing that underplating has occurred and that a discrepancy is somehow to be expected.

It is clear from Figure 7.5 that the nephelinites and ultrapotassic rocks of the Egersund Basin would not be predicted by the theory. Although no estimate of extension was available for the Netherlands region, the basanitic and ultrapotassic nature of the mafic rocks, together with their intermediate position (between Forties and Egersund) in terms of trace element enrichment (see Chapter 5), may imply that the amounts of stretching were closer to 1.5 than they were to 2.

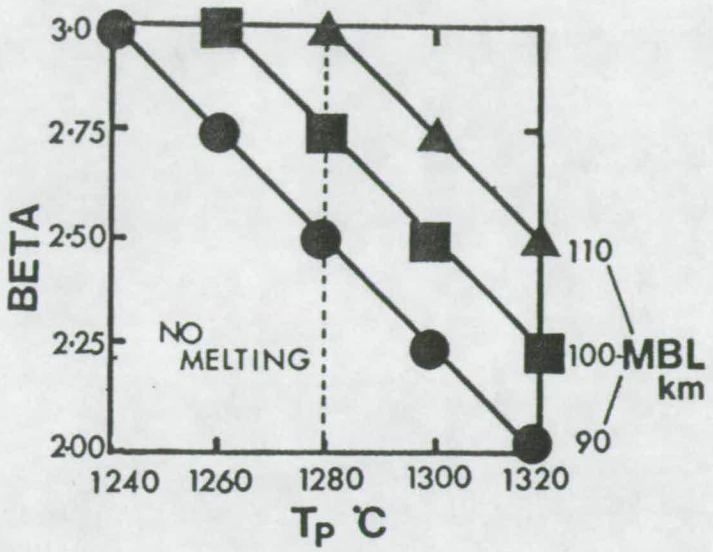

FIGURE 7.5 The effect of β (2-3) and T_p (1280±40°C) on onset of melting (0<melt %<~0.5) of dry peridotite. Circles, squares and triangles mark melting at initial MBL thicknesses of 90, 100 and 110 km respectively. The region of parameter space to the right of the dotted line and between the circles and squares is considered to be the most likely in Forties area of the North Sea.

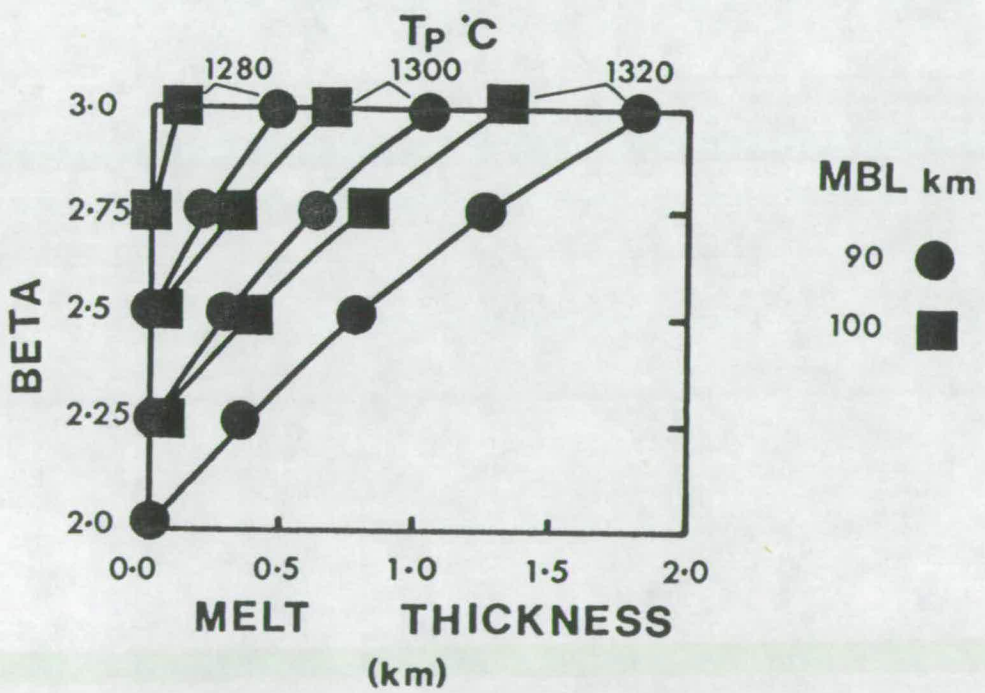

FIGURE 7.6 The predicted thickness of melt (km) in the Forties region of the North Sea as a function of β (2-3), T_p (1280, 1300 and 1320°C), and initial thickness of MBL (90 and 100 km).

7.3.2 Melt Thickness.

The Forties province is the only igneous province predicted from the theory. The total amount of mafic rock in the Forties region is uncertain. In Chapter 4 it was shown that maximum thickness estimates are between 1.5 km and 3 km. On the other hand Leeder (1983) estimated a mean thickness of basalt of only 350m while Latin *et al.* (1990 a,b) considered that a melt thickness of less than 0.5 km was most likely. Given that the basaltic rocks have undergone relatively small degrees of fractional crystallisation it is unlikely that there are large magma bodies at depth. The most likely average thickness of the melt produced in the Forties region is considered to be between 0.5 and 1 km and it is unlikely to exceed 1.5 km.

Figure 7.6 shows model predictions of melt thickness at different values of T_p, β and initial MBL thickness within the preferred region of parameter space. A melt thickness of 0.5 km is only achieved at a T_p of 1280°C if β is 3 and the initial MBL is 90 km thick. At slightly higher potential temperatures (~1300°C), however, the production of between 0.5 and 1.0 km of melt presents no problems when the MBL is initially 90 km thick. At the top of the preferred range in T_p (1320°C) the required melt thickness can be produced at all values of β and for both thicknesses (100 and 90 km) of initial MBL.

Although anomalously high values of T_p (i.e. $T_p >> 1280 \pm 40$°C) are considered unlikely (see discussion in section 7.2) it is worth considering the amounts of melt which would be expected from rifting over such high T_p regions. Figure 7.7 shows the estimated melt thickness for T_p's of 1280, 1380 and 1480°C. Note first that with a high temperature mantle plume (T_p=1480°C) very large thicknesses of melt would be predicted for the entire length of the Viking and Central Grabens. The thickness of melt in the Forties province might reach as much as 15 km. Since the crust in that region is probably less than 15 km thick (see Chapter 6, section 6.4.7 and Figure 6.21) this solution creates more problems than it solves! Lower anomalous temperatures (T_p=1380°C) lead to the production of significant thicknesses of melt (>0.5 km) in the Viking and Central Graben areas and potentially a very large thickness of melt in the Forties region (up to 5 km). In both cases it is difficult to keep the predicted melt thickness consistent with the observations. This is true even if the extreme upper limit of 3 km is used for the observed melt thickness in the Forties region.

At a "normal" potential temperature the model predictions for the thickness of melt in the Forties region do appear to be consistent with the rather approximate observational estimates.

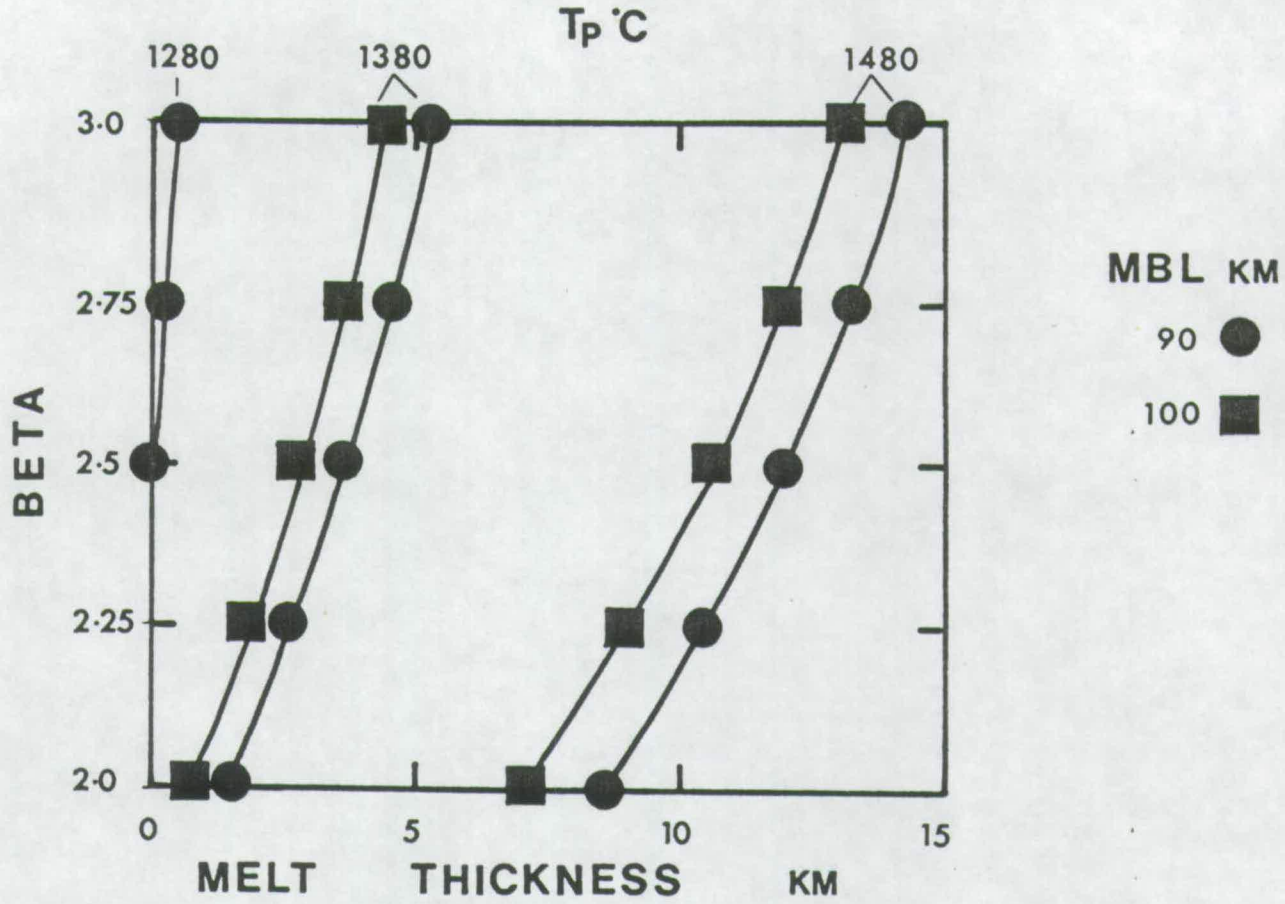

FIGURE 7.7 The predicted thickness of melt (km) at "plume" potential temperatures (1380 and 1480°C) compared with "normal" potential temperatures (1280°C).

7.3.3 Average Melt Fraction and Depth of Melting.

At a given value of T_p and initial MBL the per cent of melting increases with β (Figure 7.8 and 7.9) while the average depth (and pressure) of melting decreases (Figure 7.10). For the parameter values which are preferred for the Forties region (T_p=1280-1320°C, β=2-3, MBL=90-100 km) the point and depth average (see Chapter 2 for definition) degree of melting is predicted to be less than 5.5% and the predicted average depth of melting lies between 40 and 57 km. These values for the degree of melting lie within the range estimated from simple modal melting calculations which reproduce the ratios of immobile trace elements observed in the Forties Basalts (i.e. < 3% melting; see Chapter 5, section 5.6.3).

The predicted degrees of melting are small and therefore agree with the observed degree of fractionation of incompatible trace elements and the small volume of melt. The values for the average depth of melting (<57 km), however, appear to contradict the trace element evidence since it implies that melting occurs in the spinel stability field. The observation that the average Forties basalt, despite being highly LILE-enriched relative to average MORB, is more depleted in Y and HREE than average MORB (see Chapter 5) suggests that at least some melting took place within the garnet stability field; i.e. at depths > 60-70 km. As Figures 7.9 and 7.10 show, potential temperatures in excess of 1320°C are required before melting occurs on the *dry solidus* at depths greater than 60-70 km, the experimentally determined stability limit for garnet (see Chapter 2). As is discussed in section 7.5 (see also Latin *et al.*, 1990 a,b) there is no problem with the depth of melting if the LILE budget of the magma is largely controlled by melting on *volatile-controlled solidi* which, for a given potential temperature, are intersected at greater depths than the dry solidus. Volatile-controlled melting must be invoked to explain ultrapotassic and nephelinitic magmatism elsewhere in the North Sea so it seems likely that it will also be important in the Forties region (see sections 7.4 and 7.5). The volume of such volatile-controlled melt is, however, likely to be very small. Thus, although, they may affect the LILE budget and relative HREE depletion of the Forties basalts they are not likely to account for more than a small part of the total volume of melt in the Forties region (see section 7.5).

7.3.4 Melt Composition.

The predicted melt compositions, in terms of oxides of major elements, are shown, together with their errors, in Figure 7.11 where they are compared with the

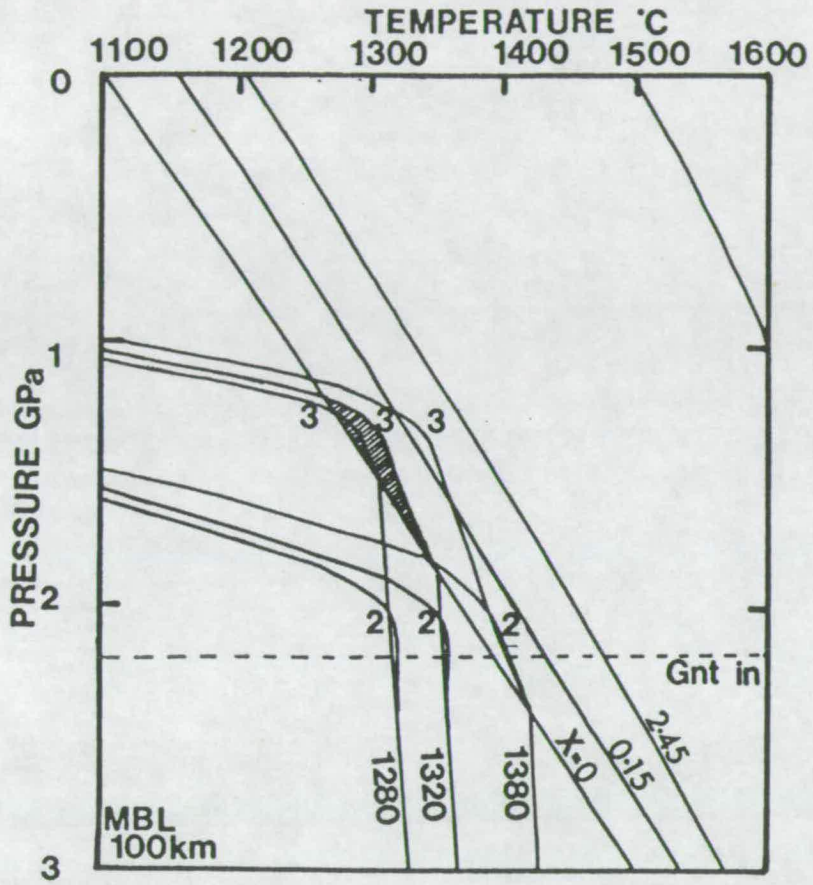

FIGURE 7.8 Convective geotherms for T_p's of 1280, 1320 and 1380°C stretched by β-factors of 2 and 3. The approximate stability limit of garnet (MacGregor, 1965; see Chapter 2) is indicated by the dashed line. Note that the region of melt production in the Forties region of the North Sea (shaded) is not within the garnet stability field.

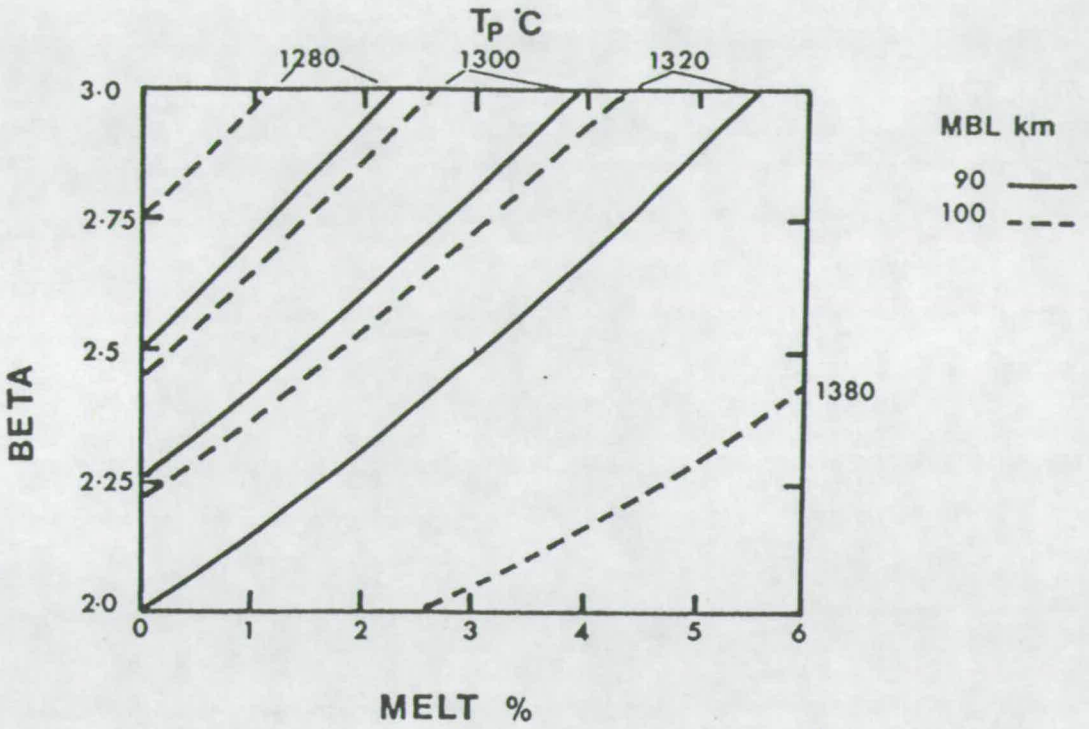

FIGURE 7.9 The variation of predicted average melt % (point and depth average, see Chapter 2) with β (2-3), T_p (1280, 1300,1320 and 1380°C), and initial thickness of MBL (90 and 100 km).

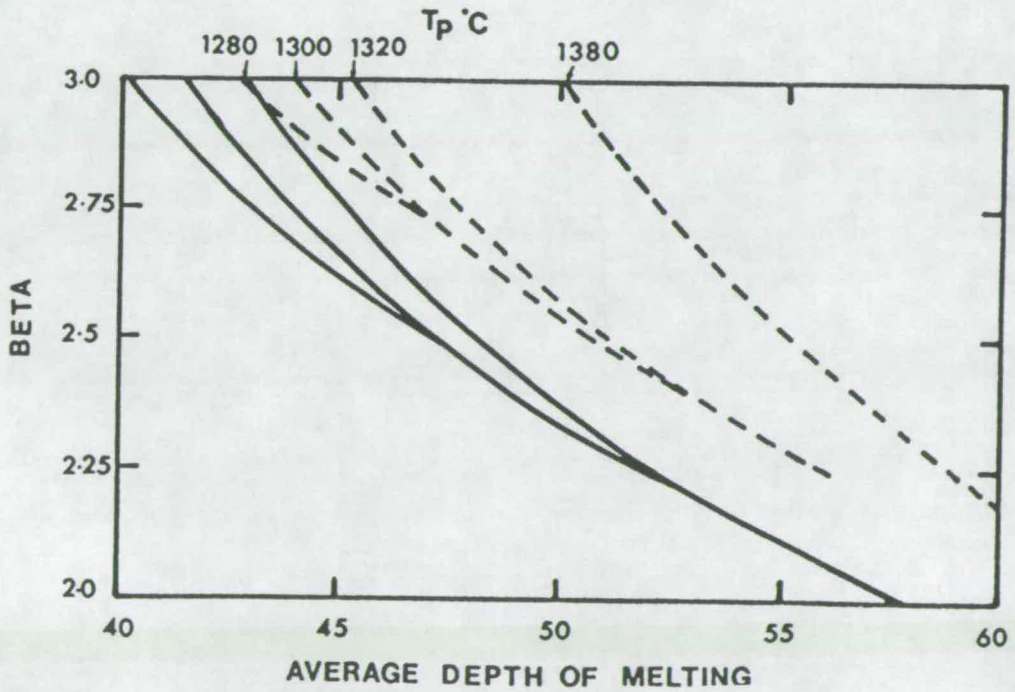

FIGURE 7.10 The variation of the predicted average depth of melting (point and depth average, see Chapter 2) with β (2-3), T_p (1280, 1300,1320 and 1380°C), and initial thickness of MBL (90 and 100 km).

freshest rocks (LOI < 4wt.%) from the Forties province. The predicted compositions are for an initial MBL thickness of 100 km and are labelled with values of T_p and β. Averages of the freshest ultrapotassic rocks from the Central Graben (30/16-A13Y, SH1) and Netherlands (F/10-1, PL1) are also shown. The position of these ultrapotassic rocks on the diagrams in Figure 7.11 will be discussed further in section 7.4.

The variation in the major element composition of the different samples from the Forties province is largely a function of clinopyroxene and olivine fractionation and accumulation (see Chapter 5). The few data points with MgO>15 wt.% are very crystal-rich ankaramites. The bulk of the samples are mafic basalts with 8<MgO<12 wt.% although there are 5 more highly fractionated (hawaiitic) samples with MgO<6 wt.%.

The key question concerns whether or not the predicted melt compositions lie within the array defined by the Forties data set. If they do not then a second question concerns whether they can be brought into coincidence with the Forties data by fractionation of olivine and clinopyroxene alone. The main conclusions to be drawn from comparing the predicted compositions with the Forties alkali basalts in Figure 7.11 are summarised as follows:

(1) The degree of fit of the predicted melt compositions with the observed compositions is, within the region of error, excellent for FeO, CaO, and SiO_2.

(2) The fit is less good for Al_2O_3 and Na_2O. In both cases the predicted compositions fall to higher values, at a given amount of MgO, than the observed compositions. These differences are difficult to explain by fractional crystallisation of olivine and clinopyroxene.

(3) The observed concentrations of TiO_2 and K_2O are between 50 and 75% higher than the predicted values

(4) Differences in T_p for a given value of β produce different predicted melt compositions. However, many of the differences introduced on melting are lost during subsequent crystallisation of olivine. One possible means of distinguishing melts from different T_p's hinges on the pressure sensitivity of FeO and SiO_2. The smallest melt fractions (those at lowest β) at higher values of T_p occur at greater depths than those at lower T_p's and are therefore more enriched in FeO and more depleted in silica. Unfortunately the FeO content of a melt is also highly dependent on the oxidation state of the source region (a poorly constrained variable; M. Wilding, pers. comm. 1990) and silica is associated with the largest error. Nonetheless the SiO_2 content of the Forties basalts is sufficiently high to preclude potential temperatures significantly greater than 1280°C (i.e. 1480°C) since at the

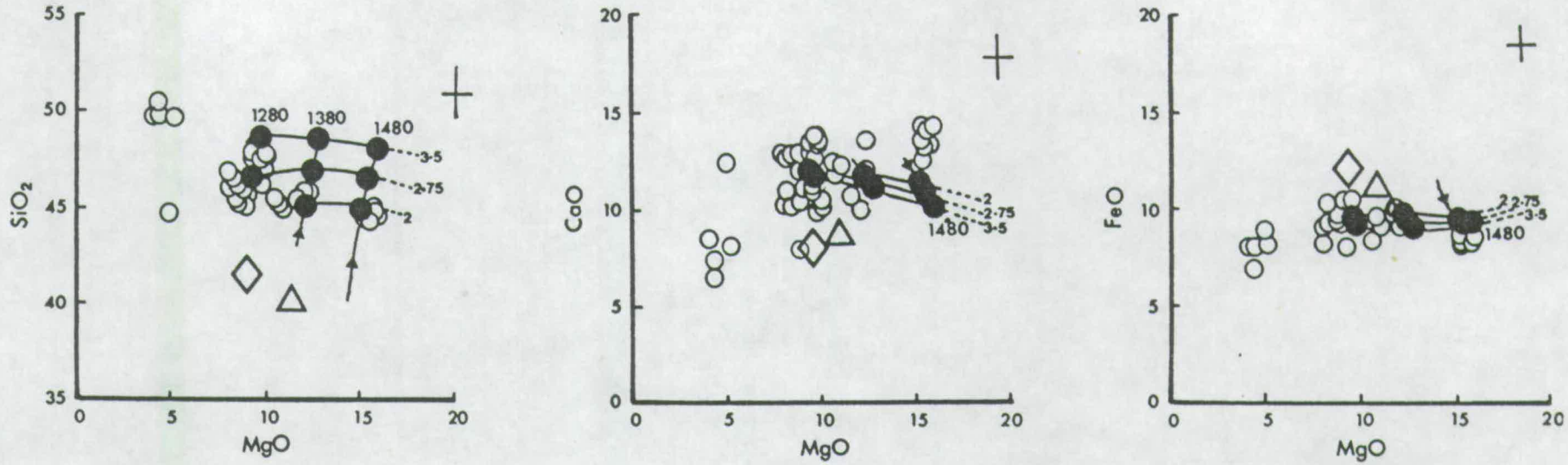

FIGURE 7.11 Predicted point and depth average melt compositions, as wt.% oxides (parameterisation (a) of McKenzie and Bickle (1988); filled circles joined by lines of constant β and constant T_p), as a function of β (2, 2.75 and 3.5) and T_p (1280, 1380 and 1480°C) for stretching of a MBL initially 100 km thick. Cross in top right hand corner of each diagram represents twice the mean error given by McKenzie and Bickle (1988). The freshest basalts from the Forties province (LOI<4 wt.%) are represented by the open circles. The diamond and the triangle represent mean compositions of fresh (LOI<4 wt.%) ultrapotassic rocks from the Central Graben and Netherlands provinces respectively (see Table 7.2).

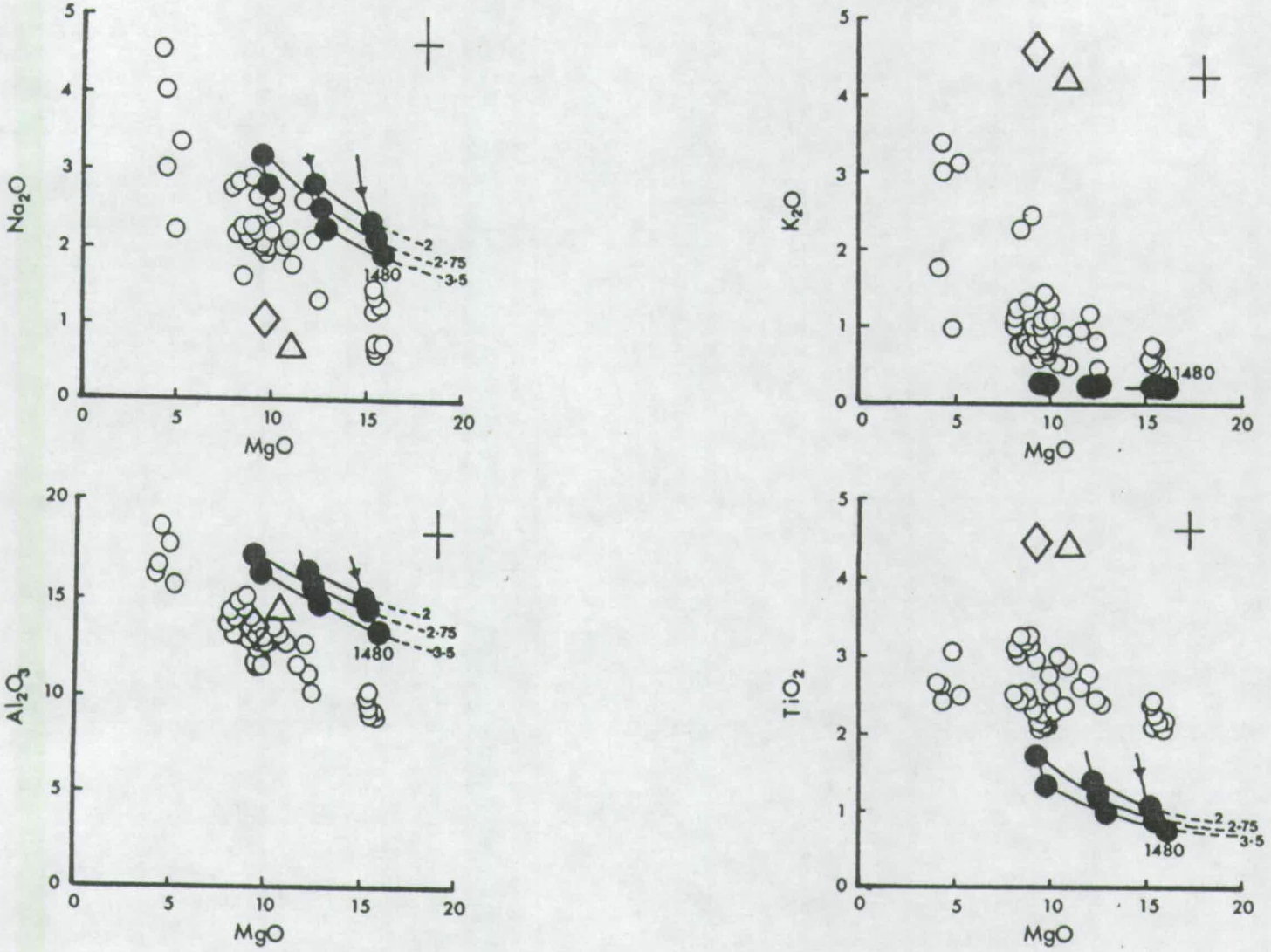

FIGURE 7.11 Continued.

high β values required (between 2 and 2.5) for these higher temperatures the amount of melt produced is likely to be too large.

Figure 7.12 shows the Forties data set, together with the point average and point and depth average melt compositions (see Chapter 2 for definitions) for stretching a MBL, initially 90 km thick, by a factor of 2.75 over asthenosphere with a T_p of 1280°C, projected from An and from Di into the normative tetrahedron of Walker *et al.* (1979); see Figure caption for details. Higher T_p compositions (not shown) plot towards Ol. The general agreement between the observations and predictions is good. The slight disagreement is due largely to the mismatch with Al_2O_3 since Na_2O, K_2O and TiO_2 are not included in this norm calculation (see Figure caption). The alkali basalts contain 3-5% less Al_2O_3 than the predicted melts (see Figure 7.11) and this leads to their relatively higher value for Q and lower value for Ol in the norm. The importance of clinopyroxene accumulation and addition of CaO during alteration of the Forties suite is clearly shown by the trend towards Di in the lower diagram in Figure 7.12.

In summary, the main conclusion from Figures 7.11 and 7.12 is that the Forties data are compositionally very similar to the melt compositions predicted from the parameterisation of McKenzie and Bickle (1988). The data are generally closer to the predictions for values of T_p which lie between 1280 and 1380°C and for values of β between 2 and 2.75. The main mismatch occurs for the values of K_2O and TiO_2 which are both much higher, and for Al_2O_3 and Na_2O which are both lower, in the basalts than they are in the predicted melts.

7.3.5 Summary and Discussion.

Of all of the Mesozoic igneous provinces in the North Sea only the Forties province is predicted by the theory. The large amount of stretching in the Forties region makes the solidus of garnet peridotite accessible to the geotherm at a normal potential temperature. The central location of the Forties province supports a coaxial rather than a non-coaxial stretching model (see Chapter 3, Latin and White (1990) and Latin *et al.*, 1990b for detailed discussion). The dry solidus is not easily attained by the more modest amounts of lithospheric thinning elsewhere in the North Sea region and magmas in other areas must therefore be produced by volatile-controlled melting.

The estimated thickness of melt in the Forties province (0.5 to 1.5 km) and average melt fraction represented by the basalts (<3%) are both consistent with the model predictions. The depth of melting is inferred to be > 60 km from the relative

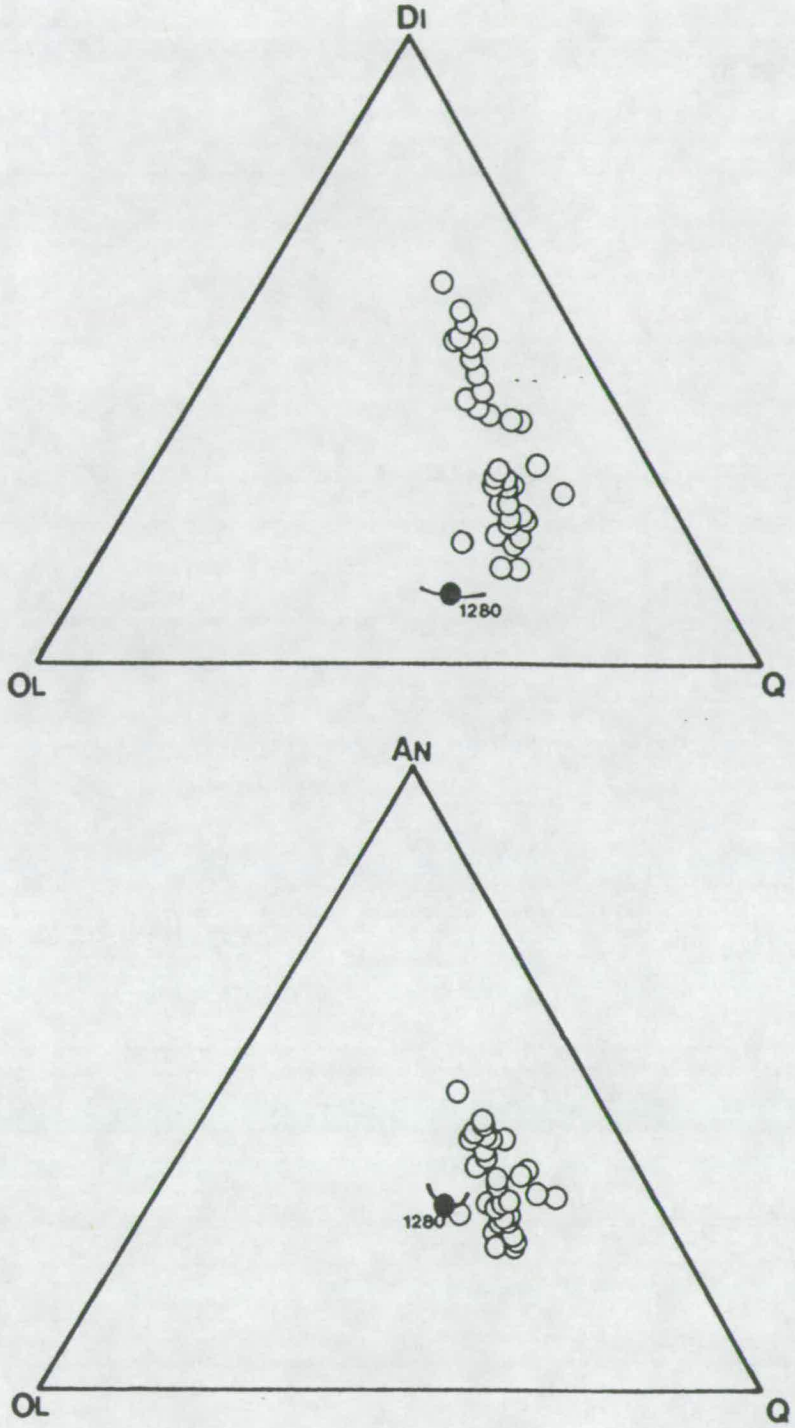

FIGURE 7.12 Predicted melt compositions (β=2.75, Tp=1280°C, MBL=90 km; filled circles = point and depth average compositions, lines = point average compositions) and melt compositions observed in the Forties province (LOI<4 wt.%) plotted in the normative projection of Walker *et al.* (1979) which excludes alkalis. The equations used in the projection are, in mol.%, An=Al_2O_3; Di=CaO-Al_2O_3; Ol=(FeO+MgO+Al_2O_3-CaO)/2; Q=SiO2-(Al_2O_3+FeO+MgO+3CaO)/2.

depletion of HREE in the Forties rocks. The predicted average depth of melting is less than 60 km. Melting at greater depths, within the garnet stability field, may only occur if the T_p is raised above reasonable normal values or if the solidus is lowered by some mechanism (see section 7.5).

The fit between predicted and observed melt compositions must be considered excellent given the reservations expressed in Chapter 2, concerning the results of melting experiments for small degrees of melting and the ability of the parameterisation to successfully predict compositions when the melt fraction is less than ~0.1. The best fit is obtained for SiO_2, FeO and CaO if a T_p between 1280 and 1380°C is chosen. The degree of fit with Na_2O and Al_2O_3 is poor and the fit with K_2O and TiO_2 is very poor. The version of the parameterisation which was used to generate the predicted compositions (Figures 7.11 and 7.12) does not, however, contain a pressure dependence for the bulk distribution coefficients of Al_2O_3 and Na_2O. Walter and Presnall (1990) have shown that the jadeite component in clinopyroxene becomes significant at high pressure. Melts at high pressures (>1.5 GPa) are likely to have lower concentrations of Al_2O_3 and Na_2O than would be predicted by the present parameterisation. A more recent version of the compositional parameterisation (Watson and McKenzie, in prep.) which includes a pressure dependency for Al_2O_3 and Na_2O and which uses an estimated composition for primary hawaiian tholeiite to constrain the compositions of small degrees of melting (< 10%) at high pressures (1.5-3 GPa), is expected to give a much better fit for Na_2O and Al_2O_3 (S. Watson, pers. comm. 1990). Inclusion of the Hawaiian data point in the new version of the parameterisation apparently results in an insignificant change in the accuracy with which it is able to predict the composition of MORB. In the next section an attempt is made to both explain the misfit and account for the compositions of the ultrapotassic rocks by adding melts, which have low concentrations of Na_2O and high K_2O and TiO_2, from a peridotite containing volatile bearing phases.

The most important conclusion of this section, and of the thesis as a whole, is that predictions made with the quantitative theory of McKenzie and Bickle (1988) are consistent with the observations in the most stretched part of the North Sea. Considering the size of the errors involved the predicted compositions and volumes fit the observations remarkably well. This section has, however, like others once again pointed towards the likely importance of volatile components in the source regions of rift basalts. Since the quantitative framework has only been developed for melts from dry-peridotite only qualitative or semi-quantitative predictions can be made where volatiles control the melting process (see next two sections).

7.4 The Origin of the Ultrapotassic Rocks.

The compositions of the ultrapotassic rocks from the North Sea (e.g. 30/16-A13Y (SH1), 29/25-1 (SH2), 17/9-1 (ES1/41,43,46) and F/10-1 (PL1); see Chapter 5) with their high concentrations of MgO (>9 wt.%) and FeO (>10 wt.%) are good candidates for magma compositions which have undergone relatively little change due to little low-pressure fractional crystallisation. Only the very freshest samples are considered in this section; i.e. those with LOI<4 wt.% which are only found in SH1 and PL1. Despite their relatively high Mg number (0.57-0.64; see Table 7.2) they contain between 4 and 5 wt. % of both TiO_2 and K_2O. In Figure 7.11 it is clear that the average compositions of these rocks (see also Table 7.2, Figure 7.13 and Appendix B) are very different to those of the predicted melts (from garnet peridotite). Most notable are their very high concentrations of K_2O and TiO_2. The K_2O content of the ultrapotassic rocks is more than 20 times that of the predicted melts and is 2-3 times that of the average Forties basalt. TiO_2 is 1.5-2 times more abundant in the ultrapotassic rocks than it is in the predicted melt composition. The value of FeO is also somewhat higher than the predicted compositions while SiO_2 and Na_2O are notably lower.

Table 7.2

Averages of analyses of ultrapotassic rocks compared with average of analyses of alkali basalts.

	SH1(3)	PL1(4)	**Forties(112)
SiO_2	41.852	40.07	45.73
Al_2O_3	13.78	14.43	12.84
$FeO_{(T)}$	12.23	10.88	9.33
MgO	9.30	11.0	10.38
CaO	7.90	8.72	11.14
Na_2O	1.00	0.72	2.04
K2O	4.60	4.25	1.44
TiO_2	4.40	4.41	2.74
*Mg#	0.57	0.64	0.66
Ni	17	43	174
Cr	5	104	529
Y	33	28	23

*Mg#=Mg/(Mg+Fe^{II})
**Only samples with >6 wt.% MgO are included.
Brackets indicate number of analyses in average.

The ultrapotassic rocks are clearly not good candidates for melts from garnet peridotite. Their undersaturated mafic character does not favour enrichment in both K_2O and TiO_2 by melting of silicic crust (see Table 7.2). Their very low concentrations of Ni and Cr suggest either a very large degree of fractional crystallisation of olivine and clinopyroxene or melting of a source which contained little olivine or pyroxene. Their generally mafic, undersaturated character does not support large amounts of fractional crystallisation.

Figure 7.13 shows the two ultrapotassic averages together with the field (dashed line) and average (circle) of the Forties data and the predicted melt compositions from Figure 7.11. Also shown in Figure 7.13 are points (filled circles) from Lloyd *et al.* (1985) which represent the compositions of experimental partial melts of a Ugandan phlogopite-clinopyroxenite at a pressure of 30 kb (3 GPa).

The similarity between the ultrapotassic compositions and the melts from phlogopite-pyroxenite in Figure 7.13 is striking. The degree of fit for SiO_2, K_2O, TiO_2, Na_2O and FeO is excellent. The fit for Al_2O_3 and CaO is not as good. This discrepancy might be explained by mixing the phlogopite-pyroxenite melts with melts from garnet peridotite. The system is, however, far too unconstrained to warrant any modelling, and while mixing might explain the relatively high Al_2O_3 and CaO contents of the ultrapotassic rocks, it would not be consistent with the very low values of Na_2O. Mixing of melts from garnet peridotite with ultrapotassic melts of the sort shown in Figure 7.13 could also produce the relative enrichment in TiO_2 and K_2O observed in the Forties basalts and noted at the end of the last section.

Figure 7.14 shows the liquidus temperatures at 2 and 3 GPa for the melts from the phlogopite-pyroxenite shown in Figure 7.13. The three geotherms in Figure 7.14 are for stretching by β's of 1.5 and 2.0 of an initial MBL 100 km thick over asthenospheric T_p's of 1280, 1320, 1380°C respectively. Note that these liquidus temperatures at pressures of 2-3 GPa are considerably lower (>200°C) than the temperature of the solidus for dry peridotite. All three geotherms easily intersect the liquidi for the phlogopite-pyroxenite melts at both values of β and in the steady state. Since the geotherms in the asthenosphere and TBL intersect the liquidi of phlogopite-pyroxenite in the steady state any of these regions are likely to have had their phlogopite-pyroxenite melts extracted (if they were ever able to produce them). This being the case the long term reservoir of phlogopite pyroxenite or similar low-melting peridotite must be in the MBL. The three near vertical dotted lines in Figure 7.14 show, for the three different values of T_p, the adiabatic trajectory for the base of the MBL as it is thinned. Notice that any phlogopite-pyroxenite that resides in the MBL is difficult to melt by large amounts even when β is 2 because the liquidus gradient is

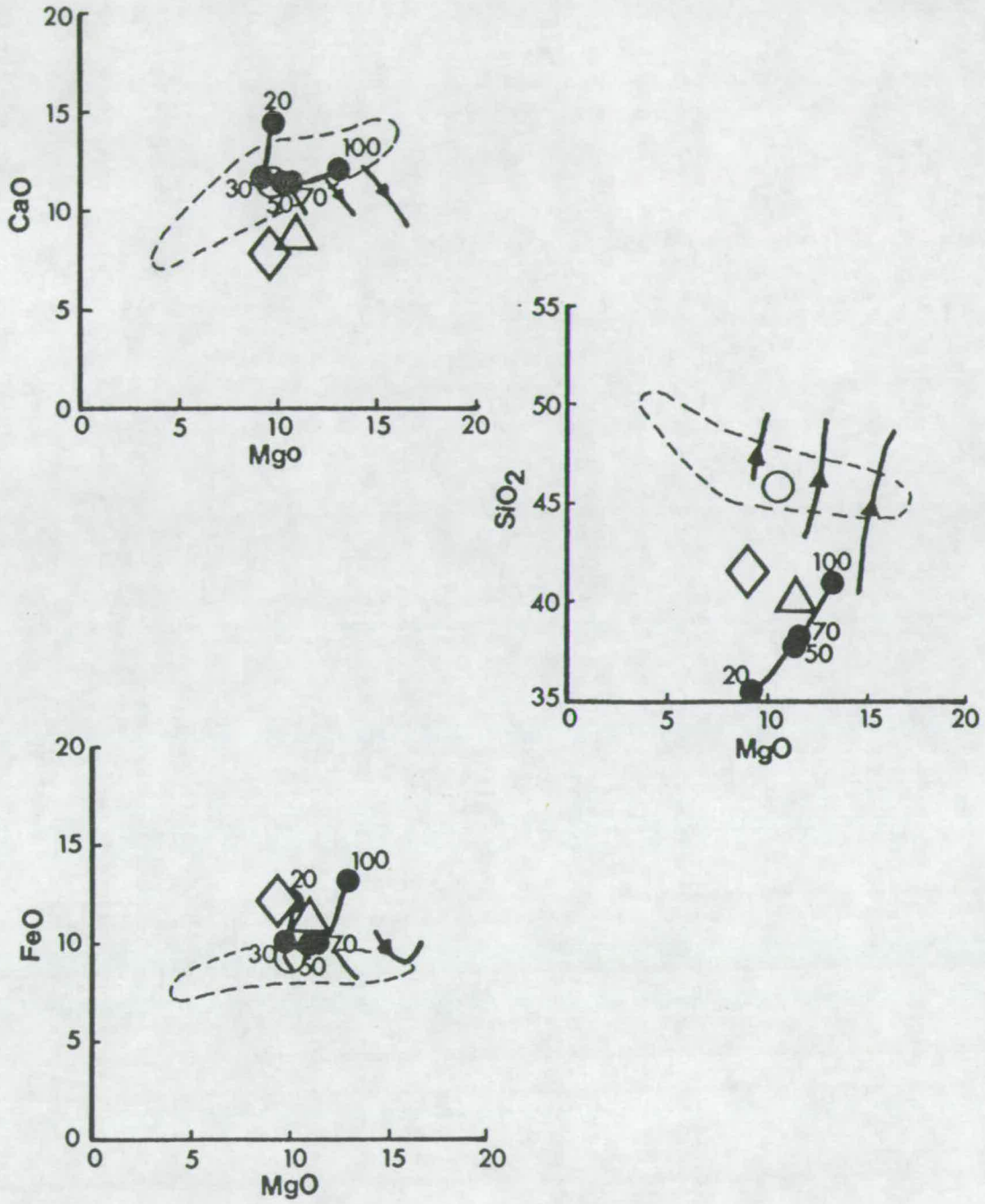

FIGURE 7.13 Compositions of partial melts from phlogopite-clinopyroxenite (filled circles labelled with per cent melt; from Lloyd *et al.*, 1985) are compared with averages of ultrapotassic rocks from the Central Graben (diamond) and Netherlands (triangle). Dashed line represents the field of alkali basalts from the Forties province whose average (see Table 7.2) is represented by the open circle. Lines with arrows mark point and depth average compositions predicted by McKenzie and Bickle (1988), shown in Figure 7.12.

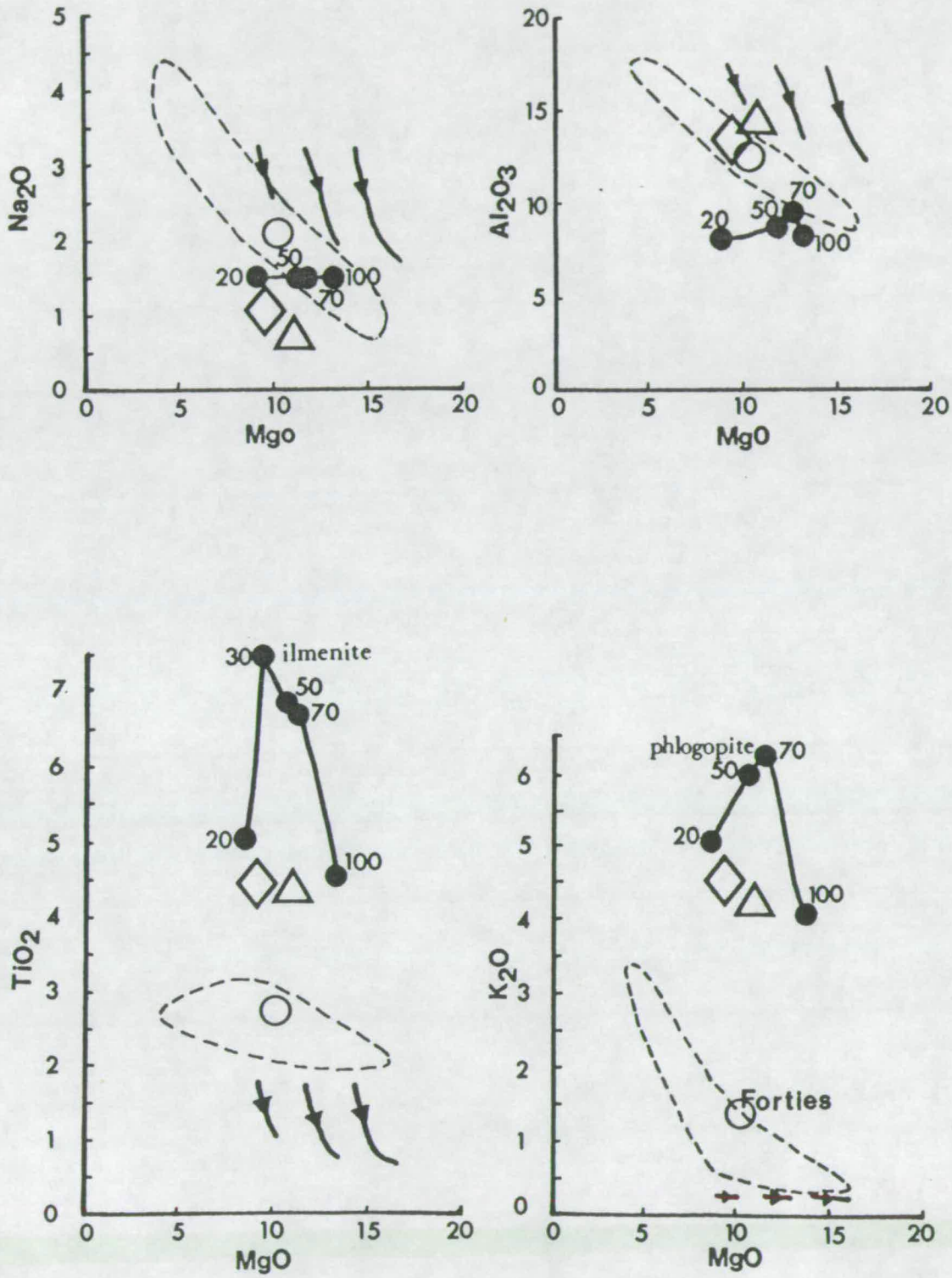

FIGURE 7.13 Continued.

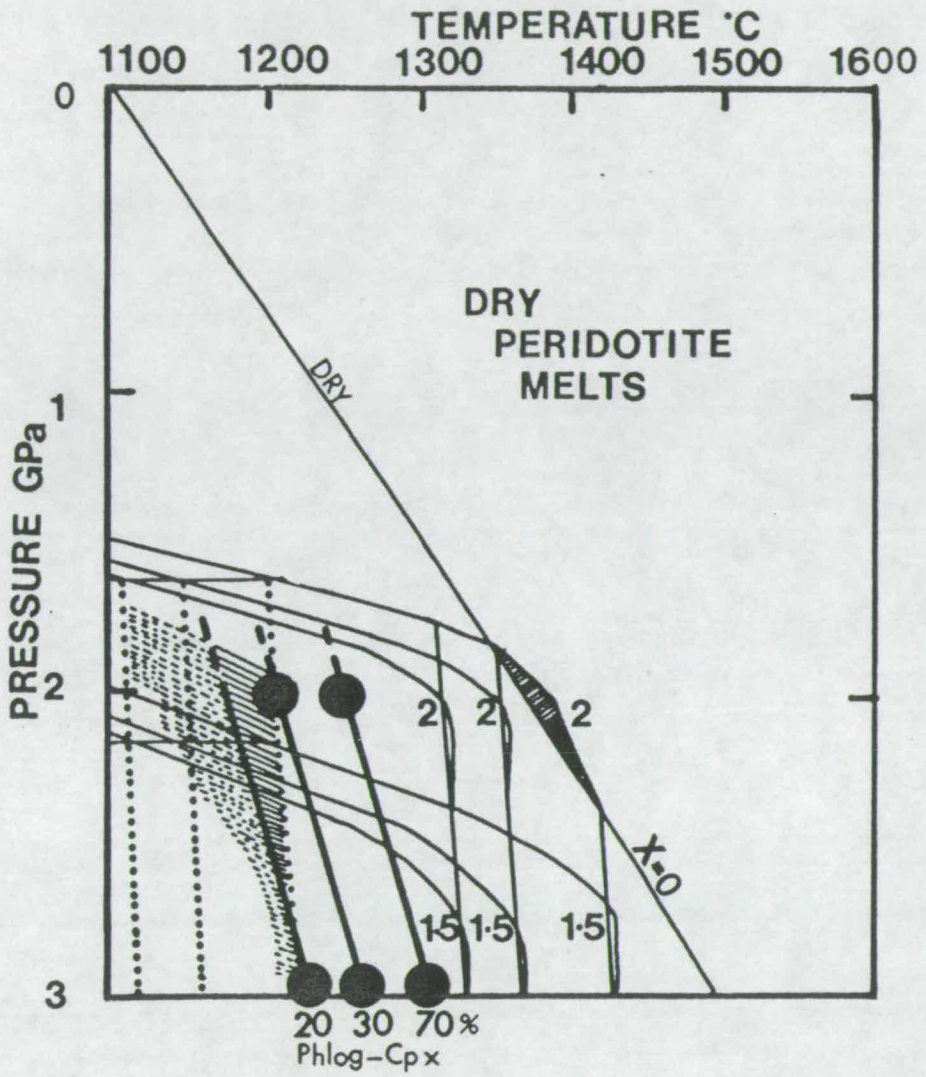

FIGURE 7.14 Liquidus temperatures, at 2 and 3 GPa, of melts from phlogopite-clinopyroxenite (filled circles labelled with per cent; from Lloyd *et al.*, 1985) compared with 3 stretched geotherms (β=1.5 and 2; T_p=1280, 1320 and 1380°C) all for an initial MBL of 100 km. The solidus for anhydrous peridotite is also shown (marked by X=0). Near vertical dotted lines trace the adiabatic decompression of the base of the MBL (shown by horizontal lines). Shaded region in lower left hand corner indicates >20% melting of phlogopite-pyroxenite while the dashed region indicates <20% melting. See text.

so similar to the adiabat. This appears to be a problem with other experimentally-determined melting curves; see section 7.5. Since Lloyd *et al.*, (1985) do not obtain solidus values in their experiments it is impossible to say whether or not melt will not be produced from the MBL when the T_p is 1280°C. For the higher values of T_p melt is released from the MBL but the degree of melting will not exceed 20% unless T_p is greater than 1320°C.

Whatever the precise nature of the source of the ultrapotassic rocks (there may be many possibilities, see Edgar (1987) and Wilson (1989) for a recent reviews) it is clear that it must contain a phase like phlogopite which has a high concentration of K_2O and TiO_2 and, by implication, H_2O. The other rocks from the North Sea (nephelinites, basanites and alkali basalts) may all be explained by melting of "normal" garnet peridotite in the presence of variable amounts of CO_2 and/or H_2O.

7.5 Volatile-Controlled Melting.

Through much of this thesis the discussion has been concerned with melting of anhydrous garnet peridotite; i.e. the dry solidus. It is nonetheless obvious that volatiles were probably involved in the production of all of the North Sea igneous rocks (see Chapters 4 and 5) and that at least some of them are not melts from garnet peridotite (see discussion above). Unfortunately the system becomes much less well constrained when volatile components are introduced. Quantitative statements are much more difficult to make. The following section summarises the major arguments for the presence of volatiles and how they are likely to effect the melting regime of the source region(s) of the North Sea basaltic rocks. In the following section a model involving melts from dry and wet asthenosphere and metasomatised MBL is shown to meet all of the requirements in the North Sea (e.g. Bailey, 1987; McKenzie, 1989; Thompson *et al.*, 1990; Pearce *et al.*, in press). It is, however, noted that many of the arguments do not preclude other models (see Latin *et al.*, 1990a), particularly those involving heterogeneous asthenosphere, favoured by other authors (e.g.; Sleep, 1984; Fitton and Dunlop, 1985; Fitton and James, 1986; Allègre, 1987; Francis and Ludden, 1990).

The main arguments for the importance of volatiles in the generation of the mafic rocks may be summarised as follows:

(1) The ocellated character of many of the Forties basalts and ultrapotassic rocks may suggest the separation of an immiscible volatile rich silicate melt (Chapter 4).

(2) The alkali basalts contain groundmass mica and amphibole both of which are volatile bearing phases. These phases dominate the petrography of the ultrapotassic rocks (Chapter 4).

(3) The undersaturated nature of the nephelinites from the Egersund Basin would be ascribed by some authors to melting in the presence of CO_2 which inhibits the melting of clinopyroxene in favour of garnet (Chapter 5; see Brey *et al.*, 1983).

(4) The buffering of Y and the HREE in the Forties basalts suggest that the trace element budget of these basalts is dominated by melting within the garnet stability field. The basalts are otherwise consistent with melting at shallower depths (on the dry solidus) in the spinel stability field (Chapter 5 and section 7.3). This argument is slightly circular because it relies on the fact that the dry solidus is accurately determined experimentally (see Chapter 2) and more importantly that the normal T_p, rather than a plume T_p, is the correct T_p.

(5) Since a T_p>>1280±40°C is considered unlikely, it is difficult to explain the presence of any of the North Sea rocks, other than those in the Forties province, without invoking volatile controlled solidi.

(6) There is no reason to expect the mantle to be completely dry. Michael and Chase (1987) consider that primary MORB magmas contain between 0.01 and 0.045 wt.% H_2O. The asthenosphere which produces MORB is therefore probably not completely dry. Latin *et al.* (1990b) calculated that if MORB represents a 20% partial melt, and if all of the H_2O enters the melt (i.e. it is infinitely incompatible), then the source of MORB may contain between 0.002 and 0.009 wt.% of H_2O. Small degree melts from this source could therefore contain relatively large amounts of H_2O. Galer and O'Nions (1986) also suggested that the asthenospheric source of MORB would not be completely dry and that it would contain <0.1% of CO_2+H_2O. More recently McKenzie (1989) has suggested that very small (10^{-3}%) volatile-enriched ultrapotassic melt fractions may separate from the asthenosphere and freeze at the base of the MBL to form a metasomatised layer.

In general the evidence for the importance of volatile C-H-O species in the source regions of alkaline magmas is widely accepted and is supported by studies of xenoliths and extreme examples of volatile-enriched magmas such as the kimberlite-carbonatite clan (e.g. Menzies and Murthy, 1980; Harte, 1983; Dawson, 1987; Menzies and Hawkesworth, 1987; Wilson, 1989). Experimental studies have shown that the presence of volatiles, particularly in excess, has a dramatic effect on the solidus position of peridotite (e.g. Green, 1969; Boettcher et al., 1975; Mysen and Boettcher, 1975; Olafsson and Eggler, 1983; Edgar, 1987).

In the context of the present study the presence of volatiles in the mantle is of importance for a number of reasons:

(1) By lowering the solidus of peridotite, volatiles allow melting to occur at normal potential temperatures in regions of the North Sea where $\beta<<2.5$; e.g. the Egersund Basin and probably the Netherlands.

(2) The H_2O/CO_2 ratio and the absolute abundance of H_2O and CO_2 in the source will have an important effect on the accessary phase mineralogy, solidus position, and resulting melt composition. Such differences may explain why igneous rocks with very high values of K_2O/Na_2O (i.e. the ultrapotassic rocks) erupt in some areas while at the other extreme rocks with low K_2O/Na_2O (nephelinites and basanites) are also found.

(3) The steady state geotherm is likely to intersect volatile-controlled solidi in the asthenosphere and TBL (see Figures 7.14, 7.15 and 7.17). In this case small amounts of melt highly enriched in volatiles and incompatible elements (particularly K, Rb and Ba) may be present in these regions and account for the geophysical low S-wave velocity zone at the base of the lithosphere. According to McKenzie (1989) upwards migration of such ultra-small melt fractions, which cannot carry sufficient heat to stray from the geotherm (their thermal Péclet number is small; see Chapter 2), may lead to metasomatism of the base of the MBL where they freeze. Metasomatic enrichment of the base of the MBL in shield regions over very long periods of time may lead to isotope signatures which are enriched relative to bulk earth. In the case of the North Sea, a metasomatised lithosphere provides a means of explaining the high concentrations of K and Ti and relatively low concentrations of HREE in the Forties basalts together with their Nd and Sr isotope ratios (which suggest time-integrated enrichment relative to MORB) without resorting to "plume" or "streaky-mantle" models for enrichment. It should be noted that metasomatic enrichment of the base of the MBL might also be responsible for the presence of reflective layers reported from an ultra-deep seismic reflection profile in the Skagerrak region (Lie *et al.*, 1990). Plume models are considered unlikely because of the observations discussed at the start of this chapter. Streaky-mantle models were developed to explain the commonly observed similarity between OIB and continental rift basalts but they are not necessarily the answer (see section 7.5.2 and Latin *et al.*, 1990 a,b).

Figure 7.15 shows the solidus and near-solidus phase reactions of volatile-enriched peridotite containing 0.3% H_2O and 0.7% CO_2 according to Olafsson and Eggler (1983). Since volatiles species are highly incompatible, partial melting of peridotite containing hydrous phases (such as in Figure 7.15) is likely to be restricted to a small T-P interval that is close to the solidus. There is therefore likely to be a

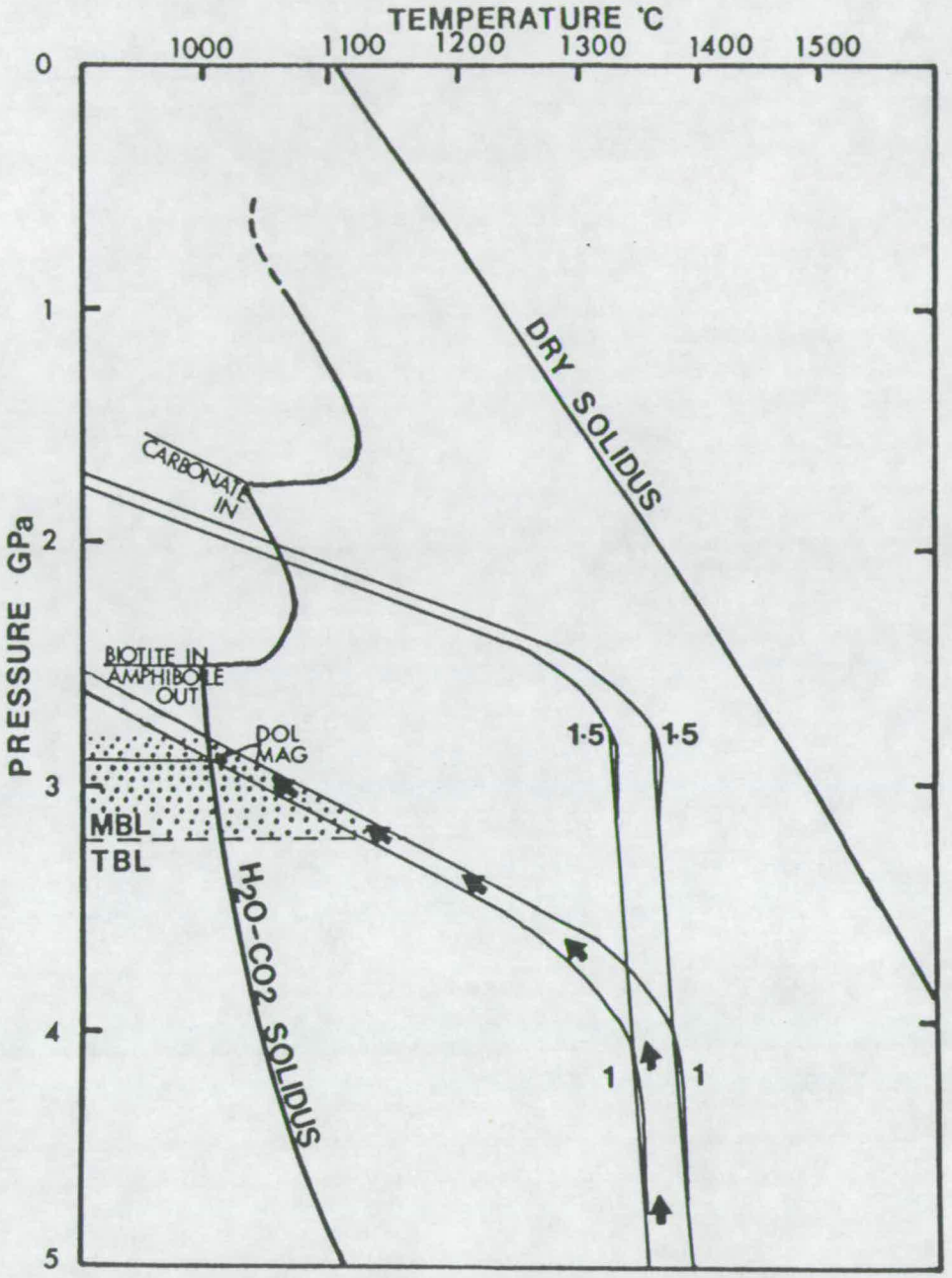

FIGURE 7.15 The volatile controlled solidus of Olafsson and Eggler (1983) compared with stretched (β=1.5) and unstretched (β=1) geotherms for T_p=1280°C and T_p=1320°C. Arrows indicate the path taken by low Péclet number, supra-solidus, small melt fractions which freeze when the geotherm at the base of the lithosphere falls below their liquidus temperatures. The dots show the region of permanent enrichment at the base of the MBL (dotted line); see caption to Figure 7.17 and text for discussion.

gap where there is no melting between the volatile-controlled and the anhydrous solidi shown in Figure 7.15. The near solidus, volatile-enriched, partial melts are likely to have distinctive compositions reflecting the nature of the minerals which are stable on the solidus (e.g. Brey *et al.*, 1983; Olafsson and Eggler, 1983). For example the ultrapotassic melts in the North Sea are probably dominated by the melting of phlogopite.

Figure 7.15 shows that the steady-state geotherm for the base of the lithosphere and asthenosphere intersects the volatile controlled-solidus within the stability field of phlogopite and magnesite. In the steady-state this region may be empty of migrating melt or there may be some steady-state flux due to the large scale convective overturn of the asthenosphere. Clearly *any* perturbation of the geotherm during rifting which results in the upwelling of asthenosphere, however small, will result in volatile controlled melting at depth and an increased flux of small melt fractions. Whether or not such melts reach the surface or freeze at the base of the lithosphere will depend on their volume and on whether they migrate by porous-media or by channellised flow (McKenzie, 1989).

In section 7.3 it was shown that the compositional parameterisation of McKenzie and Bickle (1988) failed to predict high enough concentrations of K_2O to match those of the Forties basalts. The main question at this point in the discussion concerns whether this discrepancy can be explained by addition of K_2O- and volatile-rich melts to the anhydrous melts. How much of the total thickness of melt in the Forties region could be explained by a single-stage melting event in the wet and dry portions of the asthenosphere? The amount of volatiles present in the asthenosphere is not well constrained, although earlier arguments concerning the amount of H_2O in MORB suggested that it was less than 0.01% H_2O. Since the amount of H_2O in the primary Forties magmas is not known, estimates for the H_2O content of the asthenosphere can be used to say very little about the size of the melting region. The abundance of potassium in the asthenosphere is better constrained and is estimated to be ~50 ppm from the $^3He/^4He$ isotopic ratio (O'Nions and Oxburgh, 1983). As McKenzie (1989) points out, if potassium, together with volatile species, is assumed to be completely incompatible then it will generate 0.1% of a melt containing 5% K_2O. In this case to generate 0.5 km of alkali basalt (in Forties there is between 0.5 and 1.5 km) containing 0.5 wt.% of K_2O (in Forties the most MgO rich (~15 wt.% MgO) ankaramitic basalts have >0.5 wt.% of K_2O; see Appendix A) a *column of previously unmelted asthenosphere at least 100 km thick must be upwelled over the volatile-controlled solidus.* This is a minimum estimate since potassium is probably not perfectly incompatible in the mantle (see normalised trace element patterns in

Chapter 5) and since at least some of the mantle directly beneath the lithosphere may have already have lost its volatile-enriched K-bearing melt fraction. Since the MBL (originally ~100 km thick) beneath the Forties region was thinned by no more than a factor of ~2-3 during the Jurassic it seems unlikely that more than 50-70 km of asthenosphere will have upwelled. The alkali basalts in Forties require all of the potassium from a column of mantle at least 1.5 to 2 times that size. It would appear impossible to explain the concentration of K_2O in the Forties province by single-stage melting of the asthenosphere alone (see Figure 7.16 A) since the volume of melt containing sufficient K_2O is too small. It is clear that some contribution is required from a more K_2O enriched portion of the mantle. Note that C-H-O controlled melting of the asthenosphere will occur within the garnet stability field and may therefore buffer the concentrations of Y and HREE in the Forties basalts (Figure 7.16A).

The small amounts of sodic melt (basanites and nephelinites) from parts of the Netherlands and the Egersund Basin may have been produced directly from the asthenosphere by very small amounts of volatile-controlled melting during rifting (see Figure 7.16A). The ultrapotassic rocks, however, require very large amounts of asthenosphere to pass through the volatile melting region. It seems more likely that they are the result of melting of some region of the Earth that is much more enriched in K than the asthenosphere.

The position of the steady state geotherm relative to the volatile controlled solidus (in Figure 7.15) may result in a continual or episodic flux of volatile- and LILE-enriched (K-rich) small melt fractions into the base of the lithosphere. A zone of enrichment may develop as these freeze in the MBL and TBL but since the TBL convects, this zone will only be permanent in the MBL (dotted region in Figure 7.15; see also Figure 7.17). The width of the zone will reflect the width of the melting region; i.e. the distance between the first volatile-controlled solidus and the highest temperature liquidus at a given pressure (see Figure 7.17 for explanation). In theory with time a region at the base of the lithosphere could become extremely enriched in volatile and highly incompatible components relative to the asthenosphere. Later decompression or heating of this region could liberate ultrapotassic, kimberlitic or carbonatitic melts with old, enriched isotope signatures (see Figure 7.16B). Such an explanation has been forwarded to explain occurrences of ultrapotassic rocks such as the Leucite Hills and Smoky Butte (McKenzie, 1989), ultrapotassic minettes in Colorado (Thompson *et al.*, 1990), and ultra alkaline basalts in Eastern Turkey (Pearce *et al.*, in press).

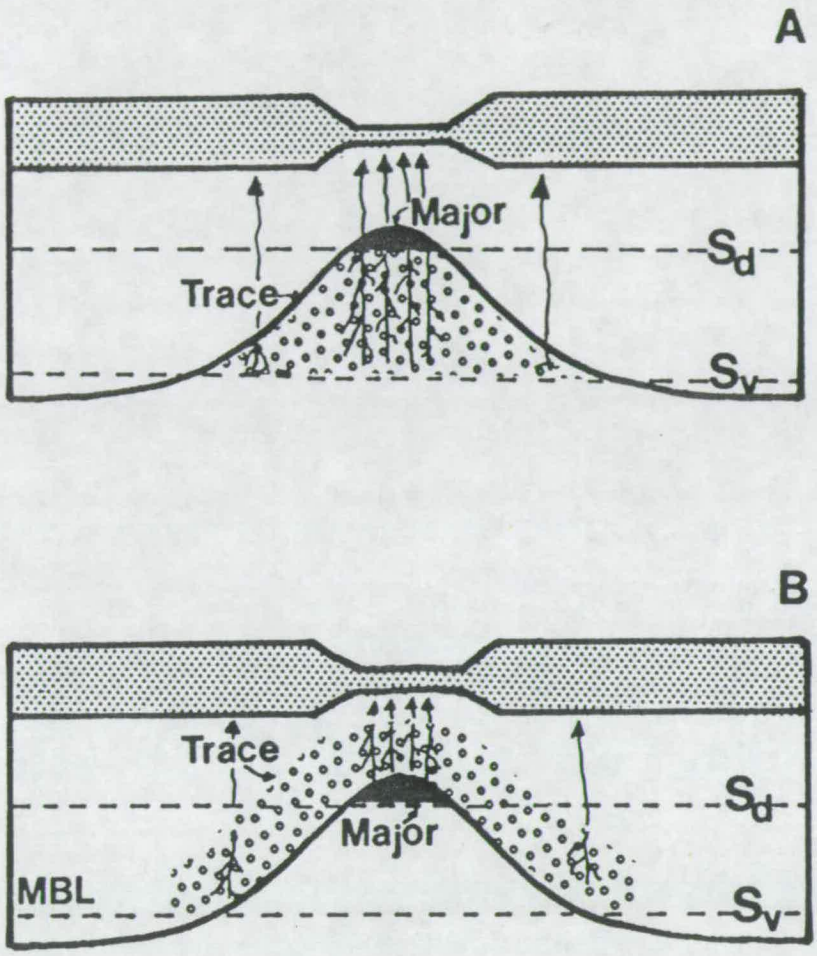

FIGURE 7.16 Cartoons to show two different models for the generation of melt during rifting of the continental lithosphere (crust dotted). See discussion in text.
A: All melting occurs in the asthenosphere on volatile controlled (S_v) and volatile free (S_d) solidi. The zone of major silicate melting (in dark shading) and the zone of trace amounts of volatile- and LILE-rich melt (circles) are also shown.
B: Large volumes of silicate melt are produced by melting dry asthenosphere while small volumes of volatile- and LILE-rich melt are produced in the MBL.

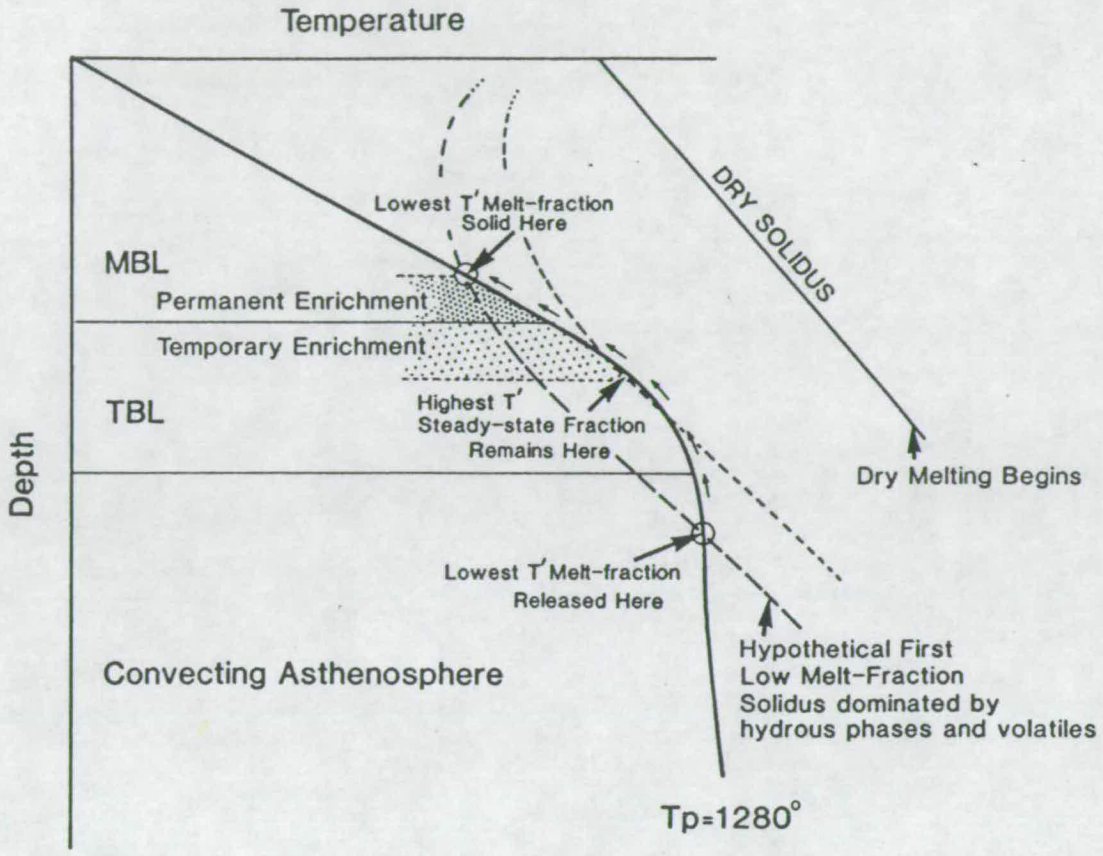

FIGURE 7.17 From Latin *et al.* (1990). The steady-state production of ultra-low melt fractions from a hypothetical mantle with a solidus (bold dashed line) dominated by hydrous phases and volatiles. The first melts are produced when this solidus intersects the geotherm. After upward migration these smallest melt fractions freeze at the lowest temperatures as an enriched layer in the MBL where the geotherm re-intersects their solidus. The largest steady state melt fractions are those produced by the largest amount of upwelling over the hypothetical solidus; they crystallise at the highest temperatures where their respective solidus (the fine dashed line) intersects the geotherm. T' is the temperature above the solidus temperature at a given pressure (see definition in Chapter 2). Arrows show the path taken (in P-T space) by the migration of melt fractions whose thermal Péclet number is less than 1 (McKenzie, 1989) and which, therefore, carry no heat. Any melts which solidify in the TBL will only reside there temporarily because of this layers' convective overturn. Melts reaching the MBL will reside permanently in steady-state conditions and will be remobilised if the geotherm is perturbed.

Despite the obvious attraction of the metasomatised MBL model (Figure 7.16B), since it allows highly LILE enriched melts to be formed relatively easily, there does appear to be a major problem. The MBL in Figure 7.15 will never be decompressed over the volatile-controlled solidus on melting! The solidus is too steep in P-T space. If the volatile controlled solidus of Olafsson and Eggler (1983) in Figure 7.15 is the correct one to use then only a rise in temperature will liberate melt from the MBL. Unfortunately there is considerable disagreement about the precise shape of such curves. Like dry melting experiments (see Chapter 2) wet melting experiments are difficult to conduct but problems are compounded because of the ease at which hydrogen ions can be lost or gained during experiments. The hypothetical curves of Latin *et al.* (1990 a) shown in Figure 7.17 may represent something closer to the real situation.

7.5.1 Discussion.

The simplest, but not necessarily the only, model for the generation of melts during rifting in the North Sea may be summarised as follows (see also Figure 7.18);
(1) There are two regions which may melt during rifting; the asthenosphere (and TBL), and the metasomatised part of the MBL. The asthenosphere and TBL are capable of producing large volumes of melt (>0.5 km) with the isotopic characteristics of MORB[2] if the dry solidus is intersected. The MBL the asthenosphere and the TBL may all produce small quantities of highly LILE-rich melt. If this melt is produced from the asthenosphere it should have the isotopic signature of MORB. Melts from the MBL (and possibly also the TBL if it only overturns episodically) will have an isotopic signature which may be enriched relative to MORB or even enriched relative to bulk earth (depending how long they have been kept separate from the asthenosphere).
(2) In its most stretched region (the triple junction) adiabatic decompression was sufficient to induce melting of anhydrous garnet peridotite in the asthenosphere. The base of the upwelled asthenospheric column may also have contributed a small amount of LILE-enriched melt (from indigenous volatile bearing phases) on volatile controlled solidi (see Figure 7.18). To explain the abundance of K_2O and their

---

[2] This model assumes that the asthenosphere, even when it melts by a small amount, has an isotopic signature which is the same as normal MORB (see Chapter 2); i.e. it is depleted relative to bulk earth. Other models invoking heterogeneous asthenosphere suggest that melts from the asthenosphere can range in isotopic composition from MORB to bulk earth.

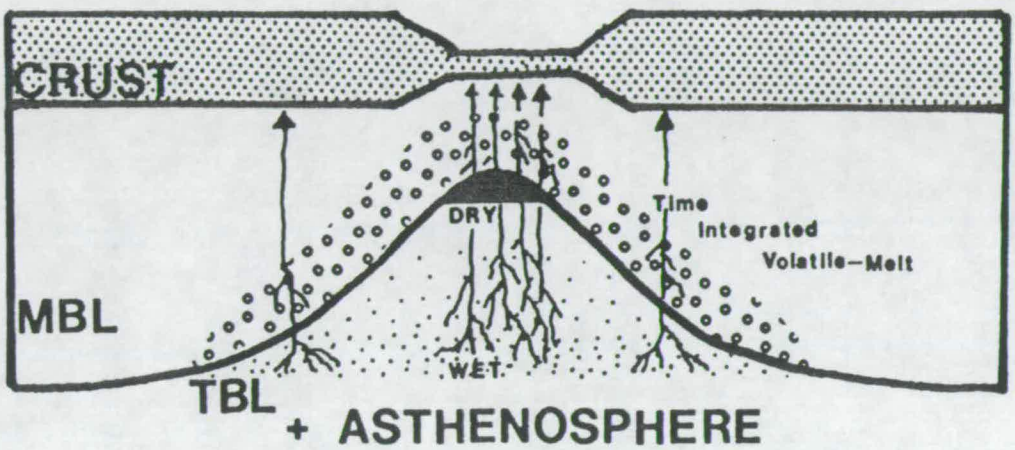

FIGURE 7.18 Cartoon showing the preferred model for magma generation in the North Sea. In the most stretched region the TBL and asthenosphere are decompressed sufficiently for the dry peridotite in the TBL to melt. Lower parts of the asthenosphere may, on decompression, liberate a small amount of volatile- and LILE-rich melt. The bulk of the volatile- and LILE- content of all of the North Sea magmas is from the MBL which is rich in these components due to a continual flux of small melt fractions as the asthenosphere overturns (see caption to Figure 7.17 and text for details). Off-axis ultrapotassic and nephelinite magmas originate mainly in the MBL.

isotopic signature (see Chapter 5) the addition of some unspecified amount of K-rich melt from the MBL is invoked.

(3) In other parts of the North Sea, where the degree of stretching was less, the anhydrous solidus was probably never attained. The basic rocks in these areas must therefore be explained by volatile-controlled melting of the asthenosphere and MBL (see Figure 7.18). Since neither the nephelinites nor the ultrapotassic rocks have MORB isotope ratios, then in this simplest model (see footnote 2), a component from the MBL must be invoked in all cases.

7.6 Uplift, Magmatism and Extension.

Although the theory accounts for the volume and alkaline composition of the Forties basalts in the most extended region of the North Sea it is unable to explain three important observations:

(1) The Central North Sea region was uplifted (at ca. 180-160 Ma) immediately prior to magmatic activity (ca. 160-150 Ma) and the main phase of faulting (<150 Ma).

(2) The Forties basalts were erupted before the main sequence of syn-rift sediments had been laid down (see Chapters 4 and 6).

(3) The subsidence of this part of the North Sea is abnormal when compared with the amount and rate of subsidence predicted by most stretching models (see Chapter 6). The syn-rift stage of subsidence is condensed or absent while the thermal stage of subsidence is extremely rapid.

At the end of Chapter 6 it was concluded that simple models involving coupled strain rates between the crust and mantle were unable to account for the subsidence observations in the triple junction region. A general qualitative model involving decoupling of strain rates was proposed. It was however noted that a simple homogeneous stretching model could probably be used to estimate the bulk strain of the lithosphere.

Figures 7.19 and 7.20 show one possible qualitative model which is proposed to account for the deviations from the simple theory (points 1 to 3 above) in the Central North Sea. Rifting is assumed to start at t_0 (see Figure 7.20) and continues until time t_2. Figure 7.20 shows the variation of strain and strain rate with time for the column of lithosphere directly beneath point X in Figure 7.19. The rates of strain in the crust and mantle in any column of lithosphere are assumed to be constant but very different. The following discussion refers to diagrams A, B and C in Figure 7.19 in sequence. Note : it is important to realise that the only constraint imposed in the

cartoons shown in Figure 7.19 is that the area under each of the curves be the same at all times during rifting.

(1) Figure 7.19 A: In the centre of the rift, (beneath point X) the mantle strain rate is very much faster than the crustal strain rate, resulting in a localised very high strain region in the mantle by time t_1. From t_0 to t_1 the central part of the rift may undergo uplift (or reduced subsidence) since $\beta_m > \beta_c$. Away from the central part of the rift where β_c exceeds β_m some small amount of subsidence may be observed although the flanks are uplifted. By time t_1 the mantle has thinned by its maximum amount (m) and $\beta_m >> \beta_c$ in the centre of the rift. The associated adiabatic decompression causes the asthenosphere and TBL of the lithosphere to cross the dry solidus and melt. This period would therefore correspond to the Bathonian-Callovian of the Central North Sea.

(2) Figure 7.19 B: During the time interval t_1 to t_2 the amount of crustal thinning increases in the central region of the rift and eventually in the very centre $\beta_c > \beta_m$ (i.e $\beta_c > m$). Subsidence in the central part of the basin begins to accelerate as β_c overtakes β_m, and as the thermal perturbation due to β_m begins to cool (the effects of this are not shown). This stage might correspond to the beginning of the Upper Jurassic phase of crustal extension in the Central North Sea. It is represented by the crossing over of the crust and mantle strain lines on Figure 7.20. Away from the centre of the rift the flanks are uplifted since $\beta_m > \beta_c$.

(3) Figure 7.19 C: As time approaches t_2 crustal thinning reaches its maximum (c) in the centre of the rift. The axis of the rift continues to subside since $\beta_c > \beta_m$ and because of conductive cooling. The flanks are uplifted and eroded. When rifting stops at t_2 the entire region will subside thermally. The amount of thermal subsidence will depend on the size of the thermal anomaly that still remains at the end of the rift phase. Subsidence of the rift flanks may give rise to onlap during the thermal phase.

Although this decoupled strain rate model is not quantitative, it may account qualitatively for the general observations in the Central North Sea while balancing the strain in the crustal and mantle sections of the lithosphere at any instant in time. One of the most important tasks still to be done is to quantify the effects of decoupled strain rates on uplift and subsidence of the lithosphere. This cannot be done until the nature of the subsidence across the triple junction area and onto the graben flanks has been determined by backstripping regional seismic lines. When such modelling is attempted the thermal effects of melting should be included in the calculations.

It is of further interest to note that the sort of model shown in Figure 7.19 does not need to be applied to the Viking Graben. The subsidence in the Viking Graben

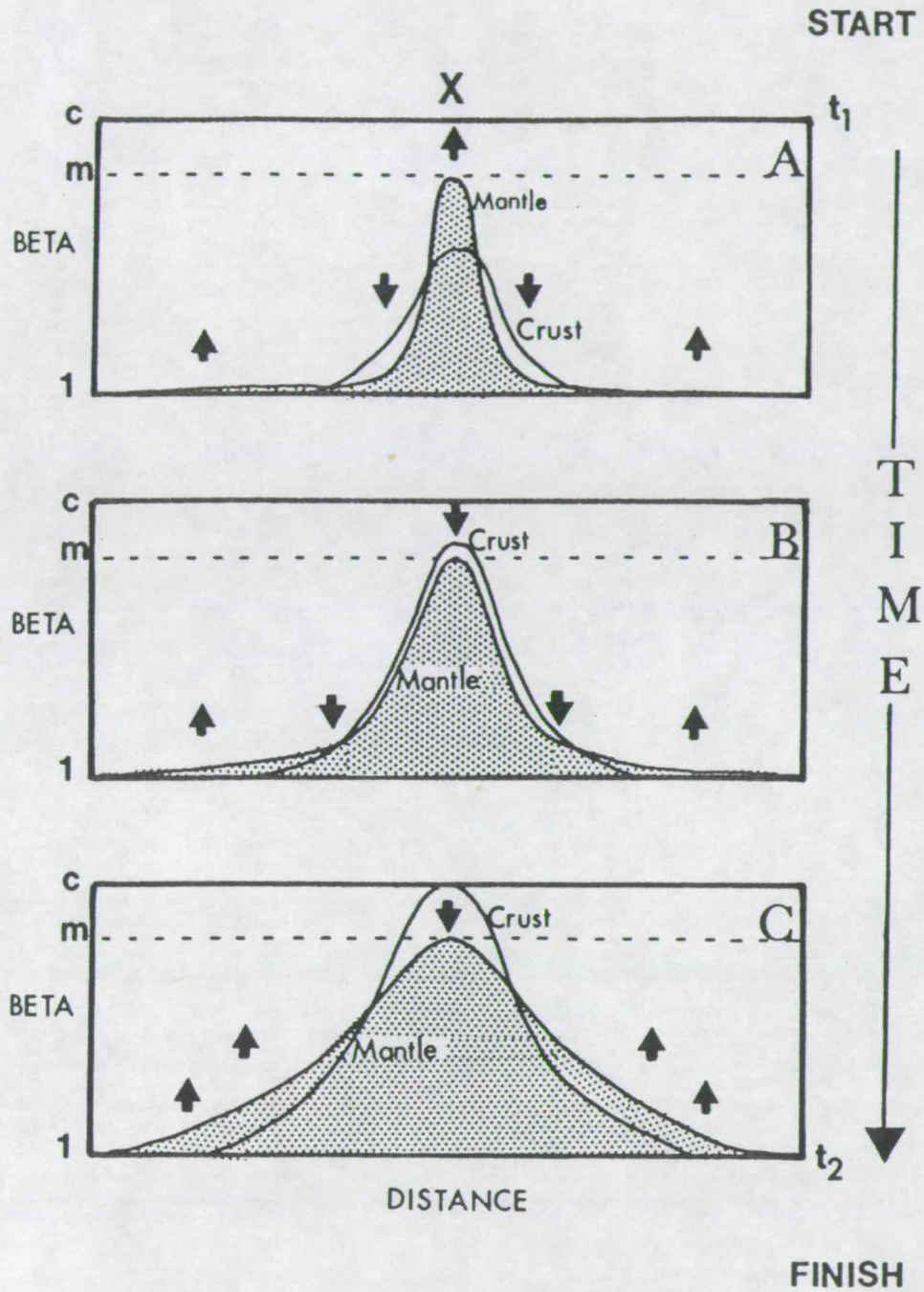

FIGURE 7.19 Cartoons showing the possible variation of crustal and mantle strain (curves) with time and according to location during rifting across the triple junction region of the North Sea. The total area beneath both of the curves (mantle is dotted) must balance across the whole rift at any instant in time. The maximum amount of mantle thinning is denoted by m, and the maximum crustal thinning is labelled as c. X marks the lithospheric column directly below the centre of the rift (see Figure 7.20). See text for detailed explanation.

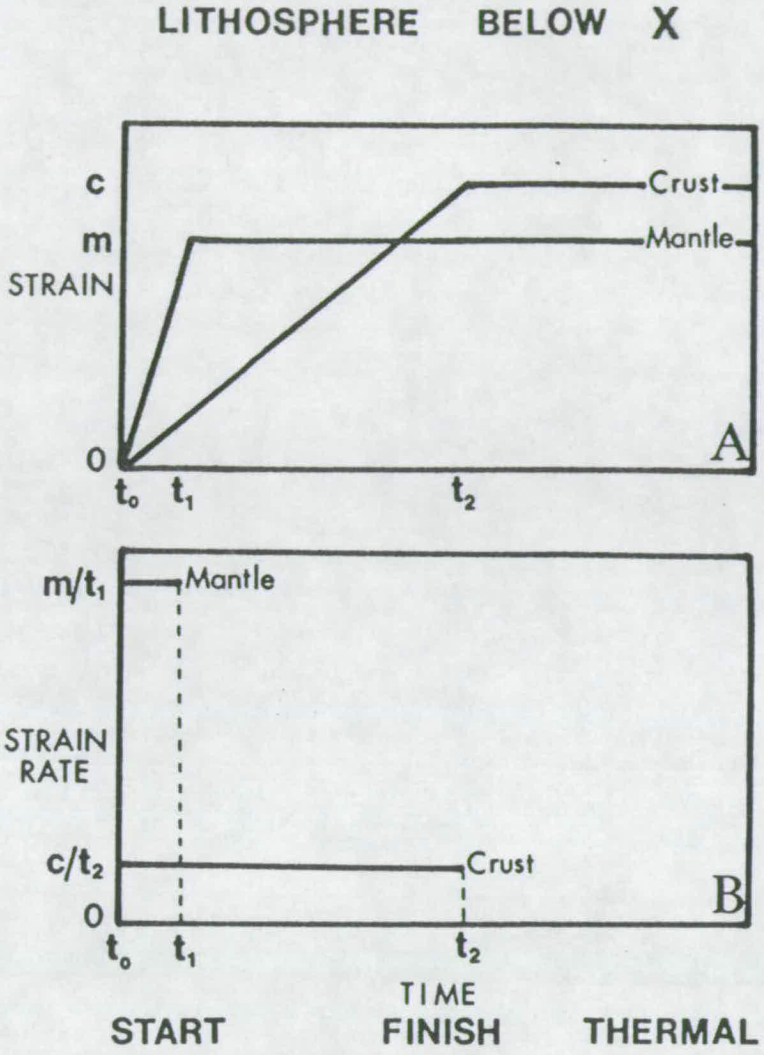

FIGURE 7.20 Cartoons showing the possible variation of strain and strain rate with time in the lithospheric column beneath point X in Figure 7.19. Rifting starts at t_0 and ends at t_2 after which the column subsides only due to cooling of the rift induced thermal perturbation. The mantle strains much more quickly than the crust and its maximum amount of stretching has occurred by time t_1.

follows the pattern predicted by a uniform stretching model of finite duration. Presumably more complex stretching models are only required to explain some parts of some rifts. Perhaps the complex stretching in the Central North Sea is a function of the 3D geometry of the triple junction region or of some rheological difference inherited from previous deformational episodes.

7.7 Discussion.

The main conclusion of this chapter is that the quantitative predictions made by the theoretical framework described in Chapters 2 and 3, and based on the model of McKenzie and Bickle (1988), are consistent with the occurrence of a small thickness (0.5-1.5 km) of alkali basalt, resulting from less than 5% melting of garnet peridotite, in the most stretched part of the North Sea. Anomalous potential temperatures are not required and are not consistent with the palaeogeographic evidence or the timing of magmatic activity in different parts of the rift system.

The doming of the Central North Sea, the abnormal subsidence curves in that region, and the eruption of the Forties province early in the rift stage conflict with existing quantitative models. An explanation may require a mechanism which allows the crust and mantle to strain at different rates from place to place and from time to time within the extending lithosphere. Since the crust and mantle are unlikely to be similar rheologically and since the past history, and therefore internal fabric, may vary from place to place, such a model is perhaps not as unlikely as it first sounds.

The ultrapotassic, basanitic and nephelinitic rocks found along the flanks of the main rift and in less extended parts of the North Sea (the Egersund Basin and Netherlands) are almost certainly the result of volatile-controlled melting which is, at the present time, difficult to quantify. It is also difficult to explain why magmatism only occurs in a few locations rather than ubiquitously. The answer presumably lies either in heterogeneous metasomatism of the MBL or in rheological differences which allow melts to escape in some areas but not in others (see Latin *et al.*, 1990 a,b for a more lengthy discussion).

CHAPTER 8

CONCLUSIONS, DISCUSSION AND FURTHER WORK

8.1 Conclusions.

A quantitative model for magma generation based on parameterisations of anhydrous batch melting experiments (McKenzie and Bickle, 1988) has been presented. The model was used to predict the volumes and compositions of melts which should have resulted from adiabatic decompression of the asthenosphere during Mesozoic rifting in the North Sea. Model predictions were then compared with observations from the North Sea region.

Middle Jurassic magmatic activity, which accompanies rifting in the North Sea, is reflected by a variably-altered suite of igneous rocks which range from mildly to highly alkaline in character. The largest volumes of melt were generated at the triple junction in the Forties region of the North Sea and were extruded subaerially, 160 to 150 Ma ago, as 0.5 to 1.5 km of alkali olivine basalt. Minor amounts of nephelinitic and ultrapotassic rocks occur on the flanks of the Egersund Basin (~170 Ma), in the Auk and Cleaver-Bank areas of the Central Graben (~150 Ma), in the Broad Fourteens and West Netherlands Basins and in the Waddensee (~155 Ma).

Many of the North Sea rocks are chemically and isotopically similar to OIB, but the ultrapotassic varieties have no oceanic equivalents. Simple single-stage melting calculations using ratios of incompatible trace elements suggest that if the source of the Forties basalts was garnet peridotite with a composition similar to either the source of MORB or bulk earth, then they were produced by very small amounts of melting; i.e. <3%. The extreme fractionation of LILE and LREE from HREE observed in other rocks from the North Sea cannot be explained by single-stage melting of such source compositions.

Modelling of subsidence and gravity data in the triple junction region suggests that the lithosphere was thinned by a factor of between 2 and 3 during the Jurassic. This is considerably more stretching than has been recorded elsewhere in the North Sea. The lithosphere in the Auk region was thinned by a factor which was less than 2, while in the Egersund basin β was probably less than 1.5. The subsidence curves

in the area of the triple junction are abnormal in that the syn-rift phase is condensed or absent while the thermal phase of subsidence is very marked. Since the wells were selected to avoid the effects of fault block rotation the observations are probably related to a more regional phenomenon which may be specific to this part of the North Sea. It was shown that, although β could be accurately estimated from the thermal portion of the abnormal curves by assuming homogeneous stretching over a finite duration, this was probably not the correct model for the critical region of the North Sea. A heterogeneous stretching model in which β_m is larger than β_c during the early stages of rifting was shown to be consistent with many of the observations.

It has been argued that the stratigraphic data together with the timing of igneous activity in different parts of the North Sea is inconsistent with migration of the region over a stationary plume in the asthenosphere. The asthenosphere is considered to have had a normal potential temperature (i.e. 1280±40°C) during rifting. The steady-state thickness of the MBL of the North Sea lithosphere is ~100 km, and its thickness prior to rifting in the Middle Jurassic was calculated to have been between 90 and 100 km, assuming that a minor rift phase occurred in the Triassic. The location of the Forties province is consistent with extension accommodated by coaxial stretching rather than by simple shear.

In the most stretched region of the North Sea the model of McKenzie and Bickle (1988) correctly predicts a small thickness (<1.5 km) of alkali basalt magma. Since the model is founded on anhydrous melting experiments it does not predict that any melting will occur in other, less-stretched regions of the North Sea. It seems likely that magmatism in these other parts of the North Sea is controlled by melting of peridotite that is more LILE- and LREE-enriched than bulk earth and which contains volatile-bearing phases. It also seems likely that an amount of LILE- and volatile-rich melt from a source peridotite containing residual garnet is an important component in the Forties basalts. The precise location of this source peridotite is not known and its chemical, mineralogical and isotopic character is uncertain. One possible model involves melting of the base of the MBL of the lithosphere which had been heterogeneously metasomatised by some unknown mechanism. Other models involving heterogeneous asthenosphere are, however, not necessarily precluded by the North Sea data.

8.2 Discussion.

One implication of the work presented in this thesis, is that when the T_p of the asthenosphere is *normal* and the initial thickness of the MBL is known, the

compositions of rift-related igneous rocks would appear to be able to be used to provide a first-order estimate of β. Nephelinitic and ultrapotassic rocks, if they occur, seem to characterise regions where the degree of lithospheric thinning is less than ~2; alkali basalts occurring at larger amounts of thinning. The model framework described in this thesis may only be used to estimate β if there is no mechanism for generating alkali basalts (or tholeiites) by smaller degrees of upwelling than are necessary for intersection of the dry solidus. It was demonstrated that the occurrence, volume and compositions of alkali basalt in the North Sea are broadly consistent with the value of β and thus with intersection of the dry solidus. What has not been considered in detail is the possibility that the base of the MBL, the TBL, or even the asthenosphere could be so modified, by the presence of fluids or hydrous phases, that *extensive* melting might occur at considerably lower degrees of upwelling than are required for dry solidus intersection. In other words does the presence of alkali basalt in rifts formed over asthenosphere of normal potential temperature always require that the dry solidus be attained, but only just crossed over? The answer to this question is, as yet, unclear but it seems possible that in some regions subduction zone processes could modify the MBL (and TBL temporarily) to such an extent as to allow the production of large volumes of alkali basalt, or even tholeiitic, melt at smaller degrees of stretching than the present model would predict. Whether or not such magmas would posess characteristic trace element patterns which would allow them to be distinguished from their "dry solidus equivalents" is also, as yet, uncertain.

One further question concerns whether or not the parameterisations of McKenzie and Bickle (1988) (or Watson and McKenzie, in prep.) correctly predict melt volumes and compositions when β is at some value which is intermediate between the most stretched part of the North Sea (β=2-3) and an ocean ridge (β=∞). The maximum value of β in the North Sea was not sufficiently large for there to have been the production of more magma which was less silica undersaturated than alkali basalt. In the Porcupine trough to the west of Ireland, which opened in the Middle Jurassic, the value of β determined from the subsidence data is ~6. The values of β derived from modelling gravity and seismic refraction profiles, however, are between 3 and 4. The initial MBL was probably close to 100 km thick. The discrepancy in β is most easily explained by the addition of ~3-4 km of melt to the base of the crust (N. White, pers. comm. 1990; Tate *et al.*, in prep.). Such a thickness of melt would be consistent with model predictions. The composition of the Porcupine median volcanic ridge is not known but it is clearly a very major feature (Tate and Dobson, 1988). Providing that large volumes of melt are not produced below the dry solidus, and so long as β is sufficiently large to induce dry melting there is, as yet, no reason

to believe that the parameterisations cannot be used to make reasonably accurate predictions of β from melt compositions and/or volumes when the T_p is normal and the initial thickness of the MBL is known. It is of course necessary to determine whether the igneous activity is sufficiently close to the start of rifting, or the rift duration is short enough (i.e. $<60/\beta^2$ Ma), that the approximation of instantaneous upwelling will be valid.

So long as alkali basalt or tholeiitic melts are not produced on volatile controlled solidi the result is potentially an important one for frontier basin exploration. If the absence of a plume during rifting can be established, the value of T_p is well constrained. Magma compositions and volumes could then be used to provide order-of-magnitude estimates of the total thinning, and therefore the size of the rift-induced thermal perturbation, in different parts of the basin. When magma compositions are more undersaturated than alkali basalt the evidence from the North Sea suggests that β is less than 2 but at the present time nothing more quantitative may be said. The controls on the locations of such undersaturated magmas are not yet understood. Not all stretched regions will show magmatism.

The theoretical framework has not yet been tested for the situation where rifting occurs over a plume. Since the theory of McKenzie and Bickle (1988) does not incorporate the effects of plume-flow and geometry on the volumes and compositions it is unlikely to be accurate. It is clear from recent work on Hawaii (Watson and McKenzie, in prep.) and Iceland (Nicholson, 1990; Nicholson and Latin, in prep.), that plumes are likely to generate larger volumes of melt which result from a smaller average extent of melting at a greater average pressure than would be predicted by the existing, one-dimensional, theory. The very large volumes of alkaline magma in East Africa require that a very large amount of mantle has been melted at depth to a very small extent. At the present time the one-dimensional parameterisations are likely to underestimate the amount of melt produced by rifting over plumes in the asthenosphere and overestimate the size of the average melt fraction; this average melt fraction will occur at greater average pressures than would be predicted. It should also be noted that if the base of the MBL is metasomatised then warming by plume passage may release ultra alkaline magmas; little or no stretching would be necessary. Given that the size of any region affected by anomalous plume temperatures is likely to be very large, the occurrence of lamproites, lamprophyres, kimberlites, melilitites, carbonatites, and associated ultra alkaline rock types within continental plates may not necessarily be due to extension, or indeed any obvious local tectonic mechanism.

Given that few rifts are as magmatically-active as the East African rift system, it seems reasonable to start by assuming that the T_p is normal during the development of most rift basins. It is more difficult to decide upon a value for the pre-rift thickness of the MBL. It does, however, seem reasonable to assume that a value of 100 km is most likely for non-shield areas unless (1) the region under consideration is still cooling from some earlier rifting event, or (2) has recently been thickened during continental collision. As was shown in Chapter 7 of this thesis the first situation can be accounted for by calculating the thermal effects. The second situation is not so amenable to modelling since an understanding of the controls on lithospheric thickening and delamination is still in its early stages.

8.3 Further Work.

There are a number of areas where there is an obvious need for further work. These can be divided into two categories, one of which is concerned with the understanding of tectonics, the other is concerned with quantifying processes in the source regions of basaltic magmas.

In terms of understanding tectonic mechanisms the decoupled stretching model outlined in Chapters 6 and 7 needs to be quantified and tested. Time-dependent Gaussian distributions for the variation of β_m and β_c across the region could be used to produce a balanced regional model for the subsidence which (1) fits the backstripped subsidence data from regional seismic lines and (2) which allows sufficient thinning to take place in the triple junction region for melting to occur within 20 Ma of the start of rifting. It is further necessary to explain why the mantle is, in some instances, apparently able to thin much faster and in a much more localised manner than the crust. The answer to this question may be found in rheological experiments using finite element methods. Initial results of stretching a layer with a depth dependent olivine rheology on a finite element mesh suggest that stretching will indeed be extremely localised at the base of the layer when stretching begins (P. England, pers. comm. 1990). Finite element modelling of sandwiches of different rheologies representing the crust and mantle (i.e. quartz and olivine) is much more difficult but is probably the way forward.

In terms of quantifying magmatic processes, the next step could be to test the model of Watson and McKenzie (in prep.), which appears able to account for the composition of melt and the rate of its production at Hawaii. Such a test could be conducted in the Indian Ocean where the Réunion plume has decompressed beneath

different thickness of oceanic plate since its Cretaceous initiation beneath the Deccan traps. The volumes and compositions of melt produced by plume decompression along this hot-spot trail (the Chagos-Laccadive ridge) should be consistent with the predictions of Watson and McKenzie (in prep.) for different the MBL thicknesses. If the model stands the test in the Indian Ocean then it might be used to study the rates of melt generation during rifting in the East African rift system.

The present quantitative theory is based on batch melting experiments. It is difficult to see how the results of the real melting process (i.e. dynamic melting) can be predicted if it cannot be experimentally duplicated. The way forward in this instance may involve a method which uses an inversion scheme for REE data to predict the variation in the extent and depth of melting (D.P. McKenzie and R.K. O'Nions, pers comm. 1990). The variation in the extent and depth of melting obtained in this way may be used as input for the compositional parameterisation of Watson and McKenzie (in prep.). The major-element compositions of the magma may then be predicted. Preliminary results suggest that the agreement between predicted and observed major-element compositions is remarkably good (McKenzie and O'Nions, in prep.).

It is abundantly clear that the theoretical framework needs to be extended to quantify the production of small melt fractions on volatile controlled solidi. Too little is known about the shape of such solidi in P-T space; existing curves do not allow the MBL ever to melt on decompression! Little is known about the cause and rate of metasomatic enrichment. Is metasomatism of the continental MBL only ever the result of processes operating at island arcs, or does it also occur in the steady state? It would be very desirable to discover whether or not the very first magmas to be erupted at an ocean island above old oceanic lithosphere (such as in the Canary Islands or Cape Verde) are more strongly potassic and volatile-rich than other oceanic rocks. It would also be interesting to see if MORB produced over downwelling limbs in the convection system (i.e. cold spots) contain less evidence for the importance of ultra-small melt fractions than normal MORB (e.g. the fractionation of U from Th or the proportion of K in the melt). If steady state convective overturn is responsible for a continual leakage of ultra-small melt fractions from the asthenosphere, then regions of downwelling should show a marked depletion in such volatile components.

REFERENCES

Ahern, J.L., & Mrkivicka, S.R. (1984). A mechanical and thermal model for the evolution of the Williston Basin. *Tectonics*, **3**, 79-102.

Ahern, J.L., & Turcotte, D.L. (1979). Magma migration beneath an ocean ridge. *Earth and Planetary Science Letters*, **45**, 115-22.

Allègre, C.J. (1969). Comportement des systemes U-Th-Pb dans le manteau superieur et modele d'evolution de ce dernier au cours des temps geologiques. *Earth and Planetary Science Letters*, **5**, 261-269.

Allègre, C.J. (1982). Chemical geodynamics. *Tectonophysics*, **81**, 109-32.

Allègre, C.J. (1987). Isotope geodynamics. *Earth and Planetary Science Letters*, **86**, 175-203.

Anderson, D. L. (1962). The plastic layer in the Earth's mantle. *Scientific American*, **205**, 2-9.

Andrews, I.J., & Brown, S. (1987). Stratigraphic evolution of the Jurassic, Moray Firth. In Petroleum Geology of North West Europe, (eds. J. Brooks & K. Glennie), Graham & Trotman, London, pp. 785-795.

Arndt, N.T. (1977). Ultrabasic magmas and high-degree melting of the mantle. *Contributions to Mineralogy and Petrology*, **64**, 205-224.

Bailey, D.K. (1982). Mantle metasomatism - continuing chemical change within the Earth. *Nature*, 296, 525-30.

Bailey, D.K. (1987). Mantle metasomatism - perspective and prospect. In Alkaline Igneous Rocks, (eds. J.G. Fitton & B.G.J. Upton), *Geological Society of London Special Publication* No **30**, pp.1-14.

Baker B.H. (1987). Outline of the petrology of the Kenya rift alkaline province. In Alkaline Igneous Rocks, (eds. J.G. Fitton & B.G.J. Upton) *Geological Society of London Special Publication* No.**30** pp. 293-312.

Baker, B.H., Crossley, R., & Goles, G.G. (1978). Tectonic and magmatic evolution of the southern part of the Kenya Rift Valley. In Petrology and Geochemistry of Continental Rifts, (ed E.R. Neumann, & I.B. Ramberg). pp. 29-50, Reidel, Dordrecht.

Barr, D. (1987). Lithospheric stretching, detached normal faulting and footwall uplift. In Continental Extensional Tectonics, (eds. M.P. Coward, J.F. Dewey, & P.L. Hancock), *Geological Society of London Special Publication*, **28**, pp. 3-18.

Barrell, J (1914). The strength of the Earth's crust. Part VI. Relations of isostatic movements to a sphere of weakness - the asthenosphere. *Journal of Geology*, **22**, 655-683.

Bartley, J.M., & Wernicke, B.P. (1984). The Snake Range decollement interpreted as a major extensional shear zone. *Tectonics*, **3**, 647-657.

Barton, P. & Wood, R. (1984). Tectonic evolution of the North Sea Basin : crustal stretching and subsidence. *Geophysical Journal of the Royal Astronomical Society*, **79**, 987-1922.

Beach, A. (1986). Some comments on sedimentary basin development in the northern North Sea. *Scottish Journal of Geology*, **22**, 1-20.

Beach, A., Bird, T., & Gibbs, A. (1987). Extensional tectonics and crustal structure: deep seismic reflection data from the northern North Sea Viking Graben. *In* Continental Extensional Tectonics (eds. M.P. Coward, J.F. Dewey, & P.L. Hancock), *Geological Society of London Special Publication*, **28**, pp. 467-476.

Beaumont, C., Keen, C.E., & Boutilier, R. (1982). On the evolution of rifted continental margins : Comparison of models and observations for the Nova Scotia margin. *Geophysical Journal of the Royal Astronomical Society*, **70**, 667-715.

Bechtel, T.T., Forsyth, D.W., & Swain, C.J. (1987). Mechanisms of isostatic compensation in the vicinity of the East African Rift, Kenya. Geophysical *Journal of the Royal Astronomical Society*, **90**, 445-465.

Bender, J.F., Hodges, F.N., & Bence, A.E. (1978). Petrogenesis of basalts from project FAMOUS area: Experimental study from 0 to 15 kbars. *Earth and Planetary Science Letters*, **41**, 277-302.

Bickle, M.J. (1978). Melting experiments on peridotitic komatiites. In Progress in Experimental Petrology, Natural Environment Research Council 4th progress report, NERC publication series D No. **11**, 187-195.

Bickle, M.J., Ford, C.E., & Nisbet, E.G. (1977). The petrogenesis of peridotitic komatiites: evidence from high-pressure melting experiments. *Earth and Planetary Science Letters*, **37**, 97-106.

Biddle, K.T., & Rudolph, K.W. (1988). Early Tertiary structural inversion in the Stord Basin, Norwegian North Sea. *Journal of the Geological Society of London*, **145**, 603-611.

Blundell, D.J., & Gibbs, A. (1990) eds. *Tectonic Evolution of the North Sea Rifts*, Oxford University Press.

Boettcher, A.L., Mysen, B.O., & Modreski, P.J. (1975). Melting in the mantle: phase relations in natural and synthetic peridotite-H_2O and peridotite-H_2O-CO_2 systems at high pressure. *Physics and Chemistry of the Earth*, **9**, 855-865.

Bosworth, W. (1987). Off-axis volcanism in the Gregory Rift, East Africa : Implications for models of continental rifting. *Geology*, **15**, 391-400.

Bott, M.H.P. (1982). *The Interior of the Earth: its structure, constitution, and evolution*. Second Edition, Edward Arnold, London, p. 403.

Bott, M.H.P. & Gunnarsson, K. (1980). Crustal structure of the Iceland-Faeroe ridge. *Journal of Geophysics*, **47**, 221-227.

Brewer, J.A., & Smythe, D.K. (1984). MOIST and the continuity of crustal reflector geometry along the Caledonian-Appalachian orogen. *Journal of the Geological Society of London*, **141**, 105-120.

Brey, G.P., Brice, W.R., Ellis, D.J., Green, D.H., Harris, K.L., Ryabchikov, I.D. (1983). Pyroxene-carbonate reactions in the upper mantle. *Earth and Planetary Science Letters*, **62**, 63-74.

Brown ,S. (1984). Jurassic. *In* Introduction to the Petroleum Geology of the North Sea (ed K.W. Glennie). pp. 133-159, Blackwell Scientific Publications, London.

Buck, W.R. (1986). Small-scale convection induced by passive rifting: the cause for uplift of the rift shoulders. *Earth and Planetary Science Letters*, **77**, 362-372.

Buck, W.R., Martinez, F., Steckler, M.S., & Cochran, J.R. (1988). Thermal consequences of lithospheric extension: pure and simple. *Tectonics*, **7**, 213-234.

Burke, K., & Dewey, J.F. (1973). Plume generated triple junctions : Key indicators in applying plate tectonics to old rocks. *Journal of Geology*, **81**, 387-405.

Calcagnile, G. (1982). The lithosphere-asthenosphere system in Fennoscandia. *Tectonophysics*, **90**, 19-35.

Carmichael, I.S.E., Turner, F.J., & Verhoogen, J. (1974). *Igneous Petrology*. New York, McGraw-Hill.

Christie, P.A.F., & Sclater, J.G. (1980). An extensional origin for the Buchan and Witchground Graben in the North Sea. *Nature*, **283**, 729-32.

Clarke-Lowes, D.D, Kuzemko, N.C.J., & Scott, D.A. (1987). Structure and petroleum prospectivity of the Dutch Central Graben and neighbouring platform areas. *In* Petroleum Geology of North West Europe, (eds. J. Brooks & K. Glennie), pp. 337-356, Graham & Trotman, London.

Cochran, J.R. (1983). Effects of finite rifting times on the development of sedimentary basins. *Earth and Planetary Science Letters*, **66**, 289-302.

Condon, P. J. (1988). *Seismic Stratigraphy and Distribution of Palaeogene Sediments West and East of Shetland.* Unpublished Ph.D. thesis, Edinburgh University.

Cottençon, A., Parant, B., & Flacelière, G. (1975). Lower Cretaceous gas fields in Holland. In Petroleum and the Continental Shelf of North West Europe, Vol 1, Geology, (ed. A.W. Woodland). pp. 403-12, Applied Science Publishers, London.

Courtney, R.C., & White, R.S. (1986). Anomalous heat flow and geoid across the Cape Verde Rise: evidence for dynamic support from a thermal plume in the mantle. *Geophysical Journal of the Royal Astronomical Society*, **87**, 815-867.

Cox, K.G., Bell, J.D., & Pankhurst, R.J. (1979). *The interpretation of igneous rocks.* Allen & Unwin, London, 450 p.

Craig, C.H., & McKenzie, D.P. (1987). The existence of a thin low viscosity layer beneath the lithosphere. *Earth and Planetary Science Letters*, **78**, 420-426.

Day, G.A., Cooper, B.A., Anderson, C., Burgers, W.F.J., Ronnevik, H.C., & Schöneich, H. (1981). Regional seismic structure maps of the North Sea. In Petroleum Geology of the Continental Shelf of North-West Europe., (eds. L.V. Illing & G.D. Hobson). pp. 76-84, Heyden, London.

Dawson, J.B. (1987). The Kimberlite clan: relationship with olivine and leucite lamproites and inferences for upper mantle metasomatism. *In* Alkaline Igneous Rocks, (eds. J.G. Fitton & B.G.J. Upton), *Geological Society of London Special Publication* No. **30**, pp. 95-101.

Delaney, J.R., Muenow, D.W., & Graham, D.G. (1978). Abundance and distribution of water, carbon and sulphur in the glassy rims of submarine pillow basalts. *Geochimica et Cosmochimica Acta*, **42**, 581-594.

DePaolo, D.J. & Wasserburg, G.J. (1976). Inferences about magma sources and mantle structure from variations in $^{143}Nd/^{144}Nd$. *Geophysical Research Letters*, **3**, 743-746.

Dick, H.J.B., & Fisher, R.L. (1984). Mineralogic studies of the residues of mantle melting: abyssal and alpine-type peridotites. In Kimberlites II: The Mantle and Crust-Mantle Relationships (ed. J. Komprobst), pp. 295-308, Elsevier.

Dick, H.J.B., Fisher, R.L., & Bryan, W.B. (1984). Mineralogic variability of the uppermost mantle along mid-ocean ridges. *Earth and Planetary Science Letters*, **69**, 88-106.

Dixon, J.E., Fitton, J.G., & Frost, R.T.C. (1981). The tectonic significance of post-Carboniferous igneous activity in the North Sea Basin. In Petroleum Geology of the Continental Shelf of North-West Europe., (eds. L.V. Illing & G.D. Hobson). pp. 121-37, Heyden, London.

Dziewonski, A.M. (1971). Upper mantle models from "pure-path" dispersion data. *Journal of Geophysical Research*, **76**, 2587-2601.

Edgar, A.D. (1987). The genesis of alkaline magmas with emphasis on their source regions : inferences from experimental studies. In Alkaline Igneous Rocks, (eds. J.G. Fitton & B.G.J. Upton) *Geological Society of London Special Publication* No.**30**, pp. 29-52.

Elthon, D. (1979). High-magnesia liquids as the parental magma for ocean floor basalts. *Nature*, **286**, 17-22.

Elthon, D. (1989). Pressure of origin of primary mid-ocean ridge basalts. In Magmatism in the Ocean Basins, (eds. M.J. Norry & S.D. Weaver), *Geological Society of London Special Publication* No. **42**, pp. 125-136.

Elthon, D., & Scarfe, C.M. (1980). High-pressure phase equilibria of a magnesian: implications for the origin of mid-ocean ridge basalts. *Yearbook of the Carnegie Institute of Washington*, **79**, 277-281.

Elthon, D., & Scarfe, C.M. (1984). High-pressure phase equilibria of a high magnesia basalt and the genesis of primary oceanic basalts. *American Mineralogist*, **69**, 1-15.

England, P. (1983). Constraints on extension of the continental lithosphere. *Journal of Geophysical Research*, **88**, 1145-1152.

Erlank, A.J., Waters, F.G., Hawkesworth, C.J., Haggerty, S.E., Allsopp, H.L., Rickards, R.S., & Menzies, M.A. (1987). Evidence for mantle metasomatism in peridotite nodules from the Kimberley Pipes, South Africa. In Mantle Metasomatism (eds. M.A. Menzies & C.J. Hawkesworth). pp. 221-311, Academic Press, London,

Eynon, G. (1981). Basin development and sedimentation in the Middle Jurassic of the northern North Sea. In Petroleum Geology of the Continental Shelf of North-West Europe (eds. L.V. Illing & G.D. Hobson). pp. 196-204, Heyden, London.

Faerseth, R.B., Macintyre, R.M., & Naterstad, J. (1976). Mesozoic alkaline dykes in the Sunnhørdland region. Western Norway : ages, geochemistry and regional significance. *Lithos*, **9**, 331-48.

Fall, H.G. (1980). *The Petrology and Geochemistry of Jurassic Igneous Rocks from the Northern North Sea.* Unpublished Ph.D. thesis. University of Sheffield.

Fall, H.G., Gibb, F.G.F., & Kanaris-Sotiriou, R. (1982). Jurassic volcanic rocks of the northern North Sea. *Journal of the Geological Society of London*, **139**, 277-92.

Fitton, J.G. (1987). The Cameroon line, West Africa : a comparison between oceanic and continental alkaline volcanism. In Alkaline Igneous Rocks, (eds. J.G. Fitton & B.G.J. Upton) *Geological Society of London Special Publication* No. **30**, pp. 273-292.

Fitton, J.G. & Dunlop, H.M. (1985). The Cameroon Line, West Africa, and its bearing on the origin of oceanic and continental alkali basalt. *Earth and Planetary Science Letters*, **72**, 23-38.

Fitton, J.G. & James, D. (1986). Basic volcanism associated with intraplate linear features. *Philosophical Transactions of the Royal Society of London*, **A317**, 253-66.

Fitton, J.G., James, D.E., & Thirlwall, M.F. (1984). *A user's guide to the X-ray fluoresence analysis of rock samples*. Unpublished report, 2nd edition, University of Edinburgh.

Fleck, R.J., Sutter, J.F., & Elliot, D.H. (1977). Interpretation of discordant 40Ar/39Ar age spectra of Mesozoic tholeiites from Antarctica. *Geochimica et Cosmochimica Acta.*, **41**, 15-32.

Foucher, J.P, Le Pichon, X., & Sibuet, J.C. (1982). The Ocean-Continent transition in the uniform lithosphere stretching model : role of partial melting in the mantle. *Philosophical Transactions of the Royal Society of London*, **A305**, 27-43.

Francis, D., & Ludden, J. (1990). The mantle source for olivine nephelinite, basanite, and alkaline olivine basalt at Fort Selkirk, Yukon, Canada. *Journal of Petrology*, **31**, 371-400.

Frey, F.A., Green, D.H., & Roy, S.D. (1978). Integrated models of basalt petrogenesis : A study of quartz tholeiites to olivine melilitites from south eastern Australia utilizing geochemical and experimental petrological data. *Journal of Petrology*, **19**, 463-513.

Fujii, T., & Bougault, D.M. (1983). Melting relations of a magnesium abyssal tholeiite and the origin of MORBs. *Earth and Planetary Science Letters*, **62**, 283-295.

Furlong, K.P., & Fountain, D.M. (1986). Continental crustal underplating: Thermal considerations and seismic-petrologic consequences. *Journal of Geophysical Research*, **91**, 8285-8294.

Furnes, H., Elvsborg, A., & Malm, O.A. (1982). Lower and Middle Jurassic alkaline magmatism in the Egersund sub-basin, North Sea. *Marine Geology*, **46**, 53-69.

Galer, S.J.G., & O'Nions, R.K. (1986). Magma genesis and the mapping of chemical and isotopic variations in the mantle. *Chemical Geology*, **56**, 45-61.

Gast, P.W. (1968). Trace element fractionation and the origin of tholeiitic and alkaline magma types. *Geochimica et Cosmochimica Acta*, **32**, 1057-86.

Gibb, F.G.F, & Kanaris-Sotiriou, R. (1976). Jurassic igneous rocks of the Forties Field. *Nature*, **260**, 23-25.

Gibbs, A.D. (1987). Deep seismic profiles in the northern North Sea. In Petroleum Geology of North-West Europe (eds. J. Brooks & K.W. Glennie). pp. 1025-28, Graham & Trotman, London.

Gibbs, A.D. (1990). Extension of the North Sea basins. In Extensional Tectonics and Stratigraphy of the North Atlantic Margins (eds. A.J. Tankard & H.R. Balkwill) *American Association of Petroleum Geologists*, Memoir **46**, 81-93.

Giltner, J.P. (1987). Application of extensional models to the northern Viking Graben. *Norsk Geologisk Tidsskrift*, **67**, 339-352.

Glennie, K.W. (1984). *Introduction to the Petroleum Geology of the North Sea.* Blackwell, Oxford 278 pp.

Green, D.H. (1969). The origin of basaltic and nephelinitic magmas in the earth's mantle. *Tectonophysics*, **7**, 409-422.

Green, D.H. & Ringwood, A.E. (1967). The genesis of basaltic magmas. *Contributions to Mineralogy and Petrology*, **15**, 103-90.

Green, D.H., Hibberson, W.O., & Jaques, A.L. (1979). Petrogenesis of mid-ocean ridge basalts. *In* The Earth: Its Origin, Structure, and Evolution (ed. M.W McElhinny), pp. 265-299, Academic Press, London.

Hallam, A., Hancock, J.M., La Breque, J.L., Lowrie, W., & Channell, J.E.T. (1985). Jurassic to Palaeogene : Part 1. Jurassic and Cretaceous geochronology and Jurassic to Palaeogene magnetostratigraphy. *In* The Chronology of the Geological Record, Geological Society Memoir No. **10** (ed. N.J. Snelling). pp. 118-40, Blackwell, London.

Haq, B.U., Hardenbol, J., & Vail, P.R. (1987). Chronology of fluctuating sea levels since the Triassic. *Science*, **235**, 1156-1167.

Harker, S.D., Gustav, S.H., & Riley, L.A. (1987). Triassic to Cenomanian stratigraphy of the Witch Ground Graben. *In* Petroleum Geology of North West Europe (eds. J. Brooks & K. Glennie), pp. 809-818, Graham & Trotman, London.

Harland, W.B., Armstrong, R.C., Craig, L., Smith, A.G., & Smith, D.G. (1990). *A Geologic Time Scale. Cambridge University Press*, in press.

Harland, W.B., Cox, A.V., Llewellyn, P.B., Pickton, C.A., Smith, A.G., & Walters, R. (1982). *A Geological Time Scale.* Cambridge University press, p. 131.

Harrison, R.K., Jeans, C.V., & Merriman, R.J. (1979). Mesozoic igneous rocks, hydrothermal mineralisation and volcanogenic sediments in Britain and adjacent regions. *Bulletin of the Geological Survey of Great Britain*, **70**, 57-69.

Harrison, W.J. (1981). Partitioning of REE between minerals and coexisting melts during partial melting of a garnet lherzolite. *American Mineralogist*, **66**, 242-259.

Hart, R.A., (1973). A model for chemical exchange in the basalt-sea water system of oceanic layer II. *Canadian Journal of Earth Sciences*, **10**, 799-816.

Harte, B., (1983). Mantle peridotites and processes - the kimberlite sample. *In* Continental Basalts and Mantle Xenoliths (eds. C.J. Hawkesworth & M.J. Norry). pp. 46-91, Shiva Publishing, Nantwich, Cheshire.

Hellinger, S.J., & Sclater, J.G. (1983). Some comments on two-layer extensional models for the evolution of sedimentary basins. *Journal of Geophysical Research*, **88**, 8251-69.

Henderson, P. (1982). *Inorganic Geochemistry.* Pergamon Press, Oxford, 353 p.

Herzberg, C.T. (1983). Solidus and liquidus temperatures and mineralogies for anhydrous garnet-lherzolite to 15 GPa. *Physics of Earth and Planetary Interiors*, **32**, 193-202.

Hess, H.H. (1962). History of ocean basins. *In* Petrologic Studies: A Volume in Honour of A.F. Buddington (eds. A.E. Engel et al.), Geological Society of America, pp. 599-620.

Hill, M.N. (1957). Recent geophysical exploration of the ocean floor. *Physics and Chemistry of the Earth*, **2**, 129-163.

Hillis, R.R. (1988). *The Geology and Tectonic Evolution of the Western Approaches Trough.* Unpublished Ph.D. thesis, Edinburgh University.

Hoffman, N.R.A. & McKenzie, D.P. (1985). The destruction of geochemical heterogeneities by differential fluid motions during mantle convection. *Geophysical Journal of the Royal Astronomical Society*, **82**, 163-206.

Hofmann, A.W. (1988). Chemical differentiation of the Earth: the relationship between mantle, continental crust and oceanic crust. *Earth and Planetary Science Letters*, **90**, 297-314.

Hofmann, A.W., & White, W.M. (1982). Mantle plumes from ancient oceanic crust. *Earth and Planetary Science Letters*, **57**, 421-36.

Holliger, K., & Klemperer, S.L. (1989). A comparison of the Moho interpreted from gravity data and from deep seismic reflection data in the northern North Sea. *Geophysical Journal of the Royal Astronomical Society*, **97**, 247-258.

Howard, K.A., & John, B.E. (1987). Crustal extension along a rooted system of imbricate low-angle faults: Colorado River extensional corridor, California and Arizona. *In* Continental Extensional Tectonics (eds. M.P. Coward, J.F. Dewey, & P.L. Hancock), *Geological Society of London Special Publication*, **28**, pp. 299-311.

Howitt, F., Aston, E.R., & Jacque, M. (1975). The occurrence of Jurassic volcanics in the North Sea. *In* Petroleum and Continental Shelf of North West Europe Vol 1, Geology, (ed. A.W. Woodland). pp. 379-88, Applied Science Publishers Ltd, Barking, Essex.

Hughes, W.F & Brighton, J.A. (1967). *Theory and Problems of Fluid Dynamics*, Schaum's Outline Series, Schaum Publishing Company, New York., 265 pp.

Ito, K., & Kennedy, G.C. (1967). Melting and phase relations in a natural peridotite to 40 kilobars. *American Journal of Science*, **265**, 519-538.

Jackson, J.A. (1987). Active normal faulting and crustal extension. *In* Continental Extensional Tectonics (eds. M.P. Coward, J.F. Dewey, & P.L. Hancock), *Geological Society of London Special Publication*, **28**, pp. 3-18.

Jacobsen, S.B., & Wasserburg, G.J. (1979). The mean age of mantle and crustal reservoirs. *Journal of Geophysical Research*, **84**, 7411-7427.

James, S.D. (1987). *Volcanism in Sedimentary Basins and its Implications for Mineralization.* Unpublished Ph.D. thesis, University of Newcastle Upon Tyne.

Jaques, A.L., & Green, D.H. (1980). Anhydrous melting of peridotite at 0-15 kb pressure and the genesis of tholeiitic basalts. *Contributions to Mineralogy and Petrology*, **73**, 287-310.

Jarvis, G.T., & McKenzie, D.P. (1980). Sedimentary basin formation with finite extension rates. *Earth and Planetary Science Letters*, **48**, 42-52.

Jeans, C.V., Merriman, R.J., & Mitchell, J.G. (1977). Origin of Bathonian and Lower Cretaceous fullers earths in England. *Clay Mineralogy Oxford*, **12**, 11-44.

Jochum, K.P., Hofmann, A.W., Ito, E., Seufert, H.M., and White, W.M. (1983). K, U and Th in mid-ocean ridge basalt glasses and heat production, K/U and K/Rb in the mantle. *Nature*, **306**, 431-436.

Jordan, T.H. (1978). Composition and development of the continental tectosphere. *Nature*, **274**, 5544-548.

Jordan, T.H. (1988). Structure and formation of the continental tectosphere. *In* Oceanic and Continental Lithosphere: Similarities and Differences, (eds. M.A. Menzies & K.G. Cox), *Journal of Petrology*, special volume, pp. 11-37.

Karner, G.D., & Watts, A.B. On isostasy at atlantic-type continental margins. *Journal of Geophysical Research*, **87**, 2923-2948.

Kay, R.W., & Gast, P.W. (1973). The rare-earth content and origin of alkali-rich basalts. *Journal of Geology*, **81**, 653-682.

Keen, C.E. (1987). Some important consequences of lithospheric extension. *In* Continental Extensional Tectonics (eds. M.P. Coward, J.F. Dewey, and P.L. Hancock), *Geological Society of London Special Publication*, **28**, pp. 67-73.

Kent, P.E. (1975). Review of North Sea basin development. *Jornal of the Geological Society of London*, **131**, 435-468.

Klein, E.M. & Langmuir, C.H. (1987). Global correlations of ocean ridge basalt chemistry with axial depth and crustal thickness. *Journal of Geophysical Research*, **92**, 8089-8115

Klemperer, S.L. (1988). Crustal thinning and nature of extension in the northern North Sea from deep seismic reflection profiling. *Tectonics*, **7**, 803-21.

Klemperer, S.L. & White, N.J. (1990). Coaxial stretching or lithospheric simple shear in the North Sea? Evidence from deep seismic profiling and subsidence. *In* Extensional Tectonics and Stratigraphy of the North Atlantic Margins, (eds. A.J. Tankard & H.R. Balkwill) *American Association of Petroleum Geologists Memoir* **46**, pp. 511-522.

Klingspor, I. (1976). Radiometric age-determination of basalts, dolerites and related syenite in Skåne, southern Sweden. *Geologiska Föreningens i Stockholm Förhandlingar*, **98**, 195-216.

Kostopoulos, D. (1988). *Geochemistry, petrogenesis, and tectonic setting of the Pindos ophiolite, N.W. Greece.* Unpublished Ph.D. thesis, University of Newcastle Upon Tyne.

Kostopoulos, D. (1990). Melting of the upper mantle: A new perspective. *Journal of Petrology*, in press.

Kushiro, I. (1968). Compositions of magmas formed by partial zone melting of the earth's upper mantle. *Journal of Geophysical Research*, **73**, 619-634.

Kushiro, I. (1972). Effects of water on the composition of magmas formed at high pressures. *Journal of Petrology*, **13**, 311-34.

Kushiro, I. (1973). The origin of some magmas in oceanic and circum-oceanic regions. *Tectonophysics*, **17**, 211-222.

Kushiro, I., & Yoder Jr., H.S. (1966). Anorthite-forsterite and anorthite-enstatite reactions and their bearing on the basalt eclogite transformation. *Journal of Petrology*, **7**, 337-362.

Kusznir, N.J. (1982). Lithospheric response to externally and internally driven stresses: a viscoelastic stress guide with amplification. *Geophysical Journal of the Royal Astronomical Society*, **70**, 399-414.

Kusznir, N.J., & Park, R.G. (1984). Intraplate deformation and the strength of the lithosphere. *Geophysical Journal of the Royal Astronomical Society*, **79**, 513-538.

Kusznir, N.J., & Park, R.G. (1987). The extensional strength of the continental lithosphere: its dependence on geothermal gradient, and crustal composition and thickness. *In* Continental Extensional Tectonics, (eds. M.P Coward, J.F. Dewey, & P.L. Hancock) *Geological Society of London Special Publication* No. **28**, pp. 35-52.

Langmuir, C.H., Bender, J.H., Bence, A.E., Hanson G.N., & Taylor, S.R. (1977). Petrogenesis of basalts from the FAMOUS area, Mid-Atlantic Ridge. *Earth and Planetary Science Letters*, **36**, 133-156.

Latin, D. & White, N. (1990). Generating melt by extension of the lithosphere : pure shear vs simple shear. *Geology*, **18**, 327-331.

Latin, D.M., Dixon, J.E., & Fitton, J.G. (1990a). Rift-related magmatism in the North Sea basin. *In* Tectonic Evolution of the North Sea Rifts (eds. D.J. Blundell & A. Gibbs), Oxford University Press, in press.

Latin, D.M., Dixon, J.E., Fitton, J.G., & White, N. (1990b). Mesozoic magmatic activity in the North Sea basin: implications for stretching history. *In* Tectonic Movements Responsible for Britain's Oil and Gas Reserves, (eds. R.F.P. Hardman & J.R.V. Brooks) *Geological Society of London Special Publication*, in press.

Le Pichon, X., & Sibuet, J.C. (1981). Passive Margins : A model of formation. *Journal of Geophysical Research*, **86**, 3708-20.

Le Pichon, X., Lybéris, N., & Alvarez, F. (1984). Subsidence history of the North Aegean Trough. *In* The Geological Evolution of the Eastern Mediterranean, (eds. J.E. Dixon & A.H.F. Robertson) *Geological Society of London Special Publication* No. **17**, pp. 727-741.

Le Roex, A.P., Dick, H.J.B., Erlank, A.J., Reid, F.A., Frey, F.A., & Hart, S.R. (1983). Geochemistry, mineralogy, and petrogenesis of lavas erupted along the southwest Indian Ridge between the Bouvet triple junction and 11 degrees East. *Journal of Petrology*, **24**, 267-318.

Leeder, M.R. (1983). Lithospheric stretching and North Sea Jurassic sourcelands. *Nature*, **305**, 510-14.

Lewis, B.T.R., & Dorman, L.M. (1970). Experimental isostasy, 2, an isostatic model for the U.S.A. derived from gravity and topographic data. *Journal of Geophysical Research*, **81**, 1903-1915.

Lie, J.E., Pederson, T., & Husebye, E.S. (1990). Observations of seismic reflectors in the lower lithosphere beneath the Skagerrak. *Nature*, **346**, 165-168.

Lister, G.S., Etheridge, M.A., & Symonds, P.A. (1986). Detachment faulting and the evolution of passive continental margins. *Geology*, **14**, 246-250.

Lister, G.S., Etheridge, M.A., & Symonds, P.A. (1990). Detachment models for the formation of passive continental margins. *Tectonics*, in press.

Livermore, R.A. & Smith, A.G. (1985). Some boundary conditions for the evolution of the Mediterranean region. *In* Geological Evolution of the Mediterranean Basin (eds. D.J. Stanley & F. Wezel), pp. 83-98, Springer-Verlag, New York.

Lloyd, F.E., Arima, M., & Edgar, A.D. (1985). Partial melting of a phlogopite-clinopyroxenite nodule from south-west Uganda: An experimental study bearing on the origin of highly potassic continental rift volcanics. *Contributions to Mineralogy and Petrology*, **91**, 321-329.

Lyon-Caen, H., & Molnar, P. (1983). Constraints on the structure of the Himalaya from an analysis of gravity anomalies and a flexural model of the lithosphere. *Journal of Geophysical Research*, **88**, 8171-8191.

Macdonald, R. (1987). Quaternary peralkaline silicic rocks and caldera volcanoes of Kenya. *In* Alkaline Igneous Rocks, (eds. J.G. Fitton & B.G.J. Upton), *Geological Society of London Special Publication* No. **30**, pp. 313-334.

MacGregor, I.D. (1965). Stability fields of spinel and garnet peridotites in the synthetic system MgO-CaO-Al_2O_3-SiO_2. *Yearbook of the Carnegie Institute of Washington*, **64**, 126-134.

Malpas, J. (1978). Magma generation in the upper mantle, field evidence from ophiolite suites, and application to the generation of oceanic lithosphere. *Philosophical Transactions of the Royal Society of London*, **A288**, 527-546.

McGeary, S. (1987). Nontypical BIRPS on the margin of the North Sea: the SHET survey, *Geophysical Journal of the Royal Astronomical Society*, **89**, 231-238.

McGeary, S., & Warner, M.R. (1985). Seismic profiling of the continental lithosphere. *Nature*, **317**, 795-797.

McKenzie, D.P. (1967). Some remarks on heat flow and gravity anomalies. *Journal of Geophysical Research*, **72**, 6261-73.

McKenzie, D.P. (1970). Temperature and potential temperature beneath island arcs. *Tectonophysics*, **10**, 357-366.

McKenzie, D.P. (1978). Some remarks on the development of sedimentary basins. *Earth and Planetary Science Letters*, **40**, 25-32.

McKenzie, D.P. (1984). The generation and compaction of partially molten rock. *Journal of Petrology*, **25**, 713-65.

McKenzie, D.P. (1985a). ^{230}Th-^{238}U disequilibrium and the melting processes beneath ridge axes. *Earth and Planetary Science Letters*, **72**, 149-157.

McKenzie, D.P. (1985b). The extraction of magma from crust and mantle. *Earth and Planetary Science Letters*, **78**, 81-94.

McKenzie, D.P. (1989). Some remarks on the movement of small melt fractions in the mantle. *Earth and Planetary Science Letters*, **95**, 53-72.

McKenzie, D.P., & Sclater, J.G. (1973). The evolution of the Indian Ocean. *Scientific American*, **228**, 62-72.

McKenzie, D.P., & Bowin, C.O. (1976). The relationship between bathymetry and gravity in the Atlantic Ocean. *Journal of Geophysical Research*, **81**, 1903-1915.

McKenzie, D.P., & Richter, F. (1976). Convection currents in the Earth's mantle. *Scientific American*, **235**, 72-89.

McKenzie, D., & O'Nions, R.K. (1983). Mantle reservoirs and ocean island basalts. *Nature*, **301**, 229-231.

McKenzie, D.P., & Bickle, M.J. (1988). The volume and composition of melt generated by extension of the lithosphere. *Journal of Petrology*, **29**, 625-79.

McKenzie, D., & O'Nions, R.K. (1990 in prep.). Partial melt distributions from inversion of rare earth element concentrations. To be submitted to *Journal of Petrology*.

McKenzie, D., Watts, A., Parsons, B. & Roufosse, M. (1980). Planform of mantle convection beneath the Pacific Ocean. *Nature*, **288**, 442-446.

McNutt, M.K., & Menard, H.W. (1982). Constraints on yield strength in the oceanic lithospheric from observations of flexure. *Geophysical Journal of the Royal Astronomical Society*, **71**, 363-394

Menzies, M.A. & Murthy, V.R. (1980). Nd and Sr isotope geochemistry of hydrous mantle nodules and their host alkali basalts: implications for local heterogeneitites in metasomatically veined mantle. *Earth and Planetary Science Letters*, **46**, 323-334.

Menzies, M.A. & Hawkesworth, C.J. (1987). *Mantle Metasomatism* (eds). Academic Press, London, p.472.

Michael, P.J., & Chase, R.L. (1987). The influence of primary magma composition, H_2O and pressure on mid-ocean ridge basalt differentiation. *Contributions to Mineralogy and Petrology*, **96**, 245-263.

Middlemost, E.A.K. (1975). The basalt clan. *Earth Science Reviews*, **11**, 337-364.

Middlemost, E.A.K. (1985). *Magmas and magmatic rocks. An introduction to igneous petrology.* Longman, London & New York, 266 p.

Mohr, P. (1982). Musings on continental rifts. In Continental and Oceanic Rifts., AGU Geodynamics Series, Vol 8 (ed G. Palmason), pp. 293-309.

Morgan, P. (1984). The thermal structure and thermal evolution of the continental lithosphere. *In* Structure and Evolution of the Continental Lithosphere, (eds. H.N. Pollack et al.,). *Physics and Chemistry of the Earth*, **15**, 107-193.

Morgan, W.J. (1981). Hot spot tracks and the opening of the Atlantic and Indian Oceans. In The Sea volume 7, (ed. C. Emiliani), pp. 443-487. John Wiley & Sons, New York.

Mutter, J.C., Buck, W.R., & Zehnder, C.M. (1988). Convective partial melting, I, A model for the formation of thick basaltic sequences during the initiation of spreading. *Journal of Geophysical Research*, **93**, 1031-1048.

Mysen, B.O., & Boettcher, A.L. (1975). Melting of a hydrous mantle: II. Geochemistry of crystals and liquids formed by anatexis of mantle peridotite at high pressures and high temperatures as a function of controlled activities of water, hydrogen, and carbon dioxide. *Journal of Petrology*, **16**, 549-93.

Mysen, B.O., & Kushiro, I. (1977). Compositional variations of coexisting phases with degree of melting of peridotite in the upper mantle. *American Mineralogist*, **62**, 843-865.

Nakamura, N. (1974). Determination of REE, Ba, Fe, Mg, Na, and K in carbonaceous and ordinary chondrites. *Geochimica et Cosmochimica Acta*, **38**, 757-775.

Nicholson, H. (1990). *The Magmatic Evolution of Krafla, NE Iceland.* Unpublished Ph.D. thesis, Edinburgh University.

Nicholson, H., & Latin, D. (1990 in prep.). Primitive basalts from Iceland: evidence for the importance of small melt fractions from a plume.

Nicholson, H., Condomines, M., Fallick, A.E., Fitton, J.G., Grönvold, K., & Rogers, G. (1990 in prep.). Geochemical and isotopic evidence for crustal assimilation beneath Krafla, Iceland.

Nickel, K.G. (1986). Phase equilibria in the system SiO_2-MgO-Al_2O_3-CaO-Cr_2O_3 (SMACR) and their bearing on spinel\garnet lherzolite relationships.

Norry, M.J., & Fitton, J.G. (1983). Compositional differences between oceanic and continental basic lavas and their significance. In Continental Basalts and Mantle Xenoliths, (C.J. Hawkesworth & M.J., Norry), pp 5-19, Shiva, Nantwich, Cheshire.

Nunn, J.A., & Sleep, N.H. (1984). Thermal contraction and flexure of intracratonic basins: A three-dimensional study of the Michigan Basin. *Geophysical Journal of the Royal Astronomical Society*, **76**, 587-635.

O'Hara, M.J. (1968). Are any ocean floor basalts primary magma? *Nature*, **220**, 683-686.

O'Hara, M.J. (1977). Geochemical evolution during fractional crystallisation of a periodically refilled magma chamber. *Nature*, **266**, 503-507.

O'Hara, M.J. (1985). Importance of the "shape" of the melting regime during partial melting of the mantle. *Nature*, **314**, 58-62.

O'Hara, M.J. & Mathews, R.E. (1981). Geochemical evolution in an advancing, periodically replenished, periodically tapped, continuously fractionated magma chamber. *Journal of the Geological Society*, **138**, 237-277.

Olafsson, M. & Eggler, D.H. (1983). Phase relations of amphibole-carbonate and phlogopite-carbonate peridotite: petrologic constraints on the asthenosphere. *Earth and Planetary Science Letters*, **64**, 305-315.

Olson, P., Schubert, G., & Anderson, C. (1987). Plume formation in the D" layer and the roughness of the core-mantle boundary. *Nature*, **327**, 409-413.

O'Nions R.K., & Oxburgh, E.R. (1983). Heat and helium in the Earth. *Nature*, **306**, 429-431.

O'Nions, R.K., & McKenzie, D.P. (1988). Melting and continent generation. *Earth and Planetary Science Letters*, **90**, 449-456.

O'Nions, R.K., Hamilton, P.J., & Evensen, N.M. (1977). Variations in $^{143}Nd/^{144}Nd$ and $^{87}Sr/^{86}Sr$ ratios in oceanic basalts. *Earth and Planetary Science Letters*, **38**, 211-236.

Oxburgh, E.R. (1980). Heat flow and magma genesis. In Physics of Magmatic Processes (ed. R.B. Hargreaves),pp. 161-199, Princeton University Press, New Jersey.

Oxburgh, E.R., & Turcotte, D.L. (1968). Mid-ocean ridges and geotherm distribution during mantle convection. *Journal of Geophysical Research*, **73**, 2643-2661.

Pallister, J.S., & Gregory, R.T. (1983). Composition of the Samail ocean crust. *Geology*, **11**, 638-642.

Parker, R.L., & Oldenburg, D.W. (1973). Thermal model of ocean ridges. *Nature*, **242**, 137-139.

Parsons, B., & McKenzie, D.P. (1978). Mantle convection and the thermal structure of the plates. *Journal of Geophysical Research*, **83**, 4485-4496.

Parsons, B., & Sclater, J.G. (1977). An analysis of the variation of ocean floor bathymetry and heat flow with age. *Journal of Geophysical Research*, **82**, 803-827.

Pearce, J.A., & Cann, J.R. (1973). Tectonic setting of basic volcanic rocks determined using trace element analysis. *Earth and Planetary Science Letters*, **19**, 290-300.

Pearce, J.A., Lippard, S.J., & Roberts, S. (1984). Characteristics and tectonic significance of supra-subduction zone ophiolites. In Marginal Basin Geology (eds. B.P. Kokelaar & M.F. Howells), *Geological Society of London Special Publication* No. **16** , Blackwell, Oxford, pp. 77-94.

Pearce, J.A., Bender, J.F., De Long, S.E., Kidd, W.S.F., Low, P.J., Güner, Y, Saroglu, F., Yilmaz, Y, Moorbath, S., & Mitchell, J.G. (1990). Genesis of collision volcanism in Eastern Anatolia, Turkey. *Journal of Volcanology and Geothermal Research*, in press.

Pederson, T., Pettersson, S.E., & Husebye, E.S. (1990). Skagerak evolution as derived from tectonic subsidence. *Tectonophysics*, in press.

Peltier, W.R. (1980). Mantle convection and viscosity. In Physics of the Earth's interior (eds A.M. Dziewonski & E. Boschi). Bologna: Societa Italiana di Fisica and Amsterdam: North Holland, pp. 362-431.

Perrot, J., & Van der Poel, A.B. (1987). Zuidwal - a Neocomian gasfield. In Petroleum Geology of North West Europe, (eds. J. Brooks & K.W. Glennie), pp. 325-35, Graham and Trotman, London.

Pitman, W.C. III. (1978). Relationship between eustasy and stratigraphic sequences of passive margins. *Bulletin of the Geological Society of America*, **89**, 1389-1403.

Presnall, D.C., Dixon, J.R., O'Donell, T.H., & Dixon, S.A. (1979). Generation of mid-ocean ridge tholeiites. *Journal of Petrology*, **20**, 3-35.

Press,W.H., Flannery, B.P., Teukolsky, S.A., & Vetterling, W.T. (1986). *Numerical Recipes. The Art of Scientific Computing*. Cambridge University Press, Cambridge, England, 818 p.

Raitt, R.W. (1963). The crustal rocks. In The Sea, (ed. Hill M.N.) volume 3, pp. 39-46, Interscience Publishers, New York & London.

Ranalli, G. (1987). *Rheology of the Earth. Deformation and flow processes in geophysics and geodynamics*. Allen & Unwin, Boston, 366 p.

Rawson, P.F., & Riley, L.A. (1982). Latest Jurassic-Early Cretaceous events and the "late Cimmerian Unconformity" in the North Sea area. *Bulletin of the American Association of Petroleum Geologists*, **66**, 2628-2648.

Ribe, N.M. (1987). Theory of melt segregation - a review. *Journal Volcanology and Geothermal Research*, **33**, 241-53.

Ribe, N.M. & Smooke, M.D. (1987). A stagnation-point flow model for melt extraction from a mantle plume. *Journal of Geophysical Research*, **92**, 6437-6443.

Richardson, S.H., Gurney, J.J., Erlank, A.J., Harris, J.W. (1984). Origin of diamonds in old enriched mantle. *Nature*, **310**, 198-202.

Richter, F.M. (1988). A major change in the thermal state of the Earth at the Archean-Proterozoic Boundary. *In* Oceanic and Continental Lithosphere: Similarities and Differences, (eds. M.A. Menzies & K.G. Cox), *Journal of Petrology*, special volume, pp. 39-52.

Richter, F.M., & McKenzie, D.P. (1981). On some consequences and possible causes of layered mantle convection. *Journal of Geophysical Research*, **86**, 6133-6142.

Richter, F.M., & McKenzie, D.P. (1984). Dynamical models for melt segregation from a deformable matrix. *Journal of Geology*, **92**, 729-40.

Ringwood, A.E. (1969). Composition of the crust and upper mantle. *American Geophysical Union, Geophysics Monograph*, **12**, 1-17.

Ringwood, A.E. (1975). *Composition and Petrology of the Earth's Mantle.* McGraw-Hill International Series in the Earth and Planetary Sciences, 618 p.

Ringwood, A.E. (1982). Phase transformations and differentiation in subducted lithosphere: implications for mantle dynamics, basalt petrogenesis and crustal evolution. *Journal of Geology*, **90**, 611-643.

Ritchie, J.D., Swallow, J.L., Mitchell, J.G., & Morton, A.C. (1988). Jurassic ages from intrusives and extrusives within the Forties igneous province. *Scottish Journal of Geology*, **24**, 81-88.

Roberts, A.M., Yielding, G., & Badley, M. (1990). A kinematic model for the orthogonal opening of the Late Jurassic North Sea Rift System, Denmark-Mid Norway. *In* Tectonic Evolution of the North Sea Rifts (eds. D.J. Blundell & A. Gibbs), Oxford University Press, in press.

Rowley, D.B., & Sahagian, D. (1986). Depth-dependent stretching: A different approach. *Geology*, **14**, 32-35.

Royden, L., & Keen, C.E. (1980). Rifting process and thermal evolution of the continental margin of eastern Canada determined from subsidence curves. *Earth and Planetary Science Letters*, **51**, 345-61.

Royden, L., Horvath, F., Nagymarosy, A., & Stegena, L. (1983). Evolution of the Pannonian Basin System 2. Subsidence and thermal history. *Tectonics*, **2**, 91-137.

Saunders, A.D., Norry, M.J., & Tarney, J. (1988). Origin of MORB and chemically depleted mantle reservoirs: trace element constraints. *In* Oceanic and Continental Lithosphere: Similarities and Differences, (eds. M.A. Menzies & K.G. Cox), *Journal of Petrology*, special volume, pp. 415-445.

Sawyer, D.S., Toksöz, M.N., Sclater, J.G., & Swift, B.A. (1982). Thermal evolution of the Baltimore Canyon Trough and Georges Bank Basin. In Studies in Continental Margin Geology, (eds. J.S. Watkins & C.L. Drake), *American Association of Petroleum Geologists Memoir*, **34**, 743-762.

Schilling, J.-G., Zajac, M., Evans, R. Johnston, T., White, W., Devine, J.D., Kingsley, R. (1983). Petrologic and geochemical variations along the Mid-Atlantic Ridge from 27°N to 73°N. *American Journal of Science*, **238**, 510-86.

Sclater, J.G., & Christie, P.A.F. (1980). Continental stretching: An explanation of the post mid-Cretaceous subsidence of the Central North Sea Basin. *Journal of Geophysical Research*, **85**, 3711-39.

Sclater, J.G., & Francheteau, J. (1970). The implications of terrestrial heat flow observations on current tectonic and geochemical models of the crust and upper mantle of the earth. *Geophysical Journal of the Royal Astronomical Society*, **20**, 509-542.

Sclater, J.G., Royden, L., Horvath, F., Burchfiel, B.C., Semken, S., & Stegena, L. (1980). The formation of the Intra Carpathian Basins as determined from subsidence data. *Earth and Planetary Science Letters*, **51**, 139-62.

Shaw, D.M. (1970). Trace element fractionation during anatexis. *Geochimica et Cosmochimica Acta*, **34**, 237-43.

Sleep, N.H. (1971). The thermal effects of the formation of Atlantic continental margins by continental breakup. *Geophysical Journal of the Royal Astronomical Society*, **24**, 325-50.

Sleep, N.H. (1984). Tapping of magmas from ubiquitous mantle heterogeneities : an alternative to mantle plumes?. *Journal of Geophysical Research*, **89**, 10029-41.

Smedley, P.L. (1986). *Petrochemistry of Dinantian volcanism in northern Britain.* Unpublished Ph.D. thesis, Edinburgh University.

Solli, M. (1976). *En seismisk skorpeudersokelse Norges-Shetland.* Unpublished M.Sc. thesis, University of Bergen.

Spiegelman, M., & McKenzie, D.P. (1987). Simple 2-D models for melt extraction at mid-ocean ridges and island arcs. *Earth and Planetary Science Letters*, **83**, 137-52.

Spudich, P., & Orcutt, J. (1980). A new look at the seismic velocity structure of the oceanic crust. *Reviews in Geophysics*, **18**, 627-645.

Steckler, M.S. (1985). Uplift and extension at the Gulf of Suez: indications of induced mantle convection. *Nature*, **317**, 135-139.

Steckler, M.S., & Watts, A.B. (1978). Subsidence of the Atlantic-type continental margin off New York. *Earth and Planetary Science Letters*, **41**, 1-13.

Steiger, R.H. & Jäger, E. 1977. Subcommission on Geochronology : convention on the use of decay constants in geochronology and cosmochronology. *Earth and Planetary Science Letters*, **36**, 359-62.

Stolper, E. (1980). A phase diagram for mid-ocean ridge basalts: preliminary results and implications for petrogenesis. *Contributions to Mineralogy and Petrology*, **74**, 13-27.

Stuart, G.W. (1978). The upper mantle structure of the North Sea from Rayleigh wave dispersion. *Geophysical Journal of the Royal Astronomical Society*, **52**, 367-382.

Sun, S. -S. (1980). Lead isotopic study of young volcanic rocks from mid-ocean ridges, ocean islands and island arcs. *Philosophical Transactions of the Royal Society of London*, **A297**, 409-445.

Sun, S. -S. (1982). Chemical composition and origin of the earth's primitive mantle. *Geochimica et Cosmochimica Acta*, **46**, 179-192.

Sun, S. -S., Nesbitt, R.W., & Sharaskin, A.Ya. (1979). Geochemical characteristics of mid-ocean ridge basalts. *Earth and Planetary Science Letters*, **44**, 119-138.

Takahashi, E. (1986). Melting of a dry peridotite KLB-1 up to 14 GPa: Implications on the origin of peridotitic upper mantle. *Journal of Geophysical Research*, **91**, 9367-9382.

Takahashi, E., & Kushiro, I. (1983). Melting of a dry peridotite at high pressures and basalt magma genesis. *American Mineralogist*, **68**, 859-879.

Tate, M.P., & Dobson, M.R. (1988). Syn- and post-rift igneous activity in the Porcupine Seabight Basin and adjacent continental margin W of Ireland. *In* Early Tertiary Volcanism and the Opening of the N E Atlantic, (eds. A.C. Morton, & L.M. Parson), *Geological Society of London Special Publication* No. **39**, pp. 309-334.

Tate, M, White, N., & Conroy, J.J. (1990 in prep.) Stretching, melting and maturation : sedimentary basin analysis west of Ireland.

Thompson, R.N. (1982). Magmatism of the British Tertiary Volcanic province. *Scottish Journal of Geology*, **18**, 49-107.

Thompson, R.N. (1987). Phase-equilibria constraints on the genesis and magmatic evolution of oceanic basalts. *Earth Science Reviews*, **24**, 161-210.

Thompson, R.N., Leat, P.T., Dickin, A.P., Morrison, M.A., Hendry, G.L., & Gibson, S.A. (1990). Strongly potassic mafic magmas from lithospheric mantle sources during continental extension and heating: evidence from Miocene minettes of northwest Colorado, U.S.A. *Earth and Planetary Science Letters*, **98**, 139-153.

Tilley, C.E., Thompson, R.N., & Lovenbury, P.A. (1972). Melting relations of some oceanic basalts. *Geological Journal*, **8**, 59-64.

Tréhu, A., Sclater, J.G., & Nabelek, J. (1976). The depth and thickness of the oceanic crust and its dependence upon age. *Bulletin of the Geological Society of France*, **18** No 4, 917-930

Turcotte, D.L., & Schubert, G. (1982). *Geodynamics: applications of continuum physics to geological problems.* John Wiley & Sons, New York, 450 p.

Turner, C. C., Richards, P.C., Swallow, J.L., & Grinshaw, S.P. (1984). Upper Jurassic stratigraphy and sedimentary facies in the Central Outer Moray Firth Basin, North Sea. *Marine and Petroleum Geology*, **1**, 105-117.

Upton, B.G.J. (1988). History of Tertiary igneous activity in the N Atlantic borderlands. *In* Early Tertiary Volcanism and the Opening of the N E Atlantic, (eds. A.C. Morton, & L.M. Parson), *Geological Society of London Special Publication* No. **39**, pp. 429-453.

Upton, B.G.J., Mitchell, R.H., Menzies, M., & Aspen, P. (1990 in prep.). Primitive olivine melan nephelinite dykes from the Orkney Islands, Scotland.

Vail, P.R., & Todd, R.G. (1981). Northern North Sea Jurassic unconformities, chronostratigraphy and sea level changes from seismic stratigraphy. In Petroleum Geology of the Continental Shelf of North-West Europe (eds. L.V. Illing & G.D. Hobson), pp. 216-235, Heyden, London.

Vail, P.R., Mitchum, R.M., Todd, R.G., Widmier, J.M., Thompson, S. III, Sangree, J.B., Bubb, J.N., & Hatlelid, W.G. (1977). Seismic stratigraphy and global changes of sea level. In Seismic Stratigraphy - Applications to hydrocarbon exploration, *American Association of Petroleum Geologists Memoir*, **26**, 49-212.

Van Hinte, J.E. (1976). A Jurassic time scale. *Bulletin of the American Association of Petroleum Geologists*, **60**, 489-97.

Van Wijhe, D.H. (1987). The structural evolution of the Broad Fourteens Basin. In Petroleum Geology of North West Europe, (eds. J.Brooks & K.W. Glennie), pp. 315-24, Graham & Trotman, London.

Verhoogen, J. (1954). Petrological evidence on temperature distribution in the mantle of the earth. *Transactions of the American Geophysical Union*, **35**, 85-92.

Voorhoeve H., & Houseman, G. (1988). The thermal evolution of lithosphere extending on a low-angle detachment. *Basin Research*, **1**, 1-9.

Walcott, R.L. (1970). Flexural rigidity, thickness and viscosity of the lithosphere. *Journal of Geophysical Research*, **75**, 3941-3954.

Walker, D., Shibata, T., & De Long, S.E. (1979). Abyssal tholeiites from the Oceanographer Fracture Zone: II Phase equilibria and mixing. *Contributions to Mineralogy and Petrology*, **70**, 111-125.

Wallis, S.M. (1989). *Petrology and geochemistry of Upper Carboniferous - Lower Permian volcanic rocks in Scotland.* Unpublished Ph.D. thesis, University of Edinburgh.

Walsh, J.N., Buckley, F. & Barker, J. (1981). The simultaneous determination of the rare-earth elements in rocks using inductively coupled plasma source spectrometry. *Chemical Geology*, **33**, 141-153.

Walter, M.J. & Presnall, D.C. (1990). Melting relations of symplified lherzolite in the system CaO-MgO-Al_2O_3-SiO_2-Na_2O (CMASN) at pressures from 14 to 28 kbar - Application to MORB genesis. *EOS*, **71**, 648.

Watson, S., & McKenzie, D. (1990 in prep.). Melt generation by plumes: A study of Hawaiian volcanism. Submitted to *Journal of Petrology*.

Watts, A.B. (1978). An analysis of isostasy in the world's oceans, 1. Hawaiian-Emperor seamount chain. *Journal of Geophysical Research*, **83**, 5989-6004.

Watts, A.B., & Thorne, J. (1984). Tectonics, global changes in sea-level and their relationship to stratigraphic sequences at the U.S. Atlantic continental margin. *Marine and Petroleum Geology*, **1**, 319-339.

Watts, A.B., & Cox, K.G. (1989). The Deccan Traps: an interpretation in terms of progressive lithospheric flexure in response to a migrating load. *Earth and Planetary Science Letters*, **93**, 85-97.

Watts, A.B., McKenzie, D.P., Parsons, B.E., & Roufosse, M. (1985). The relationship between gravity and bathymetry in the Pacific Ocean. *Geophysical Journal of the Royal Astronomical Society*, **83**, 263-298.

Wendlandt, R.F., & Morgan, P. (1982). Lithospheric thinning associated with rifting in East Africa. *Nature*, **298**, 734-735.

Wernicke, B. (1981). Low-angle normal faults in the Basin and Range province: Nappe tectonics in an extending orogen. *Nature*, **291**, 645-648.

Wernicke, B. (1985). Uniform sense simple shear of the continental lithosphere. *Canadian Journal of Earth Sciences*, **22**, 108-25.

Wernicke, B., Walker, J.D., & Beaufait, M.S. (1985). Structural discordance between Neogene detachments and frontal Sevier thrusts, central Morman Mountains, southern Nevada. *Tectonics*, **4**, 213-46.

Wilson, M., (1989). *Igneous Petrogenesis: A Global Tectonic Approach.* Unwin Hyman, London, 466 p.

White, N.J. (1988). *Extension and subsidence of the continental lithosphere.* Unpublished Ph.D. thesis, Cambridge University.

White, N. (1989). The nature of lithospheric extension in the North Sea. *Geology*, **17**, 111-114.

White, N. (1990). Does the uniform stretching model work in the North Sea? *In* Tectonic Evolution of the North Sea Rifts (eds. D.J. Blundell & A. Gibbs), Oxford University Press, in press.

White, N., & McKenzie, D.P. (1988). Formation of the `steer's head' geometry of sedimentary basins by differential stretching of the crust and mantle. *Geology*, **16**, 250-53.

White, R.S. (1984). Atlantic oceanic crust: Seismic structure of a slow spreading ridge. In Ophiolites and the Oceanic Lithosphere, (eds. I.G. Gass, S.j. Lippard & A.W. Shelton), *Geological Society of London Special Publication* No. **13**, pp. 34-44.

White, R.S. (1988). The Earth's crust and lithosphere. *In* Oceanic and Continental Lithosphere: Similarities and Differences, (eds. M.A. Menzies and K.G. Cox), *Journal of Petrology*, special volume, pp. 1-10. Oxford University press.

White, R.S., & McKenzie, D.P. (1989). Magmatism at rift zones : The generation of volcanic continental margins and flood basalts. *Journal of Geophysical Research*, **94**, 7685-7729.

White, R.S., Fowler, S.R., McKenzie, D.P., Westbrook, G.K., & Bowen, A.N. (1987). Magmatism at rifted continental margins. *Nature*, **330**, 439-44.

Whiteman, A., Naylor, D., Pegrum, R., & Rees, G. (1975). North Sea troughs and plate tectonics. *Tectonophysics*, **26**, 39-54.

Wilding, M.C. (1990). *A Study of Diamonds with Syngenetic Inclusions.* Unpublished Ph.D. thesis, Edinburgh University.

Wood, D.A. (1979). A variably veined suboceanic upper mantle - Genetic significance for mid-ocean ridge basalts from geochemical evidence. *Geology*, **7**, 499-503.

Wood, R.J. (1982). *Subsidence in the North Sea.* Unpublished Ph.D. thesis, Cambridge University.

Woodhall, D., & Knox, R.W (1979). Mesozoic volcanism in the northern North Sea and adjacent areas. *Bulletin of the Geological Survey of Great Britain*, **70**, 34-56.

Wyllie P.J. (1987). Transfer of subcratonic carbon into kimberlites and rare earth carbonatites. In Magmatic Processes : Physiochemical Principles, The Geochemical Society, Sp. Pub. No.1 (ed. B.O. Mysen), pp 107-19.

Yielding, G. (1990). Footwall uplift associated with Late Jurassic normal faulting in the northern North Sea. *Journal of the Geological Society of London*, **147**, 219-222.

Yoder, H.S. Jr. (1976). *Generation of Basaltic Magma*, National Academy of Science, Washington DC, p. 265.

Yoder, H.S. Jr. & Tilley C.E. (1962). Origin of basaltic magmas: an experimental study of natural and synthetic rocks systems. *Journal of Petrology*, **3**, 342-532.

Yuen, D.A., & Fleitout, L. (1985). Thinning of the lithosphere by small-scale convective destabilization. *Nature*, **313**, 125-128.

Zehnder, C.M., Mutter, J.C., & Buhl, P. (1990). Deep seismic and geochemical constraints on the nature of rift-induced magmatism during breakup of the North Atlantic. *Tectonophysics*, **173**, 545-565.

Zervos, F.A. (1986). *Geophysical Investigation of Sedimentary Basin Development: Viking Graben, North Sea*. Unpublished Ph.D thesis, Edinburgh University.

Zervos, F.A. (1987). A compilation and regional interpretation of the northern North Sea gravity map. *In* Continental Extensional Tectonics (eds. M.P. Coward, J.F. Dewey, & P.L. Hancock), *Geological Society of London Special Publication*, **28**, pp. 477-493.

Ziegler, P.A. (1975). North Sea history in the tectonic framework of north-western Europe. *In* Petroleum Geology and Continental Shelf of North West Europe Vol 1, Geology, (ed. A.W. Woodland), pp. 131-150, Applied Science Publishers Ltd, Barking, Essex.

Ziegler, P.A. (1981). Evolution of sedimentary basins in north-west Europe. *In* The Petroleum Geology of the Continental Shelf of North-west Europe (eds. L.V. Illing & G.D. Hobson). pp. 3-39, Heyden, London.

Ziegler, P.A. (1982). *Geological Atlas of Western and Central Europe*. Shell Internationale Maatschappij B.V., the Hague, 130 p.

Ziegler, P.A., & Van Hoorn, B. (1990). Evolution of the North Sea rift system. In Extensional Tectonics and Stratigraphy of the North Atlantic Margins. (eds. A.J. Tankard & H.R. Balkwill) *American Association of Petroleum Geologists Memoir* **46**, pp. 471-500.

Zindler, A., & Hart, S.R. (1986). Chemical geodynamics. *Annual Reviews of Earth and Planetary Sciences*, **14**, 493-571.

Zindler, A., & Jagoutz, E. (1988). Mantle cryptology. *Geochimica et Cosmochimica Acta*, **52**, 319-333.

APPENDIX A

PLATES, PETROGRAPHIC AND GEOCHEMICAL DATA

This appendix contains 18 plates (section A1 plates A to R) together with whole-rock major- and trace-element and mineral data for igneous rock samples from the North Sea (Sections A2 to A4). Since many of the samples are altered and because their petrographic character is so variable, a key is provided with each XRF analysis presented in the tables in section A2. Section A3 contains tables of REE data for selected samples and section A4 contains tables of mineral data.

SECTION A1 : Plates.

Plates A to F are included to show different extents of alteration found in the North Sea samples. They are referred to from the key for the whole-rock data presented in section A2. Plates G to R are included to show some of the features discussed in Chapter 4.

PLATE A : Ankaramitic alkali olivine basalt - plane polarised light (PPL); sample 42 from well AH1 (15/21-8a) in the Forties province. Note olivine in the centre of the field of view shows only limited alteration, along fractures, to green sheet silicate. This is the freshest sample from the Forties province. Field of view = 3.6 mm.

PLATE B : Ankaramitic alkali olivine basalt (PPL); sample 41 from well AH1 in the Forties province. Note deep orange-brown iddingsitisation of euhedral olivine phenocryst (top right) and fresh euhedral augite with thin pink-brown, more Ti-rich, veneer (bottom left). Field of view = 3.6 mm.

PLATE C : Ankaramitic alkali olivine basalt (PPL); sample 10 from well AH1 in the Forties province. The olivines in this rock have undergone several phases of alteration. Large olivine phenocryst (centre) has been altered to iddingsite and sheet silicates (as in Plate B) which have then been replaced by hydrothermal quartz (centre of phenocryst). Again note euhedral titanaugites. Field of view = 3.6 mm.

PLATE D : Altered basaltic hawaiite (PPL); sample 10 from well SO1 (22/1a-4) in the Forties province. Large olivine phenocryst (centre) is pseudomorphed by bright green sheet silicate and dark brown hydrated iron oxides. Pyroxene phenocryst (left of centre and bottom right) is pseudomorphed by carbonate. Groundmass is largely albitised microlites of plagioclase set in an altered glassy base. Carbonate-filled veins form a large part of the rock. Field of view = 3.6 mm.

PLATE E : Severely altered basaltic rock (PPL); sample 5 from well AH2 (29/14b-1) on the flanks of the Central Graben. Pseudomorphed microphenocrysts, now sheet silicate and carbonate, are after olivine and/or clinopyroxene. The groundmass is cut by veins and is pervasively altered to carbonate and chlorite. Field of view = 3.6 mm.

PLATE F : Very severely altered igneous rock (PPL); sample 2 from well FO1 (15/27-2) in the Forties province. The original igneous texture is almost completely eradicated by pervasive alteration. The only evidence for this rocks igneous origin comes from the tiny feldspar microlites preserved in dark brown veins of hydrated iron oxide. Carbonate-filled spheroidal structures may have originally been vesicles. Field of view = 3.6 mm.

PLATE G : Fresh ankaramitic alkali olivine basalt from the Forties province - cross polarised light (XPL); sample 42 from AH1 (15/21-8a). Note large fresh olivine crystal (alteration confined to cracks) and smaller, often twinned, clinopyroxenes set in a groundmass dominated by plagioclase laths and cpx. Field of view = 3.6 mm.

PLATE H Ankaramitic alkali olivine basalt (PPL); sample 44 from well AH1 (15/21-8a). Note largely unzoned clinopyroxene phenocryst has a thin highly birefringent rim of more titaniferous augite. Olivines are pseudomorphed by sheet silicates and large phenocryst has carbonate filling in the centre. Field of view = 3.6 mm.

PLATE I Ocellated hawaiite (PPL); sample 23 from well TO1 (21/3-2) in the Forties province. Notice the prominent ocellus to the left hand side of plate. A calcite and pectolite filled amygdale occurs in the centre of the ocellus which is characterised by the presence of elongate kaersutite prisms. The outer edge of the ocellus is not, in this plate, well-defined. Note large cpx phenocryst (bottom left). The groundmass is dominated by amphibole, titanaugite, and plagioclase. Field of view = 3.6 mm.

PLATE J : Vesicular hyaloclasite or flow-breccia (PPL); sample 44 from well CH1 (16/26-3) in the Forties Province. Note highly vesicular character, glassy base and highly fragmented appearance. Vesicles are largely filled with chlorite. Notice several large fragments may be identified (e.g. bottom of plate in centre, and right edge in centre). Field of view = 3.6 mm.

PLATE K : Sodalite Nephelinite (PPL); sample 8N from well 17/9-1 in the Egersund Basin. Note glommeroporphyritic aggregate of clinopyroxene (bottom left) and large euhedral phenocrysts of titanaugite. 6-sided euhedra of analcime, probably after sodalite, are prominent (upper right). Field of view = 3.6 mm.

PLATE L : Strongly porphyritic phlogopite-rich lamprophyre, possibly an alnöite (PPL); sample ES1/41 from well 17/9-1 in the Egersund Basin. A corroded "xenocryst", possibly originally orthopyroxene, now replaced by chlorite and rimmed by phlogopite, is in the centre of the plate. The large greenish pseudomorph rimmed by opaque oxides (upper left), is probably after olivine. A euhedral clinopyroxene pseudomorph, composed of granular carbonate and serpentine, can be seen next to the phlogopite in the upper right portion of the plate. Field of view = 3.6 mm.

PLATE M : Kaersutite-rich alkaline lamprophyre, a sannaite (PPL); sample 6 from well PL1 (F/10-1) on the flanks of the Central Graben (Cleaver Bank Terrace) in the Netherlands province. Note clay pseudomorph after olivine microphenocryst (centre), with zoned kaersutite phenocrysts (left), showing inclusion bearing rims and rounded, paler cores. Note that the groundmass amphibole is comparable to the dark rims. Field of view = 1.5 mm.

PLATE N : "Hornblende" basanite (PPL); sample 11 from well SH1 (30/16-A13Y) which penetrates lava flows in the Auk field. This rock is probably the extrusive equivalent of the sannaite shown in Plate M. Note the clinopyroxene microphenocryst (centre). The rock is fine grained, almost aphyric, and is dominantly composed of kaersutite and clinopyroxene , spinel and altered

feldspathoid. Note the late stage vein, containing fresh glass and prominent kaersutites, which cuts from bottom right to top left across the view. Field of view = 1.5 mm.

PLATE O : Potassic lamprophyre (PPL); sample is 3 from well SH2 (29/25-1) on the flanks of the Central Graben. Notice large resorbed phlogopite (high pressure phenocryst or xenocryst), euhedral pseudomorph (composed of carbonate and serpentine) after clinopyroxene (bottom right), and large rounded pseudomorph (top) composed of granular carbonate, possibly after xenocrystal orthopyroxene. The rock is ocellated (not in this view) and vesicular - note rounded vesicle, filled with carbonate, in top right corner. The groundmass is given its dark grown colour by abundant flakes of biotite. Field of view = 3.6 mm.

PLATE P : Leucitophyre (PPL); sample ZU6 from well Zuidwal-1 in the Netherlands province. Note abundant, icositetrahedral, pseudomorphs after leucite composed of a fine brown aggregate of carbonate. The leucite pseudomorphs range in size from 0.05 to 0.3 mm. Few other phases are present in this rock, although a small squarish carbonate pseudomorph (bottom right) may be after nepheline or sanadine. Field of view = 1.5 mm.

PLATE Q : Glommerophyric cluster of brown titaniferous salites in a leucite basanite from the Zuidwal volcano (PPL); sample ZU5 from well Zuidwal-1. Note also the small acicular crystal of aegirine in top left corner of the plate. Field of view = 3.6 mm.

PLATE R : Phenocryst of brown titaniferous salite fringed by bright green aegirine augite (PPL); sample ZU5 from Zuidwal-1 in the Netherlands. Note also the abundant small flakes of mica and smaller crystals of pyroxene in a dominantly felsic groundmass. Field of view = 1.5 mm.

A

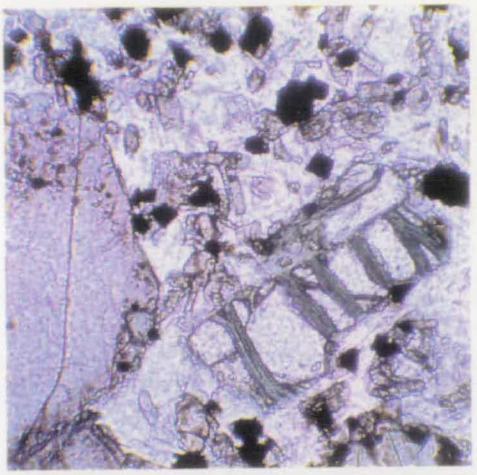

B

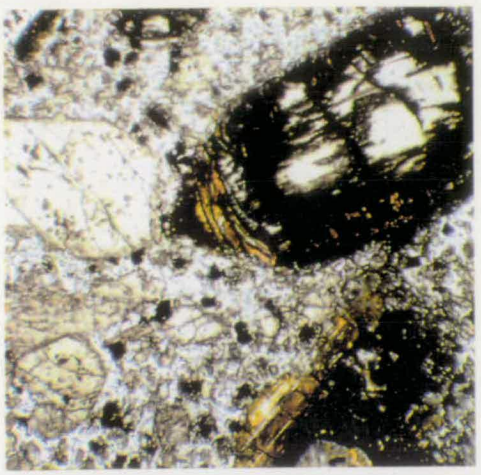

C

D

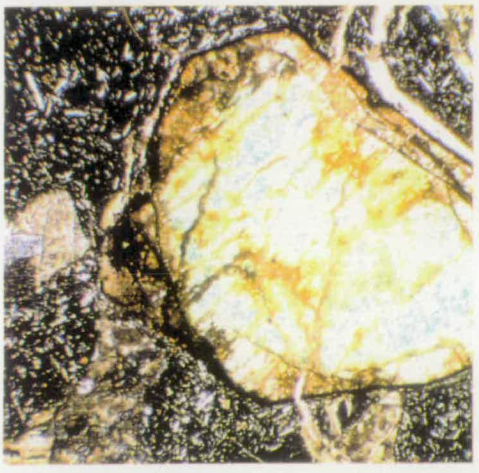

E

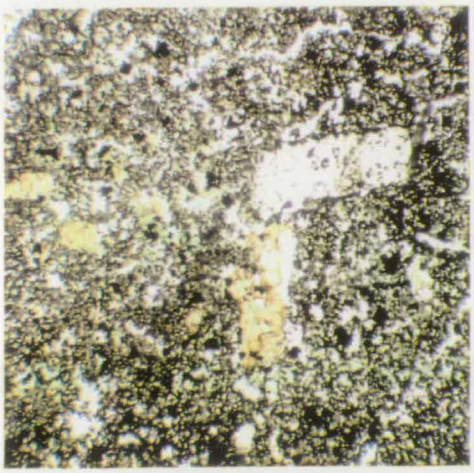

F

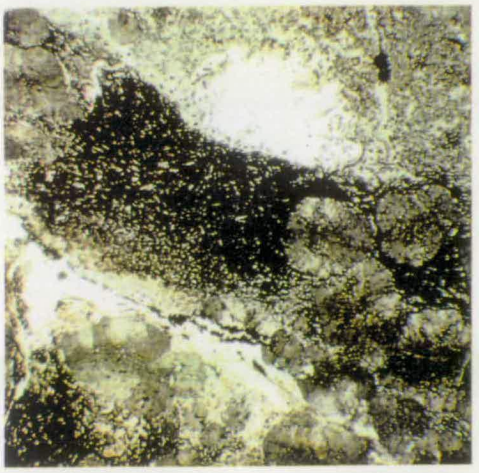

G

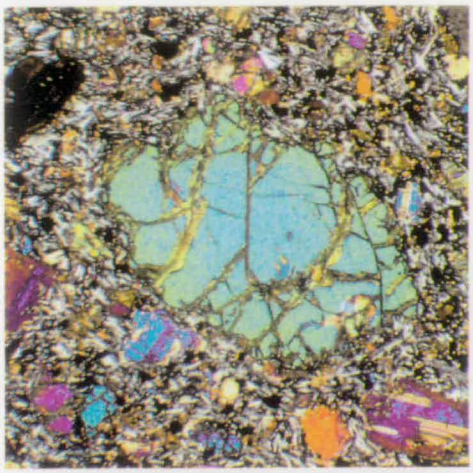

H

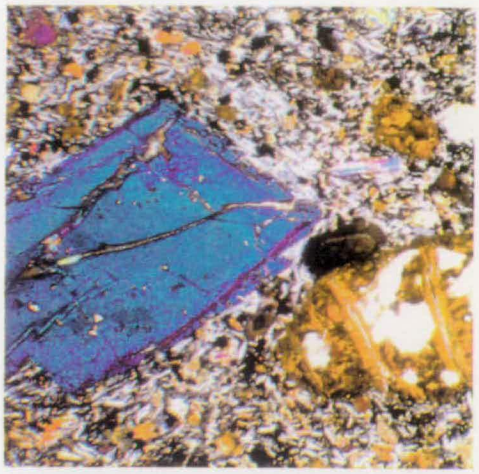

I

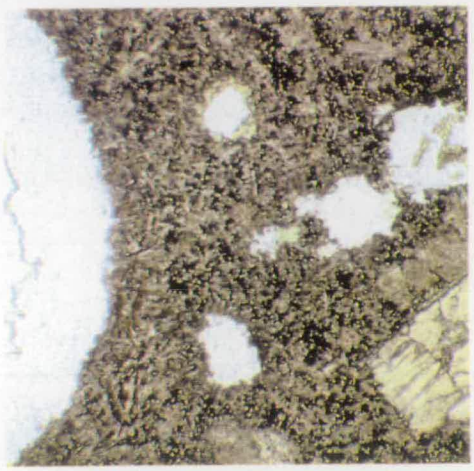

J

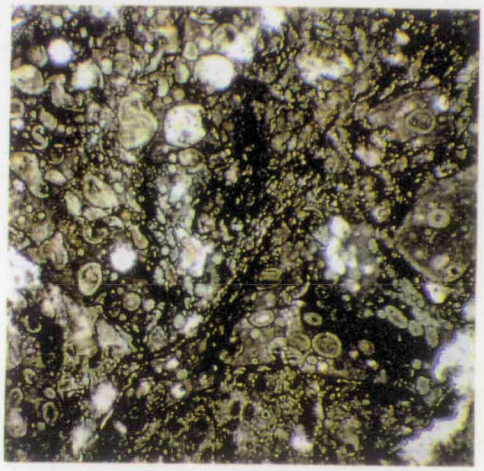

K

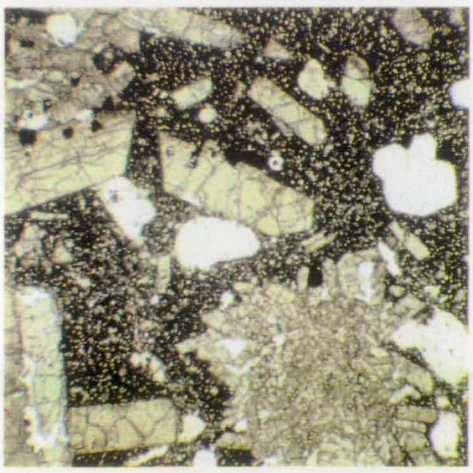

L

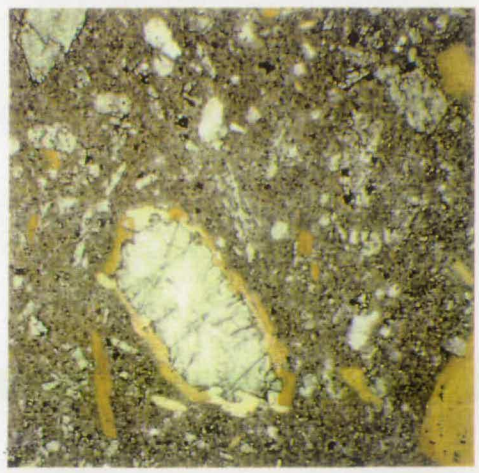

M

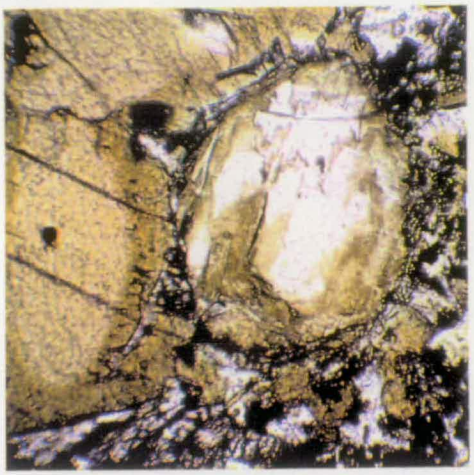

N

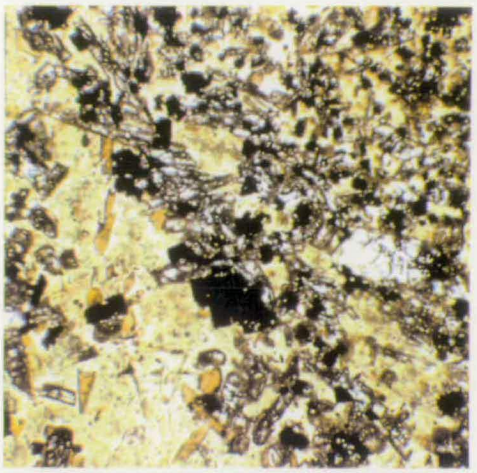

O

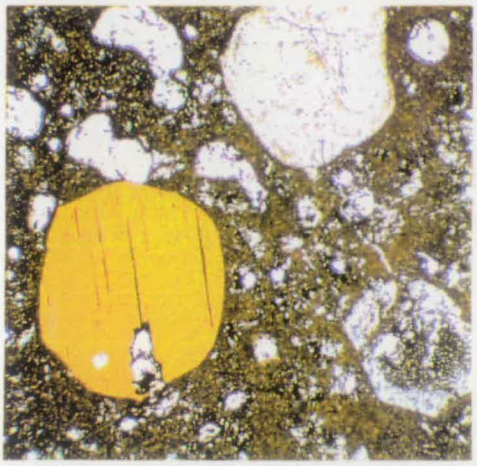

P

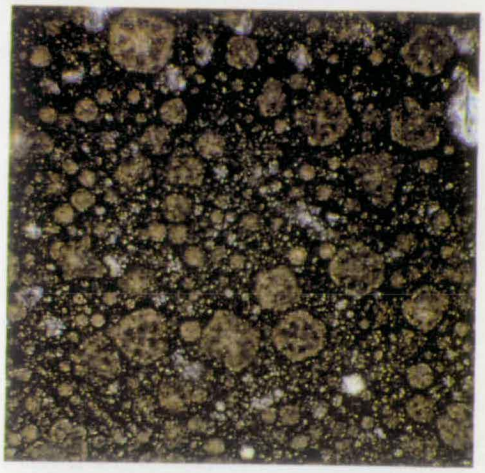

Q

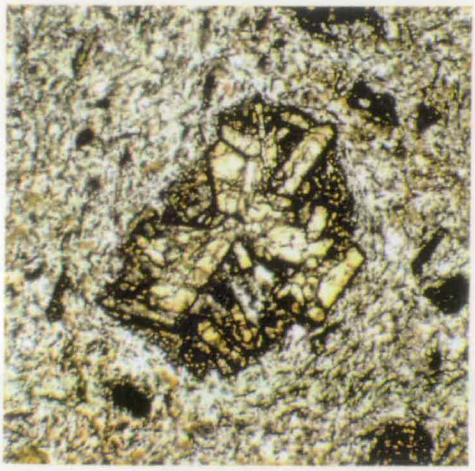

R

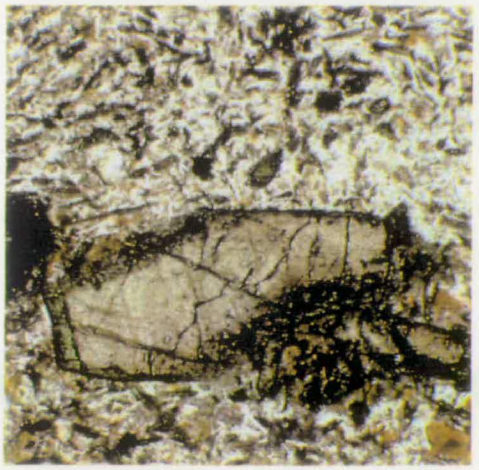

SECTION A2 : Tables of XRF Data.

The following tables present 232 analyses, each for 10 major and 17 trace elements, determined using the Philips PW1450/20 X-ray fluorescence spectrometer fitted with a Rh-anode tube. Analytical techniques were mentioned briefly in section 5.2 of Chapter 5, for further details see Fitton and Dunlop (1985), Smedley (1986) and Wallis (1989).

On each of the following pages there is also a table which provides information on the petrographic character of the rocks analysed. These descriptive tables have five columns which give the following information:

(1) *Alteration*: An index for the degree of alteration has been devised and every sample for which there was a thin section has been assigned a value from 0 to 6. Since olivine and clinopyroxene are present in most of the rocks the degree of alteration has been assessed according to their petrographic "freshness". The values, which are necessarily subjective, are defined as follows:

0 Olivines show no alteration, not even along cracks. In the absence of olivine then fresh glass is also used in identification of this unaltered type; see for example plate N in section A1.

1 Alteration is confined to olivines in where it occurs only along fractures or around edges. Fresh glass may also be present in the groundmass. See plates A and G and N in section A1.

2 Alteration is confined only to the olivines which are now completely pseudomorphed by a sheet silicate or hydrated iron oxide. There is, however, little or no veining of the host rock. This style of alteration is probably related to the cooling of the igneous body and occurs at a relatively high temperature. See Plates B and M in section A1.

3 Again only the olivines are obviously altered, but now olivines which were originally completely pseudomorphed by sheet silicates or hydroxides (type 2) are also replaced by hydrothermal quartz or carbonate (see Plates C and H in section A1); i.e. the alteration has several discrete phases. Veining is more common.

4 As in type 3 except that clinopyroxenes are now partially pseudomorphed by carbonate and ore minerals. See Plate D in section A1 for an example

5 Pyroxenes and olivines are completely pseudomorphed. The original pseudomorphing mineral assemblages may have been replaced but the original igneous texture is still apparent. See for example Plates E and Q in section A1.

6 Extreme alteration resulting in near total destruction of igneous rock texture; e.g. Plate F in section A1.

(2) *Phenocrysts*: Phenocryst and microphenocryst phases are noted. Microphenocrysts are denoted by parentheses while uncertainty or ambiguity in phenocryst type is denoted by use of a question mark. The abbreviations used for the phases are as follows: ol = olivine (magnesian), cpx = clinopyroxene (titanaugite), opx = orthopyroxene, amp = amphibole (kaersutite), bi = biotite, phl = phlogopite, sp = spinel, plag = plagioclase, lc = leucite, sod = sodalite, ne = nepheline.

(3) *Megacrysts/Xenocrysts*: Is used to note the occurrence and mineralogy of any megacrysts or xenocrysts.

(4) *Ocelli*: The presence of ocellar patches is indicated by YES in this column.

(5) *Type*: This column is used to provide information on (a) the petrographic classification of the rock (i.e. basalt vs. nephelinite, (b) their texture or mode (i.e. intrusive vs. extrusive), and (c) whether or not the sample is vesicular (or amygdaloidal). The information is provided in the form 1/2/3 and the abbreviations used are as follows:

(a) Classification: B = alkali basalt which when subscripted with Ak (B_{Ak}) is ankaramitic; H = hawaiite; B-H = basaltic hawaiite; Bs = basanite; Ne = nephelinite; P = phonolite; Tr = trachyte; L = lamprophyre.

(b) Texture/Mode: 0 = very rapid cooling (glassy); 1 = fine grained, rapidly chilled; 2 = moderately chilled; 3 = coarse slow cooled texture.

(c) Vesicles or amygdales are indicated by the symbol v.
Following the above criteria the code Bs/1-2/v would indicate a basanite which has a fine-grained to moderate texture and which is vesicular or amygdaloidal.

FORTIES PROVINCE

[15/21-8a, Amerada Hess (AH1/1-45)]

	AH1/1	AH1/3	AH1/4	AH1/5	AH1/6	AH1/7	AH1/8	AH1/9	AH1/10	AH1/11
SiO_2	39.92	41.20	50.72	48.68	49.20	47.50	45.97	46.91	45.98	46.44
Al_2O_3	13.79	15.21	17.63	15.50	14.68	13.60	12.67	12.91	11.68	12.43
Fe_2O_3	13.37	6.94	7.97	9.64	11.43	11.11	12.47	12.59	11.88	12.44
MgO	2.51	2.35	2.57	3.08	4.35	6.46	6.98	7.05	7.99	7.60
CaO	19.24	23.59	11.30	14.01	12.01	13.80	15.07	14.23	16.70	15.13
Na_2O	2.13	2.44	2.94	2.52	2.52	2.14	2.17	2.09	2.00	1.96
K_2O	1.19	1.18	1.65	1.50	1.38	0.91	0.80	0.82	0.82	0.88
TiO_2	2.52	2.75	3.32	3.00	2.67	2.45	2.27	2.30	2.14	2.21
MnO	0.29	0.28	0.11	0.19	0.18	0.12	0.16	0.14	0.17	0.16
P_2O_5	0.38	0.40	0.50	0.44	0.40	0.33	0.31	0.31	0.29	0.31
TOTAL	95.33	96.35	98.70	98.57	98.81	98.42	98.88	99.34	99.65	99.55
LOI	17.1	15.5	10.2	13.3	10.0	3.2	4.2	3.3	5.6	4.7
Ni	165	186	189	228	216	141	166	188	230	233
Cr	937	979	336	991	719	421	469	571	753	615
V	389	507	571	490	478	437	386	400	373	388
Sc	51	60	57	72	62	49	48	46	45	44
Cu	67	66	56	70	73	52	23	58	56	73
Zn	68	32	36	39	35	124	127	106	93	100
Sr	517	762	705	589	580	602	675	624	737	733
Rb	31	38	64	71	59	28	18	21	21	25
Zr	187	208	255	235	201	178	167	172	163	166
Nb	43	46	61	52	45	40	37	38	35	36
Ba	556	967	1022	792	1505	957	1672	850	734	589
Pb	1	2	*	1	2	1	*	*	0	*
Th	3	4	5	4	2	4	*	1	1	0
La	30	45	41	40	31	39	31	35	26	23
Ce	56	76	81	74	67	75	63	65	70	64
Nd	25	38	34	33	30	34	32	35	32	34
Y	17	25	22	21	22	23	22	23	22	22

	Alteration	Phenocrysts	Megacrysts/Xenocrysts	Ocelli	Type
AH1/1	6	ol?,cpx?	-	-	B_{Alk}/2?
AH1/3	6	ol?,cpx?	-	-	B_{Alk}/2?
AH1/4	6-5	ol?,cpx	-	-	B_{Alk}/2?
AH1/5	5-4	ol,cpx	-	-	B_{Alk}/2?
AH1/6	4-3	ol,cpx	-	-	B_{Alk}/2
AH1/7	3	ol,cpx	-	-	B_{Alk}/2
AH1/8	2	ol,cpx	-	-	B_{Alk}/2
AH1/9	2	ol,cpx	-	-	B_{Alk}/2
AH1/10	2	ol,cpx	-	-	B_{Alk}/2
AH1/11	2	ol,cpx	-	-	B_{Alk}/2

	AH1/12	AH1/13	AH1/14	AH1/15	AH1/16	AH1/17	AH1/18	AH1/19	AH1/20	AH1/21
SiO_2	44.77	44.69	45.61	44.67	45.10	46.00	46.17	46.11	46.47	45.54
Al_2O_3	12.72	13.17	12.26	11.64	11.72	11.69	11.44	11.97	11.94	11.66
Fe_2O_3	12.36	12.76	11.48	11.68	11.94	12.80	11.37	10.20	10.73	11.24
MgO	7.82	7.83	9.28	8.65	8.71	8.70	9.18	8.96	8.90	9.24
CaO	15.80	15.14	15.39	17.36	16.51	15.00	16.25	17.18	16.97	16.56
Na_2O	2.07	1.90	1.80	1.85	1.83	1.83	1.78	2.05	1.94	1.85
K_2O	0.82	0.84	0.70	0.62	0.63	0.77	0.79	0.60	0.76	0.58
TiO_2	2.27	2.36	2.16	2.08	2.08	2.09	2.07	2.12	2.15	2.08
MnO	0.17	0.20	0.19	0.22	0.21	0.19	0.16	0.19	0.19	0.19
P_2O_5	0.31	0.32	0.28	0.29	0.26	0.29	0.28	0.29	0.29	0.26
TOTAL	99.09	99.21	99.15	99.04	99.00	99.35	99.49	99.66	100.16	99.20
LOI	4.3	4.4	3.6	5.5	4.5	3.4	3.6	4.2	4.4	3.9
Ni	221	214	210	240	261	277	235	207	215	247
Cr	536	444	595	794	744	776	862	722	728	743
V	391	398	368	346	374	383	360	366	370	399
Sc	45	41	47	39	46	46	49	46	45	50
Cu	63	61	59	62	49	34	64	68	64	64
Zn	96	89	74	74	82	80	82	82	86	91
Sr	661	612	496	551	476	485	454	481	475	462
Rb	13	15	6	7	14	20	22	5	14	10
Zr	168	175	164	156	151	157	154	160	163	152
Nb	36	38	35	34	32	34	33	34	35	32
Ba	714	841	451	669	533	469	560	465	488	448
Pb	0	1	0	*	*	*	*	0	1	1
Th	*	2	2	0	*	3	1	0	2	*
La	31	36	30	25	29	28	29	29	26	25
Ce	71	66	60	58	56	60	52	71	64	61
Nd	34	34	34	30	30	31	28	31	30	32
Y	22	23	22	21	20	22	22	21	22	21

	Alteration	Phenocrysts	Megacrysts/Xenocrysts	Ocelli	Type
AH1/12	2	ol,cpx	-	-	$B_{Alk}/2$
AH1/13	2	ol,cpx	-	-	$B_{Alk}/2$
AH1/14	2	ol,cpx	-	-	$B_{Alk}/2$
AH1/15	2	ol,cpx	-	-	$B_{Alk}/2$
AH1/16	2	ol,cpx	-	-	$B_{Alk}/2$
AH1/17	2	ol,cpx	-	-	$B_{Alk}/2$
AH1/18	2	ol,cpx	-	-	$B_{Alk}/2$
AH1/19	2	ol,cpx	-	-	$B_{Alk}/2$
AH1/20	2	ol,cpx	-	-	$B_{Alk}/2$
AH1/21	2	ol,cpx	-	-	$B_{Alk}/2$

	AH1/22	AH1/23	AH1/24	AH1/25	AH1/26	AH1/27	AH1/28	AH1/29	AH1/30	AH1/31
SiO_2	45.89	46.50	47.05	47.37	47.59	47.61	47.81	47.52	47.42	47.49
Al_2O_3	11.57	11.47	11.53	11.59	11.98	12.24	11.90	11.60	11.84	11.74
Fe_2O_3	10.67	11.59	12.17	12.13	13.00	13.24	12.51	11.90	11.95	13.79
MgO	8.99	9.19	9.62	9.57	9.33	9.50	9.63	9.77	9.59	9.61
CaO	17.25	15.64	13.83	13.50	11.86	10.85	12.43	13.57	13.36	11.59
Na_2O	1.87	1.94	1.95	2.01	1.97	2.09	2.02	2.02	1.86	1.88
K_2O	0.58	0.69	0.73	0.75	0.92	1.04	0.90	0.84	0.83	1.09
TiO_2	2.05	2.12	2.11	2.11	2.22	2.23	2.19	2.13	2.19	2.15
MnO	0.20	0.17	0.13	0.12	0.10	0.09	0.11	0.12	0.11	0.11
P_2O_5	0.27	0.30	0.29	0.29	0.31	0.32	0.32	0.30	0.31	0.32
TOTAL	99.34	99.61	99.40	99.44	99.28	99.20	99.81	99.77	99.47	99.77
LOI	4.1	3.3	2.2	2.0	2.1	2.7	2.6	2.4	2.0	2.7
Ni	233	231	261	250	228	240	236	237	227	248
Cr	813	805	813	863	723	669	815	813	754	628
V	360	364	388	395	415	395	396	388	386	376
Sc	45	44	49	48	46	57	50	49	50	48
Cu	55	52	50	35	55	59	57	38	43	70
Zn	80	83	101	109	139	129	107	108	84	75
Sr	475	457	459	470	476	479	481	470	473	432
Rb	11	15	23	25	29	45	32	27	25	69
Zr	150	159	160	161	167	173	166	166	167	164
Nb	32	35	35	35	37	38	37	36	36	36
Ba	501	617	454	425	503	458	502	468	487	458
Pb	0	1	1	*	1	*	*	*	1	*
Th	1	*	1	1	2	*	1	1	0	2
La	30	29	32	23	29	32	29	32	28	32
Ce	62	72	59	66	57	62	64	63	66	58
Nd	30	29	30	30	29	28	27	31	30	30
Y	21	22	22	21	20	20	21	22	22	22

	Alteration	Phenocrysts	Megacrysts/Xenocrysts	Ocelli	Type
AH1/22	2	ol,cpx	-	-	$B_{Alk}/2$
AH1/23	2	ol,cpx	-	-	$B_{Alk}/2$
AH1/24	2	ol,cpx,(plag)	-	-	$B_{Alk}/2$
AH1/25	2	ol,cpx	-	-	$B_{Alk}/2$
AH1/26	2	ol,cpx	-	-	$B_{Alk}/2$
AH1/27	2	ol,cpx	-	-	$B_{Alk}/2$
AH1/28	2	ol,cpx	-	-	$B_{Alk}/2$
AH1/29	2	ol,cpx	-	-	$B_{Alk}/2$
AH1/30	2	ol,cpx	-	-	$B_{Alk}/2$
AH1/31	2	ol,cpx	-	-	$B_{Alk}/2$

	AH1/32	AH1/33	AH1/34	AH1/35	AH1/36	AH1/37	AH1/38	AH1/39	AH1/40	AH1/41
SiO_2	47.23	47.06	46.41	47.01	47.74	46.69	46.95	45.50	45.55	46.09
Al_2O_3	11.73	11.80	11.90	11.52	11.82	11.74	11.87	13.22	12.82	13.85
Fe_2O_3	12.86	12.68	14.69	12.18	11.64	12.08	12.76	13.36	13.62	11.94
MgO	9.48	9.58	9.89	9.88	9.65	9.83	9.48	8.28	9.09	8.11
CaO	12.81	13.35	10.71	13.62	13.42	13.27	12.81	12.74	12.02	12.84
Na_2O	1.96	1.89	1.82	1.92	2.13	1.94	2.07	2.24	2.03	2.13
K_2O	0.87	0.77	1.06	0.76	0.73	0.74	0.83	0.80	0.81	1.03
TiO_2	2.14	2.14	2.21	2.13	2.11	2.16	2.10	2.45	2.38	2.52
MnO	0.12	0.12	0.13	0.13	0.14	0.15	0.15	0.16	0.17	0.19
P_2O_5	0.31	0.31	0.32	0.29	0.29	0.31	0.31	0.35	0.36	0.38
TOTAL	99.51	99.71	99.13	99.42	99.66	98.92	99.33	99.11	98.84	99.09
LOI	2.2	2.7	3.4	1.9	1.1	1.9	2.0	1.7	2.1	2.2
Ni	231	233	256	207	241	256	279	187	186	135
Cr	761	720	712	760	766	699	584	337	339	268
V	378	382	390	390	363	377	356	408	410	400
Sc	48	50	51	52	46	47	43	46	44	42
Cu	45	43	41	38	34	42	80	31	31	70
Zn	77	83	75	79	77	81	78	86	89	89
Sr	459	471	384	438	471	459	483	539	521	559
Rb	35	23	39	26	14	19	21	22	15	9
Zr	165	168	169	162	163	164	167	185	185	202
Nb	36	37	37	36	36	36	38	41	42	47
Ba	481	456	473	452	557	457	663	556	533	614
Pb	*	1	3	1	1	1	*	0	*	1
Th	1	3	2	1	2	2	2	3	1	3
La	28	35	28	29	31	27	29	37	31	37
Ce	67	71	59	71	68	67	65	63	78	84
Nd	27	36	26	32	29	32	34	31	30	40
Y	22	23	20	21	22	22	22	23	23	25

	Alteration	Phenocrysts	Megacrysts/Xenocrysts	Ocelli	Type
AH1/32	2	ol,cpx	-	-	$B_{Ak}/2$
AH1/33	2	ol,cpx	-	-	$B_{Ak}/2$
AH1/34	2	ol,cpx	-	-	$B_{Ak}/2$
AH1/35	2	ol,cpx	-	-	$B_{Ak}/2$
AH1/36	2	ol,cpx	-	-	$B_{Ak}/2$
AH1/37	2	ol,cpx	-	-	$B_{Ak}/2$
AH1/38	2	ol,cpx	-	-	$B_{Ak}/2$
AH1/39	2	ol,cpx	-	-	$B_{Ak}/2$
AH1/40	2	ol,cpx	-	-	$B_{Ak}/2$
AH1/41	1-2	ol,cpx	-	-	$B_{Ak}/2$

	AH1/42	AH1/43	AH1/44	AH1/45	FO1/1	FO1/2	FO1/3	FO1/4	FO1/6	FO1/8
SiO_2	45.11	46.29	46.15	46.53	37.72	30.51	50.39	44.65	46.20	41.39
Al_2O_3	13.28	13.69	13.52	13.38	31.93	25.44	18.48	17.65	9.03	10.35
Fe_2O_3	12.54	12.15	12.22	12.56	18.67	30.51	9.12	11.60	10.85	14.05
MgO	10.71	8.58	8.85	8.75	0.87	1.51	4.40	4.90	15.81	14.11
CaO	11.81	12.87	12.65	12.56	1.58	2.24	6.56	12.37	13.44	14.66
Na_2O	2.05	2.15	2.17	2.08	0.31	0.27	3.03	2.20	1.21	1.35
K_2O	0.88	0.81	0.79	0.75	0.03	0.01	3.40	0.98	0.22	0.08
TiO_2	2.40	2.52	2.50	2.46	6.50	5.53	2.40	3.04	2.16	2.44
MnO	0.20	0.20	0.21	0.19	N.D	N.D	N.D	N.D	N.D	N.D
P_2O_5	0.36	0.37	0.37	0.36	0.61	0.84	0.91	1.15	0.26	0.30
TOTAL	99.34	99.62	99.42	99.62	98.22	96.86	98.67	98.55	99.20	98.71
LOI	1.5	2.1	2.2	2.4	17.9	18.2	2.6	2.7	3.9	14.6
Ni	127	133	142	153	73	24	69	9	365	340
Cr	277	308	306	301	50	26	2	2	1476	2290
V	383	405	406	396	619	490	259	321	289	288
Sc	44	43	45	45	25	32	5	7	53	74
Cu	63	68	65	67	57	37	9	21	56	122
Zn	85	88	90	89	193	804	165	130	50	71
Sr	482	555	557	528	991	610	1344	1653	396	208
Rb	6	6	6	4	*	*	94	15	4	5
Zr	197	196	194	189	694	634	424	386	157	155
Nb	46	45	45	42	206	174	147	126	41	43
Ba	511	549	487	508	691	758	1438	3534	353	87
Pb	2	0	2	*	7	10	1	*	3	8
Th	1	1	3	2	17	15	10	4	2	3
La	34	38	40	36	138	241	91	101	38	45
Ce	77	77	77	75	293	388	205	208	64	91
Nd	35	36	35	35	114	179	83	87	29	43
Y	24	25	24	24	27	42	34	35	18	16

	Alteration	Phenocrysts	Megacrysts/Xenocrysts	Ocelli	Type
AH1/42	1-0	ol,cpx	-	-	B_{Ak}/2
AH1/43	1-2	ol,cpx	-	-	B_{Ak}/2
AH1/44	1-2	ol,cpx	-	-	B_{Ak}/2
AH1/45	2	ol,cpx	-	-	B_{Ak}/2
FO1/1	6	?	-	-	(H/1)?
FO1/2	6	(ol,cpx)?	-	-	(H/1)?
FO1/3	3	ol,plag	-	-	H/1-2/v
FO1/4	3	plag,cpx	anorthoclase	-	H/1-2/v
FO1/6	3	ol,cpx	-	-	B_{Ak}/1-2
FO1/8	4	ol,cpx	-	-	B_{Ak}/1-2

	BP1/1	BP1/3	BP1/6	BP1/9	BP1/13	BP1/15	BP1/19	BP1/20	BP1/24	BP1/29
SiO_2	45.44	44.97	44.27	45.15	45.40	45.31	45.00	45.33	44.51	46.31
Al_2O_3	13.43	12.90	13.19	13.67	14.08	14.58	15.07	14.81	13.16	11.15
Fe_2O_3	11.01	11.91	13.52	13.03	14.10	12.75	11.97	12.13	12.08	12.04
MgO	10.53	11.05	7.84	6.82	8.34	8.84	8.99	8.48	13.06	12.35
CaO	12.46	12.36	10.64	10.02	7.81	10.46	11.10	10.20	9.13	12.22
Na_2O	2.02	1.75	2.49	2.83	3.32	2.27	2.19	1.63	1.94	2.20
K_2O	0.51	0.46	4.36	4.57	2.38	1.36	1.03	2.27	1.66	0.83
TiO_2	2.99	2.88	2.69	2.81	3.13	3.21	3.26	3.27	2.75	2.45
MnO	0.41	0.46	0.15	0.13	0.16	0.24	0.40	0.21	0.19	0.18
P_2O_5	0.44	0.41	0.44	0.47	0.50	0.51	0.52	0.53	0.39	0.30
TOTAL	99.24	99.16	99.59	99.50	99.23	99.54	99.55	98.86	98.88	100.03
LOI	2.9	3.2	7.6	7.5	4.4	3.4	2.9	2.9	5.3	3.4
Ni	110	118	66	66	74	75	65	76	162	184
Cr	291	272	110	103	121	160	132	130	333	695
V	379	357	224	275	344	338	360	384	264	305
Sc	37	35	28	26	30	32	32	33	34	45
Cu	39	35	83	40	44	44	72	60	71	37
Zn	113	85	78	69	77	117	108	132	93	76
Sr	746	695	319	342	527	811	905	876	911	457
Rb	3	2	77	85	39	20	15	49	26	5
Zr	240	229	223	234	260	263	273	279	224	185
Nb	64	58	62	66	74	75	78	78	59	45
Ba	596	582	888	935	778	793	593	913	531	359
Pb	1	2	4	5	1	4	1	4	2	2
Th	1	2	3	2	3	3	2	3	1	1
La	50	50	57	58	62	59	56	63	39	42
Ce	111	114	107	113	114	130	130	125	86	76
Nd	46	46	47	47	51	55	56	55	42	32
Y	27	26	26	28	28	30	30	30	26	25

	Alteration	Phenocrysts	Megacrysts/Xenocrysts	Ocelli	Type
BP1/1	2-3	ol,cpx,(plag)	-	-	B/2/v
BP1/3	2-3	ol,cpx,(plag)	-	-	B/2/v
BP1/4	3	ol,cpx,(plag)	-	-	B/1/v
BP1/9	2-3	ol,cpx,(plag)	-	-	B/1-2/v
BP1/13	3-4	ol,cpx,(plag)	-	-	B/2/v
BP1/15	3	ol,cpx,(plag)	-	-	B/2/v
BP1/19	3	ol,cpx,(plag)	-	-	B/2/v
BP1/20	2-3	ol,cpx,(plag)	-	-	B/1-2/v
BP1/24	3-4	ol,cpx,(plag)	-	-	B/1-2/v
BP1/29			*No Section*		

	BP1/30	BP1/33	BP1/37	BP1/43	BP1/47	BP1/50	BP1/53	BP1/57	BP1/59	BP1/64
SiO_2	45.40	45.98	45.76	45.42	45.89	44.62	46.69	46.74	46.36	46.65
Al_2O_3	11.70	12.96	12.71	11.92	10.22	10.24	14.15	13.36	12.92	14.02
Fe_2O_3	12.76	12.35	11.79	12.42	11.80	12.22	12.10	12.17	12.04	10.47
MgO	11.60	9.85	12.08	12.82	12.41	16.61	8.94	9.91	9.33	9.32
CaO	10.65	11.71	10.06	10.12	13.75	10.64	7.93	7.14	8.24	11.65
Na_2O	2.61	2.20	2.10	1.79	1.31	0.64	2.89	2.71	1.94	2.63
K_2O	0.96	0.65	1.18	1.43	0.47	1.11	2.46	3.73	4.34	0.51
TiO_2	2.61	2.74	2.75	2.57	2.42	2.26	3.11	2.78	2.75	2.95
MnO	0.19	0.25	0.15	0.17	0.27	0.15	0.15	0.16	0.14	0.29
P_2O_5	0.34	0.39	0.39	0.36	0.29	0.25	0.56	0.52	0.52	0.52
TOTAL	98.83	99.09	98.98	99.02	98.84	98.73	98.99	99.22	98.58	99.01
LOI	3.7	2.5	3.6	4.1	2.9	5.3	3.6	4.3	4.7	2.7
Ni	173	152	148	145	207	199	89	103	110	107
Cr	437	359	356	375	565	569	184	200	212	283
V	302	313	299	295	318	312	303	239	238	338
Sc	40	35	36	34	44	47	27	26	26	31
Cu	37	39	41	29	37	55	15	34	25	42
Zn	74	84	86	79	79	87	83	94	87	80
Sr	502	698	565	443	513	388	469	342	376	822
Rb	7	4	13	34	5	25	43	68	83	3
Zr	204	221	223	202	169	165	302	267	262	268
Nb	51	56	58	53	39	40	71	61	61	65
Ba	414	573	641	652	371	371	1017	760	842	466
Pb	1	4	3	6	4	4	6	6	5	3
Th	0	3	1	4	2	2	5	4	4	3
La	47	42	38	48	30	31	61	61	59	56
Ce	84	98	102	95	71	65	126	117	110	121
Nd	38	43	38	39	33	29	53	56	48	56
Y	26	27	27	26	24	20	30	26	27	29

	Alteration	Phenocrysts	Megacrysts/Xenocrysts	Ocelli	Type
BP1/30	3	ol,cpx,(plag)	-	-	$B_{Ak}/2$
BP1/33	2-3	ol,cpx,(plag)	-	-	B/2/v
BP1/37	2-3	ol,cpx,(plag)	-	-	B/2/v
BP1/43			*No Section*		
BP1/47	3	ol,cpx,(plag)	-	-	B/2/v
BP1/50			*No Section*		
BP1/53	3-4	ol,cpx,(plag)	-	-	B/2-1
BP1/57	3-4	ol,cpx,(plag)	-	-	B/1
BP1/59			*No Section*		
BP1/64	3	ol,cpx,(plag)	-	-	B/2

	BP1/65	BP1/67	BP1/69	BP1/70	BP1/71	BP1/72	BP2/1	BP2/2	BP2/3	BP2/4
SiO_2	46.78	46.45	47.21	46.60	47.26	44.68	44.95	44.35	44.36	46.98
Al_2O_3	14.37	14.14	13.83	14.26	15.03	14.18	9.89	10.26	9.92	16.10
Fe_2O_3	10.62	12.02	12.37	12.44	11.83	12.60	10.62	11.28	10.85	11.97
MgO	8.04	8.26	7.73	9.13	8.96	10.54	15.32	15.39	15.31	6.84
CaO	11.00	10.36	8.06	7.12	5.22	7.54	13.61	12.48	13.38	7.77
Na_2O	2.80	2.85	2.71	2.02	2.80	1.84	1.44	1.39	1.17	2.56
K_2O	1.16	1.24	3.20	3.65	4.09	3.77	0.53	0.71	0.73	3.88
TiO_2	3.09	3.03	3.05	3.06	3.06	3.22	2.42	2.44	2.41	3.24
MnO	0.20	0.19	0.15	0.16	0.16	0.17	0.21	0.23	0.22	0.18
P_2O_5	0.57	0.56	0.58	0.60	0.58	0.61	0.34	0.39	0.36	0.50
TOTAL	98.61	99.10	98.88	99.03	98.98	99.15	99.33	98.92	98.72	100.02
LOI	2.6	2.8	4.2	5.2	5.2	6.9	3.3	3.7	3.6	4.0
Ni	85	93	73	75	60	73	283	308	268	57
Cr	192	213	164	139	92	127	1171	1088	1647	29
V	308	297	326	328	318	340	267	271	279	352
Sc	30	28	26	27	24	26	38	40	50	28
Cu	28	41	48	49	30	30	61	66	75	136
Zn	81	113	81	91	121	118	84	96	93	118
Sr	852	814	474	426	386	489	316	326	351	799
Rb	11	28	73	91	97	91	15	20	18	85
Zr	301	297	300	306	309	313	193	201	192	308
Nb	70	70	71	74	75	75	52	57	52	92
Ba	866	854	888	835	890	1204	497	511	567	1456
Pb	4	3	4	7	6	6	6	14	10	38
Th	3	2	4	5	4	5	2	3	4	5
La	62	64	63	61	67	64	48	46	37	59
Ce	129	141	142	125	130	142	101	86	84	127
Nd	54	56	57	54	54	59	42	35	36	56
Y	30	31	30	29	27	31	21	21	21	28

	Alteration	Phenocrysts	Megacrysts/Xenocrysts	Ocelli	Type
BP1/65			*No Section*		
BP1/67	3	ol,cpx,(plag)	-	-	B/2-1
BP1/69			*No Section*		
BP1/70			*No Section*		
BP1/71	3-4	ol,cpx,(plag)	-	-	B/1-0/v
BP1/72	3-4	ol,cpx,(plag)	-	-	B/1-0/v
BP2/1	2	ol,cpx,(plag)	-	YES	B_{Ak}/2/v
BP2/2	3	ol,cpx,(plag)	-	YES	B_{Ak}/2
BP2/3	3-4	ol,cpx,(plag)	-	YES	B_{Ak}/2
BP2/4	3	ol,cpx,(plag)	-	YES	B-H/2/v

[21/3-2, Total (TO1/1-27)]

	BP2/5	TO1/1	TO1/6	TO1/8	TO1/10	TO1/14	TO1/17	TO1/18	TO1/20	TO1/21
SiO_2	44.65	45.38	44.97	44.87	44.82	44.26	44.54	44.45	48.01	47.70
Al_2O_3	9.93	9.37	9.34	8.88	11.62	9.43	9.16	9.44	12.80	12.77
Fe_2O_3	10.78	10.97	11.22	11.21	11.79	12.11	12.02	12.13	11.50	11.61
MgO	15.42	13.67	15.58	15.88	12.56	15.84	15.83	15.48	9.76	10.07
CaO	13.27	14.77	14.43	14.49	12.72	13.90	14.41	14.11	9.98	10.09
Na_2O	1.34	1.08	0.69	0.75	1.61	0.64	0.68	0.64	2.55	2.45
K_2O	0.51	0.89	0.47	0.40	0.91	0.50	0.48	0.49	1.44	1.35
TiO_2	2.51	2.29	2.09	2.08	2.51	2.37	2.25	2.21	2.27	2.31
MnO	0.20	0.16	0.18	0.18	0.17	0.19	0.19	0.17	0.20	0.23
P_2O_5	0.34	0.30	0.27	0.26	0.40	0.27	0.31	0.26	0.35	0.35
TOTAL	98.95	98.87	99.24	99.01	99.10	99.50	99.43	99.39	98.86	98.91
LOI	5.4	4.5	3.5	3.5	5.0	4.3	3.8	3.6	2.7	2.7
Ni	267	271	322	330	244	313	303	315	174	163
Cr	1329	1081	1192	1184	586	965	1018	1061	540	487
V	299	287	254	258	275	285	284	287	288	290
Sc	50	46	45	47	32	37	51	46	31	28
Cu	67	80	75	78	94	80	81	71	63	57
Zn	109	74	77	75	96	82	81	82	90	93
Sr	227	535	502	491	844	436	439	505	798	774
Rb	13	13	10	8	18	10	11	12	39	36
Zr	194	160	149	145	199	148	149	153	204	208
Nb	52	43	39	37	57	38	37	38	50	51
Ba	378	462	343	323	518	414	308	340	752	689
Pb	9	2	3	3	2	2	2	1	3	2
Th	3	*	0	*	0	0	1	0	2	1
La	50	32	30	27	35	30	27	33	39	43
Ce	96	77	65	60	97	62	56	63	84	82
Nd	38	30	28	26	41	28	25	30	37	35
Y	22	21	20	20	24	20	22	21	26	26

	Alteration	Phenocrysts	Megacrysts/Xenocrysts	Ocelli	Type
BP2/5	3	ol,cpx,(plag)	-	YES	$B_{Ak}/2/v$
TO1/1	2-3	ol,cpx,(amp?)	-	YES	$B_{Ak}/2$
TO1/6	2-3	ol,cpx,(amp?)	-	YES	$B_{Ak}/2$
TO1/8	3-4	ol,cpx,(amp?)	-	?	$B_{Ak}/2$
TO1/10			*No Section*		
TO1/14	3-4	ol,cpx,(amp?)	-	?	$B_{Ak}/2$
TO1/17	3	ol,cpx,(amp?)	-	YES	$B_{Ak}/2/v$
TO1/18	3	ol,cpx,(amp?)	-	YES	$B_{Ak}/2$
TO1/20	3-4	ol,cpx,(plag)	-	-	B-H/2
TO1/21	3	ol,cpx,(plag)	-	-	B-H/2

	TO1/23	TO1/24	TO1/25	TO1/26	TO1/27	SO1/1	SO1/2	SO1/3	SO1/4	SO1/5
SiO_2	46.25	49.67	49.57	49.73	48.38	37.11	33.53	35.76	46.98	41.45
Al_2O_3	15.18	16.55	15.67	16.27	12.68	15.87	15.18	15.40	15.77	17.02
Fe_2O_3	11.73	10.61	10.69	10.63	11.81	12.01	20.12	21.93	17.07	21.22
MgO	5.33	4.36	5.20	4.11	10.04	2.76	3.76	6.20	3.28	5.36
CaO	12.60	7.33	8.09	8.42	10.54	21.94	17.44	11.81	4.78	4.31
Na_2O	4.42	4.02	3.37	4.54	2.67	3.20	3.07	3.27	6.20	2.99
K_2O	0.06	3.02	3.14	1.78	1.11	1.36	0.60	0.38	0.54	2.13
TiO_2	2.91	2.61	2.52	2.67	2.54	4.16	3.96	4.09	4.05	4.40
MnO	0.17	0.16	0.16	0.15	0.20	0.41	0.38	0.34	0.18	0.20
P_2O_5	0.46	0.48	0.44	0.47	0.34	0.52	0.48	0.50	0.72	0.80
TOTAL	99.11	98.80	98.84	98.77	100.31	99.34	98.58	99.67	99.57	99.87
LOI	5.3	3.5	3.3	3.7	3.0	17.5	14.6	11.1	4.0	6.4
Ni	65	41	67	44	167	182	221	236	110	128
Cr	40	56	119	60	464	537	644	560	325	352
V	313	269	273	276	312	464	479	451	192	388
Sc	24	17	23	19	37	63	69	71	37	45
Cu	81	44	51	47	93	72	58	43	72	30
Zn	88	98	95	95	85	67	153	239	84	105
Sr	509	1257	881	578	919	503	505	574	592	505
Rb	*	65	73	35	36	56	20	8	14	66
Zr	237	287	268	274	190	262	248	262	288	306
Nb	70	69	65	69	48	73	70	74	95	97
Ba	37	1002	816	492	521	155	109	370	210	486
Pb	6	2	3	4	4	*	*	*	1	1
Th	5	3	5	47	*	2	0	*	4	5
La	51	59	47	51	40	49	51	52	64	82
Ce	115	113	100	106	85	108	103	103	140	145
Nd	51	50	44	48	34	48	43	41	59	55
Y	27	31	30	30	26	21	19	19	24	26

	Alteration	Phenocrysts	Megacrysts/Xenocrysts	Ocelli	Type
TO1/23	2-3	ol,cpx,(plag)	-	YES	H/2/v
TO1/24	3	ol,cpx	-	YES	H/2/v
TO1/25			*No Section*		
TO1/26	3	ol,cpx	-	-	H/2/v
TO1/27	3	ol,cpx,(plag)	-	-	B/2
SO1/1	3-4	ol,cpx	-	-	B_{Ak}/2
SO1/2	3	ol,cpx,(amp?)	-	YES	B_{Ak}/2/v
SO1/3	3	ol,cpx,(amp)	-	YES	B_{Ak}/2
SO1/4	3-4	ol,cpx,(plag)	-	-	B-H/2
SO1/5	3	ol,cpx,(plag)	-	-	B-H/2

	SO1/6	SO1/7	SO1/8	SO1/9	SO1/10	SO1/11	CH1/4	CH1/6	CH1/9	CH1/15
SiO_2	42.59	42.23	43.53	44.23	45.37	43.77	48.72	44.42	46.95	49.35
$Al2O_3$	16.17	16.28	15.27	15.82	15.91	15.45	15.59	13.66	14.44	14.13
Fe_2O_3	15.68	14.39	14.19	14.24	14.02	13.25	9.27	8.27	10.74	10.35
MgO	6.73	8.58	7.52	7.69	6.91	7.67	9.57	9.00	11.06	8.08
CaO	9.07	10.68	12.16	9.61	8.12	12.05	5.19	13.63	6.03	7.01
Na_2O	3.20	2.52	2.73	3.48	4.15	2.72	2.57	1.40	1.12	3.34
K_2O	0.87	0.50	0.42	0.49	0.48	0.48	3.68	4.66	4.91	2.41
TiO_2	4.29	4.22	3.97	4.23	4.20	3.96	3.14	2.90	3.24	2.91
MnO	0.25	0.31	0.34	0.31	0.31	0.44	0.11	0.17	0.12	0.10
P_2O_5	0.77	0.74	0.70	0.75	0.74	0.71	0.66	0.51	0.58	0.50
TOTAL	99.62	100.45	100.82	100.84	100.21	100.46	98.50	98.62	99.19	98.29
LOI	4.2	3.8	2.5	3.4	3.1	2.5	8.5	13.0	8.4	8.7
Ni	107	109	101	105	98	107	59	70	71	73
Cr	342	304	315	339	330	308	40	170	185	175
V	507	438	376	437	397	397	314	268	286	233
Sc	44	42	39	42	43	39	18	29	28	27
Cu	30	21	31	48	21	40	39	54	48	58
Zn	92	88	116	120	150	167	82	65	83	78
Sr	1131	1253	1271	1104	1001	1251	301	267	238	277
Rb	23	9	6	8	12	7	91	81	76	39
Zr	318	309	295	307	311	301	282	269	299	260
Nb	98	97	92	96	97	91	93	74	81	71
Ba	756	846	811	709	658	808	814	1046	1285	2994
Pb	1	0	0	1	*	1	5	6	4	4
Th	2	1	0	3	27	1	8	6	7	5
La	75	75	70	67	69	71	76	66	56	49
Ce	162	165	146	149	149	149	142	141	122	111
Nd	69	71	65	62	59	64	59	55	59	50
Y	26	27	25	25	24	26	31	24	21	20

	Alteration	Phenocrysts	Megacrysts/Xenocrysts	Ocelli	Type
SO1/6	4-5	ol,cpx,(plag)	-	-	B-H/2-1/v
SO1/7	4	ol,cpx	-	-	B-H/2-1
SO1/8	3-4	ol,cpx	-	-	B-H/2-1
SO1/9	3-4	ol,cpx	-	-	B-H/2-1
SO1/10	3-4	ol,cpx	-	-	B-H/2-1
SO1/11	3	ol,cpx	-	-	B-H/2-1
CH1/4	5-6	?ol,?cpx	-	-	?B-H/2-1
CH1/6	5-6	?, (plag)?	-	-	?B-H/1/v
CH1/9	5-6	ol,cpx	-	-	?B-H/2-1
CH1/15	5	ol,cpx	-	-	?B-H/2-1

	CH1/16	CH1/25	CH1/30	CH1/32	CH1/34	CH1/39	CH1/41	CH1/44	CH1/47	CH1/51
SiO_2	48.56	46.41	45.81	44.00	55.14	46.02	43.40	38.63	43.99	42.83
Al_2O_3	15.03	14.62	16.03	15.66	13.56	12.98	16.06	15.57	15.40	14.19
Fe_2O_3	9.85	11.87	11.19	12.16	8.77	14.43	14.13	15.78	12.65	14.43
MgO	8.66	13.56	12.90	13.66	9.86	15.01	14.90	17.32	13.04	11.20
CaO	6.24	3.72	2.63	2.52	2.39	2.43	1.66	4.29	4.12	6.67
Na_2O	3.60	1.22	3.29	2.81	1.99	1.40	0.94	1.13	3.01	3.10
K_2O	2.38	3.98	1.80	2.09	3.45	1.78	4.04	2.05	1.29	1.35
TiO_2	3.32	2.92	4.17	3.65	2.81	3.05	3.20	3.41	4.30	3.96
MnO	0.10	0.12	0.13	0.14	0.11	0.14	0.22	0.28	0.17	0.17
P_2O_5	0.59	0.47	0.71	0.58	0.51	0.92	0.61	0.51	0.75	0.59
TOTAL	98.33	98.87	98.65	97.28	98.58	98.14	99.23	98.97	98.71	98.49
LOI	7.8	7.9	6.8	7.3	5.9	7.1	8.1	10.4	8.2	6.7
Ni	76	117	128	128	80	148	119	116	127	113
Cr	239	226	315	274	174	263	199	181	305	266
V	262	253	391	378	199	168	115	148	340	291
Sc	29	30	48	37	28	32	31	35	41	28
Cu	63	60	66	54	14	58	58	69	31	100
Zn	70	105	101	105	77	132	117	134	96	134
Sr	196	453	484	591	478	320	226	235	297	433
Rb	39	59	31	36	57	40	79	52	58	35
Zr	302	255	345	290	270	266	307	315	339	306
Nb	83	77	103	88	81	80	96	97	106	94
Ba	1215	1050	1008	3003	1372	1294	316	159	1094	3567
Pb	7	7	5	3	2	16	6	7	7	3
Th	6	6	7	6	5	6	8	9	8	6
La	66	64	65	58	51	94	82	75	89	66
Ce	130	114	142	125	127	146	138	147	160	134
Nd	55	49	53	46	50	58	56	53	66	62
Y	23	21	22	18	19	31	25	23	23	22

	Alteration	Phenocrysts	Megacrysts/Xenocrysts	Ocelli	Type
CH1/16			*No Section*		
CH1/25	5	?ol,?cpx	-	-	?H/1-0/v
CH1/30	5	?ol,?cpx	-	-	?/1-0/v
CH1/32	5	ol,cpx	-	-	?/1-0/v
CH1/34	5	ol,cpx	-	-	?/1-0/v
CH1/39	5	ol,cpx	-	-	?/1-0/v
CH1/41	5	?	-	-	?/0/v
CH1/44	5	?	-	-	?/0/v
CH1/47	5	ol,cpx	-	-	B/2-1/v
CH1/51	5-6	ol,cpx	-	-	B/2-1/v

[16/26-4, Chevron (CH2/2-20)]

	CH1/53	CH1/56	CH2/2	CH2/6	CH2/10	CH2/12	CH2/15	CH2/17	CH2/20
SiO_2	46.65	46.52	43.49	44.63	41.64	48.55	45.58	45.32	45.53
Al_2O_3	13.60	15.02	16.20	15.29	16.58	11.11	10.94	11.65	11.21
Fe_2O_3	13.32	12.40	12.23	14.46	14.92	7.69	12.14	11.69	11.23
MgO	14.46	13.71	3.75	3.80	7.99	10.69	13.49	12.00	12.96
CaO	2.92	1.85	12.19	9.51	8.59	14.59	9.69	11.83	11.58
Na_2O	1.67	2.72	0.37	0.44	1.83	1.16	1.71	2.11	1.66
K_2O	1.62	1.77	5.71	5.71	1.90	1.84	1.54	1.14	1.09
TiO_2	3.86	3.80	3.84	3.68	4.29	2.62	2.57	2.70	2.64
MnO	0.17	0.17	0.14	0.18	0.11	0.21	0.16	0.14	0.21
P_2O_5	0.55	0.64	0.76	0.56	0.70	0.44	0.40	0.43	0.42
TOTAL	98.84	98.59	98.67	98.26	98.56	98.90	98.22	99.03	98.53
LOI	7.1	6.4	11.2	9.2	10.0	11.7	6.6	4.9	4.9
Ni	124	112	42	28	37	220	223	195	214
Cr	306	324	39	31	34	947	966	916	890
V	336	360	345	302	422	289	287	314	313
Sc	33	29	22	24	25	42	40	43	37
Cu	26	23	32	26	22	29	52	28	25
Zn	122	113	113	107	172	51	59	95	92
Sr	270	420	425	453	475	603	449	560	482
Rb	57	45	147	170	54	44	52	24	23
Zr	301	313	333	316	368	218	206	221	212
Nb	95	99	77	73	86	58	53	59	57
Ba	641	877	982	1273	829	649	903	639	722
Pb	6	4	5	4	5	4	4	2	3
Th	7	7	7	5	6	1	4	2	3
La	69	73	46	51	60	51	41	49	58
Ce	143	135	100	127	145	97	85	97	110
Nd	58	48	58	55	62	42	37	43	39
Y	23	26	30	27	22	17	19	19	20

	Alteration	Phenocrysts	Megacrysts/Xenocrysts	Ocelli	Type
CH1/53	5	ol,cpx	-	-	B/2-1
CH1/56	5-6	ol,cpx	-	-	B/2-1/v
CH2/2	5-6	?	-	-	?/1-0/v
CH2/6	5-6	?	-	-	?/1-0/v
CH2/10	6	?	-	-	?
CH2/12	4-5	ol,cpx	-	-	B/2-1
CH2/15	4-5	ol,cpx	-	-	B/2-1
CH2/17	4	ol,cpx	-	-	B/2-1
CH2/20	4	ol,cpx	-	-	B/2-1

CENTRAL GRABEN PROVINCE

[30/16-A13Y, Shell/Esso (SH1/1-11)]

	SH1/1	SH1/2	SH1/3	SH1/4	SH1/5	SH1/6	SH1/7	SH1/8	SH1/9	SH1/10
SiO_2	42.59	40.93	42.75	40.47	40.79	42.44	38.37	41.52	43.00	42.81
Al_2O_3	15.49	15.00	15.66	14.56	13.88	15.74	13.80	14.87	15.23	13.40
Fe_2O_3	17.60	16.77	14.83	17.70	16.85	15.62	17.92	17.14	15.07	15.01
MgO	8.69	10.12	9.81	10.84	9.83	9.69	10.06	9.72	11.22	8.47
CaO	2.95	6.24	4.68	4.68	7.40	3.87	7.91	4.98	2.98	8.90
Na_2O	1.08	0.96	1.31	0.97	0.89	1.38	1.06	1.40	1.21	1.18
K_2O	5.41	5.27	5.25	5.25	4.74	5.31	5.10	4.47	5.44	4.45
TiO_2	4.90	4.37	4.84	4.47	4.27	4.93	4.22	4.47	4.84	4.18
MnO	0.06	0.12	0.09	0.12	0.28	0.13	0.15	0.41	0.20	0.48
P_2O_5	1.12	1.03	1.15	1.05	1.04	1.14	1.04	1.09	1.05	0.97
TOTAL	99.88	100.81	100.37	100.10	99.96	100.25	99.64	100.06	100.23	99.85
LOI	5.4	5.6	6.5	5.3	3.8	5.8	8.7	4.4	5.0	2.5
Ni	25	19	18	18	15	25	20	29	20	15
Cr	2	*	1	0	4	5	5	0	2	*
V	404	419	347	429	414	344	446	438	347	404
Sc	32	29	29	30	24	32	28	27	33	26
Cu	21	20	17	16	16	20	31	25	26	32
Zn	169	162	101	136	152	125	114	354	177	157
Sr	719	954	659	787	1083	1168	697	1200	903	1164
Rb	90	89	68	86	76	96	69	83	88	74
Zr	436	404	439	403	402	457	385	428	423	387
Nb	130	121	132	119	111	125	109	124	120	109
Ba	894	948	801	848	886	980	795	1060	989	1046
Pb	9	5	5	6	*	9	8	14	2	6
Th	9	7	9	7	*	1	2	5	4	2
La	88	88	88	93	91	85	86	91	87	83
Ce	207	191	197	199	198	188	189	200	195	190
Nd	79	79	79	80	81	68	79	79	70	79
Y	31	34	33	37	32	26	30	33	28	32

	Alteration	Phenocrysts	Megacrysts/Xenocrysts	Ocelli	Type
SH1/1	3-4	(cpx,sp)	-	YES	HB_S/1-2/v
SH1/2	4	(cpx,sp)	-	YES	HB_S/1-2/v
SH1/3	3-4	(cpx,sp)	-	YES	HB_S/1-2/v
SH1/4	3-4	(cpx,sp)	-	YES	HB_S/1-2/v
SH1/5	3-4	(cpx,sp)	-	YES	HB_S/1-2/v
SH1/6	3-4	(cpx,sp)	-	YES	HB_S/1-2/v
SH1/7	4	(cpx,sp)	-	?	HB_S/1-2/v
SH1/8	3	(cpx,sp)	-	YES	HB_S/1-2/v
SH1/9	2-3	(cpx,sp,ol?)	-	YES	HB_S/2/v

[29/25-1, Shell/Esso (SH2/1-3 & 3U-10U)]

	SH1/11	SH2/1	SH2/2	SH2/3	3U	4U	8U	9U	10U
SiO_2	40.96	42.61	42.77	41.78	43.44	37.73	43.62	39.46	41.13
Al_2O_3	14.06	16.79	16.86	16.92	17.10	15.51	17.14	18.10	18.55
Fe_2O_3	16.18	11.42	11.43	15.32	12.14	11.10	12.51	12.62	9.16
MgO	9.65	8.51	8.59	8.97	7.02	12.65	7.49	8.17	6.70
CaO	7.42	7.98	7.98	5.65	6.05	10.36	5.36	7.73	9.58
Na_2O	0.96	1.67	1.67	1.56	1.96	1.23	1.81	1.37	1.41
K_2O	4.62	5.13	5.14	4.99	5.36	4.80	5.24	5.28	6.03
TiO_2	4.59	4.72	4.75	4.68	4.74	4.37	4.90	5.12	5.06
MnO	0.39	0.14	0.14	0.17	N.D	N.D	N.D	N.D	0.16
P_2O_5	1.10	0.75	0.74	0.69	0.78	0.63	0.68	0.73	0.79
TOTAL	99.93	99.70	100.06	100.73	98.58	98.38	98.75	98.59	98.56
LOI	4.0	13.2	11.9	9.00	9.7	15.1	9.4	15.1	13.9
Ni	20	45	63	66	20	53	98	108	53
Cr	5	67	56	55	*	54	69	59	60
V	438	477	503	509	510	501	523	589	623
Sc	30	46	46	49	34	43	49	47	44
Cu	33	16	48	95	43	9	32	12	7
Zn	161	55	97	167	158	35	166	78	34
Sr	1008	788	943	1022	956	523	1043	913	954
Rb	74	82	87	98	85	77	97	108	136
Zr	402	308	339	334	426	3247	360	386	404
Nb	115	93	104	98	117	98	106	114	119
Ba	906	896	966	980	931	828	1040	861	977
Pb	5	6	9	19	10	6	14	15	17
Th	5	4	5	1	7	8	8	9	8
La	91	61	67	74	89	76	84	87	85
Ce	194	138	147	166	183	171	171	186	198
Nd	78	60	59	69	80	77	64	76	88
Y	35	27	25	23	34	31	22	29	36

	Alteration	Phenocrysts	Megacrysts/Xenocrysts	Ocelli	Type
SH1/11	0-1	(cpx,sp)	-	YES	$HB_s/2/v$
SH2/1	3-4	phl,ol,cpx,(lc?)	opx?	YES	L/2-1/v
SH2/2	3-4	phl,ol,cpx,(lc?)	opx?	YES	L/2-1/v
SH2/3	3-4	phl,ol,cpx,(lc?)	opx?	YES	L/2-1/v
3U	3-4	phl,ol,cpx,(lc?)	opx?	-	L/1/v
4U	4-5	phl,ol,cpx,(lc?)	opx?	-	L/2-1/v
8U	3-4	phl,ol,cpx,(lc?)	opx?	-	L/3/v
9U	3	phl,ol,cpx	-	YES	L/3
10U	3	phl,ol,cpx	-	YES	L/3

[29/14b-1a, Britoil/Amerada Hess (AH2/4-11)]

	AH2/4	AH2/5	AH2/6	AH2/7	AH2/9	AH2/11
SiO_2	31.24	38.06	40.29	38.27	40.48	33.12
Al_2O_3	16.44	19.43	18.79	19.60	19.63	17.13
Fe_2O_3	22.78	9.53	15.38	9.21	18.85	23.21
MgO	7.69	5.23	5.29	5.12	4.70	6.36
CaO	10.45	12.58	8.59	13.49	4.90	7.06
Na_2O	2.14	2.69	3.99	3.06	3.93	2.36
K_2O	1.05	2.54	1.76	1.73	1.32	1.43
TiO_2	5.08	6.78	3.26	6.13	2.99	4.98
MnO	0.19	0.24	0.24	0.12	0.13	0.16
P_2O_5	1.13	1.02	0.90	1.42	0.82	1.11
TOTAL	98.19	98.09	98.49	98.16	98.06	96.92
LOI	13.4	14.7	11.9	13.8	8.3	10.6
Ni	94	38	38	122	38	67
Cr	225	76	7	248	5	226
V	469	572	376	598	302	493
Sc	31	35	13	37	5	22
Cu	26	6	7	6	8	26
Zn	116	70	539	36	646	195
Sr	267	261	426	610	334	508
Rb	23	42	25	26	22	29
Zr	447	395	909	531	759	454
Nb	137	106	297	171	271	137
Ba	363	424	405	294	392	4758
Pb	6	10	4	7	5	6
Th	9	9	32	13	29	8
La	126	51	200	245	120	74
Ce	243	119	349	460	283	165
Nd	87	66	104	147	115	68
Y	32	25	64	30	53	30

	Alteration	Phenocrysts	Megacrysts/Xenocrysts	Ocelli	Type
AH2/4	5	ol,cpx	-	-	B-B_s/2
AH2/5	5	ol,cpx	-	-	B-B_s/2
AH2/6	5-6	cpx?	-	-	?B_s/1-2
AH2/7			*No Section*		
AH2/9	5	cpx,sp,(ol?)	-	-	B_s or H/1-2/v
AH2/11	5	ol,cpx	-	-	?B/2

EGERSUND BASIN

[17/9-1, Esso (7&8N & ES1/1-46)]

	7N	8N	ES1/1	ES1/2	ES1/3	ES1/5	ES1/9	ES1/1	1ES1/15	ES1/19
SiO_2	43.11	46.24	42.68	43.10	44.07	44.07	46.03	45.51	43.19	44.29
Al_2O_3	11.43	12.40	12.44	14.43	14.50	13.18	13.14	15.09	12.21	13.36
Fe_2O_3	11.74	10.33	14.13	15.85	14.52	12.49	10.18	14.16	15.59	17.81
MgO	6.68	7.39	10.07	9.77	5.99	8.58	9.88	8.10	9.41	8.75
CaO	16.81	13.71	12.14	7.77	9.06	11.98	11.46	6.80	10.61	7.73
Na_2O	1.87	3.79	2.49	0.80	4.13	2.49	3.22	2.37	0.58	0.57
K_2O	0.84	0.57	0.50	2.16	0.92	0.85	0.50	2.08	2.40	3.06
TiO_2	3.16	3.50	3.66	3.64	3.73	3.60	3.43	3.39	3.11	3.43
MnO	0.53	0.17	0.21	0.22	0.21	0.23	0.16	0.19	0.22	0.18
P_2O_5	0.65	0.65	0.83	1.02	1.17	0.80	0.56	0.81	0.83	0.28
TOTAL	98.82	98.75	99.16	98.76	98.31	98.25	98.55	98.50	98.16	99.45
LOI	4.0	3.0	6.3	6.3	4.7	5.0	4.7	4.8	4.0	5.0
Ni	72	54	63	57	38	56	70	57	67	68
Cr	266	210	245	150	6	221	519	133	243	186
V	525	483	451	334	510	453	521	403	345	355
Sc	29	40	42	25	13	39	65	24	38	29
Cu	37	90	110	191	97	102	75	92	105	76
Zn	72	40	96	118	85	75	68	93	108	106
Sr	648	457	519	647	563	622	344	578	554	367
Rb	44	35	30	160	56	57	11	153	175	225
Zr	331	345	354	329	367	345	304	327	298	301
Nb	129	129	154	149	203	138	100	158	125	129
Ba	433	3952	293	286	776	1153	163	286	368	371
Pb	0	1	5	6	8	6	18	5	5	12
Th	10	8	10	11	16	11	32	11	9	11
La	90	87	95	134	126	109	82	105	110	123
Ce	163	183	208	263	272	216	163	212	185	167
Nd	63	76	70	93	95	84	61	70	68	54
Y	21	22	23	24	26	24	24	22	19	13

	Alteration	Phenocrysts	Megacrysts/Xenocrysts	Ocelli	Type
7N	2	ol,cpx,sod?	-	-	Ne/1-2
8N	2	ol,cpx,sod?	-	-	Ne/1-2
ES1/1	3-4	ol,cpx	-	-	Ne/1/v
ES1/2	3-4	ol,cpx	-	-	Ne/0/v
ES1/3	2	ol,cpx,sod?	-	-	Ne/1/v
ES1/5	3	ol,cpx,sod?	-	-	Ne/1-2/v
ES1/9	3-4	ol,cpx	-	-	Ne/1-2/v
ES1/11	3-4	ol,cpx	-	-	Ne/1-2/v
ES1/15	4	cpx	-	-	Ne/1-0/v
ES1/19	4	cpx	-	-	Ne/1-0/v

	ES1/22	ES1/24	ES1/31	ES1/34	ES1/36	ES1/38	ES1/41	ES1/43	ES1/46
SiO_2	43.74	45.37	42.32	44.38	43.46	41.73	42.32	36.73	35.03
Al_2O_3	11.59	11.71	14.55	13.00	13.83	14.29	15.74	19.11	17.62
Fe_2O_3	13.39	11.39	14.54	12.31	13.00	19.27	10.23	17.11	14.72
MgO	10.67	8.11	10.28	7.77	8.90	9.10	6.66	6.14	5.25
CaO	14.74	14.74	7.79	12.00	10.57	7.04	13.61	9.86	15.77
Na_2O	1.32	2.48	2.28	2.64	1.34	0.38	1.77	0.26	0.68
K_2O	0.66	0.90	0.93	0.88	1.53	2.76	3.84	3.87	4.51
TiO_2	3.42	3.31	4.19	3.76	3.92	2.83	3.09	3.44	3.34
MnO	0.22	0.26	0.20	0.20	0.21	0.27	0.18	0.29	0.31
P_2O_5	0.79	0.68	0.82	0.77	0.81	0.67	0.58	0.75	0.67
TOTAL	100.54	98.96	97.89	97.72	97.57	98.36	98.01	97.55	97.91
LOI	5.4	2.8	6.0	4.0	4.7	5.3	9.0	12.7	15.5
Ni	71	53	90	63	66	51	71	107	77
Cr	230	222	220	189	112	61	158	108	144
V	294	402	546	485	541	282	372	426	392
Sc	30	36	44	37	33	16	24	15	24
Cu	90	51	102	91	114	74	58	74	62
Zn	89	133	84	77	123	127	106	164	164
Sr	673	477	562	691	616	513	1585	1118	1271
Rb	38	46	86	59	109	208	110	131	127
Zr	326	316	416	360	422	293	370	405	400
Nb	135	120	172	140	169	116	167	214	196
Ba	2082	352	281	4751	6618	310	1675	1375	1587
Pb	0	2	6	6	5	6	9	13	12
Th	6	5	12	10	11	9	11	18	14
La	64	66	124	106	119	116	103	131	100
Ce	150	155	226	228	233	199	210	206	197
Nd	64	61	80	88	94	69	77	62	81
Y	21	19	23	24	24	21	27	31	31

	Alteration	Phenocrysts	Megacrysts/Xenocrysts	Ocelli	Type
ES1/22	3-4	cpx	-	-	Ne/1-2/v
ES1/24			*No Section*		
ES1/31	3-4	ol,cpx	-	-	Ne/1-2/v
ES1/34	3	ol,cpx,sod?	-	-	Ne/1-2/v
ES1/36			*No Section*		
ES1/38	3-4	cpx	-	-	Ne/1-0/v
ES1/41	4	phl,ol,cpx	opx?-	-	L/3
ES1/43	4	phl,ol,cpx	-	-	L/3
ES1/46	4	phl,ol,cpx	-	-	L/3/v

NETHERLANDS PROVINCE

[F/10-1, Petroland (PL1/1-12)] [Loon-op-zand/1, N.A.M. (NAM2/2-8 & DL 3-5)]

	PL1/5	PL1/6	PL1/10	PL1/11	PL1/12	NAM2/2	NAM2/3	NAM2/7	NAM2/8	DL3
SiO_2	39.47	40.47	40.44	40.22	40.13	39.04	40.71	40.60	35.43	38.05
Al_2O_3	14.41	14.13	14.59	14.76	14.45	17.13	18.14	18.32	16.34	16.35
Fe_2O_3	14.04	13.92	14.65	14.50	14.64	12.40	12.58	13.26	14.18	12.14
MgO	11.80	10.80	10.51	10.67	10.74	6.05	6.16	6.60	7.18	6.41
CaO	9.11	9.44	7.20	7.55	8.78	15.29	12.36	11.75	17.24	17.36
Na_2O	0.67	0.76	0.71	0.67	0.78	1.70	2.19	1.70	1.40	1.73
K_2O	3.87	4.18	4.99	4.75	4.18	0.93	0.75	0.77	0.74	0.71
TiO_2	4.33	4.26	4.06	4.11	4.30	3.61	3.94	4.04	3.48	3.48
MnO	0.28	0.27	0.24	0.24	0.24	0.20	0.17	0.16	0.22	0.21
P_2O_5	0.69	0.67	0.74	0.75	0.69	0.96	1.01	1.02	0.88	0.89
TOTAL	98.66	98.89	98.12	98.22	98.93	97.30	98.02	98.21	97.10	97.32
LOI	3.7	3.4	4.2	3.9	3.2	14.6	13.0	12.5	15.4	15.4
Ni	43	44	34	39	46	142	147	148	188	181
Cr	27	23	19	22	32	274	303	303	271	294
V	484	476	459	461	501	377	406	421	363	375
Sc	35	34	26	24	36	27	36	37	35	29
Cu	52	66	90	81	69	53	56	55	46	49
Zn	119	112	80	114	94	112	79	85	103	64
Sr	651	796	1174	895	883	895	1027	930	826	949
Rb	62	57	61	68	63	27	20	21	19	20
Zr	325	320	321	323	318	293	316	323	265	293
Nb	98	96	103	102	94	113	116	117	99	103
Ba	530	614	814	808	760	976	1013	1033	952	854
Pb	5	3	4	4	2	9	6	6	8	3
Th	7	6	5	7	6	6	6	7	3	5
La	87	81	81	83	67	94	88	89	88	89
Ce	177	176	182	173	160	177	166	181	190	168
Nd	67	71	69	70	67	74	60	57	72	64
Y	28	28	27	28	27	33	27	27	31	30

	Alteration	Phenocrysts	Megacrysts/Xenocrysts	Ocelli	Type
PL1/5	2-3	amp,cpx,(ol)	-	-	L/3/v
PL1/6	2-3	amp,cpx,(ol)	-	YES	L/3/v
PL1/10	2-3	amp,cpx,ol	-	-	L/3/v
PL1/11	2-3	amp,cpx,ol	-	YES	L/3/v
PL1/12	2	amp,cpx,ol	-	YES	L/3/v
NAM2/2	4	ol,cpx,(amp?)	-	YES	B_s/1-2/v
NAM2/3	4-5	ol,cpx,(amp?)	-	YES	B_s/1-2/v
NAM2/7	4	ol,cpx,(amp?)	-	YES	B_s/1-2/v
NAM2/8	4	ol,cpx,(amp?)	-	YES	B_s/1-2/v
DL3	5	ol,cpx	-		B_s/1/v

[Zuidwal/1, Petroland (ZU)]

	DL4	DL5	ZU1	ZU2	ZU3	ZU4	ZU5	ZU6	ZU7	ZU8
SiO_2	37.42	43.44	52.78	56.08	56.50	56.74	50.30	55.75	28.51	28.75
Al_2O_3	17.16	18.68	26.71	25.45	25.56	24.33	17.71	18.94	15.73	16.76
Fe_2O_3	14.18	14.06	7.77	4.39	4.77	4.49	8.38	4.14	18.02	17.54
MgO	7.03	7.74	0.67	0.66	0.80	0.78	4.78	5.72	9.61	9.74
CaO	14.34	9.27	0.65	0.63	0.62	0.62	6.43	1.69	16.37	16.49
Na_2O	1.57	1.83	1.14	2.49	1.89	3.31	5.67	4.99	0.62	0.41
K_2O	0.68	0.81	7.14	7.86	8.25	7.33	3.17	7.28	3.69	3.84
TiO_2	3.62	3.91	1.52	1.39	1.38	1.34	2.06	0.33	3.15	3.15
MnO	0.18	0.12	0.37	0.02	0.03	0.02	0.17	0.12	0.49	0.47
P_2O_5	0.92	1.00	0.27	0.22	0.24	0.23	0.45	0.03	0.37	0.41
TOTAL	97.11	100.88	99.03	99.18	101.04	99.18	99.14	99.00	96.56	97.56
LOI	13.0	9.8	8.5	5.0	4.7	4.7	4.0	6.0	21.5	21.4
Ni	181	151	21	50	44	59	40	39	267	254
Cr	302	312	4	3	5	4	9	120	1881	2098
V	396	439	157	218	203	200	135	238	480	484
Sc	31	38	*	*	*	*	*	13	30	28
Cu	54	58	802	11	294	12	143	5	182	446
Zn	119	79	137	145	175	164	137	92	213	200
Sr	852	823	2634	3086	2995	3043	2501	1992	650	577
Rb	19	24	201	176	191	165	150	64	170	176
Zr	291	311	459	522	511	450	423	329	282	287
Nb	109	109	331	319	307	302	464	157	63	63
Ba	905	1064	1630	1982	1862	2162	3616	1469	3215	1488
Pb	5	4	11	12	12	12	4	9	3	4
Th	5	8	26	21	20	18	13	15	*	*
La	94	92	90	72	64	93	137	109	59	34
Ce	180	157	180	152	135	175	190	178	62	53
Nd	70	57	53	43	32	42	30	45	20	19
Y	31	24	18	13	14	12	13	17	18	19

	Alteration	Phenocrysts	Megacrysts/Xenocrysts	Ocelli	Type
DL4	5	ol,cpx	-	YES	B_g/1-2/v
DL5	5	ol,cpx	-	?	B_g/1-2/v
ZU1	4-5	ne,?sod	-	-	P/2-1
ZU2	3-4	ne,sod,cpx	-	-	P/2-1
ZU3	4	ne,?sod,cpx	-	-	P/2-1
ZU4	4	ne,?sod,cpx	-	-	P/2-1
ZU5	3-4	ol,cpx	-	-	P-B_g/2
ZU6	4	lc,(ne)	-	-	P/2
ZU7	5	bi,cpx,ol?	-	-	?L/3
ZU8	5	bi,cpx,ol?	-	-	?L/3

[K/14-FA103, N.A.M. (DL 1-2A); ANDEL/2, N.A.M. (DL 6-7)]
[ANDEL/4, N.A.M. (DL 8-9); L/13-3, N.A.M. (001-1A,B,C)]

	DL1	DL2	DL2A	DL6	DL7	DL8	DL9	001-1A	001-1B	001-1C
SiO_2	32.56	42.78	51.11	42.23	39.63	41.07	40.17	39.95	39.88	39.05
Al_2O_3	18.73	18.28	19.78	19.85	20.70	19.73	17.82	15.15	14.82	15.33
Fe_2O_3	36.90	27.23	16.46	13.64	14.34	12.01	14.15	13.22	12.61	12.50
MgO	1.87	1.78	1.26	5.66	5.40	4.43	7.14	17.78	18.15	20.30
CaO	1.61	1.65	0.90	7.99	9.01	11.43	9.02	3.83	4.33	1.28
Na_2O	0.34	0.49	0.43	2.28	1.43	1.62	1.80	1.09	1.16	0.65
K_2O	0.38	1.27	2.28	2.38	2.45	1.70	1.71	2.60	2.73	3.26
TiO_2	3.49	3.48	3.64	3.61	3.74	4.77	4.28	3.80	3.69	3.93
MnO	1.35	0.96	0.64	0.21	0.23	0.18	0.17	0.12	0.12	0.12
P_2O_5	0.87	0.87	1.36	0.77	0.81	0.99	0.89	0.79	1.00	1.61
TOTAL	98.10	98.79	97.85	98.63	97.73	97.93	97.14	98.34	98.50	98.01
LOI	20.4	16.8	7.8	16.5	18.2	15.9	15.0	8.5	8.8	9.1
Ni	39	56	36	126	172	190	218	139	138	123
Cr	270	264	252	236	283	645	517	378	361	379
V	398	346	267	388	401	522	461	397	381	392
Sc	22	17	9	36	34	53	43	35	32	34
Cu	9	7	8	53	55	70	66	20	18	24
Zn	47	23	10	157	132	71	135	84	79	39
Sr	1432	1180	6114	732	631	1302	1430	589	577	156
Rb	19	54	84	56	52	51	44	25	26	56
Zr	434	443	456	383	395	524	447	345	338	335
Nb	154	156	164	110	115	135	120	115	111	117
Ba	142	265	387	587	702	1058	943	724	685	845
Pb	3	7	1	8	11	5	4	12	21	426
Th	6	11	*	9	9	7	5	8	8	15
La	117	108	333	96	109	110	95	113	99	96
Ce	217	198	674	177	193	214	184	201	180	160
Nd	76	65	260	68	75	82	76	76	69	55
Y	35	40	32	33	34	34	29	30	36	30

	Alteration	Phenocrysts	Megacrysts/Xenocrysts	Ocelli	Type
DL1	5-6	(?amp,cpx)	-	-	?HB$_s$/2
DL2	5-6	(cpx,?)	-	?	?B$_s$/2
DL2A	5-6	(cpx,?)	-	-	?B$_s$/2
DL6	5-6	ol,cpx,(plag,foid?)	-	YES	B-B$_s$/1-2/v
DL7	5-6	ol,cpx,(plag,foid?)	-	YES	B-B$_s$/1-2/v
DL8	5-6	ol,cpx	-	?	B$_s$/1-2
DL9	5-6	ol,cpx	-	?	B$_s$/1-2
001-1A	5-6	?ol,?cpx	-	-	?/1-2/v
001-1B	5-6	?ol,?cpx	-	-	?/
001-1C	5-6	?ol,?cpx	-	-	?/

PERMIAN

	1N	2N	3N	2D	3D	4D	5D	6D	8D	9D
SiO_2	58.91	51.42	43.22	50.49	46.78	47.17	50.04	72.74	48.65	48.48
Al_2O_3	16.52	17.80	16.36	17.05	14.97	17.41	14.89	12.06	17.34	17.20
Fe_2O_3	6.82	11.98	20.63	9.87	11.28	14.77	12.24	3.90	12.06	10.36
MgO	3.95	3.44	6.89	7.72	7.86	5.81	8.75	0.58	8.87	11.36
CaO	2.40	4.55	3.02	5.13	8.85	4.47	5.35	1.32	6.68	6.27
Na_2O	2.50	3.91	2.16	5.67	4.63	6.18	3.84	4.22	3.24	3.23
K_2O	4.47	2.33	3.16	0.53	0.69	0.77	0.95	3.91	0.51	0.54
TiO_2	3.12	3.21	2.94	2.24	2.24	2.35	2.16	0.78	1.50	1.53
MnO	N.D	N.D	N.D	N.D	N.D	0.11	N.D	0.04	N.D	N.D
P_2O_5	0.50	0.47	0.48	0.40	0.42	0.43	0.40	0.13	0.14	0.15
TOTAL	99.20	99.11	98.86	99.10	97.71	99.46	98.62	99.69	98.99	99.12
LOI	4.6	6.7	6.6	6.2	8.2	4.0	7.0	2.0	3.5	4.2
Ni	59	34	38	121	100	147	104	4	152	168
Cr	26	25	105	33	49	41	42	*	175	162
V	261	277	290	304	302	309	288	14	306	295
Sc	27	28	27	32	32	35	33	8	35	39
Cu	3	5	7	40	57	33	54	*	29	29
Zn	65	100	99	120	125	115	147	55	88	113
Sr	142	240	139	240	233	294	283	133	476	454
Rb	74	50	52	3	4	5	8	112	6	9
Zr	264	251	242	147	147	159	141	479	97	99
Nb	39	38	37	12	12	12	11	23	10	10
Ba	424	265	708	184	501	298	492	1318	249	193
Pb	4	6	12	6	9	12	6	9	22	17
Th	4	2	2	*	0	*	*	14	*	*
La	30	34	39	22	19	12	18	59	13	13
Ce	68	66	73	42	35	35	34	132	12	27
Nd	32	30	28	22	21	22	21	61	11	13
Y	29	26	26	30	29	31	24	51	19	19

	Alteration	Phenocrysts	Megacrysts/Xenocrysts	Ocelli	Type
1N	4	(plag)	-	-	H/2
2N	3-4	(plag,?ol)	-	-	H/2
3N	4	(plag)	-	-	H/2
2D	3-4	plag,(?ol)	-	-	B-H/2/v
3D	4	plag,(?ol)	-	-	B-H/2/v
4D	3-4	plag,(?ol)	-	-	B-H/2/v
5D	3	plag,(?ol)	-	?	B-H/1-2/v
6D	4	plag,(cpx)	-	-	H-Tr/1
8D	3-4	plag,(?ol)	-	?	B-H/2/v
9D	4	plag,(?ol)	-	-	B/H/2-1/v

	10D	11D	12D	13D	14D	17D	18D	19D	NAM1/1	NAM1/4
SiO_2	49.03	51.54	50.84	51.81	50.15	48.88	48.23	70.47	51.94	56.82
Al_2O_3	17.04	13.98	13.56	14.14	15.73	17.03	16.06	12.36	17.42	17.00
Fe_2O_3	11.02	12.84	10.31	11.03	10.30	11.62	12.70	5.43	8.35	7.94
MgO	8.63	5.76	8.67	9.38	9.56	1.96	6.34	0.23	6.74	6.15
CaO	8.48	5.61	10.83	7.50	7.95	11.97	8.76	1.00	9.44	8.06
Na_2O	3.20	3.68	2.40	2.80	3.24	3.08	3.51	3.01	2.68	2.44
K_2O	0.53	1.84	0.32	0.51	0.43	2.29	0.97	5.68	0.30	0.22
TiO_2	1.46	2.91	1.84	1.83	1.71	2.15	2.10	0.86	1.00	0.95
MnO	0.13	N.D	N.D	N.D	0.19	0.16	0.26	0.12	0.12	0.10
P_2O_5	0.12	0.85	0.27	0.28	0.22	0.31	0.29	0.20	0.10	0.10
TOTAL	99.64	99.01	99.03	99.29	99.48	99.45	99.75	99.34	98.10	99.78
LOI	2.5	2.5	7.4	3.8	2.4	5.7	1.5	0.6	3.9	3.7
Ni	190	17	156	168	187	87	137	13	102	90
Cr	204	78	401	448	549	51	61	7	344	334
V	295	329	258	303	330	297	277	53	287	292
Sc	33	40	35	38	41	33	25	11	38	43
Cu	25	29	52	44	33	25	13	6	90	79
Zn	74	97	75	79	78	101	228	356	262	194
Sr	482	343	319	331	353	474	474	126	210	211
Rb	4	25	3	5	3	95	20	159	8	6
Zr	102	238	147	143	161	120	192	707	97	94
Nb	9	26	11	10	10	11	16	42	7	6
Ba	291	663	145	267	184	317	368	1047	121	74
Pb	15	6	0	3	2	24	40	25	515	14
Th	*	1	*	*	*	*	*	11	6	2
La	4	34	12	15	10	10	24	96	*	*
Ce	20	73	32	33	30	20	56	146	26	28
Nd	12	35	19	19	23	13	27	76	12	11
Y	20	42	25	25	27	24	31	73	20	20

	Alteration	Phenocrysts	Megacrysts/Xenocrysts	Ocelli	Type
10D	2	(plag,cpx,?ol)	-	-	B/2
11D	3-4	(plag)	-	-	H/1/v
12D	4	(plag)	-	-	B-H/2-1/v
13D	4	(plag)	-	-	B-H/2-1/v
14D	3-4	(plag)	-	-	B-H/2-1/v
17D	3-4	(plag)	-	-	H-Tr/1/
18D	2	(plag)	-	-	H/1-2/v
19D	3	plag,(cpx)	-	-	H-Tr/0-1
NAM1/1	3-4	[plag,ol,cpx]	-	-	Dolerite
NAM1/4	3-4	[plag,ol,cpx]	-	-	Dolerite

Note : Square brackets indicate a major rock forming phase not a phenocryst.

	NAM1/13	NAM1/17	NAM1/19	NAM1/21	NAM3/1	NAM3/4	NAM3/8	NAM3/11	NAM3/12
SiO_2	45.82	45.08	44.15	43.86	47.95	47.66	48.88	65.60	48.44
Al_2O_3	16.92	12.66	11.67	11.06	16.51	16.21	15.97	14.35	16.25
Fe_2O_3	12.97	13.61	14.58	15.22	12.07	12.25	11.44	4.39	11.90
MgO	9.76	16.22	18.51	19.00	7.48	7.02	8.64	2.02	8.62
CaO	6.45	6.15	5.31	5.07	11.51	11.71	6.92	3.44	9.36
Na_2O	3.95	2.14	2.17	1.80	2.63	2.68	2.52	6.57	2.96
K_2O	0.90	0.93	0.65	0.65	0.28	0.30	2.89	1.45	0.77
TiO_2	2.24	1.61	1.65	1.53	0.94	1.12	1.20	0.81	1.08
MnO	0.18	0.14	0.15	0.15	0.14	0.16	0.33	0.10	0.18
P_2O_5	0.34	0.20	0.22	0.23	0.08	0.12	0.12	0.16	0.10
TOTAL	99.52	98.76	99.06	98.57	99.59	99.23	98.92	98.89	99.67
LOI	8.3	4.6	5.6	6.0	5.5	3.4	3.1	1.9	2.4
Ni	101	430	548	682	136	121	103	9	136
Cr	228	611	675	804	309	267	209	*	264
V	345	263	266	232	264	293	298	36	261
Sc	33	22	20	13	34	35	30	10	27
Cu	200	96	99	99	107	113	113	5	120
Zn	361	143	123	175	73	76	90	40	80
Sr	333	305	294	239	152	150	164	134	173
Rb	27	32	21	22	7	7	30	25	16
Zr	189	133	114	121	59	76	82	501	71
Nb	17	20	15	15	5	7	7	36	7
Ba	240	287	209	279	296	156	805	192	159
Pb	17	28	20	28	3	3	3	2	3
Th	0	2	1	2	*	*	*	8	0
La	10	8	10	9	4	6	14	39	4
Ce	44	36	32	26	10	21	19	82	17
Nd	28	15	15	11	10	8	10	37	11
Y	28	20	18	18	18	21	21	60	21

	Alteration	Phenocrysts	Megacrysts/Xenocrysts	Ocelli	Type
NAM1/13	4	[ol,plag,cpx,mag]	-	-	Dolerite
NAM1/17	4	[ol,plag,bi,cpx,mag]	-	-	Picritic Dolerite
NAM1/19	4	[ol,cpx,bi,plag,mag]	-	-	Picritic Dolerite
NAM1/21	4	[ol,cpx,bi,plag,mag]	-	-	Picritic Dolerite
NAM3/1	3	[plag,ol,cpx,mag]	-	-	Dolerite
NAM3/4	3	[plag,ol,cpx,mag]	-	-	Dolerite
NAM3/8	3	[plag,ol,cpx,mag]	-	-	Dolerite
NAM3/11	3	[plag,Afsp,qz,cpx,mag]	-	-	Dolerite (Syenite)
NAM3/12	3	[plag,ol,cpx,mag]	-	-	Dolerite

Note : Square brackets indicate a major rock forming phase not a phenocryst.

Typical accuracy (RMSD) and reproducibility (2σ) of XRF data.

						MEAN	2σ	RMSD
SiO2	44.97	45.02	44.58	44.42	44.51	44.70	0.22	0.26
Al2O3	12.90	12.91	12.87	12.71	12.85	12.85	0.06	0.18
Fe2O3	11.91	11.78	11.77	11.67	11.70	11.77	0.07	0.05
MgO	11.05	11.10	11.05	10.99	11.04	11.05	0.03	0.07
CaO	12.36	12.33	12.24	12.20	12.16	12.26	0.07	0.03
Na2O	1.75	1.80	1.73	1.73	1.78	1.76	0.03	0.06
K2O	0.46	0.46	0.45	0.45	0.46	0.46	0.01	0.03
TiO2	2.88	2.87	2.86	2.83	2.85	2.86	0.02	0.01
MnO	0.46	0.47	0.45	0.45	0.45	0.46	0.01	0.005
P2O5	0.41	0.41	0.41	0.42	0.42	0.41	0.01	0.01
TOTAL	99.15	99.15	98.41	97.87	98.22			
LOI	3.2	3.1	3.0	2.0	1.7			
Ni	118	116	115	115	115	116	1.04	4.3
Cr	272	271	270	270	272	271	0.80	11.0
V	357	353	353	352	351	353	1.84	11.5
Sc	35	34	33	36	38	35	1.54	2.4
Cu	35	36	30	32	32	33	1.96	5.3
Zn	85	83	84	83	82	83	0.91	5.0
Sr	695	703	701	690	697	697	4.10	9.6
Rb	2	3	3	2	2	2	0.44	3.5
Zr	229	226	225	220	221	224	2.96	14.8
Nb	58	60	60	60	59	59	0.72	2.4
Ba	582	548	557	514	541	548	19.77	39.0
Pb	2	2	2	1	1	2	0.44	4.0
Th	2	3	2	1	2	2	0.57	2.8
La	50	54	47	43	47	48	3.27	5.6
Ce	114	108	100	105	114	108	4.81	13.5
Nd	46	47	40	44	46	45	2.23	3.6
Y	26	27	27	26	26	26	0.44	3.4

Note : Measurements were conducted on 5 different fused discs and pressed powder pellets made from sample BP1/33. Major elements are given in wt. % and Fe2O3 represents total iron. Trace elements are presented in ppm. RMSD values are from Smedley 1986 for major elements, and Fitton *et al.* (1984) for trace elements.

SECTION A3 : REE Data.

REE analysis by atomic emmission spectroscopy was conducted on 40 samples using the Philips PV8210 1.5-m inductively coupled plasma spectrometer at Royal Holloway and Bedford New College. Rock powders were subjected to an HF-$HClO_4$ attack and REE were then separated from filtered solutions using cation exchange columns. Full details of the analytical procedures, standards and accuracy may be found in Walsh *et al.*(1981) and Wallace (1989). The results of the analyses are presented in the following tables. At the end of this section there is a table showing the reproducibility of the separation procedure for 4 different REE concentrations from an alkali basalt sample (AH1/42) and a nephelinite (ES1/24). The final table also shows the concentrations of blanks which were run maintain a check on the state of the separation columns. The blank values for each element are negligible.

	AH1/1	AH1/3	AH1/4	AH1/5	AH1/10
La	20.50	25.00	28.30	25.50	24.10
Ce	40.97	55.43	59.99	55.95	52.02
Pr	4.75	6.66	7.29	6.46	6.62
Nd	19.80	29.30	30.60	27.80	29.20
Sm	3.39	5.67	5.66	5.02	5.65
Eu	0.99	1.75	1.77	1.47	1.75
Gd	3.23	5.32	5.15	4.67	5.35
Dy	2.63	4.58	4.11	3.79	4.47
Ho	0.49	0.80	0.70	0.65	0.77
Er	1.41	2.18	1.87	1.78	2.09
Yb	1.17	1.77	1.41	1.35	1.64
Lu	0.20	0.26	0.20	0.19	0.24

	AH1/15	AH1/36	AH1/42	BP1/1	BP1/33
La	23.30	25.80	34.70	43.70	38.70
Ce	51.06	55.63	73.35	93.92	83.78
Pr	6.34	6.80	8.73	10.81	9.90
Nd	28.20	29.70	36.20	44.90	41.10
Sm	5.37	5.66	6.71	7.81	7.25
Eu	1.65	1.75	2.04	2.49	2.31
Gd	5.17	5.31	6.25	6.86	6.51
Dy	4.28	4.49	5.19	5.25	5.16
Ho	0.75	0.77	0.90	0.90	0.89
Er	2.02	2.11	2.45	2.39	2.42
Yb	1.60	1.67	1.97	1.82	1.88
Lu	0.23	0.24	0.29	0.26	0.27

	BP1/64	BP2/1	TO1/21	TO1/27	CH2/17
La	46.30	37.80	38.80	34.60	44.30
Ce	101.37	78.65	79.71	72.34	90.62
Pr	11.98	9.16	8.96	8.41	10.42
Nd	49.30	37.50	36.90	34.80	41.70
Sm	8.46	6.30	6.46	6.30	7.00
Eu	2.61	1.93	1.96	1.96	2.13
Gd	7.24	5.35	5.82	5.78	5.89
Dy	5.62	3.92	4.47	4.61	4.34
Ho	0.97	0.65	0.82	0.80	0.72
Er	2.61	1.69	2.22	2.13	1.88
Yb	2.02	1.24	1.81	1.67	1.40
Lu	0.29	0.17	0.27	0.26	0.19

	CH2/20	FO1/3	FO1/4	SO1/8	SO1/11
La	40.70	80.00	92.70	65.10	58.30
Ce	84.16	166.29	186.99	137.23	124.60
Pr	9.50	18.41	21.22	15.68	14.56
Nd	38.50	71.50	82.40	62.90	59.90
Sm	6.42	11.78	13.07	10.32	9.97
Eu	1.90	3.62	3.89	3.16	3.07
Gd	5.54	9.67	10.75	8.52	8.40
Dy	4.13	7.15	7.95	6.14	6.10
Ho	0.70	1.22	1.35	1.04	1.02
Er	1.81	3.26	3.57	2.72	2.69
Yb	1.35	2.53	2.68	2.02	1.96
Lu	0.19	0.37	0.38	0.29	0.28

	SH1/5	SH1/10	SH2/2	SH2/3	PL1/6
La	88.80	85.00	64.10	68.70	77.80
Ce	186.24	176.67	132.04	143.39	159.33
Pr	21.07	20.23	14.84	16.12	17.89
Nd	82.40	79.23	57.10	62.90	70.30
Sm	13.16	12.70	8.83	9.69	11.19
Eu	3.89	3.73	2.60	2.82	3.30
Gd	10.86	10.48	7.31	7.70	9.13
Dy	7.99	7.70	5.19	5.36	6.43
Ho	1.37	1.32	0.89	0.91	1.11
Er	3.60	3.48	2.31	2.40	2.86
Yb	2.65	2.54	1.66	1.79	2.08
Lu	0.38	0.37	0.23	0.26	0.31

	PL1/10	PL1/12	AH2/5	AH2/9	CH1/34
La	81.70	73.80	43.50	108.80	39.70
Ce	156.80	149.88	99.46	241.66	85.67
Pr	16.41	16.97	12.50	27.44	10.08
Nd	62.60	67.00	55.30	105.40	40.30
Sm	9.98	10.63	10.48	16.04	6.62
Eu	2.97	3.16	3.20	4.79	2.08
Gd	8.43	8.87	8.34	13.34	5.65
Dy	6.16	6.34	5.29	10.96	3.96
Ho	1.05	1.09	0.87	1.86	0.66
Er	2.73	2.85	2.20	4.91	1.78
Yb	2.08	2.09	1.54	3.57	1.40
Lu	0.30	0.30	0.21	0.51	0.20

	8U	7N	ES1/24	ES1/34	ES1/43
La	59.70	72.30	76.70	72.00	94.40
Ce	128.89	143.68	155.95	151.78	162.12
Pr	14.51	15.74	16.85	16.90	15.98
Nd	55.30	60.10	64.70	65.60	57.70
Sm	8.37	8.96	9.51	10.20	8.75
Eu	2.40	2.52	2.64	2.99	2.61
Gd	6.47	6.93	7.32	8.18	7.49
Dy	4.53	4.66	4.80	5.52	5.85
Ho	0.77	0.79	0.81	0.93	1.03
Er	2.01	2.03	2.08	2.42	2.72
Yb	1.43	1.50	1.51	1.76	2.17
Lu	0.20	0.21	0.22	0.26	0.30

	ZU5	NAM2/8	NAM1/4	NAM3/8	8D
La	92.62	58.90	10.13	5.33	8.46
Ce	159.07	120.56	22.72	13.28	20.20
Pr	15.92	13.94	2.81	1.85	2.75
Nd	49.90	50.70	13.00	10.20	13.80
Sm	7.65	8.51	2.48	2.14	3.17
Eu	2.20	2.41	0.82	0.84	1.30
Gd	5.62	6.70	3.03	3.06	3.77
Dy	4.35	5.35	3.55	3.50	3.78
Ho	0.69	0.86	0.66	0.64	0.65
Er	1.48	2.06	1.90	1.84	1.77
Yb	1.45	1.78	1.88	1.75	1.58
Lu	0.21	0.25	0.28	0.26	0.23

AH1/42

					MEAN	2σ
La	34.70	30.16	30.45	32.15	**31.87**	**1.81**
Ce	73.35	65.70	66.19	68.40	**68.41**	**3.03**
Pr	8.73	8.15	8.28	8.49	**8.41**	**0.23**
Nd	36.20	33.70	33.90	34.70	**34.63**	**0.98**
Sm	6.71	6.33	6.41	6.48	**6.48**	**0.14**
Eu	2.04	1.85	1.89	1.92	**1.93**	**0.07**
Gd	6.25	5.65	5.77	5.89	**5.89**	**0.22**
Dy	5.19	5.00	4.89	5.11	**5.07**	**0.09**
Ho	0.90	0.82	0.84	0.85	**0.85**	**0.30**
Er	2.45	2.11	2.13	2.20	**2.22**	**0.14**
Yb	1.97	1.89	1.87	1.91	**1.91**	**0.04**
Lu	0.29	0.26	0.27	0.28	**0.28**	**0.01**

ES1/24

					MEAN	2σ
La	76.70	74.45	72.45	72.66	**74.07**	**1.71**
Ce	155.95	152.40	150.11	149.94	**152.10**	**2.43**
Pr	16.85	17.51	17.27	17.22	**17.21**	**0.24**
Nd	64.70	61.70	61.30	60.80	**62.13**	**1.52**
Sm	9.51	9.89	9.83	9.73	**9.74**	**0.14**
Eu	2.64	2.51	2.51	2.48	**2.54**	**0.06**
Gd	7.32	6.90	6.95	6.82	**7.00**	**0.20**
Dy	4.80	4.94	4.93	4.88	**4.89**	**0.06**
Ho	0.81	0.77	0.78	0.77	**0.78**	**0.02**
Er	2.08	1.75	1.76	1.75	**1.84**	**0.14**
Yb	1.51	1.51	1.50	1.48	**1.50**	**0.01**
Lu	0.22	0.22	0.21	0.22	**0.22**	**0.01**

BLANKS

La	0.30	0.20	0.20	0.20	0.30
Ce	0.26	0.21	0.25	0.34	0.39
Pr	0.02	0.00	0.03	-0.01	0.04
Nd	0.20	0.20	0.10	0.20	0.30
Sm	0.04	0.05	0.02	0.03	0.06
Eu	0.01	0.00	0.01	0.01	0.01
Gd	0.04	0.03	0.04	0.05	0.07
Dy	0.03	0.05	0.02	0.03	0.08
Ho	0.01	0.00	0.00	0.01	0.01
Er	0.03	0.03	0.02	0.03	0.06
Yb	0.02	0.01	0.01	0.02	0.03
Lu	0.00	0.00	0.01	0.01	0.00

SECTION A4 : Mineral Data.

The following tables show some representative mineral analyses which are discussed with the petrographic descriptions in Chapter 4 and Appendix B (section B1) of this thesis. The analyses were produced on the Cameca Camebax Microbeam at Edinburgh. An accelarating voltage of 20 kV was used on an electron beam with a running current of 15.9 nA. A count time of 30 seconds was applied to the K-alpha peak, and 15 seconds to the background, for each element analysed. Four vertical crystal spectrometers were used (2xTAP, 1 PET and 1 LIF crystal). Na, Mg, Al, and Si were measured on the TAP spectrometers, Ca, K, Ti, and Cr were measured on the PET spectrometer, and Mn, Fe, and Ni were measured on the LIF spectrometer; they are presented below as oxides in wt.%. Jadeite, periclase, synthetic corundum, wollastonite, orthoclase, rutile and the metals Cr, Mn, Fe, and Ni, were used in the standard block. Note that total iron is given as FeO. Details of analytical procedures, precision and accuracy may be found in Wilding (1990).

Note: In the following tables phenocrysts are given as core and rim analyses. Microphenocrysts are indicated by mpxt whereas groundmass crystals are indicated by gm.

Olivines : AH1/42

	core	rim	core	rim
Na_2O	0.015	0.034	0.036	0.004
MgO	41.859	34.873	43.394	35.470
Al_2O_3	0.053	0.040	0.034	0.038
SiO_2	39.048	37.497	39.351	37.783
K_2O	0.014	0.000	0.001	0.004
CaO	0.201	0.351	0.182	0.369
TiO_2	0.010	0.038	0.030	0.052
Cr_2O_3	0.039	0.001	0.000	0.013
MnO	0.249	0.619	0.265	0.541
FeO	18.340	26.984	17.055	26.317
NiO	0.123	0.069	0.134	0.042
TOTAL	99.953	100.506	100.483	100.633

Olivines : AH1/42

	core	rim	gm	gm
Na_2O	0.005	0.034	0.004	0.019
MgO	34.650	34.091	33.469	33.915
Al_2O_3	0.032	0.030	0.051	0.042
SiO_2	37.272	36.994	37.086	37.325
K_2O	0.000	0.000	0.017	0.000
CaO	0.417	0.378	0.358	0.400
TiO_2	0.075	0.055	0.057	0.047
Cr_2O_3	0.000	0.015	0.022	0.037
MnO	0.591	0.575	0.624	0.586
FeO	27.742	28.025	29.183	28.661
NiO	0.057	0.075	0.037	0.057
TOTAL	100.842	100.271	100.907	101.088

Pyroxenes : AH1/42

	core	rim	core	rim
Na_2O	0.412	0.438	0.469	0.372
MgO	14.877	14.439	16.618	11.928
Al_2O_3	4.480	5.691	3.889	8.767
SiO_2	48.069	46.950	51.353	43.949
K_2O	0.000	0.008	0.016	0.000
CaO	21.180	21.395	21.422	22.750
TiO_2	1.403	1.535	0.579	2.836
Cr_2O_3	0.038	0.449	0.455	0.034
MnO	0.170	0.137	0.088	0.099
FeO	6.863	6.169	4.335	7.725
NiO	0.045	0.004	0.050	0.009
TOTAL	97.537	97.215	99.272	98.469

Pyroxenes : AH1/42

	core	rim	core	rim
Na_2O	0.396	0.634	0.368	0.686
MgO	16.691	12.867	15.402	10.761
Al_2O_3	3.537	5.362	4.064	10.058
SiO_2	51.022	47.684	49.107	42.265
K_2O	0.000	0.000	0.008	0.014
CaO	21.171	22.729	22.593	22.619
TiO_2	0.661	2.517	1.091	4.002
Cr_2O_3	0.152	0.041	0.140	0.094
MnO	0.151	0.187	0.114	0.176
FeO	5.104	7.047	5.357	7.745
NiO	0.009	0.015	0.024	0.008
TOTAL	98.893	99.084	98.269	98.427

Pyroxenes : AH1/42

	gm	gm	gm	gm
Na_2O	0.504	0.400	0.422	0.573
MgO	10.856	13.378	13.805	13.056
Al_2O_3	9.772	5.757	4.478	4.998
SiO_2	42.479	47.605	48.335	47.680
K_2O	0.005	0.000	0.001	0.029
CaO	22.592	21.939	22.516	22.547
TiO_2	3.942	1.935	1.893	2.470
Cr_2O_3	0.015	0.019	0.019	0.020
MnO	0.145	0.189	0.143	0.176
FeO	8.389	8.021	7.186	7.062
NiO	0.032	0.004	0.055	0.032
TOTAL	98.730	99.247	98.854	98.642

Pyroxenes : AH1/41

	core	rim	core	rim
Na_2O	0.271	0.442	0.311	0.516
MgO	14.891	13.925	16.434	13.286
Al_2O_3	4.380	6.341	2.885	5.321
SiO_2	49.396	47.776	51.357	47.616
K_2O	0.005	0.000	0.000	0.002
CaO	22.796	22.236	22.785	22.708
TiO_2	1.441	1.606	0.767	2.502
Cr_2O_3	0.158	0.107	0.680	0.007
MnO	0.115	0.133	0.102	0.160
FeO	6.068	6.725	4.207	7.251
NiO	0.052	0.023	0.041	0.000
TOTAL	99.573	99.314	99.569	99.369

Pyroxenes : AH1/41

	core	rim	core	rim
Na_2O	0.446	0.643	0.483	0.492
MgO	16.296	12.852	16.092	13.116
Al_2O_3	3.938	5.238	4.480	5.007
SiO_2	50.861	47.579	50.519	47.074
K_2O	0.017	0.008	0.000	0.000
CaO	22.106	22.583	21.737	22.628
TiO_2	0.746	2.652	0.782	2.392
Cr_2O_3	0.444	0.003	0.319	0.026
MnO	0.072	0.181	0.111	0.158
FeO	4.621	7.309	4.806	7.239
NiO	0.031	0.020	0.028	0.034
TOTAL	99.578	99.068	99.356	98.166

Pyroxenes : BP1/33

	core	rim	core	rim
Na_2O	0.468	0.484	0.408	0.398
MgO	13.389	10.761	14.608	12.512
Al_2O_3	6.413	9.544	4.890	6.394
SiO_2	47.557	42.717	49.359	46.264
K_2O	0.004	0.017	0.004	0.006
CaO	22.601	22.338	22.643	22.911
TiO_2	2.032	4.794	1.256	2.485
Cr_2O_3	0.134	0.102	0.414	0.184
MnO	0.139	0.148	0.108	0.115
FeO	6.520	8.087	4.880	6.863
NiO	0.000	0.023	0.037	0.036
TOTAL	99.256	99.015	98.607	98.168

Pyroxenes : BP1/33

	core	rim	core	rim
Na_2O	0.449	0.527	0.431	0.445
MgO	14.802	11.149	13.759	12.484
Al_2O_3	5.457	7.994	5.555	6.247
SiO_2	49.049	44.419	48.041	46.542
K_2O	0.004	0.011	0.005	0.008
CaO	22.203	22.177	22.495	22.196
TiO_2	1.538	4.442	2.182	3.156
Cr_2O_3	0.364	0.037	0.020	0.051
MnO	0.134	0.163	0.156	0.164
FeO	5.625	8.662	6.824	7.979
NiO	0.018	0.000	0.009	0.027
TOTAL	99.641	99.582	99.478	99.298

Pyroxenes : BP1/33

	mpxt	mpxt	mpxt	mpxt
Na_2O	0.462	0.499	0.384	0.360
MgO	12.524	12.479	12.678	14.285
Al_2O_3	7.276	7.203	6.974	4.212
SiO_2	45.908	45.842	46.077	49.062
K_2O	0.016	0.000	0.000	0.000
CaO	22.675	22.270	22.846	22.391
TiO_2	3.011	2.982	2.814	2.030
Cr_2O_3	0.034	0.028	0.155	0.000
MnO	0.145	0.190	0.115	0.160
FeO	7.615	7.873	6.937	6.889
NiO	0.000	0.000	0.022	0.020
TOTAL	99.666	99.366	99.002	99.409

Pyroxenes : BP1/33

	gm	gm	gm	gm
Na_2O	0.421	0.484	0.338	0.474
MgO	13.079	11.725	13.863	11.194
Al_2O_3	4.450	7.641	4.756	8.839
SiO_2	48.095	44.815	48.095	43.247
K_2O	0.024	0.028	0.010	0.030
CaO	22.140	22.459	21.697	20.829
TiO_2	2.692	4.193	2.510	4.797
Cr_2O_3	0.022	0.079	0.092	0.102
MnO	0.199	0.123	0.179	0.170
FeO	8.316	8.169	8.109	8.873
NiO	0.017	0.019	0.046	0.014
TOTAL	99.454	99.734	99.696	98.570

Pyroxenes : SH1/10

	gm	gm	gm	gm
Na_2O	0.399	0.360	0.495	0.355
MgO	13.845	13.998	13.935	13.495
Al_2O_3	4.676	4.397	4.707	4.952
SiO_2	47.359	47.203	47.667	45.419
K_2O	0.006	0.013	0.012	0.016
CaO	23.083	23.147	23.414	23.125
TiO_2	2.310	2.334	2.274	2.651
Cr_2O_3	0.022	0.035	0.028	0.018
MnO	0.300	0.196	0.189	0.227
FeO	6.764	6.849	5.985	7.269
NiO	0.052	0.103	0.041	0.122
TOTAL	98.817	98.635	98.745	97.647

Pyroxenes : PL1/10

	core	rim	core	rim
Na_2O	0.617	0.492	0.410	0.516
MgO	12.888	10.371	13.708	11.055
Al_2O_3	8.542	11.739	5.810	10.349
SiO_2	46.189	39.529	46.704	41.758
K_2O	0.006	0.011	0.000	0.018
CaO	22.594	23.043	22.987	23.192
TiO_2	2.380	5.501	2.320	4.892
Cr_2O_3	0.004	0.039	0.028	0.015
MnO	0.141	0.102	0.134	0.093
FeO	5.982	7.778	6.313	7.264
NiO	0.011	0.008	0.000	0.000
TOTAL	99.356	98.615	98.415	99.151

Pyroxenes : PL1/10

	core	rim	core	rim
Na_2O	0.624	0.154	0.361	0.483
MgO	12.885	11.056	13.996	10.234
Al_2O_3	7.896	10.417	5.330	11.333
SiO_2	45.829	41.611	47.466	39.762
K_2O	0.004	0.004	0.010	0.019
CaO	22.822	23.392	23.354	23.060
TiO_2	2.404	4.699	2.354	5.938
Cr_2O_3	0.037	0.010	0.023	0.016
MnO	0.085	0.128	0.124	0.094
FeO	6.574	6.974	6.214	7.863
NiO	0.022	0.019	0.014	0.015
TOTAL	99.182	98.823	99.246	98.818

Pyroxenes : PL1/10

	gm	gm	gm	gm
Na_2O	0.557	0.492	0.419	0.390
MgO	10.866	10.915	12.998	13.504
Al_2O_3	10.866	10.902	6.917	6.286
SiO_2	41.044	41.059	45.752	46.567
K_2O	0.013	0.087	0.002	0.022
CaO	23.146	22.817	23.239	23.154
TiO_2	5.453	5.515	3.281	3.028
Cr_2O_3	0.048	0.000	0.000	0.019
MnO	0.088	0.085	0.133	0.118
FeO	7.517	7.526	6.903	6.368
NiO	0.000	0.000	0.011	0.027
TOTAL	99.597	99.398	99.657	99.482

Pyroxenes : ES1/34

	core	rim	core	rim
Na_2O	0.371	0.228	0.280	0.252
MgO	15.381	14.570	13.071	13.663
Al_2O_3	3.889	4.718	6.522	6.530
SiO_2	49.997	48.315	46.261	45.864
K_2O	0.013	0.000	0.013	0.011
CaO	23.890	24.557	24.482	24.478
TiO_2	1.118	2.058	2.812	2.791
Cr_2O_3	0.862	0.221	0.089	0.117
MnO	0.077	0.074	0.079	0.065
FeO	3.641	4.902	6.101	5.396
NiO	0.057	0.019	0.003	0.029
TOTAL	99.295	99.662	99.714	99.194

Pyroxenes : ES1/34

	core	rim	core	rim
Na_2O	0.301	0.306	0.252	0.255
MgO	12.794	10.982	14.613	14.295
Al_2O_3	7.001	10.375	4.576	5.593
SiO_2	45.588	41.302	48.309	47.192
K_2O	0.000	0.006	0.001	0.017
CaO	24.117	23.996	24.355	24.602
TiO_2	3.209	4.919	1.885	2.464
Cr_2O_3	0.023	0.025	0.113	0.156
MnO	0.094	0.088	0.088	0.049
FeO	6.171	6.889	4.862	5.070
NiO	0.015	0.001	0.031	0.048
TOTAL	99.313	98.890	99.083	99.741

Pyroxenes : ES1/34

	core	rim	mpxt	mpxt
Na_2O	0.352	0.241	0.321	0.282
MgO	14.450	13.678	12.693	12.781
Al_2O_3	4.503	6.589	7.029	6.919
SiO_2	48.253	45.947	45.673	45.421
K_2O	0.020	0.019	0.010	0.000
CaO	24.070	24.243	24.034	24.146
TiO_2	1.947	2.966	3.316	3.279
Cr_2O_3	0.145	0.206	0.001	0.009
MnO	0.097	0.062	0.092	0.106
FeO	5.511	5.465	5.989	6.256
NiO	0.000	0.013	0.000	0.014
TOTAL	99.349	99.428	99.157	99.213

Amphiboles : PL1/10

	core	rim	core	rim
Na_2O	2.054	2.385	1.936	2.313
MgO	14.464	12.704	14.096	12.068
Al_2O_3	13.880	13.965	14.746	14.917
SiO_2	39.358	37.929	38.339	36.371
K_2O	2.029	1.519	2.353	1.620
CaO	12.414	12.446	12.092	12.338
TiO_2	4.889	6.344	4.824	6.085
Cr_2O_3	0.051	0.000	0.037	0.000
MnO	0.072	0.146	0.085	0.160
FeO	8.241	9.831	8.388	10.801
NiO	0.037	0.041	0.036	0.041
OH	2.029	2.006	2.012	1.979
TOTAL	99.518	99.315	98.942	98.694

Amphiboles : PL1/10

	core	rim	core	rim
Na_2O	1.934	2.534	2.017	2.013
MgO	14.004	11.076	13.774	14.329
Al_2O_3	14.405	14.532	14.592	14.330
SiO_2	38.923	37.394	38.971	39.182
K_2O	2.279	1.536	2.221	2.206
CaO	12.123	12.424	12.257	12.509
TiO_2	4.797	5.094	4.744	4.902
Cr_2O_3	0.010	0.025	0.047	0.108
MnO	0.067	0.229	0.088	0.105
FeO	8.518	12.080	8.828	7.801
NiO	0.042	0.006	0.008	0.018
OH	2.018	1.976	2.024	2.031
TOTAL	99.122	98.906	99.570	99.534

Amphiboles : PL1/10

	core	rim	core	rim
Na_2O	1.926	2.424	1.937	2.434
MgO	14.363	10.799	14.298	11.366
Al_2O_3	14.551	14.876	14.880	15.018
SiO_2	38.941	36.981	39.424	36.497
K_2O	2.377	1.514	2.415	1.658
CaO	12.281	12.554	12.134	12.107
TiO_2	4.687	6.340	4.787	6.929
Cr_2O_3	0.051	0.026	0.053	0.001
MnO	0.093	0.191	0.081	0.172
FeO	7.974	11.607	7.692	10.992
NiO	0.000	0.023	0.050	0.029
OH	2.024	1.987	2.041	1.988
TOTAL	99.267	99.322	99.792	99.192

Amphiboles : SH1/10

	gm	gm	gm	gm
Na_2O	2.831	2.773	2.902	2.889
MgO	12.985	12.442	13.691	13.490
Al_2O_3	12.261	13.661	11.994	12.512
SiO_2	38.160	36.780	38.846	38.998
K_2O	1.077	1.093	1.023	1.005
CaO	11.738	11.662	11.669	11.713
TiO_2	5.129	6.032	5.468	5.099
Cr_2O_3	0.000	0.004	0.025	0.034
MnO	0.266	0.291	0.334	0.271
FeO	10.181	9.952	9.438	9.752
NiO	0.126	0.056	0.081	0.061
OH	1.953	1.951	1.977	1.984
TOTAL	96.706	96.697	97.449	97.808

Feldspar : BP1/33

	core	rim	gm	gm
Na_2O	2.037	2.114	2.162	3.203
MgO	0.106	0.320	0.206	0.171
Al_2O_3	32.913	32.773	32.743	30.513
SiO_2	46.972	47.507	46.627	49.507
K_2O	0.181	0.189	0.272	0.843
CaO	16.835	16.526	16.220	13.632
TiO_2	0.085	0.112	0.127	0.133
Cr_2O_3	0.001	0.009	0.010	0.000
MnO	0.005	0.022	0.015	0.009
FeO	0.585	0.834	0.834	0.678
NiO	0.023	0.015	0.027	0.037
TOTAL	99.743	100.420	99.243	98.727

Feldspar : AH1/42

	gm	gm	gm	gm
Na_2O	3.339	3.511	7.238	7.210
MgO	0.206	0.347	0.270	0.435
Al_2O_3	31.288	30.169	23.508	22.694
SiO_2	49.103	47.618	58.176	60.435
K_2O	0.210	0.535	1.441	2.487
CaO	14.157	13.589	6.617	3.908
TiO_2	0.133	0.666	0.261	0.133
Cr_2O_3	0.016	0.007	0.012	0.013
MnO	0.017	0.035	0.032	0.033
FeO	0.533	2.024	0.788	0.759
NiO	0.003	0.024	0.107	0.110
TOTAL	99.003	98.525	98.401	98.216

APPENDIX B

RADIOMETRIC DATING OF TEN NORTH SEA SAMPLES

This appendix contains the results of a $^{40}Ar/^{39}Ar$ stepwise degassing study, commissioned by Shell U.K., on ten samples of igneous rock from the North Sea. The appendix is in three major sections. In section B1 the petrography and mineralogy and whole-rock chemsitry of each of the samples is described in detail (D.M. Latin & J.E. Dixon). Note that only 8 samples are described (B1:1 to B1:8) since sample AH1/42 was dated in both laboratories and both whole-rock and amphibole separates were dated for PL1/6. Sections B2 and B3 contain the results of stepwise degassing conducted at Cambridge University by J.A. Miller (4 samples, section B2) and at the University of Michigan by A.N. Halliday (6 samples, section B3). The results are summarised and their implications for previous interpretations of dates from the North Sea are discussed in Chapter 4 of this thesis.

SECTION B1 : Petrography (D.M. Latin & J.E. Dixon).

B1:1 PL1/6 [F10/1, Petroland, Netherlands]

Alkaline Lamprophyre.

This rock comes from a well in the Netherlands sector of the North Sea, on the flanks of the Central Graben. It is a minor intrusive encountered in the Upper Permian (Zechstein) part of the sequence. The core is veined by salt, mobilised during or after the intrusive event, but there is no evidence from the rock's petrography or chemistry that it has been modified chemically by proximity to salt.

Chemically the rock is richer in both high and low field-strength incompatible elements than alkali basalt AH1/42, and is poorer in silica (see Table B1.1). As a dry extrusive it would probably have had the modal mineralogy of a K-rich undersaturated basaltic rock - a leucite tephrite for example. As crystallisation at shallow depth has occurred, stabilising abundant K-rich, strongly nepheline-normative kaersutitic amphibole, the rock has a low final content of felsic minerals. As a porphyritic dyke-rock of alkaline type with olivine, clinopyroxene and amphibole, it is closest to *sannaite* in current lamprophyre nomenclature.

Petrography.

The rock has prominent but sparse large phenocrysts of brown *kaersutitic amphibole*, even less abundant phenocrysts of *titaniferous clinopyroxene*, with the remainder of the rock composed of euhedral microphenocrysts of amphibole, pyroxene and pseudomorphed *olivine*, with dominantly interstitial *sodic plagioclase/alkali feldspar*, fibrous *zeolite*, opaque *spinel* and prominent *apatite* prisms. The mode is :

PYROXENE	21.3%
Altered pyroxene	14.3%
AMPHIBOLE	21.2%
OLIVINE (Pseudomorphs)	3.2%
FELDSPAR	7.9%
SPINEL	10.5%
APATITE	1.9%
ZEOLITES (Interstitial)	20.6%

The most abundant phenocryst phase is amphibole, though overall, pyroxene exceeds amphibole in modal abundance. The phenocrysts of both are up to 5mm in size but a cm or more apart and so have not been distinguished in the modal analysis. The ***amphibole phenocrysts*** are euhedral short prisms. They have clear, mid-brown cores with prominent darker brown rims containing spinel inclusions similar to those in the groundmass. The cores have a rounded, probably diffusion-modified, shape with the transition from core to rim being nevertheless quite sharp and occurring between 70 and 90% of the distance from core to margin. The amphibole is a *potassian kaersutite* in the Min.Soc. of America Review nomenclature (see Table B1.2). Cores are richer in K_2O and MgO, rims are richer in Na_2O, TiO_2 (6.3% up from 4.8%), Al_2O_3 and total iron. The A-site is evidently full, the Na content rising from 0.55 to 0.7, while M4 is occupied by Ca. The essential exchange is the Ti-tschermaks substitution TiAlAl for (Mg,Fe)SiSi, probably with an increase in ferri-tschermak's molecule at the same time. A significant proportion of the rock's K_2O is thus held in the amphibole. The ***microphenocryst/groundmass amphibole*** is dark brown and has essentially the same chemistry and optical properties as the rims of the phenocrysts. It occurs as euhedral short prisms typically 0.25x0.1x0.06mm, most commonly as independent crystals but also as extensions or parallel overgrowths, sharing a common *z*-axis, on pyroxene crystals of phenocryst and groundmass generations. The texture strongly indicates simultaneous growth of both minerals throughout the crystallisation history of the rock.

Pyroxene phenocrysts reach 5mm in size and are euhedral. They have a clearly defined darker outer rim surrounding a more rounded core, comparable to that of the amphibole phenocrysts. The rims include groundmass spinels, pseudomorphs of olivine microphenocrysts and irregular inclusions of groundmass felsic minerals. Cores have a composition similar to the phenocrysts in AH1/42. They are titanaugites with rather variable alumina (5.8-8.5%) and TiO_2 at 2.4%. Rims show a sharp increase in Al_2O_3, to 11%, TiO_2 to 5.5% and an increase in total iron, some of which must be ferric to balance charges. Groundmass/microphenocryst pyroxenes probably span phenocryst rim compositions and are themselves zoned, often with marked "hour-glass" sectors. Many of the pyroxenes show some secondary dissolution along cracks and cleavage traces leaving them as optically continuous relics infilled with felsic groundmass phases and granular sphene. This alteration has not affected the amphiboles and has not resulted in amphibole growth. It may be a low-T effect.

Olivine is represented entirely by euhedral microphenocryst pseudomorphs in a colourless to pale brown, moderate birefringence, clay mineral. They reach 0.5mm in size.

The interstitial ***felsic*** component of the rock is difficult to resolve. Some clear patches of alkali feldspar are present; scattered lath-shaped grains with polysynthetic twinning are probably albite or potash oligoclase. However, the main constituent is a low birefringence, murky, slightly brownish mineral with distinct cleavage and R.I. slightly higher than K-feldspar. It has undulose or patchy extinction and many inclusions of clay or mica flakes. This groundmass phase is probably an aggregate of

pseudoleucite type after original potassic felspathoid (leucite?). It contains more than 10% K_2O but has significantly lower SiO_2 than K-feldspar. Its low sodium content may reflect further low-temperature breakdown of a nepheline component in the aggregate. The simplest possibility is that the potassium is held in two generations of K-feldspar, one high temperature, one a breakdown product of another K-rich phase (or glass). This breakdown may have occurred on cooling, in what was undoubtedly a volatile-rich rock, crystallising under sub-surface conditions.

The remaining phases are ***apatite***, which occurs as prominent prisms (some hollow), up to 1mm in length, and opaque ***spinel*** octahedra 0.07mm in size.

Crystallisation History.

As both pyroxene and amphibole phenocrysts have outer rims including spinels of groundmass size it is clear that both were present in the magma prior to and during the onset of spinel crystallisation. Microphenocryst/groundmass generations of both then nucleated and grew, accompanied by olivine, which is included as pseudomorphed "nuclei" in the pyroxene phenocryst rims. Apatite prisms are an early groundmass phase. Rimming of pyroxene by amphibole is quite common but is usually as an incomplete fringe or random projection. It appears to reflect the ease of nucleation of amphibole on pyroxene rather than the reverse and not any replacement reaction. Crystallisation of both may have continued in parallel. Minor sodic plagioclase crystallisation probably initiated the solidification of the interstitial alkali- and volatile-rich melt to some combination of leucite, nepheline and alkali feldspar to be followed by sub-solidus requilibration to lower temperature hydrous phases.

Note on the Separation Procedure.

The large phenocrysts were hand-picked from a rough crush of the rock. At this stage pyroxene phenocrysts could not be distinguished from amphibole. A gentle hand crush reduced the sample to <2mm. A pass with a hand magnet removed magnetite-bearing matrix. The finest fraction (<400 mesh) was sieved out and discarded, the sample washed and the Frantz separator was then set to remove a weakly magnetic fraction with remaining attached matrix. The remaining clean phenocryst fraction was then separated in di-iodomethane diluted to approx D=3.29. Titanaugite sank and kaersutite floated. The floated fraction was then hand-picked for stray felsic fragments and apatites.

B1:2 7N [17/9-1, Esso (Norway), Egersund Basin]

Nephelinite.

This sample is a *sodalite nephelinite* from the Norwegian part of the North sea. It is a holocrystalline, porphyritic representative of a series of flows in a thick volcanic sequence dated as Bajocian (177, 179, 180 Ma) by conventional K-Ar methods. The sequence is also fairly well constrained stratigraphically: interbedded sediments are described as Dogger (Middle Jurassic) in age. Several of the flows have glassy textures and may have erupted into water.

Petrography.

The rock has abundant phenocrysts of *titaniferous clinopyroxene* and scattered phenocrysts of pseudomorphed *olivine* in a groundmass of *pyroxene*, *sodalite*, *nepheline* (and alteration products), interstitial *zeolitic* patches after glass and *opaque spinel*. The mode of this rock is

OLIVINE (Pseudomorphed)	4%
PYROXENE Phenocrysts	31%
PYROXENE Groundmass	25%
SODALITE	12%
NEPHELINE (+alteration)	9%
ZEOLITE	11%
OPAQUE SPINEL	8%
Zeolitic infill	2%

Olivine, (pseudomorphed) is represented by scattered large euhedral pseudomorphs composed of an aggregate of clays or chloritic phases, up to 1cm across.

7N has abundant euhedral phenocrysts of a multiply twinned, titaniferous ***clinopyroxene***, which also show sector (hour-glass) and complex fine-scale oscillatory zoning. The zoning is very marked under crossed polars, as a variation in anomalous birefringence and extinction position, but is also visible in plane light as a variation in absorption and refractive index. The pyroxenes show growth patterns indicative of syneusis (amalgamation of separate nuclei). Compositionally they are titaniferous salites characteristic of undersaturated basic volcanics. The zoning reflects variation between a relatively low- Ti, Al-poor salite (wt % oxides: 1.1% and 3.9% respectively) and a high-Ti, Al-rich member which is also proportionately enriched in excess tetrahedral Al (TiO_2:4.9%; Al_2O_3:10.4%). By inference from charge balance considerations, ferric iron is also enriched in the high Ti zones. No clear core-to-rim patterns are yet apparent. The pyroxenes are up to 6mm in length. A microphenocryst generation, typically 0.7-1mm in length has similar properties and crystals of this size also form glomeroporphyritic aggregates.

Groundmass pyroxenes have not been analysed but have similar optical properties to the microphenocrysts and often clearly form outer fringes to the phenocrysts.. Typically they are fine prisms 0.1-0.2mm in length.

Sodalite occurs as rounded patches, or 6-sided micro-phenocrysts and is the most prominent felsic component. The crystals are a uniform 0.1mm in diameter and are completely isotropic, with no sign of alteration.

In the groundmass between sodalite, groundmass pyroxene and opaque spinel is a very low birefringence phase which occurs in places as sharply rectangular or hexagonal crystals. They have straight extinction but an irregular very finely fibrous character and pale green tinge. They are interpreted as coherent pseudomorphous aggregates after ***nepheline,*** probably in zeolite but possibly in other feldspathoids. Other interstitial patches of more irregular zeolitic growth are possibly after glass. No primary feldspar can be confirmed. Euhedra of opaque ***spinel*** are abundant in the groundmass. Scattered amygdaloidal patches of carbonate and zeolite, often with concentric growth zones, have clear regular outlines suggesting an original hexagonal short prism form. They are interpreted as dissolved and replaced phenocrysts of ***nepheline***, the alteration probably having taken place at low temperature.

Much of the rock's K_2O (see Table B1.1) probably resided in the nepheline. The character of the groundmass nepheline alteration suggests that it may have been early, possibly high temperature, process as the groundmass texture is intact and the pseudomorphs are optically coherent aggregates. However if the rare euhedral amygdales were in fact phenocrysts of nepheline, the pattern of K loss may have been more complex. Nevertheless the sample may yield an age close to the magmatic event, if all the alteration is associated with the initial cooling of the flows.

B1:3 AH1/42 [15/21-8a, Amerada Hess, Forties]

Ankaramitic Alkali Olivine Basalt.

This sample comes from 10m below the top of a sequence of volcanics at least 100m thick in a well on the edge of the Halibut Horst in the Forties province. The flow appears to have erupted sub-aerially from the lack of either pillowing or intrusive features. It shows extensive alteration in the top part of the interval cored, with pervasive replacement of groundmass and olivine and pyroxene phenocrysts by complex aggregates of clays and carbonate. Further down the core patches of preserved groundmass feldspar texture begin to appear, followed at greater depth by an increasing proportion of the pyroxene phenocrysts. The sample itself, from low in the cored interval, is the freshest of all Forties basalts, with LOI=1.5% (see Table B1.1), and unaltered olivine still present. The pattern of alteration, with its clear evidence of hydrothermal veining diminishing in intensity downwards from the interface with overlying sediments, suggests that a secondary hydrothermal system developed within the flow or flow-pile after burial, with the flow top acting as channel-way. How long after eruption this might have occurred is not clear. The volcanics are attributed to the Middle Jurassic Rattray Formation whereas the overlying sands are assigned to the Upper Jurassic (Upr.Oxfordian-Lr.Kimmeridgian). The core and the accompanying log are consistent with the hydrothermal activity being localised at the unconformity, downwards into the weathered top of the volcanic pile, perhaps in response to a fluid system developed at the time of active faulting, believed to be Oxfordian/Kimmeridgian.

As will be clear from the description, the sample for analysis has been selected to keep the effect of secondary mobilisation to a minimum. The feldspar and biotite containing the potassium do not appear altered.

Petrography.

The rock has abundant large euhedral phenocrysts of fresh *titaniferous clinopyroxene* and rather less abundant *olivine* phenocrysts, microphenocrysts of both phases and a groundmass of *pyroxene*, *plagioclase* and *magnetite*, with minor *biotite* and *apatite*. The mode is:

OLIVINE (phenos. & microphenos; fresh)	4%
OLIVINE (altered)	8%
PYROXENE (phenos. & microphenos.)	23%
PYROXENE (groundmass)	17.3%
FELDSPAR	35%
MAGNETITE	9.6%
BIOTITE	2.6%
APATITE	0.3%
ZEOLITE,	<0.1%

Olivine phenocrysts are euhedral and up to 5mm in length. All have a prominent green to pale brown, sheet-silicate with moderate birefringence, growing in the curving fractures. The extent of this alteration is variable: in many of the larger phenocrysts it is from 5 to 15%, but rises to 50% or more in the microphenocrysts. Some of the largest phenocrysts have undergone a separate, and by inference later, pervasive alteration to a combination of deep orange-brown clay, calcite and hydrothermal silica. The early fracture infilling stage is still recognisable but the clear green sheet silicate of that stage has been converted (oxidised?) to nontronite which has then replaced the remaining body of the olivine, accompanied by calcite.

The hydrothermal quartz, present as coalescing ellipsoidal patches, appears to be later still. This complete alteration of scattered phenocrysts is inferred to be of the same generation as the main "event" affecting the upper part of the core.

Where unaltered the larger olivines show marked zoning from Fo81 in the cores to Fo69 at the rim, with associated increase in birefringence. Microphenocrysts are slightly zoned from Fo69 to Fo67 and the smallest generation of groundmass olivines are Fo67-66.

Pyroxene phenocrysts are pale brown, up to 4mm across and generally euhedral, showing cross sections consistent with short, nearly equant prisms. They show little twinning and no evidence of syneusis. Their outer margins are darker and have glass and other inclusions. The margins are slightly ragged as they "merge" with the groundmass pyroxene and develop an intersertal fringe with adjacent plagioclase laths. The cores are augite with moderate Al_2O_3 (3.5-4.0%), TiO_2 (0.6-1.5%) and total Fe (4-5% Fe_2O_3). Some fine oscillatory zoning occurs towards Al- and Ti-rich compositions but the main feature is the prominent outer zone which is 0.1mm in width, (longer at prism terminations), where Al_2O_3 rises to 10%, TiO_2 to 4% and total iron to 7.3% Fe_2O_3. This outer zone is marker by a line of spinel inclusions and a marked colour change. ***Groundmass pyroxenes*** show a range of compositions spanning the values in this outer zone which presumably reflects post-eruption growth, probably under rising fO_2. Groundmass pyroxenes are generally 0.1mm in length but grade upwards in size to a Ti-rich microphenocryst generation 0.2-0.3mm across.

Plagioclase is a groundmass phase and occurs as finely twinned laths 0.15-0.2mm long in an intersertal texture with pyroxene and spinel. They are strongly zoned and most of the remaining interstices are filled with feldspar which appears to merge with the outer margins of the twinned laths, but lacks twinning and has irregular extinction. It reaches a potash oligoclase in composition ($An_{20}Ab_{65}Or_{15}$) with 2.5% K_2O, via sodic plagioclase. The cores of the twinned laths range from An69 to An66. The feldspar shows no alteration and should have been a stable repository for potassium.

Biotite occurs as small ragged platelets and as an interstitial phase, closely associated with spinel, which it frequently fringes. It is interpreted as essentially the last phase to crystallise, along with interstitial K-rich feldspar, and has clearly formed in part by reaction between early groundmass spinel and residual K- and H_2O-rich melt. It has normal optical properties and shows no alteration to chlorite or evidence of oxidation. It should provide a further stable K-site. ***Spinel*** has not been analysed. It occurs as opaque octahedra 0.1mm in size.

A very small fraction (less than 0.1%) of the interstitial space is occupied by fine-grained ***zeolite***.

Chemistry.

The chemical analysis (Table B1.1) is consistent with the observed alkali olivine basalt mineralogy. It is not clear that any phenocryst enrichment has necessarily occurred despite the porphyritic texture. In fact some olivine fractionation has probably occurred as olivine core compositions are not consistent with mantle olivine Fe/Mg. The K_2O content is noteworthy and is clearly an original feature of the magma chemistry.

B1:4 ES1/41 [17/9-1, Esso-Norway, Egersund Basin]

Mafic Nephelinite (Alnöite?).

This sample is composed of large ***titanian phlogopites*** (see Table B1.2) picked from the matrix of an alkaline intrusive from the same core as a series of *sodalite nephelinite* flows. The well is in the Egersund Basin, an area of Upper Jurassic subsidence east of the Forties Province. The volcanics have been dated by conventional K-Ar methods as Bajocian (177, 179 and 180 Ma), and interbedded sediments are described as Dogger (Middle Jurassic) in age. The mafic nephelinite from which these phlogopites come occurs below the nephelinite lavas in the cored interval and has a clear, irregular but steep intrusive contact with sandstones. The rock is rich in large bronzy micas and fragments of country rock and gives the impression of explosive channelling of a volatile-rich solid-charged magma. The texture is not fragmentary however and the magma was clearly silicate melt rather than tuffisite. Although this rock lies below the cored volcanics, drill cuttings from below the cored interval contain volcanic fragments. The sequence of events is either lavas/sediments/intrusive/lavas or lavas/sediments/lavas/intrusive.

Petrography.

As it contains abundant *clinopyroxene* (Ti-augite with aegirine-augite cores), *olivine* (as pseudomorphs), *phlogopite*, probable altered *felspathoidal* phenocrysts, and a groundmass with no trace of feldspar, it may well have been a mafic undersaturated rock of ***alnöite*** type.

The ***phlogopite*** occurs as slightly rounded euhedral hexagonal plates up to 2cm in size, and as a further phenocryst generation 1mm in size. The large plates sampled show a narrow outer zone of more intense reddish brown colour. The chemical analysis (Table B1.2) shows that they are Si-deficient (Si: 5.3 per 20 oxygens) with Mg number at least 84, with all iron as Fe2+. Some crystals show carbonate seams along cleavage partings. *We have not attempted to remove this from the hand-picked sample. It could be avoided by further chopping, peeling apart and selecting, or by dilute acid treatment, or both.*

The accompanying phases in the rock have not been studied in great detail. The ***pyroxene phenocrysts*** are sodic titanaugites, with occasional cores of a deep green, more aegirine rich composition. Some are partially pseudomorphed by carbonate. A separate suite of carbonate pseudomorphed grains is inferred to have been olivine, from shape and relict fractures. The groundmass is dominantly darkish brown pyroxene and phlogopite flakes in a pervasively altered matrix of carbonate, ore and unresolvable felsic material. Amygdales contain calcite and analcite.

B1:5 SH1/10 [30/16-A13Y, Shell, Central Graben]

"Hornblende Basanite".

This rock is the extrusive equivalent of the alkaline lamprophyre PL1/6, and has very similar mineralogy and chemistry (Table B1.1). However, as it contains significant modal amphibole and any original modal felspathoid it had is now represented by interstitial hydrous phases, it cannot easily be compared petrographically with typical dry undersaturated basic extrusives such as tephrites and basanites, to which it is related chemically.

The volcanics in this well are overlain by a conglomerate, belonging to the Chalk Group, with cobbles of bioclastic limestone and volcanic rocks. This is in turn overlain by Chalk. The volcanics must be older than Cenomanian. They overlie limestones of Upper Jurassic/Lower Cretaceous age. Conventional K-Ar dates by Macintyre at SURRC range between 100 and 127Ma. Other strongly potassic, incompatible-element enriched lamprophyres are found intruding Zechstein salt in adjacent parts of the Central Graben.

Petrography.

This fine-grained extrusive rock is dominantly composed of euhedral *titanaugite* and *amphibole* prisms, in a groundmass of *alkali feldspar* and a fibrous *alteration product after felspathoid*, with conspicuous *spinel* octahedra and *apatite* prisms. Very sparse microphenocrysts of pyroxene, apatite and ore occur. he mode is:

PYROXENE	16.4%
AMPHIBOLE	8.6%
FELDSPAR	26.6%
SPINEL	15.8%
APATITE	1.4%
"EX-FELSPATHOID ?"	27.2%
"LEUCOXENE"	3.8%
CARBONATE	0.2%

Pyroxene microphenocrysts are very rare. They occasionally reach 0.85mm in size but most are 0.5mm. They are most common as stellate aggregates or clusters. They are pale brown with only weak zoning and typically show partial dissolution in the core regions to fine-grained chlorite or zeolite. The majority of the *groundmass pyroxenes* are 0.2 to 0.3mm in length, by 0.02mm in width. Both generations are euhedral prisms with blunt terminations. The groundmass crystals often show irregular overgrowths and extensions of brown amphibole in structural continuity. Compositionally the pyroxenes are similar in composition to the cores of the large phenocrysts in PL1/6. Some variation towards the more Ti and Al-rich rim and groundmass compositions in PL1 occurs, but the extreme compositions of that sample are not reached, reflecting a closer approach to equilibrium crystallisation. Al_2O_3 ranges from 4.4 to 5 wt.%; TiO_2 from 2.3 to 2.7%.

Amphibole is entirely a groundmass phase, as short euhedral prisms typically 0.1mm x 0.06mm in size. They are dark brown and pleochroic as in PL1/6. Compositionally they have lower K and lower Ti than the PL1/6 equivalents and fall technically outside the *kaersutite* field, being more correctly "potassian, titanian magnesio-hastingsites" (!). Low-Ti-kaersutite is more informative. ***Spinel*** octahedra are rare as microphenocrysts but some reach 0.8mm across; 0.25mm is more usual. The abundant groundmass spinel is in 0.025mm grains. ***Apatite*** is prominent as hollow prisms typically 0.4mm long. Rarely, larger skeletal , partly resorbed prisms occur up to 0.65x0.25mm in size. ***Biotite*** is a very minor component as fringes on spinel grains.

The interstitial felsic phase in the groundmass presents similar problems to that in PL1/6. It has two main components. One is clear, untwinned ***alkali feldspar*** with sharp extinction. The other is a lower birefringence, colourless or slightly brownish phase occurring in radiating or sheaf-like aggregates, with irregular extinction and dispersed brownish inclusions. There is no clear boundary between the two in many cases, and the second phase may be an intimate ***intergrowth of K-feldspar and a zeolite***, after original felspathoid or silica-undersaturated glass. As this second phase is a probable major repository of potassium in the rock its origin

and timing has obvious implications for the interpretation of Ar release patterns. Little definite can be said however.

Crystallization History.

The crystallisation history of this rock appears straightforward. The earliest phase was spinel, which tended to aggregate in clumps. Scattered microphenocrysts of Ti-augite developed slightly later, enveloping early spinels and also growing in clusters. Apatites grew freely. Eruption initiated the simultaneous growth of pyroxene and amphibole prisms and the groundmass spinel, with interstitial space filled by alkali feldspar and the postulated feldspathoid. The latter may have recrystallised and become hydrated with the cooling of the flow.

B1:6 TO1/20 [21/3-2, Total, Forties]

Porphyritic Basaltic Hawaiite.

This sample comes from the centre of the Forties Province. The volcanic rocks in the well are inferred to rest on Triassic sediments, and are overlain by shales of probable Lower Cretaceous age. The sample comes from near the base of a core, the upper part of which is largely ankaramitic basalt. Towards the base mafic phenocrysts become less abundant and a sodic plagioclase appears as a microphenocryst phase. Although still low in silica, the petrography and inferred mineral chemistry of this rock indicate that it is more evolved than the typical undersaturated basalts of the Province, hence the term *basaltic hawaiite* (see Table B1.1). Below the point sampled in the core the volcanics are hawaiites, passing downwards into basaltic hawaiites and ankaramites.

Petrography.

The rock is strikingly porphyritic with large zoned phenocrysts of *titanaugite*, pseudomorphed phenocrysts of *olivine* in *chlorite* and *smectite*, and phenocrysts of opaque *spinel*. The groundmass has regions dominated by interlocking microphenocrysts of *sodic plagioclase*, with minor *pyroxene* and *spinel*, interspersed with regions with a finer grained intergranular texture dominated by *titanaugite*, opaque *spinel* and *plagioclase* laths. Both parts of the groundmass have interstitial pale green *chlorite*, and all the feldspar contains flakes of secondary "*clay*". Needles of *apatite* and small *biotite* flakes are common throughout the groundmass. The mode is:

PYROXENE (Phenocrysts)	12.8%
PYROXENE (Groundmass)	9.6%
OLIVINE (Pseud. phenos.)	12.0%
FELDSPAR	49.6%
SPINEL	7.0%
APATITE	0.4%
BIOTITE	0.3%
AMPHIBOLE	trace
CHLORITE	6.2%
LEUCOXENE/SPHENE	3.4%

The ***pyroxene*** phenocrysts are large (10mm), and show a range of textural features. Many are single euhedral crystals with or without simple and lamellar twinning. All are crossed by cracks and many are irregularly shaped implying fracturing and dispersal. Composite grains are also fairly common and some show

only slight discordance across the common boundary, suggesting displacement followed by annealing. All have trails and necked-off inclusions of trapped melt, now with groundmass mineralogy. Zoning is present in all and complex in detail. All show a darker rim, by inference richer in Ti, Al and total Fe, of very variable width. This darker border is also present round internal melt inclusions. The inner pale core frequently has a complex, generally rounded outer edge which in detail is often lobate or highly irregular. The outer zone shows fine oscillatory zoning, parallel to the outer margin, and these zones are sometimes truncated by the inner core, implying diffusional enlargement of the core during phenocryst growth. The very outermost few microns of the phenocrysts is marked by a zone of closely spaced spinel inclusions. Microphenocrysts of pyroxene are sparse and are mostly found as agglomerations with spinel.

Olivine was originally present as euhedral phenocrysts up to 6mm in size. Composite and broken pseudomorphed crystals are also found. The peudomorphs are now composed of a distinctive pleochroic, olive-green sheet silicate with second-order birefringence, probably a smectite. It has replaced the olivine with a high degree of structural coherence, most noticeable in the cores of the grains. Inclusions of microphenocryst spinels and pyroxene-spinel aggregates are quite common within the ex-olivines. Olivine pseudomorphs also occur within the pyroxene phenocrysts.

Opaque ***spinel*** occurs in two generations, as phenocrysts up to 1.5mm in size, closely associated with the olivine and pyroxene, and as a groundmass phase. The most conspicuous groundmass phase is feldspar as squarish crystals of ***andesine*** between 0.5 and 1mm in size. They occur packed together in clumps and strings but do not intergrow. They show marked zoning from calcic cores to sodic rims. The compositional information comes from the Ph.D thesis of Fall (19) who worked on the same core and recorded the sample depths. Fall identified potash feldspar as present in the groundmass by staining with sodium cobaltinitrite, but it is not clear whether it occurs as interstitial extensions to the andesine crystals or in the remainder of the groundmass.

The andesines are accompanied by minor brownish-pink ***titanaugites*** 0.1mm long and some spinel. Any interstitial space is occupied by a finely platy pale green chlorite, showing a radiating or cross-fibred texture. Although the feldspars clearly preserve their original compositional zoning, they all show abundant inclusions of apparently the same pale green chlorite present in between them. This must imply some post-solidification fluid permeation, perhaps channelled by inclusions of trapped residual fluid, but whether this was a separate hydrothermal event or attended cooling of the flow within the pile, is not known.

The remainder of the groundmass texture is more typical of alkali basalts elsewhere in the province. It is made up of ***plagioclase*** laths 0.1x0.02mm (i.e. much more flattened on (010) than the microphenocrysts), granular ***titanaugite***, and abundant euhedral ***spinels***. Fine-grained granular aggregates of a sphene-like phase are common, surrounding the opaques. The ubiquitous pale green chlorite is present interstitially, and as inclusions in the feldspars. The feldspars show albite twinning and moderate extinction angles.

Crystallisation History.

Mutual inclusion relations amongst the phenocrysts indicate that titanaugite, olivine and an opaque spinel were crystallising as liquidus phases. An event, either emplacement to high level or eruption, is marked by the change in pyroxene composition and probably by the nucleation and growth of groundmass pyroxene prisms. The complex zoning in the pyroxenes indicates some diffusional

readjustment of pyroxene composition at this stage. The "event" probably also caused the unzoned pyroxene-spinel aggregates to be incorporated into the magma.

The groundmass texture is then best explained by the crystallisation of intermediate plagioclase, spinel and pyroxene together until at some point alkali and water contents rose in the residual liquid to promote rapid enlargement of feldspar nuclei. These grew in the residual liquid pockets and essentially squeezed the other groundmass phases, transferring remaining residual melt to the growing feldspars. At some point a watery fluid may have separated, initiating the exchanges which led to the growth of chlorite, and probably to the breakdown of some Ti-augite to sphene and ore, liberating Mg for chlorite formation.

B1:7 BP1/33 [21/9-1, B.P., Forties]

Ankaramitic Alkali Basalt.

This sample is the freshest representative (LOI=2.5%; Table B1.1) of an amygdaloidal alkali basalt flow from near the centre of the Forties Province. The sample is from the centre of a flow which has a markedly oxidised top, and which is interpreted as subaerially erupted on to the underlying sands, believed to be of Lower Jurassic or Triassic age.

Petrography.

The rock is strongly porphyritic, with abundant large phenocrysts of *zoned titanaugite*, less abundant large, almost entirely pseudomorphed phenocrysts of *olivine*, microphenocrysts of *calcic plagioclase*, *titanaugite* and minor *olivine*, set in a groundmass of *feldspar*, opaque *spinel* and *titanaugite*. Rare amygdales are filled with a radiating fibrous chlorite/zeolite intergrowth. The mode is:

PYROXENE (Phenocrysts)	15.3%
PYROXENE (Groundmass,microph.)	29.6%
OLIVINE (Phenos.,altered)	13.3%
FELDSPAR	25.0%
SPINEL	10.6%
APATITE	0.3%
ZEOLITE+CHLORITE	5.6%

Clinopyroxene phenocrysts are 5-10mm in size when intact, and euhedral. Some are present as broken fragments. Zoning is ubiquitous: most possess a darker, Ti-rich outer zone with a moderately sharp boundary to a rounded core. However zoning is complex in detail with inner oscillatory zones truncated against the outer darker zone. A late reversion to a lighter presumably lower Ti composition is present at the outer rim. The analyses reflect this variability. The usual rise in Ti, Al and total Fe in the outer zone is found but the levels reached are more variable than for example in *PL1/6*. Al_2O_3 varies from 5.5-9.5% from core to rim, TiO_2 from 2.0 to 4.7%. Glomeroporphyritic clusters of microphenocrysts give intermediate values. The phenocrysts are conspicuously fractured and have small inclusions of altered glass, possible pseudomorphed olivines and small spinels, throughout. The fracturing is clearly syn-magmatic but post-phenocryst-growth as the broken fragments show no subsequent growth or diffusional modification of zones. Very rarely traces of brown amphibole have grown into the fractures. After solidification green fine-grained chlorite has grown along the wider cracks.

Groundmass pyroxene (titanaugite) is also variable in composition but generally matches the highest Ti and Al values of the phenocryst rims.

Olivine is preserved as rare relics in otherwise completely transformed phenocrysts 3-5mm in size, now aggregates of a brownish-green, moderately birefringent clay-mineral. ***Plagioclase*** microphenocrysts from 0.2-1.0mm in length are abundant. Some occur in stellate clusters. They show multiple twinning, complex zoning, with a very marked change in the outer 10% towards a sodic composition. Cores are calcic (bytownite) An_{81} with zoning towards An_{67}, and optical continuity into the interstitial potassium-rich alkali feldspar which reaches $An_{0.7}Ab_{16}Or_{83.3}$.

The groundmass texture is a mixture of intersertal and intergranular. The space between the plagioclase microphenocrysts is occupied by granular clinopyroxene, abundant opaque spinel, plagioclase laths, patches of green sheet silicate (possibly after groundmass olivine), apatite needles and interstitial alkali feldspar.

Crystallisation History.

The textural evolution appears straightforward. A phase of pyroxene and olivine phenocryst development was followed by some violent event (upward transport and eruption ?) which fractured the phenocrysts, possibly after some accumumulation. Plagioclase and pyroxene microphenocrysts grew and were followed by the rapid crystallisation of the groundmass.

The groundmass felsic component is notably fresh in most cases but locally the more feldspar rich patches have a trace of pale green chlorite possibly with an intergrown zeolitic phase, as sprays and veinlets a few microns across. The main development of the chlorite/zeolite intergrowth is in amygdale infills and as local pervasive replacement of groundmass feldspar within 1mm of the altered olivines, leaving the groundmass apatite, pyroxene and spinel unaffected.

The rock's K_2O content (Table B1.1) is almost entirely in feldspar and within that is concentrated in the outermost interstitial potash feldspar. As less than a few % of the interstitial feldspar shows any sign of alteration there would appear to be a good chance of argon retention in the feldpar. The late stage alteration has mostly affected the olivines, filled in vesicles and only locally replaced the groundmass phases. It may have attended cooling of the flow and so may be of the same age.

B1:8 SO1/8 [22/1a-4, Sun Oil, Forties]

Porphyritic Alkali Basalt.

This sample has many petrographic features in common with other Forties alkali basalts but is rich in groundmass plagioclase and may be somewhat more evolved. The interpretation is complicated by its high content of high field-strength incompatible elements such as Zr, Nb and Ti, which would be consistent with enrichment by fractionation, but at the same time it has very high ratios of high to low incompatible elements such as Ce/Y which are indicative of a low degree of melting at source (see Table B1.1). It is a potential candidate for a magma intermediate between the extreme, probably lithospheric, nephelinites found away from the rift axis, and the typical, potentially asthenosphere dominated, alkali basalts of the Forties region, which have significantly lower Ce/Y ratios.

As such its age is of considerable interest as it could conceivably represent a precursor to the higher degree melts more typical of the Forties province. The volcanic rocks in this well are overlain by late Oxfordian, or possibly early Kimmeridgian sands. The well does not penetrate the entire volcanic sequence, so no upper age constraint exists.

We have no microprobe data for this rock.

Petrography.

The rock is a porphyritic alkali basalt of ankaramite type, with abundant *titanaugite* phenocrysts, *pseudomorphed olivines* (in apparently coherent smectite), set in a groundmass dominated by flow-aligned *plagioclase* laths, *ore*, *pyroxene* and abundant fine-grained secondary *sphene*. The mode is:

PYROXENE (Phenocrysts)	6.6%
PYROXENE (Groundmass)	8.4%
OLIVINE (Pseudomorphs)	8.4%
FELDSPAR	54.2%
SPINEL	4.6%
APATITE	1.2%
Granular sphene	12.6%
Smectite, chlorite	4.0%

Pyroxene phenocrysts are similar to those in AH1/42. They are mostly euhedral; some are broken fragments; all are fractured and some show evidence of disorientation of component parts followed by annealing. They are from 5mm to 6mm across. They are pale brown and all show the characteristic outer, slightly darker zone, which is by inference richer in Al, Ti and total iron. Internal zoning is very slight and the outer zone is very narrow (0.01mm), parallel to the outer boundary and very sharply defined. Inclusions of pseudomorphed olivine occur in some crystals; included patches of trapped melt, now predominantly feldspar, are relatively more common.

The outer boundaries are irregular, sometimes appearing slightly resorbed. Some grains show the outer zone to have a micro-ophitic texture which then stops abruptly against the feldspar-rich groundmass rather than possessing a fringe of groundmass pyroxenes, as is more commonly the case in the ankaramitic basalts from other Forties wells.. A generation of scattered, smaller, darker microphenocrysts of pyroxene is present 0.5mm in size, which may correspond to rim compositions in the phenocrysts, but the clear impression given by the texture is that there was very little continuity between phenocryst and groundmass pyroxene growth, suggesting that here the phenocrysts may be largely xenocrystal.

Olivine pseudomorphs are up to 2.5mm in length. The majority represent euhedral sections through a single characteristic olivine shape. They are almost all pseudomorphed by what appears as a single large crystal of a greenish, moderately birefringent smectite. Only in the largest can another incoherent serpentinous phase of replacement be seen, where the coherent smectite is present only at the outer margin and along fractures. Olivine microphenocrysts grade downwards in size to patches of green smectite in the groundmass 0.05mm across. The smaller patches are darker green (nontronitic), perhaps reflecting an originally more iron rich composition.

The replacement pattern elsewhere in the core is more extreme. Higher up, the fine-grained serpentine or chlorite becomes the dominant olivine replacing phase, while the pyroxenes are replaced by carbonate and dendritic iron oxide. In the most extensively carbonated rocks the olivine pseudomorphs are a mixture of carbonate, fine-grained chlorite, clay and opaques. As these changes appear gradational with depth in the core and are clearly vein controlled in the most altered part, they probably reflect the establishment of a hydrothermal circulation system. This may not have been directly related to the initial cooling of the flow pile and could be a later event.

Apart from scattered ***spinel*** microphenocrysts 0.2mm in size, the remaining phases are present in a fine-grained groundmass. ***Plagioclase*** is the most abundant mineral and occurs as swarms of multiply twinned irregular laths 0.015mm long. They are zoned, with irregular extinction, and often pass continuously to interstitial alkali feldspar. They contain scattered minute flakes of "sericite" but this is a very minor component and the feldspar in the rock is essentially fresh. Some flow alignment is present. Diffuse circular patches a few mm. across, with weaker feldspar alignment may be ill defined ocelli. Groundmass ***pyroxene*** occurs as fine granules and rectangular grains less than 10 microns long, generally interstitial to the feldspar. Groundmass ***spinel***, is present as octahedra in the 100 to 10 micron range, also largely interstitially. Within interstitial feldspar pockets are sub-micron sized apatites.

Virtually everywhere in the section smaller groups of spinels are enveloped in finely granular ***sphene***. This has clearly replaced groundmass pyroxene as the spinels themselves appear unchanged. Over parts of the section this replacement has been pervasive so that little pyroxene remains and even pseudomorphs of pyroxene microphenocrysts are present in sphene. Sphene stringers are also found along cleavage traces in the smectite pseudomorphs after olivine, implying a fluid oversaturated in sphene component, and at least short range Ti mobility. This alteration is presumably connected to the pervasive smectite growth, via reactions in which diopside and CaTiAl molecules in pyroxene combine with ulvospinel component in magnetite to precipitate sphene, leaving Mg and Al in excess. The alteration nevertheless appears to leave feldspar intact.

Crystallisation History.

In summary, this rock shows crystallisation of pyroxene and olivine, with minor spinel, as phenocrysts. The liquid in which they were finally trapped may have undergone rather more extraction of pyroxene and olivine than that which saw these phenocrysts develop - a mixing of a phenocryst-depleted liquid and a phenocryst-enriched batch may have occurred. Solidification was then rapid presumably on eruption, and at some later stage hydrothermal alteration transformed the olivines and groundmass pyroxenes (in part), to clay and sphene.

TABLE B1.1

Whole-Rock XRF Analyses of Samples for Dating.

	AH1/42	BP1/33	7N	PL1/6	TO1/20	SO1/8	SH1/10	ES1/42
SiO_2	45.11	45.98	43.11	40.47	48.01	43.53	42.81	42.32
Al_2O3	13.28	12.96	11.43	14.13	12.80	15.27	15.01	10.23
Fe_2O_3*	12.54	12.35	11.74	13.92	11.50	14.19	15.01	10.23
MgO	10.71	9.85	8.68	10.80	9.76	7.52	8.47	6.66
CaO	11.81	11.71	16.81	9.44	9.98	12.16	8.90	13.61
Na_2O	2.05	2.20	1.87	0.76	2.55	2.73	1.18	1.77
K_2O	0.88	0.65	0.84	4.18	1.44	0.42	4.45	3.84
TiO_2	2.40	2.74	3.16	4.26	2.27	3.97	4.18	3.09
MnO	0.20	0.25	0.53	0.27	0.20	0.34	0.48	0.18
P_2O_5	0.36	0.39	0.65	0.67	0.35	0.70	0.97	0.58
TOTAL	99.34	99.09	98.82	98.89	98.86	100.82	99.85	98.01
LOI	1.5	2.5	4.0	3.4	2.7	2.5	2.5	9.0
Ni	127	152	72	44	174	101	15	71
Cr	277	359	266	23	540	315	*	158
V	383	313	525	476	288	376	404	327
Sc	44	35	29	34	31	39	26	24
Cu	63	39	37	66	63	31	32	58
Zn	85	84	72	112	90	116	157	106
Sr	482	698	648	796	798	1271	1164	1585
Rb	6	4	44	57	39	6	74	110
Zr	197	221	331	320	204	295	387	370
Nb	46	56	129	96	50	92	109	167
Ba	511	573	433	614	752	811	1046	1675
Pb	2	4	0	3	3	0	6	9
Th	1	3	10	6	2	0	2	11
La	34	42	90	81	39	70	83	103
Ce	77	98	163	176	84	146	190	210
Nd	35	43	63	71	37	65	79	77
Y	24	27	21	28	26	25	32	27

*Total iron calculated as Fe_2O_3
NOTE : Major elements are given as oxides in wt.%
trace elements are in ppm.

TABLE B1.2

Electron Microprobe Analyses of Micas and Amphiboles Separated from ES1/41 and PL1/6 respectively.

MICAS FROM ES1/41

SiO_2	36.53	34.87	35.77
Al_2O_3	16.52	15.67	15.75
FeO*	6.34	8.52	8.97
MgO	18.90	17.64	17.62
CaO	0.04	0.05	0.02
Na_2O	0.46	0.64	0.64
K_2O	9.95	9.32	9.59
TiO_2	5.61	5.69	5.11
MnO	0.06	0.09	0.05
Cr_2O_3	0.19	0.06	0.00
NiO	0.07	0.01	0.06
TOTAL	94.67	92.57	93.56

AMPHIBOLES FROM PL1/6

SiO_2	39.18	39.94	39.98
Al_2O_3	14.33	14.55	14.88
FeO*	7.80	7.97	11.61
MgO	14.33	14.36	10.80
CaO	12.51	12.28	12.55
Na_2O	2.01	1.93	2.42
K_2O	2.21	2.38	1.51
TiO_2	4.90	4.69	6.34
MnO	0.11	0.10	0.19
Cr_2O_3	0.11	0.05	0.03
NiO	0.02	0.00	0.02
TOTAL	97.50	97.24	97.33

* Total iron calculated as FeO
Major element oxides are given in wt.%

SECTION B2 : $^{40}Ar/^{39}Ar$ Dating Report (J.A. Miller).

Introduction.

Potassium-argon and other conventional dating methods allow the determination of the apparent age of rocks and minerals. They can only be applied with certainty when the rock or mineral has suffered no subsequent alteration. Should such alteration have taken place the result will represent a value somewhere between the true age of the material and the time of the alteration. It is often not possible to recognise this effect nor to quantify it and as a result misleading conclusions may be drawn.

The argon-40/argon-39 stepheating method almost invariably reveals the influence of subsequent geological events and often their timing can be determined.

As with conventional potassium-argon dating the method relies upon the decay of ^{40}K to ^{40}Ar. Samples are loaded into small quartz phials and subjected to a fast neutron flux alongside standards of known K/Ar age. A proportion of the ^{39}K in each is transmuted to ^{39}Ar, consequently a measure of the ratio of the radiogenic argon-40 to neutron induced argon-39 is a function of the apparent age and neutron absorption (J). Knowing the age of the standard, the following equation can be used to calculate J.

$$J = \frac{e^{t/\tau}-1}{^{40}Ar/^{39}Ar}$$

where t = apparent age
τ = decay of $^{40}K^{-1}$

In unaltered igneous rocks the age of the different minerals will be the same and equal to the true age of the rock. Each of the mineral types has its distinct activation energy of argon loss and potassium content. If such a rock is heated incrementally the volume of argon isotopes released at each temperature step will be different and is related to the activation energy of argon loss of the minerals, but the radiogenic argon-40/neutron induced argon-39 will be constant. This will result in a "plateau" of constant age which is equal to the true age of the rock.

Alteration of rocks results in the formation of new minerals. The rock therefore contains minerals of two ages and their presence will disrupt the simple "plateau" described above. The presence of this second age component is therefore immediately apparent.

Often these new minerals have an activation energy of argon loss significantly different from the original potassium bearing minerals. (It can be higher or lower). When this occurs the $^{40}Ar/^{39}Ar$ stepheating method can be used to determine the ages of the original and secondary components of the rock.

Whole rock samples usually contain a number of mineral types each with its own alteration product. A mixture of these minerals would be certain to give rise to a disrupted "plateau". Alteration is therefore readily detected and any conventional ages yielded by the rock can be considered with caution.

Mineral separates are usually much easier to deal with. Alteration will produce a single alteration product and enhance the change to a classical "double

plateaux" stepheat being produced. Such a result would reveal the original age and in the right geological circumstances the age of alteration as well. Problems can arise in determining the latter when there has been more than one period of alteration, but the most important thing is that its presence can be detected and erroneous conclusions avoided.

This approach has been used to investigate the ages of four whole rock samples of igneous rock from the North Sea Basin and to reconsider the interpretation of a step heating experiment made previously.

BP1/33 [21/9-1 B.P. Forties]

The two main factors that influence the argon-40/argon-39 results are the presence of most of the rock's potassium in largely unaltered K-feldspar and the occurrence of chlorite/zeolite intergrowths as amygdale infill.

Though there is evidence of alteration of olivines this will have little effect on the age spectrum as they contain essentially no potassium.

The presence of zeolite does, however, present a problem. It is well known that zeolites can contain excess argon and usually result in the rocks giving spuriously high ages. Typically the presence of excess argon is manifested in argon-40/argon-39 dating by saddle shaped age spectra which are formed when the radiogenic argon-40 and its associated argon-39 are released and depress the spuriously high apparent age. The saddle should therefore coincide with the maximum release of argon-39. The cumulative argon-39 vs. age plot for sample BP1/33 (see Figure B2.1) shows peak ages of 222 and 248 Ma with a saddle between the points at 195 Ma which coincides with the maximum argon-39 release.

Potassium feldspars have excellent argon retention characteristics and it may well be that the fall in age from 248 Ma (step 5) to 152 Ma (step 6) represents an age dominated by argon from the residue of the feldspar after the excess argon from the zeolite has been largely extracted.

The following conclusions can be drawn:

As a result of its mineralogy, the rock did not yield an isochron or "plateau". The rock contains excess argon-40 in zeolite. The age of the rock is less than 195 Ma and could be close to 152 Ma. There is no evidence of an event at 100 Ma.

PL1/6 [F10/1, Petroland, Central Graben flanks]

Potassium in the rock occurs predominantly in amphibole and in clays and/or mica flakes in the groundmass. Thin sections show clay pseudomorphs after olivine.

The groundmass is reported as containing an aggregate of pseudoleucite after original potassic feldspathoid.

There is therefore ample evidence to demonstrated that the rock has undergone some alteration and unless the alteration took place at or close to the time of formation a conventional date would be misleading.

As would be expected from the mineralogy, the rock does not yield a "plateau" age (see Figure B2.2). There is a gentle rise in apparent age to 127 Ma

from where the figures fall away to less than 100 Ma. The early steps do not define a "plateau" hence it can be said to be older than 127 Ma.

The three high temperature steps at 104, 103 and 94 Ma account for 60% of the argon-39 release. It is likely therefore that these contain significant amounts of argon from the K-rich groundmass which appears to be abundant in alteration products. The early steps therefore relate to the amphibole. It is however likely that the early part of the spectrum is influenced by some of the argon from the alteration products while the latter part is enhanced. Both sections therefore are effectively curved. It is concluded that the rock is older than 127 Ma and that alteration took place less than 94 Ma ago.

The coincidence of adjacent steps at 104 and 103 Ma is probably an artifact. There is nothing to suggest that the rock was formed at around 104 Ma because although the presence of zeolites is reported, there is no sign of a saddle shaped age spectrum.

AH1/42 [15/21-8a, Amerada Hess, Forties]

The mineralogical description of the sample describes extensive alteration in the upper part of the core which reduces markedly with increase in depth. It is suggested that the alteration was produced as the result of a hydrothermal system. The sample submitted for analysis is reported as being the freshest of all Forties basalts. Results of argon-40/argon-39 stepheating support this view. Most of the potassium is contained in biotite and feldspar. These do not appear to be altered. The rock contains virtually no zeolite.

These factors indicate that the rock is likely to yield its true age of formation. The rock yielded a "plateau" at 155 Ma containing 80% of the argon-39 (Figure B2.3).

An isochron fit of the points $^{40}Ar/^{36}Ar$ vs $^{39}Ar/^{36}Ar$ give an age of 156.8±5.3 (2σ) with a 40Ar/39Ar intercept of 300.7±14.1 (2σ) Ma compared to the current atmospheric $^{40}Ar/^{36}Ar$ ratio of 296.

The first two points of the age spectrum suggest the presence of a very slight secondary alteration which could indicate that the hydrothermal system responsible for the extensive alteration higher in the sequence was associated with some post extrusion event.

It is concluded that the rock is some 156 million years old and underwent a hydrothermal episode some time later, perhaps during the upper Cretaceous.

7N [17/9-1, Esso Norway, Egersund Basin]

From a geochronological point of view, the most important feature of this rock is the abundance of zeolite (11%) with a further 2% occurring as infill. The rock is altered with no primary feldspar detectable in the groundmass. A problem of K loss, perhaps complex, is indicated by the mineralogy.

The rock therefore contains a source of excess argon-40, some original minerals and abundant alteration products. It is unlikely that such a rock would produce reliable dates though figures of 177, 179 and 180 Ma are reported.

The age spectrum (Figure B2.4) is saddle shaped reflecting the presence of excess argon-40 from the abundant zeolites. The saddle of the age spectrum (242 Ma) is in fact a single point and must therefore be a maximum value.

If the rock is say, 155 million years old, then the reported figures are some 25 million years too high. This could be accounted for by the excess argon-40 biasing the results high with alteration introducing a young component. Stepheating has revealed that this particular sample is unsuitable for dating. It may well be that the presently accepted values of around 180 Ma are spurious for the reasons given above.

Reappraisal of Sample 8U [29/25-1, Central Graben]

Argon-40/argon-39 age spectrum (stepheating) analysis was performed on a concentrate of mica. Though the "plateau" is disturbed, when it is considered in the light of the results from samples BP1/33, PL1/6 and AH1/42 it seems likely that the early points in the age spectrum reflect the true age of the rock (157 Ma). This is supported by the "all points" $^{40}Ar/^{36}Ar$ vs $^{39}Ar/^{36}Ar$ isochron which gave an age of 160±5 Ma. Only one point lies significantly off the line and shows that the mineral has not remained completely closed over geological time. There is therefore further evidence to suggest that the rocks were affected by a post formational event or events.

Conclusions.

The limitations of conventional dating methods applied to partially altered basic rocks are amply demonstrated by these results. Only one (AH1/42) would have given a satisfactory result while the rest would have been misleading.

It is concluded that all of the rocks were formed a little over 150 million years ago and suffered subsequent hydrothermal alteration less than 94 million years ago on at least one occasion.

There is no evidence to suggest that the volcanism took place at 100 Ma and it is likely that such dates are apparent values resulting from partial overprinting of the original ages by the hydrothermal event(s).

FIGURE B2:1

BP1/33

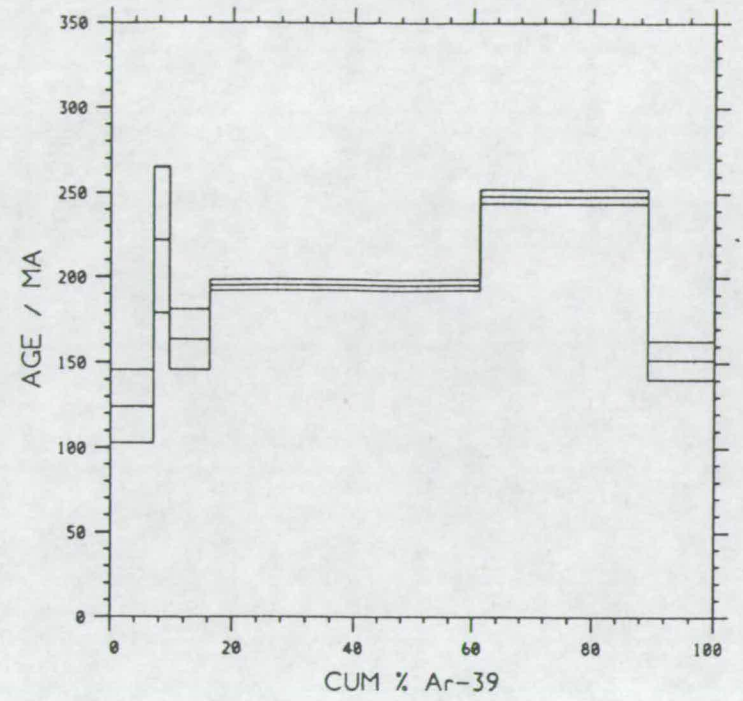

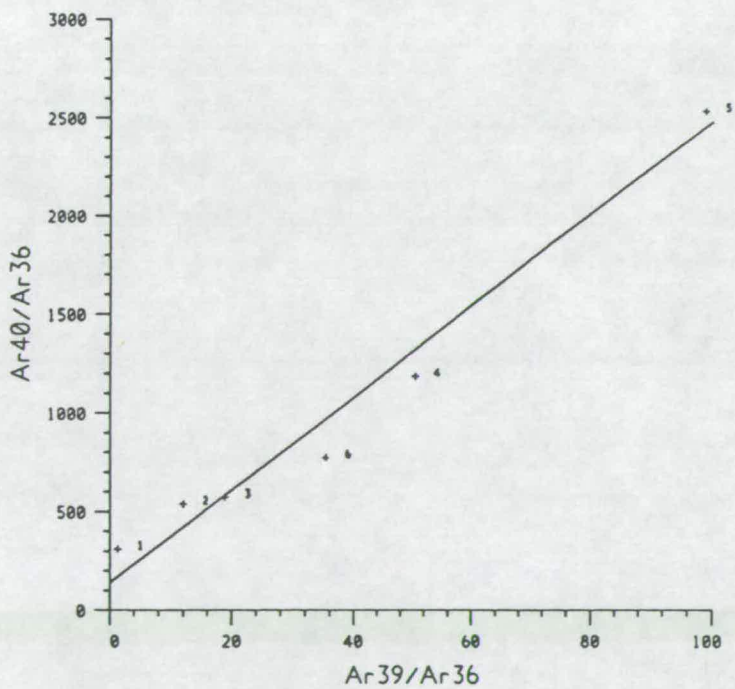

FIGURE B2:2

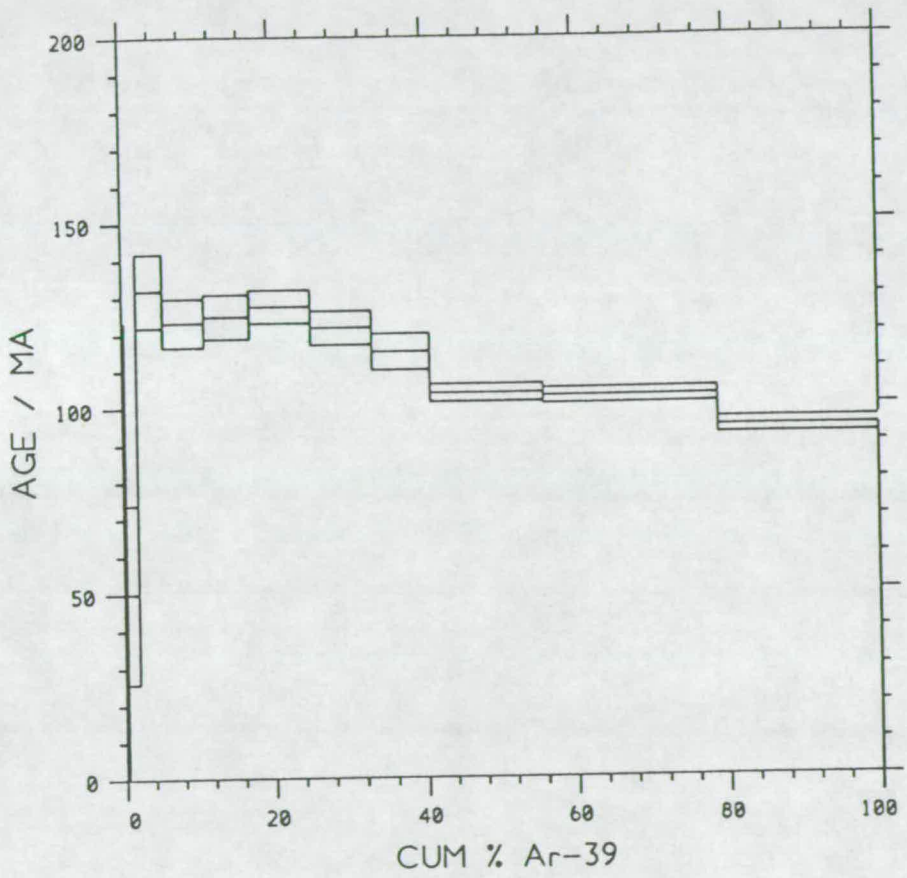

FIGURE B2:3

AH1/42

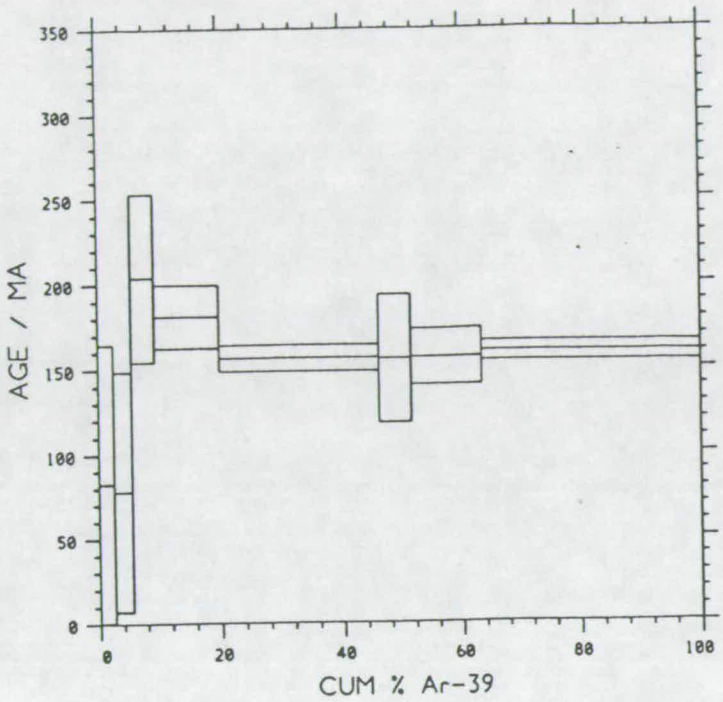

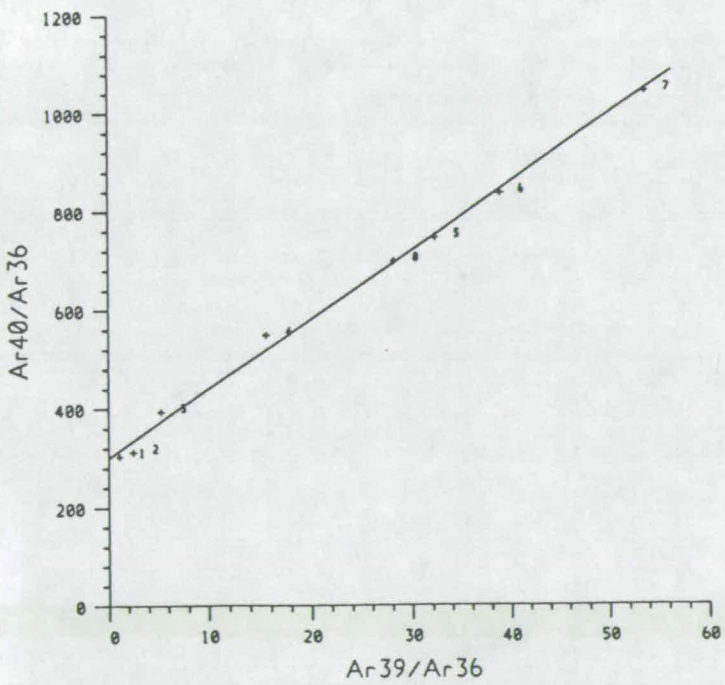

FIGURE B2:4

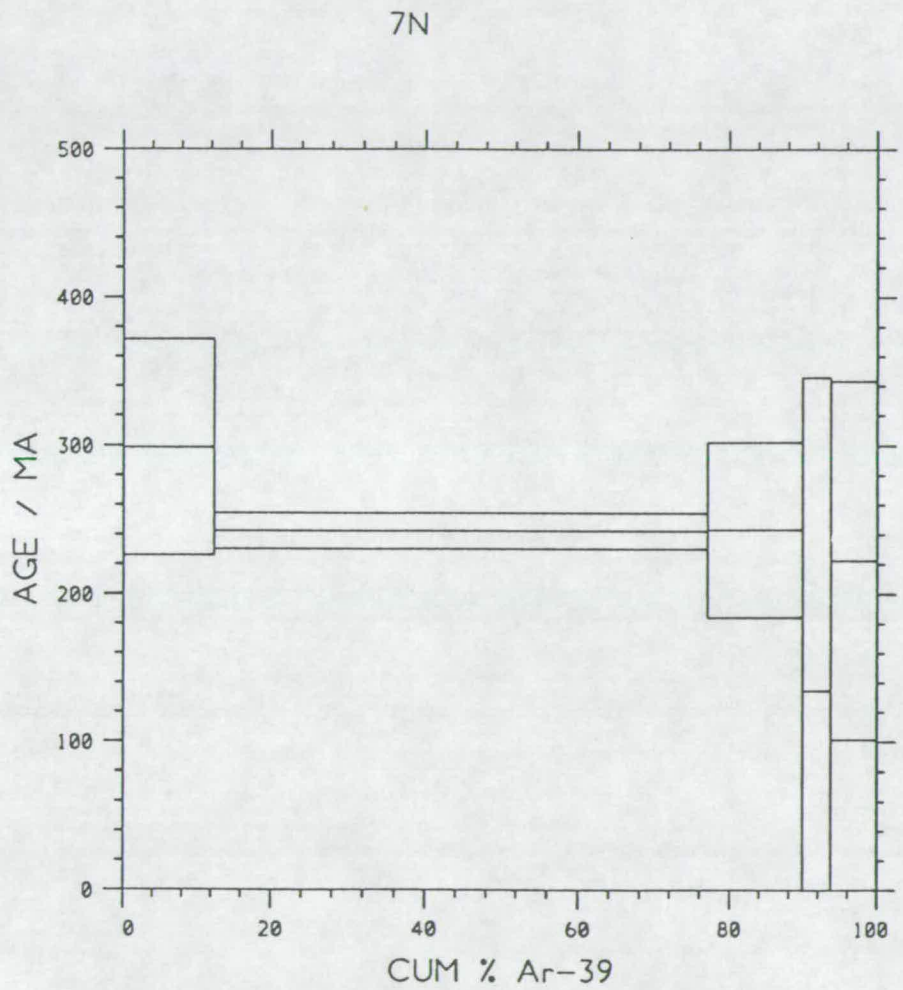

SECTION B3 : $^{40}Ar/^{39}Ar$ Dating Report (A.N. Halliday).

Techniques.

The six samples provided for analysis were weighed into Al foil capsules and irradiated along with 7 interspersed standards of known age ("monitors"). The monitor we use is the internationally recognized standard Minnesota hornblende MMhbl, the calibration of which has been documented in more detail than any other $^{40}Ar/^{39}Ar$ standard. The samples were irradiated at the University of Michigan's Ford Reactor, which has been used extensively for $^{40}Ar/^{39}Ar$ dating by a range of co-workers including Professor Mark Harrison (when at S.U.N.Y., Albany), Professor Ken Foland (Ohio State University), Professor Dan Lux (University of Maine at Orono) and Dr. John Sutter (U.S.G.S., Reston). The latest rotation device for uniform irradiation was deployed.

After irradation the monitors and samples were degassed in a low blank, small volume extraction system with a double vacuum resistively heated Ta furnace. The extraction system is online to a MAP 215 rare gas mass spectrometer with a Nier-type source and resolution set at approximately 200. Measurements were made using a single Faraday collector with a 10^{11} ohm resistor. The voltage was measured using a Solartion 7060 digital voltmeter which is operated from a Zenith XT computer, which also controls peak switching. The background on each peak was monitored prior to gas admittance and ion beam intensities for each mass were measured relative to a base line interpolated between half mass positions. The J-value (the parameter which relates the $^{40}Ar/^{39}Ar$ data of the unknown to the age of the monitor) is known to 1%.

Results.

The results are presented in Figures. B3.1 to B3.6. Only 3 out of the 6 samples defined "plateau ages", deemed suitable by virtually all $^{40}Ar/^{39}Ar$ geochronologists as the minimum of satisfactory criteria for establishing a meaningful geological event. The detailed results are as follows:

AH1/42

This sample defines an increase in apparent age to a flattish portion of the age spectrum between 30 and 90% of ^{39}Ar released, after which the age increases further to values in excess of 300 Ma. The results are ambiguous because there is no simple plateau. For example, the data could reflect a >300 Ma rock which had been largely degassed at approximately 150-200 Ma. Alternatively, the data could be interpreted as indicating a crystallization age of 183±5 Ma (the age defined by the 3 steps between 30 and 90% of ^{39}Ar cumulative release) of a basalt with some excess Ar released at the highest temperatures and some minor Ar loss recorded in the lowest temperature steps. The total degassing age (equivalent to a conventional K-Ar age) is 186±7 Ma.

TO1/20

This sample shows an initial drop in $^{40}Ar/^{39}Ar$ age, but the steps from 10 to 100% of gas released define a progressive increase in age to a highest temperature age of 270±28 Ma. This is accompanied by a drop in $^{39}Ar/^{37}Ar$ ratio, implying an

increase in the amount of Ar derived from minerals with low K/Ca ratios. Two steps for the 50-90% of cumulative ^{39}Ar release are in close agreement (weighted mean - 124±10 Ma) but do not provide convincing evidence that this is the original crysallization age. The data would, for example, be explained as the result of the partial degassing of a much older basalt around this time. Alternatively the results may reflect excess Ar being released in the highest temperature fraction. If the reported stratigraphic constraints (supposedly younger than Triassic) are valid, this clearly has to be the case. There is no doubt that the data need careful interpretation and use. The total degassing age is 107±11 Ma.

SO1/8

This sample yielded an irregular age spectrum which climbs without producing a plateau for the final 45% of ^{39}Ar release. The total degassing age is 85±12 Ma, but the crystallization age is probably better represented by at least the highest temperature age recorded (131±4 Ma).

SH1/10

This sample yielded a more satisfactory age spectrum which increases in the first 30% of ^{39}Ar release to a plateau most precisely defined by steps 7 to 9, with a mean age of 130±2 Ma. The total degassing age is 121±3 Ma. The plateau age is a reasonably reliable estimate of the age of this sample.

PL1/6 (kaersutite)

This sample yielded an extremely flat age spectrum, which suggests that there has been little if any argon loss since the kaersutite cooled through its closure temperature (in the region of 500°C). Most of the gas was released in two steps over a small temperature interval and the integrated average age for this plateau is 151±2 Ma which is the best estimate of the age of the sample. This is within error of the total degassing age of 154±5 Ma.

ES1/42 (phlogopite)

This sample similarly yielded a very uniform age spectrum with a plateau age defined by steps 3 to 7 of 170±2 Ma. This is within error of the total degassing age (172±4 Ma). These data imply that the phlogopite crystallized or last cooled through its temperature (variously estimated at between 300 and 500°C) at 170±2 Ma.

Conclusions

The best estimate of the ages of the six samples is as follows:

AH1/42	183±5 Ma
TO1/20	no commitment
SO1/8	>131±4 Ma
SH1/10	130±2 Ma
PL1/6	151±2 Ma
ES1/42	170±2 Ma

Of these, the last three warrant the greatest level of confidence.

FIGURE B3:1

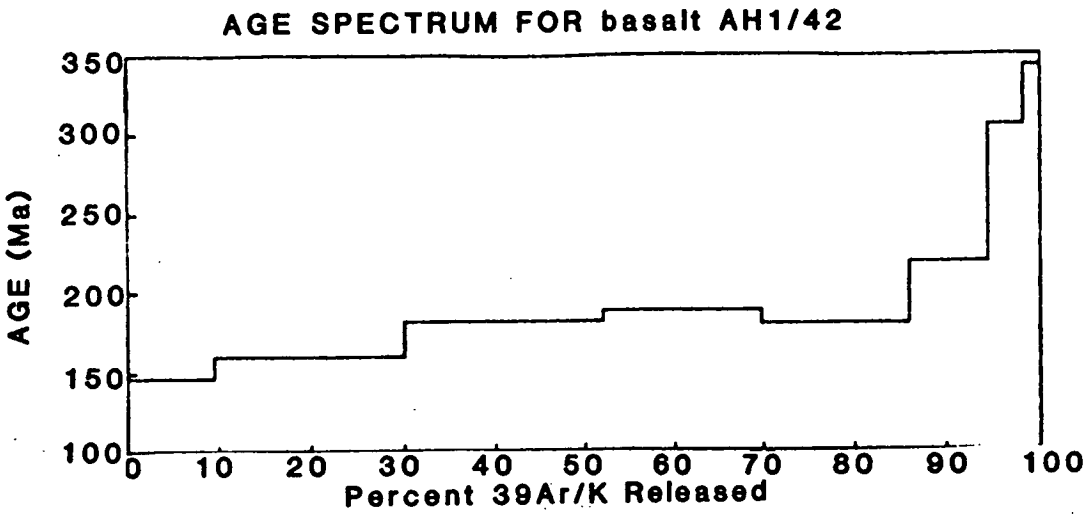

No Plateau
Total Gas Age is 185.77 7.17

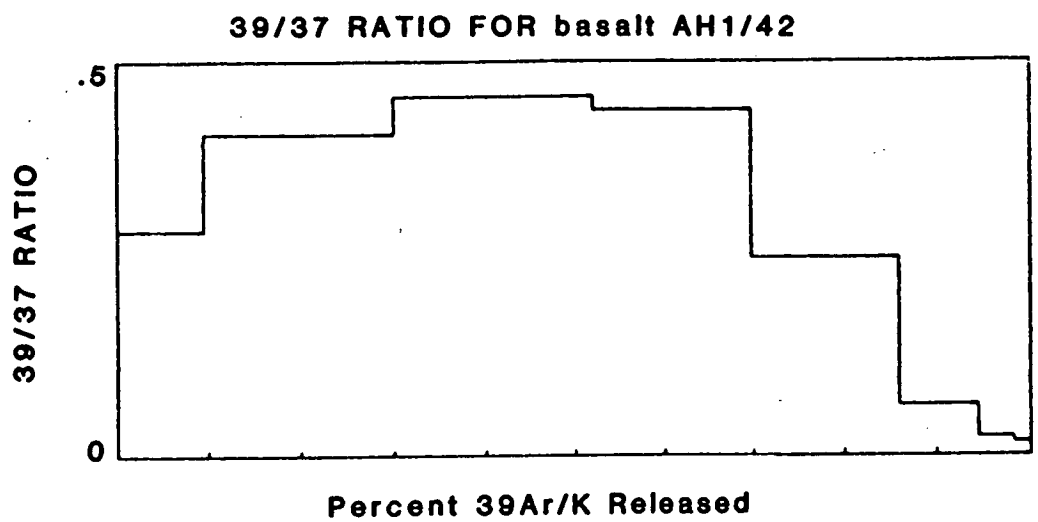

FIGURE B3:2

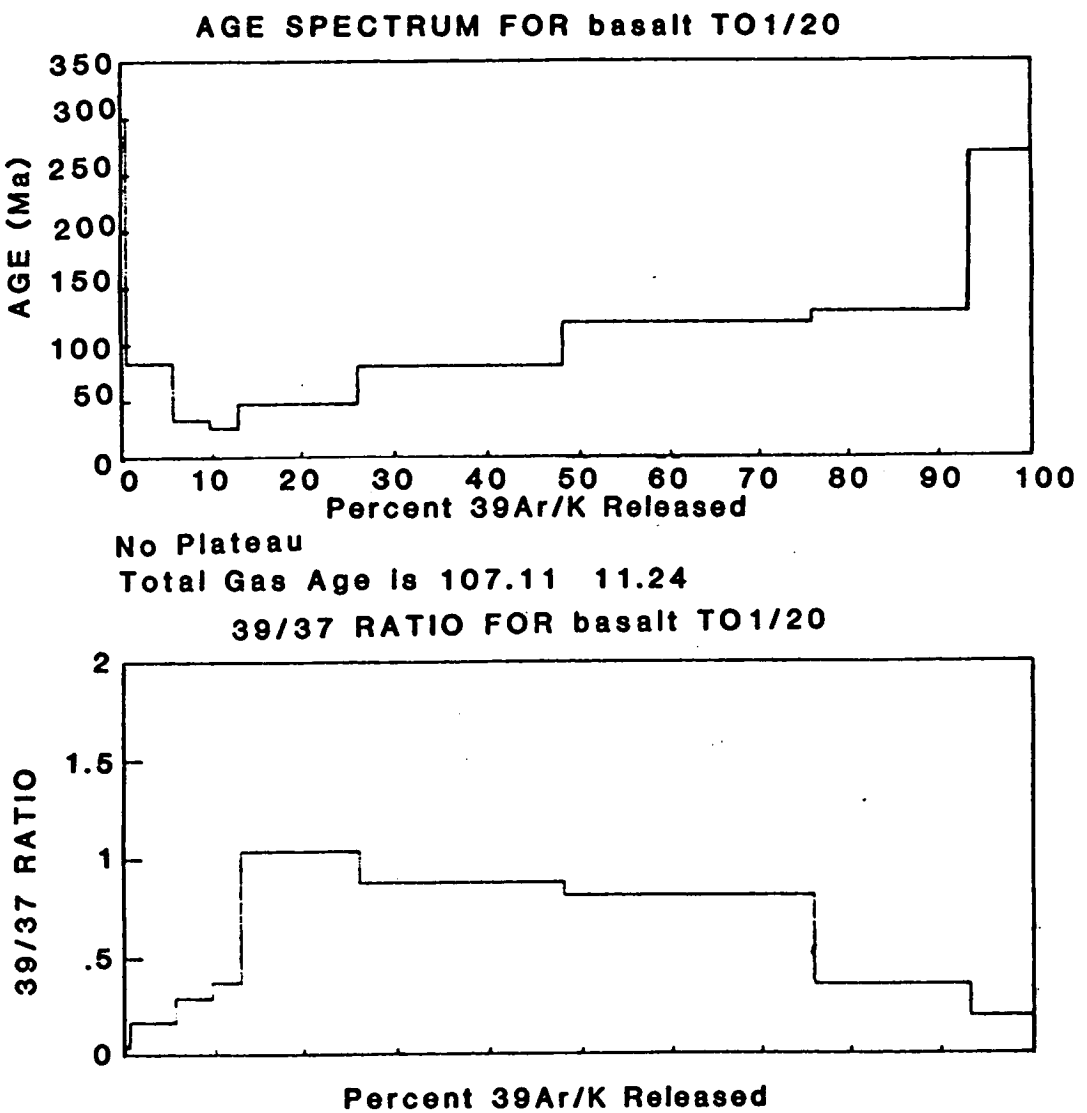
AGE SPECTRUM FOR basalt TO1/20
AGE (Ma)
350
300
250
200
150
100
50
0
0 10 20 30 40 50 60 70 80 90 100
Percent 39Ar/K Released
No Plateau
Total Gas Age is 107.11 11.24
39/37 RATIO FOR basalt TO1/20
39/37 RATIO
2
1.5
1
.5
0
Percent 39Ar/K Released

FIGURE B3:3

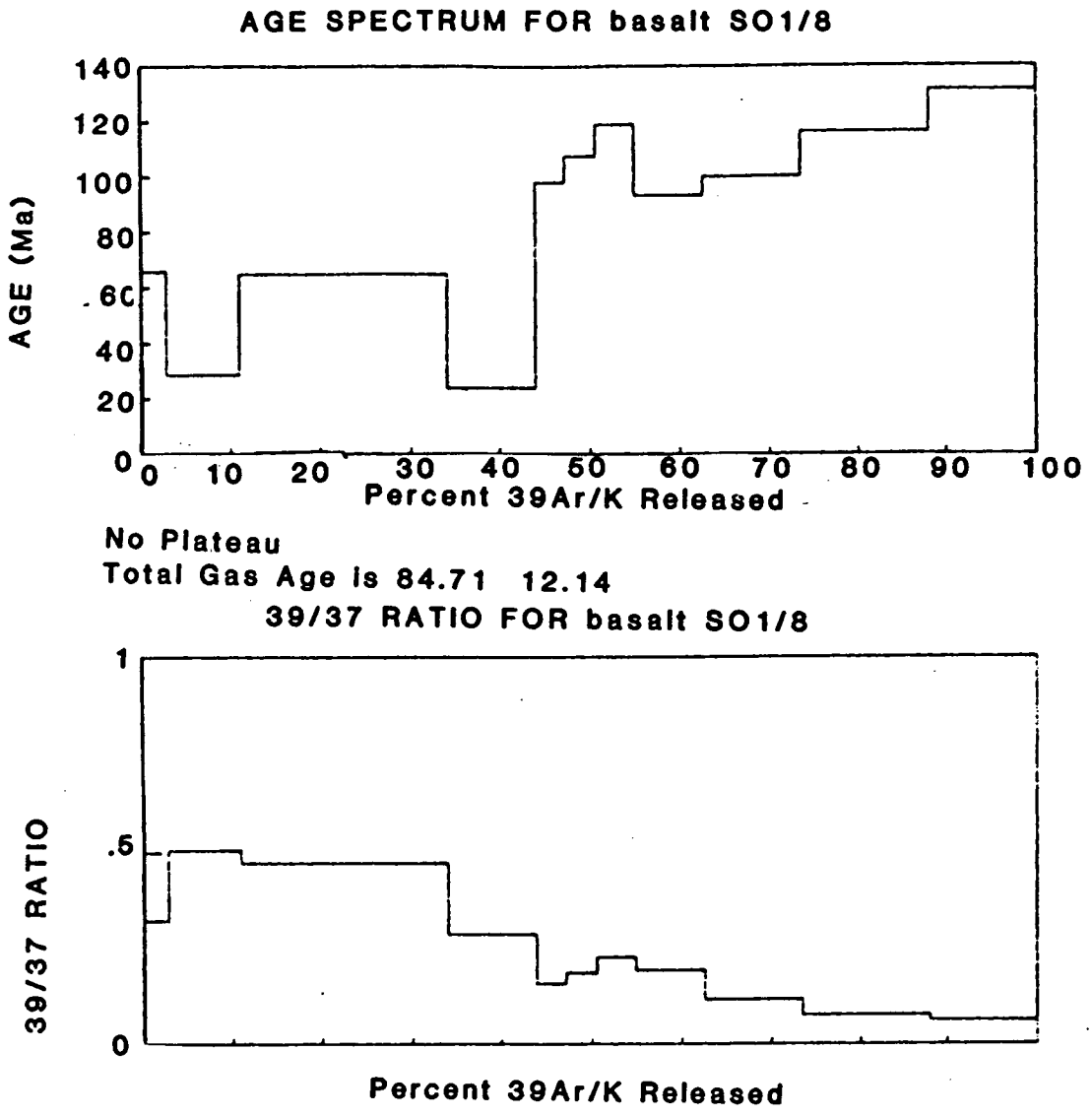
AGE SPECTRUM FOR basalt SO1/8
AGE (Ma)
140
120
100
80
60
40
20
0
0 10 20 30 40 50 60 70 80 90 100
Percent 39Ar/K Released
No Plateau
Total Gas Age is 84.71 12.14
39/37 RATIO FOR basalt SO1/8
39/37 RATIO
1
.5
0
Percent 39Ar/K Released

FIGURE B3:4

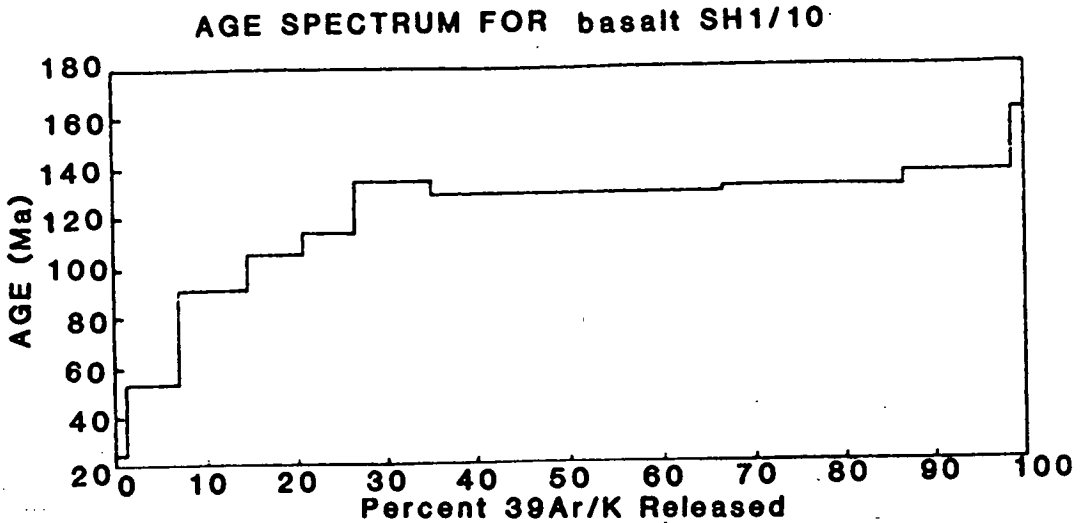

Plateau Age is 129.82 1.85 Ma
Plateau on steps 7 to 9 and contains 51.4% of the gas
Plateau min is 128.53 and Plateau max is 131.32

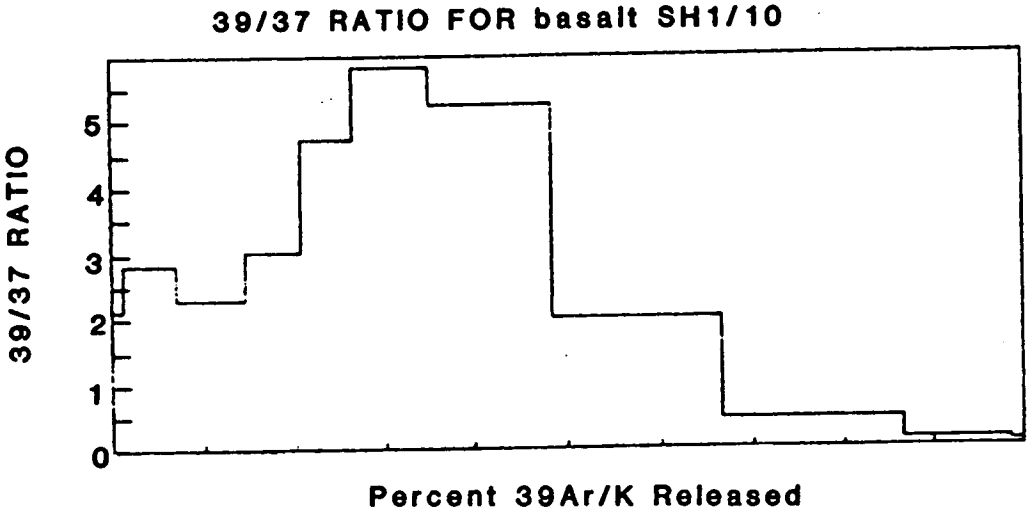

FIGURE B3:5

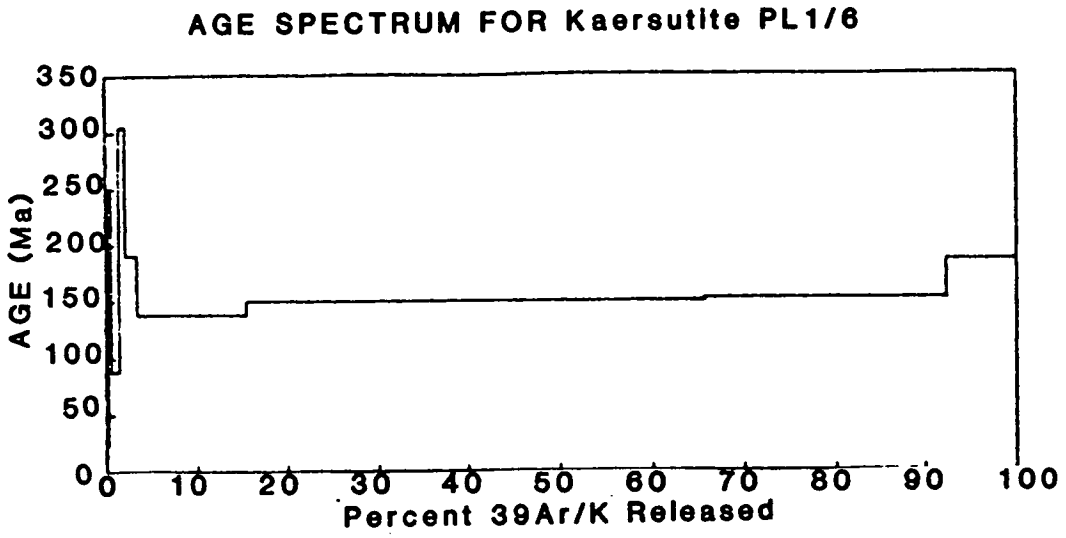

Plateau Age is 150.95 1.91 Ma
Plateau on steps 7 to 8 and contains 76.9% of the gas
Plateau min is 149.76 and Plateau max is 153.18

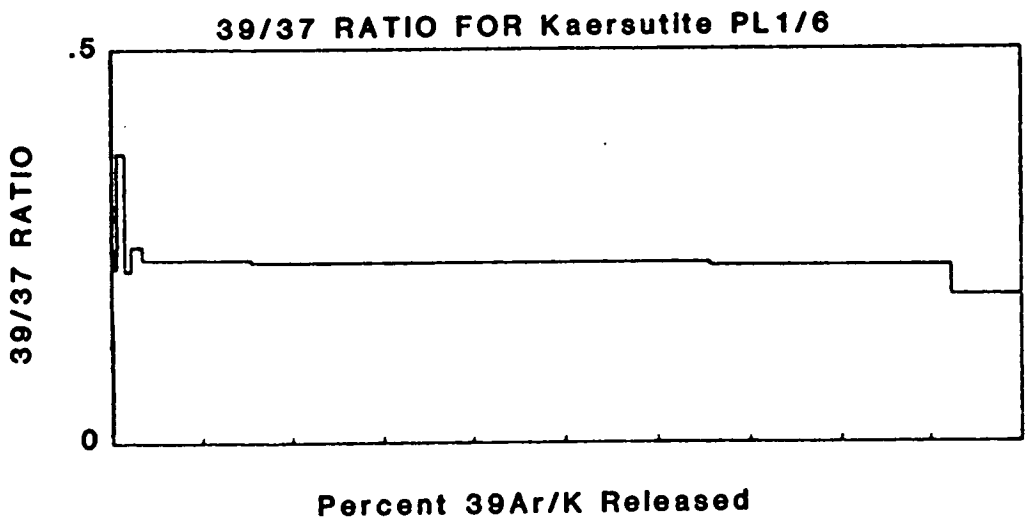

FIGURE B3:6

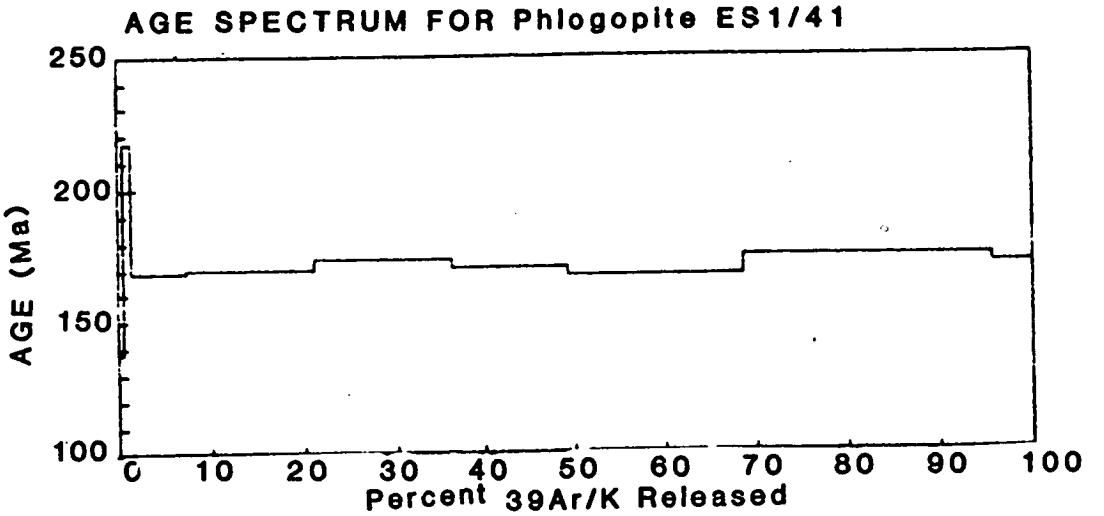

Plateau Age is 170.07 2.29 Ma
Plateau on steps 3 to 7 and contains 67.1% of the gas
Plateau min is 167.77 and Plateau max is 170.28

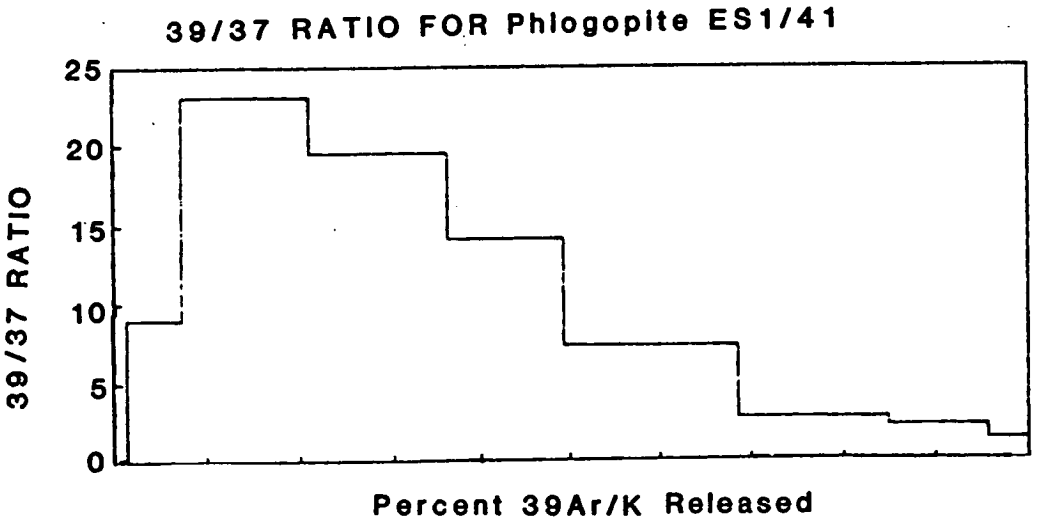

Generating melt during lithospheric extension: Pure shear vs. simple shear

Dave Latin
Grant Institute of Geology, University of Edinburgh
Edinburgh EH9 3JW, Scotland

Nicky White
Bullard Laboratories, University of Cambridge
Cambridge CB3 0EZ, England

ABSTRACT

The uniform stretching model has been used to calculate the volume and composition of melt generated by adiabatic decompression during extension of the continental lithosphere. The consequences of this approach for melt generation by lithospheric simple shear were investigated. The results show that, given an initially planar detachment fault, it is extremely difficult to generate melt from the asthenosphere, under either normal or elevated asthenospheric potential temperatures. Our conclusion is independent of the initial dip of the detachment fault and also holds when the initial dip in the lithospheric mantle is double that in the crust. In the North Sea, lithospheric simple shear fails to account for the existence and location of magmatism. These conclusions may also apply, more generally, to passive margin development.

INTRODUCTION

For the past eight years there has been considerable controversy concerning the nature of lithospheric extension. In 1978, McKenzie proposed the uniform stretching model, which stated that the lithosphere deforms by bulk pure shear during extension (Fig. 1A). On the basis of field mapping, seismic experiments, and considerations of magmatism and topography in the Basin and Range province, Wernicke (1981, 1985) argued that lithospheric extension could be accommodated by slip along a low-angle (10°–30°) normal fault that penetrates the entire lithosphere (Fig. 2A). These two models have been widely applied both to the formation of extensional sedimentary basins (e.g., Sclater and Christie, 1980; Sclater et al., 1980; Barton and Wood, 1984; Gibbs, 1987; Bosworth, 1985) and passive margins (e.g., Le Pichon and Sibuet, 1981; Sawyer et al., 1982; Lister et al., 1986).

A variety of arguments have been used to try to distinguish between these two models. For example, on the basis of seismological data from areas of active extension, such as the Aegean, Basin and Range, Yunnan (China), east Africa, and Suez, Jackson (1987) showed that active normal faults do not have dips of $<30°$ and are approximately planar down to the base of the seismogenic layer (~10 km). Others have demonstrated that the pattern of initial and thermal subsidence in older basins, such as the North Sea, is incompatible with lithospheric simple shear (White, 1989; Klemperer and White, 1989).

Here we address the same controversy by using a very different approach. We first discuss the quantitative implications of the two extension models for melt generation. Our starting point is the work of McKenzie and Bickle (1988) who suggested that the volumes and compositions of melts generated from the asthenosphere by adiabatic decompression during extension of the continental lithosphere can be related directly to the amount of upwelling and partial melting and therefore to degrees of extension. The McKenzie and Bickle model agrees well with observations of crustal thickness and composition at ocean ridges. Our aim here is to use McKenzie and Bickle's model to predict the amount of asthenospheric partial melting generated by lithospheric simple shear for different degrees of extension and then to compare these values with observations from the North Sea rift. We also briefly discuss the magmatic implications of lithospheric simple shear for the development of passive margins.

MELT GENERATION DURING EXTENSION

Adiabatic decompression during lithospheric stretching can lead to melting of the asthenosphere if the perturbed geotherm intersects the solidus for dry mantle peridotite. Minor amounts of melt may also be produced from enriched lithospheric mantle containing small amounts of volatile-bearing phases (e.g., pargasite, phlogopite, and carbonate) by more modest perturbations of the geotherm (Green, 1973; Harte, 1983; Wyllie, 1987; McKenzie, 1989; Latin et al., 1989). However, these small melt fractions tend to be chemically distinct from asthenospheric melts. In many cases they are unlikely to be significant volumetrically because volatile phases are soon exhausted during melting (e.g., Olafsson and Eggler, 1983). These minor amounts of melting are not considered further in this paper.

Figure 1 shows the results of the one-dimensional calculations by McKenzie and Bickle (1988) for uniform stretching of the lithosphere (Fig. 1A) over asthenosphere of normal potential temperature (T_p = 1280 °C; i.e., the temperature on the adiabat projected to surface pressure; Fig. 1B) and for an elevated potential temperature (T_p = 1480 °C; Fig. 1C) due to the presence of a mantle hotspot or plume (Courtney and White, 1986; White and McKenzie, 1989). The degree of partial melting of the asthenosphere was calculated for a range of stretching factors (β). The amount of melt produced and its composition can be directly related to the degree of melting and the composition of the asthenosphere. Stretching is assumed to be instantaneous, or to occur within a period that is short compared to the thermal conduction constant for the lithosphere, $60/\beta^2$ Ma (Jarvis and McKenzie, 1980). This assumption will maximize the amount of melt. The mechanical boundary layer is assumed to have an initial thickness of 100 km, which for an upper mantle kinematic viscosity of 4×10^{15} $m^2 \cdot s^{-1}$ (i.e., a dynamic viscosity of 1.32×10^{19} Pa·s) represents an effective plate thickness of about 120 km. Greater initial thicknesses for the mechanical boundary layer and larger upper mantle viscosities will decrease the amount of melt produced for a given β and T_p.

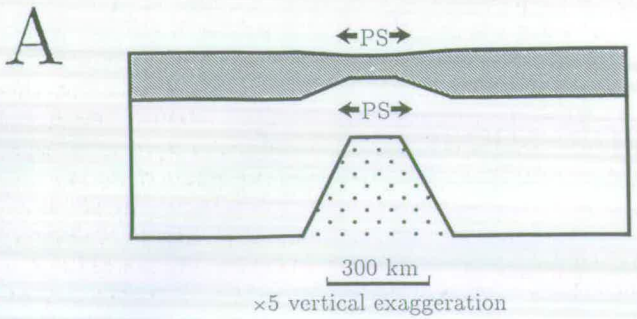

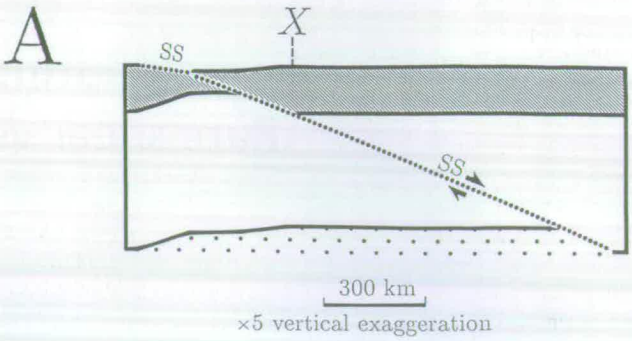

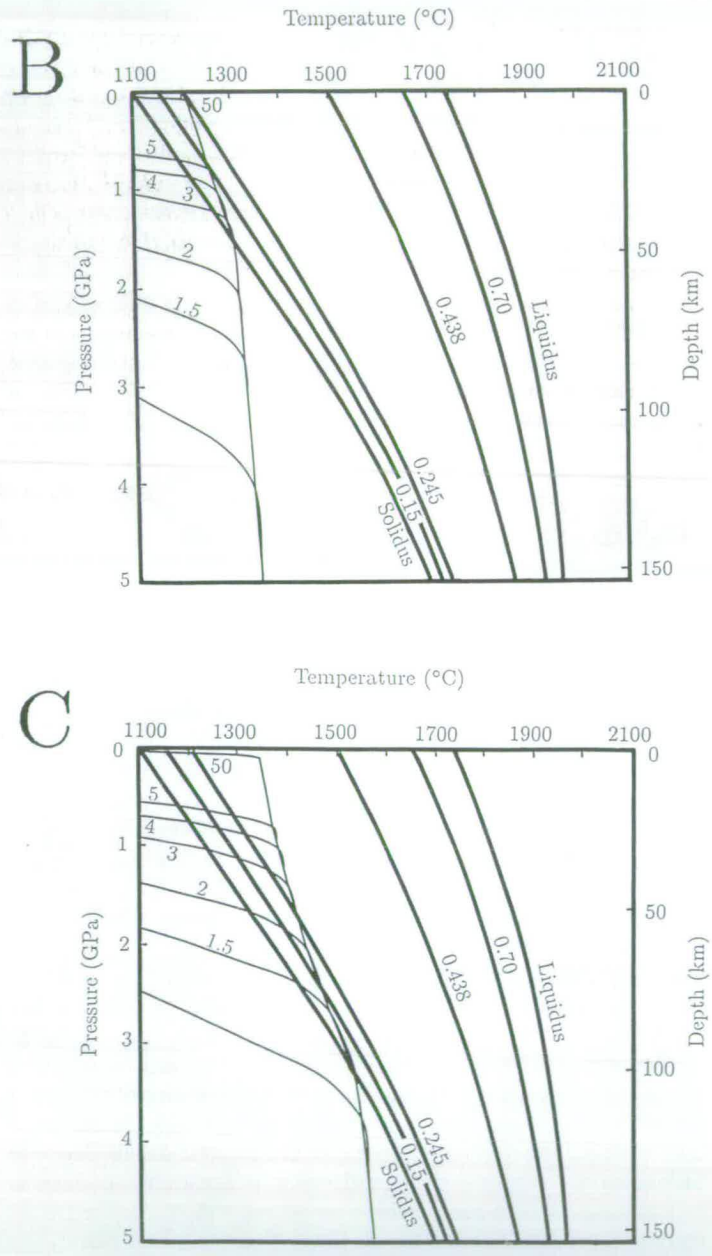

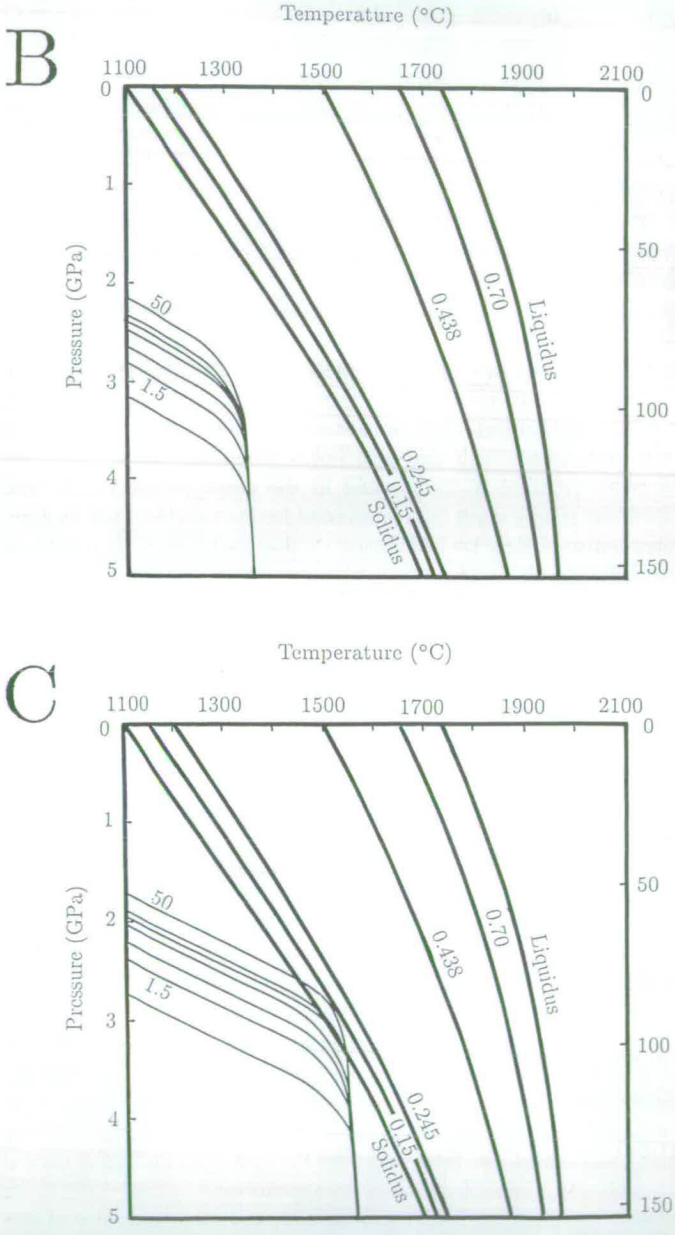

Figure 1. Uniform stretching model. A: Cartoon illustrating lithosphere geometry produced by $\beta = 2$. PS = pure shear. Gray = crust; dot pattern = upwelled asthenosphere. B: Adiabatic upwelling due to stretching of convective geotherm by different values of β, as labeled (redrawn from McKenzie and Bickle, 1988). Mechanical boundary layer thickness = 100 km; kinematic viscosity = 4×10^{15} m$^2 \cdot$ s^{-1}; interior potential temperature = 1280 °C. Curves between solidus and liquidus show melt fraction by weight. C: As for B with interior potential temperature 1480 °C.

Figure 2. Lithospheric simple shear model. A: Cartoon illustrating lithosphere geometry produced by extension on detachment fault dipping at 5° (effective $\beta_c = 2$). SS = simple shear. Gray = crust; dot pattern = upwelled asthenosphere. *X* marks position of maximum upwelling. B: Adiabatic upwelling due to stretching of convective geotherm by different values of effective crustal stretching, β_c (all parameters as in Fig. 1B). C: As for B with interior potential temperature 1480 °C. Effects of latent heat ignored.

It is straightforward to carry out similar calculations for lithospheric simple shear (e.g., Voorhoeve and Houseman, 1988; Buck et al., 1988; White, 1989). The parameters are identical to those used by McKenzie and Bickle (1988) to calculate the curves for the stretching model in Figure 1, B and C. The flexural rigidity (i.e., effective elastic thickness) of the lithosphere is assumed to be negligible, considerably simplifying the calculations and maximizing melt production. The detachment fault is assumed to be planar when extension commences, although after extension the dip of the detachment has increased considerably with depth due to isostatic rebound (Wernicke, 1985). Only the region of maximum asthenospheric upwelling is considered. This zone occurs directly below the region where the detachment fault passes along the Moho and into the lithospheric mantle (i.e., where the crust returns to its normal thickness, position X in Fig. 2A). β_c refers to the effective crustal thinning in the center of the basin. If β_c is fixed (as it would be for any particular basin), then $\epsilon \tan \theta$ is constant, ϵ being the horizontal separation of the two plates and θ the dip of the detachment fault. Therefore, *the amount of upwelling is independent of the dip of the detachment.* The perturbed geotherms shown in Figure 2C overestimate the degree of partial melting because unlike those in Figure 1, B and C, they do not take account of the change in the adiabat due to loss of latent heat upon melting.

For normal asthenospheric temperatures (T_p = 1280 °C; Fig. 2B) it is clear that the perturbed geotherm does not intersect the dry solidus even when the values of crustal thinning are extremely large (e.g., β_c = 50). No asthenospheric melt is generated because β_m, the effective thinning of the lithospheric mantle, is too small (1.5). In contrast, for the uniform stretching model the maximum degree of partial melting exceeds 20% when T_p = 1280 °C and β = 50 (Fig. 1B) and a thickness of 7 km of melt is produced with mid-ocean ridge basalt (MORB) major element chemistry. Over a mantle plume (T_p = 1480 °C), the lithospheric simple shear model (Fig. 2C) predicts no asthenospheric melting until $\beta_c > 3$. Even if $\beta_c = \infty$, the degree of partial melting cannot exceed 15% and less than 5 km of melt is produced while any crust is present. The uniform stretching model, on the other hand, can result in the production of great thicknesses of melt when T_p = 1480 °C (McKenzie and Bickle, 1988; Fig. 1C).

If the detachment fault is not initially planar, then β_m is given by

$$\beta_m = \frac{a - t_c}{a - t_c - t_c\,(1 - 1/\beta_c)\,\tan \theta_m / \tan \theta_c}, \quad (1)$$

where a is the lithospheric thickness, t_c is the crustal thickness, and θ_c and θ_m are the dips of the detachment fault in the crust and lithospheric mantle, respectively. Assuming that the dip of the detachment is initially 15° in the crust, and steepens to 30° in the lithospheric mantle, then the dry solidus will not be intersected unless $\beta_c \gg 3$ for T_p = 1280 °C and $\beta_c \geq 1.5$ for T_p = 1480 °C.

The observation that it is difficult to produce melt by lithospheric simple shear is not new (Buck et al., 1988; Lister et al., 1989). However, the simple quantitative analysis presented above suggests that the location, volume, and composition of melt produced during extension can be used to discriminate between the two extension models. We now compare these predictions with observations from the North Sea rift and from passive margins in general.

NORTH SEA

The most important and best documented episode of extension in the North Sea took place from Middle Jurassic to Early Cretaceous time (Glennie, 1986) and resulted in the development of a trilete rift system. Both the uniform stretching and the lithospheric simple shear models have been applied to the North Sea rift (Barton and Wood, 1984; Gibbs, 1987; Klemperer, 1988). It has proved difficult to decide which model is more applicable, although recent work on subsidence patterns (White, 1989; Klemperer and White, 1989) favors the uniform stretching model.

Magmatic activity associated with melting of the asthenosphere during rifting occurs principally in the triple-junction area (the alkali basalts of the Forties Volcanic Province; Fall et al., 1982; Dixon et al., 1981; Latin et al., 1989). Minor amounts of magmatism, in the form of nephelinites and ultrapotassic rocks, are observed in other areas of the North Sea, but because volatiles are inferred to have played an important role in their generation, the relation of such melts to the stretching event is unclear (Latin et al., 1989). The central location of the asthenospheric magmatic activity is of critical importance. Figure 3 shows the predicted distribution of asthenospheric melting (assuming vertical melt migration) if rifting had occurred by lithospheric simple shear. Obviously, the expected and observed distributions are in profound disagreement. Even if magmas migrated upward along the very shallow dipping detachment faults, the observed distribution of asthenospheric melt in the North Sea is difficult to explain.

Within each of the three rift arms, the maximum Late Jurassic stretching factor is ~1.5 (Sclater and Christie, 1980; Barton and Wood, 1984; White, 1988). The amount of extension at the triple junction itself is less well known, although backstripped well data suggest that β is at least 1.6 (Christie and Sclater, 1980; Wood, 1982). Geometrical considerations imply that β in this region may be as large as the square of the values within each rift arm (i.e., $\beta \sim 2.5$). The thickness of the lithosphere prior to rifting has been estimated as 125 km from the thermal time constant for

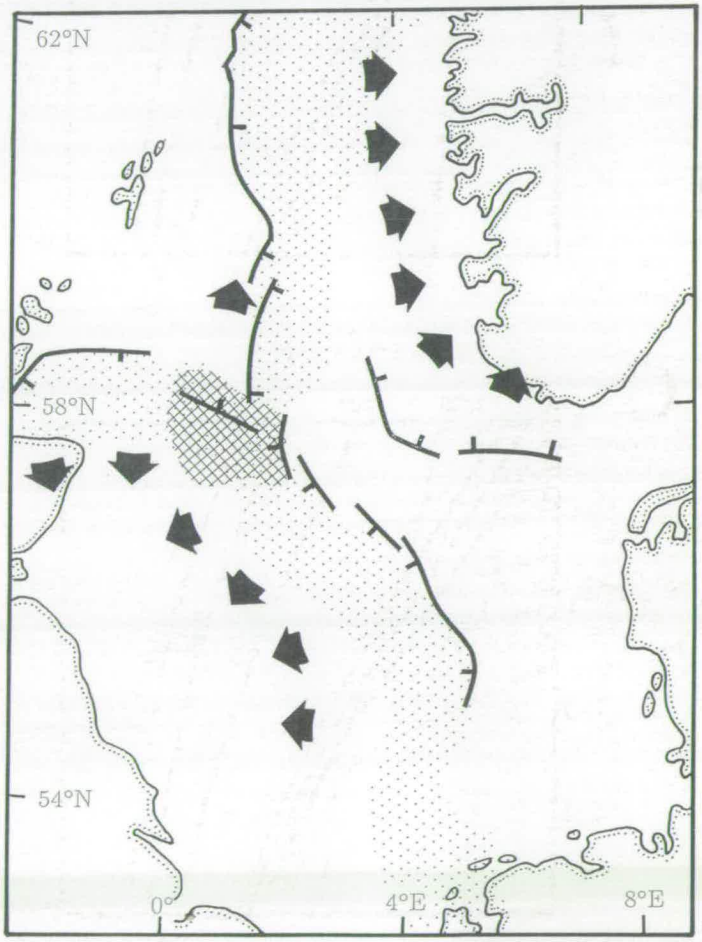

Figure 3. Simplified tectonic map of North Sea rift system. Dot pattern = trilete rift system. Cross-hatch pattern = location of Forties volcanic province. Thick lines with tick marks = detachment faults at prerift surface as proposed by Beach (1986), Gibbs (1987), and others. Arrows are positioned above point *X* in Figure 2A and indicate directions away from rift beyond which any vertically migrating melt would be expected to surface according to lithospheric simple shear model.

the subsidence, which is similar to that for ocean basins (Barton and Wood, 1984), and so assuming a mechanical boundary layer initially 100 km thick (Figs. 1 and 2) may be justified. The Forties alkalic basalts erupted within <30 m.y. of the start of rifting, so for our purposes the assumption of instantaneous extension is probably valid.

The chemistry of the Forties alkalic basalts is indistinguishable from that of ocean-island basalts; this implies an asthenospheric source (Fitton and Dunlop, 1985). Simple equilibrium melting calculations similar to those used by Fitton and Dunlop (1985) indicate that the observed compositions can be explained by <2% partial melting of asthenospheric mantle (Latin et al., 1989). The extraction of small melt fractions like these presents no difficulties in theory (M. Cheadle, 1989, personal commun.; McKenzie, 1989). Such small degrees of partial melting require the perturbed geotherm to just intersect the dry solidus. This degree of melting is only produced by a uniform stretching of $\beta \sim 2.5$ where T_p = 1280 °C (Fig. 1B). Given that β values in the North Sea rift are unlikely to exceed 2.5, it is difficult to see how the lithospheric simple shear model applies if the detachment fault is initially planar. However, if the initial dip of the detachment fault in the lithospheric mantle is double that in the crust (see equation 1), asthenospheric melt can be produced for the observed β values if T_p = 1480 °C. The spatial distribution of such melt will, however, still present problems (see above).

Note that melting in the presence of ~1 wt% of water will lower the liquidus temperature for alkalic basalt, allowing production of it at 50–100 °C below the dry solidus (Green, 1970). A small amount of water would therefore allow these melts to be generated by smaller β factors. The presence of ocelli, as well as groundmass amphibole and mica in the Forties basalts, suggests that <1 wt% of water may have been present in the magma (Latin et al., 1989). However, the asthenosphere is generally assumed to be dry, and therefore this water may have entered the melt during its passage through the lithosphere, in which case the dry solidus would still apply.

Models for the North Sea rift that require extension by lithospheric simple shear are only likely to produce the observed melt compositions in the presence of a mantle plume (T_p = 1480 °C) if the initial dip of the detachment increases rapidly with depth or if there were some water present in the asthenosphere. Even so, the location of magmatic activity still appears to disagree with this model. The uniform stretching model does not require the presence of a mantle plume (T_p = 1480 °C) in order to explain the above observations (Latin et al., 1989).

PASSIVE MARGINS

The lithospheric simple shear model has also been widely applied to the evolution of passive margins (e.g., Lister et al., 1986, 1989). Conjugate margins are described as either upper or lower plate in character, depending on their particular geometries. Emphasis has been placed on the need to produce between 5 and 15 km of melt below upper plate margins to account for permanent uplift and evidence for underplating and surface volcanism. However, it must be pointed out that White et al. (1987) and White and McKenzie (1989) would account for the development of most volcanic margins by uniform stretching over mantle hotspots. The calculations discussed in this paper suggest that little, if any, melt will be produced by lithospheric simple shear, even for very large values of β_c and extension over a mantle plume. Magmatism has also been invoked to explain the widespread and persistent uplift of lower plate margins (Lister et al., 1989). However, Figure 2A suggests that considerably less melt will be produced beneath the lower plate than is produced beneath the upper plate. Clearly, the lithospheric simple shear model fails to account for the amounts of melting required to coincide with margin formation, especially in the absence of elevated asthenosphere temperatures. The uniform stretching model has none of these problems.

Small-scale convection cells have been invoked to augment melt production during extension (Mutter et al., 1988; Buck, 1986). If these operate, then it may be possible to generate enough melt under conditions of lithospheric simple shear. However, unreasonable reductions in the viscosity of the upper mantle and large thermal gradients may be required to induce convection within the thinned thermal boundary layer.

The difficulties with lithospheric simple shear are more obvious when continental breakup and the commencement of sea-floor spreading are considered. Even when the crust is thinned to almost zero ($\beta \sim 50$), regardless of whether a mantle plume is present, little or no melt production takes place. Other models for margin formation that require a large lateral offset between crustal and lithospheric mantle stretching (e.g., Lister et al., 1989) are equally unsatisfactory for the generation of MORB. For example, suppose that the crust is stretched by a factor of 50 in one place, and the lithospheric mantle is stretched by the same amount elsewhere. Beneath the crustal rift, the base of the lithosphere rises by 16 km to a depth of about 90 km from the surface. No asthenospheric melt is predicted for T_p = 1280 °C, and only very small amounts (less than 3 km) are generated at plume temperatures. In the zone of major lithospheric mantle attenuation the upwelling is far greater, but the base of the lithosphere is still ~30 km below the surface, and therefore decompression only generates ~2 km of melt under normal asthenospheric temperature conditions. More than 15 km of melt can be generated in the presence of a mantle plume.

CONCLUSIONS

There are several ways of testing whether simple shear (Wernicke, 1985) or pure shear (McKenzie, 1978) models apply during extension of the lithosphere. Most of these arguments concern subsidence distribution (e.g., in the North Sea; Klemperer and White, 1989), the geometry of active normal faulting (Jackson, 1987), or the presence or absence of a low-angle feature on deep seismic reflection profiles (e.g., Klemperer, 1988; Gibbs, 1987). All three lines of evidence appear to favor pure shear rather than simple shear in areas of active extension (e.g., the Aegean) and in previously extended basins (e.g., the North Sea). Here we have discussed the implications of lithospheric simple shear for magma generation resulting from adiabatic upwelling of the asthenosphere during extension. Like others (Buck et al., 1988), we conclude that only very small amounts of melt are likely to be produced by this rifting mechanism.

REFERENCES CITED

Barton, P., and Wood, R., 1984, Tectonic evolution of the North Sea Basin: Crustal stretching and subsidence: Royal Astronomical Society Geophysical Journal, v. 79, p. 987–1022.

Beach, A., 1986, A deep seismic reflection profile across the northern North Sea: Nature, v. 232, p. 53–55.

Bosworth, W., 1985, Geometry of propagating continental rifts: Nature, v. 316, p. 625–627.

Buck, W.R., 1986, Small-scale convection induced by passive rifting: The cause for uplift of rift shoulders: Earth and Planetary Science Letters, v. 77, p. 362–372.

Buck, W.R., Martinez, F., Steckler, M.S., and Cochran, J.R., 1988, Thermal consequences of lithospheric extension: Pure and simple: Tectonics, v. 7, p. 213–234.

Christie, P.A.F., and Sclater, J.G., 1980, An extensional origin for the Buchan and Witchground graben in the North Sea: Nature, v. 283, p. 729–732.

Courtney, R.C., and White, R.S., 1986, Anomalous heat flow and geoid across the Cape Verde Rise: Evidence for dynamic support from a thermal plume in the mantle: Royal Astronomical Society Geophysical Journal, v. 87, p. 815–867.

Dixon, J.E., Fitton, J.G., and Frost, R.T.C., 1981, The tectonic significance of post-Carboniferous igneous activity in the North Sea Basin, *in* Illing, L.V., and Hobson, G.D., eds., Petroleum geology of the Continental Shelf of north-west Europe: London, Heyden, p. 121–137.

Fall, H.G., Gibb, F.G.F., and Kanaris-Sotiriou, R., 1982, Jurassic volcanic rocks of the northern North Sea: Geological Society of London Journal, v. 139, p. 277–292.

Fitton, J.G., and Dunlop, H.M., 1985, The Cameroon Line, West Africa, and its bearing on the origin of oceanic and continental alkali basalt: Earth and Planetary Science Letters, v. 72, p. 23–38.
Gibbs, A.D., 1987, Deep seismic profiles in the northern North Sea, *in* Brooks, J., and Glennie, K.W., eds., Petroleum geology of north-west Europe: London, Graham and Trotman, p. 1025–1028.
Glennie, K.W., editor, 1986, Introduction to the petroleum geology of the North Sea (second edition): London, Blackwell, 278 p.
Green, D.H., 1970, The origin of basaltic and nephelinitic magmas: Leicester Literary and Philosophical Society Transactions, v. 64, p. 28–54.
——1973, Experimental melting studies on a model upper mantle composition at high pressure under water saturated and water undersaturated conditions: Earth and Planetary Science Letters, v. 19, p. 37–53.
Harte, B., 1983, Mantle peridotites and processes—The kimberlite sample, *in* Hawkesworth, C.J., and Norry, M.J., eds., Continental basalts and mantle xenoliths: Nantwich, England, Shiva, p. 46–91.
Jackson, J.A., 1987, Active normal faulting and crustal extension, *in* Coward, M.P., Dewey, J.F., and Hancock, P.L., eds., Continental extensional tectonics: Geological Society of London Special Publication 28, p. 3–18.
Jarvis, G.T., and McKenzie, D.P., 1980, Sedimentary basin formation with finite extension rates: Earth and Planetary Science Letters, v. 48, p. 42–52.
Klemperer, S.L., 1988, Crustal thinning and nature of extension in the northern North Sea from deep seismic reflection profiling: Tectonics, v. 7, p. 803–821.
Klemperer, S.L., and White, N.J., 1989, Coaxial stretching or lithospheric simple shear in the North Sea? Evidence from deep seismic profiling and subsidence, *in* Tankard, A.J., and Balkwill, H.R., eds., Extensional tectonics and stratigraphy of the North Atlantic margins: American Association of Petroleum Geologists Memoir 46.
Latin, D.M., Dixon, J.E., and Fitton, J.G., 1989, Rift-related magmatism in the North Sea Basin, *in* Blundell, D.J., and Gibbs, A.D., eds., Tectonic evolution of the North Sea rifts: Oxford, England.
Le Pichon, X., and Sibuet, J.C., 1981, Passive margins: A model of formation: Journal of Geophysical Research, v. 72, p. 3708–3720.
Lister, G.S., Etheridge, M.A., and Symonds, P.A., 1986, Detachment faulting and the evolution of passive continental margins: Geology, v. 14, p. 246–250.
——1989, Detachment models for the formation of passive continental margins: Tectonics.
McKenzie, D.P., 1978, Some remarks on the development of sedimentary basins: Earth and Planetary Science Letters, v. 40, p. 25–32.
——1989, Some remarks on the movement of small melt fractions in the mantle: Earth and Planetary Science Letters.
McKenzie, D.P., and Bickle, M.J., 1988, The volume and composition of melt generated by extension of the lithosphere: Journal of Petrology, v. 26, p. 625–679.
Mutter, J.C., Buck, W.R., and Zehnder, C.M., 1988, Convective partial melting, I. A model for the formation of thick basaltic sequences during the initiation of spreading: Journal of Geophysical Research, v. 93, p. 1031–1048.
Olafsson, M., and Eggler, D.H., 1983, Phase relations of amphibole-carbonate and phlogopite-carbonate peridotite: Petrologic constraints on the asthenosphere: Earth and Planetary Science Letters, v. 64, p. 305–315.
Sawyer, D.S., Swift, B.A., Sclater, J.G., and Toksoz, M.N., 1982, Extensional model for the subsidence of the northern U.S. Atlantic continental margin: Geology, v. 10, p. 134–140.
Sclater, J.G., and Christie, P.A.F., 1980, Continental stretching: An explanation of the post mid-Cretaceous subsidence of the central North Sea: Journal of Geophysical Research, v. 85, p. 3711–3739.
Sclater, J.G., Royden, L., Horvath, F., Burchfiel, B.C., Semken, S., and Stegena, L., 1980, The formation of the Intra Carpathian Basins as determined from subsidence data: Earth and Planetary Science Letters, v. 51, p. 139–162.
Voorhoeve, H., and Houseman, G., 1988, The thermal evolution of lithosphere extending on a low-angle detachment: Basin Research, v. 1, p. 1–9.
Wernicke, B., 1981, Low-angle normal faults in the Basin and Range province: Nappe tectonics in an extending orogen: Nature, v. 291, p. 645–648.
——1985, Uniform-sense normal simple shear of the continental lithosphere: Canadian Journal of Earth Sciences, v. 22, p. 108–125.
White, N.J., 1988, Extension and subsidence of the continental lithosphere [Ph.D. thesis]: Cambridge, England, Cambridge University, 206 p.
——1989, The nature of lithospheric extension in the North Sea: Geology, v. 17, p. 111–114.
White, R.S., and McKenzie, D.P., 1989, Magmatism at rift zones: The generation of volcanic continental margins and flood basalts: Journal of Geophysical Research, v. 94, p. 7685–7729.
White, R.S., Fowler, S.R., McKenzie, D.P., Westbrook, G.K., and Bowen, A.N., 1987, Magmatism at rifted continental margins: Nature, v. 330, p. 439–444.
Wood, R.J., 1982, Subsidence in the North Sea [Ph.D. thesis]: Cambridge, England, Cambridge University, 235 p.
Wyllie, P.J., 1987, Transfer of subcratonic carbon into kimberlites and rare earth carbonatites, *in* Mysen, B.O., ed., Magmatic processes: Physicochemical principles: Geochemical Society Special Publication 1, p. 107–119.

ACKNOWLEDGMENTS

Supported by United Kingdom Natural Environment Research Council. We thank D. McKenzie for providing a copy of his geotherm program and preprints of his work; and J. E. Dixon, J. G. Fitton, J. A. Jackson, S. Klemperer, P. Molnar, T. O. Spring, and three reviewers for enlightenment. Cambridge University Department of Earth Sciences Contribution No. 1478.

Manuscript received July 19, 1989
Revised manuscript received October 19, 1989
Manuscript accepted October 26, 1989

U.S. west coast revisited: An aeromagnetic perspective

Peter R. Johnson, Isidore Zietz
Center for Basic and Applied Science, George Mason University, Fairfax, Virginia 22030
Kevin R. Bond
U.S. Geological Survey, Reston, Virginia 22092

ABSTRACT

A new compilation of magnetic data for the western conterminous United States and offshore areas provides significant information about crustal units and structures in the region. Features shown on the compilation include a magnetic quiet zone along the coast and two lineaments inland. The magnetic quiet zone correlates with the accretionary prism at the western edge of the North American plate and overlies subducted ocean crust; abrupt termination of ocean-floor magnetic anomalies at, or a short distance east of, the toe of the accretionary prism is an inferred effect of subduction-induced low-temperature metamorphism of the ocean crust.

The Puget Lowlands–San Joaquin lineament is an alignment of high-intensity magnetic anomalies that in the south, and possibly also in the north, are caused by bodies of mafic-ultramafic rocks accreted to North America during the Mesozoic and Tertiary. The lineup of the highs and the inferred lineup of the causative bodies may reflect fundamental structures that control Mesozoic and Tertiary evolution of the continental margin. The Mojave Desert lineament, a distinctive chain of short-wavelength magnetic anomalies in southern California, coincides partly with a zone of Mesozoic intrusions and the Cenozoic San Andreas fault system, but is likely to be older than both in origin and may reflect a Mesozoic or older crustal discontinuity.

INTRODUCTION

Regional-scale compilations of aeromagnetic data commonly figure among the geophysical and geologic data sets utilized by geoscientists in the course of tectonic investigations (Hinze, 1985, and references therein). Such data provide critical information about the distribution and character of crystalline rocks within the basement and of igneous rocks within the sedimentary rock cover. More important, they help to delineate contacts and structures that are concealed from direct observation by younger rocks and sediments and may suggest the presence of structures not hitherto suspected by geologists.

On the basis of a new compilation of aeromagnetic data for the conterminous western United States, we draw attention to a magnetic quiet zone and two lineaments along the western margin of the North American plate between Mexico and Canada. The compilation, reproduced here (Fig. 1) at a reduced scale of approximately 1:11 000 000, formed the basis of the 1:2 500 000-scale magnetic-anomaly map of the western United States published by the U.S. Geological Survey (Bond and Zietz, 1987) but includes a greater amount of offshore magnetic data. The compilation, furthermore, contains greater detail than the recently published *Magnetic Anomaly Map of North America* (Committee for the Magnetic Anomaly Map of North America, 1987).

INSHORE MAGNETIC QUIET ZONE

A conspicuous magnetic "quiet" zone is located at the western margin of the North American plate (Fig. 2). It extends from Canada to approximately lat 34°N as a 50- to 180-km-wide zone of low-amplitude infrequent anomalies between the region of pronounced ocean-floor magnetic stripes that mark the Juan de Fuca, Gorda, and Pacific plates to the west and regions of high-frequency anomalies inland to the east. The eastern boundary of the quiet zone encompasses the Olympic Peninsula, is offshore from Oregon, passes onshore in northern California, and extends along the California coast farther south.

The subdued magnetic relief of the zone reflects the Tertiary to Holocene accretionary prism that underlies the continental slope and coastal areas of Washington and Oregon and the accretionary prism of Cretaceous and Tertiary rocks beneath the continental slope and coastal areas of California (Cowan and Potter, 1986; Saleeby, 1986; Silberling et al., 1987). The magnetic quiet zone is underlain by subducted ocean crust, but the apparent absence of magnetic anomalies reflecting the underlying ocean crust and the abrupt nature of the termination of ocean-floor magnetic stripes at the western margin of the quiet zone are notable features of the magnetic data.

The complex subduction geology of the region is discussed in a recent paper by Clowes et al. (1987). North of approximately lat 45°N, ocean-floor magnetic stripes (anomalies 7 and 8) are preserved in the descending Juan de Fuca plate as much as 25 km east of the start of subduction of the Juan de Fuca plate beneath the North American plate (Silver, 1972; Barr, 1974; Cowan and Potter, 1986). The gradual attenuation and eventual disappearance of the stripes from the downgoing plate probably result from increasing depths to magnetic sources and/or decreasing magnetization caused by a temperature increase beyond the Curie point due to increased heat flow or greater depth of burial. In contrast, the magnetic stripes of the Gorda and Pacific plates abruptly terminate at the contact of the ocean plate and the North American plate. In the case of the Gorda plate, between approximately 40°N and 42°N, the stripes terminate at the foot of the continental slope and start of the subduction zone. South of the Mendocino fracture zone, the magnetic stripes of the Pacific plate terminate at the California trench, which marks the fossil Paleogene subduction zone between the Pacific and North American plates (Saleeby, 1986). In these two cases, the ocean-floor magnetic stripes terminate at the most seaward, and therefore the shallowest, parts of the subduction zones, rather than at some distance down the descending plate. However, there is no geologic evidence of structural causes for the termination of the stripes, such as a major fault in the ocean crust or a sudden steepening of the angle of descent of the downgoing plate that would abruptly increase the depth to magnetic source and attenuate the magnetic anomalies. Nor is there evidence—drawing on conclusions of heat-flow studies along the margin of the North American plate in British Columbia (Lewis et al., 1988)—that the stripes abruptly terminate as a result, for example, of sudden demagnetization of the descending ocean crust caused by a sudden increase in the geothermal gradient at the start of the subduction zone and a shallowing of the depth to the Curie point.

To account for the abrupt termination of the ocean-floor magnetic stripes in the Pacific and Gorda plates, we propose the existence of a lithologic contact at the boundary between the province of ocean-floor magnetic stripes and the inshore magnetic quiet zone, and we suggest that the contact results from low-temperature metamorphism of magnetic material in the ocean plates beneath the adjacent accretionary prisms. This suggestion follows the proposals of Zietz (1970) concerning magnetic quiet zones in the Atlantic Ocean and the proposals of Levi and Riddihough (1986) concerning the effective leaching of remanence-carrying iron-titanium oxides and consequent diminution of marine

GEOLOGY, v. 18, p. 332–335, April 1990